

BULGARIAN CHEMICAL COMMUNICATIONS

2016 Volume 48 / Special Issue D

*Journal of the Chemical Institutes
of the Bulgarian Academy of Sciences
and of the Union of Chemists in Bulgaria*

Preparation and characterization of antibacterial nanofibrous trimethoprim/polyvinylpyrrolidone mats as an oral fast-dissolving drug delivery system

A. Bolouri, A. Mohammad-khah*

Department of Chemistry, Faculty of Science, University of Guilan, Namjoo Street, P.O. Box: 1914, Rasht, Iran

Received May 02, 2016, Revised July 10, 2016

In this work, polymeric nanofibers, loaded with Trimethoprim– an antibiotic model drug– fabricated using electrospinning technique, as a novel method for fast-dissolving drug delivery systems applications. Polyvinylpyrrolidone K90 was used as the fibrous matrix polymer and drug carrier.

Characterization and pharmacological examinations of the specimens were carried out using a variety of techniques such as scanning electron microscope, Fourier transform infrared, differential thermal analysis and *in-vitro* drug release test. Analysis showing the smooth fabricated nanofibers with the average diameters of 220 and 350 nm at W_{PMP}/W_{PVP} of 10 and 20 weight percent, respectively. FTIR and DTA examinations revealed that the drug loses its crystalline state and becomes formulated in a nanofiber contexture amorphously.

Pharmacotechnical tests indicated that fibers are quickly moistened and dissolved in artificial saliva by less than 10 seconds. Accordingly, *in-vitro* drug release of nanofibers is a very prompt process which takes less than 30 s to release, due to the large surface area to mass ratio of nanofibers.

In-vitro bacterial inhibition test was also carried out to determine the relative activity of the released antibiotic. Results demonstrated that the medicated TMP/PVP nanofibers have an effective role in inhibiting the growth of bacteria.

Keywords: Electrospinning; Fast-dissolving Drug Delivery System; Polyvinylpyrrolidone; Nanofibers; Trimethoprim.

INTRODUCTION

There has been huge and increasing demand for patient convenient, fast and more effective forms of drugs during the past few decades. Fast-dissolving drug delivery systems (FDDSs) which may release drugs in the mouth, seems to be a promising and rapidly growing area in the pharmaceutical industry which had introduced in 1970s [1-3], in order to facilitate difficulties in swallowing traditional oral solid-dosed forms of drugs for pediatric and geriatric patients. There are many advantages of utilizing FDDS in pharmacology including; bioavailability, fast absorbability, rapid onset of action [4-6], site-specific effect (for example; sore throat) [7-9], precise dosing in addition to pleasant mouth feeling, ease of handling and transportability [10]. In this system, a palatal ligature, which is thin and easily set on the subject's tongue, forms a delivery system. The tablet where designed in FDDS is supposed to be dissolved in saliva causes its immediate hydration and sticking to the stead of the applications as fast as just a few seconds. It subsequently breaks up and deliquesces to extricate the medicine for mucosal and gastrointestinal absorption [11-13].

In drug delivery systems (DDSs), biocompatible and biodegradable polymers can be loaded with

different drugs. However, many filaments forming polymers are not suitable for oral performance and only a few polymer excipients can meet the pharmaceutical requirements for developing oral DDSs. Polyvinylpyrrolidone (PVP) as a non-crystalline vinyl polymer (Fig. 1), is possesses potentially diverse functions and benefits in the medical and drug delivery fields, due to diverse material properties such as stickiness, immense physiological consistency, low toxicity and sufficient solubility in water and most organic solvents [14]. Therefore, PVP can be used as a mat for possible oral delivery applications.

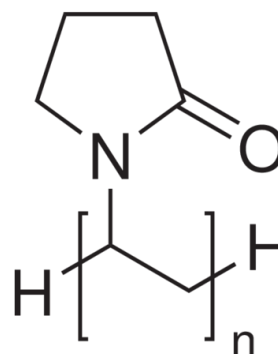


Fig 1. Chemical structure of polyvinylpyrrolidone.

Furthermore, applying nanotechnology and nanostructured materials can help the functionality of the membrane. Nanofibers, as potential

candidates for implementation in drug delivery membranes, are showing marvelous characteristics and attracting a lot of attentions due to high surface area to mass ratio, the tiny size of inter-fibrous pores with high porosity and possibilities for surface functionalization [15, 16].

Active pharmaceutical ingredient (API)-loaded nanofibers, reported by Kenawy and colleagues in 2002 [17], which mostly used for treatment of external surfaces of the human body, for instance, auxiliary therapy, transdermal DDSs and wound dressing [18-20], can be applied for oral FDDSs [12, 21, 22], although there are very limited reports in this area. Additionally, this technique can be used in a different variety of drugs from analgesics to neuroleptics and anti-psychotics due to its advantages and commonly used in drug delivery market [23, 24].

In this work Electrospinning (ES) technique has been used for fabrication of nanofibers thanks to its simpleness, cost effectiveness as well as ability to produce nanostructures continuously [25, 26]. This technique is adaptable to the wide variety of fields, especially to pharmaceutical [27-29] and biomedical [30-32] applications. Moreover, it is applicable to the most of the soluble or melted biodegradable polymers [33-35]. These specifications make the ES process probably the most suitable option for concocting such formulations.

In this technique, the high voltage direct current (DC) source is applying to induce the charge on the surface of a polymer solution, which is flowing out from a nozzle, and leading to the formation of a jet. Because of the bending instability, the jet is subsequently stretched and forms continuous and ultrathin fibers (Fig. 2) [36].

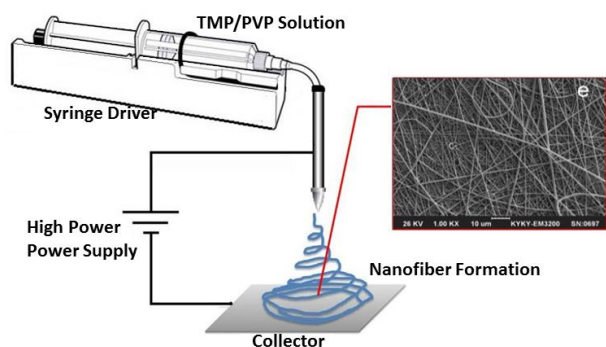


Fig 2. Schematic illustration of electrospinning setup.

The polymeric nanofibers can be loaded with different drugs to be used in the drug delivery systems (DDSs) which supposed to be transdermal, fast dissolving and implantable [37-39]. Two main factors which define drug release specifications are interactions between polymer and loaded drug as

well as the diameter of nanofibers. These so called two dimension nanofibers with macroscopic length and microscopic diameters [40] makes this medicated ultrafine fibers useful in both the nanoscale DDS in the transformation of the biopharmaceutics and pharmacokinetics specification of the drug molecules for desirable clinical results. It also makes the processing, packaging, and shipment of the drugs very facile for the common solid dosage [41, 42].

Many antibiotics have the capability to be utilized in FDDSs [43]. Many of these antibiotics such as amoxicillin trihydrate [44], cefuroxime axetil [45] and azithromycin dehydrate [46] are used in fast dissolving tablets. Among these antibiotics, trimethoprim (TMP) as an antibacterial agent is utilized in combination with sulphamethoxazole for the treatment of various infections, reported as a prototype for the provision of antibiotic-containing bandages and their use for treating wounds.

Here TMP, 5-(3,4,5-Trimethoxybenzyl) pyrimidine-2,4-diamine, (Fig. 3) has been used to load into the nanofibers. TMP is widely used in the prophylaxis and treatment of urinary and intestinal infections, senile chronic bronchitis, bacillary dysentery, enteritis, typhus, malaria and respiratory infections. It is often combined with sulfonamides (such as sulfamethoxazole) in pharmaceutical preparations to achieve synergetic effects [47].

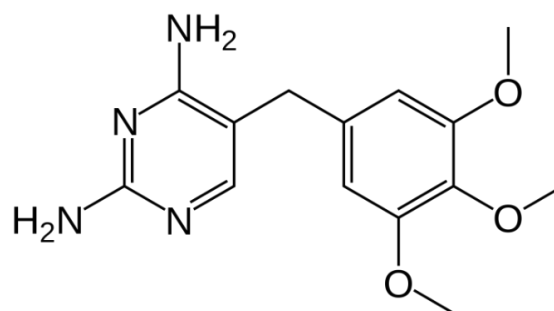


Fig 3. Chemical structure of trimethoprim.

Gupta et al. [48] introduced the solid dispersion (SD) method to increase dissolution and absorption of TMP. They had co-precipitated TMP using polyethylene glycols and PVP as carriers and chloroform as solvent and investigated the solubility enhancement of TMP. Apart from advantages, SD has two major drawbacks. First, the solvent is completely removed from viscose co-precipitations during drying and, secondly, SD process normally has incomplete outputs due to the fact that it mainly relies on pharmaceutical excipients, thus, they should be converted into concrete dosage forms when injected in patient's

body [49]. Using nanostructured materials could help to overcome the problems of the SD method.

In this study, ES technique has been used to fabricate mats of PVP nanofibers as an antibiotic delivery system loaded with TMP. The preparation of these mats will help to improve the water solubility of this drug, and could be particularly beneficial for the treatment of children with urinary infections.

Based on our knowledge, there are very limited publication and reports in literature explaining electrospun antibiotic-loaded nanofibers aimed for FDDSs. Therefore, we have tried to characterize different properties of this system. Scanning electron microscopy (SEM) has been used for morphology characterization and measurement of diameters on nanofibers as a key parameter of fabricated mats. Fourier-transform infrared (FTIR) technique is utilized to study the crystallographic and compositional characterization and differential thermal analysis (DTA) for examination of the thermal behavior of PVP nanofibers. The optical absorbance of samples was measured using UV-Vis spectrophotometer (Cary50, Varian, USA) to calculate the concentration of the samples. Also, *In-vitro* bacterial inhibition test was carried out to determine the activity of the released antibiotic in comparison with conventional solution-cast PVP films.

The main objective of this study is to explore the targeting delivery of the mats of electrospun TMP-loaded PVP nanofibers as an antibiotic delivery system toward the infected cells as well as enhancing their physicochemical traits. Dissolution and absorption of TMP and the transformation capability of TMP-loaded nanofibers as peroral slim films have also been investigated.

MATERIALS AND METHODS

Reagents

TMP (water solubility 0.4 mg/mL) was provided by Behdashtkar Co. (Rasht, Iran). PVP K90 with an average molecular weight of ~1000 kDa was provided by Rahavard Tamin Co. (Tehran, Iran). *Escherichia coli* (ATCC: 35218) and *Staphylococcus aureus* (ATCC: 33591) were purchased from Pasteur Institute (Tehran, Iran). Ethanol 96 %, sodium acetate 3 hydrate, glacial acetic acid, Mueller-Hinton agar (product no. 1054370500), nutrient broth (Cat. No: 6194390500) were purchased from Merck (Darmstadt, Germany). It is worth mentioning that all chemicals were analytically or biologically graded and used without further purification. Also, double distilled water was used for the preparation of all solutions.

Preparation of ES Solutions

Polymeric spinning solutions were prepared by dissolving PVP in ethanol/glacial acetic acid (6:1, v/v) mixed solution. After the dissolution of the polymer, TMP was added into the solution at room temperature (25 °C). The TMP content in spinning solutions was set to be 10 and 20 percent of PVP total weight ($W_{PMP}/W_{PVP} = 10, 20 \%$). This solution was added into a 20 mL plastic syringe (0.5 mm diameter). For ES process, high voltage power supply (30 kV/5mA, Fanavaran nanoazma Ltd., Iran) was applied at 15 kV to the metallic needle. The positive electrode was connected to the metal needle tip and a grounded aluminum foil used as the collector at a distance of 12 cm [12]. Electrospinning was carried out at ambient room temperature in the air condition. The polymer solutions were dispersed through the inner nozzle at the rate of 0.4 mL/h using a double syringe pump SP1000 (Fanavaran nanomeghyas, Iran). The collected nanowebs were dried at 50 °C under vacuum oven for 10 h to eliminate the residual solvents.

Film casting

TMP enclosing PVP films were also fabricated by the casting method to compare the dissolution rate of electrospun nanofibers and films. The spinning solution was cast into a Petri dish with a diameter of 8 cm. After evaporation of the solvents at room temperature and for 48 hours, the films were peeled and stored in clean condition. Additionally, the widths of the films were about 12 mm measured by Pro-Max electronic digital caliper (Mitutoyo, USA). A piece of film equivalent to about 25 mg TMP was used for dissolution tests.

The surface morphologies of drug loaded polymeric nanofibers were studied using a Digital Scanning Electron Microscope (SEM) (KyKy, China). Differential Thermal Analysis (DTA) was carried out using a PYRIS Diamond TG/DTA (PerkinElmer, USA). Sealed samples were heated at 10 °C/min from 20 to 400°C. The nitrogen gas flow rate was 35 mL/min. FTIR spectra were recorded on a Fourier transform IR spectrometer with a KBr pellet (spectrum 1, PerkinElmer, USA). The samples were prepared using the KBr disk method and the scanning range was 400–2000 cm^{-1} with a resolution of 2 cm^{-1} .

Wetting time and dissolution processes

For determination of the wetting time, a layer of filter paper was positioned on a Petri dish with a

diameter of 8 cm. When the paper was completely saturated by distilled water, the excess water was entirely drained out and a section of electrospun nanofibers was carefully placed on the filter paper by a forceps and allowed to wet completely. The time required for complete wetting of the nanofibers was denoted as the wetting time. In addition, a beaker of water was used to evaluate the rate of dissolution of the nanofibrous membranes. The wetting and dissolution processes were recorded at 20 frames per second with a digital video recorder.

In vitro release test

Electrospun nanofibrous membranes were carefully peeled from the aluminum foil and weighed exactly using a digital balance. Electrospun membrane sample and casting film with a weight of 25 mg were separately immersed in 40 mL of artificial saliva [50] at 37 °C, with magnetic stirring at 350 rpm. It must be noted that disintegration of the TMP-loaded membranes in the artificial saliva was very fast (less than 5 sec). 2 mL of prepared samples were collected after 0.5, to 10 minutes with 0.5-minute intervals and after 20 to 120 minutes with 20-minutes intervals and were analyzed by a UV-Vis spectrophotometer. The same amount of fresh water was added to the release system immediately after analyzing by the UV-Vis spectrophotometer, to maintain a constant volume.

Since TMP solution has an absorption peak at 270 nm and PVP has no detectable absorbance at this wavelength, Fig. 4, concentration of TMP/PVP can be calculated by dividing the absorbance of the two solutions at this wavelength. The concentration of TMP in the collected samples could be easily calculated using the calibration curve of pure TMP in acetate buffer pH=5 solution, see Fig. 5.

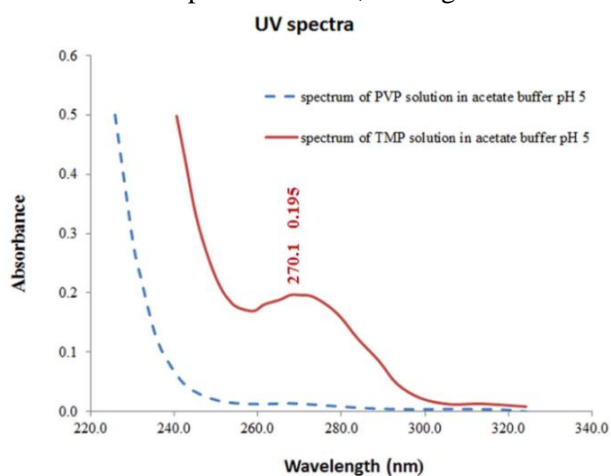


Fig 4. UV- spectra of (a) TMP solution in acetate buffer pH 5, (b) PVP solution in buffer pH 5.

The total assay of the drug in every sample of the electrospun mats or casting film was determined by UV-Vis spectrophotometer after being immersed in artificial saliva for at least 1 hour. Trimethoprim dissolved at specified time periods were plotted as the percentage released versus the time.

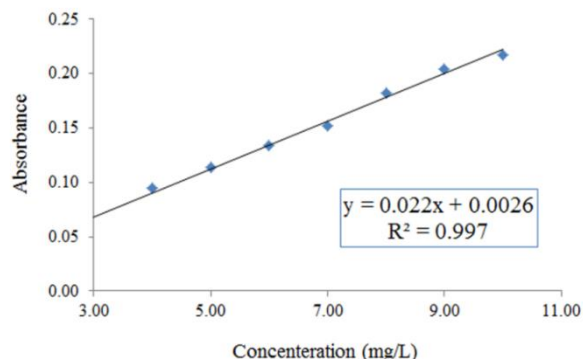


Fig 5. Calibration curve of trimethoprim at maximum 270.1 nm in acetate buffer pH 5.

Microbiological tests

TMP applies antimicrobial activity by inhibiting the reduction of dihydrofolate to tetrahydrofolate, the active form of folic acid, by sensitive organisms. It has a broad antibiotic spectrum that includes gram-negative and gram-positive bacteria [51]. In this study, the antibacterial activity of TMP-loaded PVP nanofibers was investigated using *S. aureus* as a Gram-positive model bacterium and *Escherichia coli* as a gram-negative model bacterium.

Using an antibiotic disk diffusion method, the antimicrobial property of the released PVP nanofibers loaded with TMP on *Escherichia coli* (ATCC: 35218) and *S. aureus* (ATCC: 33591) was determined. To measure the zones of inhibition, *in vitro* studies were performed using the Mueller-Hinton agar (Quelab; Canada). In both cases, first 50 µL of bacterial suspension was transferred to 2 mL of nutrient broth culture medium (beef extract, peptone, Merck Millipore). After 4 hours of initial incubation time, the surface of the solid medium was inoculated with a suspension of these bacterial cultures. McFarland turbidity standard No. 0.5 was used as the bacterial turbidity for the inoculum. In this test, samples (PVP, TMP/PVP (10 %) and TMP/PVP (20 %)) were punched to form circular discs with a diameter of 5 mm. PVP, TMP/PVP (10 %) and TMP/PVP (20 %) samples contained approximately 0, 25, and 50 µg of TMP, respectively. In separate plates samples of PVP, TMP/PVP (10 %) and PVP, TMP/PVP (20 %) were placed on agar plates and incubated at 37 °C for 12 h and 24 h, respectively, allowing the incorporated drugs to diffuse or release from the drug-loaded

mats into the agar. The bacterial inhibition zones of TMP-loaded PVP nanofibrous mats were directly visualized and measured. All tests were performed in triplicate.

In addition, minimum inhibition concentration (MIC) assays were carried out on the above mentioned bacteria. In this test, nutrient broth medium was used as the growth medium. Bacterial suspension was standardized to an absorbance value of 0.2 at 600 nm (8.0×10^7 cells/mL) with a volume of 5 mL. To each aliquot of bacterial suspension, free TMP, drug-loaded nanofibrous mat (TMP/PVP), and non-drug containing sample (PVP nanofibers) were added and, incubated at 37 °C. To evaluate the influence of TMP concentration on the antimicrobial activity, different TMP concentrations (0, 0.1, 0.2, 0.3 and 0.4 µg/mL, respectively) were added into each tube. After incubation, all tested solutions were monitored using a UV-Vis single beam spectrophotometer (Camspec 501, UK) at 600 nm. The absorbance value of the bacterial suspension was correlated directly with the concentration of bacteria in the medium. The bacterial inhibition percentage was calculated according to the following equation:

$$\text{Bacterial inhibition (\%)} = \frac{I_c - I_s}{I_c} \times 100$$

Where I_c and I_s are the absorbance of the control bacterial suspension and the bacterial suspension treated with different samples at 600 nm. Mean and standard deviation of triplicate samples for each sample were reported and all data was expressed as mean \pm S.D.

RESULTS

SEM Study

The Surface morphologies of PVP/TMP nanofibers are illustrated in Fig. 6. The SEM images indicate that the concentration of spinning solution and its parameters (distance, electrospinning speed and environment) used were acceptable as the nanofibers produced were cylindrical in shape and smooth, without forming films or beads. The mean fiber diameter is shown in table 1. In comparison, SEM image of casting film of PVP/TMP indicated that the nanofibrous structure of electrospun nanofibers created a high

Table 1. Fiber diameters.

Nanofibers composition	Fiber diameter (nm)
electrospun pure PVP nanofibers	238.7 \pm 83
electrospun TMP/PVP 10 % wt.	219.3 \pm 39
electrospun TMP/PVP 20 % wt.	347.9 \pm 109

surface to volume ratio and the potential for increasing drug load. The results of fiber diameter analyzes indicate that the increasing concentration of TMP in spinning solutions led to an average rise in fiber diameter that can increase the viscosity of spinning solution of PVP/TMP to 20 % wt.

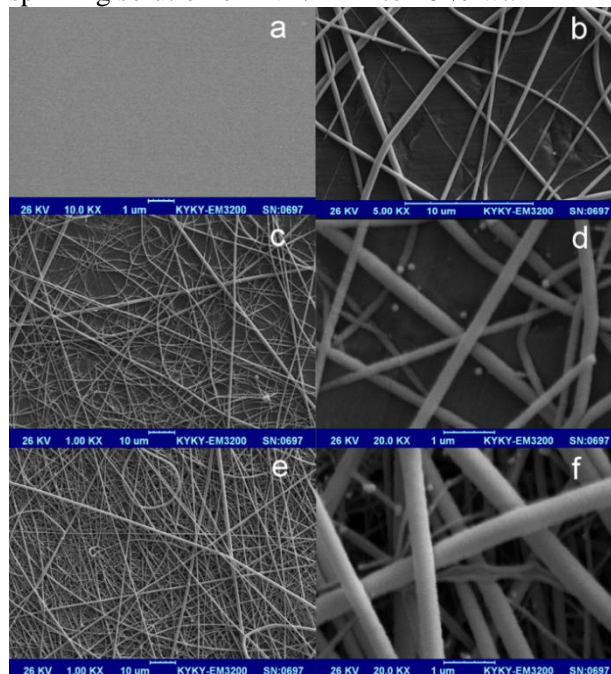


Fig 6. SEM images of (a) PVP/TMP cast film (b) electrospun pure PVP nanofibers (c) electrospun PVP/TMP 10% wt. large scale (d) electrospun PVP/TMP 10% wt. small scale nanofibers (e) electrospun PVP/TMP 20% wt. large scale (f) electrospun PVP/TMP 20% wt. small scale.

Physical status and compatibility of components

The DTA curve of pure TMP exhibited a single endothermic response corresponding to its melting point of 203°C ($\Delta H_f = -523.34 \pm 1.19$ kJ mol⁻¹). Being an amorphous polymer, PVP and TMP did not show any phase transitions or fusion peaks. DTA thermograms of the PVP nanofibers loaded by TMP did not show any peaks characteristic of TMP, suggesting that the drug was no longer present as a crystalline material; however, it had been converted into an amorphous state in all the nanofibers (Fig. 7).

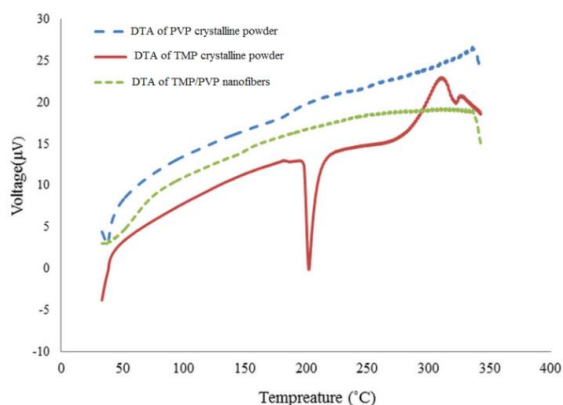


Fig 7. Differential Thermal Analysis thermogram of (a) PVP, (b) pure TMP (c) PVP/TMP electrospun nanofibers.

FT-IR spectroscopy

The infrared spectra (Fig. 8) show the characteristic peaks of trimethoprim at 1623 cm^{-1} (N-H stretching), 1560 cm^{-1} (aromatic C=C stretching), 1425 cm^{-1} (Amine C-N stretching), 1124 cm^{-1} (etheric C-O stretching), and 1494 cm^{-1} (Alkane C-H bending). The PVP spectrum shows the bands at 1661 cm^{-1} (C=O stretching), 1423 cm^{-1} (C-N stretching), 1288 cm^{-1} (-CH bending), 933 cm^{-1} (C-C breathing) and 650 and 576 cm^{-1} (N-C=O bending). The electrospun nanofibers showed no difference in the characteristic FTIR molecular mode in comparison with the individual compounds. The above data suggest that there are no physical or chemical interactions between PVP and TMP in the electrospun nanofibers.

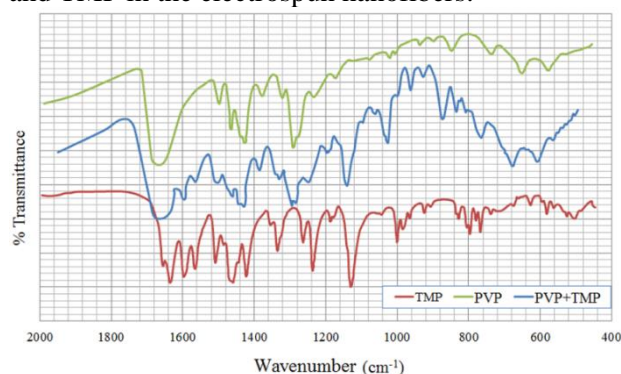


Fig 8. FTIR Spectra of PVP, PVP/TMP nanofibers and TMP.

Pharmacotechnical properties wetting and disintegrating times

The disappearance time of the samples in water was less than 5 s for electrospun PVP/ TMP (10 %) wt. and electrospun PVP/TMP (20 %) wt. Time of disappearance increased slightly as the function of increasing drug content but all electrospun samples fulfilled the requirement of fast dissolution (<30 s) (Fig. 9a).

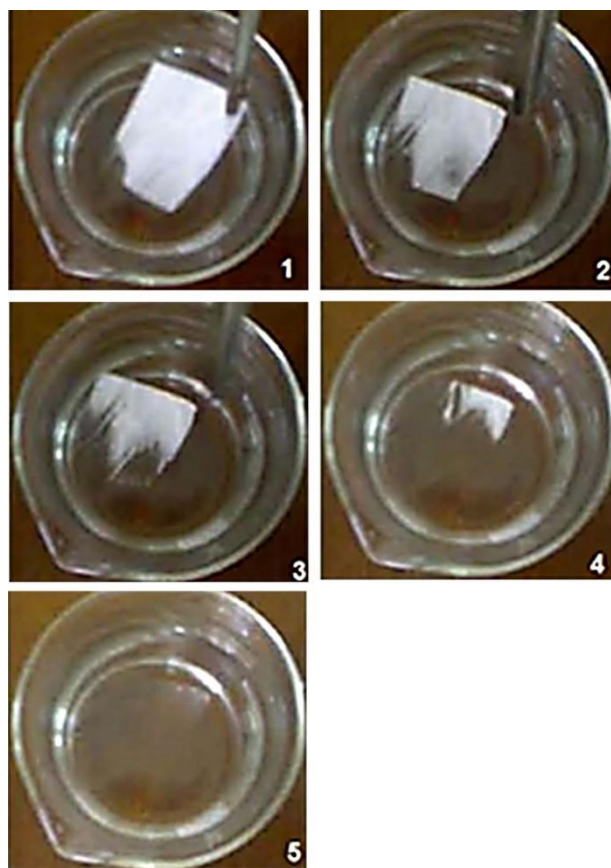


Fig 9.(a) Photographs of the disintegration process of the TMP-loaded PVP fibers, shown in sequence from 1 to 6 (with times keeps of 2 s).

As shown in Fig. 9b, the TMP polymeric nanofibrous mats quickly formed a transparent, 'gel-like' structure and lost their original white color after absorbing water from the wet paper. The wetting time was 6 s and 4 s for electrospun TMP / PVP (20 %) and electrospun TMP / PVP (10 %) wt., respectively. Also, the wet filter paper used in this research aimed to mimic the moisture available in the mouth. Thus, electrospun nanofibers possess an extremely highly porous structure, which can allow rapid penetration of saliva into the pores when placed in the oral cavity. This property can be attributed to high PVP solubility, the high degree of dispersal of TMP in the fiber and the high surface area of the fibers. These results show that electrospun PVP fibers have the potential for creating fast-dissolving DDSs for even exceptionally poorly water-soluble drugs and their derivatives.

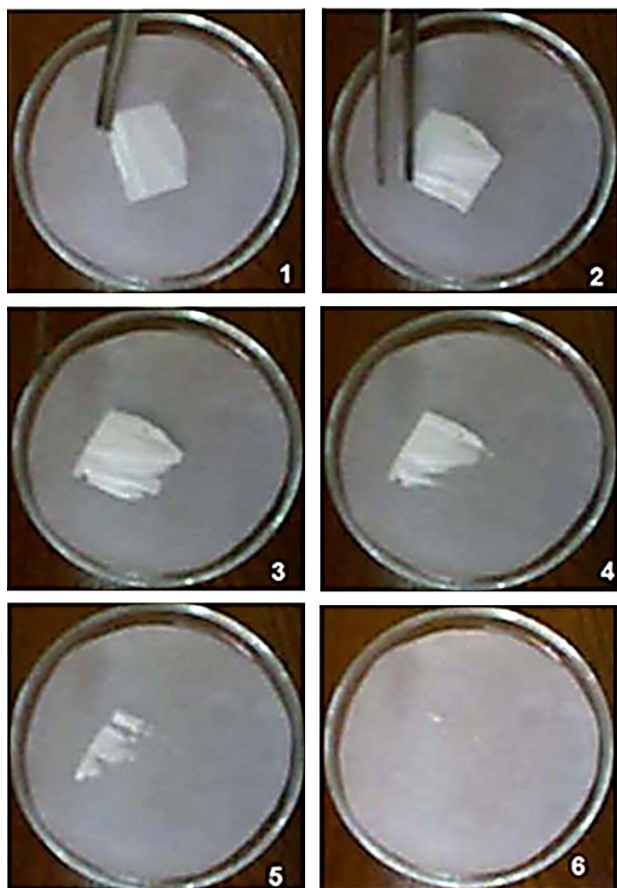


Fig 9.(b) Photographs of the wetting process of the TMP-loaded PVP fibers, shown in sequence from 1 to 6 (with times keeps of 6s).

In vitro dissolution tests

The prepared drug-loaded samples of described morphology were considered promising for oral dissolution because of good water solubility of the applied fiber-forming polymer and the huge surface of the formed fibers.

Figures 10 and 11 show the drug release profiles of electrospun webs of cast films with the same composition of electrospun TMP/PVP membranes. For TMP/PVP (10 %) and (20 %) more than 85 % and 84 % of the TMP was released within the first 30 s, respectively. After 60 s, more than 90 % of the TMP contained in these electrospun membranes were released into the dissolution medium, while only 53 % and 65 % of the TMP were released from PVP casting films during the same time respectively. The noteworthy difference between the rates of dissolution of different samples is well recognizable. The sustained release of TMP from PVP films was obtained for up to 5 min, indicating that the drug was released much more slowly and in a relatively steady manner. Dissolution of cast films was dependent on their drug content. Besides, drug release of TMP/PVP (20 %) cast films was significantly faster than that of TMP/PVP (10 %). It

is probable that the TMP present in the membrane as TMP acetate salt acts as a small molecule with good water solubility and can easily solubilize, while PVP dissolves more slowly as a macromolecule due to its long polymer chains which are less plasticized because of the presence inter- and intramolecular H-bonds. This means that PVP has a retardant effect, except in cases when the formation of a huge surface area decreases the value of the bulk entangled structure.

The electrospun webs, independently from their drug concentration, were immediately dissolved after immersion in dissolution media owing to the huge surface area. The fast release or dissolution rate of TMP from the nanofibers is due to the high specific surface area, facilitating fast drug release, and the high porosity of the nanofibers, which are able to facilitate the dissolution of the drug in the medium. Moreover, the excellent wettability of the polymer nanostructure causes a rapid penetration of water into the nanopores, promoting a remarkably fast drug release (within a few seconds).

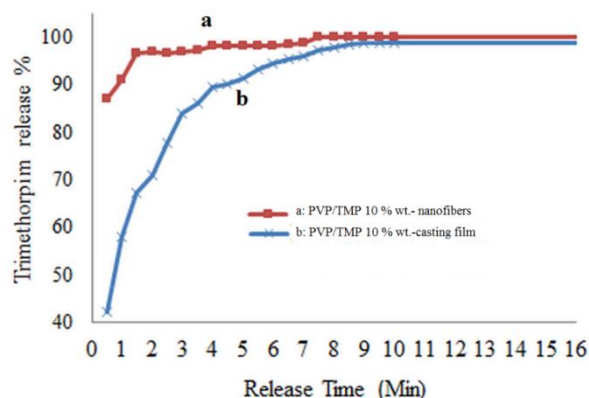


Fig 10. In vitro release profiles of 10 % TMP from (a) PVP nanofibers, (b) PVP casting film. The samples were released in artificial saliva at 37°C.

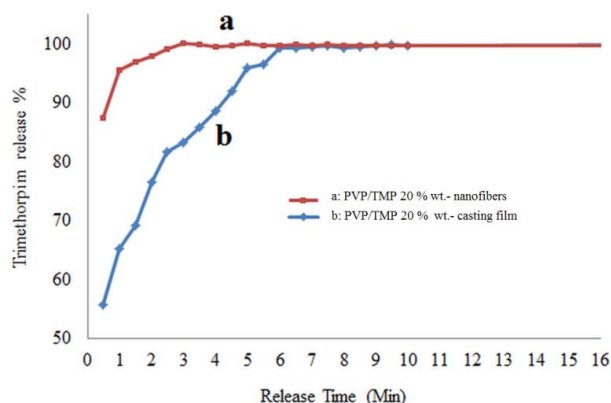


Fig 11. In vitro release profiles of 20 % TMP from (a) PVP nanofibers, (b) PVP casting film. The samples were released in artificial saliva at 37°C.

Microbiological tests

Bacterial inhibition efficacy of the TMP-mediated nanofibrous mats on *S. aureus* and

Escherichia coli was evaluated using an antibiotic disk diffusion method (Fig. 12). After incubation of *S. aureus* and *Escherichia coli* for 12 h and 24 h, respectively, the agar regions with medicated scaffolds displayed uniformly circular visible bacterial inhibition rings. Measured zones of inhibition around the disks for samples are summarized in Tables 2 and 3. These results indicate that the antibiotic drug TMP is released from the medicated nanofibrous mats and diffused onto the agar, thereby, effectively inhibiting bacterial growth. In addition, the antibacterial ability of the TMP-medicated scaffolds could still be observed after 24 h of incubation.

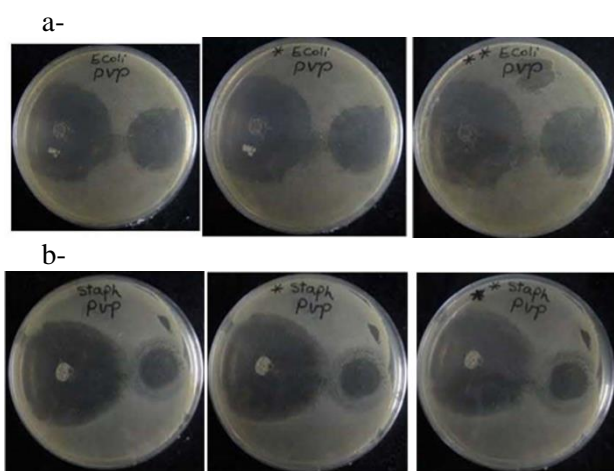


Fig 12. Digital images of the zones of inhibition against (a) *E. coli* observed after 6-h, 12-h (plate is indicated with a star), and 24-h (plate is indicated with 2 stars) (b) *S. aureus*, observed after 6-h, 12-h (plate is indicated with a star), and 24-h (plate is indicated with 2 stars). Inhibition zones in the right of each plate is related to control mats in which (no) antibiotic and Inhibition zones in the left of each plate is related to TMP mats antibiotic content 10 wt % of the polymer weight.

Also in this work, the antibacterial activity of TMP-loaded PVP nanofiber was investigated using *Escherichia coli* and *staphylococcus aureus* as model Gram negative and Gram positive bacteria, respectively.

Figure 13 shows the bacterial inhibition percentages after 24 h incubation with different concentrations of free TMP. *Escherichia coli* is more sensitive to TMP and bacterial inhibition occurs at 0.4 $\mu\text{l/mL}$. Degree of *E. coli* and *S. aureus* inhibition was 83% and 71% respectively.

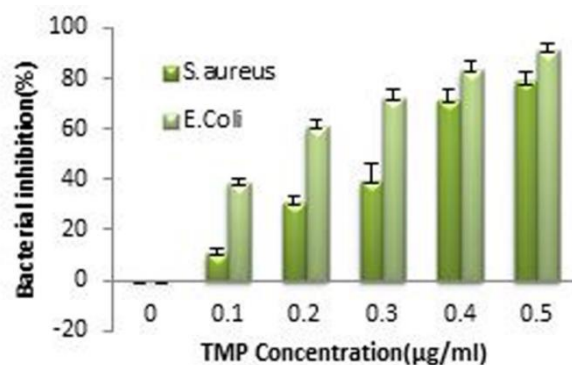


Fig 13. Inhibition of bacterial (*Escherichia coli* and *S. aureus*) growth after 24 h of incubation.

In both bacterial strains, TMP and TMP/PVP nanofiber exhibit equal bacterial inhibition and little difference between the two strains was evident.

Bacterial inhibition percentages after incubation of the bacterial suspension with different samples were shown in Fig. 14. Clearly, the sample without TMP encapsulation (PVP nanofiber) does not display significant effect on bacterial growth. In contrast, free TMP powder and drug-loaded nanofiber mat (TMP/PVP) were able to inhibit bacterial growth.

The results show that the medicated TMP/PVP composite nanofibers could be effective in inhibiting the growth of bacteria and have the potential to be used in wound dressing and tissue engineering.

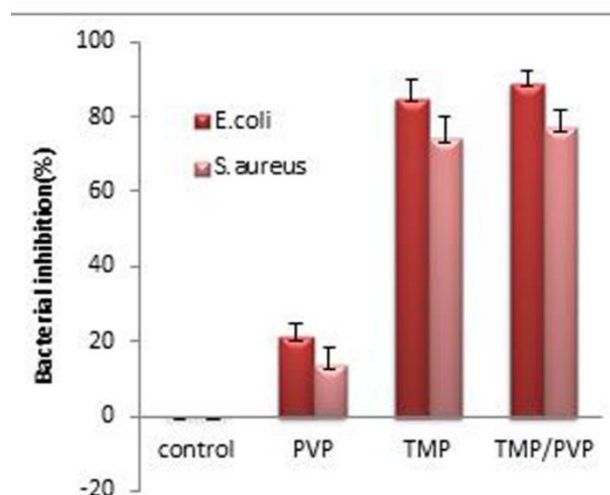


Fig 14. Inhibition of bacterial (*Escherichia coli* and *S. aureus*) growth after 24 h of incubation with free TMP, TMP/PVPs and PVP nanofiber. The concentration of free TMP and TMP in medicated sample was 0.4 $\mu\text{g/mL}$.

Table 2. Determination of bacterial inhibition efficacy of the TMP-medicated nanofibrous mats (TMP 10%) on *Escherichia coli*.

Incubation time	Inhibition zone for control mat (PVP) (mm)	Inhibition zone for sample mat (TMP/PVP) (mm)	Effective inhibition zone for sample mat (TMP/PVP) (mm)
6 h	25	39	14
12 h	27	43	16
24 h	24	38	14

Table 3. Determination of bacterial inhibition efficacy of the TMP-medicated nanofibrous mats (TMP 10%) on *S. aureus*.

Incubation time	Inhibition zone for control mat (PVP) (mm)	Inhibition zone for sample mat (PVP/TMP) (mm)	Effective inhibition zone for sample mat (PVP/TMP) (mm)
6 h	17	41	24
12 h	16	40	24
24 h	14	39	25

CONCLUSIONS

This work dealt with fast-dissolving drug delivery systems derived from electrospun PVP nanofibers and trimethoprim as a model drug. It has been shown the possibility of one-step preparation of fibrous materials from PVP loaded with trimethoprim using electrospinning.

Ultrafine nanofibers with average diameters of 220 to 350 nm and smooth surfaces were synthesis using electrospinning technique.

10 % and 20 % wt TMP/PVP drug delivery system with molecular level integration and good compatibility with no interaction between polymer and drug, has been prepared which confirmed by DTA, FTIR and SEM analysis. Pharmacotechnical tests showed that TMP/PVP nanofibrous mats had almost the equal dissolution time, about 2 s, and wetting time, about 5 s. The release measurements from the PVP nanofibrous matrices showed that the drugs can rapidly dissolve in water in a burst manner. Bioactivity studies showing that the antibacterial properties of TMP are preserved in nanofiber form.

The obtained results showed that PVP/antibiotic mats are suitable for applications that require an initial burst release of the active substances, for instance in wound dressing devices, for inhibition of pathogenic microorganisms invasion and bacterial biofilm formation.

These results proving that TMP-loaded PVP electrospun nanofibers are potentially the great candidate for implication in fast-dissolving drug delivery systems, although more research and studies are essential for the decisive approval.

Acknowledgments: The authors would like to express their thanks to the Behdashtkar Drug Company for financial support.

REFERENCES

1. D. G. Yu, L. M. Zhu, K. White, C. Branford, *Health*, **1**, 67 (2009).
2. X. Hu, S. Liu, G. Zhou, Y. Huang, Z. Xie, X. Jing, *Journal of Controlled Release*, **185**, 12 (2014).
3. T. Potrč, S. Baumgartner, R. Roškar, O. Planinšek, Z. Lavrič, J. Kristl, P. Kocbek, *Eur. J. Pharmac. Sci.*, **75**, 101 (2015).
4. A. C. Liang, L. I. H. Chen, *Expert Opinion on Therapeutic Patents*, **11**, 981 (2001).
5. V. Pillay, C. Dott, Y. U. Choonara, C. Tyagi, L. Tomar, P. Kumar, L. C. Du Toit, V. M. K. Ndesendo, *Journal of Nanomaterials*, **2013**, Article ID 789289 (2013).
6. D. G. Yu, X. Wang, X. Y. Li, W. Chian, Y. Li, Y. Z. Liao, *Acta Biomaterialia*, **9**, 5665 (2013).
7. A. Farooq, M. Yar, A. S. Khan, L. Shahzadi, S. A. Siddiqi, N. Mahmood, A. Rauf, Z. A. Qureshi, F. Manzoor, A. Chaudhry, I. Rehman, *Materials Science and Engineering: C*, **56**, 104 (2015).
8. G. Gainza, S. Villullas, J. L. Pedraz, R. M. Hernandez, M. Igartua, *Nanomedicine: Nanotechnology, Biology and Medicine*, **11**, 1551 (2015).
9. S. Um-i-Zahra, X. Shen, H. Li, L. Zhu, *Journal of Polymer Research*, **21**, 1 (2014).
10. K. H. Zhang, Q. Z. Yu, X. M. Mo, *International Journal of Molecular Sciences*, **12**, 2187 (2011).
11. S. Kunte, P. Tandale, *J Pharm Bioallied Sci.*, **2**, 325 (2010).
12. U. E. Illangakoon, H. Gill, G. C. Shearman, M. Parhizkar, S. Mahalingam, N. P. Chatterton, G. R. Williams, *International Journal of Pharmaceutics*, **477**, 369 (2014).
13. H. Yang, S. Kim, I. Huh, S. Kim, S. F. Lahiji, M. Kim, H. Jung, *Biomaterials*, **64**, 70 (2015).
14. D. Li, Y. Xia, *Advanced Materials*, **16**, 1151 (2004)
15. J. Doshi, D. H. Reneker, *Journal of Electrostatics*, **35**, 151 (1995)
16. J. M. Deitzel, J. Kleinmeyer, D. Harris, N. C. Beck Tan, *Polymer*, **42**, 261 (2001).

17. E. R. Kenawy, G. L. Bowlin, K. Mansfield, J. Layman, D. G. Simpson, E. H. Sanders, G. E. Wnek, *Journal of Controlled Release*, **81**, 57 (2002).
18. M. Sadri, S. Arab-Sorkhi, H. Vatani, A. Bagheri-Pebdeni, *Fibers and Polymers*, **16**, 1742 (2015).
19. A. Zarghami, M. Irani, A. Mostafazadeh, M. Golpour, A. Heidarinasab, I. Haririan, *Fibers and Polymers*, **16**, 1201 (2015).
20. T. He, J. Wang, P. Huang, B. Zeng, H. Li, Q. Cao, S. Zhang, Z. Luo, D. Y. B. Deng, H. Zhang, W. Zhou, *Colloids and Surfaces B: Biointerfaces*, **130**, 278 (2015).
21. X. Li, M. A. Kanjwal, L. Lin, I. S. Chronakis, *Colloids and Surfaces B: Biointerfaces*, **103**, 182 (2013).
22. F. Ignatious, L. H. Sun, C. P. Lee, J. Baldoni, *Pharmaceutical Research*, **27**, 576 (2010).
23. M. Jelvehgari, P. Zakeri-Milani, M. R. Siah-Shadbad, B. D. Loveymi, A. Nokhodchi, Z. Azari, H. Valizadeh, *AAPS PharmSciTech*, **11**, 1237 (2010).
24. Y. J. Yamanaka, K. W. Leong, *Journal of Biomaterials Science Polymer Edition*, **19**, 1549 (2008).
25. A. Balogh, R. Cselkó, B. Démuth, G. Verreck, J. Mensch, G. Marosi, Z. K. Nagy, *International Journal of Pharmaceutics*, **495**, 75 (2015).
26. B. Sun, Y. Z. Long, H. D. Zhang, M. M. Li, J. L. Duvail, X. Y. Jiang, H. L. Yin, *Progress in Polymer Science*, **39**, 862 (2014).
27. J. Choi, H. Kim, H. Yoo, *Drug Delivery and Translational Research*, **5**, 137 (2015).
28. B. P. Antunes, A. F. Moreira, V. M. Gaspar, I. J. Correia, *Carbohydrate Polymers*, **130**, 104 (2015).
29. M. F. Oliveira, D. Suarez, J. C. B. Rocha, A. V. N. de Carvalho Teixeira, M. E. Cortés, F. B. De Sousa, R. D. Sinisterra, *Materials Science and Engineering: C*, **54**, 252 (2015).
30. X. Wu, C. Branford-White, L. Zhu, N. P. Chatterton, D. Yu, *Journal of Materials Science: Materials in Medicine*, **21**, 2403 (2010).
31. A. Toncheva, D. Paneva, V. Maximova, N. Manolova, I. Rashkov, *European Journal of Pharmaceutical Sciences*, **47**, 642 (2012).
32. Z. K. Nagy, A. Balogh, B. Vajna, A. Farkas, G. Patyi, A. Kramarics, G. Marosi, *Journal of Pharmaceutical Sciences*, **101**, 322 (2012).
33. A. Rogina, *Applied Surface Science*, **296**, 221 (2014).
34. H. Brooks, N. Tucker, *Polymer*, **58**, 22 (2015).
35. L. Palangetic, N. Reddy, S. Srinivasan, R. E. Cohen, G. H. McKinley, C. Clasen, *Polymer*, **55**, 4920 (2014).
36. L. Dan, X. Younan, *Nano Letters*, **4**, 933 (2004).
37. Z. M. Huang, Y. Z. Zhang, M. Kotaki, S. Ramakrishna, *Composites Science and Technology*, **63**, 2223 (2003).
38. X. X. Shen, D. G. Yu, C. B. Ranford-White, L. M. Zhu, Preparation and characterization of ultrafine eudragit L100 fibers via electrospinning, in: The 3rd International Conference on Bioinformatics and Biomedical Engineering Shanghai, China, 2008.
39. X. Xu, X. Chen, Z. Wang, X. Jing, *European Journal of Pharmaceutics and Biopharmaceutics*, **72**, 18 (2009).
40. D. G. Yu, X. F. Zhang, X. X. Shen, C. Brandford-White, L. M. Zhu, *Polymer International Journal of ChemTech Research*, **58**, 1010 (2009).
41. Y. Dzenis, *Science*, **304**, 1917 (2004).
42. X. Chen, H. Yan, W. Sun, Y. Feng, J. Li, Q. Lin, Z. Shi, X. Wang, *Polymer Bulletin*, **72**, 3097 (2015).
43. K. Kavitha, K. Subramaniam, B. J. Hui, K. Santhi, S. Dhanaraj, M. Rupesh Kumar, *Research Journal of Pharmaceutical, Biological and Chemical Sciences*, **4**, 1510 (2013).
44. S. Kamal, K. Gautam, P. Yash, *International Journal of pharma and bio sciences*, **4**, 254 (2013).
45. N. Bhandari, N. B. Gupta, *Journal of Drug Discovery and Therapeutics*, **1**, 27 (2013).
46. S. W. Ravi, S. M. Ravikant, *Pharmacie Globale*, **4**, 1 (2012).
47. R.B. Patel, P. G. Welling, *Clinical Pharmacokinetics*, **5**, 405 (1980).
48. R. L. Guptat, R. Kumar, A. K. Singla, *Drug Development and Industrial Pharmacy*, **17**, 463 (1991).
49. D. Paramita, M. Sabyasachi, *Biology and Medicine*, **1**, 2 (2010).
50. K. Arvidson, E. G. Johansson, *European Journal of Oral Sciences*, **93**, 467. (1985)
51. R. Gleckman, N. Blagg, D. W. Joubert, *The Journal of Human Pharmacology and Drug Therapy*, **1**, 14 (1981).

Effect of benzophenone and zinc stearate on photodegradation of potato starch based low density polyethylene

M. Sasani¹, Sh. Khoramnejadian^{1*}, R. Safari²

¹ Department of Environment, Damavand Branch, Islamic Azad University, Damavand, Iran.

² Department of Biotechnology, Caspian Sea Research Institute in Ecology, Sari, Iran.

Received May 15; Revised September 9, 2016

In this research photodegradable blend of Low density polyethylene with starch were prepared. 0/4 mm dumbbell sheets were prepared and exposed to direct sunlight for 3 months. Before and after sunlight exposure mechanical properties of polymers were measured. Benzophenone and zinc stearate were used as a photosensitive and photocatalytic additive. The effects of benzophenone on photodegradation of starch based blends were studied. In these study photodegradation were confirmed by determining carbonyl index and tensile properties. Existences of the carbonyl group indicate the starting of polymer chain degradation. Benzophenone and zinc stearate enhanced the photodegradation of polymer samples.

Keywords: photo degradation, plastic, environment, sunlight, benzophenone

INTRODUCTION

Plastic materials take an important part in modern life. Using these materials has an advantage and disadvantage. Plastic materials have various applications; these materials are the best replacement for wood or metals. Plastic inventions in twenty century change the costumer behaviors. Plastics are light, cheap, and easy to use and have a different usage from industries to medicine. With all benefits plastics has a problem that they remain in the environment for long time and couldn't be degraded by natural agents. Daily plastic waste generation increased. Plastics throw away and caused problems in the environment. Plastic waste one of the source of ocean litters and dangerous for marine creatures [1].

Plastics are resistance to microorganisms. So remain in the nature for many years. Pollutions grow higher and higher, some scientists predict the depletion of fossil fuels in future, then investigation about biodegradable and natural polymers are necessary. Since 1970s many research were done about biodegradable polymers. The first generations of biopolymers were not completely biodegradable they filled up with starch or other biopolymers and after starch degradation they remained in very smaller pieces without noticeable change in polymer chain [1].

Starch has an important role in degradable polymer industries. Starch stored in the plant and has role like fat in animals. Chemical structure of starch has a linear and branches structure: amylose is linear and amylopectin is branched. The ratios of amylose to amylopectin are different in various

kind of starch. Because of similarity of linear structure of amylose to synthetic polymers they have a same behavior. Photodegradable plastics have a similar structure to other petroleum base polymers but they have some weak bonds that are break down by sunlight or they have some additive that makes them sensitive to sunlight by adsorb sun rays. UV ray know as an aging and weathering agent. In the absence of oxygen PE are resistant to UV ray, but in presence of oxygen caused the brittleness in polymer matrix [5]. Copolymerization or mixing chromophores material to polymer are the common way to produce photodegradable polymers [7]. Photodegradable plastics react with sunlight and degrade [6]. These polymers could be a good choice for sunny region. If photodegradable polymers throw out in the nature it will be degraded to water and CO₂. benzophenon has a various application. Benzophenone could adsorb UV ray and prevent its effect in higher amount. Zinc stearate also has a photo catalytic behavior. In these researches effect of benzophenone and zinc stearate on photo degradability of blend has been studied.

EXPERIMENTAL

Low density polyethylene (LDPE) with commercial grade 0200 prepared from Bandar Imam petrochemical complex, IRAN. Food grade potato starch obtained from Alvand co. IRAN. Glycerol with food grade belongs to Merck co. Germany. Polyethylene grafted maleic anhydride (PE-g-Ma) produces in Karankin Co., IRAN. Olive oil used as a moisturizer. Benzophenone obtained from Merck Germany. Samples were processed in

HBI system with 60 rpm in 160°C. Sample sheets (0.4 mm thickness) were prepared by using Hot Mini Press. Samples cut in dumbbell shape and exposed to sunlight for 3 month. The tensile properties were measured by Santam (STM-20) instrument. FTIR test was performed on each sample before and after exposure to sunlight to determine the photo degradability and carbonyl index were calculated.

RESULTS & DISCUSSION

Table 1 shows the climate of Tehran city during summer 2015. Most of days are sunny with low humidity. Believed high temperature with direct sunlight has a positive effect on photodegradation. After 3 month outdoor exposure plastic sheets were brittle.

The carbonyl index of LDPE different samples increased after exposure time (Table 2). Carbonyl index is a good way to identify photodegradation. UV ray caused generation of free radicals that forming carbonyl groups.

Any change in carbonyl index indicated that photodegradation happened [2]. Degradation rate in samples that contain benzophenone increased. Pure LDPE had shown a less sensitivity to sunlight than

Table1. Data of weathering climate at Tehran (summer 2015)

Month	Temperature (°C)	Sunshine hours	Humidity (%)
June	34	>300	20>
July	34	>300	20>
August	35	>300	20>

Table 2. Carbonyl index (CI) of LDPE samples.

Sample	CI (before)	CI (after)
LDPE	1	1.18
LDPE/potato starch	1.8	1.45
LDPE/potato starch/ benzophenone	1.76	1.4
LDPE/potato starch/ benzophenone/zinc stearate	1.14	1.2

Carbonyl index calculated according this equation:
Carbonyl index CI = peak of carbonyl/1465 (I)

Table 3. Mechanical properties of samples before and after exposure to sunlight.

Content of potato starch (%)	Elongation at break (%)		Tensile strength (MPa)	
	Before	After	Before	After
LDPE	286.846	243.321	2.85	2.01
LDPE+ Potato starch	20.74	11.1	2.17	1.26
LDPE+ Potato starch+ benzophenone	19.65	8.72	2.2	0.92
LDPE/Potato starch/benzophenone/zinc stearate	20.31	4.97	3.6	0.51

other samples. Many polymers had been attacked by UV ray and cracked. LDPE are more resistance to UV than PP. samples with starch has more porosity in polymer matrix than pure LDPE so carbonyl index increased [7]. Samples that contain benzophenone are more sensitive than other samples. Benzophenone accelerates the photooxidation. Carbonyl group appeared when the polymer oxidized. Occurrences of carbonyl group identified the polymer chain breakdown [6]. Carbonyl belongs to functional groups that caused the breakdown in polymeric chain.

Mechanical properties of blends measured before and after exposure to sunlight are shown in Table 3. Elongation at break decreased after 3 month outdoor exposure. That's shows all of the blends are sensitive to sunlight, may be zinc content make them photosensitive. All of samples contain benzophenone showed decreased in mechanical properties because in photodegradation carbonyl

groups absorb UV rays, free radical cause break down in LDPE linkage [2]. After outdoor exposure polymer sheets are brittle and broken with touching. Photodegradation of samples with benzophenone had a faster degradation. Reduction of elongation at break shown in all samples, UV ray caused the chain scission so make the samples brittle [4]. Zinc stearate has a good effect on photodegradability. It seems combination of zinc stearate and benzophenone enhanced the photodegradability.

CONCLUSION

In this research, effect of benzophenone and zinc stearate on photodegradability of starch based polyethylene has been studied. Benzophenone is a photocatalytic agent and adsorb UV ray and caused the scissoring in polymer chain. According to result samples with amount of benzophenone were shown

more photodegradability behavior than other samples. Zinc stearate has been shown same ability. These polymeric materials are a good choice for environment conservation and decrease the amount of plastic solid waste.

Acknowledgements: *This research is supported by the research fund of Damavand Branch, Islamic Azad University, Damavand, Iran.*

REFERENCES

1. L. Yu, Biodegradable polymer blends and composites from renewable resources, Willey publication, 2009.
2. E. A. Eltayeb, A. R. Mahdavian., M. Barikani, *Iranian J. Chem. Eng.*, **8**, 31 (2011).
3. Handbook of biodegradable polymer, synthesis, characterization and applications, Willy, 2012.
4. M. N. Z. Islam, N. Othman., *Sains Malaysiana*, **40**, 803 (2007).
5. P. N. Lan, N. C. Giang, N. H. Thuy, *J. Chem.*, **45**, 392 (2007).
6. A. M. Y. Nurul, M. Rahmah, A. Muhammad, *Engineering and Technology*, **77**, 814 (2013).
7. U. Ratanakamnuan, A. Duangdao, *J. Appl. Polymer Sci.*, **100**, 2725 (2006).

A new study on the derivatization of malondialdehyde by anisidine reagent with use of UV-Vis, FT-IR, ¹HNMR, ¹³CNMR techniques

B. Akbari¹, M.E.Olya^{2*}, M. Bahmaei¹, F. Najafi³

¹Department of Chemistry, Tehran North Branch, Islamic Azad University, Tehran, Iran²Environmental research Department, Institute for color science and technology, Tehran, Iran

³Department of Resin and Additives, Institute for Color Science and Technology, Tehran, Iran

Received June 26, 2015, Revised September 10, 2015

Derivative methods of malondialdehyde (MDA) as a biomarker of oxidative stress, often desire high temperature and long heating time. Some of which activate a color reaction such as thiobarbituric acid reactive substances (TBA), diamino-naphthalene, pentafluorophenyl hydrazine, and phenylhydrazine after placing in that harsh condition. Our attempts were to introduce a new derivative reaction between malondialdehyde and Para-methoxy aniline (PMA) in order to identify MDA. The derivatization of malondialdehyde (MDA) with different concentration of para-methoxy aniline (anisidine) in an acidic medium and various time, temperature, and pH was investigated. The possible reaction of malondialdehyde and Anisidine was completed after 10 min at 75°C in optimal condition. By spectrophotometric techniques, the complex formed in this process exhibits a highly specific UV spectrum with a sharp maximum at 400nm. ¹H NMR, ¹³CNMR, and FT-IR were confirmed the formed adduct.

Keywords: malondialdehyde, anisidine, colorimetric reaction, derivatization

INTRODUCTION

Malondialdehyde (MDA), as one of the great significance individual aldehyde resulting from lipid peroxidation, is a reactive unsaturated dicarbonyl that can easily bind to macromolecules such as structural and functional proteins and nucleic acids [1-5]. As of now, the great number of analytical approaches, for determination of malondialdehyde (MDA), have been proposed various derivative methods. Most procedures based on the aldehyde reactivity of MDA employed hydrazine-based derivatization reagents [6,7] Still, the classical assay "2-thiobarbituric acid (TBA) is the most general applied technology in which two molecules of TBA change with one molecule of MDA to give a colored reaction product, which can be measured spectrophotometrically at 535 nm, or by fluorescence detection with excitation at 530 nm and emission at 550 nm. [8-12] In fact, the TBA assay is a non-specific method for MDA; therefore, further developed methods were strongly suggested by researchers with use of new color reagent for detection of this prominent biomarker in order to introduce specific method. [13-15] Derivative reagents, namely, thiobarbituric acid, diamino-naphthalene (DNPH), pentafluorophenylhydrazine (PFH), pPhenylhydrazine (PH), dansylhydrazine, methylhydrazine, 2,2,2-trifluoroethylhydrazine and FMOC-hydrazine after placing in high temperature,

and long time have been proposed by researchers to measure MDA by expensive separation technology such as Reverse Phase-Liquid chromatography (RP-PLC), Gas Chromatography–Mass Spectrometry (GC-MS), and Liquid chromatography–Mass Spectrometry (LC-MS, or alternatively HPLC-MS). [6] However, the result of their investigation was far from satisfactory.

On the other hand, *p*-anisidine value would be a well-known method to measure the content of aldehydes (principally 2 alkenals and 2, 4-alkadienals) generated during the decomposition of hydroperoxides. *p*-methoxyaniline (anisidine or PMA) and the aldehyde compounds under acidic conditions provide yellowish products and absorb at 350 nm [16]. Besides, *p*-An Value is a valid indicator of oxidative rancidity in oils and fatty foods [17, 12]. However, no specific method has been developed for determination of malondialdehyde by anisidine reagent.

In this paper, based on colorimetric reaction, a new method for synthesis and identification of MDA was introduced. Investigation of complex formation (MDA-PMA) with use of variegated techniques was studied as well. In addition, it was expected that this procedure would assure a simple, selective, and sensitive measurement of MDA for further biological studies.

* To whom all correspondence should be sent:
E-mail: Olya-me@icrc.ac.ir

EXPERIMENTAL

Material and methods

Malondialdehyde, tetra butyl ammonium salt (MDA, 96%) was purchased from SIGMA ALDRICH. In addition, para methoxyaniline, butylated hydroxytoluene, glacial acetic acid, HClO₄ 0.1 M diluted in glacial acetic acid, absolute ethanol, and sodium hydroxides were from Merck Company.

Solvent selection

To find an appropriate solvent, a possible reaction between malondialdehyde, tetra butyl ammonium salt (MDA, 96%) and para-methoxy aniline (anisidine, PMA) was evaluated. Therefore, different solvents such as HPLC-grade water, absolute ethanol, glacial acetic acid, and HCl were examined. Finally, absolute ethanol and glacial acetic acid were selected as two proper solvents for MDA and Para methoxy aniline, respectively.

Preparation of anisidine reagent

p-methoxy aniline (anisidine) as a reagent was prepared at 1000 $\mu\text{M.L}^{-1}$ ($\mu\text{M} = \mu\text{M.L}^{-1} = \text{n mol/ml}$) in glacial acetic acid, by dissolving 0.0123 g of Anisidine in 100 ml of glacial acetic acid. The malondialdehyde Tetra butyl ammonium salt in 10ml of absolute ethanol. (Figure.2) This stock solution remained stable for at least 6 months and stored at -20 °C in aliquots of 250 μl in dark place while the working standard solutions had to be prepared every day MDA solution was monitored by its absorbance at 267nm [6].

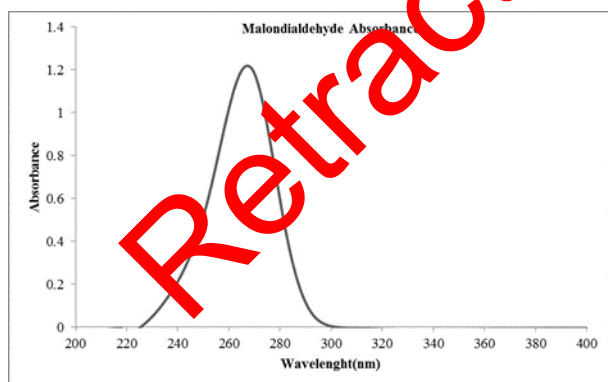


Fig. 2. Wavelength of malondialdehydetetra butyl ammonium salt diluted in absolute ethanol

The process of derivatisation

First, seven clean glass test tubes were taken and labeled them (A-G). Second, different concentrations of MDA standard stock solutions were prepared (50, 25, 10.5, 5, 2.5, 1, and 0.5 μM) and diluted by absolute ethanol. Afterwards, two ml of prepared MDA solution was transferred to

solution was protected from the light and was stored at room temperature for a daily basis. The maximum absorbance was at 273 nm (Figure.1).

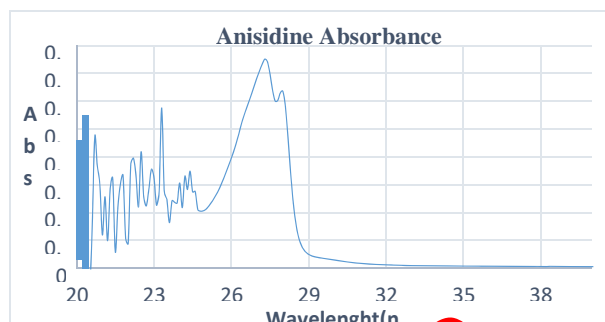


Fig. 1. Wavelength of anisidine diluted in glacial acetic acid

Anisidine was fully tested on room temperature in the dark place with two different concentrations (500 and 1000 μM) to investigate its stability in long period. Anisidine stability had a constant trend within 30 days.

2.3 Preparation of MDA stock solution

Standard stock solution of MDA (5000 $\mu\text{M.L}^{-1}$) was obtained by dissolving 0.0156 g

each labeled glass tubes. Then, two ml of anisidine (500 μM) as a color reagent was added to them and vortex the solution. Finally, the tubes were closed and placed them to any holder to keep the tubes upright during boiling at 90°C. After 10 min, immediately, the tubes were removed and were placed in ice bath to stop the reaction. At least, 15 min was needed to be cooled down. Without any extraction steps, two ml of the clear yellowish complex of each glass tubes were loaded to absorption cell for reading the absorbance at 400-404 nm by UV-Vis.

Investigation of concentration, time, and temperature

Various concentrations of MDA standards (50, 12.5, 3.125 $\mu\text{M.L}^{-1}$) and anisidine reagent (30, 50, 100, 150, 250, 500 $\mu\text{M.L}^{-1}$) were prepared by further dilution of their stock solutions. After preparing anisidine reagent in glacial acetic acid, the solution should be protected from the light within the procedure. For activating the color, derivatization was performed at different reaction times (5, 10, 20, 30, and 40 min) and at different temperature (30, 70, and 90°C) to assess the optimum conditions of MDA derivatization.

Process of complex (MDA-PMA) formation

An appropriate volumes and concentrations of anisidine, optimum temperature, and time were the significant parts of this study. In fact, in order to explore the colorimetric reaction between MDA and PMA, several tests with various concentrations of each have been done. Briefly, by our research work, various concentrations of MDA standards (50, 12/5, 3/125 μM) and anisidine reagent (150, 250, 500 μM) were prepared by further dilution of the stock solutions. Afterwards, 2 milliliter of prepared MDA solution (50) was transferred to a labeled glass tube (Complex MDA-PMA). Then, two ml of anisidine (500 μM) as a color reagent was added to the labeled tube (Complex MDA-PMA) and vortex the solution. Finally, the tube was closed and placed them to any holder to keep the tubes upright during boiling at 90 $^{\circ}\text{C}$, 70 $^{\circ}\text{C}$, and 30 $^{\circ}\text{C}$. After 10 min, immediately, the tube were removed and placed in ice bath to stop reaction. At least, 10 min was needed to be cooled down. The optimum condition provided for stable yellowish color adduct (complex A) was considered as follows: (Time:20 min, Temperature75 $^{\circ}\text{C}$, anisidine concentration 500 μM).

Synthesis of MDA-PMA adduct

The product (MDA-PMA) is not commercially available, but it can be prepared in laboratory condition. Formation of imine compound was necessary to evaluate the reaction and confirmation of MDA-PMA adduct. The derivatization procedure is based on the principle of (0.5g) of MDA reacting with (0.4g) of anisidine prepared with glacial acetic acid at room temperature.

It was found that an imine compound is produced after a few seconds. Then, yellow-orange product was dried at 30 $^{\circ}\text{C}$ for 4 h in a vacuum drying oven. The structure of this compound was confirmed by different methods namely ^1H NMR, ^{13}C NMR, and FT-IR.

Effect of pH

The pH effect of the derivatization reaction on the MDA value was investigated by previous scientists [3]. Although this new procedure was confirmed at pH= 7.4, the validity of the derivative method has been questioned in various pH (acidic or basic medium). In other words, the complete reaction should be evaluated in different pH for the future biological studies. For this reason, the pH ranges (3.2, 7.4, and 12.0) have been selected.

In normal pH (p H= 7.4), two ml of MDA (50 μM) was added to two ml of anisidine (500 μM) in a 10 ml lab tube. Then, this reaction mixture was

placed in the water bath for 10 min at 90 $^{\circ}\text{C}$. The solution was cooled and ready for the analysis by UV/Vis spectrophotometer at 400-404nm.

In the basic medium, 200 μl of 6 M NaOH was added to 1000 μl of MDA in a 10ml lab tube. By placing this mixture at 60 $^{\circ}\text{C}$ in the water bath for 30 min, allow medium to be basic. After cooling, 200 μl of anisidine reagent (500 μM) was added to this basic solution. The same as above, the reaction mixture was placed in water bath for 10 min at 90 $^{\circ}\text{C}$. The solution was cooled and ready for the analysis by UV/Vis spectrophotometer at 400-404nm.

In the acidic medium, 250 μl of HClO_4 (0.1 M) diluted in glacial acetic acid was added to 1000 μl of MDA (50 μM) in a 10ml lab tube and vortex. Then, 200 μl of anisidine reagent (500 μM) was added to the tube and finally this mixture was placed in water bath for 10 min at 90 $^{\circ}\text{C}$. The solution was cooled and ready for the analysis by spectrophotometer at 400 nm.

Techniques

Possible structure of the formed adduct (complex MDA-PMA) under above condition was confirmed by UV-Vis spectrophotometry, FT-IR, ^1H NMR, and ^{13}C NMR.

Spectrophotometric analysis

After cooling in icy bath to stop the reaction, without any extraction steps, the solution was analyzed by spectrophotometer using a Lambda Bio 20 spectrometer (Perkin-Elmer, Rotkreuz, Switzerland) using 1-cm absorption cell. Spectrum of MDA-PMA solutions was recorded from 200 to 600 nm at a scanning speed of one nm/min against of the glacial acetic acid as a blank reaction mixture. Absorbance reading was done at 404nm. Data acquisition and processing were carried out with the Perkin-Elmer UV Winlab software.

FT-IR analysis

The infrared (IR) spectra of the samples were recorded in the range 400–4000 cm^{-1} on a Fourier transform infrared (FTIR) spectrometer (model Perkin-Elmer, Rotkreuz, Switzerland) using KBr pellet method.

Nuclear magnetic resonance spectroscopy

^1H , ^{13}C NMR spectra were performed on a 250 MHz Bruker (Germany) in deuterated chloroform for both experiments at room temperature to find whether the imine was formed or not.

RESULTS AND DISCUSSION

Influence of time in derivative reaction

The yellow complex under 30 °C cannot be produced, although time and concentration of anisidine equal to 500 μM have been raised. However, at 90 and 75°C, reaction accelerates in short time (10min); this vital point can help us to consider the reaction of Imine formation or the same yellow complex in the real biological samples in order to determine MDA. As can be seen in figure 4, at 75°C, formation of yellow complex indicates a complete reaction of MDA with PMA.

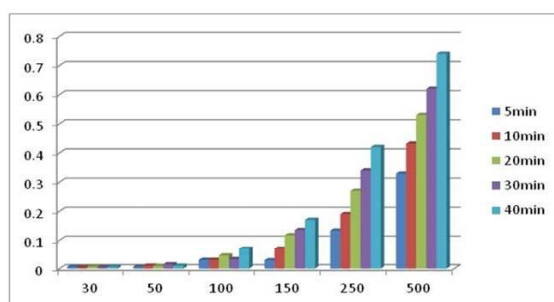


Fig4.1 at 30 °C

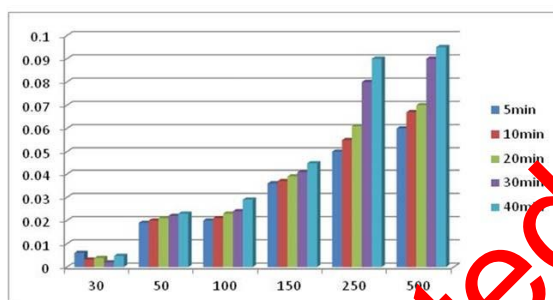


Fig4.2 at 75 °C



Fig 4.3 at 90 °C

Fig.4. Formation of yellow complex at Different time (5, 10,20,30,40 min) and different temperature (30, 75,90°C)

According to Figs. 4.1, 4.2, 4.3, the temperature of 75°C indicates the complete derivatization and the formation of the colorimetric reaction. Moreover, at 90 °C, the reaction was carried out in a short time. However, at high level of temperature, the aldehyde levels may be raised in the real samples from the actual results which makes it difficult to evaluate the data [5].Therefore, to implement this method in biological samples, using

75 °C as an optimal temperature can be suited for the analysis. Furthermore, to obtain complete derivative reaction with anisidine (500μM) at 75 °C, 20 min would be a proper time. Actually, by using 250 μM or lower concentrations of anisidine, the complex (MDA-PMA) was remained at an intermediate state and the yellowish complex will not be formed and its result will not be suitable for the real samples. Therefore, the reaction is completed by anisidine (500 μM) with optimized temperature at 75°C within 20 min. (Figure 5)

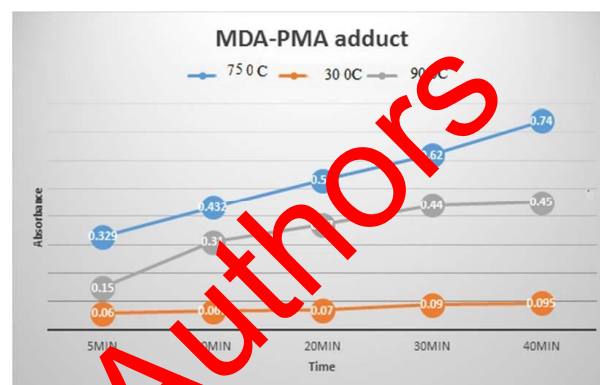


Fig. 5. The relationship between temperature and time in complex (MDA-PMA) formation (anisidine = 500 μM)

On the other hand, TFEH, and PFH as derivative reagents require harsh temperature to produce complex [6].Temperature effect on derivative procedure was considered as an important part in this research; therefore, the samples placed in a water bath at 30°C, 75°C and 90°C and room temperature, then, cooled in icy bath.

To evaluate the optimum condition for formation of the complex [MDA-PMA], different concentrations of anisidine (30, 50, 100, 150, 250, 500 μM) was added to different concentrations of MDA (3.125, 12.5 and 50 μM) in different times (5, 10, 20, 30 and 40) and in separate runs.

The results of Fig. 5 indicate that yellow adduct was not formed at 30°C and room temperature. Optimal temperature and time as the main part of derivation process were considered in this study. According to Fig.5, under low temperature (30°C), the reaction was slow and proceeded to produce an intermediate compounds. Even, by increasing in the molar concentration of anisidine and time, it produces higher concentration of intermediate compounds; this indicates that derivative adduct could not be formed in this concentration and temperature. However, when the concentration of anisidine is 10 times higher than MDA concentration, the yellow color will reduce the form of intermediate compounds and enhance the form of complex.

It seems that the procedure was completed at 90°C in 10 min which contribute to form the imine reaction or yellow adduct in this temperature while this should be considered that high temperature is not proper for this procedure, due to evaporation of malondialdehyde and solvent during derivative process, so this may be difficult to maintain the derivative concentrations.

On the other hand, at 30°C, there is no yellowish complex; therefore, it is not a proper temperature to assess the complex formation. Nevertheless, at 75°C, the reaction was completed in 40 min and the concentration of anisidine selected at 500 μM while Mao's method reaction time was 3 hours with FMOC reagent. [17]

As can be seen in Figure 6, at the wavelength of 300-380 nm, the wide peak is related to intermediate formation whereas in Figure 7, relatively high peak in the range of 400-404 nm indicates reduced concentration of intermediate and formation of adduct or the same considered complex.

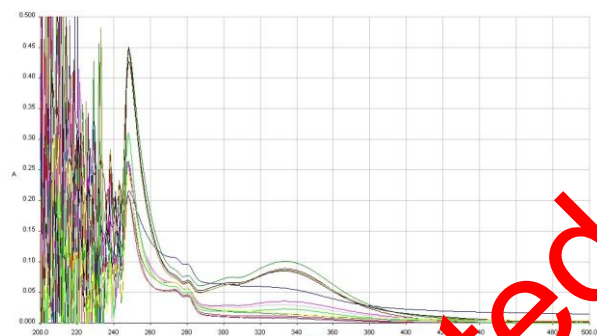


Fig. 6. Different concentration of anisidine with their absorbance spectra of derivative complex at 30 °C in complete reaction (Complete reaction)

As can be seen in Figure.7 this colorant has a strong absorbance peak in visible range in 400 nm related to electronic transference $\pi \rightarrow \pi^*$. The absorbance peaks in UV region is related to electron transference of benzene rings. [10] The obtained peak in visible range in the range of 300 to 395 is related to the formation of intermediates. The peak value decreases by high temperature. Likewise, by altering anisidine concentration, the adduct peak value increases.

Optimal condition for derivative procedure

The reaction of anisidine (para - methoxy aniline) with aldehyde groups can be considered as an addition reaction. The yellowish complex emerged from releasing H₂O molecules by which it presents a stable adduct. Investigating the reaction depended on MDA concentration indicated that the more molar concentration of anisidine, the more

increase in the concentration of yellow complex (MDA-PMA). Derivatized adduct was evaluated with the molar ratios of 1/2:1 to 1:10 (MDA: Anisidine). Figure.4 and Figure.5 depict when the molar ratio of Anisidine concentration is (10[MDA]), the derivative solution attains to a higher level; thus, the derivatisation was completed at the molar ratio of 10:1.

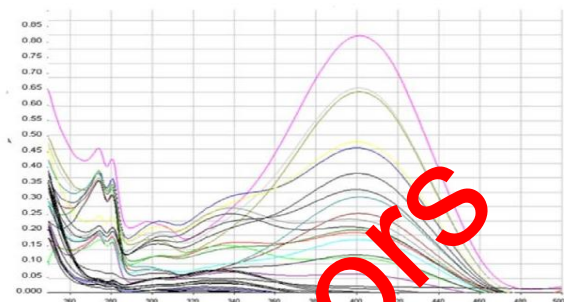


Fig.7. Different concentration of anisidine with their absorbance spectra of derivative complex at 90 °C in complete reaction (Complete reaction).

Stability

Current method is significantly different from Mao J, Zhang H, et al. [17]. Their method was time consuming procedure (4 hour) at 50 °C to reach near completion reaction [17]. In order to prevent false results, stability of malondialdehyde and anisidine as a crucial methodological aspect of this study was evaluated by UV-Vis spectrophotometry.

The absorbance reading of PMA (1000 μM and 500 μM) and MDA (stock solution (5000 μM) and its working standard solution (50 μM)) was done at 273 nm and 267 nm, respectively. It is clearly observed in Figure.8.1 that the solution of PMA was stable if it is protected from light.

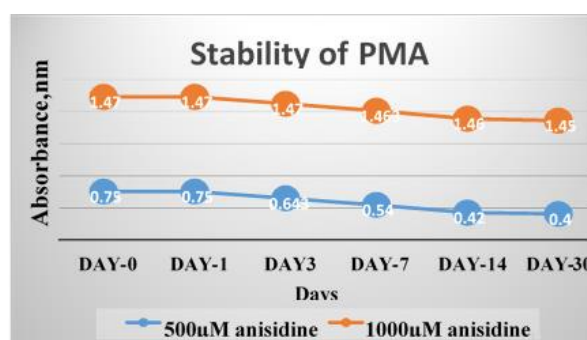


Fig. 8.1. Evaluation of PMA stability.

Nevertheless, it would be better to prepare 500 μM concentration of PMA at the time of the test. With regard to MDA stock solution stability, Figure.8.2 depicts the satisfactory results of 5000 μM concentration of MDA. However, working standard solution did not prove to be stable over 30-days period. Thus, it is only possible to use stock solution to prepare working standard solution at the

time of test because MDA become degradation less than 24 hour.

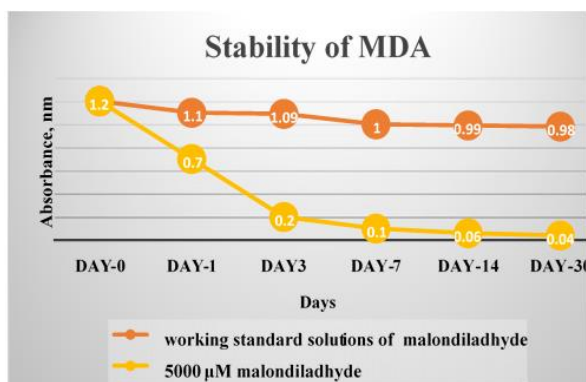


Fig. 8.2. Evaluation of MDA stability.

On the other hand, FMOC-hydrazine and DNPH (as derivative reagents) increased the derivative reaction under mild acidic conditions and lower temperatures, because of having identical hydrazine groups, which are strong nucleophiles and can readily react with aldehydes. These conditions prevent undesired artificial aldehyde formation generated during the sample pretreatment. The derivative reagents such as DNPH need several Liquid-Liquid extractions due to the excess of unreacted DNPH and thus separation of the MDA-DNPH will be difficult. Moreover, because of DNPH instability, purification of DNPH should be performed on a daily basis. [17, 12]

Consequently, based on above aforementioned results, this method did not require multiple extraction steps for anisidine reagent and thus, no residue or cloudiness was appeared during and after derivative procedure, which made this procedure preferable over the other methods. Furthermore, the yellowish adduct has no hazardous material if keep it for a long time in a laboratory. A feature which is crucial in developing a precise and accurate quantitative method is that PMA was stable for at least 1 month at room temperature if it is protected from light whereas FMOC-hydrazone (as a reagent) is only stable for 72 h at room temperature [17,12].

The effect of pH

The influence of pH in this procedure was examined. As can be seen in Figures 9.1 and 9.2, derivative complex at different pH (3.0, 7.4, 12.2) were formed after 10 min at 90 °C. The maximum yield was achieved at 400 nm in each pH. The results may contribute to apply this procedure for determination of free and total MDA in biological samples at different pH for further studies.

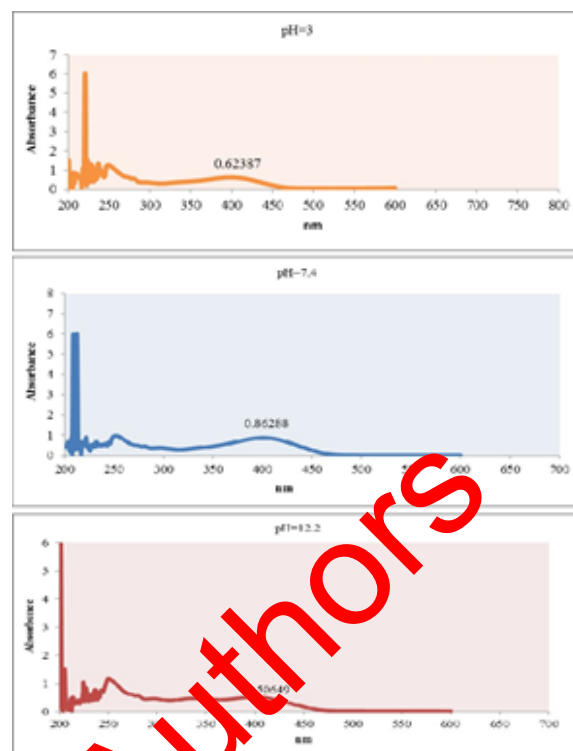


Fig.9.1 Effect of pH on complex formation

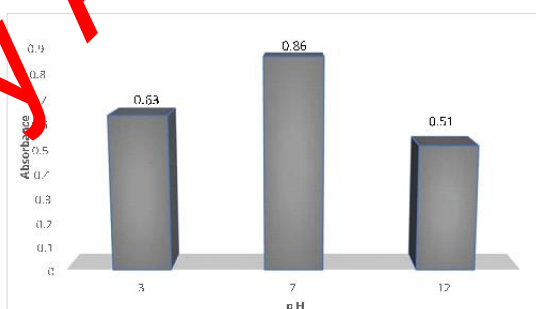


Fig. 9.2. Evaluation of different pH for complex formation.

Mechanism of imine formation

The formation of the imine is the initial step in this reaction. The imine was formed after reacting an amine (1°) with aldehydes to form a dipolar intermediate. The reaction has two steps:

- 1-NH₂ preferentially approach to carbonyl groups of aldehydes
- 2- Elimination of water group.

In current study, imine formed during the synthesis procedure identified by ¹HNMR, ¹³CNMR and FT-IR techniques were confirmed the adduct. The possible mechanism of MDA derivatization was depicted in Figure.10.

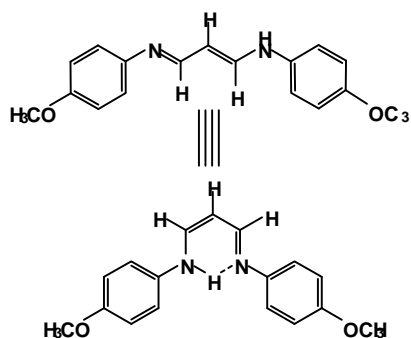


Fig. 10. The mechanism of MDA-PMA adduct.

The results of UV-Vis, FT-IR, and NMR

Spectrophotometric results

MDA and other carbonyl compounds naturally exist as byproducts of lipid peroxidation and prostaglandin biosynthesis. With regard to analytical approaches, it is better to derivatize

MDA with reagents having high molar absorptivity at longer UV wavelengths (>254 nm). In fact, the high molar absorptivity and the close proximity of the absorbance maximum to ~ 300nm make a MDA derivative almost preferably suited for detection using a diode array system [9]. (Figure.11)

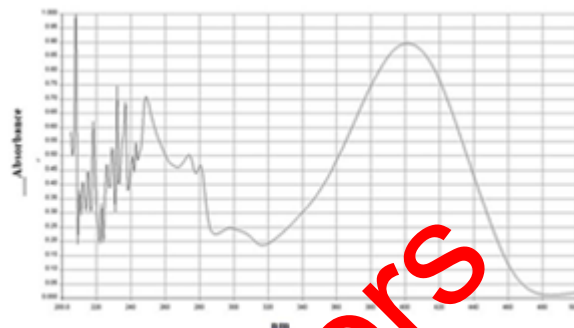
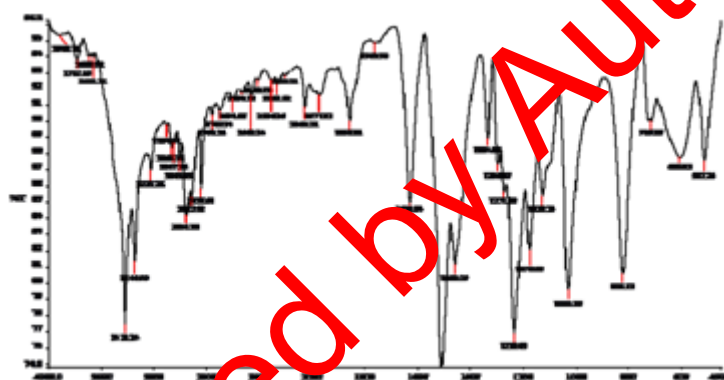


Fig. 11. A final spectrum of yellow adduct at 75°C (50 μM MDA- 500 μM PMA) FT-IR results



Retracted by Authors

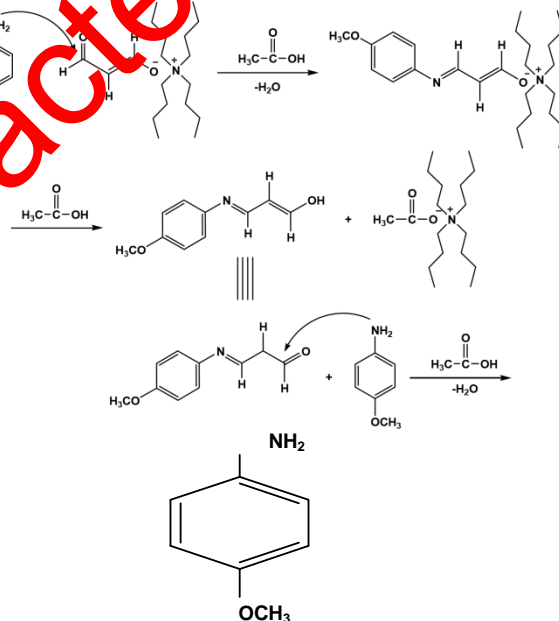


Fig. 12.1. IR-spectra of anisidine.

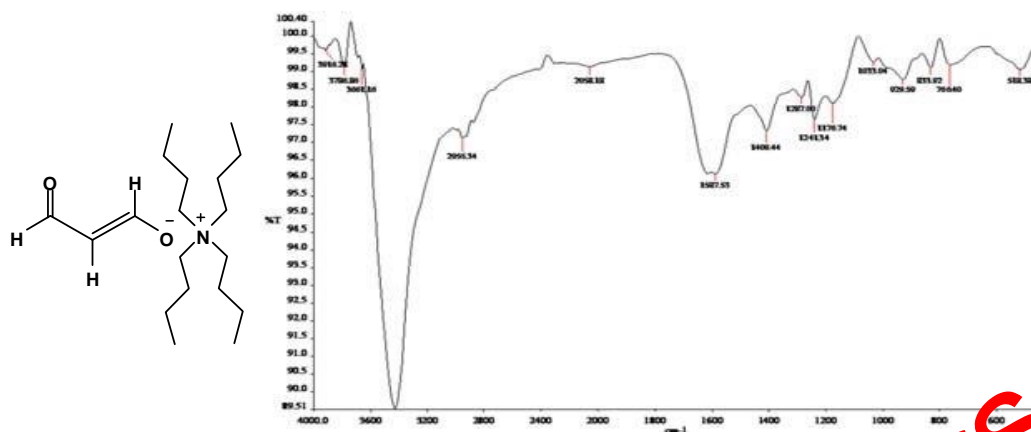


Fig. 12.2. IR spectrum of malondialdehydetetrabutyl ammonium salt molecule

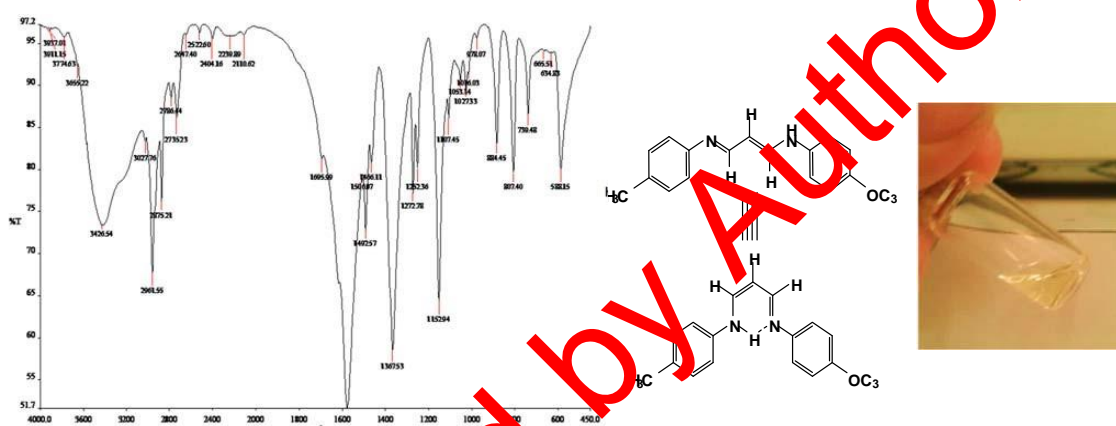


Fig. 12.3. IR spectrum of MDA-PMA and the proposed synthetic molecule

Table. 1. FT-IR results of MDA-PMA adduct

C-H = 2850 cm^{-1}	(NH group) = 3220 cm^{-1}
C-N (amine group) = 1271 cm^{-1}	CH ₃ (bending vibration) = 1287 cm^{-1}
C-O (enole form) = 1176 cm^{-1}	C=C (α , β unsaturated) = 1587 cm^{-1}
C=N (imide) = 1605 cm^{-1}	N-H = 1409 cm^{-1}

The FT-IR spectra of MDA-derivatization, primary amine and malondialdehyde were confirmed in the reaction. IR spectra were different from spectra of MDA before and after derivative reaction. The important IR bands of the compounds along with their assignments are given in Figures 12.1, 12.2, and 12.3.

Analytical data. Important infrared spectral (cm^{-1}) bands of anisidine. Figure 12.1: IR-spectra of anisidine demonstrate the N-H tension bond appears close 3346 and 3232 cm^{-1} . Another band at 3103 cm^{-1} was proved the aromatic CH tension. Furthermore, signals between 2838 cm^{-1} correspondent to the C-H aliphatic. Moreover, Band at 1510 shows the C=C and signals at 1334

and 1459 cm^{-1} depict the tension band of the CH₃ and N-H, respectively. The stretching vibration of the C-N and C-O band for the methoxy group were appeared at 1235 cm^{-1} and 1030, respectively.

Important infrared spectral (cm^{-1}) bands of malondialdehyde. Figure 12.2: IR-spectra of MDA show the C-N stretching band (calculated at 1272 cm^{-1}) related to the amine bands. The C-O stretching enole form band is clarified at 1152 cm^{-1} . The strong peak exhibits the aldehyde form of C=O at 1695 cm^{-1} . The enol form of C=C was verified by the strong band at 1580 cm^{-1} . Besides, the CH₃ and CH₂ bending at 1367 and 1492 cm^{-1} are roughly visible.

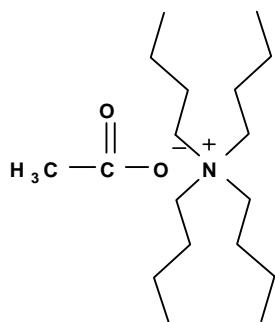


Fig. 13. The byproduct of MDA-PMA reaction.

IR spectrum of adduct. Figure 12.3: IR-spectra of adduct shows Tension signals were eliminated at 2786 and 2735 cm^{-1} (C-H) due to the reaction between anisidine and aldehyde group. Another band at 2955 cm^{-1} appeared as a result of α,β -unsaturated conjugated imides in $<2955 \text{ cm}^{-1}$.

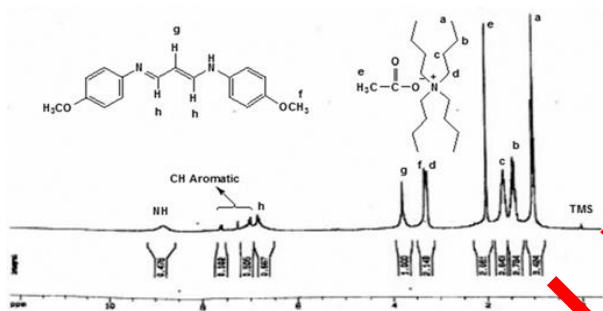


Fig.14.1: ^1H NMR spectra of the adduct (MDA-PMA)

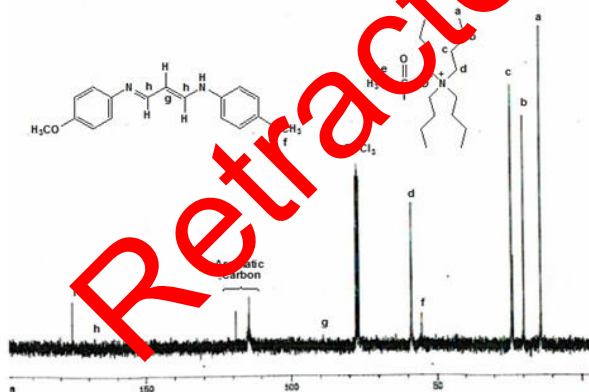


Fig.14-2. ^{13}C NMR spectra of main production with glacial acetic acid and tetra butyl ammonium salt.

The new adduct being formed in acetic acid medium is conjugated imine aromatic. Not only is acetic acid as a catalyst for the reaction of amine and MDA but also make tetra-butyl amine separate from MDA and provide possible reaction for MDA and anisidine again.

The important infrared spectral (cm^{-1}) bands of MDA-PMA are considered as follows.

Ammonium ion peak as a byproduct was appeared in a strong state at 3450 cm^{-1} . This is the byproduct which has not been fully separated completely (Figure 13).

^1H NMR and ^{13}C NMR results

The structure of adduct (MDA-PMA) is confirmed by the ^1H -NMR and ^{13}C -NMR. The protons of NH group in CDCl_3 are shown in 9.8 ppm (Figure 14).

Acknowledgements: The authors would like to express their sincere appreciation to Dr. Amir Ahmadi for her suggestions during this study.

REFERENCES

1. F. Karatas, M. Karatope, and A. Baysar, *Analytical Biochemistry*, **311**, 46 (2002).
2. D. Grotto, L.D. Santa Maria, S. Boeira, J. Valentini, M.F. Charão, A.M. Moro, P.C. Nascimento, V.J. Pombalin, S.C. Garcia., *Journal of Pharmaceutical and Biomedical Analysis*, **43**, 619 (2007).
3. D. DelRio, A.J. Stewart, N. Pellegrini, *NMCD*, **15**(4): 31 (2005).
4. P. Agarwal, S.D. Chase, *Journal of Chromatography B*, **777**, 121 (2002).
5. J. Seljeskog, T. Hervig, M.A. Mansoor, *Clinical Biochemistry*, **39**, 947 (2006).
6. M. Giera, H. Lingeman, W.A. Niessen, *Chromatographia*, **75**, 433 (2012).
7. K. Grintzalis, D. Zisimopoulos, T. Grune, D. Weber C.D. Georgiou, *Free Radical Biology and Medicine*, **59**, 27 (2013).
8. J.P.1 Steghens, A.L. van Kappel, I. Denis, C. Collombel, *Free Radical Biology and Medicine*, **31**, 242 (2001).
9. M. Czauderna, J. Kowalczyk, M. Marounek, *Journal of Chromatography B*, **879**, 2251 (2011).
10. R. Mendes, C. Cardoso, C. Pestana, *Food Chemistry*, **112**, 1038 (2009).
11. J. Pilz, I. Meineke, C.H. Gleiter, *Journal of Chromatography B: Biomedical Sciences and Applications*, **742**, 315 (2000).
12. T. Shibamoto, *Journal of Pharmaceutical and Biomedical Analysis*, **41**, 12 (2006).
13. A.S. Sim, C. Salonikas, D. Naidoo, D.E. Wilcken, *Journal of Chromatography B*, **785**, 337 (2003).
14. M. Khoubnasabjafari, K. Ansarin, A. Jouyban, *BioImpacts*, **5**, 123 (2015).
15. F. Shahidi, Y. Zhong, "Lipid Oxidation: Measurement Methods", in *Bailey's Industrial Oil and Fat Products*, John Wiley & Sons, Inc., 2005.
16. O. Aruoma, *Journal of the American Oil Chemists' Society*, **75**(2), 199 (1998).
17. J. Mao, H. Zhang, J. Luo, L. Li, R. Zhao, R. Zhang, G. Liu, *Journal of Chromatography B*, **832**, 103 (2006).

Study of the chemical compositions of Iranian rose flower essence oil (*Rosa persica*)

Mozhgan Amini, Masumeh Khosravi Rineh*, Mojtaba Yazdani

Department of Biology, Faculty of Sciences, Ashtian Branch, Islamic Azad University, Ashtian, Iran

Received June 26, 2015, Revised September 10, 2015

Iranian rose flower or varak (*R. persica* sp.) belongs to the rose flowers species. Being a perennial shrub type it has quite a lot of ramifications which propagate by seed. The purpose of this study is to identify the chemical compositions present in the essence of varak plant (*R. persica*). For this purpose, this plant was collected from the Ashtian region of Markazi province in (2014) and after drying in ambient temperature the extraction of the essence oil was carried out by implementing steam distillation method. The constituent compositions of the essence oils were separated and identified by the use of gas chromatograph (GC) devices and gas chromatograph connected to mass spectrometry (GC/MS). In the essence of these plants 56 compositions were identified so that the main part of this essence was constituted from hydrocarbon (alkanes). Among the identified compositions the active ingredient of heptacosane with (11.6) has the highest percentage and after that stands isobutyl phthalate (11.48), nonacosane (8.88), dibutyl phthalate (6.26), pentacosane (5.96), hexadecanoic acid (3.95), linalool (3.8), ethyl linoleolate (3.73), hexyl hexoate (3.67), octacosane (3.43) are the main constituent compositions of this plant.

Key words: Iranian rose flower (*Rosa persica*), essence, heptacosane

INTRODUCTION

Varak species by the scientific name of *Rosa persica* belongs to the *Rooideae* subgenus and *Rosaceae* genus. Rose genus consists of many types which are scattered across temperate regions and semi-dry northern hemisphere [1]. Varak genus is a perennial shrub type it has quite a lot of ramifications which propagate by seed. It has wooden shrubs with 30-75 cm height, thorn-like stipules and simple leaves. Yellow petals at the foot with red spots turning to brown and carpel without fluff [2]. Phenolyn compositions presence in thorny stems protects this plant against the attacks by the herbivorous insects and micro-organisms and sun ray. Plants belonging to rose genus include many different types of secondary metabolites such as flavonoids and tannins [3]. The pharmaceutical significance of antioxidants in preventing cancers and heart blockage diseases and achieving this goal by the consumption of foodstuff containing such compositions for instance acetone extracted from *Rosa persica* from Iran. Triterpenes and cyanic acids have been reported from these plant [4]

So far, except for a few researches in terms of the constituent components of essence from different species of *Rosa* in Iran and other countries have not been carried out. Jassbi et al. [6], analyzed the poly phenol antioxidant compositions of *Rosa persica* in which 5 phenol antioxidants were reported including storing and analytical

flavonoids and tannins. Nowak [8] studied fatty acid in different fruits of wild rose species. His findings showed that rose fruits are rich in non-saturated fatty acids especially in species such as *R. rubiginosa*, *R. rugosa*, *R. dumalis*. Elisabetsky et al. [5] studied the chemical compositions and antioxidant activities of essence and essential oil of *Rosa damascena* from the population of Guilan, Iran and concluded that the planted rose flower petals do not taste bitter and thanks to the potential antioxidant activity and appealing flavor can be used as the food flavor fragrant and be used as a preventive factor against many diseases.

Jassbi et al. [6] carried out a study about the photochemical and horticultural properties of *Rosa canina* which revealed that there is a significant relation between natural habitat and the time of harvesting and the amount of antioxidants, vitamin C and flavonoids.

In this study the constituent compositions of the essence of the *Rosa persica* plant were separated and identified by the use of gas chromatograph (GC) devices and gas chromatograph connected to mass spectrometry (GC/MS). This study was carried out for the first time and in order to detect the constituent compositions of the essence of the plant in natural habitat of Ashtian region.

MATERIAL AND METHODOLOGY

Plant collection and essence extraction

Iranian rose flower plant was carried out from the North and East heights of the Ashtian town and the Kahrizak valley in June of 2014-2015. In

* To whom all correspondence should be sent:
E-mail: Khosravi_rineh@yahoo.com

order to dry the plants the plant was placed in an air-conditioned room far from sun light and was kept away from any type of light until extracting essence. The drying method is very influential on the active ingredients and if drying is done by the direct sun light the plants would lose their active ingredients [7]. About 100 g of the dried plant was extracted by the use of Clevenger device and the essence was extracted by implementing Hydro distillation method for 4 hours. Essence oils were kept in dark glasses at fridge temperature until device analysis.

Detecting constituent compositions of the essence oils-GC device properties

Gas chromatograph Shimadzu 15A equipped with DB-5 column with 50 m length, internal diameter of 0/25 mm, stationary phase layer thickness of 0/25 micro m and the injection room temperature of 250 c. In heat plan the primary temperature of the column for 3 minutes was kept at 60 c and was increased up to 220 c with the speed of 5 c per minute and was stopped at 220 c for a period of 5 minutes. The detector was FID (Flame Ionization Detector) at 270 c and the carrier gas by the speed of 1ml per minute.

The features of GC/MS device

Agilent 6890 type of gas chromatograph with a column with 30 m length, internal diameter of 25% mm, layer thickness of ./25 micro m of HP-5MS type. The heat plan of the column was arranges as follows: the primary temperature of the oven was 50 c and the interval at this temperature was for a period of 5 m thermal gradient of 3 c at every minute and the rise of temperature up to 240 c by the speed of 15 degrees per minute and rise of the temperature up to 300 c and 3 minutes interval at this temperature. The injection room temperature was 290 c and helium gas was implemented as the carrier gas with the flow speed at. /8 mm per minute. The implemented Mass spectrometry was model Agilent 5973 with ionization voltage of 70 EV and the EI Ionization and the Ionization source temperature 220 c was implemented. The spectrum detection was done by the use of their retention indices and comparing with present indices in reference books and essays and by the use of mass spectrum of standard compositions and utilizing the available data at computer library [8].

RESULTS

The numbers recorded in vertical column of the chromatogram show the rate of frequency of constituent compositions of the essence and the horizontal column display the time of separation and identifying each of the essence constituent

compositions in the chromatography column (Fig.1).

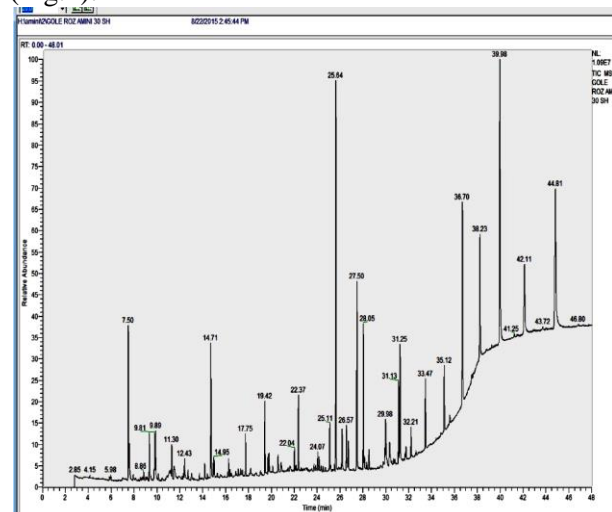


Fig1. Chromatogram of the essence of the Iranian rose flower (*Rosa persica*)

By considering the output pattern of normal alkanes and the comparison of the obtained mass spectrums from the GC-MS device with standard mass spectrums present in references it became precisely clear that each of the mass spectrums belong to what composition. In order to confirm the identification made by the mass spectrums the Kvats retention indices were implemented whose results are presented at Table 1. As it is evident from among the identified compositions the active ingredient of heptacosane with (11/6) has the highest percentage and after that stands isobutyl phthalate (11/48), nonacosane (8/88), dibutyl phthalate (6/26), pentacosane (5/96), hexadecanoic acid (3/95), linalool (3/8), ethyl linoleolate (3/73), hexyl hexoate (3/67), octacosane (3/43) are the main constituent compositions of this plant.

DISCUSSION

The study and analysis of the chromatogram and the obtained spectrums show the presence of 56 compositions. It was observed that the main part of the essence of the Iranian rose flower (*Rosa persica*) is composed of hydrocarbon compositions (alkanes). Alkanes are a group of aliphatic hydrocarbons which are totally saturated with hydrogen. The total formula for alkanes is (C_nH_{2n+2}) . Among the alkanes the highest percentage belongs to heptacosane. Heptacosane is a hydrocarbon composition as crystals with the formula $C_{27}H_{56}$ and is indivisible in water. This composition has the melting point of 60 degrees centigrade and the boiling point of 270 centigrade (at a pressure of 15 mm Hg). This composition is divisible in alcohol and it can be found in beeswax. Nonacosane is also a hydrocarbon colorless

composition with the formula $C_{29}H_{60}$ with melting point of 63 centigrade. This composition can be found in beeswax and the oil of cabbage leaves. [9] reported the chemical compositions of *Rosa damascene* essence. Among the detected compositions *linalool*, *geraniol*, *octadecane*, *nonadecane*, *geranyl acetone*, *heptadecane*, *tricosane*, *pentacosane*, *heptacosane* are similar to reported chemical compositions by the present study and at the same time the rate of *linalool* (3/8), *geranyl acetone* (0/24), *pentacosane* (5/11) confirms the obtained percentage by the

present study. Constituent components of different essences of rose (e.g. *R. persica*, *R. damascene*, *R. chinesis*, *R. rugosa*) are very close to each other and their antioxidant features and properties have been well proved [10]. Reports show that *Linanool* exists as the main ingredient of several species of aromatic plants that some of these plant species have disease treatment uses in traditional medicine [11] our research also clearly shows the presence of this chemical in chemical composition of the essence of *Rosa persica*.

Table-1 the identified constituents of the essence of the Iranian rose flower (*Rosa persica*)

No	Composition	Percentage	RI	No	Composition	Percentage	RI
1	Linalool	3.8	1098.7	29	Tetradecanal	1.87	1709.4
2	Nonanal	1.27	1102.7	30	Octyloctanoate	0.16	1776.7
3	Menthone	0.17	1155	31	Tetradecanoic acid, ethyl ester	0.42	1793.6
4	Menthol	1.51	1175.2	32	Octadecane	0.3	1798
5	Butyl caproate	0.19	1190.9	33	Hexahydrofarnesyl acetone	1.16	1844.8
6	Terpineol<alpha->	1.2	1194.2	34	Isobutyl phthalate	11.48	1870.9
7	Ethyl octanoate	1.28	1197.5	35	Nonadecane	1.03	1898
8	d-Carvone	0.61	1243.1	36	Butyl cyclohexyl phthalate	1.29	1917.6
9	Hexanoic acid, 3-methylbutyl ester	0.21	1247.9	37	Hexadecanoic acid, methyl ester	0.71	1925.9
10	Hexanoic acid, 2-methylbutyl ester	0.74	1250.6	38	Dibutyl phthalate	6.26	1965.8
11	Geraniol	0.81	1258.1	39	Hexadecanoic acid, ethyl ester	3.95	1994.3
12	Prenylhexanoate	0.43	1292.9	40	Hexadecyl acetate	0.14	2009.2
13	Undecanal	0.19	1303.9	41	Octadecanal	0.48	2020.7
14	2,4-Decadienal, (E,E)-	0.2	1316.1	42	Heneicosane	1.14	2098.9
15	Undecenal<2E->	0.39	1361	43	Methyl linolenate	0.47	2102.2
16	Hexyl hexoate	3.67	1382.3	44	Phytol	0.88	2118.2
17	Ethyl decanoate	0.47	1391.7	45	Ethyl linoleate	2.12	2162.4
18	Tetradecane	0.37	1394.9	46	Ethyl linoleolate	3.73	2169.1
19	Octanoic acid, isopentyl ester	0.4	1445.3	47	Ethyl octadecanoate	0.16	2193.4
20	Geranyl acetone	0.16	1450.2	48	Docosane	0.32	2197.8
21	Heptylhexanoate	0.16	1479.6	49	Eicosanal	0.73	2223.4
22	Tridecanal	1.04	1506	50	Tricosane	1.93	2297.1
23	Hexyl octanoate	1.87	1577.7	51	Tetracosane	1.87	2397.6
24	Lauric acid, ethyl ester	0.4	1590.1	52	n alkane	5.96	
25	Hexadecane	0.44	1594.4	53	n alkane	4.32	
26	Tridecanal	0.12	1607.6	54	n alkane	11.6	
27	Benzophenone	0.53	1629.5	55	n alkane	3.43	
28	Heptadecane	0.55	1693.8	56	n alkane	8.88	

REFERENCES

1. A. Ghahreman, Systematic Plant Chromophyts of Iran. Tehran University Publications, Volume 2, 1988.
2. J. Vlag, John, J. Studla, (2006). Herbal plants. Gognoos Publication, 7th edition, 2006.
3. R.P. Adams, Identification of Essential Oil Components by Gas Chromatography/ Quadrupole Mass Spectroscopy. Carol Stream, I11, Allured Pub. Corp., 3rd edition, 2004.
4. Cai YZ, Xing J, Sun M, Zhan ZQ, H. Corke, *J. Agric Food Chem.*, **53**, 9940 (2005).
5. E. Elisabetsky T.A. Amador, R.R. Albuquerque, D.S. Nunes, A.C. Carvalho, *J. Ethnopharmacol.*, **48**, 77 (1995).
6. A.R. Jassbi S., Zamanizadeh Najarib, S, Tahara, *J. Chem. Soc. Pakistan*, **25**, 323 (2003).
7. Y. Mikanagi, M. Yokoi, Y. Ueda, N. Satio, *Biochem. Systems Ecol.*, **23**, 183 (1995).
8. R. Nowak, *Acta Societatis Botanicorum Poloniae*, **74**, 229 (2005).
9. E. Rahimabadi, S.H. Sedagathoor, M. Qasemnejad, *Int. J. Biosci.*, **3**, 145 (2013).
10. M. Sayyah, L. Nadjafnia, M. Kamalinejad, *J. Ethnopharmacol.*, **94**, 283 (2004).
11. N. Yassa, F. Masoomi, S.E. Rohani Rankouhi, A. Hadjiakhoondi, *DARU*, **17**, 175 (2009).

Simultaneous quantitative analysis of inorganic anions in commercial waste-oil biodiesel using suppressed ion exchange chromatography

Fashe Li^{*1,2}, Zonghong Feng^{1,2}, Chengzhi Wang^{1,2}, Zhisong Liang^{1,2}, JinGao^{1,2}, Qingqing Wang^{1,2}, Jianhang Hu^{1,2}

¹Metallurgical Energy Conservation and Emission Reduction and New Energy Innovation Team, Kunming, 650093 Yunnan, China

²Faculty of Metallurgical and Energy Engineering, Kunming University of Science and Technology, Kunming, 650093 Yunnan, China

Received May 18, 2016; Revised September 10, 2016

Ion exchange chromatography was applied to simultaneous quantitative analysis of fluoride, chloride, bromide, nitrate, sulfate and phosphate anions in commercial waste-oil biodiesel. The extraction of the anions was carried out with deionized water using separation funnel. The observed limits of detection in $\mu\text{g}\cdot\text{mL}^{-1}$ were, respectively: fluoride 0.0012; chloride 0.0029; bromide 0.0116; nitrate 0.0089; sulfate 0.0094 and phosphate 0.0267. The observed amounts in $\text{mg}\cdot\text{Kg}^{-1}$ were, respectively: fluoride 1.714; chloride 8; phosphate 0.594; sulfate 1.773. The amounts of bromide and nitrate anions were lower than the limits of detection in all the studied samples and not detected. The method can be considered to be green because it uses small volumes of water, is simple, with fine recovery rates. Anions in biodiesel can be analyzed simultaneously by ion chromatography.

Key words: Ion exchange chromatography, Commercial waste-oil, biodiesel, Quantitative analysis, Inorganic anions, Separation funnel.

INTRODUCTION

Biodiesel is made from a diverse mix of feedstocks including recycled cooking oil, soybean oil and animal fats through a chemical process called transesterification. Biodiesel that meets strict technical fuel quality and engine performance specifications. Tests had shown that the addition of a small amount of biodiesel to diesel can significantly increase the lubricity of the fuel in short term [1]. However, over a longer period of time, studies showed that biodiesel loses its lubricity [2]. This could be because of corrosion over time due to oxidation of these anions.

Recently, G. Dugo et al. quantified the F^- , Cl^- , Br^- , NO_2^- , NO_3^- , PO_4^{3-} , SO_4^{2-} and I^- in commercial seed oils and virgin olive oils produced from de-stoned olives using suppressed ion exchange chromatography [3]. E.L.C. Silveira et al. determined simultaneously the acetate, formate, chloride, phosphate, and sulfate anions in biodiesel by ion chromatography, the extraction of the anions from the matrixes was performed using water with the assistance of ultrasound [4]. L.B. Caland et al. studied for the quantitative determination of sodium, potassium, calcium and magnesium inorganic cations in biodiesel samples [5]. Linlin Hu et al. determined the acetate, formate and propionate organic anions by ion chromatography [6]. Yi Zhang

et al. determined directly phosphate anion in raw *Jatropha curcas* oil by ion chromatography [7]. The content of phosphorus in biodiesel comes from the raw materials, such as seed oils and animal fats. The maximum concentration of phosphorus element allowed is $10\text{mg}\cdot\text{Kg}^{-1}$ according to the Brazilian norms, ASTM D6751 norms, DIN E 51606, ON C 1191, journal official, UNI10635 and SS 155436. However, the value according to the EN 14214 is $12\text{mg}\cdot\text{Kg}^{-1}$ and the CSN 65 6507 is $20\text{mg}\cdot\text{Kg}^{-1}$. The phosphorus compounds can inactivate the catalytic convertors of vehicles, increasing the ambient problem [8].

Like phosphorus, sulfur is also a typical poisonous catalyst and therefore can affect catalytic convertors [9]. Under China laws, the maximum sulfur concentration allowed is $10\text{mg}\cdot\text{Kg}^{-1}$. The regulated analytical methods is SH/T0689. Fluoride, chloride, bromide as the halogen elements have instability characteristics. Their presence can accelerate the corrosion of metals and can easily cause pitting [10-12]. Especially bromide, even at low concentration, can burn the surface, forming a rust corrosion. Bromide can also make sulfur dioxide oxidizing into sulfuric acid, and produce the liquid hydrobromic acid. It is fatal to the corrosion of the equipment. Therefore the application process must be paid attention to its prevention and control. In addition, the hydrogen fluoride gas biodiesel emitted is serious to our health. The maximum concentration of hydrogen fluoride allowable is 2

To whom all correspondences should be sent:
E-mail: asanli@foxmail.com

mg·m⁻³[13] in the air of workplace. A certain amount of nitrate anion is also corrosive to pipes, and with the increase of nitrate, sulfate and phosphate anions concentrations, the degree of corrosion of pipes is more severe. Therefore, simultaneous quantitative analysis of inorganic anions in commercial waste-oil biodiesel using suppressed ion exchange chromatography is extremely important [14].

Ion chromatography has been applied to a variety of matrixes, including water [15-17], environment [18], food [3, 19-24] and medicine [25-29]. However, despite its versatility, this technique is rarely used for the analysis of biodiesel. Considering the variety of biodiesel matrixes, the pretreatment procedures enjoy separation funnels and cleaner IC(C18) which are enough for the elimination of the organic matter that interferes the analysis. The aim of the present work was the simultaneous quantitation of anions in waste-oil biodiesel using this procedure and technique.

EXPERIMENTAL

Instruments

A Metrohm 883 Basic IC plus is operated with the Magic Net Basic software. The instrument equipped with a dialysis system and a high pressure pump. A Na₂CO₃ (3.2mmol·L⁻¹) and NaHCO₃ (1.0 mmol·L⁻¹) aqueous solution was used as the eluent. The volume of the sample loop was 20 μL, and the intelligent separation column is a Metrosep A Supp 5(4×150mm) IC anion column. Inline filters protect the separation column securely against possible contamination from the eluent.

Reagents, solutions and samples

Reagents. Fluoride, chloride, bromide, nitrate, sulfate and phosphate anions standard solutions were purchased from J&K (Beijing, China). The aqueous solutions were prepared with deionized water, ultrapure Type 1(18.2MΩ·cm⁻¹ at 25°C). Ultra-pure sulphuric acid (99%) was purchased from Aladdin(Shanghai, China), and used to prepare a 1.0mmol·L⁻¹ sulphuric solution for the regeneration solution of the MSM. Sodium carbonate and sodium hydrogen carbonate were of analytical grade and also purchased from Aladdin (Shanghai, China).

Solutions. All standard solutions were shook prior and then were pipetted adequate volumes of the individual solutions to the volumetric flask(marked 100mL) and diluting them with ultra-pure water to reach a final volume: fluoride(0.5; 1.0; 2.0; 4.0;10.0mg·L⁻¹),chloride(0.5; 1.0; 2.0; 4.0;10.0mg·L⁻¹), bromide(0.5; 1.0; 2.0;

4.0;10.0mg·L⁻¹), nitrate(0.5; 1.0; 2.0; 4.0;10.0mg·L⁻¹), sulfate(0.5; 1.0; 2.0; 4.0;10.0mg·L⁻¹) and phosphate(0.5; 1.0; 2.0; 4.0;10.0mg·L⁻¹). All of the standard solutions were kept tightly capped and stored in polyethylene flasks under the ambient.

Samples. The biodiesel samples prepared from waste cooking oil (WCO) was furnished by industry, and a two-step catalyzed process was adopted to prepare biodiesel [30].

Analytical procedures. Separation funnel assisted liquid-liquid extraction

For the chromatographic determination of inorganic anions, a 100ml aliquot of 400ml waste-oil biodiesel and 30ml of ultra-pure water were introduced in a separation funnel. The separating funnel is set aside to allow for the complete separation of the phases. When two layers share a surface, the top are then opened to allow pressure equalization between the inside of the funnel and the atmosphere and the lower phase namely the aqueous phase is released into a 200ml volumetric flask by gravitation. When the aqueous phase has been removed, the stopcock is closed. The upper layer, i.e. the oily one was extracted again with the same extraction durations as previously described. Aqueous phase was again recovered and added to the first extract, up to the mark with ultra-pure water, and the recoveries of all samples are 100% in this extraction method. This experiment found that the concentrations of individual analytes are highest when the extraction times were 5. The results were shown in Figure 1 which was obtained from the Origin software.

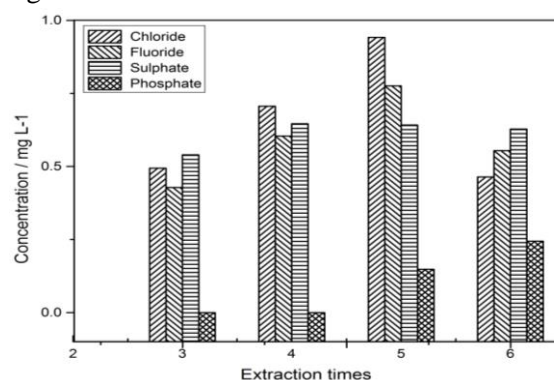


Fig. 1. The relation between extraction times and the concentration of individual analytes acquired by ion chromatography.

Assays for the spike-and-recovery

In order to verify the accuracy of the extraction process used, spike-and-recovery tests were performed by adding known concentrations of these six standard solutions to the biodiesel samples

prepared from the industry. And then by extractions and fixed the volume. Extractions were done as described above in section 2.3.1.

RESULTS AND DISCUSSION

Validation of the method

Important parameters for evaluating the determination methods are the linearity, the limits of detection, precision and accuracy.

Linearity

All standard solutions containing fluoride, chloride, bromide, nitrate, sulfate and phosphate anions were pipetted adequate volumes to the volumetric flask (marked 100mL) and diluting them with ultra-pure water to reach a final volume. The

experiment results were obtained in the Table 1, the calibration curves, $A = a + bQ$, were obtained by plotting the chromatographic peak area, the peak area is proportional to the amount of substance. The Y axis is the peak area A ($\mu\text{s}\cdot\text{cm}^{-1}\cdot\text{min}$) and the X axis is the concentrations, Q , of the analytes. The experimental correlation coefficients of the linear regression indicated a first order correlation in all analytes, Figure 2 which was exported from the IC software presented a chromatogram, the negative peak in the front of the chromatogram is the solvent peak and here is the water peak which will be contained in every chromatogram during this work.

Table 1. Linear equations of fluoride, chloride, bromide, nitrate, sulfate and phosphate anions. Analytic column: Metrosep A Supp 5(4×150mm), Eluent solution: Na_2CO_3 (3.2mmol·L⁻¹) and NaHCO_3 (1.0mmol·L⁻¹)

Anion	Concentration range (mg·L ⁻¹)					Analytical equation		r	RSD(%)
						A=a+bQ			
	a	b							
Fluoride	0.5	1.0	2.0	4.0	10.0	0.424145	0.138213	0.999987	0.062
Chloride	0.5	1.0	2.0	4.0	10.0	-0.409435	0.084848	0.999271	0.29
Bromide	0.5	1.0	2.0	4.0	10.0	-0.0610795	0.0202499	0.999805	0.036
Nitrate	0.5	1.0	2.0	4.0	10.0	-0.0468779	0.0228129	0.999792	0.042
Sulfate	0.5	1.0	2.0	4.0	10.0	-0.0256933	8.85E-03	0.99988	0.012
phosphate	0.5	1.0	2.0	4.0	10.0	-0.023412	0.0210993	0.999826	0.035

Table 2. The limits of detection (LOD) obtained for the chromatographic separation and determination of the studied anions in waste-oil biodiesel. Analytic column: Metrosep A Supp 5(4×150mm).Eluent solution: Na_2CO_3 (3.2mmol·L⁻¹) and NaHCO_3 (1.0 mmol·L⁻¹).

Anion	H _N (μS)	C ($\mu\text{g}\cdot\text{mL}^{-1}$)	H (μS)	V (μL)	C _{min} ($\mu\text{g}\cdot\text{mL}^{-1}$)
Fluoride	0.0025	0.5	1.731	20	0.0012
Chloride	0.0025	0.5	0.698	20	0.0029
Bromide	0.0025	0.5	0.173	20	0.0116
Nitrate	0.0025	0.5	0.224	20	0.0089
Sulfate	0.0025	0.5	0.075	20	0.0094
Phosphate	0.0025	0.5	0.212	20	0.0267

H_N-baseline noise peak-peak value, μS ; C-concentration of a standard solution, $\mu\text{g}\cdot\text{mL}^{-1}$;H-the chromatogram height of a standard solution, μS ; V-The volume of the sample loop, μL ;C_{min}-the minimum detection concentration, $\mu\text{g}\cdot\text{mL}^{-1}$

Table 3. RSD of the mean peak height values observed for the fluoride, chloride, bromide, nitrate, sulfate and phosphate anions.

Anion	The mean peak height value(μS)	RSD(%)
fluoride	28.044	0.062
chloride	16.713	0.290
bromide	4.008	0.036
nitrate	4.537	0.042
sulfate	1.750	0.012
phosphate	4.215	0.035

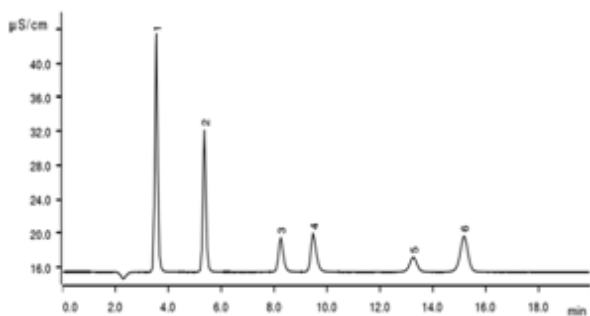


Fig.2. Chromatogram of the standard solutions. Peaks: (1) fluoride(9.992 mg·L⁻¹);(2) chloride(10.090 mg·L⁻¹); (3) bromide(10.046 mg·L⁻¹); (4) nitrate(10.047 mg·L⁻¹); (5) phosphate (10.035 mg·L⁻¹) and (6) sulfate (10.045 mg·L⁻¹).

The limits of detection

The limits of detection (LOD) is the minimum concentration of an analyte. According to the JJG 823-2014 Verification Regulation of Ion Chromatographs [31], LOD were calculated according to the following Formula 1 (The injection volume is 25µL).

$$C_{\min} = \frac{2H_N \times C \times V}{25H} \quad (1)$$

The limits of detection obtained from the proposed method in µg·mL⁻¹ were respectively: fluoride 0.0012µg·mL⁻¹; chloride 0.0029µg·mL⁻¹; bromide 0.0116µg·mL⁻¹; nitrate 0.0089µg·mL⁻¹; sulfate 0.0094 µg·mL⁻¹ and phosphate 0.0267µg·mL⁻¹. In all cases the observed LOD values were below 0.02 µg·mL⁻¹ that meets the performance indicators of IC Conductivity Detector. The obtained experimental results are shown in Table 2.

Precision. The precision was evaluated according to the repeatability and was expressed as relative

standard deviation (RSD). The chromatography parameter, the peak height values of the analyses were studied to evaluate the repeatability. A standard solution (10mg·L⁻¹) containing these studied anions was analyzed eight times by consecutive injections into the chromatograph. The mean values obtained for the peak height of the analyses and their RSD values were analyzed and shown in Table 3. It can be concluded that the method presents good repeatability because in all cases the observed RSD values were below 1%.

Accuracy

The accuracy of the proposed extraction method was evaluated through the spike-and-recovery tests. Waste-oil biodiesel samples were spiked with two different concentrations of standard solutions. All samples were filtered through cleaner IC-C18 before IEC analysis. Recoveries were calculated according to the Formula 2 obtained from analysis:

$$\text{Recovery} = \frac{\text{Found} - \text{Initial}}{\text{Added}} \times 100\% \quad (2)$$

The effect of frequency of liquid-liquid extractions was studied and the obtained results from the experiments were given in Table 4.

The biodiesel samples presented recoveries spanned from 78.4% to 110%(Table 4), indicating that the suggested extraction method was sufficiently efficient to remove the anions in the complex matrixes. Currently, in analytical procedures, recovery percentages in the range from 70 to 120% are accepted. However, depending on the complexity of matrix, this range can be extended from 50 to 120%[32].

Table 4. Recoveries of the fluoride, chloride, nitrate, sulfate anions in waste-oil biodiesel by ion chromatography.

Anion	Concentration (mg·L ⁻¹)			Recovery(%)
	Initial	Added	Found	
Fluoride	0.756	0.7	1.4077	93.1
		1.4	2.0944	95.6
Chloride	3.53	3.0	6.488	98.6
		6.0	9.188	94.3
Bromide	ND	0.1	0.089	89
		0.2	0.199	99.5
Nitrate	ND	0.2	0.22	110
		0.4	0.4068	101.7
Sulfate	0.782	0.8	1.5132	91.4
		1.6	2.2348	90.8
Phosphate	0.262	0.3	0.4972	78.4
		0.6	0.8038	90.3

ND=not detected

Analysis of the biodiesel samples

Aliquots of the biodiesel samples were analyzed by IEC after aqueous extraction according to the method described above. In all of the samples, the anions concluding fluoride, chloride, phosphate, sulfate were detected. The ion chromatographic results from this work were listed in Table 4. Figure 3 which was exported from the IC software presented the chromatogram for the waste-oil biodiesel samples purchased from the industry.

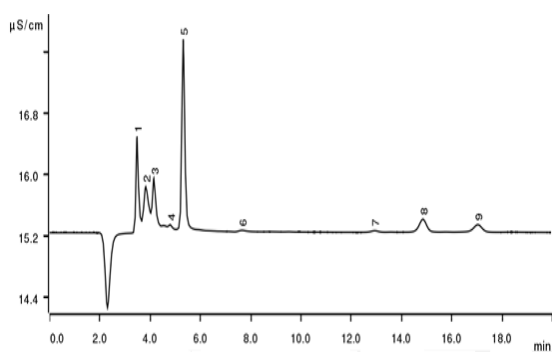


Fig. 3. Chromatogram of the aqueous extract of the biodiesel prepared from waste-oil biodiesel.

Peaks:

(1)fluoride($0.756\text{mg}\cdot\text{L}^{-1}$);(5)chloride($3.53\text{mg}\cdot\text{L}^{-1}$);(7)phosphate($0.262\text{mg}\cdot\text{L}^{-1}$);(8)sulfate($0.782\text{mg}\cdot\text{L}^{-1}$);(2,3,4,6,9):not spiked analyses

A blank experiment was done in order to verify the impact of deionized water used above on the experimental results. It found that no analyte is detected. It is also indicated that the deionized water has no effect on the study. Therefore, this work is successful and makes sense. Figure 4 which was exported from the IC software presented the chromatogram of the blank experiment.

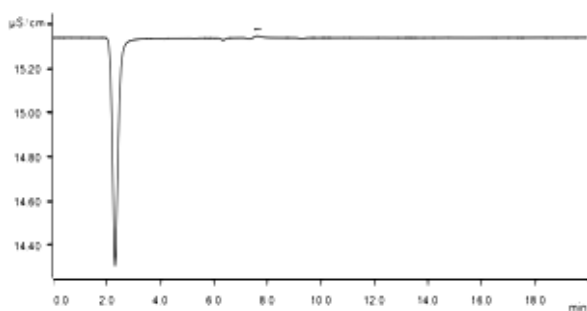


Fig.4. Chromatogram of deionized water used above in the extraction procedure. (1):not spiked analytes.

CONCLUSION

In this work, the liquid-liquid extraction procedure with water proposed was shown to be efficient. According to the results, Sulfate anion has the highest concentration in all of the samples from the industry, this may be responsible for using the

ferric sulfate in the first step of producing biodiesel. Chloride anion also presented a relatively high concentration in comparison to the other analytes acquired, it may result from the edible salt in waste-oil biodiesel. All of the analyzed samples presented low concentrations of fluoride and phosphate. Considering concentrated hydrohalic acid solutions produce visible white fumes, so this method is free from ultrasound heating for keeping from HF, HBr and HCl volatilizing, which may affect the experimental results greatly. The increasing use of biodiesel around the world implies a necessity to control the quality of this product. Therefore, the development of new and reliable analytical methods is necessary.

Acknowledgements: The authors are grateful for the support of the Project by the Special Preliminary Research of 973 Plan (2014CB460605), the General Projects of Natural Science Foundation of Yunnan Province (2015FB128) and the Doctoral Foundation of the Ministry of Education (KKQX201352004).

REFERENCES

1. H.H. Masjuki, M.A. Maleque, *J. Wear*, **198**, 293 (1996).
2. J. Hem, R.M. Bryan, T. Joe, W. Terry, *J. Biomass Bioenerg*, **34**(1), 14 (2010).
3. G. Dugo, T.M. Pellicano, L.L. Pera, V.L. Turco, Tamborrino A, M.L. Clodoveo, *J. Food Chem.*, **102**, 599 (2007).
4. E.L.C. Silveira, L.B. Caland, M. Tubino, *J. Fuel*, **124**(10), 97 (2014).
5. L.B. Caland, E.L.C. Silveira, M. Tubino, *J. Anal. Chim. Acta*, **718**(5), 116 (2012).
6. L.L. Hu, X.W. Rong, *J. Guangdong Chemical Industry*, **36**(7), 220 (2009).
7. Y. Zhang, P. Thepsithar, X. Jiang, J.H. Tay, *J. Ind. Crop Prod*, **44**(2), 459 (2013).
8. L.P. Li, J.G. He, *J. China Oils & Fats*, **39**(8), 52 (2014).
9. S.J.X. Guo, *J. Automotive Safety and Energy*, **4**(2), 161 (2013).
10. X.J. Li, Y.Z. Wang, M.Z. Yue, S.F. Bian, C.Lu, *J. Power System Engineering*, **27**(6), 13 (2011).
11. L. Niu, X. Chen, *J. Shandong Univ*, **31**(2), 190 (1996).
12. W.J. Li, R.T. Zhu, H.M. Zheng, C.P. Liu, *J. Shanxi Univ*, **36**(4), 609 (2013).
13. M.H. Zhou, H.P. Liu, W.S. Xu, *J. Chemical Fertilizer Design*, **49**(2), 39 (2010).
14. S. Cordiner, V. Mulone, M. Nobile, V. Rocco, *J. Enrgy Proced*, **61**, 953 (2014).
15. C. Lopez-Moreno, I. Viera, A.M. Urbano. *J. Desalination*, **261**, 111 (2010).
16. B.M. De Borba, R.F. Jack, J.S. Rohrer, J. Wirt, D. Wang, *J. Chromatogr*, **1369**, 131 (2014).
17. Q. Subhani, Z.P. Huang, Z.Y. Zhu, L.Y. Liu, Y. Zhu, *J. Chinese Chem. Lett*, **25**, 415 (2014).
18. P. Cheng, Y.F. Cheng, K.D. Lu, H. Su, Q. Yang, Y.K. Zou, Y.R. Zhao, H.B. Dong, L.M. Zeng, Y.H. Zhang, *J.*

- Environ. Sci*, **25**(5), 895 (2013).
19. H.B. Zhu, Y.C. Fan, Y.L. Qian, H.F. Tang, Z. Ruan, D.H. Liu, H.Wang, *J. Chinese Chem. Lett*, **25**, 465 (2014).
20. P.L. Buldini, S.Cavalli, A.J.L. Mevoli, *J. Food Chem*, **73**, 487 (2001).
21. P.L. Buldini, D. Ferri, J.L. Sharma, *J. Chromatogr. A*, **789**, 549 (1997).
22. S.D. Kumar, G. Narayan, S. Hassarajani, *J. Food Chem*, **111**, 784 (2008).
23. K. Yoshikawa, Y.Uekusa, A.Sakuragawa, *J. Food Chem*, **174**, 387-391(2015).
24. H.Z. Wang, F.J. Xia, Y.F. Zhao, Q. Han, M.X. Guo, H. Wang, Y.M. Ding, *J. Chinese Chem. Lett*, **24**, 243 (2013).
25. M. Zaveckas, S. Snipaitis, H. Pesliakas, J. Nainys, A. Gedvilaite, *J. Chromatogr.B*, **991**, 21 (2015).
26. Y.Z. Zhang, Y.C. Zhou, L. Liu, Y. Zhu, *J. Zhejiang Univ. Sci B*, **8**(7), 507 (2007).
27. P.J. Xie, M.L. Ye, Z.Y. Hu, G.W. Pan, Y. Zhu, J.J. Zhang, *J. Chinese Chem. Lett*, **22**,1485 (2011).
28. Błazewicz, M. Klatka, W. Dolliver, R. Kocjan, *J. Chromatogr. B*, **962**, 141 (2014).
29. H.W. Wu, M.L. Chen, D. Shou, Y. Zhu, *J. Chinese Chem. Lett*, **23**, 839 (2012).
30. Z.Z. Cai, Y. Wang, Y.L. Teng, K.M. Chong, J.W. Wang, J.W. Zhang, D.P. Yang, *J. Fuel Process Technol*, **137**, 186 (2015).
31. <http://www.doc88.com/p-9045754466267.html>.
32. A.G.González, M.A.Herrador, A.G.Asuero, *Talanta*, **48**, 729 (1999).

Pre-concentration, speciation and determination of As and Sb by optimized experimental design DLLME combined with GF-AAS

A.Gholami*, H. Noorizade

University of Kashan, Faculty of Chemistry, Department of Analytical Chemistry, Kashan, P.O. Box 87317-51167
Islamic Republic of Iran

Received June 26, 2015; Revised September 10, 2015

Determination of heavy metals is more important than past with the increasing their concentration in environment. Arsenic and Antimony have various forms in nature but only some forms of them are toxic. Speciation of them is impossible with common atomic absorption spectroscopy procedure. Dispersive liquid-liquid microextraction has been used for speciation includes complex formation with special ligands, extraction in organic phase and then determination with atomic absorption spectroscopy. Many factors effect on dispersive liquid- liquid microextraction procedure such as volume of disperser solvent, volume of extraction solvent, concentration of chelating agent, coexisting ions, time of extraction, pH, sample volume and salting out effect. All factors were optimized by experimental design and optimum values obtain for each other. Under the optimum condition the enrichment factor equal to 187 and detection limit 0.02 and 0.4 μgL^{-1} was obtained for Arsenic and Antimony respectively.

Keywords: DLLME, Experimental design, Speciation, Arsenic, Antimony

INTRODUCTION

Arsenic (As) and antimony (Sb) are two toxic elements that often have two oxidation states and are included in many inorganic and organic species with different physicochemical properties. Inorganic species of As and Sb are more toxic than organic species and were found in ground and surface water. Toxicity of As (III) and Sb (III) are 10-20 times more than As (V) and Sb (V) and cause several type of cancers.[1-2]

Arsenic was utilized as poisons, insecticides and wood preservatives in vast level. It is banned or limited in some fields however is used in many of others [3]. Antimony causes headaches, dizziness, and depression. Large doses of antimony such as prolonged skin contact may cause dermatitis, damage the kidneys and the liver, cause violent and frequent vomiting, and lead to death in a few days [4].

For finding sufficient information about toxicity and biotransformation of these elements, it is enough not only to determine the total concentration of them but also to speciation their species, and it is necessary to determine their concentration of each oxidation states.

Inductively coupled plasma atomic emission spectroscopy (ICP-AES) [5], inductively coupled plasma mass spectrometry (ICP-MS) [6-7] electrothermal atomic absorption spectrometry (ET-AAS) [8] and hydride generation atomic absorption

spectrometric (HG-AAS) [8-9-10] have been suggested as the sensitive and powerful analytical techniques for these kind of determinations. Today all of the mentioned analytical instrument can analyzed samples quickly by acceptable accuracy and precision, but because of the trace amounts of these elements in surface water and the importance of trace analysis of toxic species usually a preparation and pre-concentration step is needed before instrumental analysis.

Sample preparation and pre-concentration are very important for trace elements analysis especially in terms of sample cleaning and time consuming. Also, it has been observed that lower limit of detection is obtained with complete separation of analyte. The purpose of sample preparation is the interfering compounds elimination and the sensitivity enhancement. The classic liquid- liquid extraction (LLE) method is time consuming, prone to contamination and includes several steps. The new methods of extraction solve very problematic defects of LLE. Among different advanced LLE methods, dispersive liquid- liquid microextraction (DLLME) has been categorized as a developed liquid phase microextraction method (LPME) and advantages of it are as following: rapidness, low cost, simplicity or easy to operation, solvent free or solventless, miniaturized sampling devise and high enrichment factor [11]. A constant and repeatable sediment phase in each test is one of the most important points in DLLME. In addition, this method can eliminate some main disadvantages of LPME, for example elements and their species with weak partial coefficient by diffusion process cannot

To whom all correspondence should be sent:
E-mail: Agholami@kashanu.ac.ir

be extracted in LPME, but in DLLME by choosing strategy of complex formation and derivation coupled with atomic spectroscopy (include ICP and AAS) and its relative methods can determine trace or ultra-trace elements in real samples including environmental and biological samples. A disadvantage of all of LPME methods including DLLME is that these methods need to sample preparation for determination of elements in complex matrix such as blood, milk and other biologic samples. Therefore, almost most of determination by LPME method is carried out in simple matrix such as water solutions. Also, aqueous samples with high salt content such as sea water have a low enrichment factor.

Some affecting parameters on extraction process that must be optimized are: volume of extraction solvent, concentration of chelating agent, coexisting ions, time of extraction, pH, sample volume and salting out effect. One method for obtaining the best condition is using experimental design method whose goals are as follows: (1) Investigation the effect of different factors can influence on enrichment factor in the extraction procedure. (2) Identification of the factors that have higher impact on the extraction results. (3) Obtaining a better insight about the method that helps us to find optimized conditions considering the interactions between factors [12].

This study has focused on speciation and determination of As and Sb species using DLLME as an extraction and pre-concentration step followed by ETAAS method. To achieve the best results, the optimized conditions of DLLME have been obtained by using experimental design methods. Two experimental design methods called Plackett-Burman and Box-Behnken design has been applied in this work. Performing this method ensures us about achieving maximum efficiency and sensitivity of DLLME for determination and speciation of As and Sb by DLLME-ETAAS.

Literatures have suggested some compounds as the matrix modifier such as Mg, Pd, Ni and some other ones [13]. But it is including two injection solutions, first one is extracted organic phase and second one is aqueous solution involve matrix modifier. Other way is using long-term permanent chemical modifier. In this method salt of W, Ir and Mo was considered for the modification purpose [14]. Using sodium tungstate as a modifier and pyrolysing in 400 °C lead to well defined absorbance time and low background effect. Chemical modification of graphite furnace with sodium

tungstate has impressive enough for over analysis. Effect of atomization temperature is considered in 1600-2200°C. There is no significant difference between analyte signals. However time-absorbance profile disturbed to noise below 1700 °C. So 1900 and 2000 °C are chosen for As and Sb respectively [14].

EXPERIMENTAL

Reagents and chemicals

All used reagents were of analytical grade purity purchased from Merck (Germany). Stock solution of arsenic (1000 mgL⁻¹) was prepared by dissolving 1.32 g As₂O₃ in KOH 20 % and neutralized by H₂SO₄ 20 % and then diluted to 1 L. Stock standard solution of antimony was prepared by dissolving 2.743 g of potassium antimonyl tartrate hemihydrates in ultrapure water. Working standard solutions were prepared daily by stepwise diluting of stock standard solutions.

Ammonium pyrrolidine-dithiocarbamate (APDC) was dissolved in methanol as the chelating agent (0.2 gL⁻¹). Methanol and carbon tetrachloride were used as the disperser and the extraction solvents, respectively. Sodium thiosulphate was employed as the reduction agent to reducing of pentavalent species of As and Sb.

Apparatus

An atomic absorption spectrometer (Unicam AA929) equipped with continuous source background correction (deuterium lamp) and graphite furnace atomizer (GF90) were employed. Hollow cathode lamps were utilized as the radiation source for each elements. Instrumental parameters for arsenic and antimony are shown in Table 1. The pH was measured by using a pH meter (Metrohm 691 pH meter).

Preparation of graphite furnace which no need to matrix modifier

In this study, sodium tungstate was employed as the permanent matrix modifier. Cuvettes were immersed in 100 ml of a solution containing 1 gL⁻¹ Na₂WO₄·2H₂O for 12 h. After this time cuvettes were dried in 120 °C for about 4 h. Then tubes were installed on instrument and submitted to the temperatures 120, 200, 1200 and 2400 °C for 120, 120, 30 and 6 seconds, respectively, as conditioning temperature program of graphite atomizers.

Table 1. Instrumental parameters for arsenic and antimony

Instrumental parameters		Arsenic	Antimony	
Lamp current (mA)		(As HCL)	(Sb HCL)	
Wavelength (nm)		193.7	217.6	
Bandwidth		0.5	0.5	
Atomizer type		Electrographite	Electrographite	
Injected sample volume (μL)		20	20	
Background correction		D ₂	D ₂	
Furnace heating program				
Step	Temperature As ($^{\circ}\text{C}$)	Temperature Sb ($^{\circ}\text{C}$)	Hold (S)	Ramp ($^{\circ}\text{C.S}^{-1}$)
Dry	120	120	30	10
pyrolysis	1200	1200	20	50
Atomization	2600	2200	3	0
Clean	3100	2700	5	0

DLLME procedure

A sample solution containing desired analytes was adjusted in appropriate pH and placed in conical bottom propylene test tube. Then extraction and disperser solvents contain concentration of ligand was rapidly injected into the sample solution and then cloudy solution was centrifuged to remove sedimented extraction phase at the bottom of conical test tube and finally, it was placed in the graphite furnace cuvette by using a 20 microlitre Hamilton syringe to analyze.

RESULTS AND DISCUSSION

Optimization step

Some factors have influenced on determination of As and Sb and should be optimized. Therefore, enrichment factor (EF) was chosen as an analytical response under different conditions.

The enrichment factor as a response is defined in Eq. (1):

$$EF = \frac{C_{\text{sed}}}{C_0}, \quad (1)$$

Where, EF is enrichment factor and C_{sed} and C_0 are analyte concentration in sedimented phase and primary analyte concentration in aqueous phase, respectively. C_{sed} was obtained from conventional LLE-ETAAS calibration curve (extraction condition: 10 ml of standard water sample, 0.2 g L^{-1} APDC, 10 ml CCl_4 and pH at 3.1).

Extraction and disperser solvent type

Type of extraction solvent is very important and critical in DLLME process. Extraction solvent should has some properties including, density more than water, low solubility in water, low volatility, able to formed cloudy solution, able to analyte

extraction and no interfering with analyte determination technique. Accordingly, to optimize the extraction solvent, several solvents such as chloroform, carbon tetrachloride and dichloromethane were considered and according to fig. 1 chloroform was selected as extraction solvent.

Another important variable in DLLME is disperser solvent type. Disperser solvent should has some properties including, soluble in aqueous and organic phase, low toxicity, low cost and high analyte signal. Methanol, tetra hydro furan (THF), acetone, acetonitrile were tested to obtain the highest analyte signal, or in other hand to obtain the highest EF. In addition, any possible combination of extraction and disperser solvents was examined and finally, methanol was selected as disperser solvent because it shows the highest enrichment factor according to the results shown in fig. 1.

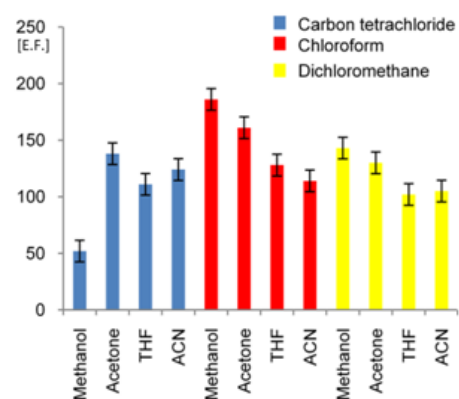


Fig. 1 Selection of extraction and disperser solvent. Methanol, tetra hydrofuran (THF), acetone, acetonitrile (ACN) were tested for highest analyte signal or in other hand to obtain highest EF.

Experimental design. Plackett burman design

Many factors effect on DLLME such as volume of extraction solvent (A), volume of disperser

solvent (B), concentration of chelating agent (C), coexisting ions (D), time of extraction (E), pH (F), sample volume (G) and salting out effect (H). The experimental design method was employed for optimization of these parameters [14]. Placket burman design is a kind of screening tools that can be reduced the number of factors by examining their main effects. In this work, a low and a high value were selected for every possible effective factors and a placket burman design with 12 run was constructed to find out main parameters ignoring their interactions. The main effects are determined based on ANOVA results. The normalized obtained results were analyzed by standardized pareto chart at 5% significance, as shown in fig. 2. The standard effect was estimated for computing the t statistic for each effect. The bars that are extended beyond the vertical line are significant at the 95% confidence limit statically. Some factors have positive rules and they increase signal by increasing their value and some factors have negative rules inversely, they are shown in hatched and smooth bars in fig. 2, respectively. As shown in fig. 2, extraction solvent volume is most effective factor with a negative rule. It's clear that because the concentration of analyte in sedimented phase will be decreased by increasing in extraction solvent volume, it has a negative rule. The next significant important having a negative effect is disperser solvent volume, because the obtained volume of sedimented organic phase will be decreased by increasing this factor and result shows that by using more than 1ml of disperser solvent volume, no sedimented phase was obtained. It is appeared that pH has a negative rule. It is because of the fact that complex formation is strongly a pH depending process and in high pH values almost complex formation is terminated. According to pareto chart, sample size has a positive effect because when this factor is passing to higher value, there is more analyte amount in sample for extraction process and it leads to a higher enrichment factor. Ligand concentration has a positive effect; its influence was investigated in the range of 0.05-0.5 gL⁻¹ and results show that the enrichment factor increases until 0.2 gL⁻¹ of ligand concentration, up to this value no significant change is observed in enrichment factor. Coexisting ion that has a negative effect was surveyed according to Table 2 for 1µgL⁻¹ of analytes. Both of time and salting effect parameters have positive and not very significant effect. Commonly, extraction time is one of the most important factors in the extraction procedure. In DLLME, extraction time is defined as the time between injecting the mixture of disperser and extraction solvents, and starting to centrifuge [15],

but in DLLME experiments show that extraction time has no effect on extraction efficiency. It has been illustrated that this founding due to the very large contact surface between the extraction solvent and aqueous phase, which it is consequence very rapid process of complexation and extraction.

Table 2: Tolerance limit of some coexisting ion

Ion	Tolerance limit C _{ion} /C _{Analyte}
Na ⁺	100000
K ⁺	60000
Ca ⁺	5000
Mg ²⁺	5000
Fe ³⁺	100
Cu ²⁺	1000
Zn ²⁺	200
Cl ⁻	100000
NO ₃ ⁻	60000
SO ₄ ²⁻	12000

For salting addition had been seen two effects as follows: Increasing in extraction solvent volume causes a reduction in enrichment factor and salting-out effect causes an increase in enrichment factor.

Considering the result of placket burman design, four variables were fixed at suitable values (chelating agent concentration of 0.2 gL⁻¹, salting addition 2 gL⁻¹, no extra time and no coexisting ion)

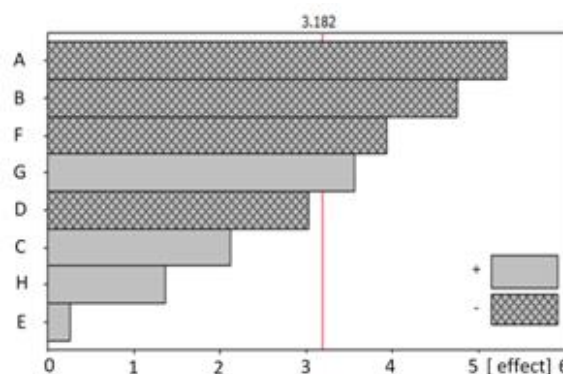


Fig. 2 Standardized (P = 0.05) Pareto chart, representing the estimated the most effective parameters, volume of extraction solvent (A), volume of disperser solvent (B), concentration of chelating agent (C), coexisting ions (D), time of extraction (E), pH (F), sample volume (G) and salting out effect (H).

Central composite design

After finding the main significant variables, next step is using a Box-Behnken experimental design to optimize four factors (pH, volume of extraction solvent, volume of disperser solvent and sample size) that are selected from plackett burman results. The optimized step can be expressed as Eq. (2) that is a second order polynomial fit, where, y is EF, b₀ is the intercept, b₁-b₁₄ are regression coefficients that

will be calculated by multivariate linear regression (MLR) techniques and x_1-x_4 are desire factors that

must be optimized. The number of run with 4 central points is 28.

$$y = 121.000 - 7.66667V_{dis} + 22.08333V_{ex} + 34.1667V_s - 31.4167pH - 18.6667 V_{dis}^2 - 19.5417 V_{ex}^2 + 3.58333V_s^2 - 33.0417pH^2 + 7.50000V_{dis} \cdot V_{ex} - 15.0000V_{dis} \cdot V_s - 22.0000V_{dis} \cdot pH - 6.25000V_{ex} \cdot V_s + 12.5000 V_{ex} \cdot pH - 3.75000 V_s \cdot pH \quad (2)$$

With R^2 value = 0.9 that is acceptable in 95% confidence limit, three dimensional plots called response surface also were prepared that show the relation between two variables and the response (EF). Six surface plots that can be explained the optimal condition are shown in fig. 3. Using obtained result the optimal condition was calculated as followings:

Volume of extraction solvent (V_{ex}): 31 μ L, volume of disperser solvent (V_{dis}):730 μ L, pH: 3.1 and sample size volume (V_s):10 mL.

Extraction in optimized conditions leads to improvement in performance of extraction procedures and obtaining higher sensitivity.

Determination of As and Sb

For determination and speciation of As and Sb, six series of water solutions were prepared including,two series solutions of As(III) and As(V) at 0.2, 0.4, 0.6, 0.8 and 1 μ g L^{-1} , andtwo series solutions of Sb(III) and Sb (V) solutions at 1.4, 1.6, 1.8 and 2 μ g L^{-1} and two series of solutions for their mixtures.

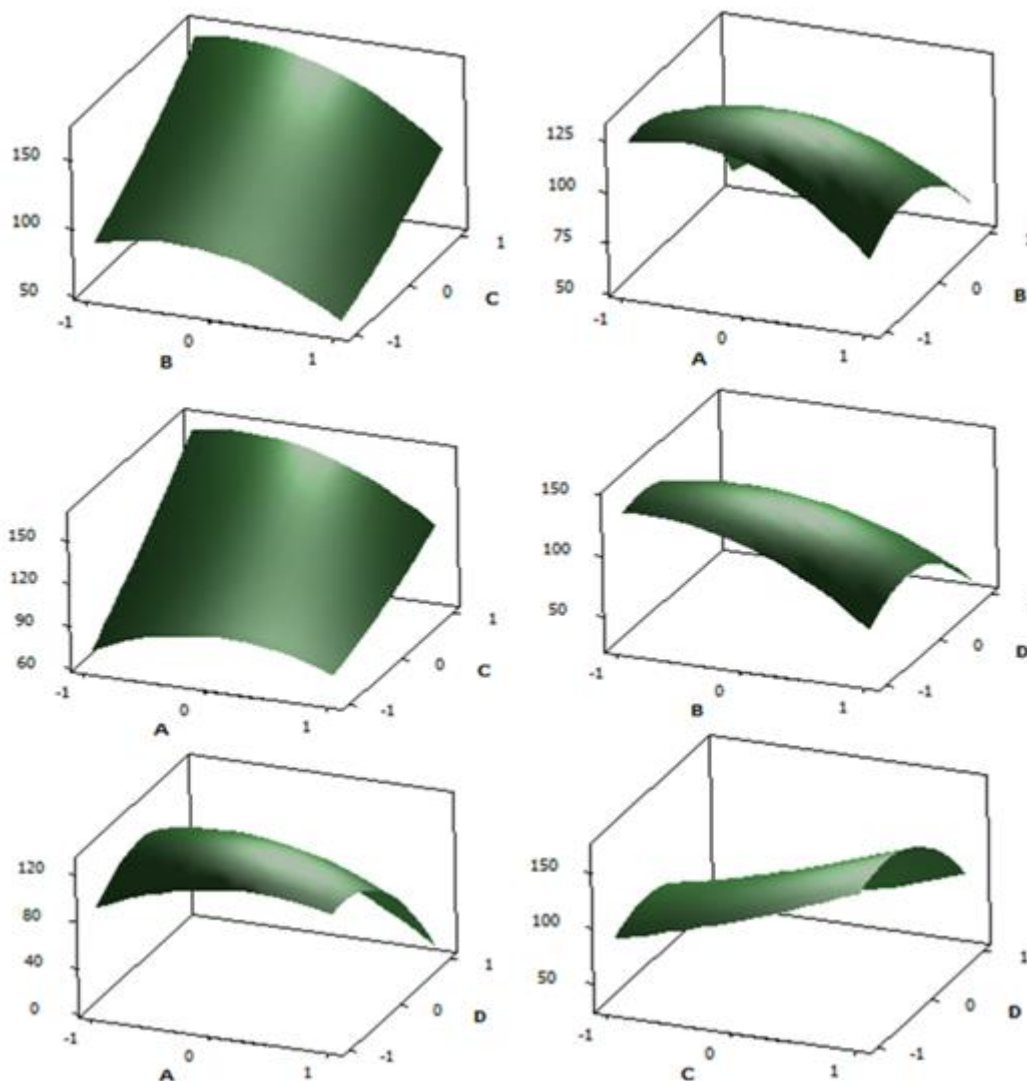


Fig. 3. Six surface plots that can be explained the optimal condition.

Table 3. Comparison of some reported determinations

Method	Analyte	Detection Method	Sample volume	Enrichment factor	Detection limit, μgL^{-1}	Reference
CPE	Sb	FI--ICP	100	872	0.09	[16]
CPE	Sb	FAAS	10	45	1.82	[17]
SPE	Sb	ETAAS	10	25	0.18	[18]
SPE	Sb	ETAAS	100	60	0.14	[19]
LC	Sb	SFIHGAAS	20	10	0.06	[20]
SDME	Sb	ETAAS	5	96	0.008	[21]
DLLME	Sb	ETAAS	5	115	0.05	[22]
DLLME	Sb	ETAAS	10	187	0.02	This work
CPE	As	ETAAS	10	53	0.01	[23]
SPE	As	FI-HGAAS	20	10	0.05	[24]
LLE	As	FI-HGAAS	250	33	0.008	[25]
LC	As	ICP-AES	3	200	0.15	[26]
LPE	As	ETAAS	1.8	150	0.05	[27]
Anion exchange resin	As	ICP-AES	20	10	0.1	[28]
DLLME	As	ETAAS	5	115	0.01	[22]
DLLME	As	ETAAS	10	187	0.004	This work

Table 4. Figure of merit.

Characteristic	Sb(III)	As(III)
Working range, μgL^{-1}	0.4-4	0.2-2
Enrichment factor	187	187
Sample size, ml	10	10
0.2 gL^{-1} APDC in methanol, ml	0.730	0.720
Carbon tetrachloride, ml	0.03	0.5
Detection limit ($3s$) ^a , μgL^{-1}	0.04	0.02
Precision (RSD, n=7), %	3.5	3.2
Calibration function (5 standard, n=3, μgL^{-1})	$A_{\text{int}}=0.005 + 0.138C_{\text{Sb}}$	$A_{\text{int}}=0.012 + 0.236C_{\text{As}}$
Correlation coefficient	0.9994	0.9991

a Calculated on the basis of three times the standard deviation for 10 replications of the blank

Since arsenic (V) and antimony (V) do not react with APDC and therefore, they do not extracted in sedimented phase, the absorbance signals of the solutions that are containing only arsenic (V) and antimony (V) are almost equal to zero (fig. 4A(a) and 4B(a)). The results of absorbance signal are different for As(III) and Sb(III) solutions because they can extracted by APDC easily. fig. 4A(b) and 4B(b) show the obtained signals for these two solutions.

The same results have been perceived for the mixtures of As and Sb species (fig. 4A(c) and 4B(c)). Theoretically if the Sb(V) and As(V) in mixture solutions were reduced to Sb(III) and As(III) by a reduction agent, the absorbance signal height must be increased. In this work, this fact was confirmed by the reduction of pentavalent species of these two elements using sodium thiosulphate (0.4M). According to result shown in fig.4A(d) and fig. 4 B(d), an obvious increase in signal intensity of mixture solution is observed after reduction. Total amounts of As and Sb were determined after reducing the pentavalent species by sodium thiosulphate (0.4M). Then, penta-valent

concentration was obtained from difference between trivalent and total amount of them. Results show that pentavalent concentrations equal to added values. In optimized condition, calibration curve is linear in the range of 0.2-2 μgL^{-1} for As according to $A_{\text{int}}=0.012 + 0.236C_{\text{As}}$ by $R^2=0.9991$. Also, Sb regression equation is $A_{\text{int}}=0.005 + 0.138C_{\text{Sb}}$, and it is linear in the range of 0.4-4 by $R^2=0.9994$, other detailed result of this method is listed in Table 3.

In Table 4, this method has been compared with other speciation methods of As and Sb in literatures. In comparison with other methods, pre-concentration using DLLME followed by ETAAS method has considerable low LOD and high enrichment factor. Other features of this method are low cost, fast, simple and no requirement of further instruments and can be used as a alternative techniques to more expensive determination and speciation methods of As and Sb in trace levels.

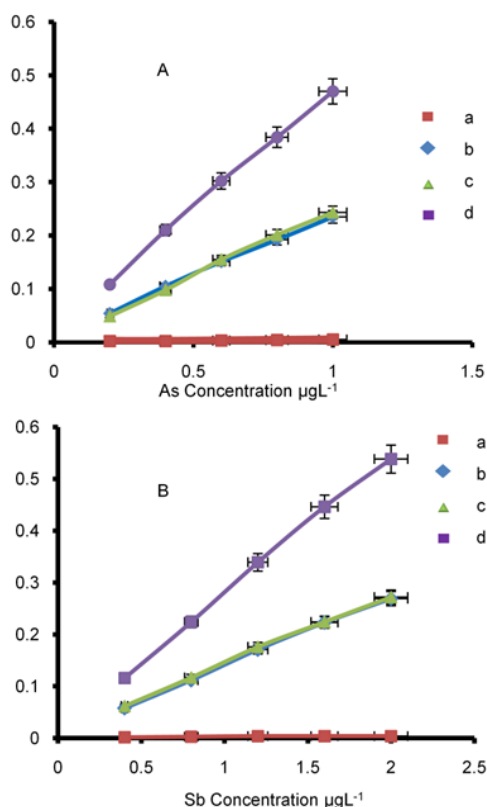


Fig. 4 Absorbance signal of the solutions that containing: pentavalent arsenic (A(a)), pentavalent antimony (B(a)), trivalent arsenic (A(b)), trivalent antimony (B(b)), mixture solution of trivalent and pentavalent arsenic (A(c)), mixture solution of trivalent and pentavalent antimony (B(c)), mixture solution of trivalent and pentavalent arsenic after reduction (A(d)), mixture solution of trivalent and pentavalent antimony after reduction (B(d)).

CONCLUSIONS

In current study, employing of experimental design caused to increasing the enrichment factor by the unfolded factor optimum values. On the other hand, LOD was decreased and determination of analytes was possible in lower level of concentration. A comparison of this method with some other methods shows that DLLME has a higher enrichment factor, lower LOD, lower sample and organic solvent consumption and shorter extraction time (less than 3 min). In addition, this method is a simple, low cost, and reproducible technique and with no need to further instrumentation. Therefore, the represented method is proposed as a proper alternative to more expensive instrument for determination of trace amount of As and Sb.

Acknowledgements: Authors are grateful to the Council of the University of Kashan for providing

financial support to undertake this work.

REFERENCES

1. Compounds W. A., Environmental Health Criteria 224, World Health Organisation, Geneva, 2001.
2. R. Poon, I. Chu, P. Lecavalier, V. Valli, W. Foster, S. Gupta, B., Thomas, *Food Chem. Toxicol.*, **36**, 21 (1998).
3. S. C. Grund, K. Hanusch, H. U. Wolf, Arsenic arsenic compounds, Ullmann's Encyclopedia of Industrial Chemistry, 2005.
4. S. Sundar, J. Chakravarty, *Int J Environ Res Public Health*, **7**, 4267 (2010).
5. J. M. Costa-Fernández, F. Lunzer, R. Pereiro-García, A. Sanz-Medel, B. N. ordel-García, *J. Anal. At. Spectrom.*, **10**, 1019 (1995).
6. X.-P. Yan, R. Kerrich, M. J. Hendry, *Anal. Chem.*, **70**, 4736 (1998).
7. C. Yu, Q. Cai, Z.-X. Guo, Z. Yang, S. B. Khoo, *Analyst*, **127**, 1380 (2002).
8. C.B. Ojeda, F.S. Rojas, J.C. Pavón, M.L. T. artín, *Anal. Bioanal. Chem.*, **382**, 513 (2005).
9. J. Y. Cabon, C.L. Madec, *Anal. Chim. Acta*, **504**, 209 (2004).
10. S. Nielsen, H E. H. ansen, *Anal. Chim. Acta*, **343**, 5 (1997).
11. M. Ezaee, Y. Assadi, M.-R. Milani Hosseini, E. Aghaee, F. Ahmadi, S. Berijani, *J. Chromatogr. A*, **1116**, 1 (2006).
12. M. Bahram, S. Khezri, *Anal. Methods*, **4**, 384 (2012).
13. B. Welz, M. Sperling, Atomic absorption spectrometry, John Wiley & Sons, 2008.
14. H. Ortner, E. Bulska, U. Rohr, G. Schlemmer, S. Weinbruch, B. Welz, *Spectrochim. Acta B*, **57**, 1835 (2002).
15. E.Z. Jahromi, A. Bidari, Y. Assadi, M. R.M. Hosseini, M.R. Jamali, *Anal. Chim. Acta*, **585**, 305 (2007).
16. Y. Li, B. Hu, Z. Jiang, *Anal. Chim. Acta*, **576**, 207 (2006).
17. Z. Fan, *Microchim. Acta*, **152**, 29 (2005).
18. K. Zih-Perényi, P. Jankovics, É. Sugár, A. Lásztity, *Spectrochim. Acta B*, **63**, 445 (2008).
19. L. Zhang, Y. Morita, A. Sakuragawa, A. Isozaki, *Talanta*, **72**, 723 (2007).
20. A. Erdem, A.E. Eroğlu, *Talanta*, **68**, 86 (2005).
21. Z. Fan, *Anal. Chim. Acta*, **585**, 300 (2007).
22. R.R. Eivas, I. López-García, M. Hernández-Córdoba, *Spectrochim. Acta B*, **64**, 329 (2009).
23. F. Shemirani, M. Baghdadi, M. Ramezani, *Talanta*, **65**, 882 (2005).
24. S. Yalçın, X. C. Le, *J. Environ. Monit.*, **3**, 781 (2001).
25. A.R.K. Dapaah, A. Ayame, *Anal. Sci.*, **13**, 405 (1997).
26. C. Xiong, M. He, B. Hu, *Talanta*, **76**, 772 (2008).
27. M. Chamsaz, M. H. Arbab-Zavar, S. Nazari, *J. Anal. At. Spectrom.*, **18**, 1279 (2003).
28. K. Jitmanee, M. Oshima, *Talanta*, **66**, 529 (2005).

Solidified floating organic drop micro-extraction (SFODME) for simultaneous separation/pre-concentration and determination of cadmium by atomic absorption spectroscopy

R. Parviz^{1*}, M. Honari²

¹Department of Chemistry, Faculty of Science, Islamic Azad University Shahr-E-Rey Branch, Shahr-E-Rey, Iran

²Department of Plant Breeding and Biotechnology, Agriculture and Natural Resources Faculty, Tehran Azad University, Science and Research Branch, Tehran, Iran

Received June 26, 2015, Revised September 10, 2015

In the present study, a method using solidified floating organic drop micro-extraction (SFODME) using atomic absorption spectroscopy was developed for determination of trace amounts of cadmium in various environmental water matrices including well water, qanat influent and effluent. Ammonium pyrrolidine-N-dithiocarbamate (APDC) acted as chelating agent. The main parameters affecting the performance of SFODME, such as pH, concentration of APDC, stirring rate, extraction time, extraction temperature, volume of the solvent (1-Dodecanol), dilution solvent (ethanol), and concentration of salt were optimized. Under the optimum experimental conditions, enhancement factors of 63 and 300 were obtained for 5 and 25 ml of sample solution, respectively. The calibration graph was found to be linear in a range of 2.0 – 400 μgL^{-1} . The limit of detection (3S) and the limit of quantification (10S) were 0.57 and 1.91 μgL^{-1} , respectively. The relative standard deviation (RSD) for 8 replicate measurements were found to be 3.04 %, 1.8%, 2.33% for 10 μgL^{-1} , 20 μgL^{-1} , and 300 μgL^{-1} of cadmium, respectively. The developed procedure was successfully applied to standard and several water samples (well, qanat and waste water) to determine trace amounts of cadmium. The method accuracy was assessed either by determination of cadmium in a certified reference material of water or by addition-recovery experiments, in which satisfactory results were obtained.

Keywords: solidified floating organic drop micro extraction; pre-concentration; cadmium ion determination; pyrrolidine-N-dithiocarbamate

INTRODUCTION

Cadmium is one of the most hazardous pollutants found in the environment. Due to its increased utilization in industries, cadmium concentration has increased which is of great concern to human health. This heavy metal is easily absorbed; it remains in tissues for a relatively long time and thus, poses serious health risks to both humans and animals. The adverse physiological effects due to high cadmium exposure commonly include depressed growth rate, anemia hypertension, damage to renal tubules and poor mineralization of bones [1]. Therefore, development of sensitive and selective methods for cadmium speciation is of great importance, and some solid-phase separation/pre-concentration systems coupled with spectro-analytical techniques (FAAS, EAAS, and ICP-MS) have been employed to eliminate matrix interferences and enhance detectability. The FAAS is one of the most commonly applied techniques for determination of trace amount of heavy metals. This method is a relatively inexpensive one, which provides adequate sensitivity and simple sample preparation as well.

Determination and analysis of untreated samples falls into two main categories, direct and indirect methods. Indirect methods employ a preliminary separation or concentration of the analyte. Typically, field samples contain high concentrations of matrix ions, which produce a high background level. An alternative method applied to improve the efficiency of these kinds of techniques is the use of a suitable ligand, which can be added to the aquatic sample to complex metal ions before their accumulation on a hydrophobic adsorbent [2]. To solve this problem ammonium pyrrolidine dithiocarbamate (APDC) is widely used to determine the metal ions, such as Cd^{+2} , Pb^{+2} , Ni^{+2} , Co^{+2} , etc., that could form slightly soluble complexes in an aqueous solution [3]. Usually, metal APDC complexes are measured by flame atomic absorption spectrometry [4], after extraction with nonpolar organic solvent [5]. Thus, development of pre-concentration methods using APDC can be very desirable for the chemical speciation using minimal sample treatment.

In other studies, pre-concentration techniques such as liquid-liquid extraction (LLE), solid-phase extraction (SPE) and cloud point extraction (CPE) have been developed and applied [6-8].

* To whom all correspondence should be sent:
E-mail: Rozaparviz@gmail.com

However, there are a few drawbacks that should be considered for these methods. They are time-consuming and require large volumes of organic solvents which are not only toxic to human health and the environment, but also are expensive. Solvent – free sample preparation methods or those employing less organic solvent are becoming increasingly important and have induced a major advance in analytical methodology. Therefore, liquid phase micro-extraction (LPME) has emerged as a new alternative for sample preparation [9]. This method has been developed in different modes, including single drop micro extraction (SDME) [9,10], direct single drop micro extraction (Direct-SDME) [11], head space single drop micro-extraction (HS-SDME) [12], liquid-liquid-liquid micro-extraction (LLL-ME) [13], continuous-flow micro-extraction (CFME) [15], hollow fiber liquid phase micro-extraction (HF-LPME) [16], dispersive liquid/liquid micro-extraction (DLLME) [15], and solidified floating organic drop (SFODME) [17-19]. The present research focuses on the SFODME. In this technique, a micro drop of the organic solvent with a density lower than water and a melting point close to room temperature (10-30°C) is floated on the surface of an aqueous sample while being agitated by a stirring bar in the bulk of the solution. After completion of the extraction, the sample is transferred into an ice bath, to freeze the organic phase. The solidified micro drop is transferred into a new conical vial, where it melts immediately. Finally, it dilutes by sufficient ethanol and injects to FAAS to determine the species in the extract. In this method, no specific holders are required for supporting the micro drop. Moreover, operation simplicity, low cost, fast operation, high enrichment factor, and low consumption of the extraction solvent are the advantages of the proposed method.

The aim of this study is to investigate the feasibility of the novel LPME technique based on solid organic drop combined with FAAS, in order to determine trace amounts of cadmium in environmental samples. The accuracy of the proposed method was assessed either by determination of cadmium in a certified reference material of water or by addition-recovery experiments.

EXPERIMENTAL

Instruments

A Varian AA-240 Flame atomic absorption spectrometer (Varian Australia Pty Ltd) coupled with an acetylene-air burner and a hollow cathode

lamp (current 4mA, 228.8nm wave length, and slit width 0.5 nm) was applied in the study.

All pH measurements were carried out using a digital pH meter equipped with a combined glass-calomel electrode (WTW-GmbH). The solution was stirred with a magnetic heater-stirrer (IKAMAG – RET, Germany). A simple water bath placed on the heater-stirrer was used for controlling the temperature of the sample solution.

Reagents and chemical

The stock cadmium standard solution, $\beta_{(Cd)} = 1000 \text{mgL}^{-1} (\text{CdCl}_2 \text{ in } \text{H}_2\text{O})$ was prepared by dissolving standard titrisol (Merck, KGaA, Darmstadt, Germany) with distilled water. The working standard solutions were prepared daily by serial dilutions of the stock solution with distilled water. The chelating agent 0.02gL^{-1} APDC solution was prepared daily by dissolving the appropriate amount of APDC (Merck Company, KGaA Darmstadt-Germany for syntheses) in distilled water. The extraction solvent, 1-Dodecanol and dilution solvent, ethanol were purchased from (Merck Company, KGaA Darmstadt-Germany for syntheses) Nitric acid (0.1molL^{-1}) and sodium hydroxide (0.1molL^{-1}) were used to adjust the pH levels 1-11.

Di - ammonium hydrogen citrate buffers (113gL^{-1}) was prepared by adding an appropriate amount of di-ammonium hydrogen citrate to ammoniac (25% w/v) to produce a pH range of 9 to 10. Coexisting ions (1000mgL^{-1}) were prepared by serial dilution of a Titrisol-Merk solution.

RESULT AND DISCUSSION

The suggested method is based on equilibrium between the analyte concentration in the sample and that in the extracting solvent. The thermodynamics and kinetic equations of LLE are demonstrated in previous studies [20]. In this method APDC forms a stable amphoteric chelate with cadmium if the pH is adjusted. It was observed that cadmium from the aqueous phase could be extracted into a small volume of 1-dodecanol. Furthermore, its stability, low vapor pressure and low water solubility at extraction conditions made 1-dodecanol the best extraction solvent to be used in the present experiment.

To obtain a suitable enrichment factor, the influence of different parameters that affect the chelate formation and the extraction conditions such as amount of APDC, sample stirring rate, extraction time, extraction temperature, volume of solvent, were optimized.

Effect of pH

The separation and pre-concentration of metal ions by SFODME involve prior formation of a complex with sufficient amount of hydrophobicity that allows it to be extracted into small volumes of organic solvent. The pH plays a unique role in the process of formation and extraction of chalets. The pH of solution (5 ml of solution involves 200ng ml^{-1} of cadmium) was adjusted between 1.0 – 11.0, using nitric acid and sodium hydroxide. The stirred solution was kept at 30°C for 20 min (300rpm) using $140\mu\text{L}$ of the organic solvent.

The results depicted in fig.1 shows the influence of pH on the analytical signal (absorbance). According to the figure, at the pH values lower than 10, as the pH increased absorbance rose from 1.0 to 9.0. At pH levels higher than 10, the absorbance showed a declining trend. The decrease in extraction efficiency at lower or higher pH levels depends on distribution of APDC between water and organic solvent at the specific pH. The highest extraction efficiency of cadmium using 1-dodecanol was obtained at $\text{pH}=9.0$. Thus $\text{pH}=9$ was selected for subsequent work and the real sample analysis.

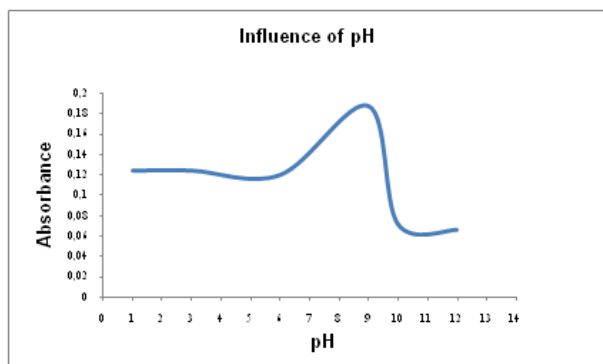


Fig 1. The influence of pH on the extraction efficiency

Effect of amount of APDC

The formation of hydrophobic ions complex strongly depends on concentration and amount of added chelate which also has influence on extraction efficiency. It is known that Cd^{+2} ions are stoichiometrically combined with ammonium pyrrolidine dithiocarbamate (APDC) to form 1:2 complexes ($\text{Cd}(\text{PDC})_2$). At constant pH levels in an aqueous phase, up to the solubility limit of the chelate in the organic phase, the value of the distribution ratio and consequently the extraction efficiency will increase as the concentration of the chelate increases [21]. Therefore the influence of concentration of APDC was studied by varying the amount of APDC 0.02 gL^{-1} between 0.2 to 1 ml. As

shown fig.2, the absorbance signal was increased by addition of 0.6ml of APDC and maximum absorbance was adjusted by addition of 0.8 ml of APDC 0.02gL^{-1} . 0.8ml was selected as the optimum amount for further studies.

Stirring rate

The stirring rate is an important parameter that enhances the kinetics of chelate formation and its extraction. According to the film theory of convective-diffusive mass transfer in the LPME system, faster sample agitation causes lower thickness of diffusion film in the aqueous phase. The optimum stirring rate was evaluated at different stirring rates, between 100 and 400rpm at a constant extraction time of 20 min. As shown in fig.3 up to 400 rpm, the absorbance signal rose as the stirring rate was increased. Afterwards, it remained constant. Higher stirring rate were not used, because at such rates, the spattering damaged the micro drops. Hence a stirring rate of 200rpm was adopted for further study.

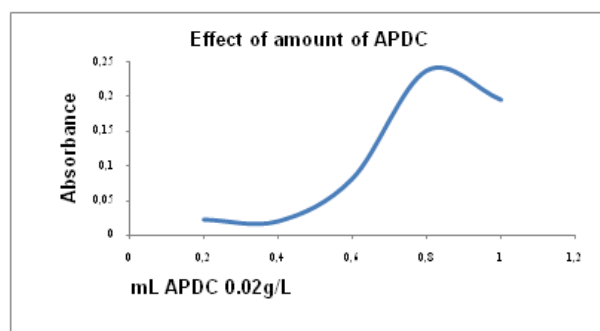


Fig 2. The effect of amount of APDC on the extraction efficiency.

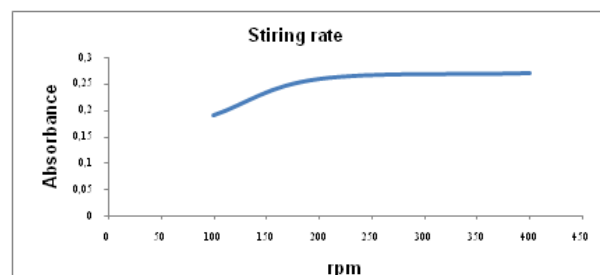


Fig 3. The effect of stirring rate on the extraction efficiency.

Effect of extraction time

The optimal extraction efficiency is obtained when equilibrium is established. The extraction time performs a very essential role in the whole process of equilibrium extraction. The effect of extraction time on the extraction efficiency was examined by varying the extraction time from 15 to 60 min at constant experimental conditions. Fig.4 shows a corresponding rise in absorbance within

time of extraction ranges between 10 and 30 minute. Micro drop was damaged on the higher extraction time. Finally, an extraction time of 30 min was selected as a reasonable compromise between enrichment factor and analysis time.

Extraction temperature

It was expected that an increase in temperature would lead to an enhancement of the mass transfer coefficients of the goal compounds from the aqueous sample into the micro drop and consequently, to higher extraction efficiencies. On the other hand, the sample temperature has significant effect on , not only the kinetics and thermodynamics of the analyte extraction, but also on those of the water molecules in the sample[22, 23].The effect of sample temperature on extraction efficiency was studied at different temperatures ranging between 30 to 60 °C(30, 40, 50, 60)°C.The lower extraction efficiencies obtained at 40°Candbelow could be due to an increase in viscosity of 1-dodecanol , resulting in a decrease of the mass transfer between aqueous solvent an organic solvent.

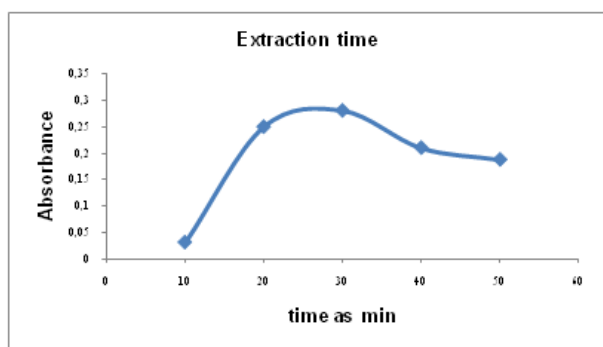


Fig 4.The effect of extraction time on the extraction efficiency.

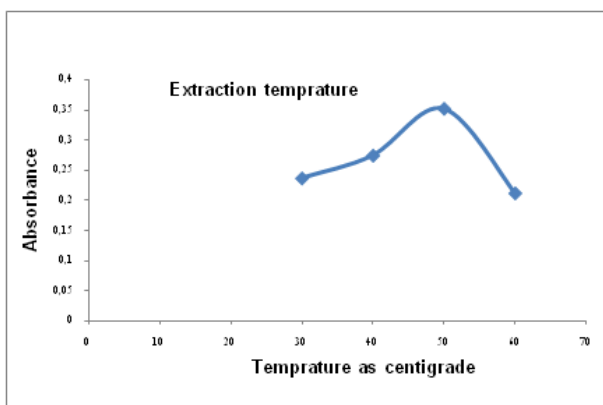


Fig 5.The effect of extraction temperature on the extraction efficiency.

In fact, a significant reduction in sensitivity was observed at higher temperature values (>50°C). This declining trend is shown in fig.5 which is

likely to be explained by considering the effects of high temperature; on the one side,it has been reported that high temperature can decrease the portion coefficients of analytes in the micro drop, resulting in a decrease of the rate of analyte adsorption on the outer surface of the micro drop. On the other side, solubility of 1-dodecanol in water decreases at temperature values higher than 50°C. So, the optimum extraction temperature was set at 50°C.

Volume of extraction solvent

Selection of an appropriate solvent is considered a crucial parameter in LPME methods. The range of proper solvents to be used in the previously mentioned method is limited as the solvent must have qualities such as, low volatility and low solubility in water, in order to be immiscible with water and as the analytes must be soluble in it. The solvent melting point should be close to the room temperature [24]. Because of low melting point, low vapor pressure, and low water solubility, 1-dodecanol seemed to be suitable for this investigation.

The influence of micro drop volume on the analytical signal was studied in the range of 50.0 to 300µL. Volume of extraction solvent was evaluated for the extraction of 5.0mL of sample containing 200.0µL⁻¹of cadmium. The stirred solution (200rpm) was kept at 50°C for 30 minute until the extraction was completed. Then, the extract was diluted using 500µLof ethanol, and its absorption was measured.

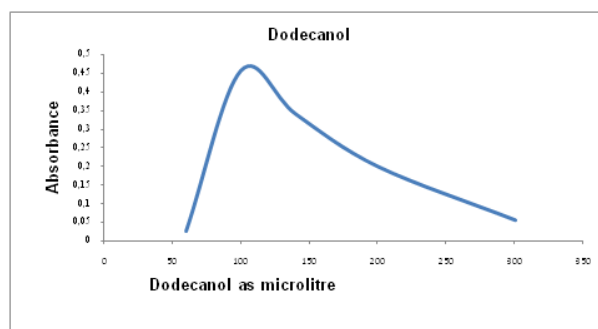


Fig 6. The effect of volume of extraction solvent on the extraction efficiency.

The result (Fig.6) shows that the rewas a corresponding growth in the absorbance of target compounds for solvent volumes ranging from 50.0 to 100.0µL. Based on LLE equations, rate of the analyte migration into the micro drop is directly related to the surface area between the two liquid phases and is inversely related to the organic phase volume [25].Thus, an increase in the drop volume raises the interfacial area following the analytical

signals. However, any further increase in the micro drop volume results in a decrease in the absorbance [26]. Hence, an organic volume of 100 μ L was selected as optimum.

Volume of ethanol as dilution solvent

Aqueous samples can be generally introduced for analysis directly without any prior treatment. But that is remarkably dependent on the viscosity of the solution; In flame atomic absorption spectroscopy (FAAS) analysis, the viscosity should be similar to that of water for which most nebulizers are designed.

Only some organic liquids such as ethanol or methyl isobutyl-keton fulfill this condition, and as a result, these solvents are often used to dilute the organic liquids; during the analysis, volatile solvents (such as methanol, acetone, diethyl ether, etc.), evaporate before reaching the flame. The burning rate is increased by expanded steam, and then increasing the gases flow into the spray chamber, leading to erratic results. Due to the high viscosity of dodecanol, the atomic absorption direct injection is not possible.

In this work, extraction solvent was diluted with ethanol prior to injection. Therefore, the influence of dilution solvent was also investigated by varying the volume of ethanol between 0.1 to 0.4 ml. As shown in fig.7, the absorbance signal was increased by additional amount of ethanol to a certain point. Further increase in the dilution solvent volume resulted in a decline in the absorbance and enrichment factor. Hence, a dilution solvent volume of 0.4mL (400 μ L) was selected as a reasonable compromise between enrichment factor and dilution solvent volume.

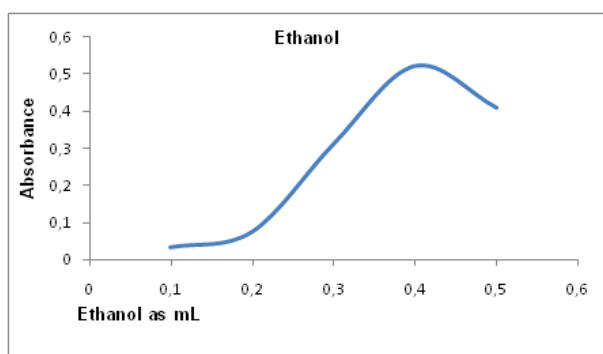


Fig 7. The effect of dilution solvent volume on the extraction efficiency

Ionic strength

The Ionic strength is one of the key parameters that must be taken into account in the extraction process. Depending on the target compounds, the presence of salt in aqueous sample can potentially

result in contrary effects: it may improve [27], not influence [28], or diminish the extraction process [29,30]. Apart from the salting-out effect improving extraction efficiency, it also leads to altered physical properties of the Nernst diffusion film in the interface of aqueous and organic phases; consequently, the diffusion rate of analytes into the solvent reduces [31,32]. To investigate this effect on the proposed LPME, the extraction was performed with a 5.0mL water sample containing various concentration of NaCl (0% to 30%, w/v). The result confirmed (figure 8) that adding salt to increase the concentration from 5%(w/v) to 10%(w/v) caused a growth in absorbance which then remained constant at concentrations up to 25%(w/v). The absorbance then showed a declining trend at higher concentrations of salt. This observation suggests the possibility of using this method for the separation and determination of cadmium from saline solutions.

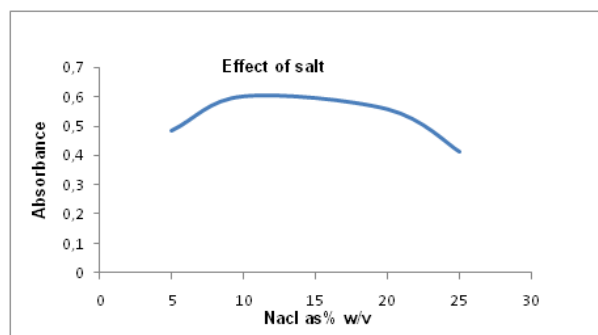


Fig 8. The effect of salt on the extraction efficiency.

Interference study

The sensitivity and utility of the SFODME in the pre-concentration of cadmium in the presence of potential interfering ions at an initial mole ratio of 5000(ion/cadmium) was examined. In these experiments, 5.0 ml of solutions containing 200 μ g/L cadmium and various amounts of interfering ions were treated according to the recommended procedure. When interference was observed, the concentration of the interfering ion was lowered. The results of this investigation are given in Table 1. A relative error of less than 5% was considered to be within the range of experimental error. As is shown, the presence of high concentrations of alkali, alkali earth cat ions, did not cause any interference, but the presence of some metals that formed ionic complex, did interfere in the determination of cadmium.

Figures of merit

Under the optimum experimental condition described above, method validation was carried out, in terms of linearity, precision, limit of detection

(LOD) and quantifications (LOQ) for each analyte. The analytical characteristics of the proposed method are presented in Table 2. The calibration curve was found to be linear in the range of 2.00 to 400 μgL^{-1} and the resulting equation was $A=0.002C+0.122$, where A is the absorbance of the extract and C is the concentration of cadmium (μgL^{-1}) in the initial solution. Precision was assessed by determination of repeatability, which could express the precision of the method under the same operating conditions

Table 1. The effect of diverse ions on the recovery of Cadmium.

Ion	Molar ratio (ion/Cd)	Recovery (%)
Pb	5000	98.87
K	5000	99.87
Mg ²⁺	5000	99.62
Ca ²⁺	5000	99
Cu ²⁺	5000	88.75
Li	5000	101.25
Na	5000	100
As	5000	91
Hg	5000	87

Concentrated volume, 5mL; cadmium concentration 200 μgL^{-1} .

Table 2. Figure of merit of the proposed method for pretreatment and determination of cadmium

Analytical parameter	Results
LR (μgL^{-1})	2-400
Slope	2.7×10^{-3}
Correlation coefficient	0.9995
LOD (μgL^{-1})	0.57
LOQ (μgL^{-1}) (LOQ)	1.91
RSD (%) (n=8, 10 μgL^{-1})	3.04
RSD (%) (n=10, 20 μgL^{-1})	1.85
RSD (%) (n=8, 300 μgL^{-1})	2.3
PF (25mL)	300
PF (5mL)	63

LR, Linearity range; (LOD) Detection limit (μgL^{-1}); (LOQ), Quantification Limit; RSD, Relative standard deviation; PF, Pre-concentration factor.

It also identified intraday precision which is explained as relative standard deviation (RSD%).

The results of 10 standard replicate measurements of 20 μgL^{-1} of cadmium is given in Table 2. The relative standard deviation was then evaluated to be 1.85% which shows acceptable error and reliability of the experiments. The limit of detection, defined as ($\text{LOD}=3S_B/m$) and quantification of limit defined as ($\text{LOQ}=10S_B/m$) where (S_B and m are the standard deviation of the blank, and the slope of the calibration curve), were 0.57 and 1.91 μgL^{-1} respectively. Furthermore, the pre-concentration factor was calculated as the ratio of the cadmium concentration in the solidified floating organic drop to that initially in the bulk phase which was 63 [33,34].

Application to real sample

Finally, the reliability of the recommended procedure, the method was evaluated by the analysis of the real samples including well, qanat and waste water. For this purpose a volume of 5 mL of each sample was pre-concentrated according to the proposed method, the result indicated that no traces of cadmium were detected in qanat and well water samples but cadmium was detected in the waste water. The accuracy of the method was verified by the analysis of the sample spiked with (50 and 200 μgL^{-1}) levels of cadmium to assess the matrix effect. The relative recovery defined as the concentration of cadmium ion ratio of a natural water sample and ultrapure water sample spiked with analytes at the same level, was applied. The relative recoveries of the analytes are given in Table 3, which varies from 98% to 101%; it shows that the influence of the matrix is not significant on the extraction.

Table 3. The results obtained from analysis of real water sample

Sample	Added Cadmium (μgL^{-1})	Found cadmium (μgL^{-1})	Recovery (%)
Well water	-	ND	-
Well water	200	201.4±0.02	101
Qanat water	-	ND	-
Qanat water	200	196.4±0.02	98.2
Waste Water	-	31±0.02	-
Waste Water	50	80.55±0.02	98.8

ND, not detected; Results are mean and standard deviation of three independent measurements (n=3).

Table 4. Comparison of the proposed method with other methods for pretreatment and determination of cadmium

Methods	LOD (μgL^{-1})	LR (μgL^{-1})	r^2	RSD (%)	Recovery (%)	PF	References
CPE-FAAS	0.3	3-250	0.999	4.0(at100 μgL^{-1})(n=7)	95.6-102.8	70	35
DLL-ME	1.2	5-150	0.9997	2.1(at100 μgL^{-1})(n=8)	69-99	34.5	36
USAE-SFODM	0.66	10-450	0.9985	3.34(at20 μgL^{-1})(n=10)	95.2-100.6	81	37
Proposed method	0.57	2-400	0.9995	1.85(at20 μgL^{-1})(n=10)	98.2-101	63	*

CPE, Cloud point extraction; DLL-ME, Dispersive liquid-liquid micro extraction; USA-SFODM, Ultrasound – assisted emulsification solidified floating organic drop micro extraction.

A comparison between the proposed FAAS-SFODM method and some of the other published methods used for extraction and determination of cadmium are summarized in table 4. The results of the investigation indicate that solidified floating organic drop micro extraction (SFODME) combined with flame atomic absorption spectrometry can be used as a simple and powerful technique for pre-concentration and determination of metal ions in aqueous samples.

CONCLUSION

In the present work, the application of the solidified floating organic drop micro-extraction (SFODME) method in determination of cadmium in aqueous samples was investigated. This technique made the separation and quantification of cadmium in the aqueous samples possible. The proposed SFODME method permits an effective separation and pre-concentration of cadmium and also its final determination using spectrometry in several categories of natural waters. The sample preparation time as well as the consumption of organic solvent was minimized and the figures of merit of the developed method were comparable to other reported methods for the determination of cadmium [35-37]. In conclusion the SFODME method is a simple, fast operation, economic, rejection of matrix constituent, high enrichment factor and environmentally friendly technique that can be applied to extraction process and can be used for determination of the cadmium ions in environmental samples in order to obtain satisfactory results. In this study, this method significantly improved the performance of the FAAS detection for cadmium. These features appears promising for the future studies on extraction of metals other than cadmium, aiming at the development of novel speciation methods that would deliver better analytical performance.

REFERENCES

1. S. Lundsted, P. Haglund, L. Oberg, *Environ. Toxicol. Chem.*, **22**, 413 (2003).
2. M. Necemer, P. Kump, *Spectrochim. Acta Part B*, **54**, 621 (1999).
3. K.V. Krishnamury, M.M. Reddy, *Anal. Chem.*, **49**, 222 (1977).
4. S.A. Popova, S.P. Bratinova, C.R. Ivanova, *Analyst*, **116**, 525 (1991).
5. H. Tao, A. Miazaki, K. Bansho, Y. Umezaki, *Anal. Chim. Acta*, **156**, 159 (1984).
6. F. Pena-Pereira, I. Lavill, C. Bendicho, *Spectrochim. Acta Part B*, **64**, 1 (2009).
7. J. Lenyicek, M. Sekyra, A.R. Novotna, E. Vaisova, D. Titeira, V. Vesely, *Acta*, **571**, 40 (2006).
8. L. Wei, Z. Wei-jun, C. Jian-bo, Y. Ming-min, *Anal. Chim. Acta*, **605**, 41 (2007).
9. M.A. Jeannot, F.F. Cantwell, *Anal. Chem.*, **68**, 2236 (1996).
10. S. Gil, M.T. C.deLoos-Vollebregt, C. Bendicho, *Spectrochim. Acta Part B*, **64**, 208 (2009).
11. A. Sarafraz-Yazdi, A.H. Amiri, Z. Eshaghi, *Talanta*, **78**, 936 (2008).
12. Y. Yamini, M. Hojjati, M. Haji-Hosseini, M. Shamsipur, *Talanta*, **62**, 265 (2004).
13. F. Zhafeng, L. Xuejuan, *Journal of Chromatography A*, **1180**, 187 (2008).
14. L. Yan, H. Yuki, L. Jin-Ming, *Analytica Chimica Acta*, **585**, 294 (2007).
15. S. Pedersen, K. Bjergaard, E. Rasmussen, *Anal. Chem.*, **71**, 2650 (1999).
16. Y. Assadi, F. Ahmadi, M.R.M. Hossieni, *Chromatographia*, **71**, 1137 (2010).
17. H. Faraji, R.M.A. Tehrani, *International Journal of Industrial Chemistry (IJIC)*, **3**, 12 (2012).
18. M.R. Khalili-Zanjani, Y. Yamini, S. Shariati, J.A. Jonsson, *Anal. Chim. Acta*, **585**, 286 (2007).
19. S. Dadfarnia, A.M. HajiShabani, E. Kamranzadeh, *Talanta*, **79**, 1061 (2009).
20. X. Chen, T. Zhang, P. Liang, Y. Li, *Microchim. Acta*, **155**, 415 (2006).
21. U. Anders, G. Hailer, *Anal. Chem.*, **278**, 203 (1976).
22. E. Aguilera-herrador, R. Lucena, S. Cardenas, M. Valcarcel, *J Chromatogr A*, **1201**, 106 (2008).
23. H.A. Mottola, *Analyst*, **118**, 675 (1993).

24. M.I. Leong, D. Hung, *Chromatogr A*, **1211**, 8 (2008).
25. L. Zhao, H.K. Lee, *Chromatogr A*, **919**, 381 (2001).
26. H. Bagheri, F. Khalilian, *Anal Chim Acta.*, **537**, 81 (2005).
27. K.E. Kramer, A.R.J. Andrews, *Chromatogr B.*, **760**, 27 (2001).
28. H.G. Uglund, M. Krogh, K.E. Rasmussen, *Chromatogr B.*, **749**, 85 (2000).
29. G. Shen, H.K. Lee, *Anal Chem.*, **74**, 648 (2002).
30. E. Psillakis, N. Kalogerakis, *Chromatogr A.*, **999**, 145 (2003).
31. H. Bagheri, A. Saber, S.R. Mousavi, *J. Chromatogr A*, **1046**, 27 (2004).
32. D.A. Lambropoulou, T.A. Albanis, *J ChromatogrA.*, **1072**, 55 (2005).
33. A. Afkhami, T. Madrakian, H. Siampour, *J. Hazard. Mater.*, **138**, 269. (2006)
34. L. Meng, B. Wang, F. Luo, G. Shen, Z. Wang, M. Guo, *Forensic Sci.Int.*, **209**, 42 (2011).
35. S. Dadfarnia, A.M. HajiShabani, E. Kamranzadeh, *J.Braz.Chem.Soc.*, **21**, 2353 (2010).
36. G. Karim-Nezhad, M. Ahmadi, B. Zare-Dizajdzizi., *J.Braz.Chem.Soc.*, **22**, 1816 (2011).
37. Z. Jing-Wen, W. Yu-Kun, D. Xin, L. Xia, M. Jing-Jun, L. Jing-Ci, *J. Braz. Chem. Soc.*, **22**, 446 (2011).

ATR-FTIR spectroscopy and chemometrics application for analytical and kinetics characterization of adsorption of 1-butyl mercaptan (1-butanethiol) on nickel coated carbon nanofibers (CNFS)

F. Karami, M. Khanmohammadi, A. B. Garmarudi

Chemistry Department, Faculty of Science, Imam Khomeini International University, Qazvin, Iran

Received June 26, 2015, Revised September 10, 2015

Mercaptans are the main compounds in petroleum derivatives that are tried to be removed. In this work, Infrared spectroscopy and chemometrics were utilized to evaluate the analytical and kinetics characteristics of adsorption of 1-butyl mercaptan from n-hexane by Ni coated carbon nanofibers (CNFs). Electroless plating was applied for coating of Ni on CNFs. Three types of adsorbents with different amounts of coated nickel were studied and compared to investigate the effect of nickel amount on modification of the surface of the adsorbent to obtain higher capacity and rate of desulfurization. In order to obtain useful information about the adsorption process, multivariate curve resolution alternating least squares (MCR-ALS) chemometrics method was used. Information about the variations in concentration of 1-butyl mercaptan and kinetics of adsorption was achieved. This study showed that the adsorbent with higher amount of coated nickel had higher rate constant of adsorption. Also, relative concentrations of 1-butyl mercaptan were calculated in different times during adsorption process.

Keywords: ATR-FTIR spectroscopy, desulfurization, MCR-ALS, chemometrics

INTRODUCTION

Sulfur is an abundant component in petroleum and consequently in petroleum based products such as fuels. Combustion of these fuels causes the exhaust of SO_x gases into atmosphere, known as one of the most important air pollutant [1]. Authorities all around the world are concerned about this problem and have made regulation to prevent production of high sulfur containing products especially fossil fuels. Euro standard is a common regulation all around the world to control and illustrate the environmental quality of fuels [2]. It is expected to attain Zero emission of SO_x gases from fuel combustion in near future due to severe research interest and focus on development of effective desulfurization approaches. There are several types of methods for desulfurization [3-5].

Desulfurization by application of adsorbents has been favorable method for researchers in petrochemical science due to its simplicity and low cost, together with effective in removal outcomes [6]. One of the valuable characteristics of adsorptive desulfurization is its potential to perform deep desulfurization of fuels which may be achieved by other methods, expensively. Thus desulfurization by application of adsorbents is going to be more and more common. The most important step in development of an adsorptive desulfurization method is to prepare high capacity

adsorbents with known properties. On the other hand it is essential to characterize the developed adsorbent. Thus application of proper tools to evaluate, characterize and comparative study of novel adsorbent are the most important requirements for researchers in this domain. Characterization and monitoring of adsorbent during the adsorption process is helpful as well. Different materials have been developed as adsorbents for desulfurization [7-12]. Nowadays, carbon nanostructures such as carbon nanofibers (CNFs) and carbon nanotubes (CNTs) have attracted the attention of the researchers [13, 14]. In some researches this structures have been used as adsorbent [15].

Among analytical characterization method, spectroscopic ones are powerful in wide range of applications in material science especially in monitoring of a chemical system (16). Infrared (IR) spectroscopy as a vibrational spectroscopic method, is attractive due to its ability in detection of chemical structures within molecular level. IR spectra regions such as finger print are unique for different analytes. This ability encourages researchers to employ IR spectroscopy as a powerful analytical method in evaluation of materials and chemical systems.

In spite of advantages for IR spectroscopy, signal overlapping is an important drawback which causes consequent difficulties to extract the spectral feature which is related to target analyte of interest. The most common solution for complicated systems is to conduct a separation procedure but

To whom all correspondence should be sent:
E-mail: mohammadkhah@guilan.ac.ir

this idea is not applicable in most cases especially in an evolutionary process. A promising route for this aim while dealing with spectroscopic data of a chemical system is to use chemometric methods [17]. Chemometrics as combination of chemistry, statistics, mathematics and computer science, tries to provide most useful knowledge from experimental data by extracting the useful information [18, 19].

In this work, carbon nanofibers (CNFs) adsorbents were prepared by electroless coating of nickel with different amounts of metal. Electroless coating is one of the plating methods that is performed without electricity current and it makes uniform deposition and resistant structure against corrosion [20]. Prepared adsorbents were used in desulfurization of model fuel sample containing 1-butylmercaptane as a well-known mercaptan in petroleum products. Variations in mercaptan concentration and adsorption kinetics were evaluated by application of MCR-ALS method on obtained infrared spectra by utilizing attenuated total reflectance (ATR) cell (21, 22). Three types of adsorbent with different nickel amount were studied. The rate and relative capacity of them were compared. Figure 1 shows the schematic diagram of the work.

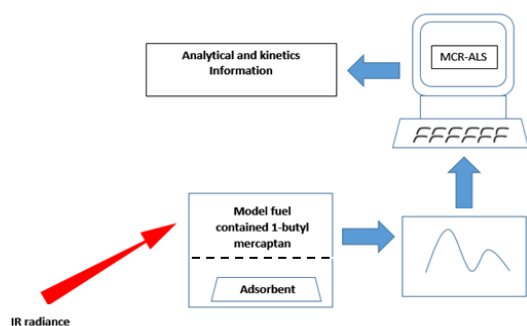


Fig. 1. Schematic diagram for characterization of adsorption process.

MATERIALS AND METHODS

Chemicals

CNFs with outer diameter of 200-600 nm and purity >95% was from neutrino Co. Hydrochloric acid (HCl), sulfuric acid (H₂SO₄ 96.2%), nitric acid (HNO₃ 65%), ammonia (NH₃), hexane, tin (II) chloride (SnCl₂·2H₂O), palladium (II) chloride (PdCl₂), sodium hypophosphite hydrate (NaH₂PO₂·H₂O) and sodium citrate (NaHC₆H₅O₇·5.5H₂O) were all of analytical grade from Merck. Analytical nickel sulfate (NiSO₄) and

1-butanethiol were from Scharlau and Acros, respectively. Double distilled water was used to prepare aqueous solutions.

Instruments

A Bomem infrared (Quebec, Canada) MB series FTIR spectrometer with DTGS mid-range detector; a KBr: Ge/Sb₂S₃, using SpectraTech (warrington, UK) in-compartment contact with sampler horizontal attenuated total reflector with a 45° ZnSe trough plate. Coated beam splitter and a SiC source, was used to record spectra. ATR cell and ultrasonic dispenser were used, too.

CNFs preparation

Known amount of HNO₃ and H₂SO₄ were mixed with CNFs in a glass flask being refluxed for 8 hours at 80°C. Oxidized CNFs were filtered to be washed with distilled water and to be dried in oven at 80°C for three hours. In order to sensitization, oxidized CNFs were added to the mixture of HCl (0.15M) and SnCl₂ (0.05M) being sonicated for 10 min. at 25°C. Then CNFs were separated by application of centrifuge. CNFs were washed by distilled water.

The next step was to activate the sensitized CNFs by adding them to HCl (0.15M) and PdCl₂ (6×10⁻⁴M) solution and sonicating for 10 min. at 25°C. Then CNFs were separated by centrifuge being washed with distilled water.

Plating of nickel on CNFs

Activated CNFs were added to the bath including NaHC₆H₅O₇·5.5H₂O as complexing agent which stabilizes the solution, NaH₂PO₂·H₂O as reducing agent as source of electrons and NiSO₄·6H₂O as the nickel source. Nickel salt solution with concentration of 20, 35 and 50 g/L, were used to prepare adsorbents with three different amounts of nickel.

Desulfurization process

1-Butanethiol solutions (500 ppm) were prepared to be used in evaluation of fabricated CNFs based adsorbents as model fuel. For each mercaptan removal experiment 1g of adsorbent was added to 100 mL of model fuel being sonicated for 5 minutes. And then mixture was stirred. Removal process was continued for 120 minutes and analysis samples were obtained from mixture solution with 20 minutes time intervals.

Chemometric data processing

Recorded spectra of sample solutions were provided the spectral data matrix. Which was then

processed by MCR-ALS inside MATLAB software environment.

MCR-ALS

The first step in performing MCR-ALS is singular value decomposition (SVD) [17] to determine the number of active components in the chemical process.

Next to SVD, initial estimation of concentration was provided by application of evolving factor analysis (EFA) [23] in which submatrices of gradually increasing size from data matrix were selected being treated by principal component analysis (PCA) [17] both from top to bottom (forward EFA) and from bottom to top (backward EFA) to study the emergence and decay of probable active components.

RESULTS AND DISCUSSION

The aim of this work was to characterize the desulfurization capability of nickel coated CNFs adsorbents with different amounts of coated nickel, prepared by electroless plating. 20, 35 and 50 g/L nickel solutions were applied and prepared adsorbents are named A-20, A-35 and A-50, respectively to be studied. Scanning Electron Microscope (SEM) was employed to admit the coating of nickel on CNFs and differences in the adsorbents prepared by different nickel concentrations as observed in Figure 2. The adsorbents prepared by more concentrated Ni solutions demonstrate more nickel nanoparticles on the surface. Also, atomic absorption measurement admitted the high amount of coated nickel on CNFs by application of nickel solution with higher concentration. Figure 3 shows the result of atomic absorption measurements.

In desulfurization process the IR spectra of the model fuel solution were recorded in increments of 20 min. The related IR spectra for each sample are illustrated in Figure 4.

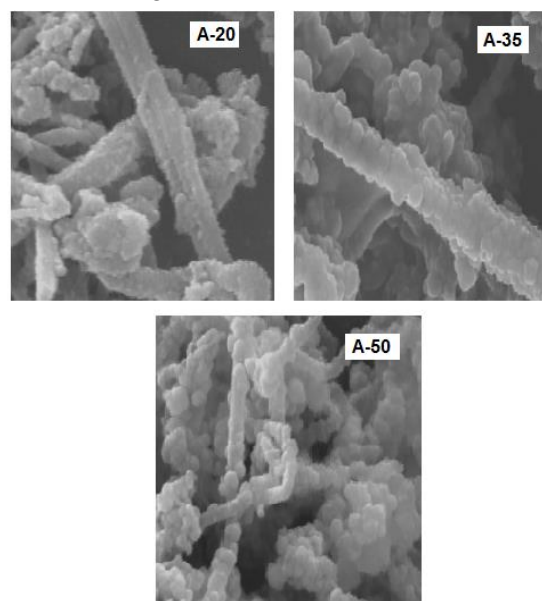


Fig. 2. SEM photos of three types of adsorbents

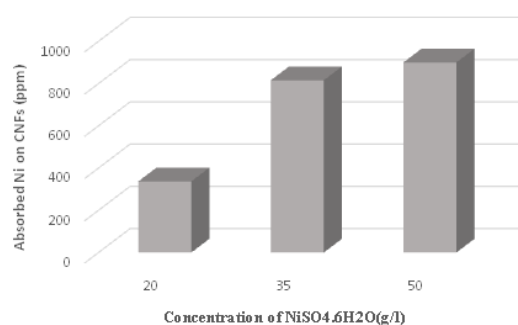


Fig. 3. The results of atomic absorption to evaluate the coated nickel amount.

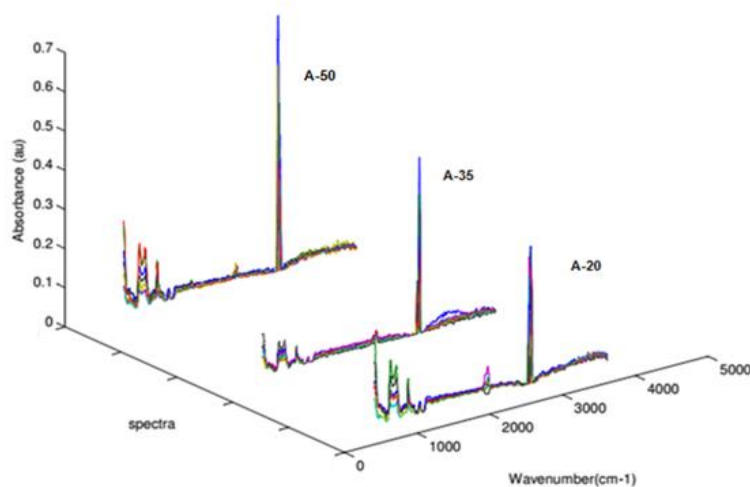


Fig. 4 Recorded IR spectra of mercaptan removing chemical system with adsorbents.

After constructing the spectral data matrix for each sample, preprocessing was conducted including baseline correction and noise removal. The next step was to perform MCR-ALS as a curve resolution method which would decompose the data matrix into two matrices of concentration (C) and spectral (S^T) profiles of data set for each component, utilizing least squares.

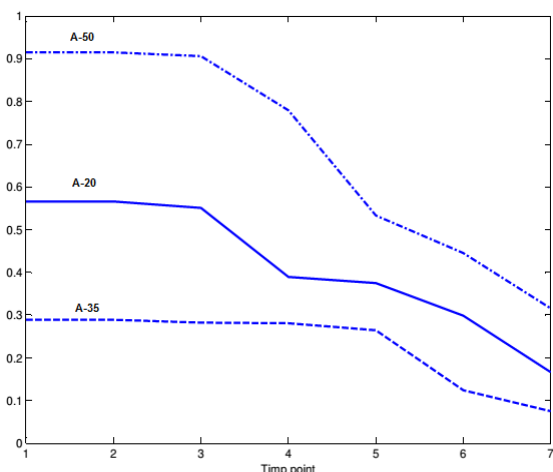


Fig. 5 Concentration profile of active component from EFA

The first step was SVD which showed only one component to be active within the system. Then EFA was performed. To obtain concentration of 1-butyl mercaptan during the removal process. Figure 5 shows the concentration profiles of active component in desulfurization process for studied samples.

The concentration profile provided by EFA was applied to start the optimization process in MCR-ALS, obtaining the spectral profile to screen the structure of active component and concentration profile to monitor its concentration variations. In some of the usual constraints of MCR-ALS were applied during optimization process to attain

assured results. Non-negativity is a constraint which proposes the calculation so that spectral profile of the active components and their related concentrations cannot have negative values. On the other hand, unimodality constraint would affect the resolved concentration profiles to obtain only one maximum in resolved profile. Figure 6 and Figure 7 show the spectral and concentration profiles of the systems, respectively.

The spectral features of the profile confirm the similarity between the active component detected in the system and 1-butyl mercaptan while concentration profiles shows gradual decrement in concentration of this component in all the samples.

Table 1 shows the relative concentration of 1-butyl mercaptan during the adsorption process determined by MCR-ALS output. The results show that the adsorbent with higher amount of nickel adsorbs higher amount of mercaptan.

Adsorption kinetics

Another role of chemometric data processing methods was to aid in calculation of kinetics model of chemical process [24, 25]. Quantitative results provided by concentration profile of the MCR-ALS model were applied to conduct a kinetics study for the adsorption process calculating the kinetics constant. For this aim, at first a predefined kinetics model was selected trying to fit the concentration data to the proposed model. Considering the initial estimation of concentration profile, first order kinetics model was selected. The equation of first order kinetics model is:

$$[A] = [A]_0 e^{-kt} \quad (1)$$

Where $[A]$ is momentary concentration of 1-butyl mercaptan, $[A]_0$ is the initial concentration, k is the kinetics constant and t is time. The calculated kinetics constant and validation parameters of MCR-ALS are shown in Table 2 for all samples.

Table 1.- Relative concentration of 1-butyl mercaptan during adsorption process

Time (min.)	A-20 (%)	A-35 (%)	A-50 (%)
0	100	100	100
20	95.54089	79.38959	78.53602
40	71.06656	62.01267	67.15535
60	73.86979	39.36603	66.86252
80	73.86979	39.36603	66.29031
100	69.96974	42.63515	40.26428
120	69.96974	42.17822	29.03991

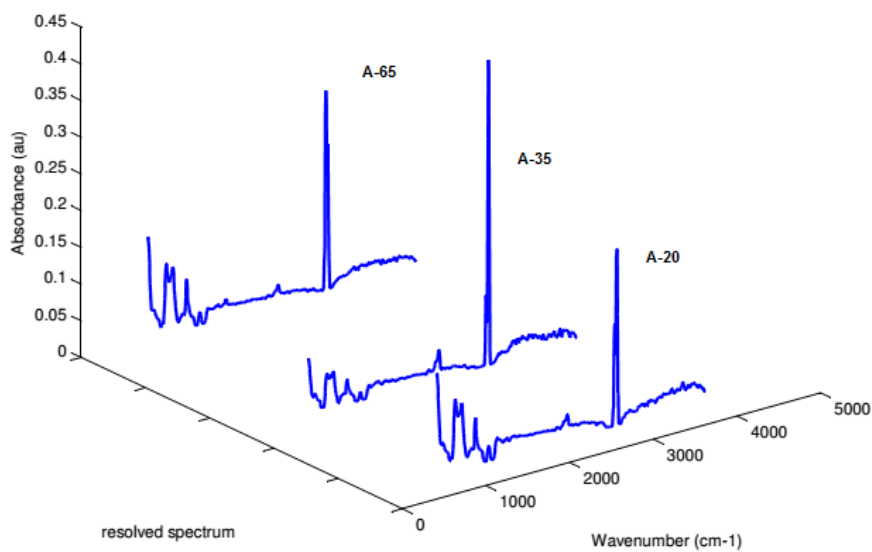


Fig. 6. Spectral profiles of mercptan.

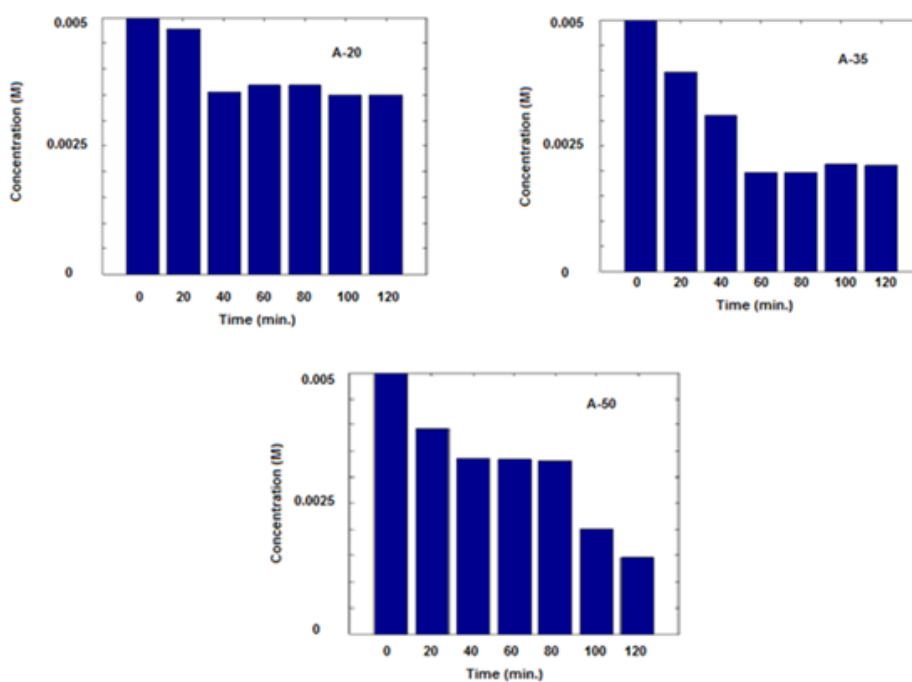


Fig. 7. Concentration profiles of A-20 (A), A-35(B) and A-50 (C).

Table 2. Kinetics and validation parameters

	A-20	A-35	A-50
k	0.7	1.2	2.3
Sum of Squares for k calculation	0.04	0.03	0.05
Standard deviation of residual vs. experimental data for MCR-ALS	0.002	0.005	0.002
R ² for MCR-ALS	0.98	0.99	0.99

It is obvious that with increasing of the amount of nickel coated on CNFs the rate constants of the adsorption have increased. The main reason for increasing the relative capacity and rate constant of adsorption for adsorbent with higher amount of metal, can be related to the making connection between the non-bonding electron pairs in sulfur and metal on the surface.

CONCLUSION

Adsorption is one of the main strategies in desulfurization of petroleum products as simple and low cost way. Improvement of this strategy needs to develop well characterized adsorbents. One of the essential needs for specialist in petrochemical science is ability to characterize the adsorbent and adsorption process in a proper way. This work applied ATR-FTIR spectroscopy with ability to detect a wide range of compounds to evaluate the adsorption of 1-butyl mercaptan as pollutant in fuel by nickel coated carbon nanofibers as new adsorbent. Evaluation was performed for three types of adsorbents with different coated nickel amount. Also MCR-ALS chemometrics method was used to obtain the concentrations variations of 1-butyl mercaptan and Kinetics constant during the adsorption process. This exploratory study showed that the adsorption of 1-butyl mercaptan has higher amount and rate for adsorbents with higher amounts of coated nickel.

REFERENCES

1. K.K Sarda., A. Bhandari, K.K. Pant, S. Jain, *Fuel.*, **93**, 86 (2012).
2. S. Brunet, D. Mey, G. Pérot, C. Bouchy, F. Diehl, *Applied Catalysis A General*, **278**, 143 (2005).
3. M. Rashtchi, G.H. Mohebbali, M.M. Akbarnejad, J. Towfighi, B. Rasekh, A. Keytash, *Biochemical Engineering Journal*, **29**, 169 (2006).
4. Z. Jiang, H. Lü, Y. Zhang, C. Li, *Chinese Journal of Catalysis*, **32**, 707 (2011).
5. Y. Fan, G. Shi, H. Liu, X. Bao, *Fuel*, **90**(5), 1717 (2011).
6. A.H.M.S. Hussain, B.J. Tatarchuk. *Fuel*, **107**, 465 (2013).
7. Y. Wang, F.H. Yang, R.T. Yang, J.M. Heinzl, A.D.Nickens, *Industrial & Engineering Chemistry Research*, **45**, 7649 (2006).
8. F. Subhan, B.S..Liu, *Chemical Engineering Journal*, **178**, 69 (2011).
9. C. Sentorun-Shalaby, S.K. Saha, X. Ma C. Song *Applied Catalysis B: Environmental*, **101**, 718 (2011).
10. X. Ma, M. Sprague, C. Song, *Industrial & Engineering Chemistry Research*, **44**, 5768 (2005).
11. M.V. Landau, M. Herskowitz, R. Agnihotri, JE. Kegerreis, *Industrial & Engineering Chemistry Research*, **47**(18), 6904 (2008).
12. A.J. Hernández-Maldonado, G. Qi, RT. Yang *Applied Catalysis B: Environmental*, **61**, 212 (2005).
13. N.M..Rodriguez, *Journal of Materials Research*, **8**(12), 3233 (199).
14. R.H. Baughman, A.A. Zakhidov, W.A. de Heer *Science*, **297**, 787 (2002).
15. V.K. Gupta, R. Kumar, A. Nayak, T.A. Saleh, M.A. Barakat, *Advances in Colloid and Interface Science*. **193–194**, 24 (2013).
16. T. Schadle B. Pejic B. Mizaikoff, *Analytical Methods*, **8**, 756 (2016).
17. R.G. Brereton, *Chemometrics: Data Analysis for the Laboratory and Chemical Plant*; Wiley; 2003.
18. M. Maeder, Y.M. Neuhold, *Practical Data Analysis in Chemistry*, Elsevier Science; 2007.
19. P. Gemperline, *Practical Guide To Chemometrics*, Second Edition, CRC Press; 2006.
20. C-Y. Huang, J-F. Pai, *European Polymer Journal*, **34**, 261 (1998).
21. J. Jaumot, R.A. Gargallo de Juan Tauler *Chemometrics and Intelligent Laboratory Systems*. **76**(1), 101 (2005).
22. K.H. Esbensen, D. Guyot, F. Westad, L.P. Houmoller, *Multivariate Data Analysis - in Practice: An Introduction to Multivariate Data Analysis and Experimental Design*: Camo Process AS; 2002.
23. H.R. Keller, D.L. Massart, *Chemometrics and Intelligent Laboratory Systems*. **12**, 209 (1991).
24. Y. Guo, Y. Ni, J. Chen, S. Kokot, *Analytical Methods*. **8**, 197 (201).
25. A. de Juan, M. Maeder, M. Martínez, R. Tauler *Chemometrics and Intelligent Laboratory Systems*, **54**, 123 (2000).

Cleaning strategy of fouled reverse osmosis membrane: Direct osmosis at high salinities (DO-HS) as on-line technique without interruption of RO operation

S.M. Tabatabaee Ghomshe*

Department of Chemical Engineering, Mahshahr Branch, Islamic Azad University, Mahshahr, Iran.

Received June 26, 2016, Revised September 10, 2016

This paper summarizes the critical examination of the cleaning performance of the polyamide RO membrane with DO-HS method as novel backwash approach for on-line membrane cleaning in RO operation. In this work, the effect of pulse injection of salt demonstrate on RO membrane cleaning. A short injection of feed water with increased salt concentrations (8 and 10% NaCl solution) with an associated osmotic pressure of 35 and 43 bar overcomes feed pump gauge pressure and reverse osmosis shifts to direct osmosis, leading to a permeate backwash stream through the reverse osmosis membrane. The results illustrate that there is more increasing in water permeate flux and permeability coefficient of RO membrane by pulse injection of 10% NaCl than the other one (8% NaCl solution). Results observed a rise of the permeability coefficient of membrane, indicating the foulant removal from the membrane. Permeability coefficient of membrane reached to approximately 90 percent after pulse injection in 10% of NaCl. As result salt concentration of 10% of NaCl is that injected to RO system was chosen as the optimal concentration.

Keywords: Membrane cleaning, Direct osmosis, Membrane fouling, Reverse osmosis, Osmotic backwashing

INTRODUCTION

The use of reverse osmosis (RO) technology has grown rapidly through the 1990's and early 2000's. The ability of RO to replace or augment conventional ion exchange saves end users the need to store, handle, and dispose of large amounts of acid and caustic, making RO a "greener" technology. Reverse Osmosis (RO) is a membrane-based demineralization technique used to separate dissolved solids and it has become one of the major technologies for producing potable water throughout the world [1]. Reverse osmosis has become one of the high potential technologies for producing either purified water or to concentrate and recover dissolved solids in the feed water [2]. In addition to providing drinking water with this method, this method is much used in industry. For example the most common application of RO in industry is to replace ion exchange, including sodium softening, to purify water for use as boiler makeup to low- to medium-pressure boilers. Other common applications of RO include: desalination of seawater, generation of high-purity water for pharmaceuticals, generation of ultrapure water for the microelectronics industry and pharmaceuticals, processing of dairy products, waste treatment for the recovery of process materials and so on. In this method, membranes in general act as perm-selective barriers, barriers that allow some species

(such as water) to selectively permeate through them while selectively retaining other dissolved species [3]. Specifically, fouling of membranes is the most important problem in reverse osmosis since economics of the process is still highly influenced by membrane fouling rate and effectiveness of fouling control [4]. Membrane lifetime and permeate productivity are primarily affected by concentration polarization and fouling at the membrane surface [5]. In this regard, the performance of a membrane due to the deposition of suspended or dissolved substances on its external surfaces, at its pore openings or within pores decreases. The mechanisms of membrane fouling are adsorption, Pore blockage, gel formation and biofouling [6]. As a result of membrane fouling, membrane resistance increases with time due to accumulation of foulants on membrane surface and inside the membrane [7]. The main results of fouling are: flux decline, permeate quality deterioration and energy consumption increase. Since operating costs of reverse osmosis highly depend on membrane useful life, fouling control is essential for increasing membrane operational life and thus reducing economics of the process [8]. The ways for fouling control are feed pre-treatment, operation conditions and membrane cleaning. Good pre-treatment avoid or minimize fouling, but in spite of good pre-treatment, membranes have to be periodically cleaned to remove reversible fouling. Operation conditions i.e. temperature, pressure and crossflow velocity can be considered to reduce fouling [9]. Despite the methods that can help to

* To whom all correspondence should be sent:
E-mail: mostafa.tabatabaee@yahoo.com

reduce fouling, membrane cleaning is necessary. Membrane fouling can be mitigated with chemical, physical and physio-chemical. In practice, physical cleaning methods includes sponge ball cleaning, forward and reverse flushing, backwashing, air flushing, Ultrasonic, electrical fields and magnetic fields followed by chemical cleaning methods and are widely used in membrane applications. However, only the chemical cleaning methods are widely applied for RO processes. In chemical cleaning the choice of the cleaning agent is critical. The optimal selection of the cleaning agent depends mainly on membrane material and type of foulant. Chemical method is an effective method to remove foulants, but this method, resulting in process downtime, membrane degradation and increased operation costs is costly and requires to stop ping the RO plant operation. Physico-chemical cleaning methods are not implemented widely in the RO industry. The applications usually consist in forward flushing with permeate between cleanings when more than one chemical cleaning is used [10], but not in a simultaneous use of physical and chemical cleaning actions. Recently innovative and non-conventional method for membrane cleaning is used. There have been significant developments in new devices for energy recovery, new membrane materials, and new sizes and orientations of RO plants, all designed to reduce costs and improving efficiency. Alternative methods of recovering RO membrane performance include Electro Magnetic Fields (EMF), [11] Direct Osmosis at High Salinities (DO-HS) [12] air scouring using compressed air [13] and combined hydrodynamic and chemical cleaning [14]. Some of these techniques have been applied to RO membranes but most work appears to have been conducted on UF membranes. There has not been a wholesale adoption of any new cleaning techniques for RO membranes [10].

Advanced processes are sought that can enhance water recovery without the limitations associated with the current processes [15]. Forward osmosis (FO) or Direct Osmosis (DO) as a novel process has attracted much interest because of its potential applications in seawater desalination [16], wastewater reclamation [17], energy production

[18-19-20-21-22-23-24], and so on. The water permeation in the DO process is brought about by an osmotic pressure difference across semi-permeable membranes. The water molecules can be transferred from a low concentration solution to a high concentration solution without applied hydraulic pressure. The DO process has great potential to enable versatile novel applications such as pure water drawing for product enrichment, hybrid desalination [25], energy production, and so on. Although a few DO processes have already been commercialized, further efforts are required to achieve their industrial use worldwide [26]. Pressure driven backwashing is common practice in filtration processes, including microfiltration and ultrafiltration, offering an effective means of fouling control. However, it was not extensively employed for membranes used in RO, due to high back-pressure required for a hydraulically driven backwash since it may rupture the composite membrane used[27]. In this study, Osmosis-assisted cleaning of polyamide RO membrane carried out using direct osmosis (DO) in RO plant operation in continues mode without stopping of RO plant. In these experiments the membrane fouling trend is shown and then high concentration solution of salt injected in order to create osmotic pressure. This means that the permeate flow is improved .The aim of this project is to investigate the optimum concentration of salt for the implementation of this method and identify practical feasibility of this approach.

MATERIALS AND METHODS

Membrane characteristics

A polyamide Dow Filmtec membrane was used, which was flat sheet, hydrophilic, with a nominal pore size of 0.01 μ m. Some other specifications of membrane given in Table 1.

Test equipment

In this project for cleaning the polyamide RO membrane assisted by directly osmosis with saline solution, the semi-industrial pilot plant is designed and built.

Table 1. Membrane Specifications

Membrane	Part number	Active area, ft ² (m ²)	Feed spacer thickness (mm)	Permeate flow rate, gpd (m ³ /d)	Stabilized salt rejection (%)	Minimum salt rejection (%)
polyamide Dow Filmtec	Lc-HR-404	94(8.7)	28	2900(11)	99.7	99.5

The pilot includes pumps, tank (Super Duplex stainless steel) for feed, saline solution container, air regulator (R07-200-RNKA), feed temperature gauge, membrane chamber and membrane inlet and outlet gauge pressure. A NaCl solution as the high salinity solution and cooling water as feed solution were connected to Membrane chamber. The feed solutions were recirculated by high pressure pump (Wanner Engineering, Inc., USA, F20-111-2400/B) and a pulse of high concentration solution called hypersaline solution (HS) injected in to feed water after the membrane contaminated by organic and mineral foulants. Feed tank is capable of holding

about 20 liters of the solution. In order to discharge of solution after each test, the bottom of the tank is made bowl shaped and located on center. Tank outlet is equipped with a drain valve to full drain the solution from tank. Since the tests carry out at intervals of 2 to 4 hours, and during this time, by pumping the fluid, tank's temperature rises, in order to control the feed temperature, a cooling coil is placed vertically in the tank. This tank to provide pump's NPSH, have been installed at the proper height. Fig. 1 shows a schematic diagram of a pressure assisted osmosis evaluation system.

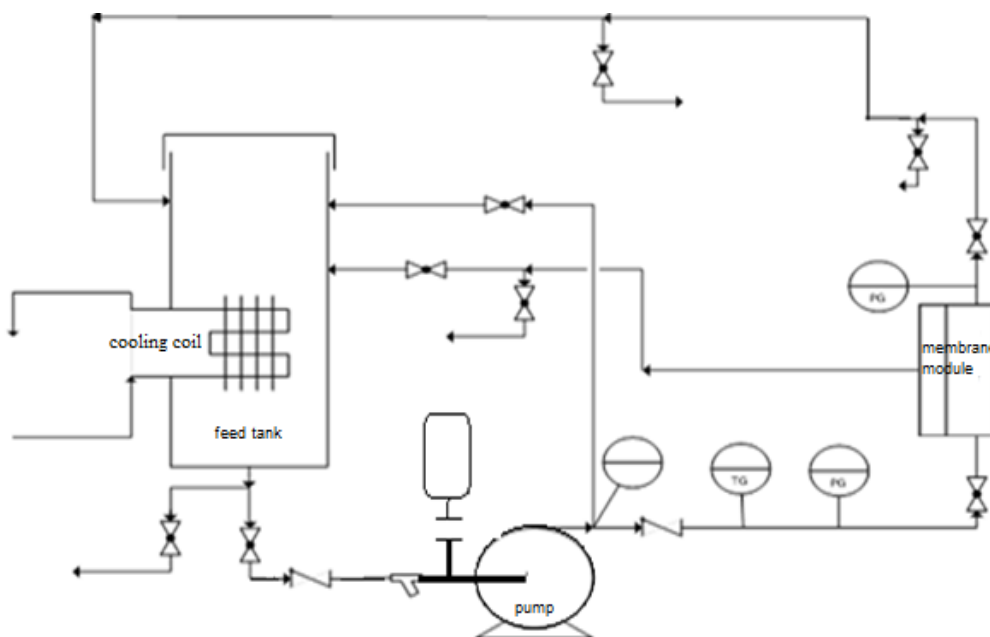


Fig.1. Schematic diagram of RO semi-industrial pilot plant

Determination of pure water permeability of clean membrane

After sealing the system, the Demineralized Water (DM) flux at pressures of 2, 4, 6, 8, 10 and 12 bar was measured. When the pressure was adjusted, at least certain time passed, the flux measurements were taken. This allowed the membrane to reach a steady state flux. So at least certain time passed, the volume of water that collected through membrane was recorded. From this data, the pure water flux was calculated at each different pressure. The general equation describing the water flux in direct osmosis (DO), reverse osmosis (RO), or pressure-retarded osmosis (PRO) is as follows [28]:

$$j_w = A(\Delta\pi - \Delta P), \quad (1)$$

Where, J_w is the water flux, A is the water permeability constant of the membrane, $\Delta\pi$ is the

osmotic pressure difference across the membrane, and ΔP is the applied hydraulic pressure difference.

In equation 1 the calculation of osmotic pressure is an important consideration. The van't Hoff equation provides the basis for that through the following simple relation for the estimation of osmotic pressure (π) for any dilute solution [29]:

$$\pi = MRT, \quad (2)$$

Where, M is the molar concentration of the solution, R is the universal gas constant, and T is the absolute temperature. If the solute is a strong electrolyte that completely dissociates in water and contains m ions, then the Van't Hoff equation becomes the following [30]:

$$\pi = \frac{m x_1 RT}{V_2}, \quad (3)$$

Where, x_1 is the mole fraction of species 1 (electrolyte) and V_2 is the molar volume of water. Pure water permeability coefficient calculation were done at 2, 4, 6, 8, 10 and 12 bar. Osmotic

pressure calculated by equation 2. Based on experimental data by calculating the slope of J_w versus $(P-\pi)$ membrane permeability coefficient obtained.

Fouling experiments

Fouling studies with cooling water (collected from cooling tower of Marun petrochemical company, Mahshahr, Iran) as feed at 25°C and pressures of 2, 4, 6, 8, 10 and 12 bar were conducted until a steady-state flux was observed. Other than measuring the water fluxes produced in RO tests, the conductivities were measured per day in order to determine either the solute rejection or the reverse solute transport across the membrane. The conductivities of the feed solution, draw solution and permeate were measured using a conductivity meter (1214000, Thermo Scientific Orion, Beverly, MA), and the solute rejection were then calculated. Prior to using the conductivity meter, calibration curves associating individual solute concentration in water with conductivity were conducted to facilitate the calculation of solute concentration following the measurement of conductivity during the tests. By calculating the solute concentration before and after each experiment, the solute rejection can be determined using the equation as shown in Eq. (4) for RO experiments.

$$\text{Rejection, \%} = \frac{C_{\text{feed,initial}} - C_{\text{permeate,final}}}{C_{\text{feed,initial}}} 100\%, \quad (4)$$

In order to investigate the membrane fouling, the tests were carried out at different pressures in 11 days. Permeability coefficients at different pressures calculated in the 11 days and its results will be reported.

Membrane cleaning experiments

The cleaning procedures applied were either: (1) physical cleaning, which involved recirculating DM water for 20 min with no permeation. (2) osmotic cleaning, which consisted of recirculating a high salinity feed solution for 21 second followed by physical cleaning as described above in procedure 1. In these experiments the RO system was adjusted on pressure of 10 bar. Pulse duration should be longer than the residence time for a maximum achievable cycle-averaged permeation rate. A shorter pulse is ineffective in inducing osmotic permeation. In fact, short pulse is significantly diluted on the membrane surface to the point where its concentration may drop below that required for inducing osmotic flow. The pulse concentration and duration must be optimized if efficient osmotic cleaning is to be achieved throughout the full length of a membrane train. So osmotic backwash cycle 60

induced by seven pulse of high concentration solution of NaCl during 21 second that create osmotic pressure more than hydraulic pressure. Duration of each pulse was 3 second. Two draw concentration 8% and 10% NaCl solution are injected to RO system. Simultaneously with per pulse permeate flow is almost zero and DO were made. After the injection of salt solution and stability of RO system; the tests take place to measure the permeate flux again. Salt injection into the system at both levels will continue to 6 days. Permeate flow is measured per day in each of concentration separately.

RESULTS AND DISCUSSION

Permeability coefficient calculation of clean membrane

The result of permeate flux of clean membrane at different pressures is given in Table 1.

Permeability coefficient calculated by equation 1.

As can be seen in table 1, the permeate flux increased with increasing ΔP because the additional applied hydraulic pressure could work as a high driving force in all experiments. By calculating the slope of J_w versus $(P-\pi)$ membrane permeability coefficient obtained. Result given in figure 2.

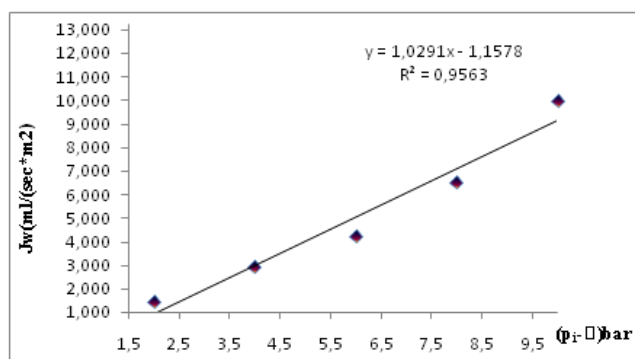


Fig. 2. Permeate flux of clean membrane at different pressures

Membrane fouling

Permeate flux of fouled membrane at different pressures in 11 days measured and subsequently the permeability coefficients of membrane calculated by equation 1. The results are given in Table 2.

As can be seen, permeability coefficients of membrane are reduced per day which this indicates fouling of membrane during these days. According to measurement taken within 11 days and taking into account the operating pressure is 10 bar, the reduction in permeate flow and the TDS concentration of feed, permeate and rejection flow are given in Table 3 & 4.

Table 2. Water permeate flux of clean membrane

i	P _{in} (bar)	P _{out} (bar)	t(sec)	V(ml)	Q _p (ml/s)	Temp(C)	J _w (ml/m ² .sec)
1	2	0.6	20.29	258	12.71	37	1.462
2	4	1.4	20.58	523	25.41	37	2.921
3	6	2.1	20.35	750	36.85	37	4.236
4	8	4	20.46	1158	56.59	37	6.506
5	10	7.4	20.31	1760	86.66	37	9.961
6	12	10.5	20.23	2329	115.12	37	13.233

Table 3. Permeability coefficients of fouled membrane in 11 days

	First day	Second day	Third day	Fourth day	Fifth day	Sixth day	Seventh day	Eighth day	Ninth day	Tenth day	Eleventh day
Permeability Coefficient (ml/m ² .s.bar.)	1.01	1.0	0.98	0.93	0.83	0.8	0.78	0.74	0.69	0.65	0.6

Table 4. Results of membrane fouling at pressure of 10 bar

Test number (day)	TDS _F (mg/lit)	Cond _F (µs/cm)	TDS _R (mg/lit)	Cond _R (µs/cm)	TDS _P (mg/lit)	Cond _P (µs/cm)	Q _P (Lit/s)	Reduction of permeate flow(%)
First	285	570	340	680	2.4	4.6	0.086	0
Second	303	604	342	687	2.35	4.6	0.083	3
Third	287	574	353	705	2.4	4.75	0.08	6.82
fourth	391	782	469	936	3.7	7.3	0.083	3.09
fifth	438	875	627	1255	3.7	7.4	0.058	32.29
sixth	1370	2750	1528	3100	5.1	10.3	0.057	33.93
seventh	1370	2750	1528	3100	5.1	10.3	0.051	40.54
Eighth	1650	3300	1817	3640	6.2	12.3	0.062	28.26
Ninth	1970	3940	2350	4700	6.5	13	0.051	40.54
Tenth	2270	4530	2430	4870	8	16.1	0.049	43.02
Eleventh	2530	5110	3310	6600	17	34	0.047	45.35

As it is seen, conductivity and subsequent TDS increase during 11 days, it means that the membrane fouling is increasing. With putting the RO system in service and daily calculation of important parameters such as TDS, conductivity for feed, permeate and rejection flow, Input and output pressure of the membrane and calculation of permeate flux, the percentage of membrane clogging is investigated. The results show that the

percentage of fouling in the membrane of the 11 days is increased approximately 45 percent.

Osmosis-assisted cleaning of fouled membrane

The osmotic pressure assisted operation has a potential use in membrane cleaning by high salinity solutions. Therefore, to estimate the potential use for salinity solutions, we investigated the effect of salt concentration of NaCl on permeate flux in RO membrane and membrane cleaning during DO

process. Draw solutions used in the osmotic cleaning experiments are NaCl solutions with a concentration of 80 and 100 gr/l. These concentrations of salt create osmotic pressure of 35 and 43 bar respectively.

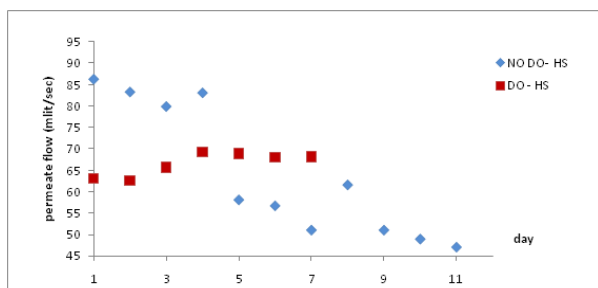


Fig. 3. Influence of performing DO process on permeate flow (pulse injection salt's concentration of 8%)

The change of permeate flux after salt injection with concentration of 8% at pressure of 10 bar is given by Table 5.

In the pulse injection, desorption process take place. Since desorption is endothermic process, so the temperature of system reduce. As shown in the table above, after a week of injection high salinities (8% NaCl solution), permeate flux increased about 45 percent than the last day before injection. Influence of performing DO process on permeate flow illustrate in figure 3.

In order to create a strong net driving force of 43 bar for the DO backwash process high-saline solution made of 10% NaCl could be injected into the feed stream over a few seconds before the injection of high-solution, the RO system put in service to membrane fouling reached up to 35 %.

Table 5. Result's data after pulse injection in 8% of salt concentration

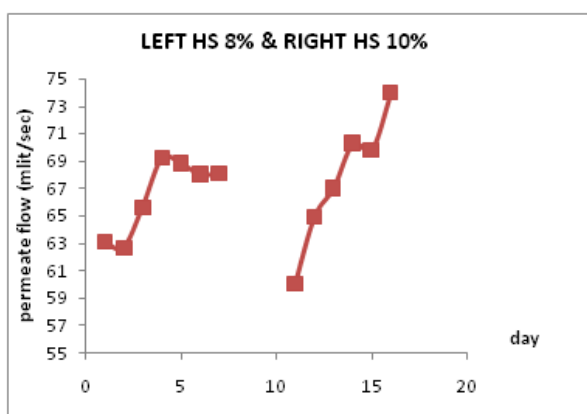
P _{in} (bar)	Test number (day)	P _{out} (bar)	Cond _p (μs/cm)	Q _p (ml/s)	J _w (ml/m ² .s)	T (°C)
10	The day before salt injection	8.7	16.7	47	5.387	33
10	1	8.9	3.54	63.12	7.205	30
10	2	9	3.07	64.69	7.21	29
10	3	9	2.78	65.65	7.55	29
10	4	9	2.5	67.85	7.63	29
10	5	8.95	2.41	68.04	7.71	28
10	6	8.95	2.23	68.04	7.82	28
10	7	8.95	2.1	68.12	7.83	28

Table 6. Result's data after pulse injection in 10% of salt's concentration

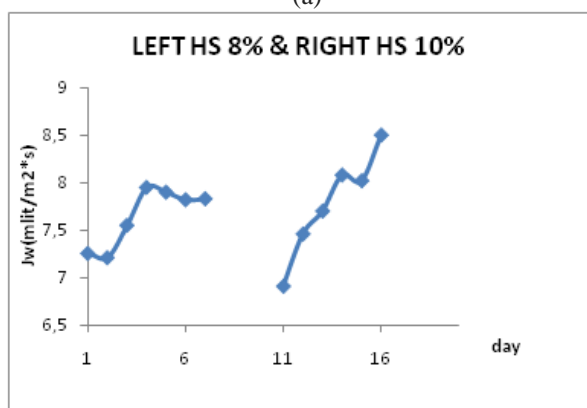
Test number (day)	P _{in} (bar)	P _{out} (bar)	Cond _p (μs/cm)	Q _p (ml/s)	J _w (ml/m ² .s)	T (°C)
The day before salt injection	10	9.2	7.2	55.26	6.35	31
1	10	9.25	6.94	60.10	6.91	30
2	10	9.3	2.49	64.94	7.46	29
3	10	9.25	2.57	67.03	7.70	30
4	10	9.2	2.89	70.29	8.08	30
5	10	9.2	3.18	69.81	8.02	30
6	10	9.2	3.7	73.96	8.5	30

Table 7. Result's data after and before pulse injection in 8,10% of salt's concentration

	P _i (bar)	P _{out} (bar)	Q _p (ml/s)	J _w (ml/s.m ²)	T (°C)	Π(bar)	Permeability Coefficient (ml/s.m ² .bar)
Before salt injection	10	7.4	86.66	9.961	37	0	1.0291
After salt injection with concentration of 8 %	10	8.9	68.12	7.83	28	0.00578	0.88
After salt injection with concentration of 10%	10	9.2	73.96	8.5	30	0.023	0.924



(a)



(b)

Fig 4. Significant increasing in the a(permeate flux b)permeate flow after solution injection.

As shows Table 5, after 6 days of injection high-saline permeate flow increased about 34% Than the last day before injection. Increase permeate flow after day solution injection has been demonstrated in figure 4.

Figure 4 indicate that the slope of permeate flux and permeate flow with a short injection of feed with increased salt concentration (10% NaCl solution) with an associated osmotic pressure of 43

bar is growing faster than the other one(8% NaCl solution).also it is indicate that an increase in salt concentration, caused more stable system and increasing in permeate flow and permeate flux can be observed. The reversible flow helps to dislodge any foulants (mineral and organic foulants) and scaling on the membrane surface and promotes lifting, sweeping and removing of the concentration polarization CP layer. In this case the percent of salt rejection calculated by equation 4 is 99.5% after solution injection. so this method considered as effective and potentially technique that able to membrane cleaning.

Permeability coefficient calculation of membrane after salt injection with concentration of 8 and 10% NaCl

As in the starting up of process the permeability coefficient calculated by DM water, at this stage instead of cooling water (feed) ,DM water is used and permeability coefficient calculated after salt injection. Results showed in Table 6.

As can be seen permeability coefficient of membrane is 1.02 at first day (before salt injection) while it is reached to approximately 90 percent of itafterpulse injection in 10% of salt concentration. Also in the short time we have achieved the desired result by injection in 10% of salt concentration.

CONCLUSION

There is clearly much scope for the development of assisted pressure process like DO for membrane cleaning. In general this method is considered an innovative, effective and potentially chemical-free cleaning technique and was used as a novel backwash approach for on-line polyamide membrane cleaning in RO operation without stopping the RO pump in this research. In the system studied, foulant removal was facilitated by

the combined effect of DO process by high saline solution of NaCl with RO process. Draw strength (concentration of salt) optimization may be achieved by considering the amount of permeate flux and toleration of osmotic pressure by polyamide membrane. Results showed that there is more increasing in permeate flux by pulse injection of 10% NaCl than the other one (8% NaCl solution). On the other hand, there was not polyamide membrane rupture under osmotic pressure. Permeability coefficient of membrane reached to approximately 90 percent after pulse injection in 10% of NaCl as well as. So 10% NaCl as salt concentration. To the best of our knowledge the current study is one of the first one to have demonstrated the application of DO process in polyamide RO membrane cleaning. It can be concluded from the work reported here in that the membrane cleaning by hypersaline solutions ensured stable operation with significantly improved membrane performance, consistently reduced low pressure drop and increased membrane salt rejection. Nevertheless it deserves further study.

Acknowledgments: The author would like to gratefully acknowledge financial and technical support of Marun petrochemical company and Department of Chemical Engineering, Mahshahr Branch, Islamic Azad University, Mahshahr, Iran.

REFERENCES

1. J. Kucera, Reverse Osmosis, design, processes and applications for engineers, WILEY, 2010.
2. A. Al-Amoudi, W.L. Lovitt, *Journal of Membrane Science*, **303**, 4 (2007).
3. J.-J. Qin, B. Liberman, K.A. Kekre, *The Open Chem. Eng. J.*, **3**, 8 (2009).
4. G.Z. Ramon, *Chemical Engineering Journal*, **218**, 173 (2013)..
5. J.J. Sadhwani, J.M. Veza, *Desalination*, **139**, 177 (2001).
6. M.F.A Goosen, S.S. Sablani, H. Al-Hinai, S. Al-Obeidani, R. Al-Belushi, D. Jackson, *Separation Sci. Technol.*, **39**, 2261 (2004).
7. K.G. Tay, L. Song, *Desalination*, **177**, 95 (2005).
8. F.H. Butt, F. Rahman, U. Baduruthamal, Characterization of foulants by autopsy, 1997.
9. T. Mohammadi, M.K. Moghadam, S.S. Madaeni, *Desalination*, **151**, 239 (2002).
10. S. Ebrahim, *Desalination*, **96**(1-3), 225 (1994).
11. H. Y. Ng, H. Winters, A Novel 16-Inch RO System for Water Reuse and Desalination. (Israel Desalination Society Annual Conference, 19-20 December), 2006.
12. W. Seng Ang, N.Y. Yip, A. Tiraferri, M. Elimelech, *Journal of Membrane Science*, **382**, 100 (2011).
13. J.-J. Qin, M.H.O. Kiran, A. Kekre, Herry Seah Optimization of Direct Osmosis - High Salinity Cleaning for RO Fouling Control in Water Reuse, Technology & Water Quality Office, Public Utilities Board, Singapore, 2010,
14. S.A. Avlonitis, K. Kouroumbas, N. Vlachakis, *Desalination*, **157**, 151 (2003).
15. J. Qin, H. Oo, K. Kekre, B. Liberman, *J. Membr. Sci.* **346**, 8 (2010).
16. A.D. Khawaji, I.K. Kutubkhanah, J.M. Wie, *Desalination*, **221**, 47 (2008).
17. A. Achilli, T.Y. Cath, E.A. Marchand, A.E. Childress, *Desalination*, **239**, 10 (2009).
18. M. Xie, L.D. Nghiem, W.E. Price, M. Elimelech, *Environ. Sci. Technol.*, **47**, 13486 (2013).
19. A. Achilli, T.Y. Cath, A.E. Childress, *J. Membr. Sci.* **343**, 42 (2009).
20. Q. She, X. Jin, C.Y. Tang, *J. Membr. Sci.*, **401-402**, 262 (2012).
21. K.L. Lee, R.W. Baker, H.K. Lonsdale, *J. Membr. Sci.*, **8**, 141 (1981).
22. S. Loeb, *Desalination*, **143**, 115 (2002).
23. N.Y. Yip, A. Tiraferri, W.A. Phillip, J.D. Schiffman, L.A. Hoover, Y.C. Kim, M. Elimelech, *Environ. Sci. Technol.*, **45**, 4360 (2011).
24. Y.C. Kim, M. Elimelech, *Environ. Sci. Technol.*, **46**, 4673 (2012).
25. P.H.H. Duong, T.-S. Chung, *J. Membr. Sci.*, **452**, 117 (2014).
26. M. Shibuya, M. Yasukawa, T. Takahashi, T. Miyoshi, M. Higa, H. Matsuyama, *Desalination*, **365**, 381 (2015).
27. G. Ramon, Y. Agnon, C. Dosoretz, *Journal of Membrane Science*, **364**, 157 (2010).
28. T.Y. Cath, A.E. Childress, M. Elimelech, *J. Membr. Sci.*, **281**, 70 (2006).

Analysis of the effects of alcohol on displacement performance of the micro-emulsion system through ε - β -fish-like phase diagram

D. Yin*, K. Liu, Y. Zhou

College of Petroleum Engineering, Northeast Petroleum University, Heilongjiang, Daqing, 163318

Received February 18, 2016; Revised September 10, 2016

In the article, a more accurate and intuitive ε - β -fish-like phase diagram is adopted to study the effects of different kinds of alcohols with various concentrations on phase changes of the micro-emulsion system and solubilisation parameters by analyzing the pros and cons of different phase diagrams. We already know that the solubilisation parameters and mid-phase region ranges change with alcohols, so the mixed alcohols composed of n-propanol and n-butyl alcohol (1:1) are chosen as co-surfactants. The micro-emulsion system (1:1 oil-water ratio) is composed of sodium dodecyl sulfonate (AS) with a concentration of 2%, mixed alcohols of 3% and NaCl of 5%. This system is adopted as the formula to conduct the displacement experiments. Compared with the experiments without micro-emulsion or systems with a single type of alcohol, the result shows that this micro-emulsion system can reduce water content by up to 23.7% and increase the displacement efficiency by 13.31% through water displacement. Thus the article has reasonably proved that this formula turns out more effective in terms of water content and displacement efficiency.

Keywords: Micro-emulsion, ε - β -fish-like phase diagram, Solubilisation parameter, Oil displacement experiment, Alcohol

INTRODUCTION

One of the major advantages of micro-emulsion in the flooding process is the high solubility parameter, ultra low interfacial tension and large middle phase area, which are mainly determined by the properties of surfactant [1-2]. Alcohol, as a type of co-surfactant, can improve the performance of surfactant system [3]. Therefore, it is necessary to understand the effects of different concentrations and types of alcohol on the performance of micro emulsion. In the article, for the study of the range of phase solubilisation parameters of micro-emulsion system, we have chosen the ε - β -fish-like phase diagram method, which can directly estimate the hydrophilic lipophilic degree of surface active agent, three-phase region size and the efficiency of solubilisation of oil and water. We find that the shorter the carbon chain is, the higher the alcohol fraction mass in the interfacial film, or rather, the lower the solubility is, but the larger the middle phase region is [4-5]. As a result, the n-propyl alcohol/n-butyl alcohol is adopted as the assistant surfactant. Then a displacement experiment is carried out by using the AS/mixed-alcohol/octane/NaCl micro-emulsion formulation. The results show that the mixed alcohol system is more effective in terms of water

content and displacement efficiency. In the article, an efficient and cost-effective formulation is finally determined by taking only micro-emulsion into account, the results of which could provide a reasonable and reliable basis for future research [6-7-8].

RESEARCH METHOD FOR THE PHASE BEHAVIOR OF MICRO-EMULSION

The methods to study the phase behavior of micro-emulsion mainly include the Winsor phase diagram, δ - γ -fish-like phase diagram and ε - β -fish-like phase diagram. The Winsor phase diagram can only represent a qualitative phase change state, on the basis of which the δ - γ -fish-like phase diagram and the ε - β -fish-like phase diagram are able to calculate the relevant physicochemical parameters. Besides, parameters obtained from ε - β -fish-like phase diagram tends to be more reliable.

The Winsor phase diagram

The Winsor phase diagram illustrates the phase change in the system, phase volume, the minimum alcohol concentration and alcohol width required for the formation of middle phase micro-emulsion. In the Winsor phase diagram, when the concentration gets low, the system turns into Winsor I micro-emulsion, in which a phase equilibrium is reached between the micro-emulsion and the remaining oil. With the increase of the concentration of alcohol in the system, the middle

* To whom all correspondence should be sent:
E-mail: yindaiyin@163.com

phase micro-emulsion appears and a Winsor III micro-emulsion is formed together with the oil and the water phase. Continue increasing the concentration of alcohol, the middle phase micro-emulsion disappears and the Winsor II micro-emulsion appears with a phase equilibrium of micro-emulsion and residual water. However, when the middle phase micro-emulsion and single phase micro-emulsion are formed, it will be difficult for the Winsor phase diagram to determine the composition of the equilibrium interfacial film and the solubilisation properties of the whole system.

δ - γ -Fish-like phase diagram

The δ in the δ - γ -fish-like phase diagram is a mass fraction between the surfactant and alcohol; γ is the mass fraction of alcohol and surfactant in the system. Therefore, the drawn fish-like phase diagrams seem noticeably "head" up and "tail" down, which describes the whole process of micro-emulsion phase transition. At the point of "fish head", the middle phase micro-emulsion and the "fishtail" single-phase micro-emulsion appears. The area below the "fish belly" indicates the O/W type micro-emulsion and the area above of that means the type of W/O micro-emulsion. The center lines of the "fish head", "fish tail" and the "fish belly" in micro emulsion fish-like phase diagram correspond to the equilibrium positions of the lipophilic and hydrophilic action. Therefore, the component of interfacial film can be calculated when the average curvature is zero based on the theory of constant interface composition. δ - γ -fish-like phase diagram has many advantages over the Winsor phase diagram. For example, we can calculate through the fish-like phase diagram the components of the system's composition, the equilibrium interfacial film composition, the surface active agent, alcohol in the oil phase solubility of the middle phase and single phase micro-emulsion. However, the δ - γ -fish-like phase diagram also has its deficiencies. It can not directly reflect the changes of the phase state nor the changes of the volume of each phase. The center line of the three-phase region corresponding to the lipophilic hydrophilic balance equation in this phase diagram appears steeper and it is difficult to obtain an accurate curve, leading to a larger error. Furthermore, E point of "fish tail", γE , reflects the total mass fraction of alcohol and surfactant in the system, but it fails to reflect directly the least required surface active agent and the amount of alcohol when the single phase micro-emulsion appears.

ϵ - β -fish-like phase diagram

In the ϵ - β -fish-like phase diagram, ϵ is the mass fraction of the alcohols and β is the mass fraction of the surfactants in the micro-emulsion system. Its difference with the δ - γ -fish-like phase diagram is that the "fish head" pitches down and the "fish tail" pitches up, which means the amount of alcohols (ϵ) that is used to form a mid-phase microemulsion increases as the surfactant content (β) increases. We can see directly from the whole phase diagram that the phase state of the micro-emulsion system changes with the concentration of alcohol. The x-coordinate of the "fish tail" reflects the minimum amount of surfactant required for the formation of single phase micro-emulsion when oil and water are dissolved by the same amount. Y-coordinate reflects the minimum amount of alcohol required. Therefore, we are able to calculate accurately the various physical and chemical parameters through the ϵ - β -fish-like phase diagram; it can also reflect directly the least surface active agents and the amount of alcohol required for the formation of a single phase micro emulsion and to evaluate the solubilisation ability of the micro-emulsion system more comprehensively. In order to observe the whole process of phase change and to calculate accurately the minimum alcohol concentration required to form the single phase micro-emulsion with the same amount of oil and water, we have compared the solubilisation parameters of different systems according to the characteristics of each phase. In the article, the ϵ - β -fish-like phase diagram is adopted to study the effects of different concentration and types of alcohol in micro-emulsion system [9-10-11-12].

THE INFLUENCE OF ALCOHOL CONCENTRATION ON PHASE CHANGE OF MICRO-EMULSION

The addition of low carbon alcohol can increase the solubility of the surfactant, and thus increase the ability of the surfactant to tolerate salt, which will finally lead to the phase change state of the system. Therefore, under a certain salinity, a specific alcohol concentration is required for any surfactant to facilitate the formation of a middle phase micro-emulsion system. The ϵ - β -fish-like phase diagram is adopted to study the phase change state of the system AS/ n-butanol / n-butane /NaCl, and the minimum alcohol content in the formation of the optimum phase micro-emulsion, or the solubilisation property of the system. In the micro-emulsion system, the mass fraction of AS is 2%, the mass fraction of co-surfactant alcohol is

3%, the concentration of NaCl is 5%, the ratio of oil and water is 1:1 [13-14-15-16].

Major instruments and chemicals

Experimental equipment: FA1104 electronic balance, 80-B2 constant temperature box, 800 centrifugal precipitator, Set thermal type DF-101S magnetic heating agitator.

Experimental agents: Twelve sodium alkyl sulfonate (AS) of the analysis grade of purity, used after recrystallization for the experiment, Octane, Butyl alcohol; double deionized water; the other reagents are A.R. grade.

Experimental method

First, add surface active agents with different qualities to a series of test tubes; keep the mass ratio of 5% of brine, and normal octane as 1; drop into different quality alcohol into a series of tubes; place the test tubes in a chamber under a constant temperature of 40 degrees Celsius for a week. When the balance is achieved, take notes of the volume of phase in the test tube.

EXPERIMENTAL RESULTS AND DISCUSSION

Method to determine the position of heads and tails in coordinates

To draw the ε - β -fish-like phase diagram of the AS/ n-butanol / n-butane of /NaCl system, we need first determine the coordinates of heads and tails. The head of coordinates is where the middle phase micro-emulsion begins to appear and the volume is zero. Fish tail coordinate is where water and aliphatic hydrocarbons of the same amount are solubilized completely in single-phase micro-emulsion phase with zero additional volume, that is the moment the middle phase micro-emulsion disappears. When determining the positions of the heads and tails, the reading error is relatively large for the micro-emulsion system subjected to transient changes, thus the extrapolation method is used. First, plot the relations of ratios of the volume fraction of the middle phase micro-emulsion to the entire system (φ) and the mass fraction of the surface active agent to the total volume (β); then fit a straight line. When the value of φ is 0 or 1, the extrapolated values of β corresponds to the abscissas of heads and tails. The relation between φ and β is shown in Fig.1.

According to the linear equation of the relation: $\varphi = 11.11\beta - 0.044$, when φ is 0, $\beta_b = 0.004$ at the fish head; when φ is 1, $\beta_E = 0.094$ at the fish tail.

The ε - β -fish-like phase diagram

The fish-like phase diagram of AS/ butanol / octane /NaCl micro-emulsion system is shown in Fig.2.

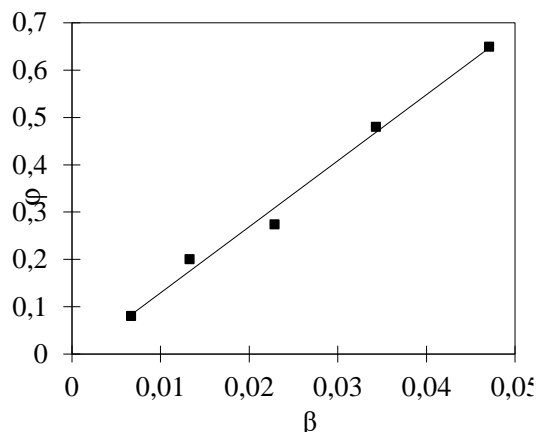


Fig.1. The relation of volume fraction φ - β in middle phase micro-emulsion

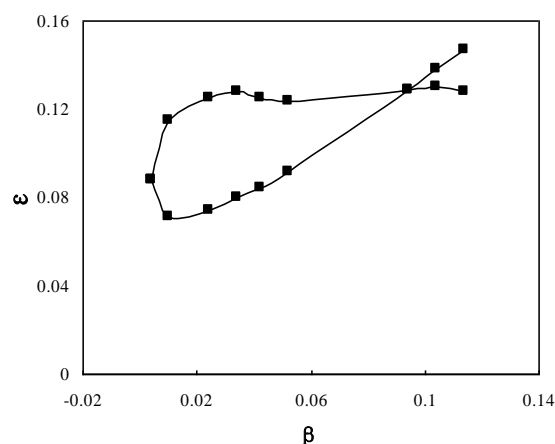


Fig.2. The ε - β -fish-like phase diagram of AS/ butanol / octane /NaCl micro-emulsion system

Concluding discussion

We can see from the fish-like phase diagram that when β remains constant, the whole micro-emulsion system is transformed from type Winsor I to type Winsor III and to type Winsor II with the increase of the concentration of alcohol [5]; with the increase of surface active agent, the alcohol concentration required to form a middle phase micro-emulsion will increase; the alcohol width that corresponds to the ε difference of the middle phase micro-emulsion between appearance and disappearance will decrease. The alcohol width decreases with the increase of surfactant concentration, and is affected by the curvature of the interfacial film, or rather, when surfactant concentration is low, the change of the curvature of the interfacial film from the formation of the middle phase micro-emulsion to its disappearance is larger due to little solubilisation; when the

concentration is higher, the change of curvature of the interfacial film gets smaller due to the increasing solubilisation. Therefore, with the increase of surfactant concentration, both the variation amplitude of the curvature of the interfacial film and the alcohol width will decrease.

Statistically, in the system of AS/butanol/octane/NaCl, when the surfactant concentration reaches 0.004mol/L and the alcohol concentration 0.088mol/L, the middle phase micro-emulsion begins to appear. When the surfactant concentration reaches 0.094mol/L and the alcohol concentration 0.129mol/L, the micro-emulsion disappears, and the single phase micro-emulsion will begin to appear.

THE INFLUENCE OF THE TYPE OF ALCOHOL ON PHASE CHANGE OF MICRO-EMULSION SYSTEM

Alcohol, as a facilitating surfactant, is one of the indispensable factors for the formation of micro-emulsion. Different types of alcohols have different effects on the structure of the interfacial film, and the effect varies due to different types of alcohol to change the optimal salinity of the system by changing the curvature of the micro emulsion droplets either in the form of concave or convex towards the oil phase, so it is necessary to select carefully the best type of low carbon alcohol to increase the solubility of surfactants and thus to improve the efficiency of the surfactant and reduce costs.

Major instruments and chemicals

Experimental equipment: FA1104 electronic balance, 80-B2 constant temperature box, 800 centrifugal precipitator, Set thermal type DF-101S magnetic heating agitator.

Experimental agents: Twelve sodium alkyl sulfonate (AS) of the analysis grade of purity, used after recrystallization for the experiment; Octane, n-propanol, Butyl alcohol, n-amyl alcohol, double de-ionized water; the other reagents are A.R. grade.

Experimental method

First, add surface active agents with different qualities to a series of test tubes; keep the mass ratio of 5% of brine and normal octane as 1; drop different amounts of n-propanol into a series of tubes; place the test tubes in a chamber with a constant temperature of 40 degrees Celsius for a week. After a balance is achieved, take notes of the volume of phase in the test tube. Similarly, the corresponding phase volume data is recorded when the normal butyl alcohol and butyl alcohol are

added.

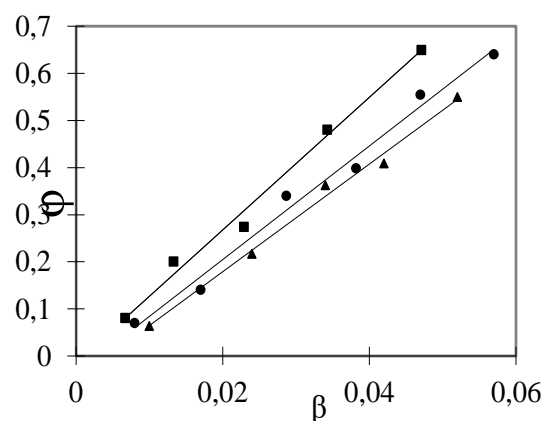


Fig.3. The relation of volume fraction ϕ - β in middle phase micro-emulsion

Experimental results and discussion

Method to determine the positions of heads and tails in coordinates

The relation between ϕ and β is shown in Fig.3. According to Fig. 3, when n-propyl is used as co-surfactant in the micro-emulsion system, the fitting linear equation is: $\phi = 6.58\beta - 0.013$. When ϕ is 0, $\beta_B = 0.002$ at the fish tail; when ϕ is 1, $\beta_E = 0.154$ at the fish tail. The fitting linear equation of Butyl alcohol is: $\phi = 11.11\beta - 0.044$. When ϕ is 0, $\beta_B = 0.004$ at the fish tail point; when ϕ is 1, $\beta_E = 0.094$ at the fish tail point. The fitting linear equation of n-amyl alcohol is: $\phi = 14.085\beta - 0.014$. When ϕ is 0, $\beta_B = 0.001$ at the fish tail point; when ϕ is 1, $\beta_E = 0.072$ at the fish tail point.

The ε - β -fish-like phase diagram

According to the calculated results of head and tail coordinates, we have drawn an AS/ n-propyl alcohol (Butyl alcohol, n-pentanol) / octane / NaCl system phase diagram (Fig.4.).

Calculation of physical and chemical parameters of the ε - β -fish-like phase diagram

The dotted line connecting point B and point E is the center line of the three-phase region. The oil-water interface composition of micro-emulsion system in this line has just reached a hydrophilic lipophilic balance. At this moment, the average curvature of the oil-water interfacial film is zero, and the micro-emulsion is the best medium phase micro-emulsion. The HLB equilibrium equation at each point of the center line is:

$$\varepsilon = \frac{A^s - F\alpha}{1 - A^s + F\alpha} \beta + \frac{F\alpha}{1 - A^s + F\alpha} \quad (1)$$

Where

$$F = \frac{A^o S^s - S^o A^s}{1 - S^o - A^o} \quad (2)$$

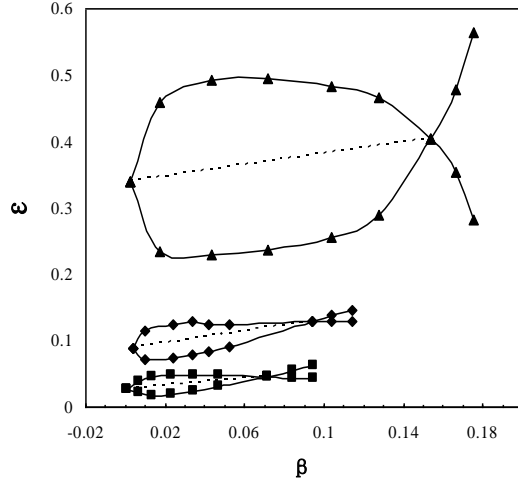


Fig.4. The ε - β -fish-like phase diagram of the AS/n-propyl alcohol (Butyl alcohol, n-pentanol) / octane / NaCl system

S^o and A^o represent the solubility of the surfactant monomer molecules and the alcohol molecules in the oil phase respectively; S^s and A^s represent the mass fraction of the surfactant and the alcohol in the mixed interfacial film respectively.

The phase center line is a straight line with the slope and intercept as K and I . A^s can be obtained by:

$$A^s = \frac{K + I}{1 + K} \quad (3)$$

S^s can be calculated by:

$$S^s = 1 - A^s \quad (4)$$

Surfactant and alcohol in the interfacial film can be determined by Equation (5,6). When the system has achieved a lipophilic hydrophilic balance:

$$C_s = \beta_E - \frac{\beta_B(1 - \beta_E - \varepsilon_E)}{(1 - \beta_B - \varepsilon_B)} \quad (5)$$

$$C_A = \varepsilon_E - \frac{\varepsilon_B(1 - \beta_E - \varepsilon_E)}{(1 - \beta_B - \varepsilon_B)} \quad (6)$$

Therefore, the mass fraction of the alcohol in the interfacial film can also be expressed as:

Table 1. Calculation results of the physical and chemical parameters of the ε - β -fish-like phase diagram.

Alcohol	β_B	ε_B	β_E	ε_E	A^s	S^o	A^o	C_s	C_A	A_{eff}^s
N-propyl alcohol	0.002	0.34	0.154	0.403	0.534	0.003	0.507	0.1526	0.1741	0.533
Butyl alcohol	0.004	0.088	0.094	0.129	0.372	0.007	0.162	0.0906	0.0537	0.372
N-pentanol alcohol	0.001	0.0263	0.0719	0.0453	0.232	0.002	0.048	0.071	0.0214	0.232

$$A_{\text{eff}}^s = \frac{C_A}{C_s + C_A} \quad (7)$$

Surfactant and alcohol solubility in oil phase S^o and A^o can be determined by Equation (8,9).

$$S^o = \frac{\beta_B}{\alpha + (1 - \alpha)(\beta_B + \varepsilon_B)} \quad (8)$$

$$A^o = \frac{\varepsilon_B}{\alpha + (1 - \alpha)(\beta_B + \varepsilon_B)} \quad (9)$$

A_{eff}^s represents the mass fraction of the interface membrane of n-propyl alcohol, Butyl alcohol and n-pentanol alcohol, which are 0.533, 0.372 and 0.232 respectively. The results are consistent with A^s calculated by corresponding systems, which has verified the accuracy of these two methods. All the calculated physical and chemical parameters according to the ε - β -fish-like phase diagram are shown in table 1.

Discussion over the performance of micro-emulsion

We can see from the ε - β -fish-like phase diagram that there are only small differences in the chain length of the three types of alcohols, while the difference in the phase diagram is noticeable. The longer the added alcohol carbon chain is, the smaller the formation of the micro-emulsion phase diagram will be, that is, the smaller the range of the formation microphase emulsion. But A^s decreases from 0.534 to 0.372 then to 0.232, which means that the solubilisation ability of the whole system has become larger, that is: n-pentanol alcohol > Butyl alcohol > n-propyl alcohol.

OIL DISPLACEMENT EXPERIMENT

Through the experiments above, we learn that the chain length of the alcohol is very sensitive to the phase state change of the whole micro emulsion system. In order to obtain a better solubility and a larger middle phase micro-emulsion region, the mixture of n-propyl alcohol / Butyl alcohol will be used as surfactant for oil displacement experiment. The results suggest that the mixed alcohols system has a better displacement efficiency to enhance oil recovery when compared with that of the micro-emulsion system with n-butyl alcohol only.

Experimental equipment and chemicals

Experimental equipment: core cutting machine, high pressure cleaning apparatus, drying box, vacuum pump, electronic balance, constant speed and pressure displacement pump, piston container, core holder, confining pressure device, thermostat, pressure gauge, cylinder etc.

Experimental agents: twelve sodium alkyl sulfonate (AS) of the analysis grade of purity, used after recrystallization for the experiment; octane; n-propyl alcohol, butyl alcohol, double deionized water, the other reagents are A.R. grade.

Experimental core: 2.5 × 2.5 × 30cm Daqing ultra low permeability natural core.

Experimental water: simulated formation water.

Experimental procedure

(1) Connecting device: connect the displacement device, pressure detecting device, liquid collection device and check leakage.

(2) Select full diameter core from Daqing outskirts low permeability oilfield; cut it into a series of cylinder-shaped samples. After extraction, dry them and measure the cores' dry weight, permeability, porosity and size. 3 cores with close permeability and porosity have been selected as experimental cores.

(3) Vacuum the core and saturate them with simulated formation water: immerse the 3 cores selected in simulated formation water; start the vacuum pumping device. Start the time recorder when the pressure of the vacuum gets below 0.098MPa, and vacuum for 24 h. In order to reduce errors, the mass difference of core saturation before and after saturation was measured by the weighing method; then calculate the saturated water volume.

(4) Put the core into the core holder; start flooding until no more oil will be recovered. Record the volume of water in the recovery liquid and calculate the initial oil saturation of the core.

(5) Waterflood the cores and record the outlet oil and water volume at different time and the pressure difference at both ends of the core until the water content of the sample reaches 95%.

(6) Select a piece of core, continue water flooding until the water content reaches 100%. Select another core and start injecting AS/ Butyl alcohol /octane /NaCl micro-emulsion system by 0.5PV and continue water flooding until the water content reaches 100%. Inject the last piece of core

with AS/ mixed alcohol /octane /NaCl micro-emulsion system by 0.5 PV and continue water flooding until the water content reaches 100%. Record the oil and water volume in the recovery liquid at different time and the pressure difference at both ends of the 3 cores [17-18-19-20].

Experimental results and discussion

The experimental results without micro-emulsion system, the experimental results with the injection of AS/ Butyl alcohol /octane /NaCl micro-emulsion system and the experimental results with the injection of the AS/mixed alcohol/octane/NaCl micro-emulsion system are showed in table 2.

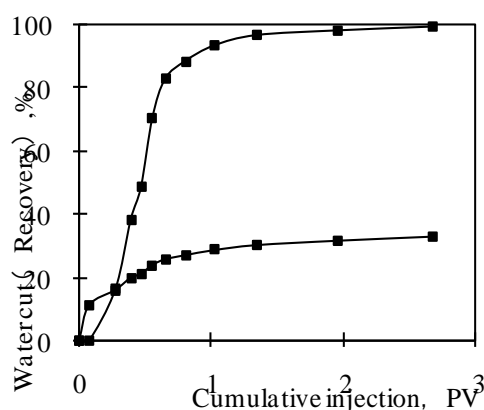


Fig.5. Experimental results of oil displacement without micro-emulsion System

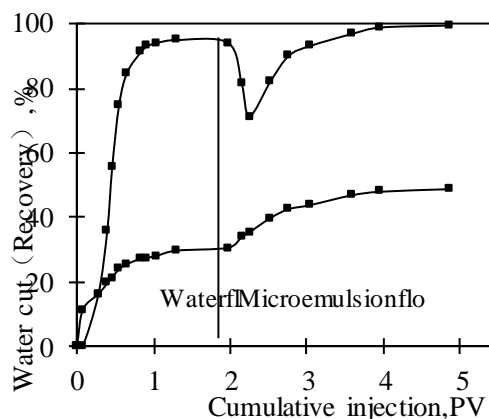


Fig.6. Experimental Results of oil displacement with AS/ Butyl alcohol / octane /NaCl micro-emulsion system.

Table 2. Experimental results.

Core number	Length of core(cm)	Diameter of core(cm)	Porosity(%)	Permeability(10 ⁻³ μm ²)	Irreducible water saturation(%)	Final recovery(%)
1-1	8.2	2.5	12	7.8	0.34	33.1
1-2	6.7	2.5	15	9.2	0.30	40.60
1-3	7.4	2.5	14	8.4	32	48.7

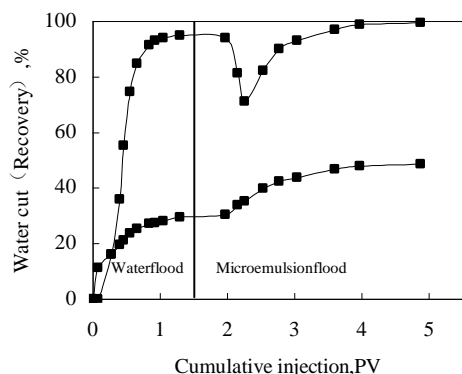


Fig.7. Experimental results of oil displacement with AS/ mixed alcohol / octane /NaCl micro-emulsion system (the proportion of n-pentanol alcohol and butyl alcohol is 1:1)

It can be seen from the results that for low permeability samples, the water flooding recovery is 33.1%. The efficiency reaches 40.6% when Butyl alcohol is used as the co-surfactant in the micro-emulsion system, and 48.7% when the co-surfactant is mixed with alcohol. From the perspective of water ratio, when water ratio reaches around 95%, the micro emulsion can be injected into the water. The water ratio can be reduced by up to 17% for Butyl alcohol and 23.7% for mixed alcohol.

CONCLUSION

In the article, the effects of concentration and the types of alcohol on phase behavior and the solubilisation effects of the AS/ alcohol / octane /NaCl system were studied with the ϵ - β -fish-like phase diagram. We have learnt that the micro-emulsion system with Butyl alcohol / n-pentanol (1:1) as the co-surfactant has better solubilisation ability and wider middle phase zone. The oil displacement experiment was carried out using the formulation of AS/mixed alcohol/octane/NaCl micro-emulsion system, which is composed of 2% of sodium alkyl sulfonate, 3% of mixed alcohol, 5% of NaCl and an oil and water ratio of 1:1. The results indicate that the system has higher displacement efficiency in practical application.

(1) The ϵ - β -fish-like phase diagram provides a visual illustration of the phase changes and solubilisation performance of the micro-emulsion system. Meanwhile, the physicochemical parameter such as mass fraction of alcohol in the interfacial film can be calculated more accurately when the system reaches the oil-wet or water-wet balance.

(2) For the AS/ alcohol/ octane /NaCl

micro-emulsion system, the alcohol width of n-propyl alcohol is 0.262mol/L, 0.0513mol/L for butyl alcohol, and 0.0291mol/L for n-pentanol alcohol. We can see that in terms of alcohol width, n-propyl alcohol > butyl alcohol > n-pentanol alcohol. From the view of solubility, the minimum alcohol concentration required is 0.403mol/L for the n-propyl alcohol system, 0.129mol/L for the butyl alcohol system, and 0.0453 mol/L for the n-pentanol alcohol system when an optimum medium phase micro-emulsion is to be formed. Thus in terms of solubility properties: n-pentanol alcohol > butyl alcohol > n-propyl alcohol.

(3) AS/ alcohol / octane /NaCl system has a wider range of middle phase micro-emulsion and a better solubility when the mixture of n-propyl alcohol and butyl alcohol (1:1) is used as co-surfactant. We have verified through flooding experiments that the recovery rate of the system with butyl alcohol can be improved by 7.5% than water flooding, meanwhile, the water content can be reduced by up to 17%, while the mixed alcohol system recovery can be improved by 15.6% than water flooding and the water content can be reduced by up to 23.7%.

Acknowledgements: This work was supported by the National Natural Science Foundation of China under Grant No. 51474071.

REFERENCE

1. G. P. Willhite, D. W. Green, D. M. Okoye, & M. D. Looney, in: SPE, **20**(6), 459 (1980).
2. X. D. Yang, H. Y. Zhang, J.L. Chai, *Adv.Mater.Res.*, **875-877**, 308 (2014).
3. Y. Li, B. Huang, M.L. Huang, K.S. Zhao, T.Q. Xu, *Chinese Journal of Applied Chemistry*, **05**, 424 (2003).
4. K. Kaizu, L. Alexandridis, J. Paschalis, *J. Colloid Interface Sci.*, **466**, 138 (2016).
5. M.L. Zhu, Phase behavior and solubility of surfactant in the medium phase micro-emulsion system formed by mixed surfactant, Shandong Normal University, 2012.
6. S. Somayyeh, A. Sadeqhi, D. Rahmat, *Fluid Phase Equilibria*, **377**, 1 (2014).
7. X. Xia, H. Liu, Y. Xia, Q.Q., Fang, *J Chem Eng Chin Univ*, **25**, 12 (2011).
8. J.L. Chai, J.R. Zhao, X.D. Yang, C.J. Wu, *Colloids Surf., A*, **302**, 31 (2007).
9. J.R. Zhao, Study on the beta epsilon phase diagram method of anionic and cationic surfactants and their mixtures in micro-emulsion, Shandong Normal University, 2007.
10. J. Liu, C.K. Qin, *Hebei Chemical Engineering and Industry*, **01**, 3 (2009).
11. J.L. Chai, G. Z. Li, G. Y. Zhang, *Colloids Surf., A*, **231**, 173 (2003).

12. H.L. Li, *Shanxi Chemical Industry*, **04**, 23 (2008).
13. H.L. Li, Progress in the research and application of various phase diagrams of micro-emulsions, Shandong Normal University, 2008.
14. H. Kraack , B.M. Ocko, P.S. Pershan, E. Sloutskin, L.Tamam, M. Deutsch, *Langmuir*, **20**, 5386 (2004).
15. J.F. Chen, Study on the phase behavior of micro-emulsion and the solubility of water in aqueous solution by the optimum micro-emulsion dilution method, Shandong Normal University, 2008.
16. K. D. Shah, D. W. Green, M. J. Michnick, G. P. Willhite, R. E. Terry, *Soc. Pet. Eng. J.*, **21**, 763 (1981).
17. X.J. Liu, Study on homogeneous micro-emulsion flooding, Xi'an Shiyou University, 2005.
18. R. N. Healy, R. L. Reed, C. W. Carpenter, *SPE*, **15**, 87 (1975).
19. R.N. Healy, R.L. Reed, *SPE*, **17**, 129 (1977).
20. H.J. Zhu, P.H. Yang, *Petrol Explor Devel.*, **02**, 74 (1994).

Thermodynamics of NO₃⁻ adsorption on different kinds of anion exchange resins

J. Wang*, H. Huang

College of Environmental Science and Engineering, Xiamen University of Technology, Xiamen 361024, China

Received June 8, 2016; Revised September 6, 2016

The thermodynamic behavior of NO₃⁻ adsorption from water on 201×7(717), Amberlite IRA 402 and Amberlite IRA 900, strong-base anion-exchange resin, were researched. After reaching equilibrium about adsorption of NO₃⁻ on three resins, adsorption capacity and adsorption efficiency were analyzed. Freundlich and Langmuir isotherm model were fitted for the behavior of resin adsorbing NO₃⁻. The thermodynamic functions of adsorption process were calculated. The results indicate that the adsorption effect of NO₃⁻ for IRA 402 resin is the best, 717 is the second, and IRA 900 is the last, but there are an insignificant difference. Adsorption efficiency was very high for adsorption of 5-20 mg N/L NO₃⁻ on three resins, which greater than 96%, but slightly lower than adsorption efficiency of the dynamic ion exchange column. Whereas the ion exchange resins have certain saturation capacity for the exchange of ions. The Langmuir equation could well describe the resins adsorbing NO₃⁻. The adsorption process was spontaneous for Gibbs free energy change (ΔG) value was negative. The enthalpy change (ΔH) and entropy change (ΔS) were positive, which indicate that adsorption of NO₃⁻ is endothermic and entropy increasing process. Therefore increasing temperature is conducive to the more complete and faster adsorption.

Key words: NO₃⁻, Anion exchange resin, Adsorption isotherm model, Thermodynamics.

INTRODUCTION

Concentrated urban population, relatively low urban wastewater treatment rate, industrial waste water and exhaust, as well as excessive fertilizer of agricultural production, which result in nitrate pollution in water body [1]. High levels of nitrate in water can cause met-hemoglobin hematic disease. Furthermore, nitrate is reduced to carcinogenic nitrosamines, which make a serious threat to human health [2]. Therefore, to study how to remove nitrate in water and to protect the water ecological environment, maintaining the healthy development of the people and water in harmony, have certain theoretical and practical significance [3-4-5-6-7].

Compared with the other method, ion exchange technology due to its simplicity, effectiveness and good selectivity, easy recovery of inorganic ions and the cost is relatively low, which is more suitable for applied to remove the nitrate nitrogen in water [8-9-10-11]. Moreover, new preparation research based on ion exchange adsorption technology and how to improve the efficiency of ion exchange resin, which caused global attention increasingly [12-13-14-15-16].

Strong basic anion exchange resin, 201 x 7 (717), has been widely used in research on nitrate nitrogen adsorption [1, 2]. So we chose two kinds of new type of strong basic anion exchange resin, IRA 402 and IRA 900, produced by American

Rohm Haas Company, and attempted to study NO₃⁻ adsorption thermodynamics experiments of the three resins, expecting to find the ideal of NO₃⁻ selective adsorption resin.

MATERIALS AND METHODS

Experimental materials

Experimental reagents. 1 mol/L HCl and 1 mol/L NaOH solution were acid and alkaline detergent respectively. 5.0, 10.0, 15.0, 20.0 mg N/L KNO₃ solution were nitrate simulation wastewater.

Strong basic anion exchange resin, 201 x 7 (717) (sand, 1 mm in diameter, yellow, easy to conglomerate things), was produced by Shantou Xilong Chemical Plant, Guangdong Province. Strong basic anion exchange resin, AMBERLITE IRA 402 (granular, fine, canary yellow, has certain adhesivity), and IRA 900 (bead-like structure, 1.5 mm in diameter, white, not easy to conglomerate things) were all produced by American Rohm Haas Company. Performance parameters of these three resins were shown in Table 1.

The pretreatment of ion exchange resin. Took certain amount (2 g) of resin in a 150 ml conical flask, poured 1 mol/L HCl solution inside the conical flask, which liquid level was above the resin 2-3 cm and the resin was soaked for 2-4 hours. After soaking by dilute hydrochloric acid solution, the resin was rinsed repeatedly with distilled water until the pH to neutral. Then poured 1 mol/L NaOH solution inside the conical flask, and operation method was the same as the first and

* To whom all correspondence should be sent:
E-mail: wangjp@xmut.edu.cn

second step. Finally, use 1 mol/L HCl solution soaking the resin for 2 hours, again washed the resin with distilled water until the pH to neutral.

Experimental apparatus

The analyses of nitrate-nitrogen were performed using the Shimadzu 2550 ultraviolet-visible spectrophotometer (Shimadzu, Japan) and the Dionex ICS-1000 ion chromatography equipment (Dionex, USA).

Experimental method

The static adsorption method was used for the need to study the thermodynamic behavior of resin adsorption NO₃⁻ at different temperature. 100 ml KNO₃ solution of different concentrations (5.0, 10.0, 15.0, 20.0, 30.0, 20.0, 30.0 mg N/L) was poured into seven conical flasks containing resins with a volume of 150 ml. Then these conical flasks were fixed in the water-bathing constant temperature vibrator, and set different temperature (25 °C, 35 °C, 45 °C) vibrating for a period of time. After fully exchange adsorption reaching equilibrium (according to the actual experimental conditions), ultraviolet spectrophotometry was used to determine residual nitrate nitrogen concentration in the solution [17]. Adsorption capacity, adsorption efficiency and the residual nitrate nitrogen concentration after adsorption equilibrium on resins for different initial concentrations of KNO₃ solution at different temperature were calculated. Freundlich and Langmuir isotherm model were fitted for the behavior of resin adsorbing NO₃⁻. The thermodynamic function of adsorption process was calculated.

The computation formula of adsorption capacity and adsorption efficiency are as follows.

$$q_e = \frac{(c_0 - c_e) \cdot V}{G} \quad (1)$$

$$E = \frac{c_0 - c_e}{c_0} \cdot 100\% \quad (2)$$

Where q_e is equilibrium adsorption capacity (mg/g); c_0 is initial concentration of nitrate nitrogen (mg/L) ; c_e is nitrate nitrogen equilibrium

concentration after adsorption (mg/L) ; V is volume of solution (L) ; G is resin quality (g) ; E is adsorption efficiency (%).

RESULTS AND DISCUSSION

Adsorption capacity and adsorption efficiency for resin adsorption of different initial concentration of NO₃⁻

Adsorption capacity and adsorption efficiency for resin adsorption of different initial concentration of NO₃⁻ at different temperature were shown in table 2. Adsorption of 5-20 mg N/L NO₃⁻ on resins had high efficiency, which was greater than 96%. Adsorption capacity had increased gradually. Compared with dynamic adsorption in the ion exchange column, adsorption efficiency in this experiment was slightly lower [18] It illustrate contact area of dynamic adsorption is greater than that static adsorption, and large area is conducive for resin to fully contact with the liquid phase. As the initial concentration of NO₃⁻ solution increasing to 30 mg N/L, adsorption efficiency showed the decrease tendency and equilibrium adsorption capacity changed little. Which indicate the ion exchange resin have certain saturation capacity on the exchange of ions. The NO₃⁻ equilibrium adsorption capacities for the three kinds of resin were all 1.55 mg/g approximately. With the increase of temperature, so did the NO₃⁻ equilibrium adsorption capacity and adsorption efficiency for resin. It show that temperature rising is helpful to the resin adsorption, but the influence of temperature is not significant (Table 2).

From Table 2, data showed NO₃⁻ adsorption effect for IRA 402 resin was the best, 717 was the second, and IRA 900 was the last. At 45 °C, for the initial concentration of 5 mg/L of nitrate nitrogen, the adsorption efficiency was as high as 99.7% for IRA 402, 717 was 99.4%, and IRA 900 was 99.2%. At 25 °C, adsorption efficiency for 717, IRA 402 and IRA 900 are 99.0%, 99.3% and 98.6% individually. It show that these three kinds of resin can be very good selective adsorption of NO₃⁻

Table 1. Performance parameters of the three kinds of resin.

Resin type	Moisture content/%	Total exchange capacity/(mmol/g)	Functional group	Wet superficial density/(g/mL)	Granularity (0.315~1.25mm) /%	Factory pattern
717	42~48	3.6	[—N(CH ₃) ₃]	0.66~0.75	≥95	chloro-type
IRA 402	50~56	3.8	[—N(CH ₃) ₃]	0.66~0.73	≥95	chloro-type
IRA 900	50~60	4.0	[==N==]	0.65~0.73	≥95	chloro-type

Table 2. Adsorption efficiency and adsorption capacity for three resins adsorption of different initial concentration of NO₃⁻ at different temperature.

Temperature (°C)	Initial concentration (mg/L)	717		IRA 402		IRA 900	
		E (%)	q _e (mg/g)	E (%)	q _e (mg/g)	E (%)	q _e (mg/g)
25	5	99.0	0.25	99.3	0.25	98.6	0.25
	10	98.3	0.49	98.9	0.49	97.9	0.49
	15	97.4	0.73	97.9	0.73	97.0	0.73
	20	97.2	0.97	97.6	0.98	96.1	0.96
	30	90.2	1.35	90.8	1.36	89.3	1.34
	40	75.7	1.51	77.9	1.56	73.5	1.47
	50	63.7	1.59	63.8	1.59	60.1	1.50
35	5	99.3	0.25	99.5	0.25	99.0	0.25
	10	98.6	0.49	98.8	0.49	98.1	0.49
	15	97.9	0.73	98.2	0.74	97.6	0.73
	20	97.5	0.98	97.7	0.98	97.0	0.97
	30	90.6	1.36	90.9	1.36	90.0	1.35
	40	77.4	1.55	78.2	1.56	75.1	1.50
	50	63.8	1.60	64.2	1.61	60.9	1.52
45	5	99.4	0.25	99.7	0.25	99.2	0.25
	10	99.0	0.49	99.0	0.49	98.3	0.49
	15	98.6	0.74	98.7	0.74	98.0	0.74
	20	97.7	0.98	98.2	0.98	97.3	0.97
	30	90.7	1.36	91.3	1.37	90.4	1.36
	40	77.6	1.55	80.0	1.60	75.5	1.51
	50	63.9	1.60	64.8	1.62	62.0	1.55

Isothermal adsorption model for resin adsorption of NO₃⁻

In the process of ion exchange adsorption, adsorption isotherm can be used for analysis of adsorption behavior for adsorbent and the specific adsorbate [19]. According to the previous experiences, the resin adsorption capacity (*q_e*) depends on adsorption equilibrium concentration of adsorbate ion (*c_e*) in the liquid phase and the temperature (T) under the specific conditions. When the temperature is constant, the function equation between *q_e* and *c_e* is adsorption isotherm. Langmuir and Freundlich isothermal adsorption model are commonly used as common adsorption isotherms to describe adsorption equilibrium between solid and liquid phase [20]. Langmuir adsorption isotherm model can predict resin maximum adsorption capacity, who assumes that adsorption process occurs on the surface of the adsorbent, and has the same affinity on adsorbate. Adsorbate transfer into the adsorbent surface and form into monolayer adsorption, without considering inhomogeneous adsorption [21]. Freundlich model is the liquid-solid empirical adsorption equation, considering inhomogeneous adsorption. However, it cannot predict the situation of adsorption balance, and have no actual physical meaning, is believed as purely empirical [22].

Adsorption isothermal equation

(1) Freundlich adsorption isothermal model

$$q_e = k_f (c_e)^{\frac{1}{n}} \tag{3}$$

The logarithmic form is

$$\ln q_e = \ln k_f + \frac{1}{n} \ln c_e \tag{4}$$

where, *k_f* and *1/n* are constant related to the adsorption intensity and capacity; *q_e* and *c_e* is as in the above case.

(2) Langmuir adsorption isothermal model

$$\frac{1}{q_e} = \frac{1}{b} \times \frac{1}{c_e} + \frac{1}{q_m} \tag{5}$$

where *q_m* is the maximum uptake value; *b* is coefficient related to the adsorption capacity (*b=q_m/k_l*); *k_l* is Langmuir dissociation constant of adsorption equilibrium; *q_e* and *c_e* is as in the above case.

Adsorption isotherm model analysis

According to equilibrium concentration of NO₃⁻ in the solution and adsorption capacity after adsorption, drew the adsorption isotherm of NO₃⁻ at different temperature (25 °C, 35 °C, 45 °C). Experimental data were respectively fitted with the Freundlich and Langmuir adsorption isotherm

equation. Fitting results were shown in figure 1, 2, 3, and the fitting parameters were listed in table 3.

Figures 1~3 and Table 3 showed that adsorption isotherm of three kinds of resin at different temperature were coincide with the Langmuir adsorption model, and the correlation coefficient (R^2) were greater than 0.95. In compared, R^2 of Freundlich was around 0.89, slightly smaller than that of Langmuir. The adsorption thermodynamics experiment was conducted in 150 ml flask, and adsorbent were evenly lay on the flat surface, which conform to the adsorption conditions of Langmuir adsorption model. Langmuir adsorption model also shows that adsorption of NO₃⁻ on resins will not always increase with the increment of initial concentration, but has its maximum uptake value, namely the saturation capacity. With temperature rising from 25 °C to 45 °C, q_m increased and k_f decreased in the adsorption process, which indicate that temperature is advantageous to the adsorption. At different temperature, Freundlich constant n was all greater than 1, showing that the three kinds of

resin have strong adsorption ability for KNO₃ solution (Table 3).

Analysis and calculation of thermodynamic function

At the temperature of 25 °C (298k), 35 °C (308k) and 45 °C (318k), thermodynamic parameters for NO₃⁻ adsorption on resins in water can be estimated based on the following equations.

Gibbs change of adsorption process (ΔG).

Change of the Gibbs free energy (ΔG) in the process of NO₃⁻ adsorption on resins was estimated by Van't Hoff isothermal formula [23].

$$\Delta G = -RT \ln K_0 \tag{6}$$

Where, R is gas constant, and the value is 8.314 J/(mol.K). T is temperature, and the unit is K. K_0 is the adsorption equilibrium constant, which is equal to K_f as estimated by Freundlich equation fitting parameters [23]. And K_0 is equal to $1/K_l$ and b/q_m as estimated by Langmuir equation fitting parameters [24]. We used Langmuir equation parameters to calculate K_0 (Table 4)

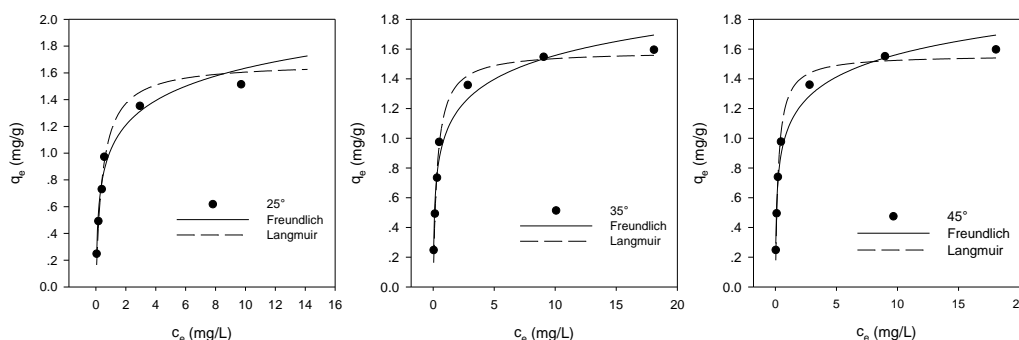


Fig. 1. Freundlich and Langmuir equation fitting curve for 717 resin.

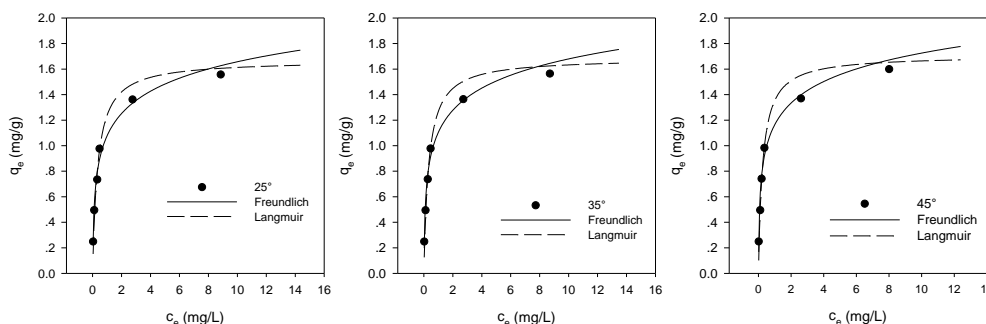


Fig. 2. Freundlich and Langmuir equation fitting curve for IRA 402 resin.

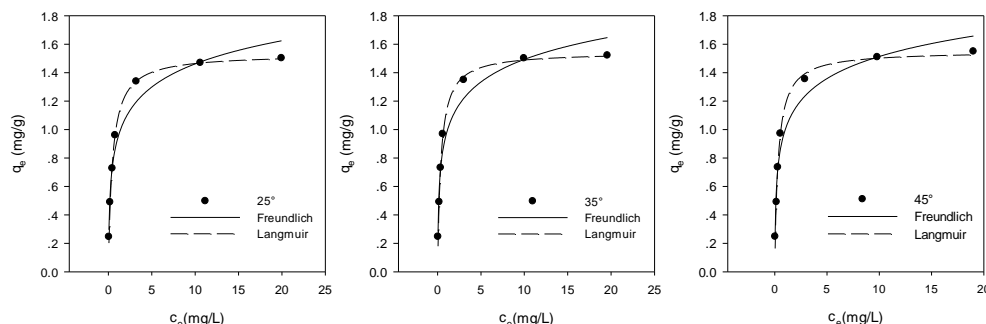


Fig. 3. Freundlich and Langmuir equation fitting curve for IRA 900 resin.

Table 3. Freundlich and Langmuir isotherm parameters for adsorption of NO₃⁻ on three resins at different temperature.

Resin type	Temperature/K	Parameters for Freundlich equation			Parameters for Langmuir equation			
		K_f	n	R^2	b	q_m	k_l	R^2
717	298	0.84	3.37	0.89	6.10	1.27	0.22	0.98
	308	0.87	3.48	0.89	8.00	1.31	0.16	0.97
	318	0.91	3.70	0.89	9.71	1.33	0.14	0.99
IRA 402	298	0.89	3.53	0.90	8.55	1.14	0.15	0.98
	308	0.91	3.62	0.91	11.49	1.21	0.10	0.96
	318	0.96	3.80	0.91	18.87	1.30	0.06	0.95
IRA 900	298	0.78	3.32	0.88	4.22	1.24	0.32	0.99
	308	0.82	3.45	0.88	5.95	1.29	0.22	0.98
	318	0.85	3.55	0.88	7.69	1.37	0.16	0.97

Table 4. Thermodynamic equilibrium parameters for adsorption of NO₃⁻ on three resins at different temperature.

Resin type	T (K)	K_0	ΔG (kJ/mol)	ΔH (kJ/mol)	ΔS [J/(mol·K)]
717	298	4.65	-11.51	16.35	93.51
	308	6.29	-16.10		105.37
	318	7.29	-19.28		112.05
IRA 402	298	6.57	-16.28	29.76	154.52
	308	9.53	-24.40		175.86
	318	16.58	-43.85		231.48
IRA 900	298	3.09	-7.65	22.86	102.40
	308	4.63	-11.86		112.73
	318	6.18	-16.35		123.32

ΔG of NO₃⁻ adsorption process was negative at different temperature for three kinds of resin. It illustrate the adsorbate tend to adsorbing from solution to the surface of resin and the adsorption process can occur spontaneously. And with the increase of temperature, absolute value of ΔG increases, which further demonstrate that temperature rising accelerate the process of NO₃⁻ adsorption on resins.

Enthalpy change of adsorption process (ΔH). Enthalpy change (ΔH) in the process of NO₃⁻ adsorption on resins was estimated by the following Van't Hoff equation (7) [24]. Using $\ln(1/c_e)$ and $1/T$, a linear relationship model was built, and the slope was obtained. After conversion, ΔH can be estimated.

$$\ln(1/c_e) = A + (-\Delta H/RT) \quad (7)$$

In order to calculate ΔH , NO₃⁻ adsorption experiments with a concentration of 5 mg/L were added for three kinds of resin at 30 °C (303 k) and 40 °C (313 k). NO₃⁻ equilibrium concentration after adsorption was measured and drew with different temperature (Figure 4). ΔH for three kinds of resin was obtained by the slop in the figure.

As shown in table 4, the enthalpy change affected by the temperature was insignificant,

therefore the enthalpy change at different temperature was identical. ΔH was all greater than zero for three kinds of resin. K_0 increased as the temperature rising, showed that the adsorption behaviors were endothermic process for the three kinds of resin. Temperature helps NO₃⁻ adsorbing on resins.

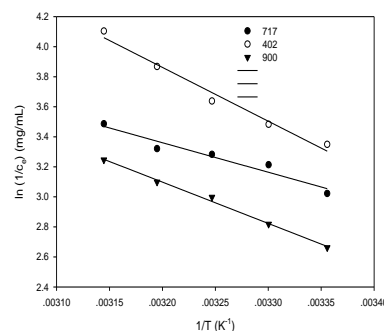


Fig. 4. The liner fitting curve between $\ln(1/c_e)$ and $1/T$ for three resins.

Entropy change of adsorption process (ΔS).

$$\Delta S = (\Delta H - \Delta G) / T \quad (8)$$

The entropy change (ΔS) in the process of NO₃⁻ adsorption on resins was estimated by the following Gibbs-Helmholtz equation (8) [24].

The calculation results were shown in table 4, ΔS are greater than zero for three kinds of resin, which show that NO₃⁻ adsorption on the resin is an

entropy increase process. For the solid-liquid adsorption behavior, adsorbate molecules adsorbing to the resin surface by liquid phase will lose some freedom, which is a process of entropy decrease. Adsorbate adsorbs on the adsorbent (resin), and exchange with the ion exchange group of resin phase. The group and the hydration water molecules releasing into the liquid phase is the process of entropy increase. So the total entropy of adsorption processes are the sum of the both [24-25]. Due to the large volume of the exchange groups of three kinds of resin, especially for the 717 and IRA 402 (Table 1), therefore ΔS is positive in the adsorption process.

CONCLUSION

This paper studied NO_3^- adsorption thermodynamic properties on strongly basic anion exchange resin, 717, IRA 402 and IRA 900. Two kinds of adsorption isotherm at different temperature were measured and thermodynamic parameters, ΔG , ΔH and ΔS in the adsorption process were estimated.

The adsorption effect of NO_3^- for IRA 402 resin is the best, 717 is the second, and IRA 900 is the last, but there are an insignificant difference. Adsorption efficiency was outstanding for adsorption of 5 mg N/L NO_3^- on three resins, which greater than 98% and indicate these three kinds of resin have excellent selectivity on adsorption of NO_3^- . Compared with the common 717 resin, IRA 402 and IRA 900 also can be better resins for NO_3^- adsorption.

Adsorption efficiency was very high for adsorption of 5-20 mg N/L NO_3^- on three resins, which greater than 96%, but slightly lower than adsorption efficiency of the dynamic ion exchange column. As the initial concentration of KNO_3 solution rising to 30 mg N/L, adsorption efficiency appeared decrease trend. It indicate ion exchange resin have certain saturation capacity for the exchange of ions. With the increase of temperature, so did the NO_3^- equilibrium adsorption capacity and adsorption efficiency for resin. It demonstrate that temperature rising is helpful to the resin adsorption, but the influence of temperature is not significant.

Freundlich and Langmuir equation fitting correlation coefficient R^2 of NO_3^- adsorption isotherm for three kinds of resin were greater than 0.85. And the Langmuir equation coefficient was greater, more than 0.95, which indicated that the Langmuir isotherm equation can well describe the adsorption process of NO_3^- .

ΔG of NO_3^- adsorption process was negative at different temperature for three kinds of resin.

Which illustrate the adsorption process can occur spontaneously. And with the increase of temperature, absolute value of ΔG increases, which further demonstrate that temperature rising may accelerate NO_3^- adsorption process for resin.

ΔH and ΔS were all greater than zero in the process of NO_3^- adsorption on three kinds of resin, showing that adsorption of NO_3^- is endothermic and entropy increasing process. Therefore increasing temperature is conducive to the more complete and faster adsorption. Therefore, increasing temperature is conducive to the adsorption process more complete and faster.

The research conclusion for strongly basic anion exchange resin to remove nitrate from water have certain guiding and application significance. In the future, adsorption dynamics of NO_3^- on strongly basic anion exchange resin and elution recycling can be further analyzed and discussed. Our goal is using cheap, available and good selective adsorption resin to dispose nitrogen wastewater, and reduce the damage and pollution to the environment.

Acknowledgments: We gratefully acknowledge the generous support provided by Natural Science Foundation of China (No.51378446), Natural Science Foundation of Fujian Province, China (2013J01211), Science and Technology Plan Project of Xiamen City, China (3502Z20131157).

REFERENCES

1. S.N. Milmile, J.V. Pande, S. Karmakar, A. Bansiwala, T. Chakrabarti, R.B. Biniwale, *Desalination*, **276**, 38 (2011).
2. A. Bhatnagar, M. Sillanpaa, *Chem. Eng. J.*, **168**, 493 (2011).
3. A.P. Murphy, *Nature*, **350**, 223 (1991).
4. P.M. Vitousek, J.D. Aber, R.W. Howarth, G.E. Likens, P.A. Matson, D.W. Schindler et al., *Ecol. Appl.*, **7**, 737 (1997).
5. Y. Wu, *Chin. Agr. Sci. B.*, **27**, 284 (2011).
6. S.R. Carpenter, N.F. Caraco, D.L. Correl, R.W. Howarth, A.N. Sharpley, V.H. Smith, *Ecol. Appl.*, **8**, 559 (1998).
7. P. Jiang, Y. Yu, *Guangzhou Chem. Ind.*, **40**, 31 (2012).
8. A. Kapoor, T. Viraraghavan, *J. Environ. Eng.*, **123**, 371 (1997).
9. S. Ghafari, M. Hasan, M.K. Aroua, *Bioresour. Technol.*, **99**, 3965 (2008).
10. L.H. Liu, *Chin. J. Environ. Sci.*, **14**(2), 63 (1993).
11. B.U. Bae, Y.H. Jung, W.W. Han, H.S. Shin, *Water Res.*, **36**, 3330 (2002).
12. H.O. Song, Y. Zhou, A.M. Li, S. Mueller, *Desalination*, **296**, 53 (2012).

13. H.O. Song, Z.J. Yao, M.Q. Wang, J.N. Wang, Z.L. Zhu, A.M. Li, *J. Environ. Sci.*, **25**, 105 (2013).
14. G.H. Tong, C.S. Peng, Y.G. Jia, Y. Cao, *Ind. Water Wastewater*, **39**, 73 (2008).
15. Y.L. Fei, G.M. Cao, L.H. Zhang, F. Chi, D. Li, *Water Purif. Technol.*, **30**, 20 (2011).
16. Y.L. Liu, J. He, T.F. Xie, *Water Purif. Technol.*, **21**, 30 (2002).
17. Editorial Committee of the State Environmental Protection Administration (ECSEPA), *Water and wastewater monitoring analysis method*, 4th ed. Beijing: Environmental Science Press of China, 2002.
18. J.P. Wang, T. Lin, Q.S. Li, D.H. Chen, *Chin. J. Environ. Eng.*, **8**, 5091 (2014).
19. J.N. Wang, Y. Zhou, A.M. Li, L. Xu, *J. Hazard. Mater.*, **176**, 1018 (2010).
20. A. Mittal, L. Kurup, J. Mittal, *J. Hazard. Mater.*, **146**, 243 (2007).
21. J.M. Chern, Y.W. Chien, *Water Res.*, **36**, 647 (2002).
22. K. Vijayaraghavan, T.V.N. Padmesh, K. Palanivelu, M. Velan, *J. Hazard. Mater.*, **133**, 304 (2006).
23. S.S. Tian, X. Wang, H.Q. Wang, *Chin. J. Process Eng.*, **12**, 648 (2012).
24. N.H. Zhang, J.H. Qiu, *Ion Exc. Adsorp.*, **27**, 26 (2011).
25. Z.H. Li, H.Q. Pi, B.L. He, *J. Funct. Polym.*, **13**, 1 (2000).

Experimental study on the effect of combined modified aluminum and magnesium and phosphorus removal of zeolite

Li Xu^{1, 2*}, Tao Jiang¹, Pengfei Yu¹, Qiuju Zhao¹

¹ School of Municipal and Environmental Engineering, Shenyang Jianzhu University, Shenyang, Liaoning, China, 110168

² College of Land and Environment, Shenyang Agriculture University, Shenyang, Liaoning, 110866

Received June 18, 2016; Revised September 10, 2016

Zeolite is an excellent water treatment agent, packing for the artificial wetland. Will have broad application prospects in the field of water treatment, the data showed that zeolite adsorption of ammonia nitrogen amount is larger, but phosphorus adsorption in water quantity is small, this undoubtedly denitrification and phosphorus removal for wastewater caused great limit. Therefore, the modification research of zeolite are valuable. Salt modification method is determined, by using MgCl₂ and AlCl₃ solution soaking, high temperature calcination method by certain proportion of zeolite was modified to improve its adsorption of phosphorus removal performance. Through the contrast test alone, finally determine the zeolite: MgCl₂: the mass ratio of 3:1:1 AlCl₃ as the optimal conditions. Conform to the Langmuir and Freundlich isothermal equation as a result, under the condition of the experiment, the modified zeolite adsorption of phosphorus were 1.1924 mg/g, 9.54 times that of 0.125 mg/g before modification. The experimental results show that the method of modified zeolite adsorption quantity of phosphorus increased significantly, the effect is good, is applied to the artificial wetland and other water treatment method is more in the promotion value.

Key words: Zeolite, Salt modification, Adsorption, Phosphorus removal, Elution regeneration.

INTRODUCTION

Zeolites are widely distributed in the earth's crust, porous aluminosilicate an aqueous alkali metal or alkaline earth metal. Zeolite with 400m²/g surface area, so much better chemical and biological stability. It is a kind of polar adsorbent, has good adsorption properties and exchange properties [1, 2], can be adsorbed with polar molecules of bacteria. So the natural zeolite is a kind of biological carrier ideal. Characteristics of zeolite is cheap, non-toxic side effects, regeneration method is simple, the sewage treatment effect is good, no two pollution, therefore suitable as substrates in constructed wetland.

Some experts and scholars have modified zeolite to do some research. [3] studied the preparation of modified zeolite and its adsorption of ammonia nitrogen. The adsorption properties of natural zeolite to ammonia nitrogen is better, but the adsorption capability of phosphorus. The zeolite modified to improve a lot on the adsorption properties of ammonia nitrogen, but the study on modified zeolite adsorption of phosphorus is less, and the modification method of zeolite modified with acid, alkali modification and organic modification of the economic costs of these

methods are high [4], so to carry out the test of salt modified natural zeolite for adsorption of phosphorus.

THE MECHANISM

Natural zeolite is a kind of aluminosilicate minerals, a frame structure, crystal has a large number of internal connect to each other, connected to the outside world, the channel hole; the internal structure of zeolite by silicon oxygen tetrahedron and stepwise formation unit loop, dual ring, multi ring cage [4, 5] constitute the main three-dimensional space frame shaped crystal polyhedron. Therefore, the zeolite has a large surface area, and the special molecular structure formation of electrostatic larger. The adsorption properties of zeolites and silica alumina ratio of zeolite [6, 7], the cation exchange is one of the important characteristics of. Zeolite contained K⁺, Na⁺, Ca²⁺ and the crystal structure of the combination is not tight, therefore, in the solution of other cations and reversible exchange. In zeolite Mg²⁺, and Ca²⁺, Fe²⁺, Al³⁺ can occur chemical reaction to generate precipitation and phosphate ions in wastewater. In the phase interface, material concentration automatic accumulation or enrichment and adsorption. Although adsorption can occur in different phase interfaces, but in water treatment, basic is the use of porous solid material, so that one or more substances in waste water was adsorbed on the solid surface and achieve the

* To whom all correspondence should be sent:
E-mail: xuli319@sina.com

purpose of removal.

We usually by isothermal adsorption equation to determine the theoretical maximum adsorption capacity and adsorption type adsorbent, adsorbent adsorbed on the basis of comparison. The adsorption isotherm equation commonly used are two, respectively is Langmuir and Frenundlich isothermal adsorption equation.

The Langmuir isothermal adsorption equations: the equations by assuming that conditions for the adsorption material is only for single molecule layer derived from solid medium, can determine the theoretical maximum adsorption capacity and adsorption strength through the equation.

$$c/m = C/Xm + 1/Km$$

The Frenundlich isothermal adsorption equations: the equation is the empirical formula, K, n are empirical constants, said the relationship between the equilibrium solute concentrations of solid surface adsorption and liquid.

$$\ln m = 1/n * \ln c + \ln K$$

Among them, C is the original solution concentration, mg/L; C equilibrium concentration, the adsorption of mg/L; m mg/g; Xm maximum adsorption capacity, adsorption capacity, mg/g; Km, N, K are the model constants.

MATERIALS AND METHODS

Material

Natural zeolite (30 eyes), MgCl₂, AlCl₃, K₂S₂O₈, K₂SbC₄H₄O₇, KH₂PO₄, ammonium molybdate, ascorbic acid, sulfuric acid and other reagents were analytically pure.

Table 1. Experiment with zeolite main performance index.

Features	Density	Bulk density	Proportion	Void fraction	Specific surface area
Unit	g/cm ³	g/cm ³	g/cm ³	%	m ² /g
Specific parameters	1.8	0.95	1.6	40-50	500

Modification methods

Salt of zeolite modified test method: take 100 g dry 30 purpose test zeolite packing, quality ratio is shown in Table 2.

The five groups according to the mass ratio between the amount added zeolite filler, MgCl₂ and AlCl₃, MgCl₂ and AlCl₃ mixing with water to dissolve, static 24h, filtration, washed two times with distilled water, filtering to obtain zeolite, at a temperature of 105°C oven drying to constant

weight of filler, 1H culture at Ma Eph furnace are put into the 250°C, cooled out after preparing the modified zeolite standby.

Table 2. Zeolite and magnesium salt and aluminum salt mass ratio table.

Zeolite: MgCl ₂					
The serial number	1	2	3	4	5
Design quality ratio	1:1	2:1	3:1	4:1	5:1
Actual quality ratio	1.08:1	2.04:1	3.15:1	3.98:1	5.16:1
Zeolite: AlCl ₃					
Design quality ratio	1:1	2:1	3:1	4:1	5:1
Actual quality ratio	1.15:1	1.92:1	3.06:1	4.13:1	4.97:1

Phosphorus adsorption test method

Preparation of phosphate solution method: Phosphorus Solution of certain concentration gradient. A certain amount of dry KH₂PO₄ the preparation of 5,10,20,30, 40... 180, 190mg/L except for the first group outside with 10mg/L as the gradient of the solution of the 20 groups. 2G each dry 30 to 5 groups each of 3 copies of packing. In the centrifuge tube, with 50ml solution at 25°C, constant temperature oscillator, 200r/min oscillation in 24h, static 2h, phosphorus content of each supernatant.

Method: Determination of molybdenum antimony anti spectrophotometry; calculation formula: M = (C-c) V / (1000W)

Among them, adsorption, M adsorption of mg/g; C, C concentration, as before and after adsorption of phosphorus in L solution mg/; V the solution volume, taken as the adsorption test of mL; W as adsorbent dosage, G.

RESULTS AND ANALYSIS

Magnesium and aluminum salt proportion on the effect of modification of zeolite

Zeolite MgCl₂ and AlCl₃ soaked after 280°C calcination at high temperature 1H, the water inside the zeolite can be removed, and some volatile components were removed by calcination of zeolite, hydroxy will go, at the same time will generate some metal oxide, the metal oxide coordinatively unsaturated, in aqueous solution and water molecules ligand the reaction, which can cover the hydroxyl on the surface of zeolite, so more conducive to PO₄³⁻ ions to form coordination complexes, in order to increase the P adsorption capacity, you will have the following effect.

In the other conditions are the same, the magnesium salt and aluminum salt of different proportion of alone of zeolite was modified test, the quality of magnesium and aluminum salt on zeolite than were 1:1 supreme, but compared to the first three groups were matched, the modification effect and drug use is not a linear relationship between the 5, fourth, change the group the effect of decreased a lot. It is from the economic considerations, third group of 3:1 ratio of modified optimal. Therefore, selection of zeolite: the mass ratio of $MgCl_2:AlCl_3$ to 3:1:1 for further comprehensive test.

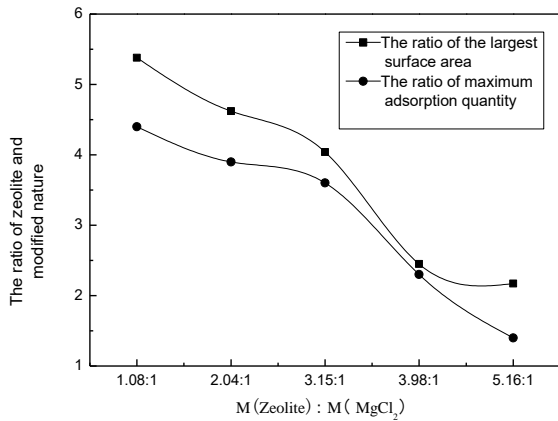


Fig. 1. Magnesium salt modified test.

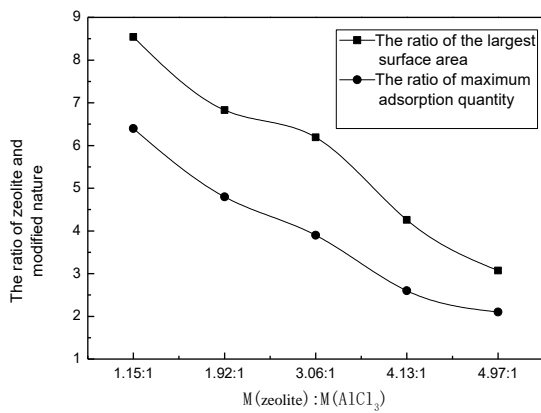


Fig. 2. Aluminium salt modified test.

Change the adsorption effect of phosphorus and analysis

We can see from Figure 3, the amount of phosphorus adsorption on modified zeolite increased significantly with the increase of concentration, and the adsorption capacity increased faster. At the same time simulation of isothermal adsorption of modified zeolite, with the former method.

Before modification zeolite theory of phosphorus adsorption quantity biggest is 0.125 mg/g, modified zeolite theory of phosphorus adsorption quantity

biggest is 1.1924 mg/g, 9.54 times that of before modification. In the process of modified zeolite framework in the position of the Si is the Al^{3+} ions in the solution, increased the amount of Al in the zeolite framework, at the same time increase the PO_4^{3-} and Al^{3+} exchange. The Mg^{2+} cation can compensate the excess charge instead of silicon,

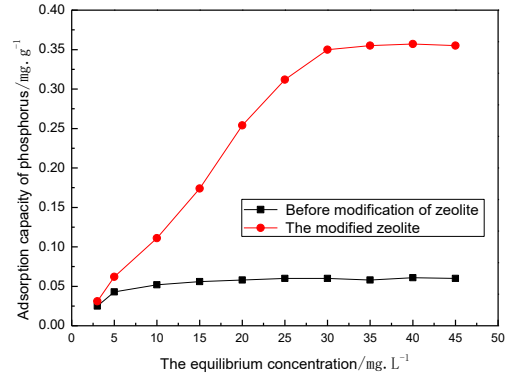


Fig. 3. Modified zeolites with different initial concentration of phosphorus adsorption quantity contrast figure.

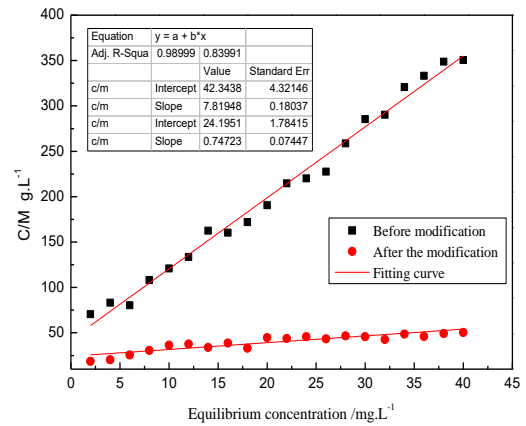


Fig. 4. Before and after the modification of zeolite to phosphorus Langmuir isotherm equation fitting curve.

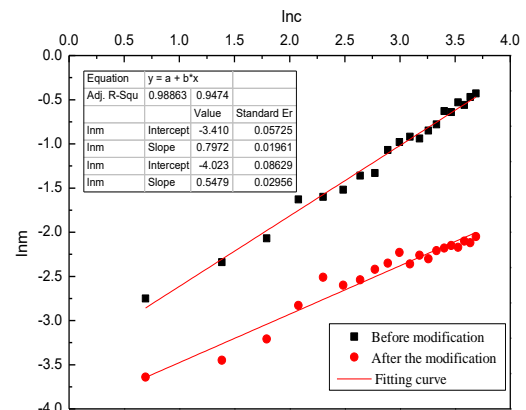


Fig. 5. Fitting curves of Freundlich isothermal equation of phosphorus in modified zeolite before and after modification.

and can work with zeolite channel K^+ , Na^+ , Ca^{2+} ions in ion exchange effect, so that the zeolite

channel more unobstructed; Too much of the Cl⁻ ions can also enter the zeolite ion exchange reaction channel, to improve its internal environment. Therefore, specific surface area and the modified zeolite internal structure all the corresponding improvement.

Table 3. Zeolite modified phosphorus isothermal adsorption equation and its parameters.

Before and after modification The fitting equation	Langmuir fitting equation		Frenundlich fitting equation	
	Formula	Decision coefficient	Formula	Decision coefficient
In front of the zeolite modified fitting equation	$y=7.8194x+42.343$	$R^2=0.9899$ $X_m=0.1250$	$y=0.5479x-4.023$	$R^2=0.9502$ $n=2.1164$
Zeolite modified fitting equation	$y=0.7472x+24.195$	$R^2=0.8399$ $X_m=1.1924$	$y=0.7972x-3.410$	$R^2=0.9892$ $n=1.3847$

CONCLUSIONS

Zeolite adsorption of phosphorus effect is relatively poor, by using MgCl₂ and AlCl₃ solution soaking, high temperature calcination methods of zeolite was modified to improve its adsorption of phosphorus removal performance. Zeolite modified filler to Langmuir isotherm equation fitting and Frenundlich isothermal equation fitting.

This low-cost adsorbent preparation, the method is simple, does not produce secondary pollution after use, after adsorption saturation of the adsorbent, using 1L 15 % NaOH + 5% NaCl eluent [8] the elution solution regeneration, control the eluent velocity, time after 1.5 h, adsorbent for phosphorus adsorption capacity can be up to 94% of the original sample regeneration can be recycled after processing, can be used as a plant of nitrogen and phosphorus compound fertilizer, has a certain economic and social benefits.

Acknowledgments: The authors wish to thank the China Fund program: National Science and Technology Major Project for the Control and Treatment of Water Pollution (2014ZX07202-011).

REFERENCES

1. J. Li, J. Qiu, Y. Sun, *J Micormporous and Mesoporous Materials*, **5**, 365 (2000).
2. H. Hu, *J. Mineral Resources Protection and Utilization*, **25** (1996).
3. Z. Li, K. Fu, Q. Xia, *J South China University of Technology*, **35**, 6 (2007).
4. M. Ma, Y. Wei, Y. Zhang, *J Anhui Agricultural Science*, 2061 (2007).
5. Chemical physics institute of Dalian, Chinese academy of sciences molecular sieve group, Zeolite molecular sieves, Beijing: science press, 1978, p.20.
6. C.S. Cerjan-Stefanovic, *Water Res.*, **31**, 1379 (2007).
7. G. Chen, *J Mineral Resources Protection and Utilization*, **6**, p. 55 (2007).
8. X. Quan, W. Jin, Y. Li, *J Non-Metallic Minerals*, **25**, 48 (2002).

Liquid–liquid equilibrium for the ternary systems of water + acetic acid + ethyl acetate at T=298.2 K

M. Manteghian¹, M. Shahbazi^{2,*}

1- Department of Chemical Engineering, Tarbiat Modares University, Tehran, Iran

2- Department of Chemical Engineering, Separation Processes, Islamic Azad University, North Tehran Branch, Tehran, Iran

Received June 26, 2016; Revised September 10, 2016

The concentration of each phase was determined by acidimetric titration, the Karl Fischer technique. The reliability of the experimental data was determined through the Othmer–Tobias and Hand plots. Distribution coefficients and separation factors were evaluated over the immiscibility regions. The results show that ethyl acetate is satisfactory solvent for extraction of acetic acid from water.

INTRODUCTION

Liquid-liquid equilibrium (LLE) data are of interest in extraction operations and recovery of valuable products [1-2]. Nowadays, liquid-liquid extraction has become one of the main separation technologies for separation of complex liquid mixtures.[3]Owing to that, there has been a significant growth in the number of publications devoted to the study on LLE of ternary and quaternary mixtures, including experimental data and correlation parameters.

Studies of phase equilibria of ternary systems are very important in both theoretical and industrial applications [4]. Precise LLE data of aqueous mixtures with organic solvents are needed in the evaluation of industrial units for solvent extraction processes. The accurate interpretation of phase equilibria and thermodynamic behaviour for the different ternary mixtures is a fundamental and important key to improving solvent extraction techniques [4-11].

Acetic acid is one of the most widely used organic acids, which has many industrial applications. The pure acetic acid is extensively used as an additive in the food industry. Therefore, the efficient separation of acetic acid from aqueous solutions, by solvent extraction technique, is of considerable economic importance in the chemical industry [12-13]. The type of solvent is one of the most important factors, which influence the equilibrium characteristics of extraction of the acid from aqueous solutions. Solvents that are used in the liquid-liquid extraction process must have the

following properties: 1- High capacity that decreases the amount of solvent required. Capacity determines the conditions and size of the separator. 2- High selectivity that leads to products produced with desirable purity. 3- Capability to form two phases at reasonable temperatures and capability of rapid phase separation. 4- Boiling point temperature of solvent should be as varied as possible from the boiling point temperature of components of mixture. 5- Low toxicity, non- corrosiveness and finally, the use of solvent is desired economic justification [14-17].

Many organic solvents have been tested as extractants for the recovery and purification of acetic acid from water. Heavy alcohols, ketones and ethers have been used for extraction of acetic acid from aqueous solutions [18].

As a continuation of that previous work, we present the LLE results for the ternary system (water + acetic acid + ethyl acetate) at T = 298.2 K. The distribution coefficients and separation factors were obtained from experimental results and are also reported. The tie lines were determined and were correlated by the methods of Othmer-Tobias and Hand on a mass-fraction basis. In this work, distribution coefficients (k) and separation factors (S) were determined to establish the possibility of the use of this solvent for the separation process [18-20].

EXPERIMENTAL

Materials

Analytical grade acetic acid, ethyl acetate (mass fraction purity > 0.99) were supplied by Merck. Bi-distilled water was used throughout all the experiments. The purity of the acid was checked through acidimetric titration with 1 N NaOH.

Apparatus and procedure

* To whom all correspondence should be sent:
E-mail: Mehdi.shahbazi72@yahoo.com

The water content of the organic phase was measured by the Karl-Fischer method using Metrohm-870 KF Titrino plus Karl-Fischer titrator. The titrator was calibrated with a standard solution of sodium tartrate. The sample weighing was carried out with an AND electronic analytical balance (model HR-200) with an accuracy of ± 0.0001 g.

Details of the experimental apparatus, procedure and measurements are similar to that of previous work. Solubility or LLE data for the water + acetic acid + ethyl acetate system at T = (298.15) K were determined by the cloud point method.

Tie-line data were determined for the ternary systems at T = 298.2 K. Experiments were carried out in a jacketed 250 ml glass cell. The temperature was estimated to be accurate to within ± 0.1 K. The prepared mixtures were placed in the extraction cell and were vigorously agitated by a magnetic stirrer for 2 h. For all the mixtures, the resting time for phase separation was 4 h. The mass fractions of the acid in both the phases were obtained by potentiometric NaOH titration. The solvent was added by an automated microburette with an accuracy 5.10^{-3}cm^3 . The concentration of water in the organic-rich phase was measured by the Karl-Fisher method.

(Liquid + liquid) equilibrium (LLE) data for the ternary mixtures of {water (1) + acetic acid and (2) + ethyl acetate (3)} were determined at T = 298.2 K and atmospheric pressure.

RESULTS AND DISCUSSION

Experimental LLE results. The experimental solubility data and experimental LLE data of (water + acetic acid) with ethyl acetate at T = 298.2 K are presented in table 1 and 2 [18-20].

The effectiveness of acetic acid extraction done using the solvent ethyl acetate is given by its separation factor (S), which is a measure of the ability of solvent to separate the acid from water. To show the selectivity and extraction strength of the solvent to extract acetic acid, distribution coefficients, d_i , for water ($i = 1$) and acetic acid ($i = 2$) and separation factors, s , were calculated as follows:

$$1) d_i = w_{i3}/w_{i1}$$

$$2) S = \frac{\text{distribution coefficient of acetic acid}}{\text{distribution coefficient of water}} = \frac{w_{23}}{w_{13}} = \frac{w_{21}}{w_{11}}$$

where w_{23} and w_{21} are the acetic acid concentrations insolvent-rich and water rich phases, respectively, and w_{13} and w_{11} are the water concentrations in solvent-rich and water rich phases, respectively. The distribution coefficients and separation factors at T = 273 K and atmospheric pressure are shown. The effectiveness of extraction of acetic acid by ethyl acetate is given by its separation factor, which is an indication of the ability of ethyl acetate to separate acetic acid from water. This quantity is found to be greater than 1 (separation factors varying between 2.397 and 6.981) for the system reported here, which means that extraction of acetic acid by ethyl acetate is possible. The separation factor is not constant over the whole two-phase region.

The distribution coefficients D2 versus w_{21} were plotted in Fig 1 and the separation factors S versus w_{21} were plotted in Fig 2. As shown in fig 1, the distribution coefficients in all cases decreased and increased with increasing of the mass fraction of acetic acid in water-rich phase

The variation of experimental separation factor of the acid as a function of the mass fraction of the solute in aqueous phase for each ternary system is shown in Fig. 2. As shown in these figures, the selectivity in all cases decreased with increasing of the mass fraction of acetic acid in water-rich phase.

Selectivity. Selectivity diagrams on a solvent-free basis are obtained by plotting $w_{23}/(w_{23} + w_{13})$ vs. $w_{21}/(w_{21} + w_{11})$ for system (water + acetic acid + ethyl acetate) in figure 3. The effect of a mass fraction of ethyl acetate in the aqueous phase change on the selectivity values was found to be significant.

Consistency of tie-line data. The reliability of experimental tie-line data can be determined using the Othmer–Tobias and Hand correlations for each solvent, as shown in the following equations:

$$3) \ln ((1-w_{33})/w_{33}) = A + B \ln ((1-w_{11})/w_{11})$$

$$4) \ln (w_{21}/w_{11}) = A' + B' \ln (w_{23}/w_{33})$$

where w_{23} the mole fraction of phosphoric acid in organic phase and w_{11} is the mole fraction of water in aqueous phase; A, B, A', and B' are the parameters of the Othmer–Tobias and the Bachman correlations, respectively.

Table 1 : LLE Data for (Water + Acetic acid + Ethyl acetate) at T = 298.2 K and atmospheric pressure.

Data	M ₃ (gr)	M ₂ (gr)	M ₁ (gr)	W ₃	W ₂	W ₁
1	660.6	670.5	462.15	239.0	204.0	556.0
2	035.8	081.4	301.7	413.0	2109.0	376.0
3	323.8	670.3	090.5	487.0	215.0	298.0
4	829.8	092.3	590.3	569.0	199.0	231.0
5	441.9	590.2	842.2	634.0	174.0	192.0
6	610.9	053.2	622.2	672.0	144.0	183.0

Table 2. Experimental tie-line data in the organic phases for [water (1) + Acetic acid (2) + Ethyl acetate (3)] at 298.2 K

Data	1	2	3	4	5	6
d ₁	0.4701	0.4598	0.4461	0.250	0.1765	0.1534
d ₂	1.179	1.132	1.070	111.1	205.1	096.1
S	508.2	462.2	397.2	444.4	824.6	981.

Table 3. Experimental data of (water + acetic acid + ethyl acetate) ternary system for Tobias Fig

Data	1	2	3	4	5	6
Ln((1-w ₃₃ /w ₃₃))	-/008	-/034	-/088	-/481	-/481	-/991
Ln((1-w ₁₁ /w ₁₁))	-/2818	-/3474	-/368	-/964	-1/355	-1/553

Table 4. Experimental data of (water + acetic acid + ethyl acetate) ternary system for Hand Fig

Data	1	2	3	4	5	6
Ln((w ₂₃ /w ₃₃))	-0.780	-0.828	-0.880	-1.123	-1.356	-1.617
Ln((w ₂₁ /w ₁₁))	-1.072	-1.095	-1.093	-1.386	-1.694	-1.827

Table 5. Constants of Othmer–Tobias and Hand equations for the (water + acetic acid ethyl acetate) system (R²: regression coefficient).

Tobias equatio			Hand equation		
A	B	R ²	A'	B'	R ²
-2886.0	2924.1	99250.	-0.2788	0.9862	0.9792

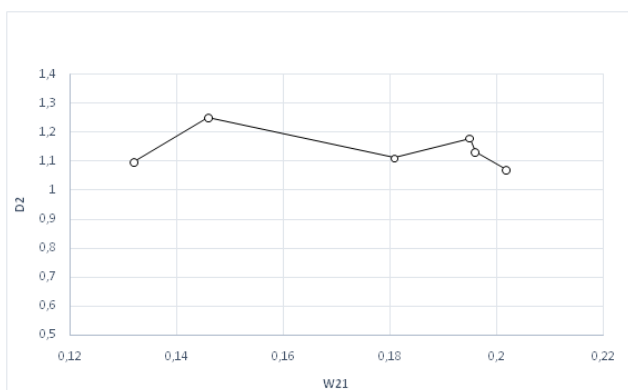


Fig 1 : Distribution coefficient of acetic acid,D2, as a function of the mass fraction of acetyl acetate in the aqueous phase, w21 for the systems of water (1) + acetic acid (2) + ethyl acetate (3)

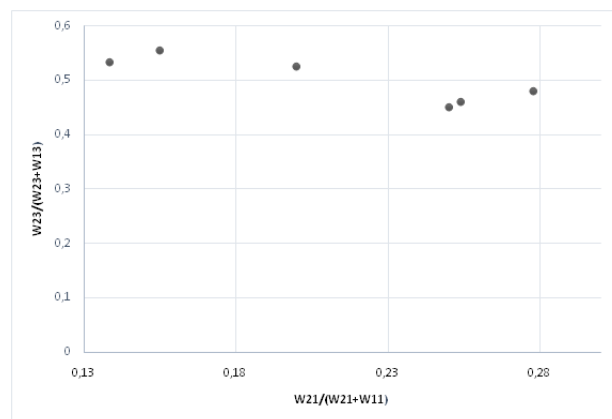


Fig 3 . Selectivity diagram for [water (1) + Acetic acid (2) + Ethyl acetate (3)] at 298.2 k

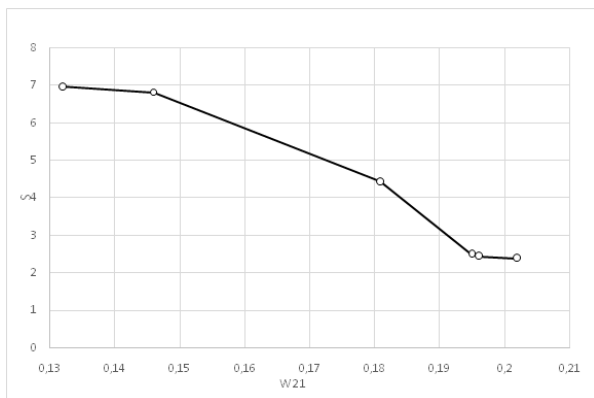


Fig 2: Separation factor, S, as a function of the mass fraction of acetic acid in the aqueous phase, w21 for the systems of water (1) + acetic acid (2) + ethyl acetate (3)

The parameters of the Othmer–Tobias and Hand correlations, at T = 298.2 K, are listed in table 7. For these investigated systems, the Othmer–Tobias and Hand plots are shown in figures 4 and 5, respectively. The correlation factor (R²) is approximately unity, and the linearity of the plots indicate the degree of consistency the measured LLE results in this study.

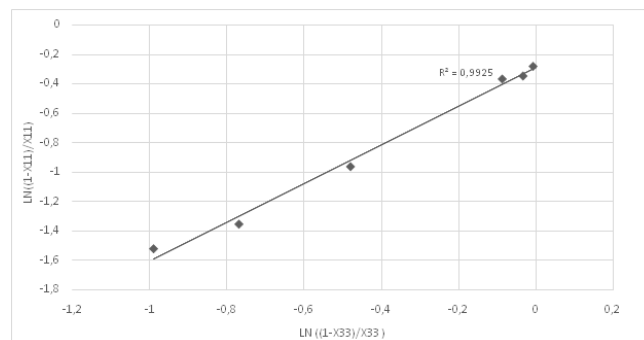


Fig. 4. Othmer–Tobias correlation for the system of water + acetic acid + ethyl acetate at 298.2 K.

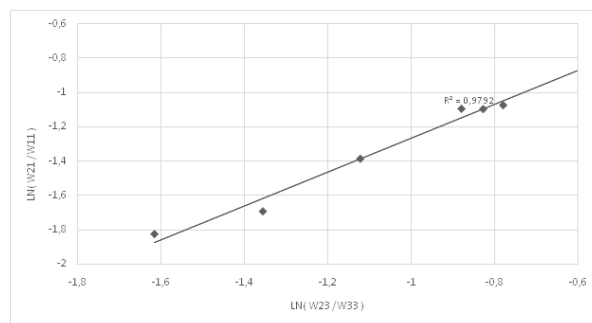


Fig. 5. Hand correlation for the system of water + acetic acid + ethyl acetate at 298.2 K.

CONCLUSION

LLE data for acetic acid + water + ethyl acetate systems were obtained at 298.2 K. Experimental results showed that ethyl acetate have low solubility in water and high solubility for acetic acid. Thus, they can serve as extractors to extract acetic acid from the mixture of acetic acid and water and can serve as an entrainer to separate acetic acid and water via heterogeneous azeotropic distillation. The tie-line data of the system were satisfactorily ascertained by the Othmer–Tobias and Hand correlating equations. The separation factors and distribution coefficients for the solvents used in this work were calculated. The obtained separation factors confirm the ability of these solvents

for extraction of acetic acid from water. As well as the selectivity in all cases decreased with increasing of the mass fraction of acetic acid in water-rich phase.

REFERENCES

1. S. de Moura, J. dos Santos, F. da Silva, *Amer. J. Phys. Chem.*, **2**, 117 (2013).
2. J.C. Upchurch, M. Van Winkle, *Ind. Eng. Chem.*, **44**, 618 (1952).
3. H. Ghanadzadeh, A. Ghanadzadeh, Z. Aghajani, S. Abbasnejad, S. Shekarsaraee, *J. Chem. Thermodyn.*, **42**, 695 (2010).
4. A. Senol, *Fluid Phase Equilibria*, **227**, 87 (2005).
5. A. Arce, A. Blanco, P. Souza, I.J. Vidal, *J. Chem. Eng. Data*, **40**, 225 (1995).
6. S. Ismail Kırbaşlar, S. Sahin, M. Bilgin, *J. Chem. Thermodyn.*, **38**, 1503 (2006).
7. D. Ozmen, S. Cehreli, U. Dramur, *J. Chem. Thermodyn.*, **37**, 837 (2005).
8. H. Ghanadzadeh, A. Ghanadzadeh, *J. Chem. Eng. Data*, **49**, 783 (2004).
9. H. Ghanadzadeh, A. Ghanadzadeh, R. Sariri, *J. Chem. Thermodyn.* **36** (2004)1001.
10. H. Ghanadzadeh, A.K. Haghi, *Fluid Phase Equilibria*, **45**, 243 (2006).
11. C. Hanson, *Recent Advances in Liquid-Liquid Extraction*, Pergamon, New York, 1971.
12. R. Blumberg, *Solvent Extr. Rev.*, **1**, 93 (1971).
13. J.F. McCullough, L.L. Frederick, *J. Agric. Food Chem.*, **24**, 180 (1976).
14. A. Arabi, J. Mahmoudi, H. Saradar, A. Jafarzade, *Korean J. Chem. Eng.*, **28**, 917 (2011).
15. C.-T. Hsieh, W.-Y. Ji, H.-M. Lin, M.-J. Lee, *Fluid Phase Equilibria*, **271**, 69 (2008).
16. A. Orjuela, A. J. Yanez, P. K. Rossman, D.T. Vuc, D. Bernard-Brunel, D. J. Miller, C. T. Lira, *Fluid Phase Equilibria*, **290**, 68 (2010).
17. C.R. Bhupesh, M. R. Awual, M. Goto, *Applied Sciences*, **7**, 1053 (2007).
18. T. Afolabi, A. Alao, *Fluid Phase Equilibria*, **379**, 19 (2014).
19. E. Ince, Y. Selim, *Fluid Phase Equilibria*, **370**, 19 (2014).
20. H. Ghanadzadeh Gilani, A. Ghanadzadeh Gilani, M. Sangashekan, *J. Chem. Thermodyn.*, **58**, 142 (2013).

The effect of nitrate ions on the electrodeposition of PbS semiconducting film: electrochemical and surface analysis

A. Lorparizangen^{1*}, M. Jafarian¹, F. Gobal², S. Miandari¹, M.G. Mahjani¹

¹Department of Chemistry, K.N. Toosi University of Technology, P.O. Box 15875-4416, Tehran, Iran

²Department of Chemistry, Sharif University of Technology, P.O. Box 11365-9516, Tehran, Iran

Received June 26, 2016; Revised September 10, 2016

The aggressive effect of NO_3^- ion, present in electrolyte solvent, on the electrodeposition of PbS film was studied by cyclic voltammetry (CV), cyclic potentiodynamic polarization (CP), and electrochemical impedance spectroscopy (EIS) methods. The CV curves confirmed that presence of NO_3^- 0.1 M in the solution leads to a dramatic increase in amplitude of current and considerable damage to the passive layer at breakdown potential (E_b) of 0.16 V/SCE. Cyclic polarization studies revealed that I_{corr} goes up from 44.08 $\mu\text{A}/\text{cm}^2$ to 551 $\mu\text{A}/\text{cm}^2$ as NO_3^- concentration increases from 0.05 M to 2 M. However, 0.01 M NO_3^- solution notably improved passivation of PbS thin films. The capacitive semicircle with low R_{ct} at medium frequency in the Nyquist plot, indicated structural change in passive layer (PbS film) and pitting corrosion on its surface. X-ray diffraction (XRD) and scanning electron microscopy (SEM) were used to investigate the aggressive behavior of NO_3^- and deformation of the surface.

Keywords: Lead sulfide; cyclic polarization; electrochemical impedance spectroscopy; pitting corrosion

INTRODUCTION

Lead sulfide (PbS) is a well-known semiconductor with a narrow band gap of 0.41 eV and relatively large excitation Bohr radius¹⁻³. These characteristics make it a basic industrial material. Lead sulfide has been widely used in many areas such as infrared detection applications, Pb²⁺ ion selective sensor, solar energy absorption, photography, photo resistors, and diode lasers [1-3].

PbS thin film is deposited by various deposition methods which are basically categorized into two main types:

1) electrochemical [3-6] and

2) chemical [4-8] methods. Extensive research has been devoted to production of PbS thin film by various electrodeposition techniques. Unlike routine deposition methods, electrodeposition approach provides advantages such as operation at ambient temperature and pressure [9, 10], low cost, and easy control of thickness of the film [11].

So far several studies on the electrodeposition of PbS in a variety of electrolytes have been carried out [6] and considerable effort has been focused on PbS properties in different media [12-15] using a wide variety of electrochemical methods. However, there are few reports on the effect of electrolytes on the PbS layer and its corrosion in aqueous media. Semiconducting properties of PbS films are adversely influenced by aggressive ions. PbS films are susceptible to corrosion as PbS becomes

oxidized. This process is depicted in the Pourbaix diagram for the lead/water system [7, 12, 15]. Recently, the aggressive effects of NO_3^- ions on aluminum rods [16] and stainless steel [16] have been studied. The aggressive nature of NO_3^- in the corrosion of Pb in different media has also been reported [16-18].

In this work, we have studied the influence of KNO_3 solution on deposition of PbS in sodium sulfide medium and found its optimum concentration. We investigate the effects of NO_3^- on breakdown and structural change of the passive film. Cyclic voltammetry, chronoamperometry, and electrochemical impedance spectroscopy methods were used to characterize the mechanism of this process in detail. These studies were accompanied by surface analysis methods, i.e. XRD and SEM [19].

EXPERIMENTAL

Sodium sulfide, potassium nitrate, and potassium hydroxide used in this work were Merck products of analytical grade and were used without further purification. Electrochemical studies were carried out in a conventional three electrode cell powered by an electrochemical system comprising of a potentiostat/galvanostat (EG&G, model 273A) controlled by a PC through M270 and M398 software (GPIB interface), and a frequency response analyzer (EG&G, model 1025). The frequency range of 100 kHz – 10 MHz and modulation amplitude of 5mV were employed in electrochemical impedance studies. The working

* To whom all correspondence should be sent:
E-mail: aminlorpari@yahoo.com

electrode employed in the present study was made of very pure lead rod (purity 99.999%, w/w of Pb) in shape of a cylindrical rod, welded to Cu wire for electrical contact, and mounted to expose 1cm² area to the electrolyte. Graphite as a counter electrode, and a saturated calomel electrode (SCE) as a reference electrode were used. Prior to each experiment, the surface pre-treatment of the working electrode was performed by mechanical polishing of the electrode surface with successive grades of emery papers down to 2000 grit. The electrode was rinsed with ethanol and distilled water and then was dipped in the electrolyte. All the electrochemical experiments were performed at room temperature.

XRD analysis was performed on X-Pert pro MPD (PAN analytical) diffractometer with CuK α radiation ($\lambda = 1.5406 \text{ \AA}$) in the 2θ range of 10 to 90°.

SEM images were created using the electrode surface after potentiostatic polarization at the potential of 0.55 V for 60s. SEM examinations were performed by a TESCAN (model VEGA-TS 5136MM) electron microscope using various magnifications to observe different aspects of the surface.

RESULTS AND DISCUSSION

Cyclic voltammetry

The potentiodynamic studies of Pb electrode were performed in three different solutions: 1) 0.1 M Na₂S, 2) 0.1 M Na₂S mixed with 0.1M KNO₃, and 3) 0.1 M Na₂S mixed with 0.1 M NaOH. The potential was swept from -2 to 2 V/SCE at the sweep rate of 50 mV/s. The potential was then swept back for a second time from 2 to -2 V/SCE at the same rate. Fig. 1(a,a') presents the cyclic voltammogram of Pb electrode in Na₂S solution with two anodic peaks at -0.2 and 1.3 V/SCE. First peak (A₁) was observed in potential region of -0.4 to 0.2 V/SCE, (Fig. 1a'). This potential region is related to oxidation of Pb to Pb²⁺ and formation of PbS as reported by Yang et al¹⁹. Second peak (A₂) was in potential region of 0.4 to 1.4 V/SCE (Fig. 1a). Passive region is formed from -0.25 to 1.3 V/SCE. At potential of 1.3 V, the oxygen evolution on the Pb surface leads to removal of PbS film from the surface, which in turn prevents the passivation of the electrode [20, 21]. Therefore, the second anodic peak enhances passivity breakdown of the layer at a certain potential (breakdown potential, E_b) [14]. The cyclic voltammograms show that the A₂ peak rises more upon addition of NO₃⁻ than OH⁻. In contrast, A₁ peak does not demonstrate considerable change upon addition of either NO₃⁻ than OH⁻.

These observations confirm that despite the stability of the highly adhesive PbS film, formation of PbO results in breakdown of the passive PbS film [14]. Since the solubility constant of PbS is approximately 10⁸ times less than that of Pb(OH)₂, (K_{sp}=1.42×10⁻²⁰) formation of oxide layers is not expected. XRD results confirm formation of PbO and Pb₃O₂(OH)₂ layers. Reactions involved in formation of PbO are described below²⁰.

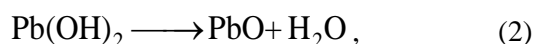


Fig.1b shows the effect of addition of NO₃⁻ solution with different concentrations on the passivation of PbS. Increasing the concentration of NO₃⁻ caused no significant change in the first anodic peak, however, the second anodic peak raised markedly. Upon addition of 0.01 M NO₃⁻ solution, the passive region spanned a relatively wide range of potential. Upward shift of curve 2, reflecting a slight increase in current density, is due to higher conductivity of electrolyte solution. An increase in nitrate concentration up to 0.05 M created an E_b at 0.41 V/SCE and caused the anodic current to increase. Further increase in the NO₃⁻ concentration caused E_b to shift to more negative potentials (E_b=0.16 V/SCE in 0.1M). The current density increased as well.

In 0.01 M and 0.05 M NO₃⁻ solutions the cathodic curve was found at higher current density level than the anodic curve (Fig. 1b'). In contrast, in 0.1 M NO₃⁻ solution the cathodic curve was found in lower current density level than the anodic curve. This difference indicates that the passive layer was significantly damaged at nitrate concentration of 0.1 M [16, 22].

Formation of a large anodic peak with a high current density level in the potential range between PbS formation potential (-0.2V/SCE) and O₂ evolution potential (1.3V/SCE) indicates the aggressive effect of NO₃⁻ on PbS passive layer (Fig. 1b). This effect is further confirmed by the displacement of E_b potential toward formation potential of PbS, and conversion of the anodic peaks to a single peak. Lower value of repassivation potential (E_{rep}) compared to breakdown potential (E_b) indicates cessation of pit growth in PbS passive layer, and formation of lead oxide and lead hydroxide compounds in PbS film layer [23].

In order to recognize the effectiveness of NO₃⁻ in causing pits in the film layer, breakdown potential versus the logarithmic concentration of NO₃⁻ was plotted (Fig. 1c). The aggressive behavior

of a given anion is more prominent if the curve representing equation (3) is close to a straight line [22, 24]. The value of B for NO₃⁻ was 0.526. The relationship between E_b and logarithmic

concentration of NO₃⁻ was found to be linear which suggests the aggressive behavior of NO₃⁻ ions.

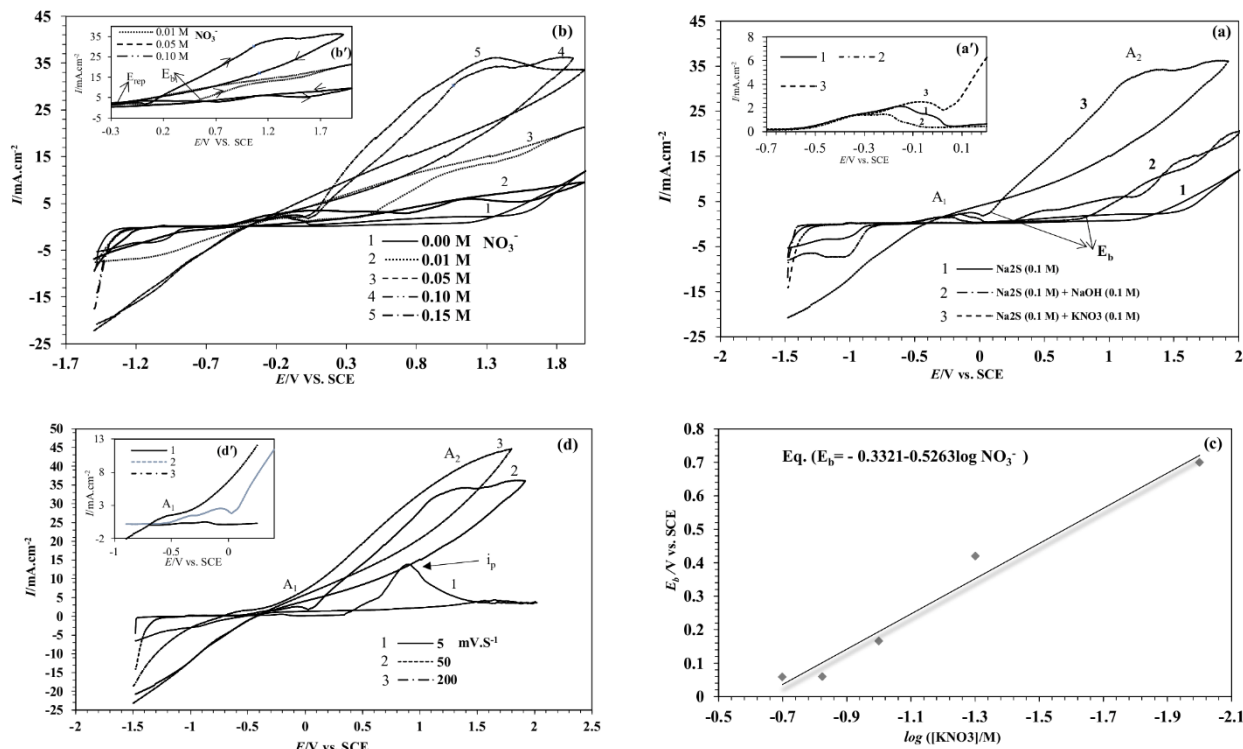


Fig. 1. Cyclic voltammograms for Pb electrode (a) in three different media with scan rate of 50 mV/s (b) in solution containing Na₂S and different concentrations of 0.0 – 0.15 M (c) in 0.1 M Na₂S + 0.1 M KNO₃ mixed solution at different scan rates of 5, 50 and 200 mV/s (d) Plot of pitting potentials versus log []

$$E_b = A - B \log C_x, \quad (3)$$

A and B are constants and C_x is the concentration of aggressive ion. E_b, critical breakdown potential, is the potential above which film breakdown occurs [23-25].

The influence of scan rate (5, 50, and 200 mV/s) on the potentiodynamic polarization curves of Pb in a solution with Na₂S concentration of 0.1 M and KNO₃ concentration of 0.1 M was studied. As scan rate increased, the anodic peak current density (i_p) shifted toward more positive values (Fig. 1d) and the potential value of A₁ peak shifted toward more negative values (Fig. 1d').

A₁ peak in Fig. (2a) shows the formation of PbS in the Na₂S solution. With increasing scan rate, i_p went up. Nevertheless, the PbS formation peak in Na₂S+KNO₃ solution (A₁) did not exhibit a significant change. In reverse scan, reduction peaks C₁ (-0.8 V/SCE) and C₂ (-1.3 V/SCE) were generated by reduction of compounds were oxidized in A₂ and A₁, respectively. As the scan rate increased, C₁ tended to overlap with C₂ to make a single peak. This overlap is thought to be

due to rapid formation of a solid layer of PbS (K_{sp}=3.0×10⁻²⁸) according to the following reaction:

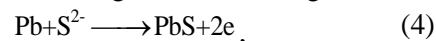


Fig. (2a') shows the linear dependency of anodic peak current density (i_p) on the square root of scan rate (v^{1/2}) [26]. Fairly straight lines with correlation coefficients of 0.98 were obtained suggesting that diffusion of reacting species dominantly control the kinetics of anodic processes [27].

Chronoamperometry studies

The pitting corrosion effect of NO₃⁻ can be related to the adsorption competition between NO₃⁻ and S²⁻ ions on the PbS surface sites. We attempted to verify this assumption by applying potentiostatic methods at the potential of the second anodic peak (0.55 V/SCE) for 60 s.

Fig. (2b) shows the chronoamperograms of lead electrode in three different electrolytes. Curves 1 and 2 show a decrease in current density. The reason is nucleation of the passive layer [28] and continued S²⁻ flux. This nucleation process led to thinning of PbS layer. In other words, the oxidation

process was overtaken by slow mass transfer to the surface. The current densities in curves 1&2 are smaller than that in curve 3 due to mass transfer limitations of different electrolytes. An increase in the current density in the presence of NO_3^- as an aggressive anion (curve 3) corresponds closely to passivity breakdown of the passive film at early stages of the process (pit growth time) [29]. The passive layer was partially re-established.

Polarization gradually caused a decrease in current density according to the ohm law, $V = IR$, where R is the electrical resistance of the electrolyte plus any passive film inside of pit region. IR drop was thus related to the potential difference between the pit bottom at metal interface and the passive surface [16]. Fluctuations of corrosion current in curve 3 confirmed that the flaws were present in the film.

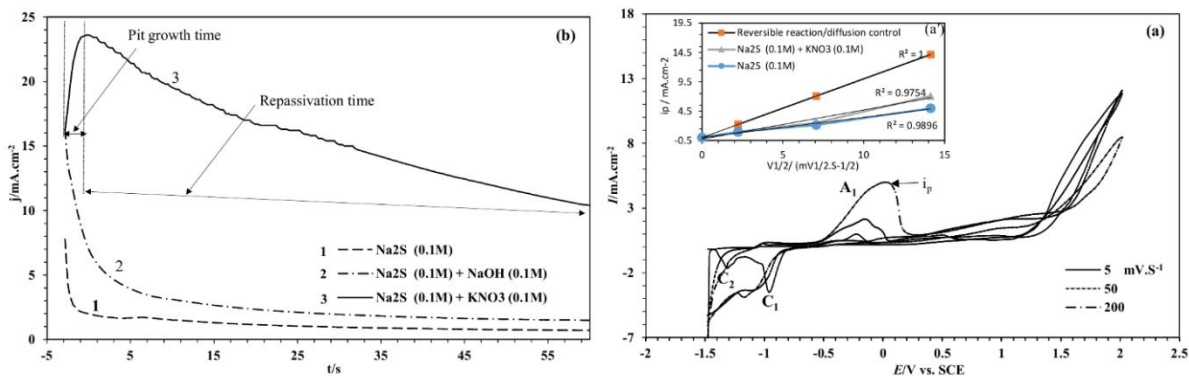


Fig. 2. (a) Cyclic Voltammograms for Pb electrode in 0.1 M Na_2S solution between -1.5 and 2 V/SCE at different scan rates of 5, 50 and 200 mV/s . (b) Chronoamperograms of lead electrode in different electrolytes, $E_{\text{apply}} = 0.55$.

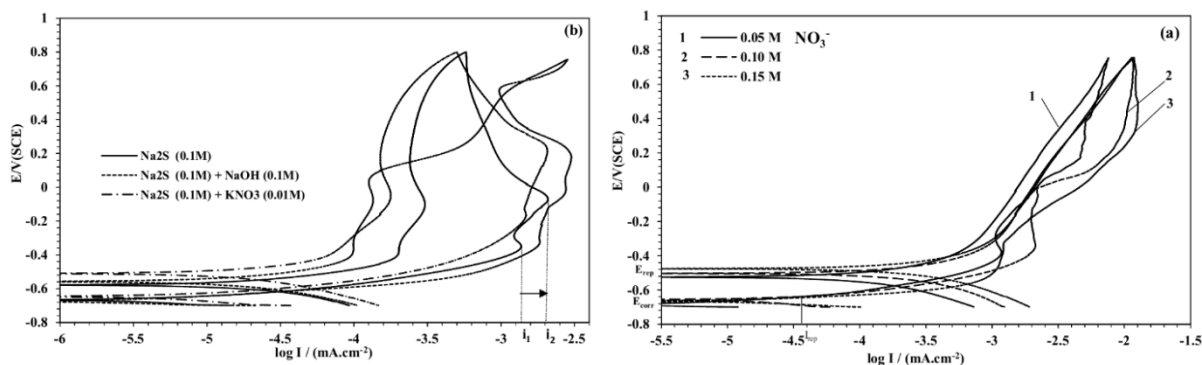


Fig. 3. Cyclic polarization curve of PbS in different media (a) without aggressive effect (b) with aggressive effect.

Cyclic potentiodynamic polarization

Fig. (3a) shows the cyclic polarization curves of the potentiodynamically deposited thin film layers on the Pb electrode in three different electrolytes. In all cases, the cyclic polarization curves were swept between -700 to 750 mV with 10 mV/s scan rate. The cyclic polarization curve of 0.1 M Na_2S solution exhibited the corrosion potential (E_{corr}) of -668 mV/SCE and corrosion current density (I_{corr}) of 30.44 $\mu\text{A/cm}^2$. The cyclic polarization curve of 0.1 M $\text{Na}_2\text{S} + 0.1$ M NaOH solution yielded E_{corr} of -674 mV/SCE and I_{corr} of 81.12 $\mu\text{A/cm}^2$. In 0.01M NO_3^- solution, E_{corr} and I_{corr} were -647 mV/SCE and 44.08 $\mu\text{A/cm}^2$, respectively.

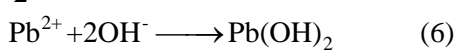
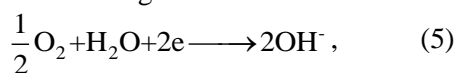
These data show an increase in I_{corr} which was not due to pit formation on the surface of PbS layer. Based on [16], we concluded that incorporation of water molecules into the PbS passive film formed concentration gradients across metal-film and film-

solution interfaces. These gradients caused flaws in the passive layer which increased the critical current density from i_1 to i_2 [30], (Fig. 3a).

Upon addition of 0.01 M NO_3^- solution to Na_2S solution, NO_3^- ions help to distribute the current, generated in the flaws, all over the passive film. Thus, a film forms on the uniformly polarized surface at higher potentials. An increase in concentration of NO_3^- to 0.05M makes the passive film unstable (Fig. 3b). This can lead to localized corrosion on the PbS surface. Dissolution of passive layer advances a flaw to a pit [16]. Upon addition of 0.1 M NO_3^- solution, E_{corr} and I_{corr} measured -658 mV/SCE and 0.15 mA/cm^2 , respectively. Value of I_{corr} in case of addition of NO_3^- to Na_2S solution was 2 to 5 times larger than addition of OH. An increase in the value of pitting current density (I_{pit}) confirms that the film did not have a stable passive state. The corrosion, passivation, breakdown, and re-passivation

parameters are calculated by the cyclic polarization method and are summarized in the paper.

The 0.1M solution of OH⁻ showed a large hysteresis loop (Fig.3a). Crevice corrosion did not propagate immediately after corrosion initiation at -118 V which resulted in surface polarization and subsequent formation of passive layer on the surface. This layer was found to be compact and favorable because it contains Pb(OH)₂ formed according to the following reactions:



Moreover, hysteresis loop was larger in 0.1 M OH⁻ curve (Fig.8) than 0.1 M NO₃⁻ curve (Fig.3b). This observation indicates that NO₃⁻ causes a larger increase in the current, although the conductivity of NO₃⁻ and OH⁻ are close.

Electrochemical impedance spectroscopy

Typical Nyquist and Bode-phase plots are presented in Fig. 4a,b. Curve 1 is plotted for the Pb electrode in the Na₂S solution. It has one capacitive loop with a resistance value of about 400 Ω.cm² against the charge transfer process for deposited PbS film. Value of charge transfer resistance was found to be very large when the OH⁻ anions were added to Na₂S solution (Nyquist plots, curve 2) which was due to the formation of stable and compact passive film in the solution. This result is in accordance with the cyclic polarization studies (Fig. 3a). In the corresponding Bode-phase plot (Fig. 4b, curve 2) the capacitive response was observed with 60 degree phase angle in the intermediate frequencies. Addition of NO₃⁻ ions resulted in two overlapping capacitive loops (curve 3). At high frequencies, semicircle of NO₃⁻ solution curve was smaller than those of NO₃⁻-free solution and NO₃⁻+OH⁻ solution which was owing to decreased stability of passive layer and increased porosity of the film. Nitrate ions penetrated the passive film [31] and caused structural changes in

the surface which in turn led to a remarkable decrease in diameter of the semicircle (R_{ct}). Nitrate anions were then adsorbed on the film-solution interface at OCP. This behavior is shown in the Bode-phase spectrum (Fig.4b, curve 3) with the phase value of 20 degrees in high frequencies. The PbS layer was then removed and lead oxide layer was formed. Small values of second charge transfer resistance (25 Ω.cm²) and phase (10 degrees) indicate low resistivity and high permeability of the passive film which is owing to the formation of lead oxide. In addition, the presence of one inductive loop at low frequency range indicates that the pitting process occurred on the surface after passivation process [32]. However, [33] mentioned an inductive loop associated with the synchronized adsorption ↔ desorption process (i.e. adsorption of lead oxide ↔ desorption of lead sulfide). Our experimental data revealed the aggressive effects of NO₃⁻ culminating in structural change and pitting corrosion of passive layer (PbS film).

Nitrate, as a chaotropic anion [34] with a weak electric field, can become adsorbed on or even penetrate into the film-solution interface. Hydroxylic ion is a kosmotropic anion with a strong electric field at short distance [35]. Therefore, OH⁻ was less likely than NO₃⁻ to be adsorbed on the passive film-solution interface which resulted in generation of more cation vacancies that migrate to the metal-film interface [36].

X-ray diffraction studies

Fig. 5 shows XRD pattern of the product prepared potentiostatically on the Pb surface in a 0.1M Na₂S + 0.1M KNO₃ solution in 60 s. The XRD pattern demonstrated the presence of H₂Pb₃O₄ with tetragonal structure (JCPDS card no.77-1895), PbO with orthorhombic structure (JCPDS card no.77-1971), and PbS with cubic crystal structure (JCPDS card no.78-1057). PbO was detected in the passive layer according to the XRD pattern of the film (Fig.5).

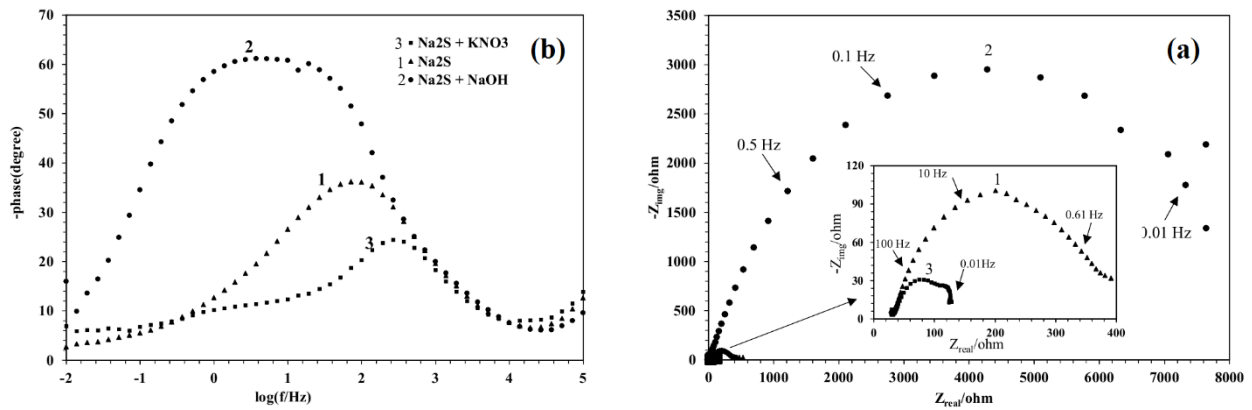


Fig. 4. a) Nyquist plots and b) Bode-Phase spectra of deposited passive film in solutions containing 0.1 M concentration of different electrolytes, at the OCP.

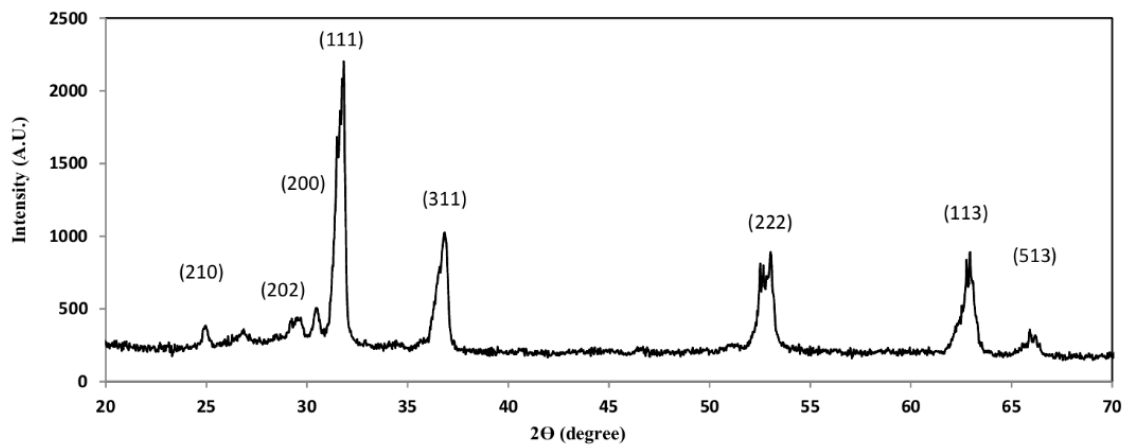


Fig. 5. XRD pattern of potentiostatically oxidized Pb electrode in 0.1 M Na₂S+0.1 M KNO₃ solution at 0.55 V/SCE. *SEM and morphology of surface*

Reduction of NO₃⁻ is thermodynamically easier than Pb²⁺ in the potential used in our experiment (0.55 V/SCE) because of the fact that reduction potential of NO₃⁻ [$E_{\text{NO}_3^-/\text{NO}_2^-}^\circ$ (-0.234 V/SCE)] is more positive than that of Pb²⁺ [$E_{\text{Pb}^{2+}/\text{Pb}}^\circ$ (-0.36 V/SCE)].

Reduction of NO₃⁻ leads to the formation of OH⁻ according to the following reaction,



OH⁻ ions and Pb²⁺ ions were generated at the same time on the surface of anode and cathode respectively. When direct current passed through the electrochemical cell, Pb²⁺ ions reacted with OH⁻ ions to production of Pb(OH)₂, which was then hydrated to form PbO [16].

Obtained SEM images (Fig. 6) showed the morphology of the passive film on the Pb surface after potentiostatic treatment in three different solutions: 1) 0.1 M Na₂S, 2) 0.1 M Na₂S mixed with 0.1 M KNO₃, and 3) 0.1 M Na₂S mixed with 0.1 M NaOH. Bare surface of Pb was scanned by SEM (Image a). Electrochemically treated surface of Pb in the pure solution of Na₂S had an uneven surface with no evidence of pitting is observed (Image b). Upon addition of NO₃⁻ to Na₂S solution, the entire surface of the electrode was damaged and covered with irregular holes (Images c, e). A hole of testicular shape and 5.3×3.5 μm diameter was observed (Image g). PbS surface had superficial defects in case of OH⁻ solution (Images d, f), whereas the surface was observed to have clear holes in case of NO₃⁻ solution (Image e). The effect of NO₃⁻ on the pitting corrosion of passivated thin film was clearly demonstrated in the SEM images.

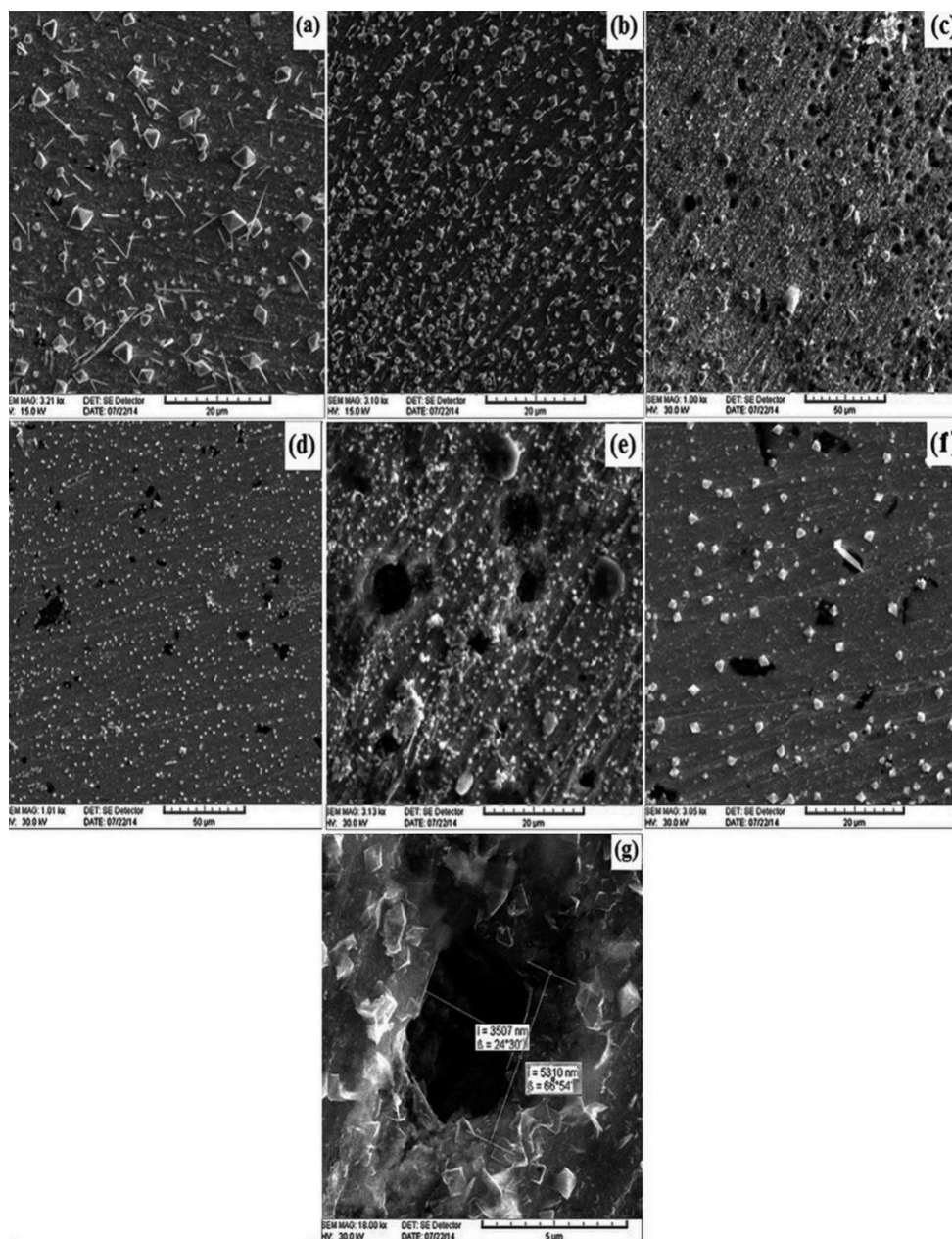


Fig. 6. SEM images of Pb surface (a), and Pb surface after potentiostatic polarization at 0.55 V/SCE for 60 s in 0.1M Na₂S (b), 0.1 M Na₂S+0.1 M KNO₃ (c,e,g) and 0.1 M Na₂S+0.1 M NaOH (d,f) solutions.

CONCLUSIONS

Potentiodynamic polarization of nitrate-free solution exhibited two anodic peaks corresponding to the formation of PbS and oxygen evolution. Addition of NO₃⁻ ion caused these peaks to merge and induced abrupt increase in current density. This increase is related to more aggressive behavior of NO₃⁻ in compared with that of optimum concentration of NO₃⁻ was obtained to be 0.01 M. An increase in the concentration of NO₃⁻ in sodium sulfide solution to values larger than the optimum induced pitting attack at a certain potential (E_{pit}). The pitting corrosion of PbS increased with increasing NO₃⁻ concentration. Chronoamperometric studies revealed an IR drop at the

bottom of pit at pit growth initiation. XRD pattern showed deformation of passive film due to aggressive behavior of NO₃⁻ ions. Three-phase mixture of H₂Pb₃O₄, PbO, and PbS and presence of pits on the electrode surface were also confirmed using XRD.

Acknowledgment: We gratefully acknowledge the support of this work by K.N. Toosi University of Technology Research Council.

REFERENCES

1. M. Mozafari, F. Moztarzadeh, *J. Colloid Interface Science*, **351**, 442 (2010).
2. M. Barote, A. Yadav, T. Chavan, E. Masumdar, *Digest J. Nanomater. Biostruct.*, **6**, 979 (2011).

3. A. O. Nejo, A. A. Nejo, R. V. Pullabhotla, N. Revaprasadu, *J. Alloys Compounds*, **537**, 19 (2012).
4. A. Aghassi, M. Jafarian, I. Danaee, F. Gobal, M. Mahjani, *J. Electroanal. Chem.*, **661**, 265 (2011).
5. P. Nair, V. Garcia, A. Hernandez, M. Nair, *J. Physics D: Applied Physics*, **24**, 1466 (1991).
6. F. B.E. Nisanci, U.M. Demir, *Langmuir*, **28**, 8571, (2012).
7. M. Alanyaloğlu, F. Bayrakçeken, Ü. Demir, *Electrochimica Acta*, **54**, 6554 (2009).
8. M. Takahashi, Y. Ohshima, K. Nagata, S. Furuta, *J. Electroanal. Chem.*, **359**, 281 (1993).
9. A. P. Gaiduk, P. I. Gaiduk, A. N. Larsen, *Thin Solid Films*, **516**, 3791 (2008).
10. Z. Zeng, S. Wang, S. Yang, *Chemistry of Materials*, **11**, 1999, 3365.
11. J. Valenzuela-Jauregui, R. Ramirez-Bon, A. Mendoza-Galvan, M. Sotelo-Lerma, *Thin Solid Films*, **441**, 104 (2003).
12. M. Sharon, K. Ramaiah, M. Kumar, M. Neumann-Spallart, C. Levy-Clement, *J. Electroanal. Chem.*, **436**, 49 (1997).
13. Y. J. Yang, *Materials Science and Engineering: B*, **131**, 200 (2006).
14. Y. J. Yang, L. Y. He and Q. F. Zhang, *Electrochem. Commun.*, **7**, 361 (2005).
15. Y. Mikhlin, A. Kuklinskiy, E. Mikhlina, V. Kargin I. Asanov, *J. Appl. Electrochem.*, **34**, 37 (2004).
16. E. E. Stansbury, R. A. Buchanan, Fundamentals of electrochemical corrosion, ASM International, 2000.
17. B. M. Rosales, M. Iannuzzi, *Mater. Sci. Eng.: A*, **472**, 15 (2008).
18. S.-I. Pyun, K.-H. Na, W.-J. Lee, J.-J. Park, *Corrosion*, **56**, 1015 (2000).
19. R. Newman and M. Ajjawi, *Corrosion Sci.*, **26**, 1057 (1986).
20. M. A. Amin, S. S. Abdel Rehim, *Electrochimica Acta*, **49**, 2415 (2004).
21. M. El-Naggar, *J. Mater. Sci.*, **39**, 2747 (2004).
22. P. Veluchamy, M. Sharon, H. Minoura, Y. Ichihashi, K. Basavaswaran, *J. Electroanal. Chem.*, **344**, 73 (1993).
23. J. Galvele, *Corrosion Sci.*, **47**, 3053 (2005).
24. A. Montaser, P. Veluchamy, H. Minoura, *J. Electroanal. Chem.*, **419**, 47 (1996).
25. C. Chao, L. Lin, D. Macdonald, *J. Electrochem. Soc.*, **128**, 1187 (1981).
26. S. M. Sayyah, S. S. Abd-Elrehim, R. E. Azooz, F. Mohamed, *J. Korean Chem. Soc.*, **58**, 24 (2014).
27. A. J. Bard, L. R. Faulkner, *Electrochemical methods: fundamentals and applications*, Wiley New York, 1980.
28. S. Saidman, J. Bessone, *J. Electroanal. Chem.*, **521**, 87 (2002).
29. M. A. Amin, *Electrochimica Acta*, **54**, 1857 (2009).
30. D. Li, P. P. Conway, C. Liu, *Corrosion Sci.*, **50**, 995 (2008).
31. Q. Wang, J.-E. Moser, M. Grätzel, *The J. Phys. Chem. B*, **109**, 14945 (2005).
32. M. Jafarian, F. Gobal, I. Danaee, R. Biabani, M. Mahjani, *Electrochimica Acta*, **53**, 4528 (2008).
33. M. Lashgari, M.-R. Arshadi, S. Miandari, *Electrochimica Acta*, **55**, 6058 (2010).
34. J.-L. Trompette, L. Massot, L. Arurault, S. Fontorbes, *Corrosion Sci.*, **53**, 1262 (2011).
35. K. D. Collins, G. W. Neilson, J. E. Enderby, *Biophysical Chem.*, **128**, 95 (2007).
36. M. Alvarez, J. Galvele, *Shreir's Corrosion*, Elsevier, Oxford, 2010, p.772.

Application research on coating to adjust the cohesive force between dust and polar plate

Y. Zhang, Wei Yu*, Min Li

School of Automotive and Transportation, Qingdao University of Technology, Shandong, Qingdao, 266520, China

Received June 6, 2016, Revised September 8, 2016

In order to improve the dust collecting efficiency of electrostatic precipitator, starting from the polar plate material, established mechanical model of dust collecting process, analysed the influence of polar plate material to dust collecting, designed experimental device to measure dust cohesive force, measured the dust collecting effect when use coating, results showed that: according to the different nature of the dust, used reasonable Polar Plate coating can improve ESP dust collecting effect.

Keywords: electrostatic precipitator, dust, experiment device, cohesive force.

INTRODUCTION

Mine underground dust is the main factor to cause silicosis. Electrostatic precipitator (ESP) is widely used for mine dust capturing and recovery. Its basic principle is the use of high-voltage discharge, the gas ionization, charged dust move to collecting dust polar plate, then dust separate from the gas stream, so achieve the purpose of purifying gas. At the same time, many factors influence on ESP's collecting dust effect, such as temperature, humidity especially electrostatic dust characteristics. Conventional ESP is suitable for collecting dust with 10^4 - $10^{11}\Omega\cdot\text{cm}$ resistivity, while for high resistivity dust, the cohesive force between dust and collecting polar plate is large and difficult to rapping and fighting off, and the dust deposited on the collecting plate has slow discharge rate, which is prone to generate the phenomenon of anti-corona and "secondary emissions" for the low resistivity dust. In order to improve the performance of ESP, many domestic and foreign experts have done a lot of research [1-6], Tang Min-kang [7] studied on particle coagulation and high resistivity dust characteristics, Zhi Xue-yi, Ye Qing studied on dust formation mechanism, growth pattern and coagulation mechanism [8, 9]. In order to improve the mine ESP efficiency, article starting from the relationship between polar plate material and dust cohesive force, adjust cohesive force between dust and polar plate, solve the rapping problem, improve the dust collection efficiency.

EFFECT OF POLAR PLATE MATERIAL ON THE DUST CHARGE

According to the theory of molecular heat physics, any matter has certain degree thermoelectric in high temperature conditions, but emit a lot of electron only when the temperature reaches the critical emission temperature. Different materials have different critical emission temperature, according to the temperature environment in underground mine, can choose a suitable electronic work function lower polar plate material, the polar plate can be stable emit electron in ESP, make dust charging, achieve the purpose of energy efficiency.

Analysis electron how to escape from materials surface

For the different environment especially under different temperature conditions, it is not a definite concept that ESP polar plate material electron work function is the good to improve dust collection efficiency. The work requirement vary according to the change of external conditions, article through reducing definition formulas to describe the main factors of affecting electron work function, to provide the scientific basis for selecting suitable polar plate material.

The application of single electron approximation method to discuss the energy behavior of plurality electron. Assuming no electronic interaction, and motion in the potential field of a single finite barrier. Single electron statewave function can be obtained by means of the Schrodinger equation:

$$\left[-\frac{1}{2}p^2 + U_{eff} \right] \Psi_i = E_i \Psi_i \quad (1)$$

* To whom all correspondence should be sent:

E-mail: zhyoliang@163.com

U_{eff} is effective surface potential.

In the infinite surface potential should be constant constant potential. In the positive colloid, independence total electron energy is:

$$E_T = 2 \sum_t^{\text{occ}} E_i \quad (2)$$

Here to consider the electron spin. Occ said all electron number if its occupied state, represented by the density of states:

$$E_T = 2 \int_{-\infty}^{E_F} E \rho_t(E) dE \quad (3)$$

E_T can be divided into two parts: body and surface, the surface energy:

$$E_S = 2 \int_{-\infty}^{E_F} E \rho_s(E) dE \quad (4)$$

Because the surface caused the presence of small changes in the density of states at the Fermi level, the excess electron is empty offset, these electrons on the surface energy contribution is negative:

$$-2 \int_{-\infty}^{E_F} E \rho_s(E) dE$$

Expressions of surface energy is:

$$\begin{aligned} E_S &= 2 \int_{-\infty}^{E_F} (E - E_F) \rho_s(E) dE = \\ &= 2 \int_{-\infty}^{E_F} (E - E_F) \left[-\frac{1}{4} \delta(E) + \frac{1}{\pi} \frac{d\eta(E)}{dE} \right] dE = \\ &= \frac{E_F}{2} + 2 \int_0^{E_F} \frac{d\eta}{dE} \times \frac{E - E_F}{\pi} dE \end{aligned} \quad (5)$$

Application condition of electrical neutrality $\eta(E_F) = \pi/4$, obtained

$$E_S = \frac{2}{\pi} \int_0^{E_F} E \frac{d\eta}{dE} dE \quad (6)$$

The above results based on hypothesis of isolated electronic. But the actual situation is much more complicated, when the electron motion energy exceed surface energy, electron will escape from the surface material Choice ESP polar plate material in the actual, not only to consider the interaction between electrons, but also consider the effect of orientation of the metal crystals.

The work function of dust space collision

When ESP working, polar plate material because of its nature or affected by the outside world, electron escape phenomenon often appear, and the escaping electrons and dust happen elastic collision in space and make dust become charged objects. These phenomena generated due to electron work fuction plays a considerable influence on ESP work efficiency.

The so-called electron escape depth (also known as the mean free path) refers to the electronic

experience average distance before elastic collision. The electron mean free path and its kinetic energy have direct relationship with polar plate material. D.R.Penn proposed the theoretical formulais:

$$\lambda(E_k) = \frac{E_k}{a(\ln E_k + b)} \quad (7)$$

$\lambda(E_k)$ is the mean free path when the electron kinetic energy is E_k ; a , b are two parameters related to the plate material properties

Used this formula can calculate the mean free path of common materials.

Although the electron mean free path changes with the electron kinetic energy and material properties need to continue to study, but a large number of experimental results shown that, the relationship between escape depth and kinetic energy trend seems to be a general curve, as shown in Figure1.

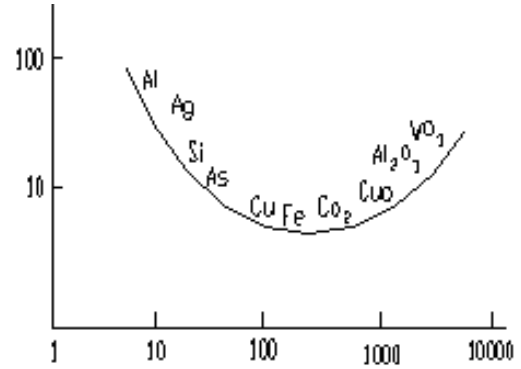


Fig. 1. Relation diagram between escape depth and kinetic energy.

In general, $\lambda(E_k)$ varies with the nature of the material, the energy is generally in the range between 200 and 2000 eV, in this energy range, $\lambda(E_k)$ change with $E_k/2$, approximately, namely $\lambda = k\sqrt{E}$, k is constant.

For various kinds of dust, they collision can not produce energy more than 200 eV, according to above derivation data, kinetic energy of dust collision can not make electron escape, so the study of ESP can ignore the work function when dust collision in space.

THE INFLUENCE OF COATING ON FORCE CONDITIONS OF DUST

The existing theory of dust trapping considers that, when dust gets into the border region of laminar flow where Coulomb force plays the role, and attaches to the collecting dust polar plate, the dust can be arrested on the set.

After dust particles in the electric force field are separated from the airflow and attached to the

collecting dust polar plate, dust whether re-entering the flow or not depends on the force conditions of the dust particles. If the cohesive force is greater than the bonding force, the dust particles can be firmly attached to, or may be desorption and re-entering the flow which results in the so-called "secondary dust" phenomenon. After particles attached to the polar plate, the main forces are as following:

The molecular force between dust layer and polar plate, f_1 , which has a small effective distance about 10-8cm, and

$$f_1 = \pi UDL \quad (8)$$

Where, U - intensity per unit area;

D - diameter of dust layer;

L - the effecting distance of molecular force on the contacting face.

The molecular force between dust particles, f_2 , and

$$f_2 = \pi U \frac{D_1 D_2}{D_1 + D_2} L \quad (9)$$

Where, D_1, D_2 - diameter of particles.

The gravity of dust layer, f_3 , and

$$f_3 = mg = A \delta_d r_d \quad (10)$$

Where, A - area of deposited dust;

δ_d - dust layer thickness;

r_d - the heap rate of dust layer.

The brushing force of wind power, f_4 , is given by

$$f_4 = 0.5 \xi v^2 r S \quad (11)$$

Where, ξ - resistance coefficient;

v - air flow speed;

r - the gas density;

S - the projected area of dust particles on the air flow direction.

Electric force, f_5 , and

$$f_5 = \varepsilon_0 (\varepsilon_d E_d^2 - E_p^2) / 2 \quad (12)$$

Because $E = \rho j$, the equation (12) can be rewritten as:

$$f_5 = \varepsilon_0 j^2 (\varepsilon_d \rho_d^2 - \rho_p^2) / 2 \quad (13)$$

Where, ε_0 -vacuum dielectric constant;

ε_d -dust relative dielectric constant;

E_d -the average field strength within dust layers;

E_p -dust space field strength;

j -current density;

ρ_d, ρ_p -apparent resistivity of dust layer and electric field respectively.

Whether dust attaches to polar plate stably or not, it does not depending on the electric field force which performances adhesive force or bonding force, but depending on the resultant force of those

forces acting on dust particles which performances adhesive force or bonding force. Under normal conditions, the electric force changes with the dust particles resistivity, and other forces have little influence on dust resistivity.

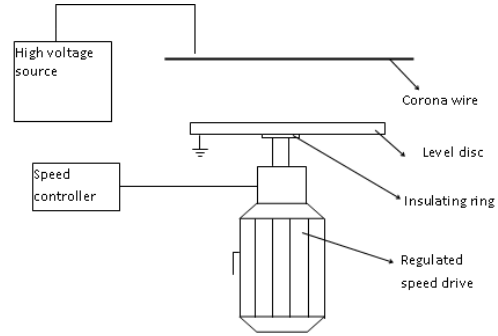


Fig. 2. Centrifugal force measuring device.

In view of the difference of dust resistivity, to discuss the stable attachment of dust on the polar plate, F_0 can be used to represent the resultant force of $f_i (i=1, 2, 3, 4)$, that is, $F_0 = \sum f_i$, then the total force acted on particles is $f = f_0 + f_5$, and if with a coating $F = F_0 + f_5$. The greater dust resistivity is, the greater f_5 is, and also the greater the coating resistivity is, the greater f_5 is.

Through discussion [10], we can see that the field force used to maintain a suitable cohesive force between dust layer and polar plate is generated mainly by the coating. The resistivity of the coating should be in the range of $1.1 \times 10^5 \Omega \cdot \text{cm}$ to $1.1 \times 10^{12} \Omega \cdot \text{cm}$. For the selection of coating materials, using lipid polymer as the main raw material is quite suitable. In experiments, we have selected the polyurethane which contains 23% graphite to be the coating material. Coating thickness has little impact on coating resistivity, which can be ignored, and in the experiments, we have set the coating thickness of $10 \mu\text{m}$.

EXPERIMENTAL STUDY ON THE IMPACT OF COATING TO DUST COHESIVE FORCE

The principle of centrifugal force determination

Centrifugal force method is to use centrifugal force to measure the dust cohesive force. Dust is placed on a flat steel plate which is mounted on a centrifuge, so that the dust will rotate along with centrifuge. Therefore, dust receives the action of centrifugal force $f (f = mr\omega^2)$, when the centrifugal force is just greater than the dust cohesive force, the dust will fly out from the plate. At that time, measure the centrifuge speed and the

horizontal position of dust out of steel plate, and then by doing force analysis we can determine the quantity of the cohesive force of dust layer.

Experimental device

A set of centrifugal force measuring device is designed and assembled in laboratory, as shown in Figure 2.

Force analysis of dust on the centrifuge

The main forces acting on dust in the rotating disc are gravity (mg), supportive (N), friction ($F_{friction}$), centrifugal force ($F_{centrifuga}$), cohesive force between dust ($F_{1cohesive}$), as well as the cohesive force between dust and disc ($F_{2cohesive}$), as shown in Figure 3.

In the vertical direction, the equation of force balance:

$$N = mg + F_{2cohesive} \quad (14)$$

In the horizontal direction, the force balance equation:

$$F_{1cohesive} + F_{friction} = F_{centrifugal} \quad (15)$$

At the moment when the dust just flying out, dust should be subject to the maximum static friction force, that is

$$F_{friction} = \mu_s \cdot N \quad (16)$$

Where, μ_s - the largest static friction coefficient of dust with steel plate.

The micro-dust gravity can be neglected, then have

$$N \approx F_{2cohesive} \quad (17)$$

Generally, the quantity of cohesive force between dust and steel plate is 2~3 times larger than that of among dusts, if take 2 times, have

$$F_{1cohesive} + F_{friction} = F_{1cohesive} + 2\mu_s F_{1cohesive} = (1 + 2\mu_s)F_{1cohesive} \quad (18)$$

For centrifugal force, have

$$F_{centrifuga} = m\omega r^2 \quad (19)$$

Considering equations (15), (18) and (19), hence

$$(1 + 2\mu_s)F_{1cohesive} = m\omega r^2 \quad (20)$$

Finally, the calculated formula of adhesive force is:

$$F_{1cohesive} = \frac{m\omega r^2}{1 + 2\mu_s} \quad (21)$$

The cohesive force between dust and polar plate is $F_{cohesive} = 2F_{1cohesive}$.

Experimental Results

By using centrifugal force measuring device, data of cohesive force between high resistivity dust, which is lime powder, and polar plate at different high voltage are measured. We found that with the polar plate coated or uncoated, the cohesive force between lime powder and polar plate has big changes. In order to see the changes directly, the measured data are plotted in Figure 4.

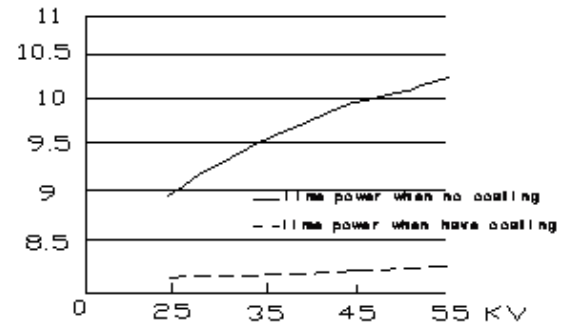


Fig. 4. Cohesive force between lime powder and polar plate with coating or no coating.

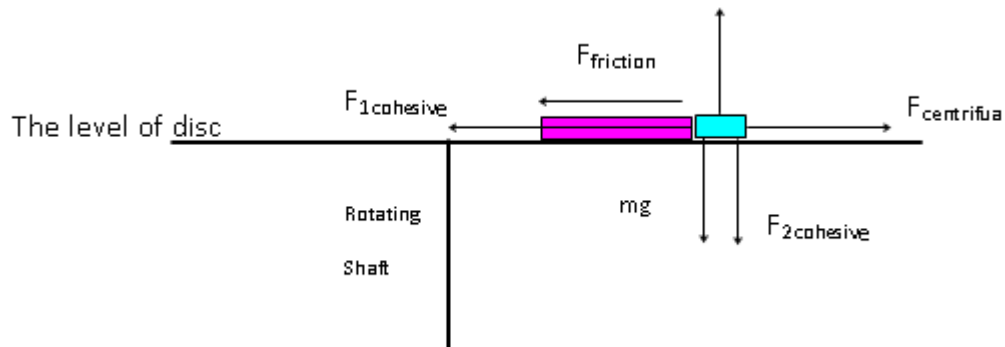


Fig. 3. Force analysis of dust on the rotating disc.

CONCLUSIONS

(1) ESP electronic work function of polar plate material had great influence on the efficiency of removing dust.

(2) Designed and assembled a set of centrifugal force measuring device to measure cohesive force between polar plate and dust, the determination result is accurate.

(3) According to the different nature of the dust, used reasonable Polar Plate coating can improve ESP dust collecting effect.

Acknowledgment: This research was financially supported by the National Science Foundation funded project (51204100), China Postdoctoral Science Foundation Special funded project (2014T70658), University Science and Technology Development Program of Shandong Province (J14LH03), the Science and Technology Development Plan Project of Shandong province (2014GSF116020), Qingdao Science and Technology Project (14-2-4-95-jch).

REFERENCES

1. Y.L. Zhang, M.K. Tang, *Metal Mine*, **9**, 91, (2010).
2. D.M. Li, *Disaster Adv.*, **5**, 263 (2012).
3. Y.L. Zhang, S.J. Cai, *Functional Materials*, **45**, 1865 (2010).
4. B.H. Han, Experimental Study of a Moving Electrode Electrostatic Precipitator (Proceeding of the 7th inter-national Conference on Electrostatic Precipitation Jan 2008), China, p. 321.
5. Y.L. Zhang, S.J. Cai, H.Y. Chen, *Amer. J. Chem.*, **6**, 198 (2010).
6. S.A. Selt, Experimental Study of Collector Plate Rapping and Re-entrainment in Electrostatic Precipitators (Proceedings of the 4th international Conference on Electrostatic Precipitation, Jan. 2005, China), 2005, p. 231.
7. M.K. Tang, *Ind. Safety Dust Proof*, **7**, 42 (1997).
8. Z.X. Yhi, South Metallurgy Institute Graduation Thesis, **6**, 82 (2009).
9. Q. Ye, South Metallurgy Institute Graduation Thesis, **6**, 65 (2004).
10. W. Fang, Northeastern University Graduation Thesis, **6**, 38 (1997).

Investigating the efficiency of nanocomposite membranes synthesized by polyacrylonitrile polymers containing single-walled carbon nanotubes in decreasing chemical and biological pollution indicators of greywater

A. Mohsenibandpey¹, A. Eslami¹, H.K. Maleh², M.M. Rabori^{3*}

¹Department of Environmental Health Engineering, School of Public Health, Shahid Beheshti University of Medical Science, Tehran, Iran

²Department of Chemistry, Graduate University of Advanced Technology, Kerman

³Department of Environmental Health Engineering, School of Public Health, Shahid Beheshti University of Medical Science, Tehran, Iran

Received June 18, 2016; Revised September 10, 2016

One of the most important concerns of human society is successive droughts and water resource shortage. To overcome water shortage crisis, water consumption pattern together with wastewater treatment regarding water resources recycling are necessary. The best and cheapest practical solutions are to decrease per capita water consumption in homes as well as treatment of greywater. The purpose of the present study was to determine the efficiency of nanocomposite membranes synthesized by polyacrylonitrile polymers containing Single-Walled Carbon Nanotubes (SWCN) in decreasing chemical and biological pollution indicators of greywater. To synthesize the membrane of SWCN, polyacrylonitrile polymer with the molecular weight of 1.5×10^6 g/mol and SWCNT produced by US Research Nanomaterials with the purity of 96% and approximate diameters of 9-15nm as well as DMF solvent were used. In order to prepare nanofiber, the electrospinning process with ultrasonic was used. Then, to evaluate the efficiency of the prepared membranes in greywater treatment, parameters such as COD, BOD₅, TSS, TDS, Detergent, and Fecal Coliform and Total Coliform were used. Data were analyzed in SPSS 19 and the results were presented using graphs, figures, tables, mean, and standard deviation. Among synthesized nanocomposite membranes, PAN+2.5%CNT showed the highest efficiency. The application of this membrane in treating the gray water led to decreased parameters including COD, BOD₅, TDS, Detergent, Fecal Coliform, and Total Coliform by 98%, 89.62%, 91.4%, 88.4%, 90.9%, 100%, and 99.28%, respectively. The results showed that nanocomposite membranes synthesized by polyacrylonitrile polymer containing carbon nanotubes can be effective in decreasing pollution indicators of the greywater with high efficiency. The results showed that the use of nanocomposite membranes containing CNT in greywater treatment can be effective in dealing with water shortage and preserving water resources and environment.

Keywords: Nano-composite, Nano fiber, single-walled carbon nanotubes (SWCNT), gray water, purification, electro spinning, bathroom shower.

INTRODUCTION

Global warming and water shortage are among the most important concerns of human societies in the decades ahead [1]. To deal with these crises, various solutions should be used. One of the practical solutions to preserve water resources is greywater reuse [1,2]. Greywater is referred to wastewaters resulted from laundry, shower, and kitchen except toilet [3-5]. Of course, many scholars do not consider wastewaters from kitchen among greywater [6-9]. Up to now, numerous efforts have been done regarding greywater treatment and reusing it. One of the most important methods is filtration with soil, using wetlands, rotating biological contactor (RBC), sequenced batch reactor (SBR) reactor, ultrafiltration UF, and membrane

bioreactors MBR [10-13]. Parameters including TSS, TDS, BOD, COD, pathogens, coliforms, detergents, nitrogen compounds, and phosphates are among the most important pollution factors of greywater. The results of a study showed that with greywater reuse in toilet's flash tank, about 30% water consumption saving occurs [14]. Also, it is possible to use this water to wash car, irrigation of golf courses, camps [15], fire-fighting, boilers, or cement production [16].

Various studies have shown that the use of Single Wall Carbon Nanotubes (SWCNTs) can increase the flow passing through the polymer membranes. The results of a study showed increasing the flow by 50000 times in carbon nanotubes led to attention to producing carbon nanotubes in industrial scale [17]. Polymers, particularly polyacrylonitrile (PAN), are widely used in nanocomposite membrane production [18-21]. Single-walled carbon nanotubes compared to multi-walled carbon nanotubes have higher length

* To whom all correspondence should be sent:
E-mail: mmehdipoor@sbmu.ac.ir or yahoo.com

to diameter ratio; therefore, they have higher application potential [22].

The most important issue regarding the application of nanocomposite membranes is the investigation of morphological features such as diameter, matrix structure, and permeability of the matrix bed [23]. In order to produce membranes containing CNTs and fibers with sub-micron diameter, the easiest and most effective method is to use electricity process [23, 24]. Electrospun fibers can be used with functionalized additives and fillers as nanocomposite fibers [25]. In electrospinning method, it is possible to modify nanofiber structure by adding some of nanostructure materials to achieve desirable and new properties. Additives can influence properties and interactions in the solution as well as diameter and morphology of nanofibers. CNTs are widely used as fillers for electrospun fibers [21, 26-30] that were identified by Iijima [31]. So far, various methods have been used to treat greywater and these methods include physical [31,33] chemical [33] physiochemical [34,35] and biological methods [36-40]. Investigating the conducted studies in this context shows that many of physical, chemical, and biological processes cannot satisfy necessary needs to reuse greywater[10]. Therefore, the treated greywater by these methods could not provide standard quality criteria for quick recycling. On the other hand, none of the mentioned methods could make recycling and treatment of gray water as practical for quick recycling in consumption process.

The purpose of the present study was to determine the efficiency of nanocomposite membranes made by polyacrylonitrile polymers containing SWCN in decreasing gray water pollution indicators as well as quick recycling of gray water in consumption process.

MATERIALS AND METHODS

Materials

Pure and white color powder of polyacrylonitrile polymer was prepared from Isfahan's Polyacrylamide Company with the molecular

weight of 1.5×10^6 g/mol. Di-methyl-formamide (DMF) with the purity percentage of 99.9% and density of 0.945 g/ml were prepared from Merk Company in Germany. SWCNT was prepared from US Research Nanomaterials Inc with the approximate diameter of 9-15 nanometers. The analysis of SWCNT's main components by X-ray Diffraction Spectroscopy showed that these nanotubes contain 96.30% of pure carbon. Physical and morphological properties of these nanotubes are shown in Fig.1.

Preparation of CNT dispersions in PAN matrixes

To prepare PAN solution containing 1.82% and 2.5% CNT, first, PAN polymer was solved in DMF in controlled condition and temperature of 80 °C by magnetic stirrer for 30 minutes. Also, SWCNT were solved in DMF for 30 minutes at the temperature of 80 °C. In the next step, after mixing PAN and CNT to create uniform distribution of CNT in PAN, ultrasonic homogenizer machine (1500 W) with 50% power and timing of 3 seconds working and 7 seconds resting was used for 30 minutes in controlled condition.

Electrospinning process

According to previous studies [41-43], PAN polymer solution with 0-2.5% CNTs was prepared. In this study, Full Option Lab. ES electrospinning device made by Nanoazma Company was used. In this device, 5 ml syringe was used to inject polymer solution with robotic controlled infusion pump with the infusion rate of 1 cc per hour and 100 RPM with nuzzle diameter of 18 Gage. Other parameters of this process are shown in Table 1. Since the electrospinning chamber is surrounded, flow and air pressure measurements were ignored.

After producing synthesized nanocomposite membranes, the morphological structure of nanofibers produced by SEM images was evaluated after coating a thin layer of gold with an electron microscope (KYKY-EM3200). Figures 3A, 3B, and 3C show morphological structure of synthesized nanocomposite membranes.

Material	SWNT	MWNT	Steel
Young's modulus (GPa)	1054	1200	208
Tensile Strength (GPa)	150	150	0,4
Density (g/cm ³)		2,6	7,8
Thermal Conductivity W/m.K	3000		
Electrical Conductivity S/m	10 ⁵ – 10 ⁷		

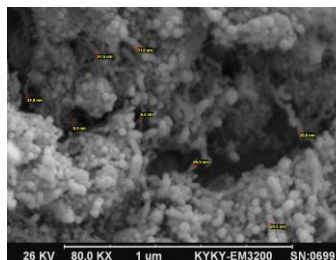


Fig.1. SEM image of SWCNT with the physical properties.

Table 1. Parameters in electrospinning process of synthesized nanocomposite membranes

Parameters in electrospinning process /type of synthesized nanocomposite membranes	Pure PAN	PAN+1.82% SWCNT	PAN+%2.5 SWCNT
Voltage (Kv)	20	11.6-15	22
Distance between nozzle tip to collector (cm)	9	8	21
Injection rates (ml per hour)	1.1	1	1.3
The horizontal movement collector (Scan) cm	3	2	5

Table 2. Maximum, minimum, mean, and standard deviation values of primary parameters as well as final parameters.

Parameter	Initial grey water samples(n=10)			Mixed Greywater	References no. Standard method[44]
	Min-Max	Mean	Standard Deviation		
Temperature ^{0C}	28-37	31.30	2.91	25	-
pH	6.9- 8.9	7.850	0.72	7.85	2520
Turbidity _{NTU}	38-109	79.60	27.02	73	2130A
COD _{mg/L}	110-645	312.80	167.10	258	5250C
BOD ₅ _{mg/L}	52-294	141.60	75.92	135	5210A
TSS _{mg/L}	26-94	58.70	23.72	58	4500H
TDS _{mg/L}	49-301	180.00	91.53	155	1030
Detergent _{mg/L}	0.56-1.86	1.13	0.41	1.13	5540C

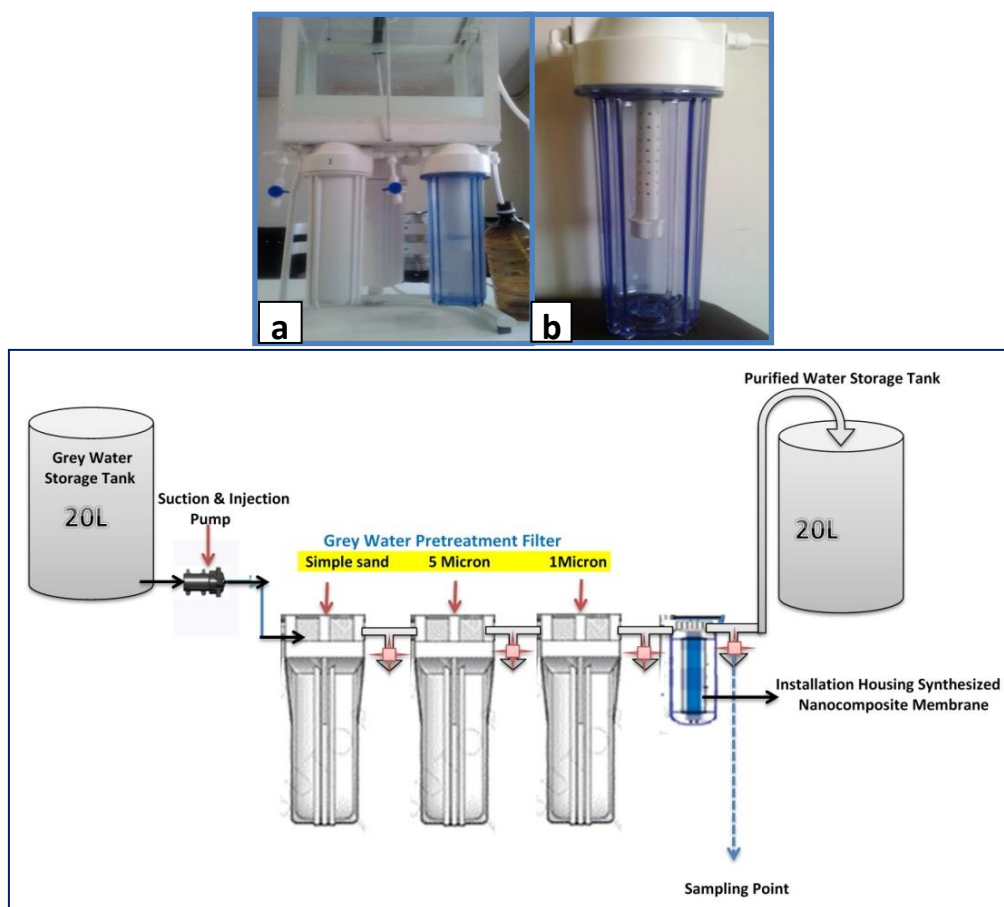


Fig. 2. a) Pilot device in this study b) Chamber for nanocomposite membranes installation c) Schematic of greywater treatment pilot equipment.

Sampling process

The greywater of 5 private bathrooms and 5 public bathrooms were collected (3L) and stored at the temperature of 4°C and transferred to the laboratory. In the laboratory, all samples were mixed in a big plate. All 10 primary samples were taken and the final sample was examined regarding chemical and biological parameters based on standards methods (44). Table (2) shows physiochemical properties of the primary samples and the final sample. To determine the efficiency of the membranes in the absence of biological factors, a synthetic solution was used. This solution was prepared from adding half McFarland (1.5×10^8), fecal coliform (E.Coli), and 2.8×10^2 total coliform to 1 liter physiological serum in OD=620nm.

Pilot design and launching

To examine the efficiency of synthesized membranes in the treatment and recycling of greywater, a pilot device was designed and launched. This device consists of a storage chamber of greywater, suction pump, and pilot infusion with 1.6 liters per minute flow rate and optimized pressure of 130 PSI, Simple Sand Filters, 1 and 5 micron fiber filters and nanocomposite membranes installation that was used to install synthesized nanocomposite membranes with cross section of 0.05m², 2(18*14 cm). Fig.2 shows the pilot device used in this study and Fig.3 shows its schematic view.

Pilot testing

Twenty liters of the final sample size (30L) was picked to be stored in pilot chamber. During three steps, nanocomposite membrane installations were done. In each step, only one of the pure PAN, PAN+1.82% CNT, and PAN+2.5% CNT membranes were installed. In each step, 3L grey water was passed by 1.6L per minute under the pressure of 130 PSI from the pilot device (including filters and membranes) and the output wastewater was examined based on standard methods in Table (2) to determine the physiochemical parameters including COD, BOD, Turbidity, TSS, TDS, and Detergent to specify the efficiency of synthesized nanocomposite membranes in the treatment and recycling of greywater.

Bacteriology testing

To conduct testing in order to determine the efficiency of synthesized nanocomposite membranes in the absence of total and fecal coliforms, first, filters were sterilized in UV device

and then, were installed at biological test pilot. Physiological serum with the concentration of half McFarland (1.5×10^8 cfu/100ml) and total coliform (2.8×10^2 cfu/100ml) added to the primary physiological serum, was passed through each membrane separately. Then, from the greywater passing through the membrane, final sampling was done in sterile glass (100cc). Samples were cultured based on 15-tubes MPN method (standard method 9221). First, in order to identify total coliforms in lactose medium, inoculation process was done at 35 ± 0.5 . After 48h, the initial results of positive and negative tubes were calculated based on table and Thomas formula. At the same time, with the culture of samples passing through membranes, control sample culture was done, too. In the final step, from 50% of positive carbonated tubes in the first step in the medium EC inoculation was done. After 48h in incubator at the temperature of 44.5 C, the presence of fecal coliforms was examined. The results of investigating the presence of total and fecal coliform bacteria available in control and final samples are presented in Table (3).

RESULTS AND DISCUSSION

The morphology of electrospun nanofibers (PAN+SWCNT)

In Fig.3, the structure of synthesized membrane nanofibers with statistical mean of nanofiber's diameter are shown. Mean and standard deviation of nanofiber's diameter produced by Pure Pan, PAN+1.82% CNT, and PAN+2.5% CNT were 867.75 ± 318.25 nm, 1131.7 ± 445.39 , and 280.95 ± 91.86 nm, respectively. The results of this study are consistent with a study conducted in 2009 (41). To have more accurate investigation, the nanofiber diameter produced by SEM images with 500 x zoom was used (Fig.3). As can be seen from figures 3 and 4, the pore diameter in PAN+2.5%CNT is lower compared to Pure PAN and PAN+1.82%CNT.

Investigating the effect of key parameters on nanofiber electrospun

The effect of polymer solution concentration

With increased concentration of polyacrylonitrile polymer containing CNT, the mean of nanofiber diameter increases and this is due to increased physical entanglement of polymer chain (45). The physical entanglement of chains in the solution and increasing with concentration has led to increased viscosity of the solution and resistance against tensile force resulting from the available loads within the flow increases and finally

leads to increased diameter. This is consistent with Deitzel et al. (45)

The effect of electric voltage: electric voltage is one of the effective parameters in electrospinning process of nanofibers. By increasing the voltage by 15 KW, the mean diameter of fibers increases and then decreases. On the other hand, with increased voltage, the electronic flow still increases. It is obvious that with increased voltage, due to increased homogenous loads, more flow passes through surface water in time unit and the surface density increases. Increased flow with increased voltage is consistent with Wan et al. (46). In this study, voltage changes (11.6-22KW) were due to preventing bead formation at the tip of nuzzle and the surface of produced membrane surface as well as decreased wasted polymer solution (PAN+CNT).

The effect of distance between tip of the needle and collector: with increased distance between needle and collector, the electronic flow and the mean diameter decrease. Also, with increased distance, the electric intensity decreases and as a result, the jet speed decreases to towards the

collector. Therefore, the flight duration increases and finally, leads to decreased diameter. On the other hand, if this distance is too much, due to the weakness of the electric field and lower strain, the mean diameter increases that can be observed at 20 cm (47)

The effect of flow rate: with increased flow rate by 1 ml/h, the mean diameter of fibers increases and after that decreases. However, with increased flow rate, the electric flow does not follow a fixed trend. In fact, with increased infusion rate, the output volume increases while the voltage is fixed. But after that at 1.5ml/h flow rate, due to increased unspun drops under the influence of output solvent volume from the tip of the needle, the solution that is used for fiber production decreases and the mean diameter of the fibers decreases. The results of empirical observations that were mentioned above are consistent with Ramakrishna et al.(47) regarding the effect of flow rate on fibers' diameter. On the other hand, in higher flow rates and due to increased output solution volume from the tip of the needle, the drop corporations increase.

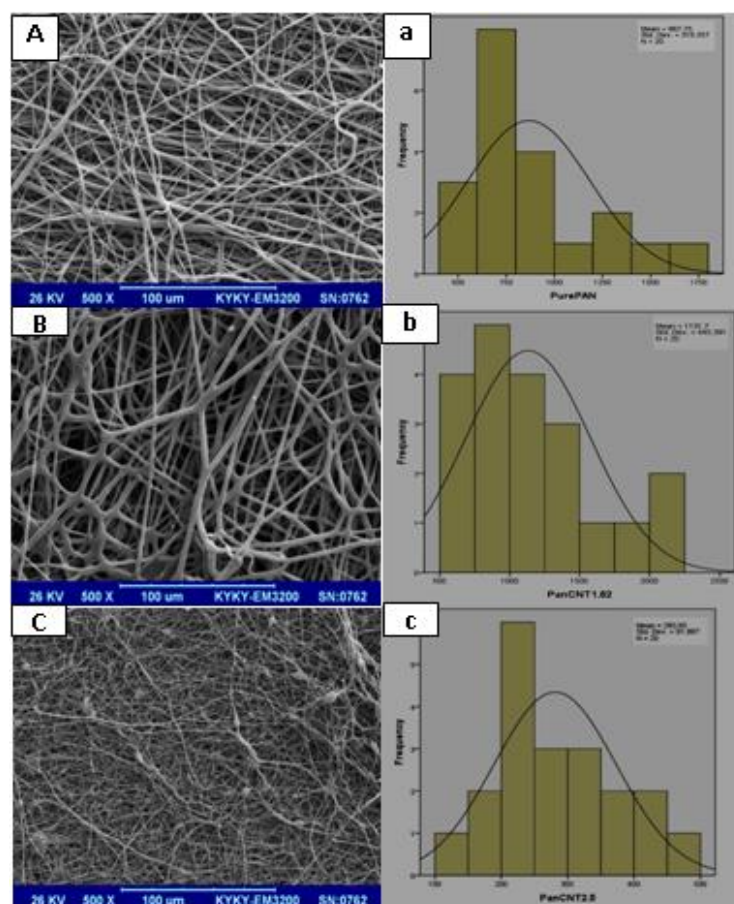


Fig. 3. A, B, and C show SEM images (500 x zoom) of Pure PAN polymer nanofibers, PAN+1.82% CNT, and PAN+2.5% CNT, respectively and a,b,c show nanofiber's diameter of Membranes a)- Pure PAN, b)- PAN+1.82% CNT, c)-PAN+2.5% CNT.

Table 3. Average influent and effluent grey water characteristics treated by pure PAN Nano composite membrane, PAN +1.82% SWCNT and PAN +2.5% SWCNT.(Q=1.6LPM, Hydraulic pressure=130 PSI .

parameter	Initial Influent grey water Avg.	Treated Effluent characterization /membrane type					
		Pure PAN		PAN +1.82% SWCNT		PAN +2.5% SWCNT	
		E. Avg.	R. P %	E. Avg.	R. P %	E. Avg.	R. P %
Temp.°C	25	25	-	25	-	25	-
pH	7.85	7.2	-	7.6	-	7.5	-
COD, mg/L	258	69	73.25	117	54.65	25	98
BOD, mg/L	135	28	79.25	58	57	14	89.62
TSS, mg/L	58	17	70.68	24	58.62	5	91.4
TDS, mg/L	155	21	86.45	33	78.7	18	88.4
Detergent _{mg/L}	1.1	0.5	54.5	0.6	54.45	0.1	90.9
Turbidity NTU	110	10	91	18	83.7	5	95.45
Fecal Coliform _{cfu/100ml}	1.5*10 ⁸	ND	100	ND	100	ND	100
Total Coliform _{cfu/100ml}	2.8 * 10 ²	<2	99.28	4	98.57	<2	99.28

E.Avg.: Effluent Average , R.P: Removal Percent %, ND: Not Detected

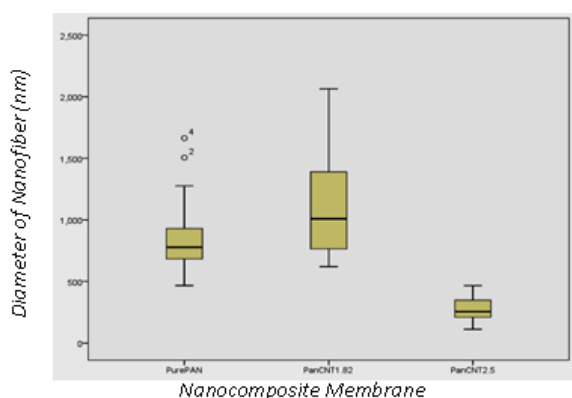


Fig. 4. Min, max and mean diameter of membrane nanofibers

In a study in 2015, it was shown that Pure Pan electrospinning leads to nanofibers production with the diameter mean of 515.34nm, but after adding 1% and 3% molecular weight of MWCNT, the structure and diameter mean of the produced nanofibers changed to 536 and 531nm, respectively [48]. It is consistent with the results of this study. Some scholars believe that the addition of CNTs to polymer matrix increases uniformity and mean of nanofiber diameter. The relative increase of the diameter can be due to increased viscosity of the final PAN/CNT solution [43]. However, in the present study, the addition of CNTs to the polymer matrix increased the nanofiber diameter and then, decreased it. This can be due to increased distance between nozzle and the collector and also voltage and flow changes. The results of this study have relative correspondence with the results of the present study. In another study by adding Halloysite Nano Tubes (HNTs) to PAN in

concentrations of 0, 1, and 3, improved electrospinning process and increased produced nanofiber diameter from 484nm to 556nm and 570nm were reported 49). Others reported the Pure PAN nanofibers diameters between 200 to 300nm and by adding 2% CNT to the primary solution, increased diameter to 500 and 600nm was reported 42)(that is consistent with the results of this study.

Analyzing biological and chemical experiments

In Table (3), the chemical and biological parameters, before and after the passage of greywater from synthesized nanocomposite membranes as well as the efficiency of these membranes in decreased indicators are shown.

All experiments were conducted at the standard temperature of 25 °C by applying error coefficient. The pH level after passing through three membranes based on Table (4), shows a little change.

The results of this study showed that PAN+1.8% SWCNT, Pure Pan, and PAN+2.5% SWCNT could decrease COD in primary greywater by 70.25%, 54.65%, and 98%, respectively. Also, BOD reduction percentages in water passing through these three membranes were 79.25, 57, and 89.62%, respectively. Therefore, the efficiency of PAN+2.5% SWCNT in COD and BOD reduction is significantly higher than other two membranes. The Pure Pan membranes compared to PAN+1.8% SWCNT showed more desired performance in decreasing these two indicators. By investigating the morphology of the mentioned membranes, it can be inferred that in the third membrane (Fig.3C), the pore diameter is very low among the nanofibers

and this can be effective in attracting more pollutants. Also, due to increased pore diameter between the second membrane nanofibers (Fig.3B), the efficiency has been decreased.

In study by [36], RBC process was used to treat the greywater. In this study, the synthetic of biological reaction was investigated. The results of this study showed that the decline rates of COD and BOD were 84-89% and 64%, respectively [37].

Hocaoglu et al. [49] in a study using MBR process, in 60 days, reported BOD and COD removal efficiencies as 97% and 96.4%, respectively. The findings of this study are consistent with the results of the present study[50]. However, the mentioned results, due to increased treatment time and incapability of quick greywater recycling, are less important compared to the present study.

In another study, the use of ultrafiltration membrane led to decreased COD from 451mg/l to 117mg/l and BOD decreased from 274mg/l to 53mg/l [40]that compared to the present study and due to efficiency higher than 98% in the removal of COD and 89.6% in the removal of BOD, has better performance compared to ultrafiltration membrane.

The removal efficiency levels of greywater pollution indicators are shown in Fig.7 by each of the synthesized nanocomposite membranes.

In another study in 2013, the physiochemical processes were used to treat the greywater. The results showed the used process can decrease COD by 63%[51]. that compared to the present study has high weakness.

In another study where ultrafiltration, nanofiltration, and reverse osmosis membranes were used to treat the greywater, the efficiency of COD removal by ultrafiltration, nanofiltration, and reverse osmosis membranes were 53.5%, 93.36%, and 97.7%, respectively[52]. The results of this study are consistent with the results of the present study regarding the membrane and shows better performance compared to ultrafiltration membranes, but compared to reverse osmosis membrane, has lower efficiency that can be due to lower level of nanocomposite membrane in this study. In a study in 2004, the efficiency of nanofiltration membrane in removing the organic matters in greywater was 94% [53] that is a little bit better than the results of the present study. In another report in 2005, the reverse osmosis could decrease BOD from 82 to 2 mg that shows the efficiency of 98% that is more efficient compared to the present study regarding BOD removal [52]

In another study where ultrafiltration membrane with pore diameter of 0.05micron was used to treat

greywater, BOD level declined from 195 to 86mg that shows 56% efficiency. The application of this membrane could not provide necessary standards for non-drinking uses of greywater [53,54] in this study [52] and compared to the results of the present study, shows lower efficiency in decreasing BOD. In a study in 1998 [40] by applying the relative ultrafiltration resistant membrane, BOD and COD levels declines from 451 and 271 mg/l in the input to 117 and 53 mg/l in the output that shows lower efficiency compared the results of the present study.

In a study in 2007, by implementing MBR with 0.01 μ m pores, the decline rates of COD and BOD were reported from 109 to 15 and 59 to 4mg/l, respectively [11, 46, 47].In a study in 2008, TSS-turbidity-BOD-COD declined from 29-43-23-55 mg/l to 9-4-9-22 mg/l 35)(that shows weaker efficiency compared to the present study. In another study in 2007, by implementing MBR membrane system, researchers could decrease COD by 96.7% and BOD by 95.7%[50]

TSS decline levels in output water from three mentioned membranes were 70.68, 58.62, and 91.4%, respectively. Also, the decline levels of TDS were 86.45, 78.7, and 88.4%, respectively. These results show that the efficiency of PAN+2.5% SWCNT is higher compared to other two membranes. This efficiency is significant in TSS decline. PAN membrane efficiency in TDS decline is at upper limit and is almost similar to PAN+2.5% SWCNT. The reason for high efficiency of PAN+2.5% SWCNT in removing TSS compared to TDS can be due to smaller pore diameters and the possibility for TDS penetration. Turbidity removal rate in PAN+2.5% SWCNT is high and determined as 95.45% that compared to other two membranes has higher efficiency. In several studies, the efficiencies of processes such as microfiltration and ultrafiltration in removing the organic matters (TDS and BOD) were not successfully evaluated, but about turbidity, TDS, and pathogens removals, acceptable performance was indicated. So that, turbidity and TSS removal efficiency were reported as 100% [40,52,53,56]

In 2013, in a study using MBR process and modelling the biological decomposition of greywater pollutants during 60 days, TSS declined from 51 to lower than 2mg/l (95.9%) [50] In a study in 2010, TSS and turbidity decline levels were evaluated as 83% and 90% using RBC process [37] and the findings of the present study show better efficiency compared to this study. However, in RBC method, time has a crucial role in greywater pollution decline; an issue that shows the

superiority of the present study due to higher speed compared to other mentioned methods.

Also, in a study where ultrafiltration was used for greywater treatment, the final turbidity declined to NTU 1 [57]. There is in a relative consistency with the present study.

In another study in 2007, by implementing MBR, researchers could decrease TSS from 51 to 2 mg/l (96%) [57]. The results of this study are a little bit better than the present study regarding TSS removal and this can be due to increased utilization time from MBR.

In a study in 2013 where physiochemical processes were used to treat greywater, TSS removal was reported as 35% [51] that shows lower efficiency compared to the present study. In this study, the removal rate of linear surfactants (LAS) was 72% and in physiochemical processes, it was expected to have higher efficiency, but in comparison with the results of the present study, has lower efficiency. Detergents' removal rate in greywater by PAN+2.5% SWCNT nanocomposite membrane has the highest efficiency (90.9%), but in other two membranes, shows almost similar efficiency (54.5%) that can be due to large pore diameters compared to PAN+2.5% SWCNT.

Somewhere else in 2007, nanomembranes were used for greywater filtration that showed 92-98% of anionic surfactants and 88-92% non-anionic surfactants were removed by this membrane [58]. The results of this study regarding surfactants' removal are consistent with the present study. In another study, incapability of coagulation process in greywater treatment was reported. However, in this report, COD removal and anionic surfactants efficiencies were 70% and 90%, respectively [34]. The results of this study in microbial part showed that all three synthesized membranes have desired efficiency in removing pathogens and fecal coliforms, so that all membranes can remove the fecal coliforms and this can be due to the large diameter of various *E. coli* bacteria between 0.2 to 2.4 micron (200-2400 nm [59]). It is larger compared to viruses with the diameter of 25 nm [10]. But in total coliform removal, PAN+2.5% SWCNT and Pure Pan showed similar efficiency (99.28%), but PAN+1.82% SWCNT showed lower efficiency (98.57%) in total coliforms removal.

In a study in 2010 using RBC process in greywater treatment, the coliforms removal by this process was 99.99% [37] that has a little bit higher efficiency compared to the present study.

In a study where ultrafiltration process was used for greywater treatment, *E. coli* removal rate was satisfying [57]. In a study in 2008, total coliform

and fecal coliform levels in all samples were lower than 1 in 100 ml [35]. The results showed that fecal and total coliform decline are consistent with the present study. In another study where MBR process with the pore diameter of 0.03-1µm was used, the decline level of coliforms were 4-6 log [60] that is consistent with the present study. In 2007 and by using MBR (0.01 µm) in the greywater treatment and recycling, it was shown that fecal coliform declined from CFU/100ml 1.4×10^5 to 68 in 100 ml that is not consistent with global and state standards [54, 55]. However, according to the country standards, it is suitable for agriculture [54]. The results of this study ([11]) have lower efficiency in fecal coliforms decline rate compared to the present study. However, the required quality of the recycled greywater for each application according to the specific geographical zone is defined, but it should have the least criteria of organic matters, solids and biological requirements. One of the most important criteria is BOD5 lower than 10mg/l, turbidity lower than 2 NTU, and fecal coliforms at 100 ml [61].

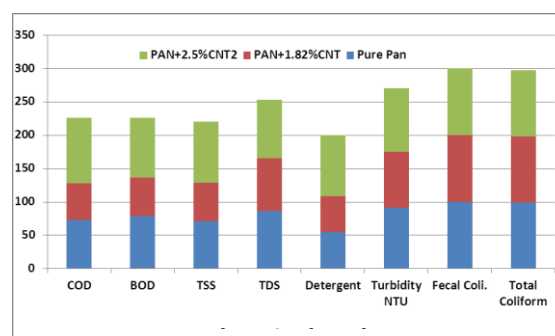


Fig. 7. Contribution of each treatment by Nanocomposit membrane synthesized to the removal of indicator pollutants from grey water

CONCLUSION

In sum, it can be concluded that according to the results obtained from this study, to dominate the most important challenges of water crisis in the future, modern technologies should be used to recycle water resources. One of the most important solutions can be the use of polyacrylonitrile polymer nanocomposites containing CNTs that have potential capability in removing greywater pollutants. Therefore, in near future, these fibers can be used to treat and reclamation of greywater in industrial scale. This can be effective step towards decreased water consumption per capita and water recycling.

REFERENCES

1. E. Eriksson, K. Auffarth, M. Henze, A. Ledin *Urban water*, **4**, 85 (2002).
2. B. Jefferson, J.E. Burgess, A. Pichon, J. Harkness, S.J. Judd, *Water research*, **35**, 2702 (2001).
3. R. Otterpohl, A. Albold, M. Oldenburg, *Water Science and Technology*, **39**, 153 (1999).
4. E. Eriksson, Potential and problems related to reuse of water in households. Ph. D. Thesis: Technical University of Denmark, Department of Environmental Science and Engineering, 2002.
5. P.A. Wilderer, *Water Science and Technology*; **49**, 7 (2004).
6. L. Allen, J. Christian-Smith, M. Palaniappan. Overview of greywater reuse: the potential of greywater systems to aid sustainable water management. Pacific Institute, 2010, p. 654.
7. D. Christova-Boal, R.E. Eden, S. McFarlane, *Desalination*, **106**, 391 (1996).
8. O.R. Al-Jayyousi, *Desalination*, **156**, 181 (2003).
9. F. Li, K. Wichmann, R. Otterpohl, *Science of the Total Environment*, **407**, 3439 (2009).
10. C. Merz, R. Scheumann, B. El Hamouri, M. Kraume, *Desalination*, **215**, 37 (200).
11. B. Jefferson, S. Judd, C. Diaper, Lens, P, Zeeman, G, Lettinga, G, Eds. , *Systems and Implementation*, **334**, 53 (2001).
12. D.A. Okun, *American Water Works Association Journal*, **89**, 52 (1997).
13. E. Santala J. Uotila, G. Zaitsev, R. Alasiurua R. Tikka, J. Tengvall, Microbiological greywater treatment and recycling in an apartment building. Proceedings of the 2nd International Advanced Wastewater Treatment, Milan, Italy. 1998, p.1416.
14. K.P. Lee, T.C. Arnot, D. Mattia, *Journal of Membrane Science*. **370**, 1 (2011).
15. M. Whitby, N. Quirke, *Nature Nanotechnology*, **2**, 87 (2007).
16. D. Mattia, K.P. Lee, F. Calabrò, *Current opinion in chemical engineering*, **7**, 32 (2014) .
17. D. Esrafilzadeh, M. Morshed, H. Tavanai , *Synthetic Metals*, **159**, 267 (2009) .
18. M. Wu, Q. Wang, K. Li, Y. Wu, H Liu, *Polymer Degradation and Stability*, **97**, 1511 (2012).
19. H.G. Chae, Polyacrylonitrile/carbon nanotube composite fibers: reinforcement efficiency and carbonization studies: ProQuest, 2008.
20. S. Prilutsky, E. Zussman, Y. Cohen, *Nanotechnology*, **19**, 165603 (2008).
21. W.J. Li, C.T. Laurencin, E.J. Caterson, R.S. Tuan, F.K. Ko, *Journal of biomedical materials research*, **60**, 613 (2002).
22. M.K. Pilehrood, P, Heikkilä, A. Harlin, *AUTEX Research Journal*, **12**, 1 (2012).
23. D.H. Reneker A.L. Yarin H. Fong , *Journal of Applied physics*, **87**, 4531 (2000).
24. H. Ye, H. Lam, N. Titchenal, Y. Gogotsi, F. Ko *Applied physics letters*, **85**, 1775 (2004).
25. Y.Q. Wan, J.H. He, J.Y. Yu, *Polymer International*, **56**, 1367 (2007).
26. S. Park, S. Jo, D. Kim, W. Lee, B. Kim, *Synthetic Metals*, **150**, 265 (2005).
27. H. Lam, N. Titchenal, N. Naguib, H. Ye, Y. Gogotsi, F. Ko, eds. Electrospinning of carbon nanotube reinforced nanocomposite fibrils and yarns. MRS Proceedings; Cambridge Univ Press .,2003:
28. L. Vaisman, E. Wachtel, H.D. Wagner, G. Marom, *Polymer*, **48**, 6843 (2007).
29. Y-W. Ju, G-R. Choi, H-R, Jung W-J. Lee, *Electrochimica Acta*, **53**, 5796 (2008).
30. M. Ward, Treatment of Domestic Greywater Using Biological and Membrane Separation Techniques: MPhil Thesis, Cranfield University; 2000.
31. S. Prathapar, M. Ahmed, S. Al Adawi, S. Al Sidiari, *International journal of environmental studies*, **63**, 283 (2006).
32. E. Eriksson, K. Auffarth, A.M. Eilersen M. Henze, A. Ledin, *Waters*, **29**, 135 (2003).
33. Y. Chang, M. Wagner, P. Cornel, *Gewässerschutz Wasser Abwasser*, **206**, 32 (2007).
34. M. Pidou, L. Avery, T. J. Stephenson, P, Effrey S.A. Parsons, S. Liu, *Chemosphere*, **71**, 147(2008).
35. T.A. Elmitwalli, R. Otterpohl, *Water Research*. **41**, 1379 (2007).
36. A. Baban, S.M. Hocaoglu, E.A. Atasoy, K, Gunes, S. Ayaz, M. Regelsberger, *Desalination and Water Treatment*, **23**, 89 (2010).
37. M. Elmitwalli, C. Shalabi, R. Wendland Otterpohl, *Water Science and Technology*, **55**, 173 (2007).
38. L. Hernandez, G. Zeeman, H. Temmink A. Marques, C. Buisman eds., in: Proc IWA conference on Sanitation challenges, Wageningen, Netherlands, 2008.
39. R. Birks, Biological aerated filters and membranes for greywater treatment: MSc thesis, Cranfield University; 1998.
40. P. Heikkilä, L. Wikström, A. Pasanen, P. Kauranen, A, Harlin eds., Preparation of electrospun pan/cnt composite fibres. (ICCM17 Edinburgh 17th international Conference on Composite Materials 17 Jul 2009-31 Jul 2009), Edinburgh, UK; 2009.
41. N. Khenoussi, E. Drean, L. Schacher, D. Adolphe, H. Balard, *Materials Technology*, **24**, 36 (2009).
42. G. Mathew, J. Hong, J. Rhee, H. Lee, C. Nah *Polymer Testing*, **24**, 712 (2005).
43. A. Apha, WPCF, Standard methods for the examination of water and wastewater. American Public Health Association/American Water Works Association/Water Environment Federation, Washington DC, USA. 1995.
44. J.M. Deitzel, J. Kleinmeyer, D. Harris, N.B. Tan, *Polymer*, **42**, 172 (2001).
45. Y-Q. Wan, J, He, J. Yu, *Iranian Polymer Journal*, **15**, 265 (2006).
46. S. Ramakrishna, K. Fujihara, W-E Teo, T-C Lim, Z. Ma, World Scientific; 2005.
47. O. Eren, N. Ucar, A. Onen, N. Kizildag, *Marmara J. Pure Appl. Sci., Special Issue-1*: 95 (2015).
48. M. Makaremi, R.T. De Silva, P. Pasbakhsh, *The Journal of Physical Chemistry C*, **119**(14), 7949 (2015).

49. S.M. Hocaoglu, E. Atasoy, A. Baban, D. Orhon *Journal of Membrane Science*, **429**, 139 (2013).
50. C. Noutsopoulos, A. Andreadakis, N. Kouris, P. Mendrinou, I. Mantziaras, Physicochemical treatment of greywater, Proc. 14th Int. Conference on Environmental Science and Technology, Rhodes, Greece, 3-5 September 2015.
51. S. Šostar-Turk, I. Petrinić Simonič, M. *Conservation and Recycling*, **44**, 185 (2005).
52. G. Ramona, M. Green, R. Semiat, C. Dosoretz, *Desalination*, **50**, 170 (2004).
53. Organization WH. Guidelines for the Safe Use of Wastewater, Excreta and Greywater: Excreta and greywater use in agriculture: World Health Organization; 2006.
54. Epa U. Guidelines for water reuse. Environmental Protection Agency, Municipal Support Division Office of Wastewater Management Office of Water Washington, DC Agency for International Development Washington DC, EPA/625/R-04/108, Cincinnati, OH US EPA/625/R-04/108. 2012.
55. K-H. Ahn, J-H. Song, H-Y. Cha, *Water Science and Technology*, **38**, 373 (1998).
56. F Li, J. Behrendt, K. Wichmann, R. Otterpohl *Water Science and Technology*, **57**, 1901 (2008).
57. N. Funamizu, Y. Kikyo *Gewässerschutz Wasser Abwasser*, **206**, 35 (2007).
58. Nelson DE, Young KD. *J. Bacteriol.*, **182**, 1714 (2000).
59. C. Chiemchaisri, Y. Wong, T. Urase, Yamamoto, *Water Sci. Technol.*, **25**, 40 (1992).
60. B. Jefferson, A. Palmer, P. Jeffrey, R. Stuetz, S. Judd, *Water Sci. Technol.*, **50**, 157 (2004).

A novel modified integral PES/PVB nanofiltration membrane and its application in wastewater treatment

S. Zarinabadi*

Department of Chemical Engineering, Mahshahr Branch, Islamic Azad University, Mahshahr, Iran

Received June 26, 2016; Revised September 10, 2016

This study describes the preparation Novel polyethersulfone (PES)/poly(vinylbutyral) (PVB)/titanium dioxide (TiO₂) nanoparticles integral nanofiltration membranes were prepared by dip-coating of PES membrane in PVB and TiO₂ nanoparticles aqueous solution. Glutaraldehyde (GA) was used as a cross-linker for the integral polymer membrane in order to enhance the chemical, thermal as well as mechanical stabilities. TiO₂ nanoparticles with different concentrations (0, 0.1, 0.5, 0.8 wt.%) were coated on the surface of PES/PVB integral membrane. The morphological study was investigated by atomic force microscopy (AFM), scanning surface microscopy (SEM). In addition, the membranes performances, in terms of contact angle, permeate flux, COD rejection and swelling factor were also studied. It was found that the increase in TiO₂ solution concentration can highly affect the surface morphology and filtration performance of coated membranes. The contact angle measurement and studies indicated that the TiO₂ nanoparticles successfully were coated on the surface of PES/PVB integral membranes. However, rougher surface was obtained for membranes by TiO₂ coating. The filtration performance data showed that the 0.5 wt.% TiO₂-modified membrane presents higher performance in terms of flux and COD rejection as a pollution index. Finally, TiO₂ modified membranes demonstrated the lower degree of swelling.

Keywords: nanofiltration, polyethersulfone, modification, poly (vinyl butyral) , TiO₂ nanoparticles

INTRODUCTION

With the development of global economy, the lack of water resource is becoming an increasingly crucial problem. Membrane separation such as nanofiltration (NF) technology now has been becoming an important way in the treatment and the recycling of wastewater [1, 2]. The main advantages of this process are low operating pressures, high fluxes, high rejections of multivalent salts, low investment and operation costs leading to gaining attention in many separations, and treatment processes namely water softening, waste water treatment, color removal, chemical and biological oxygen demand reduction (COD and BOD respectively), pharmaceutical and biochemical industries[3-7]. As with any other membrane process, nanofiltration is susceptible to fouling caused by adsorption of various types of foulants including: colloidal (clays, flocs) [8], organic (oils, polyelectrolytes, humics) [9, 10] and scaling (mineral precipitates) [11, 12], either in membrane pores or on membrane surfaces. Membrane fouling can cause severe flux decline and affect the quality of the water produced. Severe fouling may require intense chemical cleaning or membrane replacement. This increases the operating costs of a treatment plant and

consequently increases the overall energy consumption of separation process. So it is vital to investigate the ways and methods to develop antifouling nanofiltration membranes. In general, the fouling occurs more seriously in the hydrophobic membranes than in the hydrophilic ones because of the interactions between the solutes, microbial cells and membrane surface [13]. The preparation and characterization of nanofiltration membrane based polymer materials have aroused a great deal of interest among researchers over the past few years. PES is a commercially available, thermally stable polymer, which is used in high-performance applications due to its toughness, good thermal resistance and chemical inertness [14]. As a result, PES is one of the most important polymeric materials and is widely used in separation fields [15, 16]. Though PES and PES-based membranes have been broadly applied in separation processes, they have some disadvantages. The main disadvantage of the PES membranes is related to their relatively hydrophobic character [15]. Their hydrophobicity leads to a low membrane flux and poor anti-fouling properties, which have a great impact on PES membrane application and useful life [17]. A general method to suppress membrane fouling, especially irreversible fouling is to inhibit natural organic matter adsorption on the membrane surface by increasing hydrophilicity of the membrane surface [18]. Many investigations have revealed

* To whom all correspondence should be sent:
E-mail: szarinabadi1@yahoo.com

that increasing the membrane surface hydrophilicity can effectively reduce the membrane fouling [19]. Therefore, efforts have focused on increasing PES hydrophilicity by chemical or physical modifications such as UV irradiation [20], addition of additive [21], plasma treatment [22], and so on. Therefore there is a need to improve the hydrophobic properties of this membrane, which might be achieved by coating. One of candidate of these material which is coated to PES is poly(vinyl butyral) that is introduced in this paper.

Poly(vinyl butyral) (PVB) is a product of the reaction between poly(vinyl alcohol) (PVA) and butyl aldehyde in the presence of an acid catalyst. Its structural formula is shown as below (Fig. 1) [23].

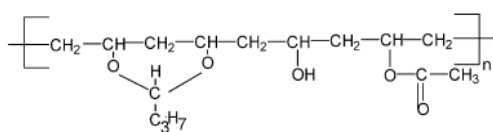


Fig. 1. Structural formula of poly(vinyl butyral).

Being an innocuous and tasteless polymeric material, PVB can endure the low temperature, light, change in humidity, bacteria, microorganism, alkali and diluent acid [24]. PVB has immense potential as membrane material because of its hydrophilicity and film forming characteristics. Swelling of PVB membrane in aqueous medium may lead to an open structure, which affects the membrane performance particularly the membrane rejection [23]. Hence there is a need to balance the hydrophilic and hydrophobic properties of such membranes. by cross-linking to PES this balance might be achieved. PVB similar to poly(vinyl alcohol) (PVA) can be cross-linked by using multifunctional compounds, such as dialdehydes [25] and dicarboxylic acids [26], which are capable of reacting with the PVB hydroxyl groups. Cross-linking improves the stability of such membranes. In this approach, glutaraldehyde (GA) was used as cross linking agent. As mentioned before, a concerning subject in membrane application is fouling. Successful utilization of membrane technology has been seriously limited by membrane fouling. A recently established method to improve the membrane antifouling properties is using TiO₂ nanoparticles on membrane structure as well as surface. TiO₂ nanoparticle has been extensively studied owing to its outstanding physical and chemical properties [27]. TiO₂ nanoparticle is usually used in the form of nanoparticles with high surface area, activity and excellent chemical stability. This nanoparticle (TiO₂) has been the

focus of numerous investigations for innocuity, resisting and decomposing bacteria, UV-proof and super hydrophilicity in recent years. Therefore, it has been applied to a variety of problems associated with water and air purification as well as environmental issues. Composite membrane with TiO₂ has better filtration performance [28] and the membrane modification with such material will introduce photocatalytic activity, which can be exploited for antifouling and regeneration purposes. In this work, the modification of PVB/PES composite nanofiltration membrane by depositing the nano-sized TiO₂ particles on the surface of PVB coated PES membranes is attempted. SEM and AFM analysis are used to examine the surface morphology of the composite nano filtration membranes. Finally as practical study, the effect of TiO₂ concentration on the COD rejection, contact angle and degree of swelling are investigated.

EXPERIMENTAL

Material

Polyethersulfone (Ultrason E6020P, MW= 58,000 g/mol) supplied from BASF company was employed as basis polymer of the membranes. TiO₂ nano powder (<40 nm), N-methyl-2-pyrrolidone (NMP) (>99.5 %), glutaraldehyde (GLU) 50% (w/w), sulfuric acid and polyvinyl pyrrolidone (PVP K 40) purchased from Merck (Germany) were used as solvent and pore former, respectively. PVB, 45–49% of butyl aldehyde group was supplied from Shanghai Chemical Reagent Company, PR China. Water used in this work was deionized beforehand.

Preparation of membranes

Polyethersulfone (PES) ultrafiltration prepared in the binary PES–solvent casting solutions by the immersion–precipitation process in which the solvent was NMP. The homogeneous solution was prepared by dissolving 16 wt.% PES in N-methyl-2-pyrrolidone (NMP) with 2 wt.% polyvinyl pyrrolidone (PVP) by stirring for 48 h at 50 °C. The polymeric solutions were subsequently coated on nonwoven-fabric, which was cut for 150mm×100mm by a stainless steel scraper at 25 °C. The scraper clearance was 200 μm (unless otherwise specified). Then, these solution films together with the nonwoven-fabric were immersed into a water bath at ambient temperature (25°C). Immediately phase inversion started, and after few minutes the resulting membranes with nonwoven-fabric separated off the stainless steel support spontaneously. The obtained membranes were then

repeatedly washed with water and wet stored. The homogeneous PVB solution which was prepared by dissolving 2 wt.% of PVB in N-methyl-2-pyrrolidone (NMP) at 50 °C for 24 h, was coated on the surface of PES barrier layer based on dip coating technique. The PVB coated membranes were then immersed in the cross-linking solution containing 5 wt.% of GA and 0.5 wt.% of H₂SO₄ for 2 min at room temperature in order to reduce the membrane swelling by chemical cross-linking. H₂SO₄ was used as catalyst of the reaction. For modification of PVB/PES composite nanofiltration membrane, TiO₂ nanoparticles with concentrations of 0.1, 0.5 and 0.8(wt.%) were dispersed in distilled water by sonication for 1 h and stirred vigorously for 45 min. Subsequently, the PVB coated membranes were immersed in TiO₂ nanoparticles solution. All modified membranes were heat treated in temperature of 110 °C for 5 min.

Scanning electron microscopy (SEM)

Structure of the prepared membranes was examined by scanning electron microscope (KYKY-EM 3200, China). For preparing the images of the cross section, the membranes were first frozen in liquid nitrogen and then fractured. After sputtering with gold, they were viewed with the microscope at 25 kV.

Atomic force microscopy (AFM)

Atomic force microscopy (AFM) was studied to analyze the surface morphology and roughness of the prepared membranes. The AFM analysis carried out by (BioScope TM, USA) using the tapping mode. All specimens with dimensions of (1cm×1cm) were cut and glued on glass substrate. The membrane surfaces were imaged in a scan size of 5 μm×5 μm.

Contact angle measurement

Membrane hydrophilicity was quantified by measuring the contact angle between the membrane surface and water. The contact angles were measured using a contact angle measuring instrument (G10, KRUSS, Germany). The contact angle values of each sample were obtained at four various positions of the sample and then the average value was recorded.

Swelling studies

The extent of membrane swelling was determined by the sorption experiments. These experiments are helpful to determine the interaction of the membranes with the liquid penetrates. The

weighed samples of circularly cut membrane pieces (3 cm diameter) have been soaked in deionized water. The membranes were weighed accurately (±0.1 mg) and kept in different soaking mixtures for 48 h. The degree of swelling (%), DS was calculated as [29]:

$$DS(\%) = \frac{M_s - M_d}{M_d} \times 100, \quad (1)$$

Where M_s and M_d are the weight of wet and dry membranes, respectively.

Nanofiltration experiments

All experiments were carried out at room temperature (25 °C) and transmembrane pressure (TMP) of 5 bar using a cross flow nanofiltration set-up with effective membrane surface area of 24 cm² in batch mode. The membranes performance was characterized by pure water flux (PWF) and yeast waste water rejection. The pure water flux was calculated by the following equation [30]:

$$J = \frac{Q}{A \times t}, \quad (2)$$

Where J is the permeation flux (L/m²h), A is the effective membrane surface area (m²) and Δt is the sampling time (h).

After pure water filtration, the feed reservoir was emptied and refilled with the feed solution in order to its filtration. The feed solutions were yeast manufacturing industry wastewater.

The solute rejection was calculated using Eq. (2) [30]:

$$R(\%) = \left(1 - \frac{C_p}{C_f}\right) \times 100\%, \quad (3)$$

Where C_p and C_f are the concentrations of the solute in permeate and feed solutions, respectively. In general, cross flow filtration system was utilized for measuring the flux and COD level of the permeate phase.

RESULTS AND DISCUSSION

AFM analysis

AFM images of the modified and unmodified membranes were shown in Fig. 2. Images recorded for PVB/PES composite membranes confirm that TiO₂ nanoparticles were successfully coated onto the membrane and produced rougher surfaces. The virgin PVB/PES membrane has smoother structure than the modified membranes with TiO₂ nanoparticles. The surface roughness parameters of membranes in scan size of 5 μm×5 μm were calculated by DME SPM software and are presented in Table 1. Ra is the mean value of surface area relative to the central plane, for which the volume enclosed by the image above and below this plane is equal. Root-mean-square (RMS) height

is a key physical parameter obtained from the AFM analysis, and defines as the mean of the root for the deviation from the standard surface to the indicated surface. The high RMS means high surface roughness. As shown in Table 1, the surface roughness of membranes modified with TiO₂ is higher than unmodified membranes.

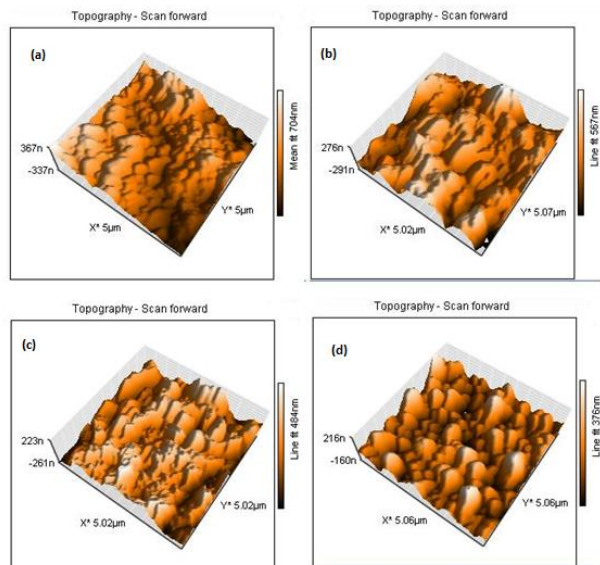


Fig. 2. AFM images of: (a) unmodified PVB/PES composite membrane, (b) 0.1 wt.% TiO₂ modified membrane, (c) 0.5 wt.% TiO₂ modified membrane, and (d) 0.8 wt.% TiO₂ modified membrane

Membrane morphology

The morphologies of unmodified PVB/PES composite membrane and PVB/PES composite modified membranes with TiO₂ nanoparticles were observed by SEM images and the obtained results are shown in Figs.3 and 4. As can be seen, in the modified PVB/PES membranes a porous top layer was formed, and a finger-like structure was observed in the sublayer of resulting membranes. The porosity of top layer is increased by increasing TiO₂ nanoparticles content. An increase with higher content of TiO₂ nanoparticles (up to 0.5 wt. %), significant agglomeration takes place. It can be seen by comparing the surface SEM images of unmodified and TiO₂nanoparticles modified membranes that there is an amount of TiO₂ nanoparticles embedding on the surface of PVB/ TiO₂ nanoparticles composite membrane. Many aggregates or chunks randomly distributed on the top surface of PVB/PES modified membranes, especially at high concentration of TiO₂

nanoparticles. Hence, the TiO₂ nanoparticles tended to form aggregates and dispersed onto the PVB/ PES membrane surface. The self-assembly of TiO₂ nanoparticles on the surface of PVB/ PES composite membrane depends on hydroxyl functional groups. The presence of hydroxyl functional groups on the surface of PVB/PES composite membrane can guarantee the self-assembly of TiO₂ and establishment of a strong bond with PVB polymer, prevents washing and removing of nanoparticles from membrane surface.

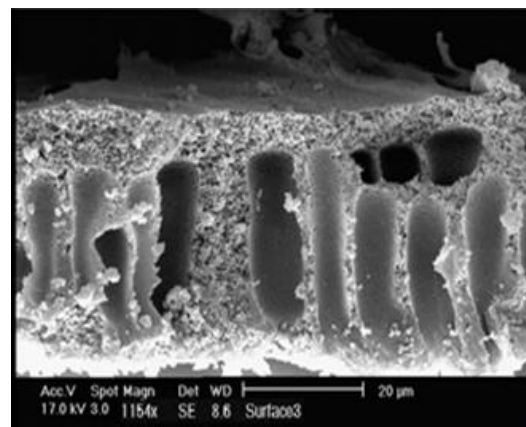


Fig. 3. The cross section SEM image of top layer of PVB/PES composite membrane.

Contact angle measurement

Fig.5 shows the effect of addition of TiO₂ nanoparticles on the contact angle and in other words wettability of the membranes. As shown, the membranes prepared with addition of TiO₂ nanoparticles present higher hydrophilicity (lower water contact angle) in comparison with the unmodified PVB/PES membrane. The highest water contact angle and in other words, the highest hydrophobicity belong to the pure PES membrane.

Coating with PVB and modified by TiO₂nanoparticles significantly improved hydrophilicity of this membrane. Water contact angle of the PVB/ PES composite membrane remarkably decreased from 71.7° to 32.3° after adding 0.5 wt. % of TiO₂nanoparticles and then slightly increased with adding 0.8 wt. % of TiO₂ nanoparticles.

Table 1. Roughness parameters of membrane surface calculated with DME SPM software

membrane	R _a (nm)	RSM(nm)
PVB/TiO ₂ (0%)	31.2	13.3
PVB/TiO ₂ (0.1%)	35.6	24.65
PVB/TiO ₂ (0.5%)	37.2	26.3

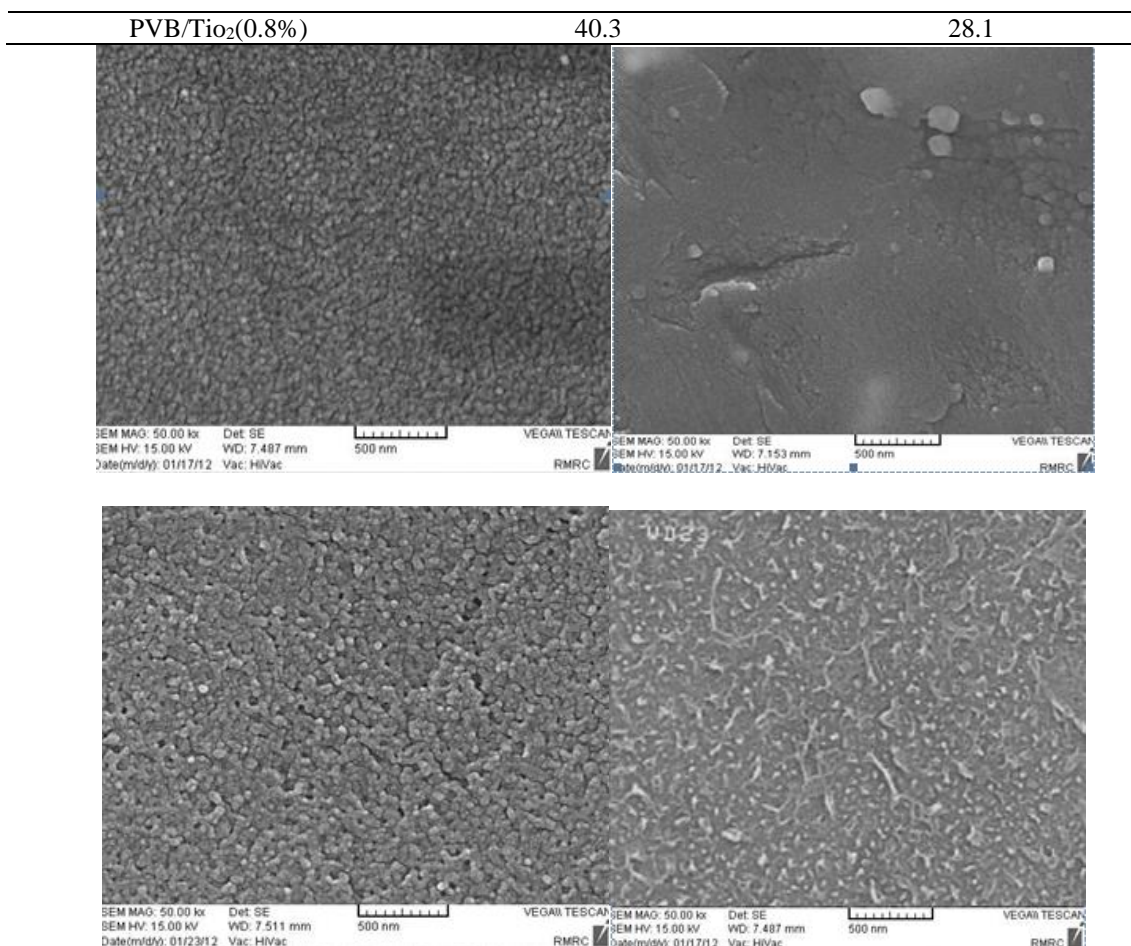


Fig. 4. SEM photographs for PVB/TiO₂ composite polymer membranes: (a) 0 wt.% TiO₂ nanoparticles; (b) 0.1 wt.% TiO₂ nanoparticles; (c) 0.5 wt.% TiO₂ nanoparticles; (d) 0.8 wt.% TiO₂ nanoparticles

Higher hydrophilicity of the modified PVB/ PES membranes in comparison with the unmodified PVB/ PES membrane can be related to hydrophilic nature of TiO₂ nanoparticles and the created hydroxyl groups on the membrane surface due to the presence of TiO₂ nanoparticles. These polar groups can interact with water molecules through van der Waals' force and hydrogen bond. Consequently, the permeation rate of water through the TiO₂ modified PVB/PES composite membranes must be high in comparison with the unmodified one. The accumulation of this nanoparticle at further concentration (more than 0.5 wt.%) on the surface can result an increase on the contact angle of membrane.

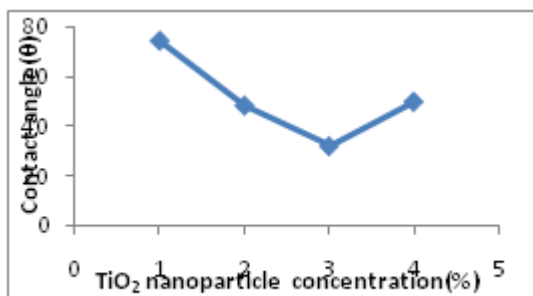


Fig. 5. Contact angle of the prepared membranes.

Pure water flux (PWF)

Fig. 6 reveals the effect of TiO₂ nanoparticles concentration on PWF of the prepared membranes at TMP of 5 bar. As shown, PWF of all modified PES/PVB membranes increased in comparison with that of the virgin PES/PBS membrane. For example, PWF of the membranes increased from 22.1 l/m² h to 55.6 l/m² h after adding 0.5 wt. % of TiO₂ nanoparticles and then slightly decreased with addition of 0.8 wt. % TiO₂ nanoparticles. The above trend confirms the results observed from the aforementioned surface SEM images. In fact, the membranes with higher porosity on top layer presented higher PWF. It is evident that there is a direct relationship between the porosity and permeability at 0.8 wt. % TiO₂ nanoparticles, the flux cannot be improved further as the nano-sized TiO₂ particles coalesce.

Flux and rejection

The effect of TiO₂ concentration on the permeability of the nanofiltration membranes during filtration of yeast wastewater for 90 min is

shown in Fig. 7. The permeability of TiO₂ modified PVB/PES composite membranes are higher than unmodified PVB/ PES membrane. Moreover, the decline in flux of unmodified PVB/PES membrane is highest in comparison with TiO₂modified PVB/PES membranes. The high permeability of TiO₂ modified membranes can be attributed to the high hydrophilicity of membrane surface. The surface of unmodified PVB/PES composite membrane is changed due to the self-assembly of TiO₂ nanoparticles and the surface roughness of TiO₂ modified PVB/PES membrane increased here in (see Table 1). However, the surface hydrophilicity of the membrane also increases with the increase of membrane surface roughness [31].

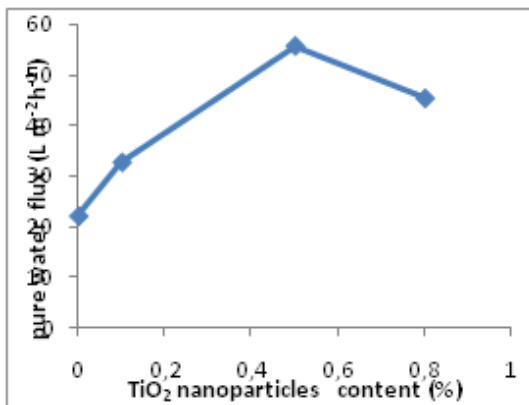


Fig. 6. Effect of TiO₂ nanoparticles concentration on pure water flux

On the other hand, the content of hydroxyl functional group on the membrane surface increases due to the incorporation of TiO₂ nanoparticles into membrane surface. The results of COD rejection of yeast wastewater obtained by utilizing the prepared membranes are illustrated in Fig. 8. As observed, all the modified PES/PVB membranes revealed higher rejection in comparison with the virgin PES/PBS membrane. An increase in TiO₂ nanoparticles concentrations up to 0.5 wt. % resulted in increasing the rejection, however, further increase in TiO₂ nanoparticles concentration up to 0.8wt. %, resulted in decreasing the COD rejection of the wastewater. Adding TiO₂ nanoparticles in to top layer of membranes change the morphology of membranes and reduce the interaction between hydrophobic particles and membrane's surface. Therefore, in general the rejection is increased.

Swelling measurements

The swelling behavior of membranes was determined in distilled and deionized water. Dry membrane pieces (601 cm² square cut) were placed in distilled and deionized water kept at a constant

temperature, 25°C. The degree of swelling (%) calculated from Eq. (1) for all membranes are plotted as a function of TiO₂ nanoparticles concentration at 25°C (see Fig. 9). PVB uncoated Membrane swell rapidly, and the equilibrium is achieved in about 15 min. It is observed that this membrane has the highest degree of swelling compared to all the other membranes over the studied range of feed water compositions. Swelling degree of the coated membrane decreased from 80 to 38 with increasing TiO₂ nanoparticles concentration. It might be explain that the cross linked PVB/TiO₂ nanocomposite membrane have less accessible free volume for the water and that causes the swelling effect to reduce significantly.

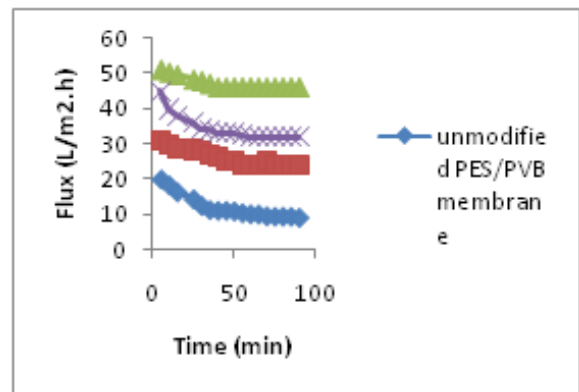


Fig. 7. Permeability of unmodified and modified membranes as a function of TiO₂ content

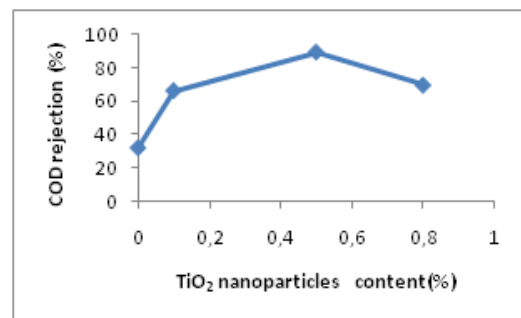


Fig. 8. Effect of TiO₂ nanoparticles content on COD rejection of membranes

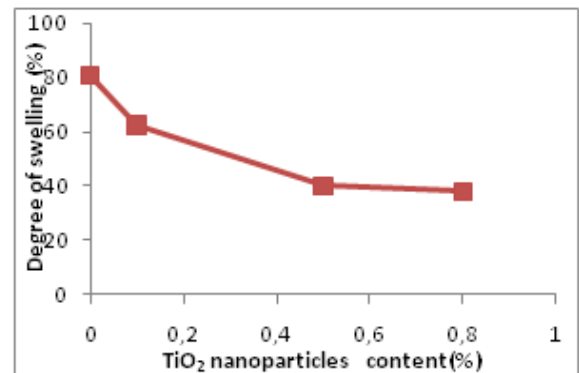


Fig. 9. Degree of swelling of membranes as a function of TiO₂ nanoparticles content.

Binding TiO₂ nanoparticles with PVB hydroxyl groups leads to a compact structural membranes that are in agreement with results obtained from swelling data. Actually, the presence of TiO₂ nanoparticles may improve the roll of cross linking agent and hinder the fact of membrane swelling.

CONCLUSION

In this work, new PVB/PES integral membranes were fabricated and modified by adding TiO₂ nanoparticles on their surfaces to improve the membrane performance and surface properties. The SEM and AFM images confirmed the settling of TiO₂ nanoparticles on the surface of PVB/PES integral membranes. The contact angle measurement indicated that the hydrophilic property of PVB/PES integral membrane was significantly improved by coating of TiO₂ nanoparticles. The water permeability of TiO₂ modified PVB/PES integral membranes were higher than unmodified PVB/PES membrane. Moreover, the flux decline of unmodified PVB/PES membrane was highest. As final result, the COD rejection as a pollution index enhanced considerably from 32 % for unmodified membrane to 89.6% for 0.5% TiO₂ modified membrane which was a superior finding for such membrane performance.

REFERENCES

1. P. Cote, D. Thompson, *Water Sci. Technol.*, **41**, 209 (2000).
2. B. Jefferson, A.L. Laine, S.J. Judd, T. Stephenson, *Water Sci. Technol.*, **41**, 197 (2000).
3. C.N. Lopes, J. Carlos, C. Petrus, H.G. Riella, *Desalination*, **172**, 77 (2005).
4. S. Chakraborty, M.K. Purkait, S. DasGupta, S. De, J.K. Basu, *Sep. Purif. Technol.*, **31**, 141 (2003).
5. M. Mantta ri, K. Viitikko, M. Nystrom, *J. Membr. Sci.*, **272**, 152 (2006).
6. V. Uyak, I. Koyuncu, I. Oktem, M. Cakmakci, I. Toroz, *J. Hazard. Mater.*, **52**, 789 (2008).
7. S. Bouranene, P. Fievet, A. Szymczyk, M. El-Hadi Samar, A. Vidonne, *J. Membr. Sci.*, **325**, 150 (2008).
8. E.M. Vrijenhoek, S. Hong, M. Elimelech, *J. Membr. Sci.*, **188**, 115 (2001).
9. S. Hong, M. Elimelech, *J. Membr. Sci.*, **132**, 159 (1997).
10. Q. Li, M. Elimelech, *Environ. Sci. Technol.*, **38**, 4683 (2004).
11. N. Her, G. Amy, C. Jarusutthirak, *Desalination*, **132**, 143 (2000).
12. S. Bhattacharjee, G.M. Johnston, *Environ. Eng. Sci.*, **19**, 399 (2002).
13. J.G. Choi, T.H. Bae, J.H. Kim, *J. Membr. Sci.*, **203**, 103 (2002).
14. A. Rahimpour, S.S. Madaeni, *J. Membr. Sci.*, **360**, 371 (2010).
15. C. Zhao, J. Xue, F. Ran, S. Sun, *Prog Mater Sci.*, **58**, 76 (2013).
16. A. Ananth, G. Arthanareeswaran, H. Wang, *Desalination*, **287**, 61 (2012).
17. N. Maximous, G. Nakhla, W. Wan, K. Wong, *J. Membr. Sci.*, **341**, 67 (2009).
18. P. Xu, J.E. Drewes, T.U. Kim, C. Bellona, G. Amy, *J. Membr. Sci.*, **279**, 165 (2006).
19. Y.Q. Wang, L.Y. Su, Q. Sun, X.L. Ma, Z.Y. Jiang, *J. Membr. Sci.*, **286**, 228 (2006).
20. N.K. Saha, M. Balakrishnan, M. Ulbricht, *Desalination*, **249**, 1124 (2009).
21. Q. Shi, Y. Su, X. Ning, W. Chen, J. Peng, Z. Jiang, *J. Membr. Sci.*, **347**, 62 (2010).
22. K.R. Kull, M.L. Steen, E.R. Fisher, *J. Membr. Sci.*, **246**, 203 (2005).
23. F. Shen, X. Lu, X. Bian, L. Shi, *J. Membr. Sci.*, **265**, 74 (2005).
24. S.B. Seymour, C.E. Carraher, *Polymer Chemistry—An Introduction*, 2nd Ed., Marcel Dekker, New York, 1988.
25. B. Gebben, H.W.A. van den-Berg, D. Bargeman, C.A. Smolders, *Polymer*, **26**, 1737 (1985).
26. V. Macho, M. Fabini, M. Rusina, S. Bobula, M. Harustiak, *Polymer*, **35**, 5773 (1994).
27. A. Sotto, A. Boromand, R. Zhang, P. Luis, J. M. Arsuaga, J. Kim, B. Van der Bruggen, *J. Colloid Interface Sci.*, **363**, 540 (2011).
28. A. Rahimpour, S.S. Madaeni, A.H. Taheri, Y. Mansourpanah, *J. Membr. Sci.*, **330**, 297 (2009).
29. D. Tanyolac, H. Sonmezis, A.R. Ozdural, *Biochem. Eng. J.*, **22**, 221 (2005).
30. E. Saljoughi, S.M. Mousavi, *Sep. Purif. Technol.*, **90**, 22 (2012).
31. W.Y. Chuang, T.H. Young, W.Y. Chiu, *J. Membr. Sci.*, **172**, 241 (2000).

Organic pollutant adsorption on pristine, defected and Al-doped carbon nanotube: a dispersion corrected DFT study

Z. Izakmehri¹, M. Ardjmand², M. Darvish Ganji^{3*}

¹Department of Chemical Engineering, Science and Research Branch, Islamic Azad University, Tehran, Iran

²Chemical Engineering Department, Islamic Azad University, South Tehran Branch, Tehran, Iran

³Department of Nanochemistry, Faculty of Pharmaceutical Chemistry, Pharmaceutical Sciences Branch, Islamic Azad University, Tehran - Iran (IAUPS)

Received June 18, 2016, Revised September 10, 2016

The effective enrichment and detection of organic pollutants in the environment has been attracted many attentions because of the enormous human health concerns. Using dispersion-corrected density functional theory (DFT-D2), we studied the interactions between 2, 3, 7, 8-tetrachlorodibenzo-p-dioxin (TCDD) and pristine, defected and Al-doped carbon nanotubes. The TCDD molecule physical adsorption on pure and defected CNTs with a binding energy of about -0.52 eV and -0.34 eV. The accuracy of our method was validated by hybrid B3LYP levels of theory and it was shown that there is worthy agreement between two respected methods. However, the binding energy rises to -0.85 eV when TCDD binds to Al-CNT. The increase in binding is due to charge transfer from the TCDD molecule to the Al-CNT. Furthermore, the obtained DOS spectra show that the electronic properties of Al-CNT change considerably by the adsorption of TCDD whereas no such variations are observed for the other considered CNTs. Consequently, the Al-CNT is a promising candidate for the TCDD sensing and detection. Our *first-principles* results present evidence for a rational benchmark for the applicability of the Al-CNT for TCDD adsorption and detection.

Keywords: Al-doped CNT; TCDD; DFT-D; adsorption; Hazardous materials

INTRODUCTION

Dioxins refer to a group of chemicals, the polychlorinated dibenzo-dioxins (PCDD), which are known to be highly toxic and chemically stable. It causes immune toxicity, reproductive effects and carcinogenicity, so it is very important to monitor and control its exposure in both industrial and residential environments [1, 2]. The most toxic PCDD isomer is 2, 3, 7, 8 tetrachlorodibenzo-p-dioxin (TCDD) and is classified as a carcinogenic component (group 1 carcinogen) to humans according to IARC. It can be formed from the combustion organic compounds in waste incinerators such as municipal waste, medical waste, army stockpiles (chemical agents), and herbicide overuse, thus TCDD removal to well below (1 ng/m^3) is generally required [3].

Since 1991, different sorbents such as activated carbon has been widely adopted for dioxin removal [4, 5]. Carbon nanotubes (CNTs), discovered Iijima in 1991, are quasi-one-dimensional nanostructures with unique thermal and electronic properties that has attracted much interest to develop for applications in nanoelectronics. It has been shown

that CNTs can detect molecules such as NH_3 , O_2 and, NO_2 in small concentrations but H_2O , H_2 , CO cannot be detected using intrinsic CNTs since they are only adsorbed weakly on the tube wall and there is almost no charge transfer between the tube and molecules [6]. To overcome these limitations, a few strategies, such as creation of defects, chemical functionalization, and heteroatom doping, were proposed to alter the chemical nature of CNTs and enhance their sensitivity and selectivity [7, 8-14]. Little information is known about the types of defects that might be introduced during nanotube synthesis, but vacancy defects, i.e., defects resulting from missing carbon atoms, are likely candidates [9-11].

Recent investigations by using temperature-programmed desorption (TPD) on multi-walled nanotube showed that CNTs have more efficient sorbent than activated carbon for dioxin removal [4]. Great efforts have been devoted to find a suitable material for efficient dioxin adsorption and detection [15-20]. Among the well-established computational techniques to study the adsorption properties of metals and CNTs, the density functional theory (DFT) calculations have been used as a standard tool for large system with reliable compromise between accuracy and efficiency [15]. Kang et al. [16] studied the dioxin

* To whom all correspondence should be sent:
E-mail: ganji_md@yahoo.com

interaction with SWCNT and metal-doped (Fe, Li and Na) graphene sheet by using DFT calculations. Using the first principle calculations, Fagan et al. [17] demonstrated TCDD adsorption on SWCNT and predicted that dioxins can be adsorbed onto the surface of the CNTs stronger than the nanotube with lattice defect. Pan et al. [18] have reported the inclusion of TCDD with β -cyclodextrin by performing quantum mechanics and molecular dynamics (MD) calculations. It was found that β -cyclodextrin may serve as a potential substrate enriching TCDD. They further studied that 1-butyl-3-methylimidazolium dicyanamide ionic liquid can be used as efficient sorbent for TCDD using combined (MD) simulation and quantum chemical (QM) calculation [19]. Zhang et al. [20] examined the binding of TCDD molecule on a graphene sheet. It was found that they can be effective adsorbents for dioxin in the presence of calcium atoms. Doubtless, the solution of this problem will come from the development of dioxin sensors based on nanostructured material such as nanowires, nanoribbons, nanotubes and another unique material that exhibit a wide band gap and has potential application [21].

In this work, we report our theoretical studies of interaction between Al-doped CNT and TCDD by using the DFT calculations. The computational details for calculating the adsorption energies and the method of construction of TCDD/nanotubes complexes are given in detail in the next section.

COMPUTATIONAL APPROACH

In this work, all calculations were performed by using the *ab initio* DFT package SIESTA, which is based on localized basis set and the method of pseudopotentials [22]. In this software the electronic wave functions are constructed by linear combination of locally-confined atomic orbitals (LCAO's) [23].

The wave functions for the valence electrons were represented by a linear combination of pseudo-atomic numerical orbitals, while core electrons were represented by improved Troullier-Martins [24] pseudopotentials. We utilized soft confinement potentials [25] to produce double- ζ polarized (DZP) basis set for all species with the confinement regions corresponding to the energy shift of 50 meV which is appropriate for evading nasty overestimation of binding [26, 27]. For all systems under consideration, all atoms were allowed to relax freely until the forces on each atom were less than $0.03 \text{ eV}\text{\AA}^{-1}$. The structural relaxations as well as total energy calculations were carried out within the Generalized Gradient Approximation (GGA)

with the exchange-correlation functional of Perdew Burke Ernzerhof (PBE) [28]. Conventional DFT functional do not take into account dispersion forces, that is, London dispersion. Thus, it is essential to choose the suitable computational approaches that should consider the correct description of long-range electron correlation to incorporate the long distance van der-Waal's interaction between the adsorbent and adsorbate. We expect that long-range dispersion interactions will play a significant role in aromatic molecules adsorption on extended carbon based systems [29-32]. The present study employs the DFT-D2 method within the PBE functional for the systems under consideration. The Brillouin zone was sampled by $1 \times 1 \times 5$ special k -points using the Monkhorst-Pack scheme for all structural configuration relaxations. Furthermore, to clarify the electronic nature of the dioxane molecule and CNTs, the Hirshfeld charge [33] analysis is computed and discussed.

To evaluate the stability of adsorbed species onto nanotubes, we calculate the binding energy, E_b , of interacting systems by using the following equation:

$$E_b = E(\text{NT/TCDD}) - [E(\text{NT}) + E(\text{TCDD})], \quad (1)$$

where $E(\text{NT/TCDD})$ is the total energy of the nanotube interacting with TCDD molecule, $E(\text{NT})$ is the total energy of the perfect nanotube and $E(\text{TCDD})$ is the total energy of an isolated TCDD molecule. In such a depiction, $E_b < 0$ corresponds to an energetically favorable configuration. The accuracy of our DFT-D2 calculations has been evaluated by state-of-the-art *first principles* method at the B3LYP level of theory.

RESULT AND DISCUSSION

First, we considered the adsorption of single TCDD molecule on the perfect (10, 0) CNT. Two possible configurations are investigated, including when the two six-member carbon rings of TCDD were parallel/perpendicular to the CNT surface (Fig.1). The geometry of the (10, 0) CNT nanotube, TCDD molecule and various configuration of CNT/TCDD complexes are optimized to find the most stable adsorption configuration. The most stable adsorption configurations in which the TCDD molecule is placed parallel to the tube axis are shown in Fig.2 (e). The calculated adsorption energy, charge transfer, and the binding distance are summarized in Table 1. After the adsorption of TCDD molecule, interaction distances between the closest atoms of the TCDD molecule and CNT is about 3.401 \AA , which are very close to the value (3.42 \AA) found in

the case of our previous study[34].The bond lengths and especially the angle between two adjacent benzene rings in TCDD molecule were altered. Besides that, the C-C bond length near the adsorbate almost remains unchanged. The corresponding binding energy is obtained to be approximately -0.52eV , which is comparable to that Ganjiet al [34]. There are is little charge (0.037 e) transferred from the tube to TCDD molecule. These small E_b values, charge transfer and large interaction distances indicate that the TCDD molecule adsorbs weakly due to van der Waals interaction CNT and TCDD[35-42].

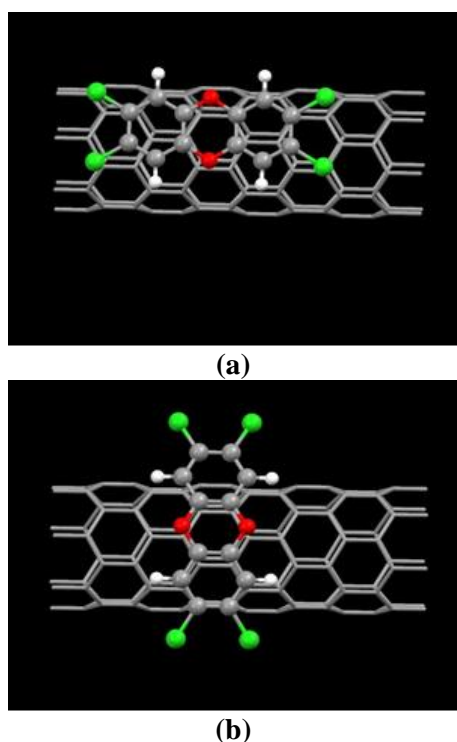


Fig. 1. Models for a TCDD molecule interacting with CNT (10, 0) with molecular axis (a) parallel and (b) perpendicular orientation to the tube axis.

There are some theoretical studies of defected CNT, showing that the formation of defected CNT was a useful way of modifying in electronic, mechanical, and adsorption properties [43-46].Hence, we studied the interaction of the defected CNT with a TCDD molecule using similar computational procedure. Among various native defects, we focused on defect, in which showed the most stable optimization structure of C-vacancy (V_C) as shown in Fig.1 (f).To investigate the TCDD adsorption on the V_C defect in (10, 0) CNT, we initially placed a TCDD molecule above a vacant site. We now consider the adsorption nature of TCDD molecule onto the V_C defect using similar computational procedure.Fig.2 (g) represents the optimized structures and calculated equilibrium distances between the two closest atoms from the two entities and angles for the adsorption of TCDD molecule. The calculated binding energy for the energetically most favorable configuration and equilibrium distance between the closest atom between V_C defect and TCDD are determined to be about -0.34 eV and 3.498 \AA , respectively. Our calculated results show that there is no enhancement of TCDD adsorption on the defected CNTs. Furthermore, after performing full structural optimization procedure for the configurations with lowest binding energy, the geometrical parameters for TCDD molecule remained almost unaltered during the adsorption process. It can be found from the calculated binding energies that in all the cases the vacancy defect in CNT caused a decrease in the interaction between the two entities in comparison to that of perfect CNT. From the above discussions, it can be obviously seen that TCDD adsorption ability of vacancy defected CNTs is weaker than that of perfect CNT. In Table 1 we listed the binding energies and equilibrium distances for the energetically most stable configurations.

Table 1: Calculated binding energies, bonding distances and charge transfers with DFT-D method for TCDD molecule interacting with perfect CNT, defected CNT, Al-CNT

Entry	System	Binding energy(eV)	$d_{A-S}(\text{\AA})$	$Q_T (e)$
1	TCDD/CNT(10,0)-Par	-0.52	3.401	-0.037
2	TCDD/CNT(10,0)-Perp	-0.35	3.502	-0.021
3	TCDD/CNT(10,0)-def-Par	-0.34	3.278	+0.131
4	TCDD/CNT(10,0)-def -Perp	-0.30	3.203	-0.019
5	TCDD+Al-dop-CNT-10,0--Cl-Cl-Par	-0.86	2.480	+0.36
6	TCDD+Al-dop-CNT-10,0--Cl-Cl-Perp	-0.55	2.623	+0.294
7	TCDD+Al-dop-CNT-10,0--C-Ring-Par	-0.62	2.968	+0.313
8	TCDD+Al-dop-CNT-10,0--C-Ring-Perp	-0.62	2.461	+0.322
9	TCDD+Al-dop-CNT-10,0--O-O-Par	-0.62	3.244	+0.331
10	TCDD+Al-dop-CNT-10,0--O-O-Perp	-0.43	3.318	+0.292

The results indicate that the average bond length of the Al-C in Al-CNT for the energetically favorable state decreased after the adsorption. In the case of TCDD molecule only the average bond length of C-Cl is slightly increased and other bond length such as C-C, C-O are decreased after adsorption on the Al-CNT. The angle between two adjacent benzene rings in TCDD molecule was also increased. A more negative E_{ad} between the Al-doped and TCDD indicates that the doping of Al in CNT can improve the reactivity of tube toward the TCDD molecule, which is in agreement with the usual mechanism that is proposed for such binding: the TCDD binds at the exposed Al atom which is electron deficient and can receive electrons from chlorine. As a result for Al-CNT system, a significant enhancement of about 65% in binding energy was observed which is significantly stronger than the pure CNT.

We also determined the electronic density of states (DOS) of the TCDD/CNT, TCDD/defected CNT and TCDD/Al-CNT complexes to fully understand the bonding nature of this TCDD through electronic structure. Fig. 5 shows the total electronic DOS for the most stable state of TCDD/CNT, TCDD/defected CNT and TCDD/Al-CNT complexes. It can be seen from the figure that

the electronic spectra near the Fermi level remained unchanged after the adsorption process. Indeed, the energy spectra for the TCDD/CNT, TCDD/defected CNT are almost the same as those for perfect CNT and no significant change can be observed on the DOS near the Fermi level upon the adsorption of TCDD molecule and corresponding CNTs.

This result emphasizes also that the adsorption of TCDD on both the perfect CNT and defected CNT does not change its structural and electrical properties. In the case of the TCDD/Al-CNT complex, however, the DOS near the Fermi level has obvious change due to adsorption of TCDD molecule. By comparing the DOS of the considered systems, we find that the adsorption of TCDD molecule leads to the additional peak pinned at the Fermi level which take part in the bonding process, as shown in Fig. 5(c). On the other hand, the difference in the Fermi level of the Al-CNT ($E_F = -4.66$ eV) and TCDD/Al-CNT ($E_F = -4.46$ eV) clearly shows a charge transfer between the Al-CNT and TCDD in the adsorption process. This result rationalizes the observation that Al dopants have a strong influence in TCDD adsorption systems.

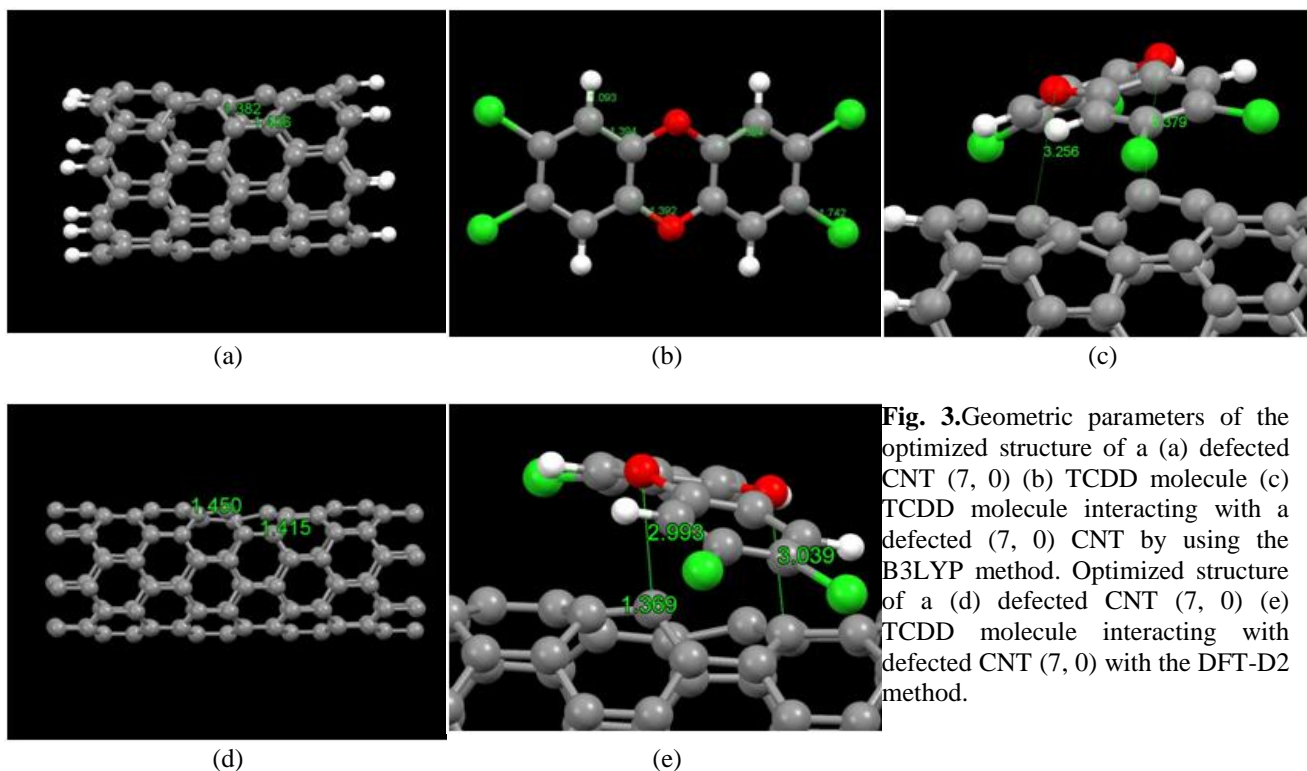


Fig. 3. Geometric parameters of the optimized structure of a (a) defected CNT (7, 0) (b) TCDD molecule (c) TCDD molecule interacting with a defected (7, 0) CNT by using the B3LYP method. Optimized structure of a (d) defected CNT (7, 0) (e) TCDD molecule interacting with defected CNT (7, 0) with the DFT-D2 method.

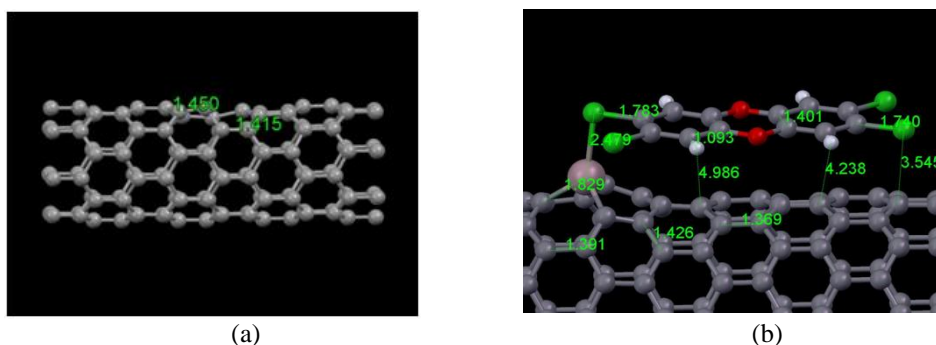


Fig.4. Schematic representation of (a) geometric parameters of the optimized Al-CNT (10, 0) and (b) energetically favorable TCDD/Al-CNT (10, 0) - complex.

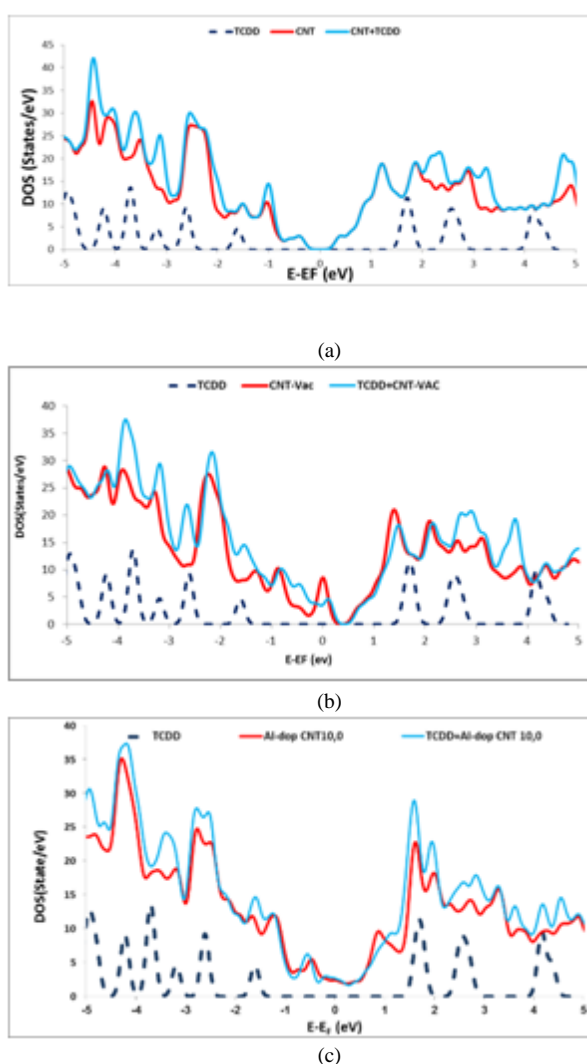


Fig. 5. Comparison between the density of states (DOS) for (a) an isolated TCDD molecule, an isolated CNT (10, 0), and the combination of the two at equilibrium geometry, and corresponding DOSs for energetically favorable (b) TCDD/CNT (10,0) with defect systems, (c) TCDD/Al-CNT(10, 0) (d) additional one peak appear above the Fermi level which take part in the bonding process TCDD/Al-CNT(10, 0)

To further investigate the change in the electronic structure in the present systems and enhancement effect of dopant on the TCDD adsorption, the charge transfer between the TCDD and Al-CNT/CNT system was calculated. Electron charge transfer plays an important role in the

electronic properties and stability of interacting systems. The charge analysis was analyzed based on Hirshfeld method which is shown to be more reliable and yield chemically meaningful charges compared to Mulliken and Bader methods [49–52]. Charge analysis indicates that about 0.36 e charge

has been transferred from the TCDD molecule to the Al-CNT while for TCDD/CNT complex about 0.03 *e* was found to be transferred from the CNT to the TCDD molecule. The enhancement in the TCDD adsorption on Al-CNT in comparison with the CNT can be explained in terms of charge analysis. This is confirmed by the Hirshfeld charge analysis, the strong binding nature of TCDD/Al-CNT complex in comparison with the TCDD/CNT system.

CONCLUSION

In conclusion, we have carried out first-principle calculations using dispersion-corrected density functional theory (DFT-D2) to investigate the adsorption of a TCDD molecule onto a CNTs. It is established that the TCDD weakly interacts with a perfect and defected CNT surface could be significantly enhanced to region of chemisorption by doping Al into structure of CNT. The doped Al induced altering in the electronic structure of CNT and facilitates adsorption of the TCDD molecule. Adsorption energies calculated from the GGA-PBE method are in good agreement with the corresponding B3LYP values. The results showed that TCDD molecule prefers to be adsorbed onto the Al-CNT with the binding energy of about -0.86 eV.

The obvious structural changes, significant binding energies and charge transfer of the TCDD/Al-CNT system reveal that it is strong interaction. The binding nature of TCDD molecule adsorbed on the CNTs surface is also investigated by the DOS analysis. Results of the electronic structure and Hirshfeld analyses indicate that in the case of TCDD/pure CNTs system there is no significant hybridization between the respective orbital but the adsorption of TCDD on the Al-CNT surface strongly suggests an orbital mixing between TCDD molecule and respected substrate near the Fermi level. Therefore, the Al-CNT would have unique application potential in chemical sensors and promising candidate for TCDD adsorption.

REFERENCES

1. B. Hileman, *Chem. Eng. News*, **37**, 55(2000).
2. D. Mackay, W. Y. Shiu, Ma, K. C. Polynuclear Aromatic Hydrocarbons, Polychlorinated Dioxins and Dibenzofurans. Handbook of Physical Chemical Properties and Environmental Fate for Organic Chemicals; Lewis Publishers: Ann Arbor, MI, 1992.
3. H. Fiedler, *Organic Pollutants*, **3**, 45 (2003); H. U. Harstenstein, In: Activated Carbon for Flue-Gas Polishing of MWIs (Proceedings of International Specialty Conference, VIP-32; Municipal Waste Combustion Conference, Williamsburg, VA, March 1993); Air and Waste Management Association: Pittsburgh, PA, 1993, p. 87.
4. R. Q. Long, R. T. Yang, *J. Am. Chem. Soc.*, **123**, 2058 (2001).
5. S. Iijima, *Nature*, **354**, 56(1991).
6. S. Peng, S. Cho, *Nano Letters*, **3**, 513 (2003).
7. J. Kong, M.G. Chapline, H. Dai, *Adv. Mater.* **13** 1384 (2001).
8. L. Duclaux, *Carbon*, **40**, 1751 (2002).
9. R.H. Telling et al., *Nat.Mater.* **2**, 333(2003).
10. A.V. Krashennnikov., *Phys. Rev. B*, **65**, 165423 (2002).
11. G.G. Samsonidze, G.G. Samsonidze, B.I. Yakobson, *Phys. Rev.Lett.*, **88**, 065501 (2002).
12. S.B. Fagan et al., *Nano Letters*, **4**, 1285(2004).
13. L.B. da Silva, S.B. Fagan, R. Mota, *Nano Letters*, **4** 65 (2004).
14. S.B. Fagan, A.J.R. da Silva, R. Mota, R.J. Baierle, A. Fazzio, *Phys. Rev. B*, **67**, 033405 (2003).
15. S. Basri, S.K. Kamarudin, W.R.W. Daud, Z. Yaakub, *Int. J. Hydrogen Energy*, **35**, 7957 (2010).
16. H. S. Kang, *J. Am. Chem. Soc.*, **127**, 9839 (2005).
17. S.B. Fagan, E. J. G. Santos, A. G. Souza Filho, J. Mendes Filho, *Chem Phys Lett.*, **437**, 79 (2007).
18. W. Pan, D. Zhang, J. Zhan, *J. Hazard. Mater.*, **192**, 1780 (2011).
19. W. Pan, Y. Qi, R. Wang, Zhe Han, D. Zhang, *J. Hazard. Mater.*, **91**, 157 (2013).
20. H. Zhang, W. He, X. Luo, X. Lin, X. Lu, *J Mol Model*, **20**, 2238 (2014).
21. Z. L. Wang, *Mater. Today*, **7**, 26 (2004).
22. J. M. Soler, E. Artacho, J. D. Gale, A. Garcia, J. Junquera, P. Ordejon, D. Sanchez-Portal, *J. Phys. Condens. Matter.*, **14**, 2745 (2002).
23. E. Artacho, E. Angladaet, *J. Phys.: Condens. Matter*, **20**, 064208 (2008).
24. N. Troullier, J. L. Martins, *Phys. Rev. B.*, **43**, 1993 (1991).
25. J. Junquera, O. Paz, D. Sanchez-Portal, E. Artacho, *Phys. Rev. B.*, **64**, 235111(2001).
26. R. Rurali, N. Lorente and P. Ordejon, *Phys. Rev. Lett.*, **95**, 209601 (2005).
27. A. Hauschild, K. Karki, B. C. C. Cowie, M. Rohlfing, F. S. Tautz and M. Sokolowski, *Phys. Rev. Lett.*, **95**, 209602 (2005).
28. J. P. Perdew, K. Burke and M. Ernzerhof, *Phys. Rev. Lett.*, **77**, 3865 (1996).
29. M. Dion, H. Rydberg, E. Schröder, D. C. Langreth, B. I. Lundqvist, *Phys. Rev. Lett.*, **92**, 246401 (2004).
30. T. Thonhauser, Valentino R. Cooper, Sh. Li, A. Puzder, P. Hyldgaard, D. C. Langreth, *Phys.Rev.B* **76**(12), 125112 (2007).
31. G. Román-Pérez and J. M. Soler, *Phys. Rev. Lett.*, **103**, 096102 (2009).
32. J. D. Wuesta, A. Rochefort, *Chem. Commun.*, **46**, 2923 (2010).
33. F. L. Hirshfeld, *Theor. Chim.Acta*, **44**, 129 (1977).
34. M. D. Ganji, H. Alinezhad, E. Soleymani, M. Tajbakhsh, *Physica E: Low. Dimens. Syst. Nanostruct.*, **67**, 105 (2015).
35. M.D. Ganji, *Nanotechnology*, **19**, 025709 (2008).
36. M. Darvish Ganji, H. Mazaheri, A. Khosravi, *Commun. Theor. Phys.*, **64**, 576 (2015).
37. M. Darvish Ganji, A. Bakhshandeh, *Commun. Theor. Phys.*, **60**, 341 (2013).

38. M. D. Ganji, *Diamond Related Mater*, **18**, 662 (2009).
39. M. D. Ganji, M.T, M. Laffafchi, *Sol .State.Sci*, **12**, 1547 (2010).
40. M. D. Ganji, A.Mirnejad, A .Najafi, *SciTechnolAdv Mat.*, **11**, 045001 (2010).
41. M.D. Ganji, B. Ahaz, *Commun. Theor.Phys.*, **53**, 742 (2010).
42. Z. Izakmehri, M. Ardjmand, M. D. Ganji, E. Babanezhad, A. Heydarinasab, *RSC Adv.*, **5** 48124 (2015).
43. Y. J .Xu, J.Q.Li, *Chem. Phys. Lett* , **412**, 439 (2005).
44. Z.R .Tang, *Physica B*, **405**, 770 (2010).
45. M. D.Ganji, M .Goodarzi, M .Nashtahosseini, A.Mommadi-Nejad., *Commun. Theor.Phys*, **55**, 365 (2011).
46. Y.J.Xu., Li.J.Q, *Chem .Phys.Lett.*, **400**, 406 (2004).
47. A. Schäfer, C. Huber and R. Ahlrichs, *J. Chem. Phys.*, **100**, 5829 (1994).
48. F. Neese, *Wiley Interdisciplinary Reviews: Comp. Mol. Sci.*, **2**, 73 (2012).
49. G. Te.Velde, F. M. Bickelhaupt, E. J. Baerends, C. Fonseca ,Guerra, S. J. A. Van Gisbergen, J. G. Snijders, T. Ziegler, *J. Comput. Chem.*, **22**, 931 (2001).
50. C. Fonseca Guerra, J. W. Handgraaf, E. J. Baerends and F. M. Bickelhaupt, *J. Comput. Chem.*, **25**, 189 (2004).
51. A.E. Clark, J.L. Sonnenberg, P.J. Hay, R.L. Martin, *Chem. Phys.*, **121**, 2563 (2004).
52. S. Tsushima, *Dalton Trans.*, 6732 (2011).

Thermal conductivity of silane cross-linked polyethylene composites

Md. Poostforush, H. Azizi*, I. Ghasemi,

Plastics Dept., Processing Faculty, Iran Polymer and Petrochemical Institute P.O.Box.14965/115, Tehran, Iran

Received June 26, 2015; Revised September 10, 2016

Silane cross-linked polyethylene (XLDPE) composites contained aluminum (Al) particles and carbon fiber (CF) prepared via melt mixing. The effect of filler loading and cross-linking on thermal properties of composites were investigated. Thermal conductivity was calculated from thermal diffusivity multiplying by specific heat capacity by density. Thermal stability was investigated by thermogravimetric analysis (TGA) and morphology of composites studied by scanning electron microscopy (SEM). Thermal stability of composites didn't affected by cross-linking. Thermal conductivity increased with enhancement of degree of cross-linking and reached to 3.81 and 0.9 $\text{W}\cdot\text{m}^{-1}\text{K}^{-1}$ for composites contained 60 vol% Al and 15 vol% CF, respectively. With increasing filler content the filler- filler interaction would be enhance and three dimensional thermal conductive pathways formed in all compositions leading to increase of thermal conductivity of composites.

Keywords: Thermal conductivity, Polymer composites, Silane cross-linked polyethylene

INTRODUCTION

Thermal conductive polymers have wide applications in various fields such as electronics, solar cells, automotive, heat exchanger equipment and etc. There are several methods for enhancement of thermal conductivity of bulk polymers. Typical methods mainly focused on introduction of heat transport networks by addition of thermal conductive inorganic fillers into polymer matrix which can enhance the thermal conductivity of prepared composites. The enhanced thermal conductivity of such composites doesn't reach theoretical expectations as a result of high thermal contact resistance at polymer-filler interfaces [1]. The other way for controlling thermal conductivity of polymers is enhancement of intrinsic thermal conductivity by changing structural design [2], crystallinity [3] and introducing cross-link bonds (high density) [1] between polymer chains.

Polyethylene is the most widely used polymer which has a great potential in geothermal pipe applications but it suffered from low thermal conductivity and thermal stability. Highly Cross-linking of PE can improve the thermal conductivity and thermal stability of bulk resin by opening new heat paths and directly contributes to the increase in abovementioned [4]. The main application of thermally conductive XLPE is in piping systems in geothermal heat exchangers [5]. Higher heat dissipation in thermal conductive pipes led to length reduction of heat exchanger pipes and better efficiency of heat pumps.

Chrissafis et al [6] enhanced the thermal conductivity of cross-linked high density PE by addition of carbon nanotubes (CNT) from 0.17 $\text{W}\cdot\text{m}^{-1}\text{K}^{-1}$ up to 0.51 $\text{W}\cdot\text{m}^{-1}\text{K}^{-1}$ at 5 wt% of nano filler. In other attempt, Roumeli et al [7] enhanced the thermal conductivity of cross-linked high density PE by addition of low nano filler contents of nanodiamonds (NDs) and NDs/CNT hybrids. They enhanced the thermal conductivity of Si-XLDPE/NDs (0.5 wt%) from 0.17 $\text{W}\cdot\text{m}^{-1}\text{K}^{-1}$ up to 0.5 $\text{W}\cdot\text{m}^{-1}\text{K}^{-1}$ and in the case of Si-XLDPE /NDs (3 wt%) /CNT (5 wt%) nanocomposites thermal conductivity enhanced up to 0.45 $\text{W}\cdot\text{m}^{-1}\text{K}^{-1}$. There are limited scientific reports on enhancement of thermal conductivity of silane crosslinked polyethylene by addition of micro fillers.

In this work for the first time we attempt to investigate the effect of addition of Al and CF as micro fillers in order to enhance the thermal conductivity of XLDPE composites. We investigate the effect of crosslinking on thermal conductivity, thermal stability and morphological properties of XLDPE composites.

EXPERIMENTAL

Materials

PE-g-Si was chosen as a matrix in thermal conductive composites CF and Al powder considered as effective and commercialized thermal conductive fillers in this study. Table 1 summarizes the characteristics of used materials.

* To whom all correspondence should be sent:
E-mail: H.Azizi@ippi.ac.ir

Table 1. Material properties

Material	Size [μm]	Density [g·cm ⁻³]	Thermal conductivity [W·m ⁻¹ K ⁻¹]	MFI 190°C/5 kg [g/10 min]	Manufacturer
LDPE-g-Si	-	0.952	0.31	1.1	Hyundai Eng. Plastics
CF (COAL TAR PITCH)	Chop length: 3600 Filament diameter: 11	2.12	140	-	DIALEAD
Al	<180	2.7	205	-	K.P.M

Sample preparation

PE-g-Si and fillers (Al & CF) were first dry mixed on desired volume percentages. Formulations were designed at three different filler volume content.

The composites were prepared by W50EH internal mixer (Brabender GmbH & Co., Duisburg, Germany) at 60 rpm for 10 min at the temperature 190°C. After the melt mixing step, prepared composites were cooled down at the room temperature and hot pressed at 30 MPa at 195°C for 5 min in a press machine Ttoyoseiki, Japan). Abrasive paper was used to make a disc sample manually with 10 mm diameter and 1 mm thickness to measure the thermal diffusivity by the laser flash method.

CHARACTERIZATION

Scanning electron microscopy

A field emission scanning electron microscope [(FE-SEM), S-4500, JEOL Co.LTD, Tokyo Japan] at an accelerated voltage of 10 kV was used to observe the morphology of the fillers and fractured surface of the composites. The composites were cryogenically fractured in liquid nitrogen. The samples were Pt-coated using a sputter coater (Sputter Coater 108 auto, Cressington Scientific, Watford, UK) for 2 min before imaging to avoid charging during observation.

Thermal stability

Thermal gravimetric analysis (STA 625 from Rheometric Scientific) used in order to investigate thermal stability of different samples under N₂ atmosphere. The heating rate considered at 20°C/min. A mass of about 100 mg of samples was heated at temperatures ranging from 30 to 700°C. TGA analysis gives an idea of the thermal stability of samples

Gel content

The gel content of cross-linked samples was determined according to ASTM D 2765. Xylene used as solvent in the gel content analysis.

Thermal conductivity

Thermal conductivity (W·m⁻¹k⁻¹) was given by the product of the thermal diffusivity (mm²/s), multiplying by specific heat capacity (J·g⁻¹ K⁻¹) and density (g·cm⁻³). The thermal diffusivity of the composites was measured by a laser flash method (TC-7000, ULVAC Co. Japan) at 30°C. The laser flash technique was introduced in 1961 by Park et al.[8]. Laser heat pulses irradiated on the front side of the disc sample; the heat was transmitted through the sample thickness direction and was measured by an infrared camera. The time to reach the half of the maximum temperature (t_{1/2}) at the back side of the sample was chosen to calculate the heat diffusivity calculated by Equation 1:

$$\alpha = 1.38 L^2 / \pi^2 \cdot t_{1/2} \quad (1)$$

The parameter α is thermal diffusivity and L is the thickness of the samples. DSC N-650 instrument equipped with specific heat capacity calculation software was used for measuring the specific heat. For this purpose, a three-curve analysis method was used including obtained DSC sample curve, baseline and reference material data. Sapphire was selected as a reference material. Then thermal conductivity was calculated from thermal diffusivity by Equation 2:

$$K = \alpha \times \rho \times C_p \quad (2)$$

RESULTS AND DISCUSSION

Morphological characteristics

The morphology of Al, CF and composites were observed by SEM. As shown in Figure 1, Al particulates (Figure 1a-c) have irregular shapes meanwhile CF (Figure 1d-f) has perfectly straight

shape and smooth surface. The aspect ratio of CF is about 330.

The morphological structure of the prepared composites was also investigated. SEM micrographs of cryogenically fractured disk shaped samples, shown in Figure 2. Composites (Figure 2d-i), has rough surface compared to virgin PEX (Figure 2a-c). With enhancement of Al content, the roughness of composites surfaces will be more pronounced. Al powder content enhancement led to decrement of average inter-particle space and formation of more agglomerates. As it can be seen at high magnifications, there is a great interaction between Al surface and XLDPE. The surface of all Al particles has well coated with the matrix. It could be as result of condensation reaction of Si-OH groups in silane grafted PE and OH groups on the surface of Al particles [9]. Formation of 3-dimensional pathways inside the matrix is seen clearly at high filler concentrations.

In the case of XLDPE/CF composites, at low filler contents (5 Vol%, Figure 3a-c), the inter-particle space between the fibers are high and CFs are mostly separated without any contacting each other. Comparing to Al particles, there isn't any reaction possibility between XLDPE and CF surfaces. It would be as result of different surface chemistry of CF and XLDPE. Attendance of

several cylindrical holes on the fractured surface is completely clear for all composites.

By increasing the volume content of CF (15 % vol., Figure 3d-f), the average inter-particle space become smaller and local networks would be form.

Thermal stability

The different behavior of the LDPE-g-Si, XLDPE and their composites showed that the influence of thermal conductive fillers on the thermos-oxidation process resulted in a superior thermos-oxidative stability in composites. Thermal stability of samples investigated by TGA and presented on Figure 4. Under a nitrogen atmosphere LDPE-g-Si and XLDPE degrade in a single step and reached near zero at the last. Addition of thermal conductive fillers led to improving of overall thermal stability and enhancement of onset temperature thermal degradation in XLDPE/Al and XLDPE/CF composites about 8-9°C. However, the thermal degradation behavior of composite samples is completely different with non-filled XLDPE. From Figure 4 it can be concluded that thermal stability of XLDPE didn't change significantly in comparison with LDPE-g-Si. Attendance of silane cross-linked networks hardly affected the thermal properties of our materials.

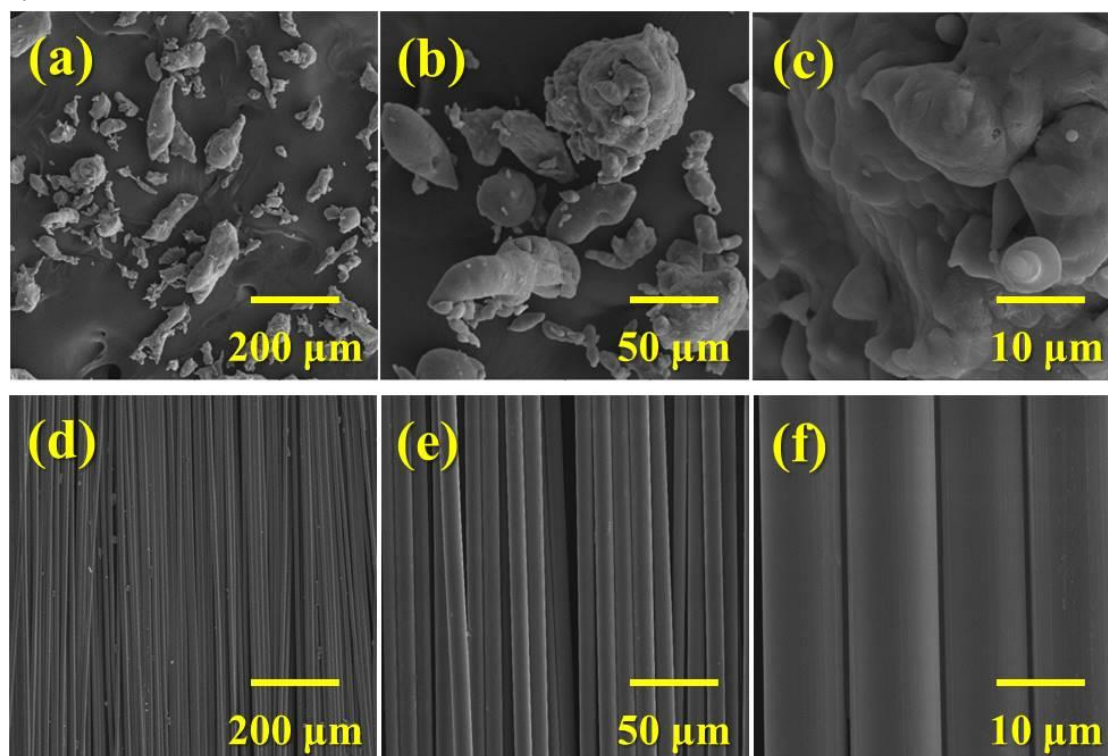


Fig. 1. SEM images of Al (a-c) and CF (d-f) at different magnifications X 250, X 1000 & X 5000 respectively.

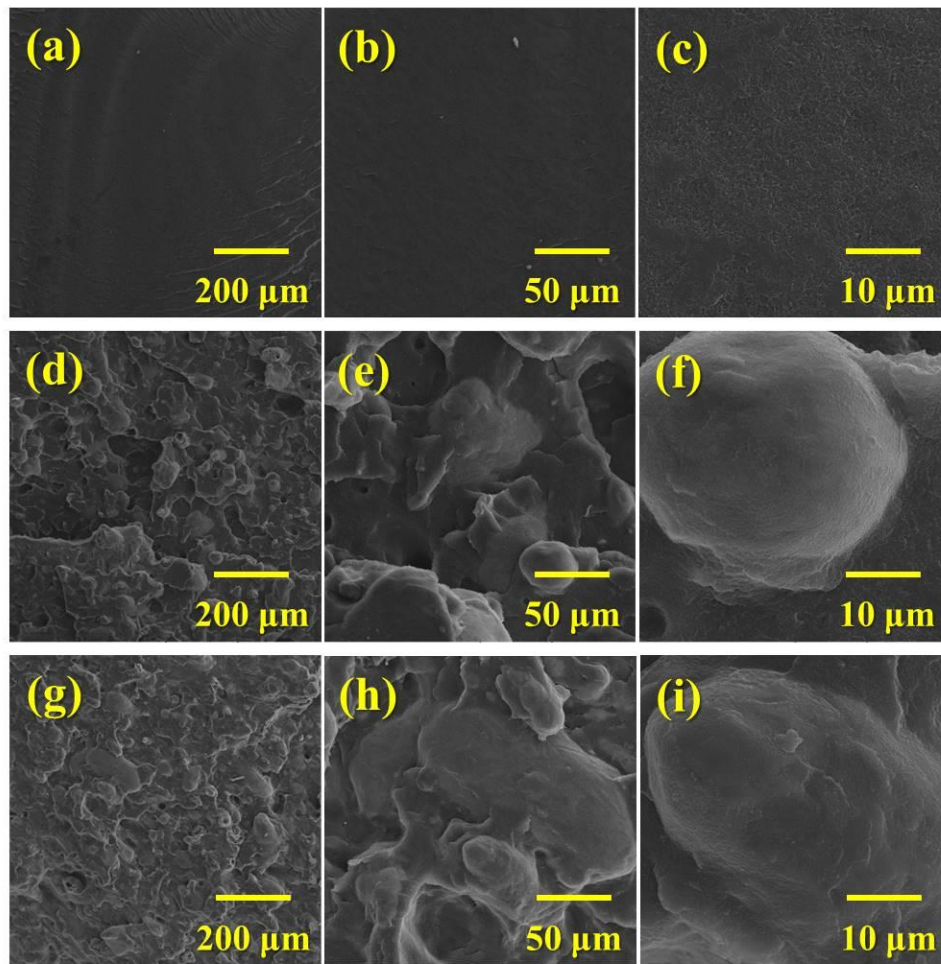


Fig.2. SEM images of XLDPE (a-c) and XLDPE/Al composites at different volume concentrations (vol%): XLDPE/Al (d-f, 40 vol%), XLDPE/Al (g-i, 60 vol%).

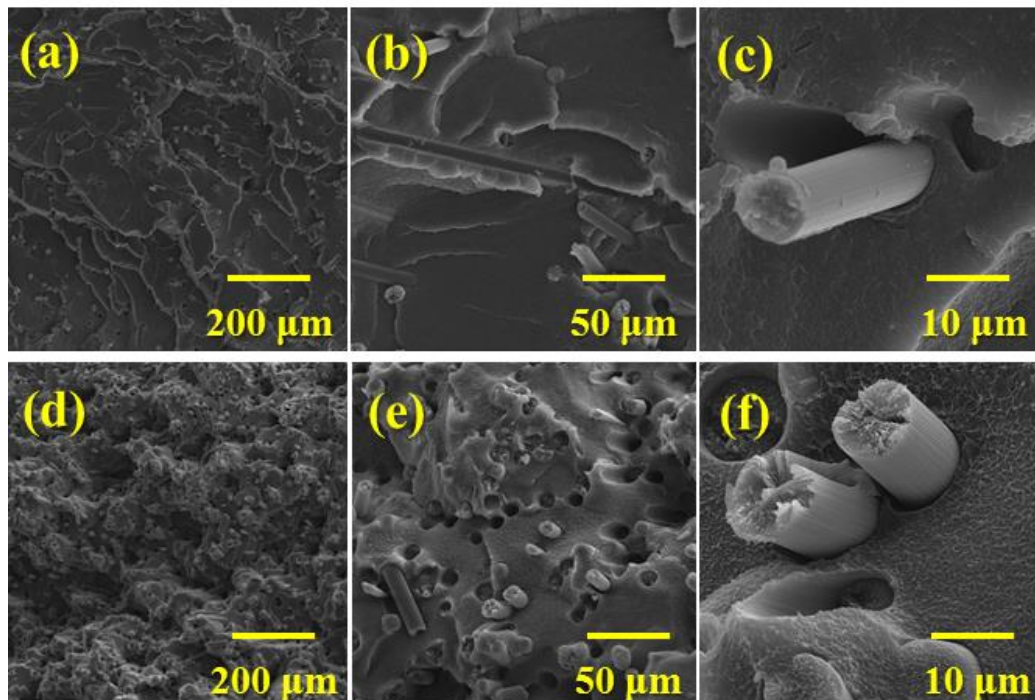


Fig. 3. SEM images of and XLDPE/CF composites at different volume concentrations (vol%): XLDPE/CF (a-c, 5 vol%) & XLDPE/CF (d-f, 15 vol%).

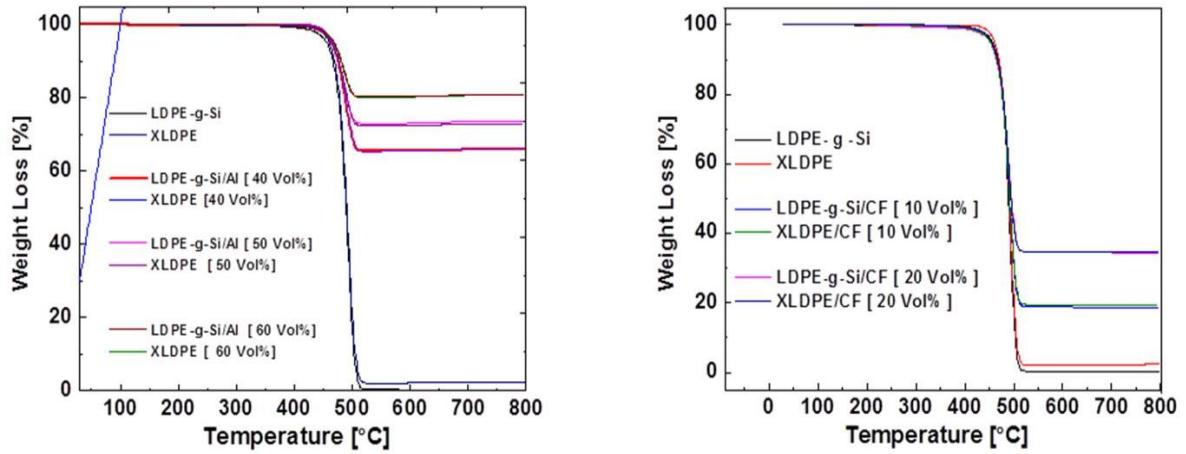


Fig. 4. TGA curves of XLDPE, LDPE-g-Si and their composites with (a) Al and (b) CF.

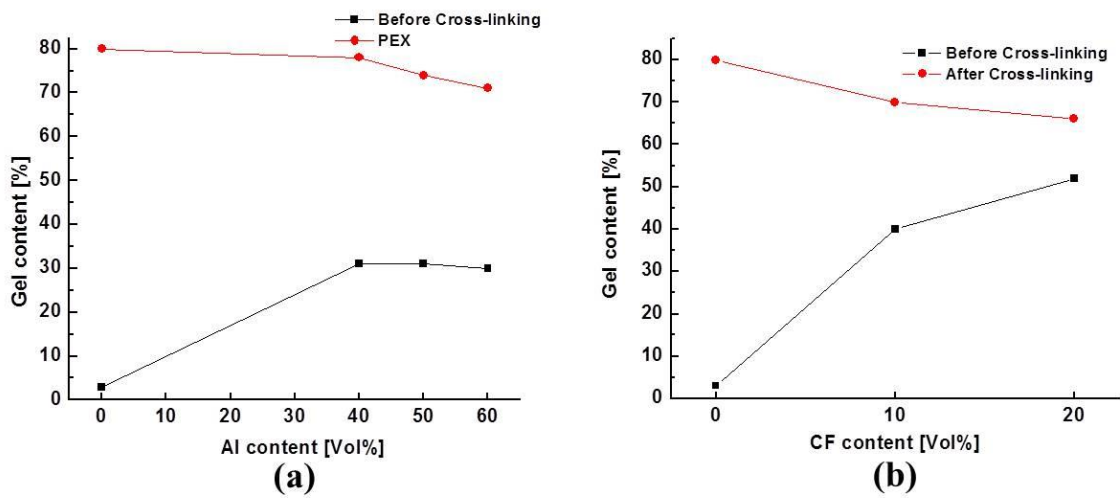


Fig. 5. Effect of filler volume fraction on gel contents of composites containing (a) Al and (b) CF as a filler.

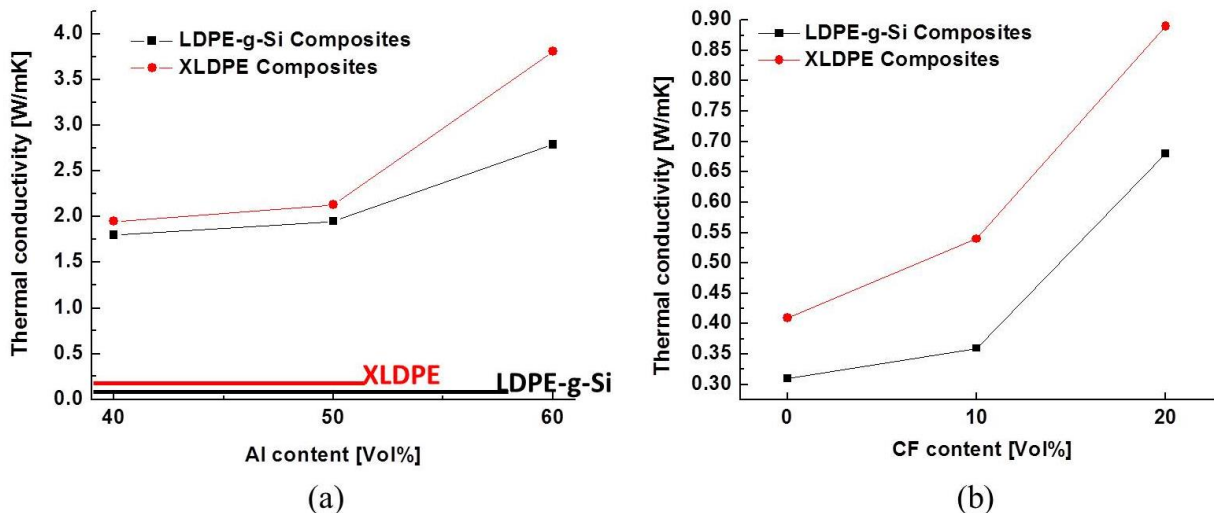


Fig. 6. Thermal conductivity of composites contain (a) Al and (b) CF as a filler.

Gel content

The effect of Presence of thermal conductive fillers on the gel content of samples investigated before and after crosslinking and results are

depicted in Figure 5. Cross-linking would be happened even before moisture curing as a result of unavoidable atmospheric moisture during raw material storage and melt blending. Existing of

filler affected the cross-linking level before and after moisture curing of composites. Before moisture curing and crosslinking process, addition of filler enhanced the gel contents meanwhile after moisture curing, the reverse trend was found. Before moisture curing step, gel content enhanced from 2% up to 30 % and 50% for LDPE-g-Si/Al and LDPE-g-Si/CF composites at the highest filler contents, respectively. For XLDPE composites presence of fillers would be hinders of condensation of silanols to form Si-O-Si crosslinks which negatively influence the gel content. By introduction of different type of fillers in the polymer matrix, the possibility of formation of bridges between the chains during moisture curing would be decrease. The gel content decreased from 80 for XLDPE to about 70 at highest concentrations of fillers.

Thermal conductivity

There are limited investigations on thermal conductivity of XLDPE composites. Thermal conductivity of composites before and after moisture curing investigated and results depicted in Figure. 6. Thermal conductivity of Al and CF contained composites enhanced with increment of filler loading as result of formation thermal conductive pathways through the matrix especially at high filler loadings. The thermal conductivity of LDPE-g-Si/Al (Figure 6a) and LDPE-g-Si/CF (Figure 6b) composites increased from $0.31 \text{ W}\cdot\text{m}^{-1}\text{K}^{-1}$ up to $2.79 \text{ W}\cdot\text{m}^{-1}\text{K}^{-1}$ at (Al-60 % vol.) and $0.68 \text{ W}\cdot\text{m}^{-1}\text{K}^{-1}$ (CF-20 vol %) of fillers respectively. Moisture curing of LDPE-g-Si led to enhancement of thermal conductivity of matrix (XLDPE) as a result of introduction heat pathways and these paths directly contributes to increment in thermal conductivity [4]. In our study, thermal conductivity of XLDPE reached to $0.41 \text{ W}\cdot\text{m}^{-1}\text{K}^{-1}$. The similar results found for XLDPE composites. Thermal conductivity of XLDPE/Al and XLDPE/CF composites rose up to $3.81 \text{ W}\cdot\text{m}^{-1}\text{K}^{-1}$ and $0.9 \text{ W}\cdot\text{m}^{-1}\text{K}^{-1}$ at highest filler contents. Combination of high density cross-linking and formation of 3D conductive filler pathways provided such a high thermal conductivity. In the case of XLDPE/Al composites, there is a great interaction between the XLDPE and Al surface which can reduce the amount of defects in composites and subsequently decrease the Umklapp-scattering. In the case of

XLDPE/CF composites, there isn't any interaction between the CF surface and XLDPE due to different surface chemistry of CF sizing and matrix. Based on above results, thermal conductivity of composites is closely related to performance of filler and matrix. These results can open up application of such thermal conductive fillers in production of heat exchanger pipes and similar applications.

CONCLUSION

XLDPE composites successfully prepared by melt mixing of LDPE-g-Si in presence of Al and CF at different loadings and thermal conductivity, gel content and morphology of prepared composites were investigated. Thermal conductivity of composites was calculated after measurement of the thermal diffusivity, specific heat and density of samples. By introducing high density cross-linking and increasing of filler content, thermal conductivity of nanocomposites enhanced. The highest thermal conductivity was surprisingly more than 12 times superior than LDPE-g-Si. With considering our results, these types of composites can be applied as a thermal conductive pipes in thermal management applications , semi-conductive products and so on.

REFERENCES

1. H. Guo-Jie, C Bing-Yang, L Yuan, *Chinese Physics Letters*, **31**, 86501 (2014).
2. S. Shen, A. Henry, J. Tong, R. Zheng, G. Chen, *Nature Nanotechnology*, **5**, 251 (2010).
3. J. Yu, B. Sundqvist, B. Tonpheng, O. Andersson, *Polymer*, **55**, 195 (2014).
4. G. Kikugawa, T. Desai, G. P.Keblinski, T.Ohara, *J. Appl. Phys.*, **114**, 034302 (2013).
5. E. Roumeli, A. Avgeropoulos, E. Pavlidou, Vourlias, G.; Kyratsi, T.; Bikiaris, *D. RSC Advances*, **4**, 45522 (2014).
6. E. Roumeli, A.Markoulis, T. Kyratsi, D. Bikiaris, K.Chrissafis, *Polymer Degradation and Stability*, **100**, 42 (2014).
7. E. Roumeli, E. Pavlidou, A. Avgeropoulos, G.Vourlias, D. N. Bikiaris, K. Chrissafis, *The J. of Physical Chemistry B*, **118**, 11341 (2014).
8. W. J. Parker, R. J.Jenkins, C. P. Butter, G. L. Abbot, *J. of Applied Physics*, **32**, 1679 (1961).
9. J. Li, X. Zhang, M. Yuen, K. Zhang, L. Liu, C.H. Ku. *Electronic Packaging Technology (ICEPT)*, **329**, 65 (2014).

Preparation, characterization and optical properties of nanostructured undoped and Cu doped ZnO thin films

Esmaeil Amaki, Reza Sahraei*

Department of Chemistry, University of Ilam, P.O. Box: 65315-516, Ilam, Iran.

Received June 26, 2016; Revised September 10, 2016

In this work, undoped and Cu-doped ZnO (ZnO:Cu) nanostructured thin films were synthesized by chemical bath deposition method. UV-Visible and photoluminescence (PL) spectroscopy have been used to investigation of optical properties of the samples in detail. The band gap energy of undoped and Cu-doped ZnO films is blue-shifted by ≈ 0.3 eV with respect to the bulk value (3.37 eV), probably due to the quantum size effect as expected from the nanocrystalline nature of the films. The photoluminescence (PL) spectra of the ZnO:Cu thin films exhibited two emission peaks, one blue peak located at 491 nm and a intense deep level-green peak at 521 nm. The intensity of photoluminescence emission is enhanced with increasing Cu concentration and deposition temperature. The intensity of peaks is optimized at Cu:Zn ratio of 0.29% for the ZnO:Cu thin films. Fourier transform infrared (FTIR) spectroscopy shows two peaks in 427.22 and 532.71 cm^{-1} which is attributed to ZnO and CuO bonds, respectively. The x-ray diffraction and scanning electron microscopy techniques indicated that the films have hexagonal phase of ZnO.

Keywords: Nanostructures; Zinc oxide; Cu doped; Thin films; Optical properties

INTRODUCTION

Zinc oxide (ZnO) with a wide band gap (3.37 eV) [1] and a large exciton binding energy of 60 meV [2] is one of the excellent semiconductors which can be applied to light emitting diodes, solar cells, and gas sensors [2-5]. Among metal oxides, ZnO has been studied intensively due to its rich optical properties. Besides, it can be prepared at a lower temperature. Owing to these properties, ZnO has attracted increasing attention as a promising candidate material for potential applications in optoelectronic devices [6-10]. The emission properties of undoped and doped ZnO films have been widely studied [11-13]. Recently, some researchers have found some doping elements, such as Ga, Ni, and Mg can influence the luminescence properties of ZnO films [14-16]. Copper is a prominent luminescence activator in II-VI compounds [17]. It is significant to investigate ZnO film doped with Cu for its possible luminescence application. The techniques used for ZnO growth include chemical vapour deposition (CVD), molecular beam epitaxy (MBE), Rf or dc sputtering, pulsed laser deposition (PLD) [18-20], and chemical bath deposition (CBD) [21-23], etc. Among these methods, chemical bath deposition is an attractive technique for obtaining thin films and has the advantage of easy control of the film composition and easy fabrication of large area thin

film with low cost [24]. In this paper, we fabricated undoped and Cu-doped ZnO (ZnO:Cu) thin films on glass substrates through chemical bath deposition at range of 45-76 °C. The effect of fabrication conditions including the concentrations of Cu precursor and kinetic parameters (temperature and deposition time) on the structural, optical and photoluminescence properties of the ZnO:Cu thin films were investigated. The films are characterized by several techniques such as X-ray diffraction, scanning electron microscopy (SEM), UV-visible and fluorescence spectrophotometer.

EXPERIMENTAL

Undoped and Cu-doped ZnO (denoted by ZnO:Cu) thin films were deposited on glass substrates by chemical bath deposition. The precursor materials used prepare undoped and doped ZnO films are zinc chloride (ZnCl_2), hexamethylenetetramine ($\text{C}_6\text{H}_{12}\text{N}_4$), copper acetate monohydrate [$\text{Cu}(\text{CH}_3\text{COO})_2 \cdot \text{H}_2\text{O}$] and ethanol (for seed layer of ZnO:Cu films, solutions of 0.1M ZnCl_2 , in ethanol). Aqueous solutions of 0.1M ZnCl_2 , and 0.1M $\text{C}_6\text{H}_{12}\text{N}_4$ with ratio 1:1 were mixed in a beaker for deposition undoped and Cu-doped ZnO thin films at 45-76 °C and deposition times of 1-8 h. In order to adjust the Cu concentration, the desired amounts of copper acetate solution were added (5×10^{-2} – 5×10^{-7} M and 1–10 mL).

The nanostructure and morphology of the films were studied by X-ray diffraction Xpert MPD with

* To whom all correspondence should be sent:
E-mail: reza_sahraei@yahoo.com

Cu K α radiation (40 kV and 30 mA) and scanning electron microscope (SEM, S-4160 Hitachi), respectively. Photoluminescence (PL, Cary Eclips FL III MO25) measurements were carried out at room temperature. The optical properties of the sample were investigated by a UV-Visible (UV-Vis, Cary 300 Bio). Inductively coupled plasma atomic emission spectroscopy (ICP-AES, Varian Vista-Pro) confirmed the presence of copper atoms with different percentages as an impurity. Infrared spectrum was recorded on (FTIR, Vertex 70). Also, the thickness of the films was measured by thickness gauge needle (Dektak³).

RESULTS AND DISCUSSION

X-ray diffraction (XRD)

XRD patterns of the undoped and Cu-doped ZnO thin films prepared at 76 °C are presented in Fig. 1. It is apparent that four peaks can be designated to (100), (002), (101) and (102) planes of hexagonal wurtzite in ZnO thin films [25]. Fig. 1b shows double phase of ZnO:Cu and secondary phase can be detected, it is apparent that a (110) peak of monoclinic appears in ZnO:Cu thin films that correspond to copper oxide phase [26]. Fig. 1 shows, the intensity peaks ((100), (002), (101) and (102)) of ZnO:Cu decreased than to pure ZnO due to the presence of copper in the structure of ZnO can be attributed to changes in the make-up atoms. Also, It has happened angular shifting at the peak with adding copper, and according to Braggs rule, can be attributed change in atomic plates distance and layers compaction.

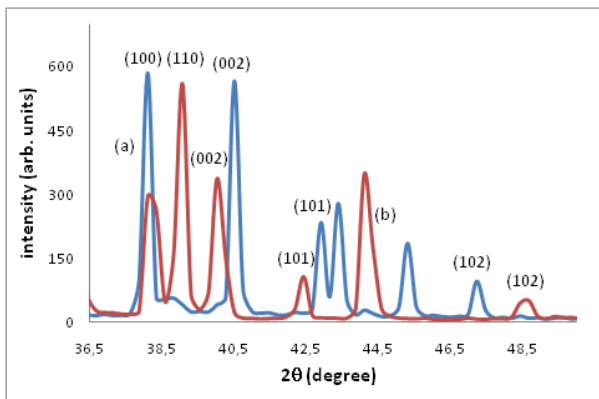


Fig. 1. XRD patterns of (a) ZnO (b) ZnO:Cu (Cu=0.5×10⁻⁵ %) thin films.

Fig. 2 shows X-ray diffraction measurements on the Cu-doped ZnO films for different Cu concentrations, the peaks intensity hexagonal structure of ZnO decreased with increasing copper concentration, but the peak intensity increased corresponding Miller indices (110) monoclinic

structure of CuO, that differences of intensities can be attributed to how to arrange of atoms in structure. XRD pattern of the Cu-doped ZnO thin films prepared at 56°C is presented in Fig. 3, and compared to Fig. 2a, the full width at half maximum (FWHM) of peaks is wider and indicates the smaller sized nanoparticles according to Braggs rule at 56 °C is formed. Also, the intensity of the (110) peak decreased which indicated that the dominant hexagonal phase is more stable than the monoclinic phase at 56°C.

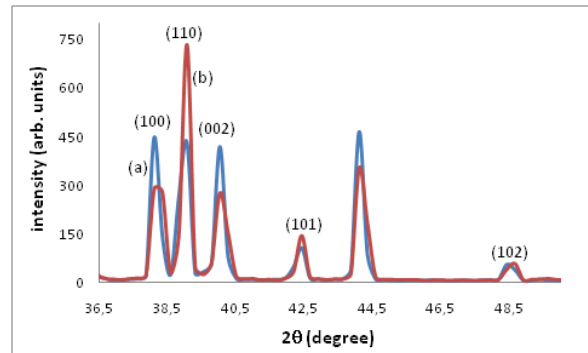


Fig. 2. XRD patterns of ZnO:Cu prepared at 76 °C (a) Cu=0.45×10⁻⁴ % (b) Cu=0.03%

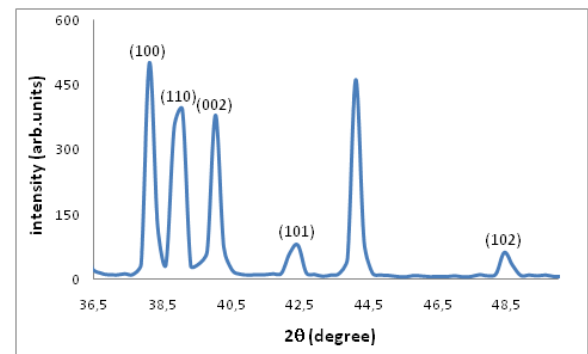


Fig. 3. XRD pattern of ZnO:Cu (Cu=0.45×10⁻⁴ %) prepared at 56°C.

The broadening of peaks is related to small crystallite sizes and lattice strains:

$$B_r = B_{\text{crystallite}} + B_{\text{strain}} \quad (1)$$

The using Equation (2) for calculated B_r :

$$B_r = \sqrt{(B_0 - B_i)^2 + (B_0^2 - B_i^2)} \quad (2)$$

Where, the remaining width B_r is due to the combined effects of crystallite size and lattice strain, if the observed x-ray diffraction peak has a width B_0 and the width due to instrumental effects is B_i ($B_i=1.74 \times 10^{-3}$ rad).

The quantity $B_r \cos \theta$ can be plotted versus $\sin \theta$ according to Eq. (3):

$$B_r \cos \theta = \eta \sin \theta + \frac{K\lambda}{L} \quad (3)$$

Where k is a constant ($k=0.94$), λ is X-ray wavelength (CuK α , $\lambda=0.15406$ nm), L is crystallite sizes. The plot of $B_r \cos\theta$ against $\sin\theta$, can be used to calculate from the intercept $K\lambda/L$ and the slope η the crystallite size (L) and lattice strain (η), respectively [27, 28]. Fig. 4 and Fig. 5 shows plot of $B_r \cos\theta$ versus $\sin\theta$ for ZnO:Cu at 76 °C and 56 °C respectively. The values of lattice strain and crystallite size for ZnO:Cu thin films were shown in Table 1. The results shown, the full width at half maximum (FWHM) is more at 56 °C. Thus, the nanocrystal size is smaller and with lower lattice strains.

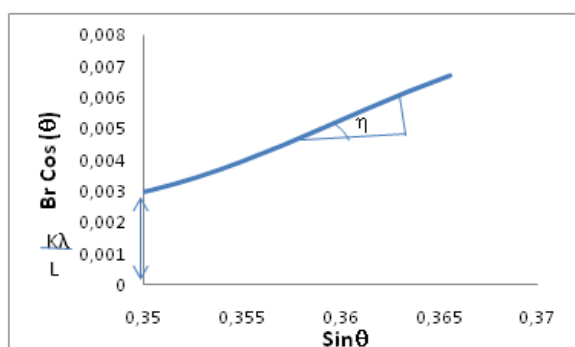


Fig. 4. Plot of $B_r \cos\theta$ versus $\sin\theta$ for ZnO:Cu ($\text{Cu}=0.45 \times 10^{-4}$ %) at 76°C.

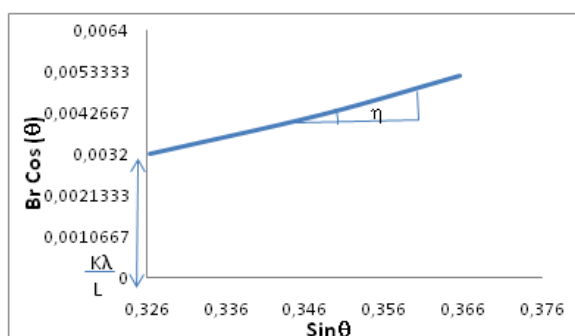


Fig. 5. Plot of $B_r \cos\theta$ versus $\sin\theta$ for ZnO:Cu ($\text{Cu}=0.45 \times 10^{-4}$ %) at 56 °C.

Table 1: The values of lattice strains (η) and crystallite sizes (L) of ZnO:Cu

Temperature (°C)	(η)	L (nm)
56	0.0095	43.32
76	0.0101	46.21

Surface morphology by scanning electron microscopy (SEM)

The surface morphology of the undoped and Cu-doped ZnO thin film deposited on glass substrates at 56-76°C were studied by scanning electron microscope. Fig. 6 show the SEM images of ZnO thin film prepared at 76 °C. It exhibits a sheet like structure. Also SEM studies indicated that the

product was hexagonal phase of ZnO thin film, which good agreement with the XRD results.

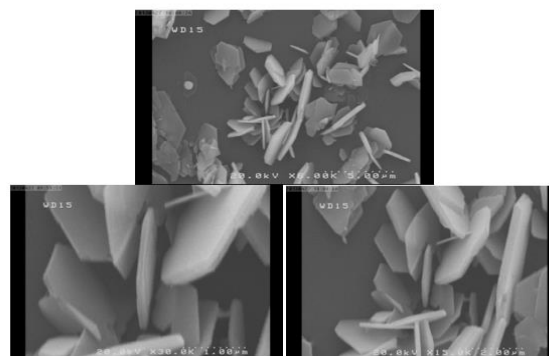


Fig. 6. SEM images of ZnO thin films.

In Figs. 7-8 the SEM images show ZnO:Cu thin film (seed layer). SEM studies indicated that the product was hexagonal and monoclinic phase attributed to ZnO and CuO respectively, which good agreement with the XRD results. Fig. 7 shows the SEM images of ZnO:Cu film deposited at 76 °C from different deposition times. The nanocrystal size increased with increasing deposition time. The size of ZnO:Cu nanocrystals due to seed layer is greater than ZnO pure (at the same time, compared with Fig.6), Also, after 8 hours deposition were completed hexagonal nanocrystals shown in the Fig. 7d. The photoluminescence peak intensities optimized with 0.45×10^{-4} at % Cu doped ZnO at 76 °C (Fig. 7b).

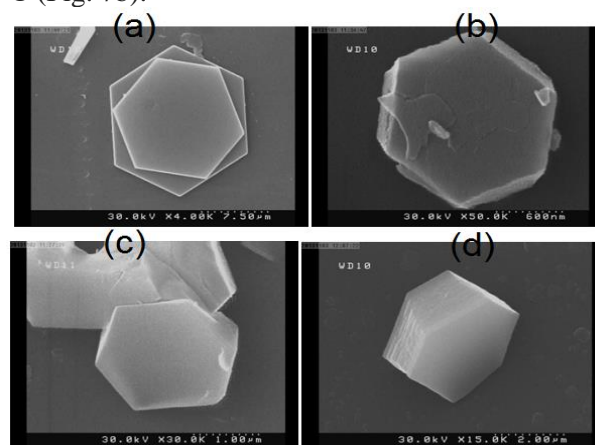


Fig. 7. SEM images of ZnO:Cu ($\text{Cu}=0.45 \times 10^{-4}$ %) thin films prepared at different deposition times and at 76 °C (a) 1.5 h (b) 2.5 h (c) 4 h and (d) 8 h.

Fig. 8 show the SEM images of ZnO:Cu films deposited at 76 °C for different Cu doped. As can be seen, the images show that the monoclinic phase of copper oxide in comparison with Fig.7 is formed. Also, photoluminescence results show that increasing of copper concentration was decreased the intensity of emission due to electron capture by copper ions.

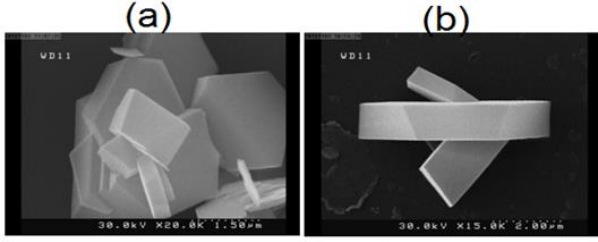


Fig. 8. SEM images of ZnO:Cu thin films prepared at different Cu concentrations and at 76°C for 4 h (a) Cu=0.004 % and (b) Cu=0.03 %

Optical properties

The energy gap of semiconductors represents fundamental physical aspects that characterize their optical and electronic properties. The optical energy (E_g) determines the threshold for absorption of photon in semiconductor. The energy gap of all the films is determined from the absorption coefficient (α) which can be calculated from the transmittance (T) of the ZnO thin films. The absorption coefficient (α) is calculated by the following formula:

$$\alpha = \frac{1}{d} \ln \frac{1}{T} \quad (4)$$

where d is the film thickness. The absorption edge was analyzed by the following equation [29]:

$$(\alpha hv)^2 = A (hv - E_g) \quad (5)$$

where A is a constant, hv is the incident photon energy and E_g is the optical band gap energy. Based on the Eq. (5) the plots of $(\alpha hv)^2$ as a function of incident photon energy (hv) were obtained for the undoped and Cu-doped ZnO thin films and are shown Fig. 9, 10, and 11 indicate that the films are direct transition-type semiconductors. The linear portion is extrapolated to $\alpha=0$, on energy axis, which corresponds to the E_g undoped and Cu-doped ZnO thin films shown in Table 2. Kinetic parameters (temperature and time deposition) are influenced on the band gap energy, where with increasing temperature and deposition time the band gap energy of films is decreased.

Brus for the first time considered the correction of exciton energy and energy of the quantum confinement in the Schrödinger wave equation. So using equation (6) one can calculate the radius (R) of the ZnO nanocrystals using following equation [30-32]:

$$E_g^{NC} = E_g^B + \frac{h^2}{8R^2} \left(\frac{1}{m_e} + \frac{1}{m_h} \right) - \frac{1.8e^2}{4\pi\epsilon R} \quad (6)$$

where E_g^{NC} is band gap energy of nanocrystals, E_g^B is band gap energy of the bulk, h is Planck

constant, e is electric charge of electron, ϵ is relative dielectric constant ($\epsilon=8.66$ for wurtzite ZnO), m_e and m_h is electron effective mass and hole effective mass respectively ($m_e=0.28m_0$ and $m_h=0.78m_0$ for wurtzite ZnO), m_0 is the electron mass at rest [33-35]. The nanocrystals radiuses for undoped and Cu-doped ZnO thin films are shown in Table 2. With increasing deposition kinetic parameters, the nanocrystals radius of the undoped and Cu-doped ZnO thin films increased due to quantum effects.

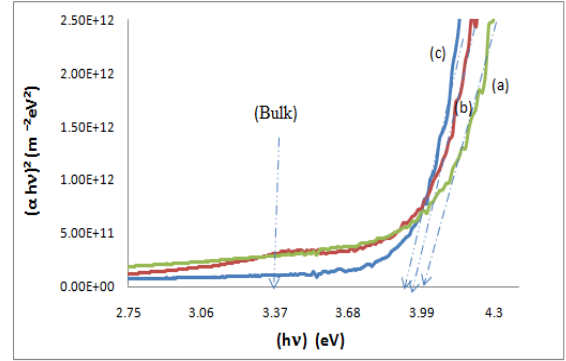


Fig. 9 Plot of $(\alpha hv)^2$ versus hv for the ZnO thin films prepared at 60°C and at different deposited times (a) 3 (b) 6 (c) 8 h.

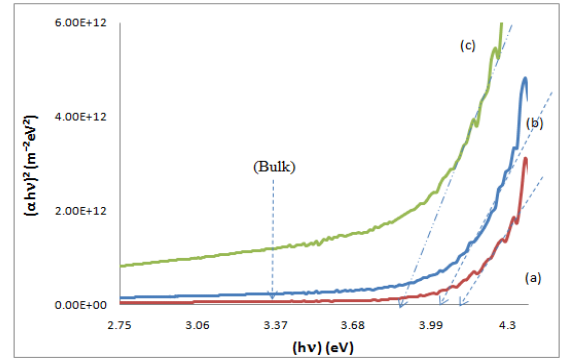


Fig. 10 Plot of $(\alpha hv)^2$ versus hv for the ZnO thin films prepared at different deposition temperatures (a) 45 (b) 60 (c) 76 °C.

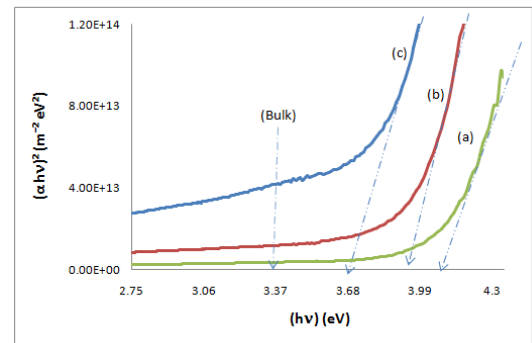


Fig. 11 Plot of $(\alpha hv)^2$ versus hv for the ZnO:Cu thin films prepared at 76 °C and at different deposited times (a) 1.5 (b) 3 (c) 4h.

PHOTOLUMINESCENCE STUDIES

Fig. 12 shows the photoluminescence (PL) spectra of the undoped and Cu-doped ZnO prepared at various Cu concentrations and at 76°C. The PL measurements were performed at excitation wavelength of 330 nm. Two emission bands are apparently observed in PL spectra of the undoped and Cu-doped ZnO thin films: one is blue luminescence centering at 491 nm, and the other is deep level-green luminescence at 521 nm, which correspond to excitonic emission. The concentration of the Cu²⁺ ions is another factor which is necessary to be optimized. Just as Fig. 12 shows, PL intensity increased with increasing of Cu²⁺ concentration and reached a maximum at 0.45×10⁻⁴ at % Cu doped ZnO. Increasing of the dopant content would rationally increase the number of dopant-related states in the band gap and subsequent enhancement of the recombination process through these states [36]. Nonetheless, addition of Cu²⁺ dopant ions, more than the 0.45×10⁻⁴ %, gives rise to appearance of concentration quenching effect due to non-radiative transitions between the neighboring dopant ions. Many researchers report this effect in transition metal-doped II-VI QDs [37-39].

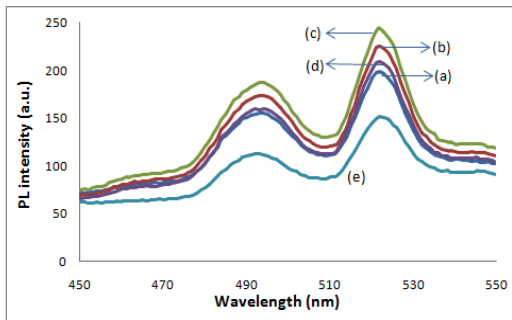


Fig. 12. PL spectra (a) pure ZnO and Cu doped ZnO prepared at different Cu concentrations (b) 0.5×10⁻⁴, (c) 0.45×10⁻⁴, (d) 0.03 and (e) 0.5.

Fig. 13 shows the PL spectra of ZnO:Cu thin films prepared at different temperatures and at 4 h deposition. The intensity of emission increases with increasing of temperature, which may be originate from the intrinsic defects such as oxygen vacancy [40] and oxygen interstitials [41]. Fig. 14 shows the PL spectra of ZnO:Cu thin films prepared at different deposition times and at 76 °C. The crystal lattice defects decrease with increasing deposition time and become more perfect in the nanocrystals. So, the photoluminescence peak intensities decreased with increasing deposition time.

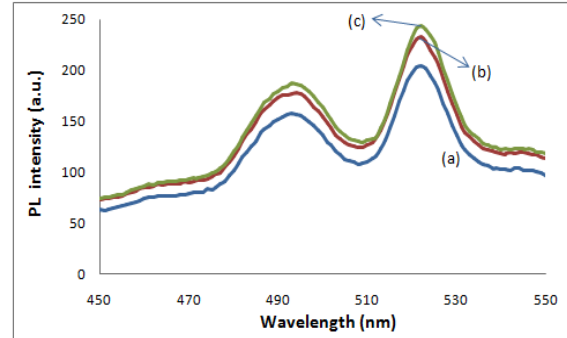


Fig. 13 PL spectra of ZnO:Cu (Cu=0.45×10⁻⁴) thin films prepared at different temperatures (a) 56 °C, (b) 66 °C and (c) 76 °C for 4 h deposition.

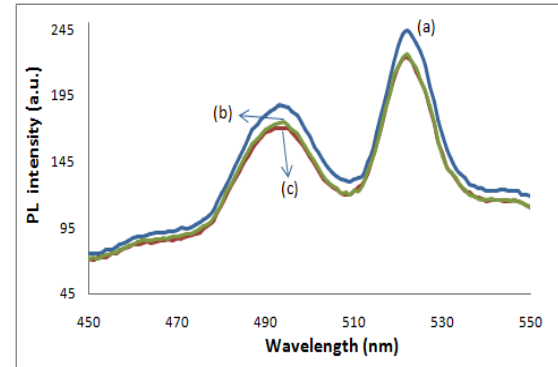


Fig. 14. PL spectra of ZnO:Cu (Cu=0.45×10⁻⁴) thin films prepared at temperature 76 °C and after different time (a) 4h (b) 6h (c) 8h.

Table 2: Band gap energy (E_g^{NC}) values and nanocrystals radius (R) of the undoped and Cu-doped ZnO thin films

Sample	deposition temperature (°C)	deposition times (h)	Cu doped (%)	E_g^{NC} (eV)	R (nm)
ZnO	60	3	-	3.96	1.75
ZnO	60	6	-	3.93	1.8
ZnO	60	8	-	3.91	1.83
ZnO	45	5	-	4.10	1.58
ZnO	60	5	-	4.00	1.7
ZnO	76	5	-	3.86	1.93
ZnO	76	2	-	3.97	1.74
ZnO:Cu	76	2	0.45×10 ⁻⁴	3.94	1.79
ZnO:Cu	76	1.5	0.45×10 ⁻⁴	4.05	1.63
ZnO:Cu	76	3	0.45×10 ⁻⁴	3.91	1.83
ZnO:Cu	76	4	0.45×10 ⁻⁴	3.70	2.35

Elemental analysis

Chemical composition of ZnS:Ni thin films were analyzed by ICP-AES and FTIR measurements. Table 3 shows the Cu/Zn atomic percent ratios for the ZnO:Cu films prepared at different Cu concentration and at 76 °C. ICP-AES analysis shows, with increasing in Cu precursor, the Cu/Zn atomic ratios in the films increase. The co-deposition of ZnO and CuO quite difficult, because of the CuO ($K_{sp}=1\times 10^{-19.7}$) is much less soluble

than the ZnO ($K_{sp}=1\times 10^{-16.7}$). Therefore, during the deposition process, the concentration of Cu precursor should be very lower than the concentration of Zn precursor. Hence, at very low amount of Cu precursor, ZnO can form the main phase, whereas Cu^{2+} ions are present as an impurity and can be incorporated gradually into the ZnO crystal lattice, depending on the concentration of Cu precursor.

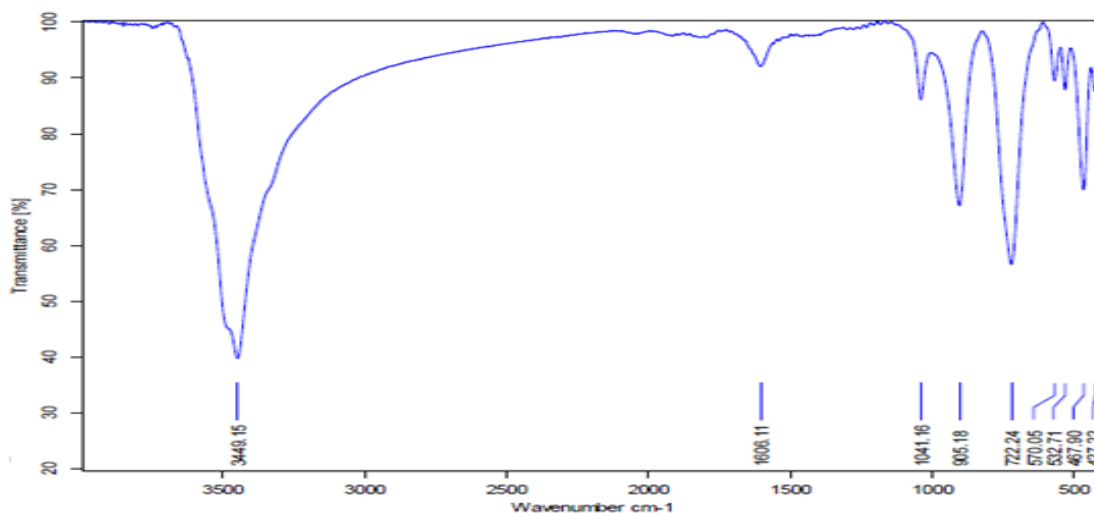


Fig. 15. FTIR spectra of ZnO:Cu thin films prepared at 76 °C for 8 h.

Table 3: The atomic ratio values of ZnO:Cu films prepared at 76 °C for 4 h.

Cu doped (%)	Cu:Zn (%)
0.5×10^{-5}	0.041
0.45×10^{-4}	0.29
0.4×10^{-4}	0.55
0.4×10^{-2}	1.24
0.03	3.57

In order to investigate the presence of organic compounds as impurities in the ZnO:Cu thin films, the FTIR spectrum of films was obtained and studied. Fig. 15 shows the FTIR spectrum of ZnO:Cu thin films prepared at 76 °C for 8 h. The various vibration bonds of ZnO:Cu thin films were listed in Table 4. FTIR spectrum shows two main peaks in 427.22 and 532.71 cm^{-1} which are attributed to ZnO and CuO bonds, respectively [42-44]. Some very weak peaks related to partial decomposition of $C_6H_{12}N_4$ molecules are observed in the films. Also, two peaks were observed in the FTIR spectrum, one very weak peak at 1606.11 cm^{-1} and another broad peak at 3449.15 cm^{-1} that must be related to the stretching and bending modes of trace amounts of adsorbed water on the film.

Table 4: The vibration bonds of the ZnO:Cu thin films

Wavenumber (cm^{-1})	bond
3449.15	OH
1606.11	OH
1041.16	C-N
905.18	C-H
722.24	C-C
532.71	CuO
476.9	Zn(OH) ₂
427.22	ZnO

CONCLUSIONS

Undoped and Cu-doped ZnO thin films have been prepared by chemical bath deposition method with potential applications in optoelectronics and solar cell engineering. The effect of Cu:Zn molar, temperature and deposition time on the structural, optical and photoluminescence properties of the ZnO:Cu thin films were investigated. The XRD patterns and SEM images showed that the films consisted of small ZnO:Cu nanocrystals, showing quantum size effects. The green emission at 521 nm of the ZnO:Cu films can be related to the d-d optical transitions of Cu^{2+} luminescent centers formed in the ZnO host crystals. Furthermore, with

increase in the Cu concentration, the PL emission intensity of the ZnO:Cu films is improved that can be attributed to the decrease of crystal defects density and also an enhancement in number of the radiation centers.

REFERENCES

1. B.K. Meyer, *Phys. Status Solidi B*, **241**, 231 (2004).
2. O. Madelung (ed), *Data in Science and Technology: Semiconductors*, Springer, Berlin, 1992.
3. S.H. Nam, M.H. Kim, D.G. Yoo, S.H. Jeong, D.Y. Kim, N.E. Lee, J.H. Boo., *Surf. Rev. Lett.*, **1**, 121 (2010).
4. Y. Hamesa, Z. Alpaslan, A. Kosemen, S.E. San, Y. Yerli, *Sol. Energy.*, **84**, 426 (2010).
5. R. Khan, H.W. Ra, J.T. Kim, W.S. Jang, D. Sharma, Y.H. Im, *Sens. Actuators B Chem.*, **150**, 389 (2010).
6. S. Singh, M.S.R. Rao, *Phys. Rev. B*, **80**, 045210 (2009).
7. S. Cho, J. Ma, Y. Kim, Y. Sun, *App. Phys. Lett.*, **75**, 2761 (1999).
8. D.M. Bagnall, Y.F. Chen, Z. Zhu, *Appl. Phys. Lett.*, **70**, 2230 (1997).
9. Z.K. Tang, G.K.L. Wong, P. Yu, *Appl. Phys. Lett.* **72**, 3270 (1998).
10. X.T. Zhang, Y.C. Liu, Z.Z. Zhi, *J. Lumin.*, **99**, 149 (2002).
11. S.M. Chung, S.H. Han, K.H. Son, *J. Lumin.*, **114**, 227 (2005).
12. K. Vanheusden, W.L. Warren, C.H. Seager, D.R. Tallant, J.A. Voigt, B.E. Genade, *J. Appl. Phys.*, **79**, 7983 (1996).
13. P. Che, J. Meng, L. Guo, *J. Lumin.*, **122**, 168 (2007).
14. Z.F. Liu, F.K. Shan, J.Y. Sohn, S.C. Kim, G.Y. Kim, Y.X. Li, Y.S. Yu, *J. Electroceram.*, **13**, 183 (2004).
15. D.J. Qiu, H.Z. Wu, A.M. Feng, Y.F. Lao, N.B. Chen, T.N. Xu, *Appl. Surf. Sci.*, **222**, 263 (2004).
16. F.K. Shan, B.I. Kim, G.X. Liu, Z.F. Liu, J.Y. Sohn, W.J. Lee, B.C Shin, Y.S. Yu, *J. Appl. Phys.*, **95**, 4772 (2004).
17. P. Dahany, V. Fleurovy, P. Thurianz, R. Heitzz, A. Hoffmannz, I. Broserz, *J. Phys.: Condens. Matter.*, **10**, 2007 (1998).
18. A. Ohtomo, A. Tsukazaki, *Semicond. Sci. Technol.*, **20**, 1 (2005).
19. K. Ellmer, *J. Phys. D: Appl. Phys.*, **33**, 17 (2000).
20. S. Fay, U. Kroll, C. Bucher, E.V. Sauvain, A. Shah, *Sol. Energy Mater. Sol. Cells*, **86**, 385 (2005).
21. A. Drici, G. Djeteli, G. Tchangbedji, H. Derouiche, K. Jondo, K. Napo, J.C. Bernede, S.O. Djobo, M. Gbagba, *Phys. Status Solidi*, **201**, 1528 (2004).
22. A. Goudarzi, G. Motedayen Aval, R. Sahraei, H. Ahmadpoor, *Thin Solid Films*, **516**, 4953 (2008).
23. R. Sahraei, G. Motedayen Aval, A. Baghizadeh, M. Lamehi-Rachti, A. Goudarzi, M.H. Majles Ara, *Mater. Lett.*, **62**, 4345 (2008).
24. M. Wang, L. Zhang, *Mater. Lett.*, **63**, 301 (2009).
25. H. Mcmurdie, *Powder Diffraction*, **1**, 76 (1986).
26. J. Langford, D. Louer, *J. Appl. Crystallogr.*, **24**, 149 (1991).
27. C. Suryanarayana, M. Grant Norton, *X-Ray Diffraction A Practical Approach*, Plenum Press. New York and London, 1998.
28. R. Sahraei, S. Noshadi, A. Goudarzi, *RSC Adv.*, **5**, 77354 (2015).
29. S. Major, A. Banerjee, K.L. Chopra, K.C. Nagpal, *Thin Solid Films*, **143**, 19 (1986).
30. L.E. Brus, *J. Chem. Physics*, **80**, 4403 (1984).
31. G. Hodes, S. Gorer, *J. Phys. Chem.*, **98**, 5338 (1994).
32. R. Sahraei, G. Motedayen Aval, A. Goudarzi, *J. Alloys Compd.*, **466**, 488 (2008).
33. S.J. Pearton, D.P. Norton, K. Ip, Y.W. Heo, T. Steiner, *Progress In Materials Science*, **50**, 293 (2005).
34. S. Adachi, *Properties of Group-IV, III-V and II-VI Semiconductors*, John Wiley and Sons, Ltd, West Sussex, England, 2005.
35. H. Hartnagel, A.L. Dawar, A.K. Jain, C. Jagadish, *Semiconducting transparent thin films*, Institute of Physics Publishing, Bristol and Philadelphia, 1995.
36. R. Sahraei, S. Darafarin, *Spectrochim. Acta Part A*, **149**, 941 (2015).
37. R. Sahraei, S. Darafarin, *J. Lumin.*, **149**, 170 (2014).
38. Y. Song, Y. Li, X. Wang, X. Su, Q. Ma, *RSC Adv.*, **5**, 6271 (2015).
39. S. Darafarin, R. Sahraei, A. Daneshfar, *J. Alloys Compd.*, **658**, 780 (2016).
40. K. Vanheusden, C.H. Seager, W.L. Warren, D.R. Tallant, J.A. Voigt, *Appl. Phys. Lett.*, **68**, 403 (1996).
41. S.A. Studenikin, N. Golego, M. Cocivera, *J. Appl. Phys.*, **84**, 2287 (1998).
42. J.R. Ferraro, *Low-Frequency Vibrations of Inorganic and Coordination Compounds*, Plenum, New York, 1971.
43. R. Sahraei, A. Daneshfar, A. Goudarzi, S. Abbasi, M.H. Majles Ara, F. Rahimi, *J. Mater. Sci.: Mater. Electron.*, **24**, 260 (2013).
44. M.R. Johan, M.S. MohdSuan, N.L. Hawari, H.A. Ching, *Int. J. Electrochem. Sci.*, **6**, 6094 (2011).

Research on extinction performance of expanded graphite at band of 3 millimeter wave

T. Shen*, B. Wang, M. Yao, W. Yang

Xi'an Research Institute of High Technology, Shannxi China, 710025

Received June 3, 2016, Revised September 16, 2016

Expanded graphite is a kind of materials with good capability of electromagnetic wave absorption. In order to explore the extinction and scattering characteristics of expanded graphite in 3mm wavelength passive interference, the integral equation and the formula of extinction, scattering, absorption and backscattering cross sections are established based on the electromagnetic field theory. The method of moment (MOM) is used to solve the integral equation. The relationships between infrared extinction cross section of expanded graphite and the conductivity, magnetic permeability, the fiber length and diameter are analyzed and calculated. Theoretical calculation results show that the factors of length, radius, conductivity and magnetic permeability are closely related with the performance of expanded graphite in extinction, scattering, absorption cross section and back scattering in 3mm band. And the properties can be improved when the conductivity and magnetic permeability of the expanded graphite are increased properly. This research provides a valuable insight into the improvement of interference performance of expanded graphite in 3 millimeter wave.

Key words: Expanded graphite, Scattering, Absorption, Infrared extinction.

INTRODUCTION

Expanded graphite is high-temperature puffing products of graphite intercalation compound, which has unique structure, good floatation and conductivity. In recent years, expanded graphite is widely used in the military field as shielding interference material in millimeter wave band. Compared with the traditional interference materials, such as chaff, foil and glass fiber coated with aluminum, expanded graphite has the advantages of masking jamming characteristics in wide band (can work in 3 mm and 8 mm simultaneously), dispersion and environment coordination. At present, the research on expanded graphite interfering millimeter wave at home and abroad is mainly aimed at the experimental study on attenuation performance. Based on the theory of computational electromagnetism, the research on extinction, scattering characteristics and influence factors of expanded graphite in millimeter wave band is necessary, which can provide a theoretical basis for the improvement of the extinction performance.

THE INTEGRAL EQUATION FOR EXPANDED GRAPHITE

Pocklington integral equation

Expanded graphite external appearance presents

cylinder as follow Pic.1. Suppose expanded graphite particle radius as a , length as $2h$, conductivity as σ , relative permeability as μ_r , relative dielectric constant as ϵ_r . When plane electromagnetic wave irradiates expanded graphite, its surface produces current flow $\mu(s)$ and the current flow radiation can produce scattered field. Suppose the incident angle of electromagnetic wave as θ_i , scattering angle as θ , as follow Figure 1-2.

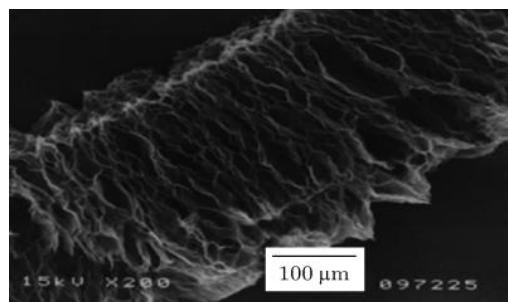


Fig. 1. Expanded graphite external appearance.

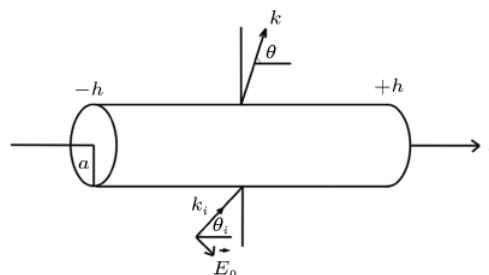


Fig. 2. Expanded graphite and incident electromagnetic wave angle.

* To whom all correspondence should be sent:
E-mail: luckyshentao@163.com

According to Maxwell equation and Pocklington integral equation, the expanded graphite surface induced current equation can be get as follows [1][2].

$$E_0\sqrt{1-q^2}e^{isq} = \int_{-x}^x u(s')G(s,s')ds' + \int_{-x}^x E(s')F(s,s')ds' \quad (1)$$

$$q = \cos \theta_i, p = \cos \theta, s = kz, y = ka, x = kh, k = 2\pi / \lambda \quad (2)$$

$$G(s,s') = [1 + \frac{\partial^2}{\partial s^2}]g(s,s'), F(s,s') = \frac{y^2}{2R} \frac{\partial}{\partial R} g(s,s') \quad (3)$$

$$g(s,s') = \frac{e^{iR}}{R}, R = \sqrt{(s-s')^2 + y^2} \quad (4)$$

Obviously, to finite length expanded graphite, the particle terminal induced current disappeared. Then $u(\pm x) = 0$, equation (1) is changed into equation (5) as following.

$$E_0\sqrt{1-q^2}e^{isq} = \int_{-x}^x u(s')G(s,s')ds' + E(s) \quad (5)$$

If the electromagnetic wave is vertical incidence, then $q = 0$. The surface electric field is equal to the arithmetic product of surface impedance and surface induced current.

$$E(s) = \eta_s u(s) \quad (6)$$

If the electromagnetic wave is not vertical incidence, then

$$E_0\sqrt{1-q^2}e^{isq} = \int_{-x}^x u(s')[G(s,s') + \eta_s F(s,s')]ds' \quad (7)$$

Moments method solution

The method of moment (MOM) is used to solve the integral equation. Dividing expanded graphite into N parts along with Z axis, the unknown induced current is expanded by pulse primary function as following [3].

$$P_i(s) = \begin{cases} 1, & s \in i, \\ 0, & \text{others} \end{cases} \quad (8)$$

$$u(s) = \sum_{i=1}^N \alpha_i P_i(s) \quad (9)$$

(9) is substitute in (8), Select point matching weight function to multiply formula(7),

$$\sqrt{1-q^2}e^{isq} = \sum_{i=1}^N \alpha_i \int_{cell_i} [G(s_j, s') + \eta_s F(s_j, s')]ds', i, j = 1, 2, 3, \dots, N \quad (10)$$

The induced current distribution inside the expanded graphite can be obtained by solving the matrix equation above.

In far field condition, According to formula (9), the expanded graphite scattered field is [4]

$$f(q,p) = \sqrt{1-p^2} \int_{-x}^x ds [u(s) - (\frac{ka}{2})^2 E(s)] \exp(-ips) \quad (11)$$

(6) is substitute in (11)

$$f(q,p) = \sqrt{1-p^2} [1 - (\frac{ka}{2})^2 \eta_s] \int_{-x}^x ds u(s) \exp(-ips) \quad (12)$$

To unit amplitude incidence wave, the scattered

field can be obtained from above and the expanded graphite scattering cross section is:

$$\sigma_s(q) / \lambda^2 = 2\pi \int_0^\pi |f(q,p)|^2 dp \quad (13)$$

the expanded graphite absorption cross section is

$$\sigma_a(q) / \lambda^2 = -\frac{1}{\pi} \text{Im}(\eta_s) \int_{-x}^x ds |u(s)|^2 \quad (14)$$

Extinction cross section is composed by absorption cross section and scattering cross section, that is

$$\sigma_e = \sigma_a + \sigma_s \quad (15)$$

Calculation parameter solution

The dielectric constant of expanded graphite is[5]

$$\varepsilon = \varepsilon_0 \varepsilon_r + \varepsilon_0 (\varepsilon' - j\varepsilon'') \quad (16)$$

Adopting four-point probe method, the average electric conductivity in normal room-temperature is about $1.13 \times 10^4 \text{ S} \cdot \text{m}^{-1}$.

The magnetic conductivity is

$$u = u_0 u_r + u_0 (u' - ju'') \quad (17)$$

Common expanded graphite is not magnetism, in calculation relative permeability $u_r = 1$.

NUMERICAL CALCULATION AND DISCUSSION

According to theory above, the code of expanded graphite scattering cross section, absorbing cross section, extinction cross section and RCS model are programmed based on Matlab [6][7]. The relationships between each cross section and grain size, electric conductivity and magnetic conductivity of expanded graphite are analyzed and calculated [8].

Effect of expanded graphite length

To verify the method valid of this paper, it is compared with the calculus of variation about conduction fiber scattering cross section [3]. The calculation parameters are followed:

Frequency $f = 94.5 \text{ GHz}$, angular frequency $\omega = 2\pi f$, wavelength $\lambda = 3.17 \text{ mm}$, fiber radius $a = 0.12 \text{ mm}$, dielectric constant $\varepsilon = 8.85 \times 10^{-12} (15.54 - 4.76i)$, electric conductivity $\sigma = 1 \times 10^4 \text{ S} \cdot \text{m}^{-1}$, magnetic conductivity $\mu = \mu_0 \mu_r = 4\pi \times 10^{-7}$, incidence angle $\theta = \pi/4$, length variation range $h = 0.3 - 1.8 \text{ mm}$. The relationship between each cross section and particle length is followed as Figure 3.

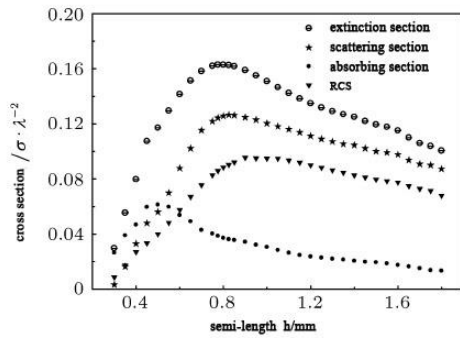


Fig. 3. Relationship between each cross section and expanded graphite particle length.

From Figure 3 above, to 3mm incident wave, when the length of expanded graphite is short, the value of each cross section is small. The absorption effect is most. The longer the length of expanded graphite is, the larger the each cross section value is. When the length of expanded graphite is longer than 1mm, the scattering effect is most. When the length is 1 mm, 1.55 mm and 1.65 mm individually, the value of the absorbing cross section, scattering cross section and extinction cross section is the maximizing. With the length of expanded graphite increases, the absorbing cross section, scattering cross section and extinction cross section decrease gradually.

Effect of expanded graphite radius

The expanded graphite is long column, its grain size includes the length and the radius. The calculation parameters are followed as 3.1 above. Suppose the length $h = 0.75$ mm, the radius variation range $a = 0.01 \div 0.24$ mm. The relationship between each cross section and particle radius is followed as Figure 4.

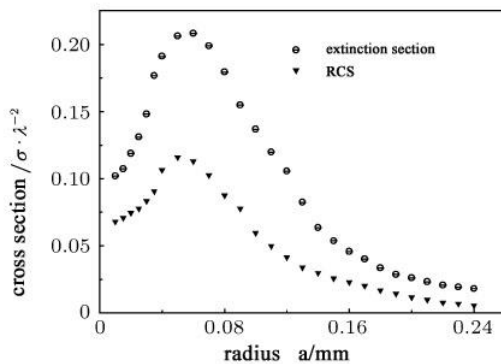


Fig. 4. Relationship between 3mm wave extinction cross section, RCS and expanded graphite radius.

From Figure 4 above, extinction cross section changes with the expanded graphite radius.

When the expanded graphite radius is small value, the extinction cross section and RCS gradually enhances with expanded graphite radius. The extinction peak value appears on the

corresponding radius $a = 0.05$ mm. After the peak value, the extinction cross section and RCS gradually decrease with expanded graphite radius increment. That is because the expanded graphite extinction effect on millimeter wave includes not only scattering effect, but also absorbing effect. So, the expanded graphite radius is too thin or too thick, that decreases the extinction cross section and RCS.

Effect of expanded graphite electric conductivity

The interference materials extinction effect on electromagnetic wave is combined with scattering effect and absorbing effect. It is decided by the interference materials form, dimension and electromagnetic character commonly. The calculation parameters are followed as 3.1 above. Suppose the length $h = 0.75$ mm, the electric conductivity variation range $\sigma = 2.5 \times 10^2 - 1 \times 10^6$ S \cdot m⁻¹. The relationship between each cross section and expanded graphite electric conductivity is followed as Figure 5.

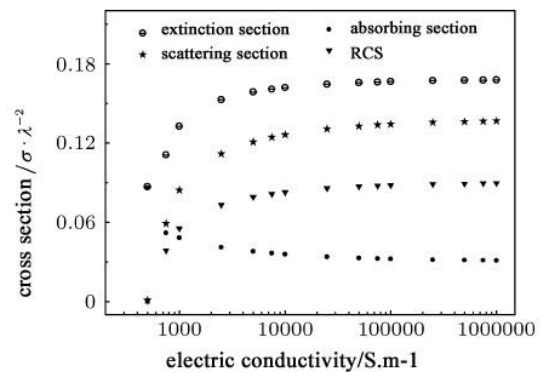


Fig. 5. Relationship between 3mm wave extinction cross section, RCS and expanded graphite electric conductivity.

From Figure 5 above, the absorbing cross section decreases with the expanded graphite electric conductivity increasing. When the electric conductivity is small value, the absorbing effect is the main extinction effect. To extinction cross section, scattering cross section and RCS, the values increase with the electric conductivity increasing.

Effect of expanded graphite magnetic conductivity

The expanded graphite calculation parameters are followed as 3.1 above. Suppose the length $h = 0.75$ mm, the magnetic conductivity variation range $\mu = (1-5) \times 4\pi \times 10^{-7}$ (H/m). The relationship between each cross section and expanded graphite magnetic conductivity is followed as Figure 6.

From Figure 6 above, when the magnetic conductivity is small value, the absorbing cross section increases with the expanded graphite magnetic conductivity increment. When the

magnetic conductivity reaches 1.6, the absorbing cross section appears peak value. After the peak value, the absorbing cross section decrease with expanded graphite magnetic conductivity increment.

To extinction cross section, scattering cross section and RCS, the values increase with the magnetic conductivity increasing. When the relative

magnetic conductivity is greater than 2, the influence on expanded graphite extinction, scattering performance and RCS are not obvious.

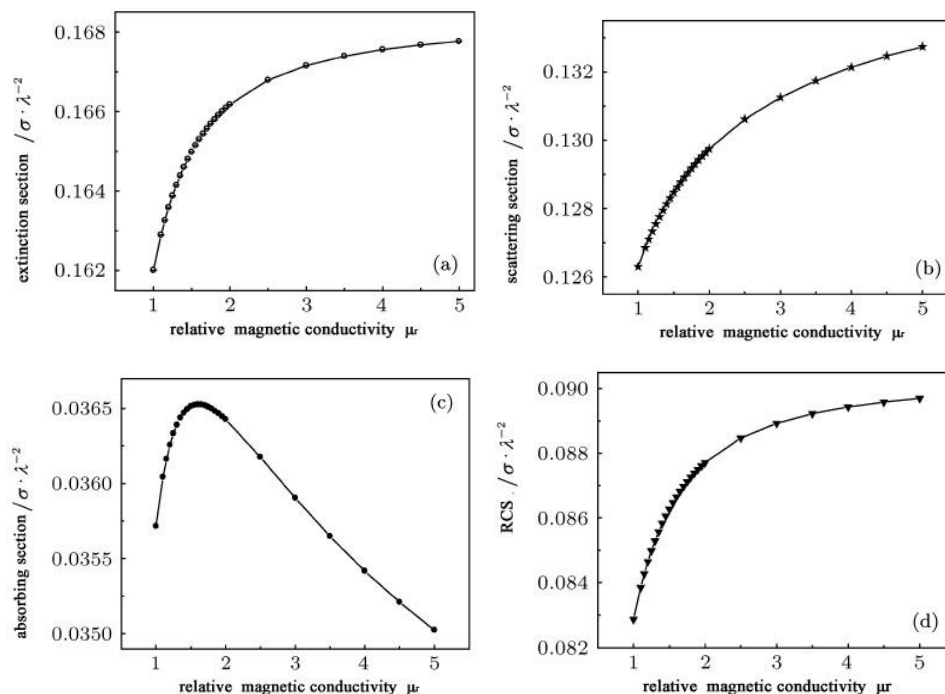


Fig. 6. Relationship between 3mm wave extinction cross section, RCS and relative magnetic conductivity.

CONCLUSION

(1) The expanded graphite extinction performance on 3 mm wave agrees with semi-wavelength theory and the optimum extinction radius is 0.05 mm. When particle length is near the semi-wavelength, the extinction and scattering performance are most intensive. If the expanded graphite radius is too thin or too thick, it can abate the extinction and scattering performance.

(2) The expanded graphite extinction and scattering performance increase with the electric and magnetic conductivity increment. When the electric conductivity is greater than $1 \times 10^4 \text{ S} \cdot \text{m}^{-1}$ and the magnetic conductivity is greater than 2, the influence on expanded graphite extinction and scattering performance is not obvious.

(3) The calculation result shows that the extinction and scattering performance on 3 mm wave can be intensified by controlling expanded

graphite particle size, increasing expanded graphite electric and magnetic conductivity.

REFERENCES

1. H. Guan, G.P. Pan, L. Jiang, *J. Infrared Millimeter Waves*, **23**, 72 (2004).
2. I.M. Afanasov, V.T. Gustaaf, *Carbon*, **49**, 352 (2011).
3. Y.H. Zhang, Q. Lin, Y. Fan, *J. Infrared Millimeter Waves*, **30**, 38 (2011).
4. M.S. Zhou, C.J. Li, M. Xu, *J. Inorg. Mater.*, **22**, 509 (2007).
5. H. Ren, F.Y. Kang, Q.J. Jiao, *New Carbon Mater.*, **21**, 24 (2006).
6. P.C. Waterman, *J. Opt. Soc. America*, **22**, 2430 (2005).
7. A. Sharhabeel, *Electromagnetic scattering and absorption by a finite conducting thin fiber*, New Mexico State University, 2006.
8. A. Sharhabeel, *Trans..Antennas & Propagation*, **55**, 1856 (2007).

Microstructure interpretation of macromechanical behaviour of poly urethane eletrospun nanofiber webs

A.S. Maryan^{1*}, M. Gorji²

¹Department of Chemistry, Ardabil Branch, Islamic Azad University, Ardabil, Iran

²Department of Textile Engineering, Amirkabir University of Technology, Hafez Avenue, Tehran, 15914, Iran.

Received June 18, 2016, Revised September 10, 2016

In this study, the effect of electrospinning duration, polymer concentration, solvent mixture and fiber orientation on stress-strain behavior of thermoplastic polyurethane (TPU) nanofiber web is investigated. The tensile behavior of PU network obeys nonlinear elastic that were interpreted in regard to the polymer molecular chain and network morphologies. With increasing electrospinning duration, polymer content and increasing of DMF in THF/DMF solvent, fiber diameter, thickness of fiber network and tensile strength increased but the behavior of elongation was different. Also, the results show that with increasing electrospinning duration, thickness of nano-fiber web increased nonlinearly.

For investigating the effect of fiber orientation, the stress strain curve of PU membrane is compared with PU yarn. The results show that initial hardness of stress-strain curve of PU mat is due to the fiber oriented normal to elongation direction.

The initial hardness of stress strain curve is the results of the fibers normal to the elongation direction.

Keywords: Electrospinning, Nanofiber, Mechanical properties, Polyurethane

INTRODUCTION

Investigation of the Stress-Strain Behavior of electrospun nanofibers is a very wide and popular research area, nowadays [1, 2, 3]. Due to the high surface area and interconnected porosity, electrospun nanofibrous webs are an important area in nanotechnology applications [4, 5, 6].

TPUs is considered as “bridging the gap between rubber and plastics”, since TPUs not only offer mechanical performance characteristics of rubber, but also it can be processed as thermoplastics [7]. These randomly segmented copolymers composed of hard and soft segments form a two-phase microstructure. The hard segments, composed of polar materials, can form carbonyl to amino hydrogen bonds and thus tend to cluster or aggregate into the ordered hard domains, whereas the soft segments form amorphous domains resulting phase separation [7].

Tensile behavior of thermoplastic polyurethane elastomer (TPUE) is investigated by different researchers [1,8]. These works reported that electrospun TPUE fibre mats showed non-linear elastic and inelastic characteristics which may be due to the slippage of crossed nanofibers (i.e. non-bonding or physical bonding structure) and breakage of the nanofibers at junctions (i.e. point bonded or chemical bonding structure).

Some research showed that the mechanical properties of electro-spun nano fiber mat are affect-

ed by the nature of solvent that has been used [9]. With using DMF in electrospinning of TPU as solvent, the tensile strength is much more than the mat that used THF as solvent [10]. Other parameters that affect mechanical properties of nanofiber mat are the concentrations of polymer in electrospinning solution [11]. The fiber orientation also has important effect on mechanical properties of mat. Tensile strength increases through an increase in fiber orientation [12, 1]. In previous work, it has been shown that electrospun nanofibrous web has a good potential as membrane for using in protective clothing applications [1, 2, 4]. Although some researches have been carried out on studying the mechanical properties of the electrospun nanofibers, comprehensive investigations are necessary for studying the effects of micro structure on macro mechanic of PU electrospun nanofiber mat.

In this study the effect of solvent mixture, polymer concentration, fiber orientation and electrospinning duration has been studied on tensile behavior of TPU electrospun nanofibrous web. Also, the effect of these parameters on fiber diameter, web thickness, tensile strength and elongation has been investigated and interpreted. The stress-strain behavior of PU membrane has been interpreted with regards to polymer structure and web morphology.

* To whom all correspondence should be sent:
E-mail: alisadeghian60@yahoo.com

EXPERIMENTAL

Electrospinning

Electrospinning solution was prepared from 13,14 and 15 percent wt./vol of commercial TPU (Mw: 65,000, Bayer, Germany) which was dissolved in tetrahydrofuran (THF) and N,N- dimethylformamide (DMF) mixture (60:40, 55/45 ,50/50, v/v). In order to obtain different thickness and studding the effect of mesh thickness electrospinning process was done with different durations (2,4, and 6 hours).

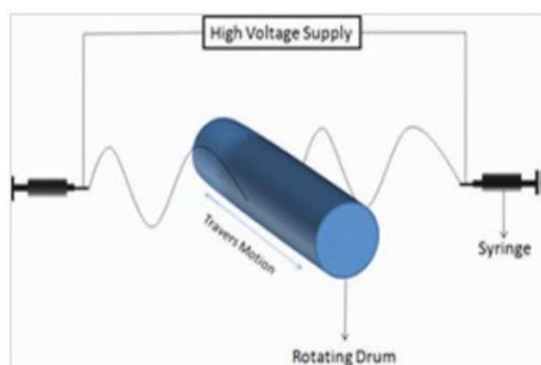


Fig. 1. Schematic diagram of double nozzle electrospinning machine with rotating drum.

In this research an electrospinning machine with 2 nuzzles has been used. In the electrospinning process, PU solution from two opposite needles was electrospun simultaneously on one rotating drum. The optimum distance between nozzle and collector was 13 centimetre. The rotation speed and traverse speed of drum and applied voltage was respectively 150 RPM, 400mm/min and 13KV. The average of 20 points is reported as thickness of mat with using a micrometer (Dial Thickness Gage, Mitotoyo, Japan). Morphology of electrospun polyurethane fibres was studied using scanning electron microscopy (SEM) and diameter of the nanofiber was measured from SEM image using Image analyzer software. Five dumbbell-shaped specimens in machine direction (MD) and five dumbbell-shaped specimens in transverse direction (TD) were examined for characterization of mechanical properties according to ASTM D-638. Figure 2 shows a typical SEM of electrospun PU web.

To study the effect of fiber orientation on tensile behaviour of electrospun web an aligned yarn was produced by the setup that is proposed by Najafi and Gharehaghaji [5]. For producing aligned nanofibers in yarn formation zone, two nuzzles with opposite charge were used. These nuzzles were connected to 1 ml syringes that were fixed on the syringe pump. Polymer solution was electrospun

and produced jets were moving towards each other and then were joined together on the surface of aluminum collector. The aluminum drum was used as a temporary collector. Consequently, twisting and winding units were used to align and twist the nanofiber strand. During this transformation, a tensile load was exerted on nanofibers and a spinning triangle was formed.

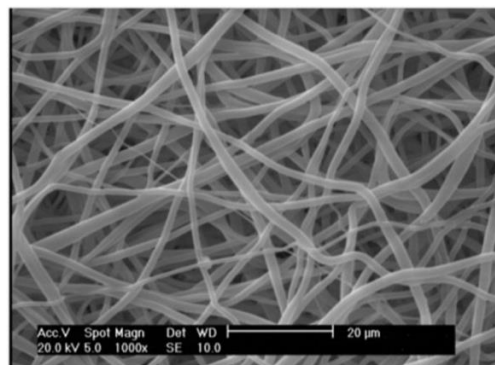


Fig. 2. A typical SEM of electrospun PU web.

The nanofibers orientation distribution was calculated by a program which was encoded in MATLAB Software (version 7.0.0.1920) as explained in previous work [1]. The summary of results is shown in Table 1.

RESULTS AND DISCUSSION

Stress-strain behavior of electrospun PU

The data from uniaxial tensile tests showed the perfectly non-linear elastic behavior of the electrospun PU nanofiber web. Figure 3 shows the typical stress-strain curve of PU nanofibrous webs. The load-elongation curve shows a high initial modulus that after approximately 15 mm elongation is followed with a slightly slope and around 150 mm elongation this slope increased again.

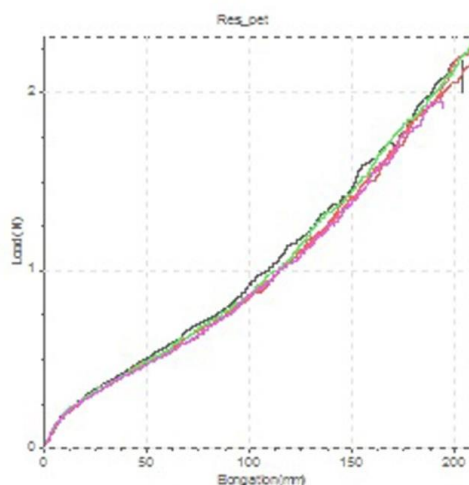


Fig. 3. The typical stress-strain curve of PU webs

Table 1. Characterization of produced sample

Sample Code**	Mat thickness (mm)		Tensile at break (N)				Elongation at break (%)			
	Mean	S. D.	Machine Direction		Cross Direction		Machine Direction		Cross Direction	
			Mean	S. D.	Mean	S. D.	Mean	S. D.	Mean	S. D.
III 2h 13%	0.039	0.010	1.46	0.272	2.19	0.144	200.30	14.52	206.10	8.03
III 2h 14%	0.031	0.002	1.12	0.35	1.57	0.32	194.60	8.59	184.40	24.87
III 2h 15%	0.040	0.006	1.54	0.30	2.09	0.16	197.90	0.09	204.00	9.52
II 2h 13%	0.029	0.003	0.82	0.10	1.20	0.09	135.30	6.56	153.3	12.05
II 2h 14%	0.039	0.008	1.05	0.20	0.90	0.08	140.40	11.10	100.20	8.10
II 2h 15%	0.038	0.004	1.19	0.57	0.70	0.05	144.6	10.28	105.8	8.02
I 2h 13%	0.039	0.014	1.33	0.213	1.53	0.30	198.5	6.02	198.00	12.16
I 2h 14%	0.044	0.011	0.66	0.09	8.84	0.15	96.02	12.86	170.70	14.81
I 2h 15%	0.056	0.014	1.34	0.17	1.92	0.15	156.80	8.11	182.40	11.16
III 4h 13%	0.077	0.014	1.99	0.70	2.51	0.08	166.9	17.00	154.20	6.81
III 4h 14%	0.092	0.005	1.97	0.30	3.37	0.2	0.213	13.13	180.10	7.42
III 4h 15%	0.114	0.019	1.93	0.37	2.41	0.12	260.70	4.27	187.30	10.80
II 4h 13%	0.080	0.014	1.43	0.53	1.86	0.10	126.80	19.28	128.70	7.03
II 4h 14%	0.087	0.007	0.87	0.15	1.23	0.18	135.50	10.12	164.00	14.05
II 4h 15%	0.082	0.015	3.35	0.90	3.96	0.27	191.40	12.57	191.60	8.71
I 4h 13%	0.090	0.013	2.15	0.70	3.41	0.22	156.30	15.44	177.30	9.22
I 4h 14%	0.095	0.005	2.00	0.32	2.95	0.20	183.70	15.30	189.90	9.63
I 4h 15%	0.070	0.011	2.92	0.33	3.66	0.44	124.70	13.94	134.90	6.09
III 6h 13%	0.112	0.015	3.58	0.39	5.53	1.12	163.50	0.35	169.60	40.29
III 6h 14%	0.142	0.004	4.72	0.44	6.35	0.76	230	16.12	226.30	21.06
III 6h 15%	0.085	0.019	4.61	1.14	6.21	0.72	234.60	9.47	221.00	13.73
II 6h 13%	0.099	0.010	2.84	0.61	3.66	0.39	145.20	15.63	153.40	18.00
II 6h 14%	0.114	0.034	2.92	0.96	3.51	0.14	139.1	25.74	131.70	6.09
II 6h 15%	0.113	0.020	3.60	1.14	3.32	0.11	153.50	16.50	139.80	4.02
I 6h 13%	0.136	0.016	3.13	0.48	4.29	0.48	153.9	8.02	154.10	16.38
I 6h 14%	0.153	0.029	3.42	0.50	5.31	0.81	189.30	18.35	200.70	25.02
I 6h 15%	0.160	0.027	0.02	0.52	2.58	0.19	97.98	9.40	120.90	9.45

** Sample coding: solvent mixture (I=60/40, II=55/45 and III=50/50(THF/DMF)), Electrospinning duration (2h=2hours, 4h= 4hours and 6h= 6hours) and Polymer content.

The PU web gives a characteristic response to elastomeric materials -sigmoidal in shape-, with strain hardening resulting from molecular orientation at high degrees of strain. This behaviour can be interpreted with regards to two sources; firstly fiber polymer's molecular structure and secondly network morphology.

The segmented polyurethanes are consisted of hard and soft segments. Hard domains act as physical crosslinks and impart the material's elastomeric behavior. At room temperature, soft domains are above their glass transition temperature and impart the material its rubber-like behaviour; hard domains are below their glass or melt transition temperature and are thought to control and regulate the high modulus and tensile strength [7].

The electrospun PU mesh has stress-strain responses resulting from molecular orientation within the fibres as a result of electrospinning, and a strain-induced orientation of the electrospun fibre mat. When a strain is applied to the electrospun mat, fibers oriented in the direction of cross-head displacement are stretched uni-axially, while fibers oriented at some angle relative the principal strain direction experience a rotation. As the strain in the electrospun mat increases and more fibers become oriented in the direction of strain, the relative number of fibers stretched in comparison to the fibers rotated, increases and the stress in the electrospun mat increases. The electrospun mat is globally isotropic, the individual fibers comprising the web have a certain degree of molecular orientation prior to stretching. The strain applied to the electrospun mat serves to orient both fibers and molecules within the fibers. The apparent molecular orientation in the electrospun fibers also leads to the pronounced reduction in elongation to failure of the electrospun mat.

In the beginning of the tensile process the electrospun nanofiber mesh has Hookian behavior, and structural morphology does not change. After a critical level of stress the weaker fibre breaks or the bonding between the fibres where fibres cross each other, break up and nanofibers slip on each other. Because the breaking force of fibre is significantly higher than the forces needed for breaking the bonding between fibre, this point bonding starts to break up at an average extension of 20 %, then the slope of graph decreases. Because of the bonding break up stress, quality of the bonding between fibres and fibre diameter deviation, a long transition is observed in graph.

Federico and Gasser [13] in studying the non-linear elasticity of biological tissues with statistical fiber orientation showed that the comparison poten-

tial terms with the fibres allowed to resist compression, are convex with the isotropic fibre distribution, for all deformation states tested, and non-convex with the anisotropic fibre distribution, for most of the deformation states tested. In contrast, the anisotropic ensemble potential terms with tension-only fibres is convex for all tested combinations of fibre orientation and deformation state. Their result suggests that the assumption of fibres having asymmetric behaviour in tension and compression is not only more realistic, but also needed from the point of view of mathematical consistency, in order to achieve convexity. In the other words, when the nanofibrous web is loaded the fiber in the other direction resist to buckle and this imparts a convexity to tensile behavior (This is the reason of initial high moduli), and after overcoming to this resistance (when fiber in perpendicular direction is buckle) the curve continue with smaller slope. The comparison between load-elongation of electrospun nanofiber web with fiber oriented in different directions (fig. 3) and load-elongation of aligned nanofiber yarn with fiber aligned in loading direction (fig. 4) confirms this assumption.

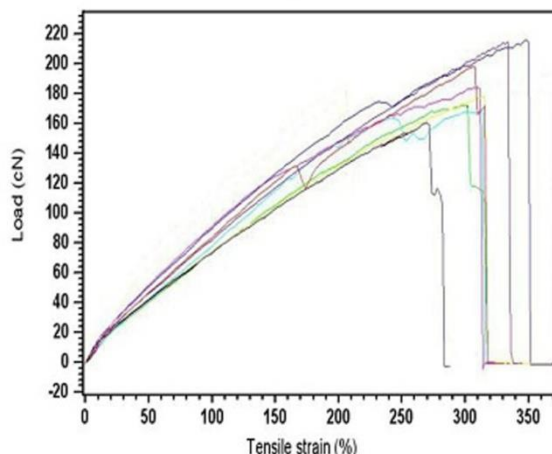


Fig. 4. The typical stress-strain curve of PU webs.

As it can be seen from figure 4, the initial slope in nanofiber yarn stress-strain curve is smaller than figure 3 that is because of fiber orientation distribution in PU electrospun nanofibrous web.

Stress softening (Mulins effect)

Figure 5 shows the softening behavior during the cyclic loading. In cyclic tests, the stress-strain curve in the second cycle is far more compliant than that of observed in the first cycle. The stress-strain behavior tends to be stabilized after four cycles and most softening occurring during the first cycle. As the strain upon reloading approaches the maximum strain achieved in prior cycles, the stress tends to approach to the stress level of a first cycle

test at that strain and unloading paths after a given strain all follow the same curve, independent of cycle number. Softening depends on strain history, where larger strain produces greater softening and the residual strain occurs predominantly after the first cycle, and no significant height changes are observed after the additional cycles. Stable curves are typically observed after only 4 cycles.

The stress-strain elastic nonlinear behaviour and stress softening of electrospun nanofibrous PU web are similar to the bulk behaviour of thermoplastic polyurethane that reported by Qil and Boyce [7].

The domain structure of segmented polyurethane is responsible for the softening effect. It is found that the stress inhomogeneity in the soft domains could lead to the rotation of hard domains in order to minimize the overall energy of deformation. It is also found that at large stretch the hard domains would break down to further accommodate stretch. To achieve the high degree of hard block orientation, it was necessary that hard domains undergo the plastic deformation, which was accompanied through the breakage and reformation of hydrogen bonds [7].

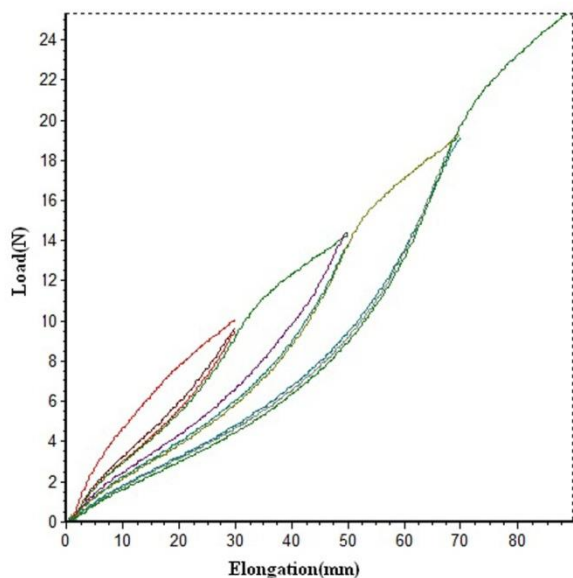


Fig. 5. Cyclic uniaxial tension test.

On the other hand, the network microstructures can cause the stress softening effect. Electrospun fibers are held together through connecting sites such as crossing and bonding between fibres [8]. The point-bonding and physically crossed structure occurred for electrospun PU. The relatively weak non-bonded structures tend to break or slip-apart, under loading resulted in the stress-softening behaviour in cyclic loading-unloading tests. It is stated that the non-bonding structures do not contribute effectively for carrying the load in comparison with

the point-bonded structures [14]. It can consider that the point bonding and the non-bonding (physical crossed structure) in electrospun fibrous network play the role of the hard segment and soft segment in the PU molecular chain, respectively.

The effect of electrospinning duration

Statistical analysis shows a significant difference between mean diameters of fibre among different levels of electrospinning duration (2, 4 and 6 hours). The results show that with increasing electrospinning duration that resulted in increasing web thickness the diameter of fiber increased (fig 6). It seems that with increasing fiber on collector drum, the charge carrying capacity of the jet decreases, thereby subjecting it to lower tension when the electric field is applied. Lower tension resulted in decreased elongation forces exerted on the jet, yields a coarser fiber.

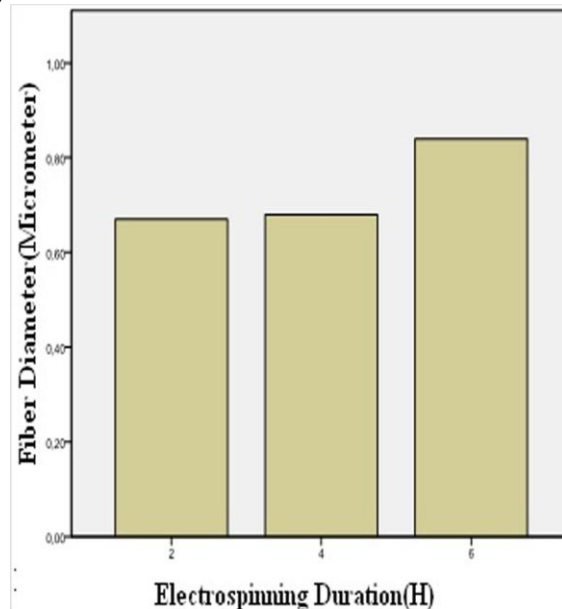


Fig.6. The effect of electrospinning duration on diameter of fibers.

One of the most important factors that affect the mechanical properties of fibrous material is the thickness of structure. The test result shows that with increasing process duration the weight and thickness of layers increase linearly but the increase in slope of thickness is larger than weight. It is described that as the fibers reach the collector the charge intensity decreased and this caused that next fiber with a lower speed moved in distance between nozzle and collector and the thicker web produced. On the other hand the as spun fibers have some electrical charged ions that repel other fiber that yielded to more voluminous network.

With increasing electrospinning duration, the tenacity of layers increased and elongation of them

decreased. The results indicate that these layers have good strength as a result of point bonding due to the residual solvent.

As figure 7 show a nonlinear relation is governing between strength at break (N) and electrospinning duration (H). The regression model ($R^2=98\%$) is as below:

$$\text{Tenacity (N)} = 0.562 + 0.036 \text{Electrospinning Duration(h)}^2$$

This regression equation suggests that the rate of strength increasing is being increasing with increasing electrospinning duration (web thickness). This is due to this fact that with increasing the web thickness the residual solvent should pass a longer way to leave the nanofibrous web and the nanofibers have more time to connect each other by residual solvent and produce network have more chemical connection and strength.

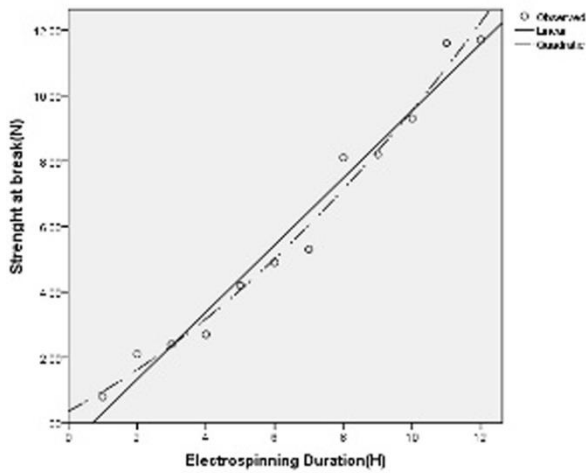


Fig. 7. Strength at break versus electrospinning duration

The effect of fiber orientation distribution

The results of this experiment show that tenacity in cross direction (CD) is about 28% more than the machine direction (Fig.8) but no significant difference occurred in elongation at break. Figure 9 shows typical fibres orientation in different directions of samples. As this figure demonstrates, the fibres are more oriented in cross direction than machine direction.

Strength in different directions of electrospun nanofiber webs is due to the orientation distribution of the nanofibers in various directions [15]. In this work traverse motion of the drum causes the fibre bundle get more oriented in cross direction.

The results obtained by Pedicini and Farris[16] indicate that molecular orientation is induced by the electrospinning process and is a contributing factor

to the ‘stiffer’ stress–strain behaviour of the eletrspun PU mat.

They showed that the molecular orientation function ($f = [3\cos^2\alpha - 1]/2$ where α is mean molecular angle) for oriented electrospun PU fibers is an order of magnitude larger than f for the isotropic electrospun fibers and PU film. This means that in cross direction oriented mat not only the fiber get more oriented in a cross direction but also the molecular chain is more oriented in cross direction and these two factors increased the strength in this direction.

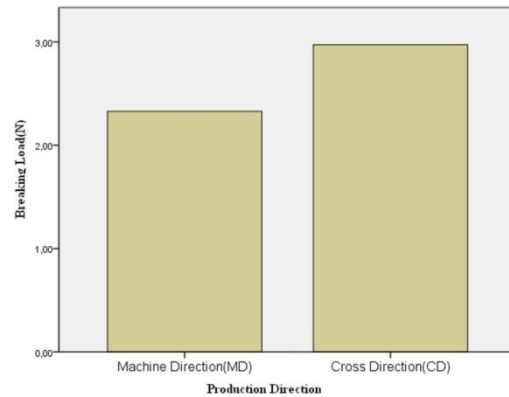


Fig. 8. The effect of production direction on load at break

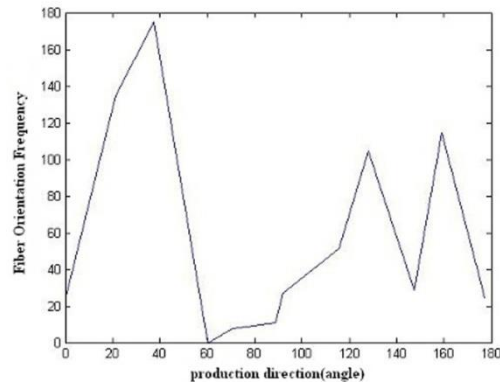


Fig. 9. Typical fibre orientation distribution.

The effect of polymer concentration

Solution concentration plays an important role in the fiber diameter. ANOVA analysis shows the significant effect of polymer content on tensile behavior of PU web (tab. 2). The result shows that with increasing polymer content, tenacity and elongation was increased (Fig. 9).

The polymer concentration that controls solution viscosity is one of the biggest determinants of fiber diameter and morphology when spinning polymeric nanofibers. Increasing the solution viscosity by increasing the polymer concentration caused that fiber diameter, web thickness, tenacity and elongation of PU electrospun web increased as shown in Table 3.

Table 2. Analysis of variance for the effect of polymer content and solvent mixture on load and elongation at break.

Source	Dependent Variable	Type III Sum of Squares	df	Mean Square	F	Sig.
Polymer Content (P.C)	Maximum Load	7.123	2	3.562	14.170	.000
	maximum elongation	3755.813	2	1877.906	9.958	.000
Solvent Mix- ture(S.M)	Maximum Load	37.741	2	18.870	75.072	.000
	maximum elongation	101033.576	2	50516.788	267.867	.000
P.C * S.M	Maximum Load	14.774	4	3.694	14.694	.050
	maximum elongation	2247.130	4	561.783	2.979	.065
Error	Maximum Load	41.224	164	.251		
	maximum elongation	30928.578	164	188.589		
Total	Maximum Load	1965.974	213			
	maximum elongation	6161941.690	213			
Corrected Total	Maximum Load	447.620	212			
	maximum elongation	292769.327	212			

Table 3. The effect of polymer content on morphology and tensile behaviour of PU mat

Polymer content (%)	Fiber diameter (nm)	Mat thickness (mm)	Tensile at break (N)	Elongation at break (%)
13	610	0.075	2.53	159.95
14	810	0.086	2.68	167.41
15	950	0.102	2.76	169/66

Table 4. The effect of polymer mixture on morphology and tensile behaviour of PU mat

solvent mixture (THF/ DMF)	Fiber diameter (nm)	Mat thickness (mm)	Tensile at break (N)	Elongation at break (%)
50/50	920	0.095	3.00	195.90
55/45	850	0.077	2.56	157.36
60/40	710	0.080	2.35	159.96

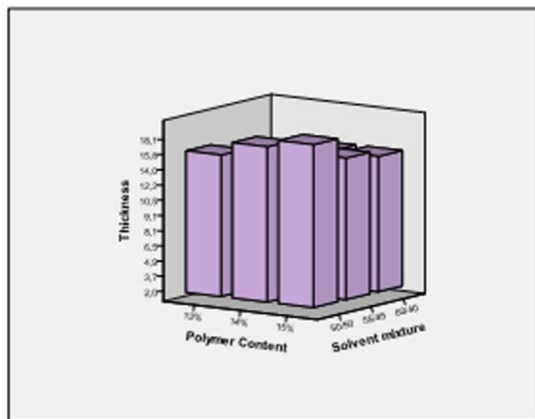


Fig. 10. The effect of polymer content and solvent mixture on strength of PU web.

The elongation of electrospun sample with 13%wt. polymer content had smaller value than two other samples but no significant difference between elongation of sample with 14% and 15% polymer concentration was observed.

The effect of solvent mixture

Rapid solvent evaporation and phase separations due to alternation of the jet are a common phenomenon in electrospinning process. Solvent volatility plays a major role in the formation of nanostructures through influencing the phase separation process. Also the electrolytic nature of the solvent is an important parameter in electrospinning [6].

As Table 2 shows, the solvent mixture has also significant effect on tensile behaviour of PU mat. It can be seen from Table 4 and figure 10 that with increasing DMF in THF/DMF mixture the strength and elongation of electrospun nanofibrous web increased.

With increasing THF content fiber diameters and web thickness increased. Data indicate that the mat tensile strength is sensitive to the fiber diameters and web thickness.

On the other hand, since the volatility of DMF is less than THF, the electrospun nanofiber by more DMF have a more time for connect to each other by residual solvent and this resulting to increasing strength.

It should be noted that increasing the DMF in THF/DMF content not only increased the web strength but also significantly increased the elongation of PU webs. Increasing in elongation is due to the more point bonded created by residual solvent as a result of less volatility of DMF. Then the sample with 50/50% THF/DMF solvent mixture can be considered as optimum condition having the best elongation and strength.

CONCLUSIONS

Because of the wide application of electrospun PU membrane, the stress strain behaviour as a key factor in macro mechanical properties of electrospun membrane is investigated with regards to some micro structures parameters like nanofiber diameter, web thickness and fibre orientation.

In the present work, ultrafine elastic fibers with submicron diameters have been successfully produced through electrospinning the polyurethane solutions. This research investigated some important production parameters (electrospinning duration, polymer concentration and solvent mixture) on stress-strain behaviour of poly urethane nanofiber. It has shown that nonlinear elastic and stress softening in electrospun PU nanofibrous mat is arised of two source; PU molecular chain and network microstructures. Fibre diameters increase with increasing electrospinning duration, polymer content and DMF content in THF/DMF mixture. The results of this study show that some mechanical properties of PU mat such as breaking load increase linearly with increasing electrospinning duration. These results also show that with increasing THF content tenacity and elongation of layers decrease.

This research showed that mechanical properties of PU membrane is mainly effected by morfological properties of mat that changed with changing production parameters and structures.

REFERENCE

1. M. Gorji, Ali. A. A. Jeddi, A. A. Gharehaghaji, *Journal of Applied Polymer Science*, **125**, 4135 (2012).
2. R. Bagherzadeh, M. Gorji, M. Latifi, S. S. Najar, M. A. Tehran, L. Kong, *Textile Research Journal*, **82**(1), 70 (2011).
3. K. Molnar, L. M. Vas, T.Czigany, *Composites:B*, **43**, 15 (2012).
4. M. Gorji, A. Ali, A. Jeddi, A. A. Gharehaghaji, "The effect of electrospinning duration on some physical and mechanical properties of Polyurethane Electrospun nano web", Polymer Processing Society (PPS), Asia/Australia Regional Meeting, Kish Island, Iran, November 15-17, 2011.
5. S. J. Najafi, A.A. Gharehaghaji, S. M. Etrati, "Fabrication and Characterization of Polyurethane Nanofiber Yarns For Orthopedic Dressing", International congress of innovative textiles (ICONTEX), Istanbul, Turkey. 20-22 October , 2011.
6. A. Patanaik, R. D. Anandjiwala, R. S. Rengasamy, A. Ghosh, Harinder Pal, *Textile Progress*, **39**, 67 (2007).
7. web.mit.edu/cortiz/www/Jerry/jmps_softening.pdf.
8. K.H. Lee, B.Lee, C. Kim, H. Y. Kim, K.W.Kim, C.W.Nah, *Macromolecular Research*, **13**, 441 (2005).
9. Y. J. Ryu, K. W. Kim, S. W. Choi, *Journal of Polymer Science Part B: Polymer Physics*, **41**, 11 (2003).

10. D. I. Cha, K. W. Kim, G. H. Chu, H. Y. Kim, K. H. Lee, N. Bhattarai, *Macromolecular Research*, **14**, 331 (2006).
11. S. Ramakrishna, K. Fujihara, W.E.Teo. T-C. Lim, Z. Ma, An Introduction to Electrospinning and Nanofibers, World Scientific Publishing Co. Pte. Ltd., 2005.
12. P. Brown, K. Stevens "Nanofibers and Nanotechnology in Textiles", Woodhead Publishing Series in Textiles, 2007.
13. S. Federico, T.C. Gasser, *J. R. Soc. Interface*, **7**, 955 (2010).
14. K.H. Lee, H. Y. Kim, Y. J. Ryu, K.W. Kim, S.W. Choi, *J. Polym. Sci.; Part B: Polym. Phys.*, **41**, 1256 (2003).
15. Z. J. Pan, H. B. Liu, Q. H.Wan, *JFBI*, **1**, 1 (2008).
16. A. Pedicini, R. J. Farris, *Polymer*, **44**, 6857 (2003).

Synthesize of nano silver using cellulose or glucose as a reduction agent: the study of their antibacterial activity on polyurethan fibers

A. Sadeghian Maryan^{1*}, M. Gorji²

¹Department of Chemistry, Ardabil Branch, Islamic Azad University, Ardabil, Iran

²Department of Textile Engineering, Amirkabir University of Technology, Hafez Avenue, Tehran, 15914, Iran.

Received June 26, 2015, Revised September 10, 2015

Silver nanoparticles are used an increased attention for various biomedical and medical applications. In this paper, the synthesis of nano silver was investigated and compared to using chemical reduction of silver nitrate by glucose and cellulose in neutral and alkaline media. The reducing properties of glucose and cotton cellulose showed that cellulose acted as a strong reducing agent. The antibacterial activity of synthesized nano silver on polyurethane fiber using exhaustion method was measured. The synthesis of nano silver in an aqueous solution was illustrated with an adsorption spectrophotometer. Moreover, the TEM images demonstrated the size and shape of the nano silver particles. Silver nitrate salts were reduced using cellulose in alkaline media, and nano silver particles were subsequently synthesized with the sizes of 30-40nm. Antibacterial properties of treated polyurethane fibers with synthesized nano silver were good.

Keywords: Nano Silver, Chemical Reduction, Glucose, Cellulose, polyurethane fibers.

INTRODUCTION

Metal nano particles have attracted a great deal of attention in recent years due to their optical, physical and chemical properties that differentiates them from bulk material properties. There is wide application in various fields like catalysis, photonics, optoelectronics, information storage, antibacterial applications, etc. Silver powders, having ultra fine and uniformly distributed particle size, are of considerable use in the electronics industry as thick film conductors in integrated circuits due to their unique properties such as high electrical and thermal conductivity, high resistance to oxidation [1].

Silver is a safe and effective bactericidal metal because it is non-toxic to animal cells and highly toxic to bacteria such as *Escherchia coli* (*E. coli*) and *Staphylococcus aureas*. Colloidal silver, nano silver coated fabric, nano silver metal oxide granules and nano silver coated ceramic materials are used for antibacterial applications. Nano silver in the form of powders as well as suspensions, due to the high surface to volume ratios, has been used in the above said applications as it enables the loading of small quantities of silver and thus makes the product cost effective [2].

Many methods and approaches have been reported for the synthesis of AgNPs by using chemical, physical, photochemical and biological routes. Each method has advantages and disadvantages with common problems being costs, scalability, particle sizes and size distribution. Physical and photochemical methods to prepare

nanoparticles are usually need the very high temperature and vacuum conditions, and expensive equipment [3].

There are several aqueous based chemical methods reported in the literature to produce nano silver. While most of these reports deal with inorganic bases such as NaOH to control the pH to above 9, the contamination of silver with metals ions will cause limitations in specific applications such as electronics, and hence organic bases are required in the nano silver synthesis, as reported by Hsu and co-worker [4].

Generally, nano silver particles is synthesised by chemical reduction of metal salt, using stabilizing agent, including a polymer or a surfactant. A great deal of studies was carried out on the effect of stirring, temperature control and pH, on the size of particles [5-9].

The chemical reduction method involves the reduction of AgNO₃ by a reducing agent in the presence of a suitable stabilizer, which is necessary in protecting the growth of silver particles through aggregation. In the formation of silver nanoparticles by the chemical reduction method, the particle size and aggregation state of silver nanoparticles are affected by various parameters, such as initial AgNO₃ concentrations, reducing agent/AgNO₃ molar ratios, and stabilizer concentrations [10].

In one of the methods of chemical reduction, high dispersed silver particles with size of 20–80 nm were prepared by reducing silver nitrate with glucose using protective agent as poly vinyl pyrrolidone (PVP). The addition of the sodium hydroxide enhanced the reaction velocity. The PVP

has protected the silver particles from agglomeration. In another study, PVP was used as dispersant agent in the reaction between silver ions and glucose [11, 12]. An approach based on the polyol process for the large-scale synthesis of silver nanowires with uniform diameters was demonstrated. It was involved the reduction of silver nitrate by polyol in the presence of PVP as stabilizer. This method had been successfully illustrated with the production of silver nanowires 30-60 nm in diameter and 1-50 μ in length [13].

In another work, silver nanoparticles were prepared by a green method from reduction of silver nitrate. Carboxymethyl cellulose sodium (CMS) was employed as both a reducing and a stabilizing reagent and silver ion can be reduced by hydrolyze of CMS to form silver nanoparticles. Results were also shown that the concentration of CMS has very small effect on the size distribution of silver and nanoparticles prepared was uniform and stable, which was stored at room temperature for 2 months without any visible change [14].

Polyurethane (PU) is one of the most important engineering polymers and widely used in commercial applications, including construction, automotive, food packaging and storage, transportation, textiles, foot-wear and wound dressing materials. With the growing public health awareness of the pathogenic effects and stain formations caused by microorganisms, there is an increasing need to develop antimicrobial PU for improving the properties. Besides antibiotics, silver salts and silver nanoparticles can be used as filler or coating material in the preparation of antimicrobial PU. Comparatively speaking, silver nanoparticles show more efficient antimicrobial property than silver salts due to their extremely large surface area. The effective biocide concentration of silver nanoparticles is at a nano molar level in contrast to a micromole level of silver ions. Therefore, application of nano silver antibacterial agent would be a better alternative. The silver nanoparticles coated PU could serve as water filter to remove bacteria from water [15].

In the present work, we have synthesised silver nanoparticles by an aqueous chemical method with cellulose or glucose. The size of synthesized nanoparticles compared and analysed. Electrospun polyurethane was treated nano silver colloid. The antibacterial activities of the fibers were assessed against both Gram-positive *Staphylococcus aureus* (*S. aureus*) and Gram-negative *Escherichia coli* (*E. coli*).

MATERIALS AND METHOD

The substances and materials used in this study, including cotton fabric as cellulosic substrate, electrospun polyurethane fibres from china, silver nitrate, glucose, sodium hydrosulphite and sodium hydroxide, were all catered by Merck Company, Germany. All experiments were carried out following with Table 1, using distilled water at 60°C for one hour.

Table 1: The methods of experimental

Sample code	AgNO ₃ 1%	Cellulose 322g/m ²	Glucose 1%	pH
NS	2 cc/l	0	0	12
NCS	2 cc/l	20 g/l	0	12
NG	2 cc/l	0	4.5 cc/l	7
NGS	2 cc/l	0	4.5 cc/l	12
NCG	2 cc/l	20 g/l	4.5 cc/l	7
NCGS	2 cc/l	20 g/l	4.5 cc/l	12

Then, after synthesizing of nano silver, polyurethane (PU) Samples were treated using 3 g/L nano silver colloid for 60 min at 70° C and pH = 7.

Adsorption spectra of synthesised samples were measured by Camspec UV-vis spectrophotometer; model M-350, England. Microscopic images were prepared from suspension samples by a transmission electron microscope (TEM), model EM 208, from Philips Company, Netherlands. The distribution range of particles of synthesised samples was obtained using a dynamic light scattering (DLC), Malvern model, England.

Quantitative experiments, investigating the strength and decrease in microbial agents, were conducted according to AATCC 100-2004 standard test method, using gram-positive *Staphylococcus aureus*, gram-negative *Escherichia coli* bacteria. In this method, the number of colonies of bacteria was counted according to colony forming unit (CFU) and the decrease in microbial agents (C) was determined using equation 1, where M₁: the number of colonies in control microbial suspension and M₂: the number of colonies existing in the suspension after being co-located adjacent to treated samples.

$$C = \frac{M_1 - M_2}{M_1} \times 100 \quad (1)$$

RESULTS AND DISCUSSION

Adsorption spectrophotometry

Figure 1 shows the UV-vis spectra of silver nitrate, reduced silver nitrate with cellulose in

alkaline media, and silver nitrate in alkali media in absence of the reducing agent.

The adsorption spectra illustrated in fig. 1 indicate that silver nitrate has created a peak at wavelength of 302nm, and then the silver nitrate reduced by cellulose in alkali media, shows a peak at 408nm. This peak prove the synthesis of nano silver in experiment conditions; while, the silver nitrate in alkaline media without cellulose is not reduced and it has no peak at 400nm. Thus, nano silver particles have not formed in the absence of cellulose. Figure 2 shows the UV-vis spectra of silver nitrate was reduced by cellulose and glucose in alkali media.

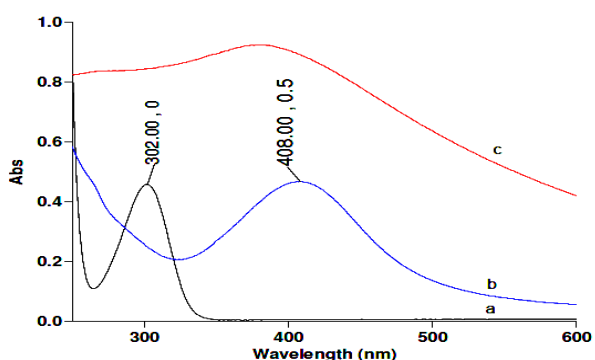


Fig. 1. Adsorption spectra of silver nitrate in different condition, a :AgNO₃ 1% · b :NCS·c:NS

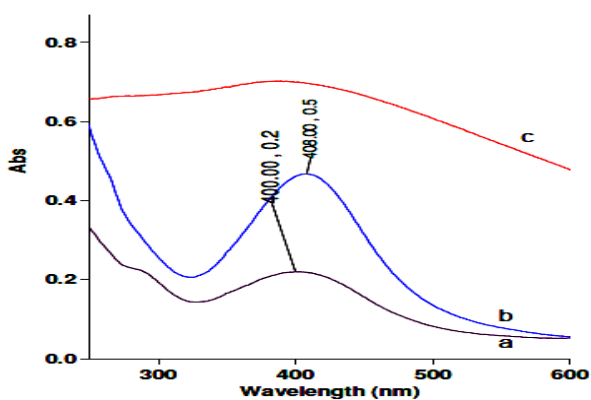


Fig. 2. Adsorption spectra of the silver nitrate, reduced by cellulose and glucose, a: NCGS, b: NCS, c: NGS

The adsorption spectra of silver nitrate in Figure 2 indicate that silver nitrate was reduced by both cellulose and glucose because of peak at 400nm. This indicates that presence of glucose and cellulose, was caused that silver nitrate was reduced in alkali media and nano silver particles is synthesised based on reaction has shown in figure 3. These results indicate the cellulose or glucose oxidation through reduction of silver nitrate, resulting in formation of nano silver.

Considering to adsorption spectra and previous studies, it seems that using of glucose in reduction reaction has helped avoiding the aggregation of

particles and leads to the creation of an appropriate peak at 400nm.

DLS analysis, TEM and SEM

Dynamic light scattering (DLS) was used to determine the size distribution of small particles in solution. Fig 4 shows the distribution curve of nano silver particles, It could has founded from the curves, nano silver particles has synthesized by cellulose and are formed at a range lower than 100 nm (The measurement range of DLS is limited to the size range of hydrodynamic particles, which is 10% larger than the actual size). If silver nitrate is reduced by cellulose along with glucose using sodium hydroxide, the size of nano silver particles has decreased to 10nm.

It could has founded from the curves, nano silver particles has synthesized by cellulose and are formed at a range lower than 100 nm (The measurement range of DLS is limited to the size range of hydrodynamic particles, which is 10% larger than the actual size). If silver nitrate is reduced by cellulose along with glucose using sodium hydroxide, the size of nano silver particles has decreased to 10nm.

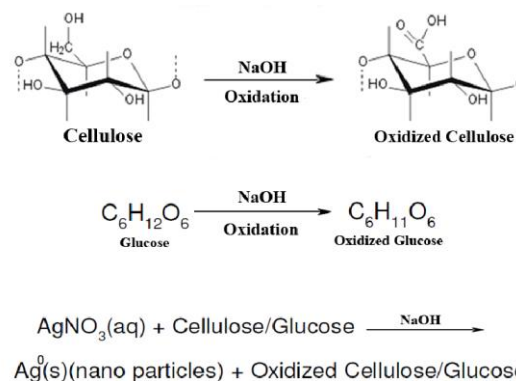


Fig. 3. Schematic reactions: Oxidation of cellulose and glucose and synthesis of nano silver by cellulose and/or glucose in alkaline media.

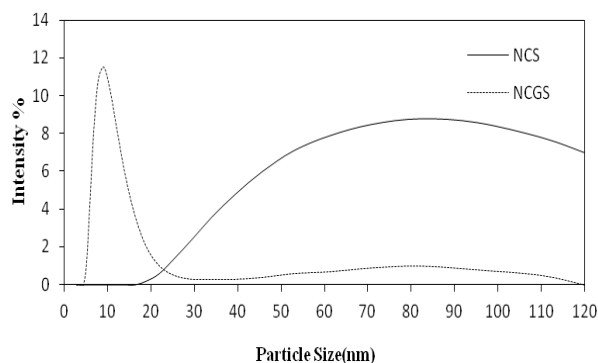


Fig. 4. Size range diagram of synthesized Nano silver particles

Figure 5 shows the TEM images of nano silver particles was synthesized by cellulose along with

glucose in alkali media. It is obvious that synthesized nano silver particles using cellulose and glucose have been less aggregated and the size of particles is less than 100nm. It seems that synthesized particles using cellulose alone were aggregated and size of them is more than 50nm; thus, Glucose acts as a stabilizing agent in reduction process of silver nitrate to nano silver.

Figure 6 shows the SEM images of untreated and treated substrate cellulosic (cotton). While the surface of untreated substrate (fabric) is smooth with no particles, the synthesized silver nanoparticles were uniformly distributed on the surface of the cellulosic substrate treated in reduction of silver nitrate. Thus, it proves that nano silver particles has been synthesized well by substrate cellulosic (cotton fiber) along with glucose.

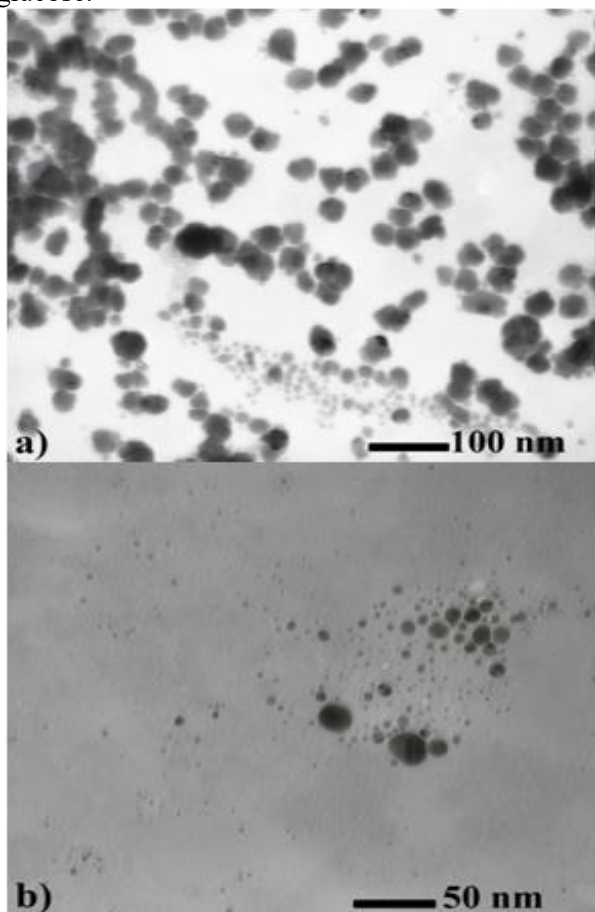


Fig. 5. TEM images of Nano silver particles, synthesized with cellulose in an alkaline media (a) and synthesized using cellulose and glucose at the same time (b)

SEM pictures and Antibacterial activity

The morphologies of untreated PU fiber, PU fiber treated with nano silver are shown in Figure 6. The SEM image of untreated fiber showed no particles on the surface of the fibers. However, the synthesized nano silver particles are well distributed on the surface of treated fibers. No

agglomeration detected on the sample treated with nano silver, indicating the synthesis of silver nano particles with smaller size. Therefore, cellulosic material was acting as a stabilizer through nano silver synthesis preventing nano particles agglomeration.

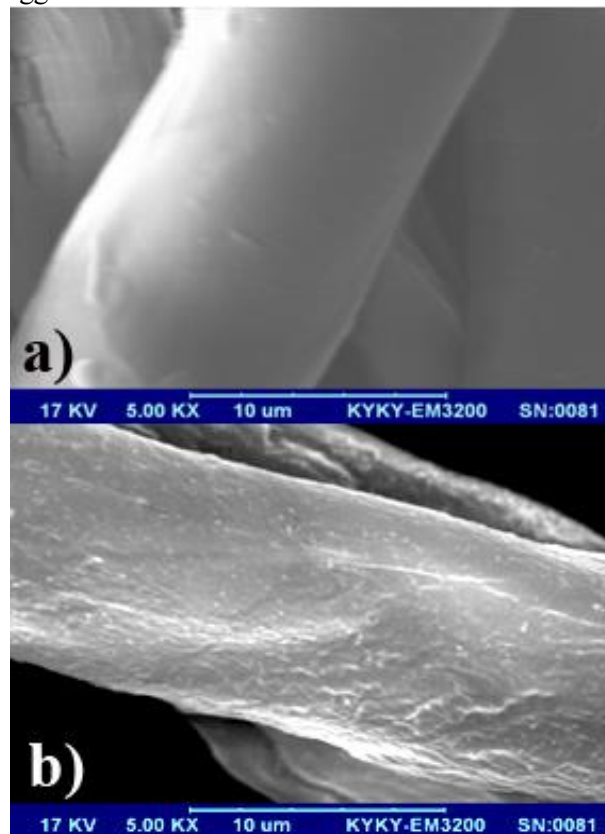


Fig. 6. SEM images of different samples, a: Untreated PU fiber, b: treated PU fiber with nano silver

The decrease in the number of colonies by the samples treated with nano silver nitrate after being placed adjacent to the Gram-negative and Gram-positive bacteria are presented in Table 2. Generally, textile goods without antibacterial modifications provide an excellent environment for microorganisms to grow. The PU fiber treated with nano silver indicated a good antibacterial activity thus they were effective in inhibitory and killing microorganisms. Treated sample with synthesized nano silver with cellulose have antibacterial activity than other samples, because of the small size of nanoparticles. the comparison of bacteria's colonies of PU fibers are shown figure 7.

Table 2: Antibacterial activities of different samples

Bacteria type samples	<i>E. coli</i>	<i>S. aureus</i>
Untreated	0	0
glucose	89.1	90.4
Cellulosic	97.6	96.2

material

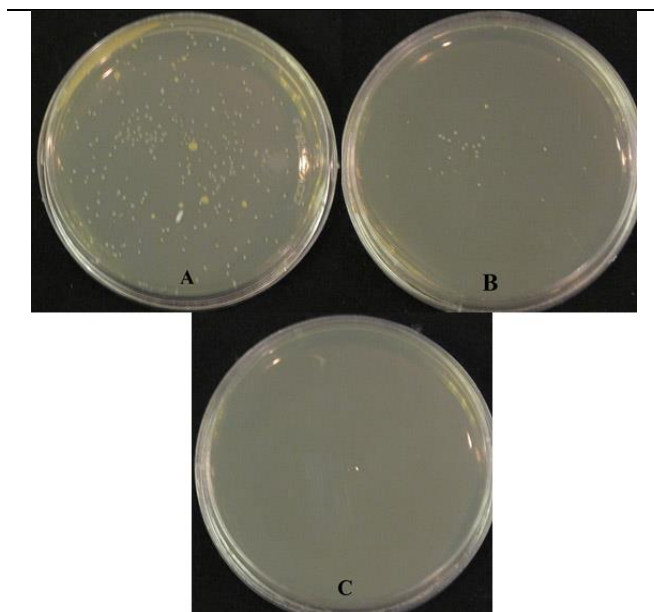


Fig. 7. Comparison of bacteria's colonies of PU fiber, A: untreated sample, B: treated sample with synthesized nano silver with glucose, C: treated sample with synthesized nano silver with cellulosic material.

CONCLUSIONS

In this research, synthesis of nano silver particles through chemical reduction of silver salt has been studied and electrospun fiber PU was treated with synthesized nano silver. Nano-silver particles have been stable and not aggregated, with no sedimentation. In this study, nano silver particles were successfully synthesized by cellulose and or glucose in an alkali media. The nano particles were synthesized through chemical reduction using cellulose along with glucose have

had a size of 10nm. Thus glucose has prevented the aggregation of synthesized particles and acted as stabiliser in chemical reduction. Treated PU fibers with synthesized nano silver using cellulosic material have high antibacterial activity.

REFERENCES

1. R. Janardhanan, M. Karuppaiah, *Polyhedron*, **28**, 2522 (2009).
2. U. Klueh, V. Wagner, S. Kelly, A. Johnson, J. D. Bryers, *J Biomed Mater Res*, **53**, 621 (2000).
3. J. Natsuki, T. Natsuk, *Int. J. Materials Sci. Applications*, **4**, 325 (2015).
4. S.L.C. Hsu, R.T. Wu, *Mater. Lett.*, **61**, 3719 (2007).
5. Z.J. Jiang, C.Y. Liu, Y. Liu, *Appl. Surface Sci.*, **233**, 135 (2004).
6. M. Cai, J. Chen, J. Zhou, *Appl. Surface Sci.*, **226**, 422 (2004).
7. A. Sileikaite, I. Prosycevas, J. Puiso, A. Juraitis, A. Guobiene, *Materials Sci.*, **12**, 287 (2006).
8. G. Lee, S. Shin, Y. C. Kim, S. G. Oh, *Materials Chem. Phys.*, **84**, 197 (2004).
9. K. S. Chou, Y. S. Lai, *Materials Chem. Phys.*, **83**, 82 (2004).
10. K. Chang Song, S. Min Lee, *Korean J. Chem. Eng.*, **26**, 153 (2009).
11. H. Wang, X. Qiao, J. Chen, S. Ding, *Colloids and Surfaces A: Physic Chem. Eng.*, **256**, 111 (2005).
12. H. Wang, X. Qiao, J. Chen, X. Wang, S. Ding, *Materials Chem. Phys.*, **94**, 449 (2005).
13. Y. Sun, B. Mayers, T. Herricks, Y. Xia, *Nano Letters*, **3**, 955 (2003).
14. J. Chen, J. Wang, X. Zhang, Y. Jin, *Materials Chem. Phys.*, **108**, 421 (2008).
15. J. Prashant, T. Pradeep, *Biotechnol. Bioeng.*, **90**, 59 (2005).

Optimal semi large scale synthesis of copper and copper oxide nanoparticles by electrical explosion of wire

M. Darvishpour*, M. Feyzi, M. Joshaghani

Faculty of Chemistry, Razi University, P.O.Box: +98-67149, Kermanshah, Iran.

Received June 26, 2015, Revised September 10, 2015

Copper and copper oxide nanoparticles (CNPs and CONPs) were produced in large scale by the Electrical Explosion of Wire process (EEW). Characterization of the Cu compound was carried out using TEM, EDX, XRD, FT-IR, and UV-Vis. X-ray diffraction spectroscopy was carried out to characterize the size of nanoparticles. The influences of wire diameter, feed rate, electrode distance and voltage in the exploding wire chamber on the particle size were analyzed by a design of experiments (DOE). This design was carried out using the Response Surface Methodology (RSM) that shows the particle size increases when the voltage decreases and decreases when other factors increase.

Keywords: Semi-large scale synthesis; copper nanoparticles; copper oxide nanoparticles; electrical explosion of wire process; response surface methodology.

INTRODUCTION

Copper nanoparticles (CNPs) and copper oxide nanoparticles (CONPs) with uniform shape and narrow size distribution are gaining increased technical importance. Cu will gain increasing importance as is expected to be an essential component in the future nanodevices due to its excellent thermal and electrical conductivity as well as good bio-compatibility and surface enhanced Raman scattering activity, nonlinear optical devices and giant magnetic resistances at a cost much less than other nanoparticles [1-4]. The oxides of transition metals are an important class of semiconductors. Among these transition-metal oxides, copper oxide (CuO); one of the important-type semiconductors with a narrow band gap of 1.4 eV [5] has attracted much attention. CuO is used as optical switch, pigment, fungicide, metallurgy reagent, gas sensor, magnetic storage media, field emission (FE) emitter and solar cells owing to its photoconductive and photochemical properties [6,7].

The most important problem of wide application of CNPs and CONPs is the dependence of their properties on the production conditions. There are a wide variety of methods for preparation of CNPs and CONPs based on various chemical and physical techniques [4, 8, 9]. All of these methods require costly precursors, templates, and very high temperature. There is a specific need to find an economically variable method for preparing nanomaterials.

The wire explosion technique which is basically a physical vapor deposition technique has been used for the production of nanopowders due to several advantages which are: (a) ability to produce nanopowders with high purity, (b) high energy efficiency, and (c) feasibility to be used for mass production [10]. This technique can be considered to be making use of both top-down and bottom-up approaches. The generation of nanoparticles from this technique can be considered to be going through two processes as follows: (i) the top-down process during which the solid wire is disintegrated into vapor by the joule heating effect to produce a supersaturated vapor and (ii) the subsequent bottom-up process during which nanoparticles will be formed through the nucleation and subsequent growth of nuclei from the supersaturated vapor [11].

The results of experiments with underwater electrical explosion of conical arrays of copper wires are presented, too [12]. Several investigations have been carried out to determine the effect of various experimental factors on the characteristics of powder produced from the wire explosion. Some of these factors are: (i) ambient gas species and pressure [13, 14, 15] (ii) energy deposited into the wire [16-18], and (iii) initial crystalline structure of wire [19].

Many papers have been published on different aspects of this method. Although studies on these factors have been performed, literatures on optimization conditions for various effects by EEW are scanty and still not well explained. Furthermore, almost all reports focused on laboratory scale synthesis and there is no report on semi large scale synthesis of CNPs.

The objective of this study was optimization of

* To whom all correspondence should be sent:
E-mail: maryamdarvishpour@gmail.com

semi large scale selective synthesis of CNPs and CONPs based on the Electrical Explosion of Wire (EEW) by using design of experiments (DOE) with Response Surface Method (RSM) and prediction of particle size under different conditions [20].

EXPERIMENTAL

Material and methods: X-ray diffraction (XRD) patterns for the samples were recorded on an Inel French, EQUINOX 3000 model X-ray diffractometer with Cu K_α radiation (λ= 1.5406, 30 kV, 20 mA). Transmission electron microscopy (TEM) analyses were performed using a Jeol JEM-2100 transmission electron microscope with an accelerating voltage of 200kV. Fourier transform infrared (FT-IR) spectra were recorded as KBr pellets using a Shimadzu 470 FT-IR spectrophotometer. The optical absorption of the nanoparticles were performed using a Shimadzu double beam double mono-chromator spectrophotometer (8453) using quartz cells of 1 cm optical path in the wave-length range of 190–900 nm with a resolution of 0.5 nm. All these absorption spectra were recorded keeping air as the reference. Energy-dispersive X-ray (EDX) analyses of CNPs were carried out using a scanning electron microscope (SEM), Philips XL 30 and S-4160, with gold coating. DOE software Version 7.0.0 was used to investigate the statistical analysis of preparation of CNPs by EEW.

Typical procedure for the synthesis of nanoparticles by EEW: The EEW experiments were carried out using a designed apparatus for semi large scale synthesis of nanoparticles consists of a wire feeding system which continuously conducts wire into the explosion chamber with a defined rate. The main components of the apparatus have been shown in Fig. 1.

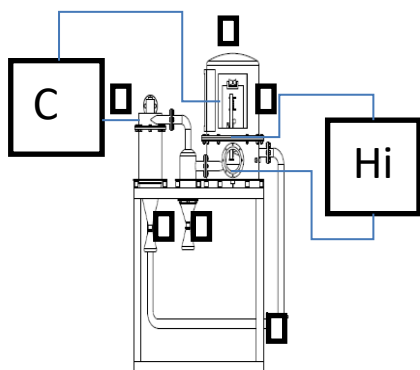


Fig. 1. Schematic diagram of the equipment used for manufacturing metal nanopowders via the wire electrical explosion process. 1-Evaporation chamber, 2- Wire feeding system, 3- Mesh filter of micro particles, 4- Nanoparticles collection vessel, 5- Fan, and 6- Pulse power.

After setting up, the chamber was evacuated to 0.1 Pa range and purged with argon three times. A thin wire is evaporated by passing a high current through it which is usually produced by the discharge of a capacitor bank. Due to the high-density current (10⁴–10⁶ Amm⁻²) through the wire, the temperature of the wire rises by joule heating, followed by melting, and finally reaches the boiling point and eventually superheating of the vapor. During this heating, some surface evaporation from the wire material takes place before melting the wire completely. This surface evaporation leads to a formation of nearby plasma of the wire materials and the ambient gases, conducting a part of the total current. As the wire materials completely melt, the current through the wire decreases due to the expansion of the vapor and continues until the vapor is sufficiently thick. When the concentration of the vapor decreases to a particular value, an arc discharge occurs. At this stage, a column of ionized plasma is formed. Subsequently, the plasma begins to expand due to the enormous difference in the temperature and pressure between the plasma and the ambient gas. The expanded plasma particles are rapidly cooled down during the expansion and a supersaturated vapor is formed which undergoes a homogeneous nucleation of nanoparticles [11, 21, 22]. The nanoparticles were collected and subjected to particle size analyzing. The results were used for further statistical investigations using ANOVA analysis of variance.

RESULTS AND DISCUSSION

Experimental design and mathematical model: It is difficult to obtain a model similar to the real, so it is important to analyze a large number of influences, but by careful planning of experiments to take account of economic and the duration of the experiment (23). Design of experiments is a statistical approach for modeling of an experimental response *y* by considering the most important effective factors *x*₁, *x*₂, ..., *x*_{*k*} as shown in eq.1:

$$y = f(x_1, x_2, \dots, x_k) \quad (\text{eq. 1})$$

The experimental data obtained was used to determine the coefficients of the polynomial model with RSM (eq. 2) [24].

$$Y = \beta_0 + \beta_i X_i + \beta_j X_j + \beta_{ii} X_i^2 + \beta_{jj} X_j^2 + \beta_{ij} X_i X_j + \dots \quad (\text{eq. 2})$$

Where, *i* and *j* are the linear and quadratic indexes, respectively, and β is the regression coefficient. *X*_{*i*} and *X*_{*j*} are the studied independent variables. β₀ is the interception coefficient, β_{*i*} and β_{*j*} are the linear terms and β_{*ii*} and β_{*jj*} are the quadratic

terms. P value with 95% confidence level was considered to evaluate the effectiveness of the model terms.

For Design of experiment of copper nanoparticles, four parameters containing wire diameter, feed rate, electrode distance and voltage were studied in five levels design with RSM. The ranges and levels of the variables in coded and actual units are given in Table 1. Particle size was selected as the numerical response. The experimental conditions and results obtained are shown in Table 2.

The ANOVA results: ANOVA results for CNPs size are presented in Table 3. The Model F-value of 10979.75 implies the model is significant. There is only a 0.01% chance that a "Model F-Value" this

large could occur due to noise. Values of Prob > F less than 0.0500 indicate all A, B, C, D terms are significant. The Lack of Fit F-value of 0.93 implies the Lack of Fit is not significant relative to the pure error. The Prediction R-Squared of 0.9992 was in reasonable agreement with the Adjusted R-Squared of 0.9993. Adequate precision was 389.217 indicating an adequate signal. Plots of the residuals in Supplementary Fig. S1 reveal that they have no obvious pattern and unusual structure. They also show equal scatter above and below the x-axis. This implies that the model proposed is adequate and there is no reason to suspect any violation [24]. Also, the validity of model was also evaluated using another graphs (Supplementary Fig. S2).

Table 1. Experimental range and levels of the independent variable based on ultimate design by RSM method.

Variables	unit	Range and levels				
		+2 α	+ α	0	- α	-2 α
Wire diameter (A)	mm	0.1	0.2	0.3	0.4	0.5
Feed rate (B)	cm/s	1	2	3	4	5
Electrode distance (C)	cm	1	2	3	4	5
Voltage (D)	kV	5	7.5	10	12.5	15

Table 2. Experimental conditions and CNPs size by EEW used in RSM design.

Run	Variables				Particle size (nm)
	A	B	C	D	
1	0.4	4	4	7.5	135.95
2	0.3	3	3	15	38.4
3	0.3	1	3	10	57.1
4	0.4	2	4	7.5	112.6
5	0.4	2	2	12.5	34.85
6	0.2	2	2	7.5	64.55
7	0.3	3	1	10	44.05
8	0.3	3	3	10	78.75
9	0.4	4	2	12.5	59.45
10	0.2	2	2	12.5	23.05
11	0.2	4	2	12.5	47.9
12	0.3	3	3	5	120.5
13	0.4	2	2	7.5	75.25
14	0.3	5	3	10	102.1
15	0.3	3	5	10	116.1
16	0.4	4	2	7.5	98.75
17	0.1	3	3	10	68.2
18	0.5	3	3	10	92
19	0.4	2	4	12.5	71.25
20	0.2	2	4	12.5	59.65
21	0.3	3	3	10	79.15
22	0.4	4	4	12.5	95.35
23	0.3	3	3	10	80.7
24	0.2	2	4	7.5	99.65
25	0.3	3	3	10	80.1
26	0.3	3	3	10	79.8
27	0.2	4	4	12.5	82.15
28	0.3	3	3	10	79.15
29	0.2	4	2	7.5	86.45
30	0.2	4	4	7.5	122.65

Table 3. ANOVA results for Response Surface Linear Model. ^a

Source	Sum of squares	df	Mean square	F value	P-value (Prob>F)
Model _a	21764.93	4	5441.23	1097.975	< 0.0001
A	876.04	1	876.04	176.75	< 0.0001
B	3215.54	1	3215.54	648.56	< 0.0001
C	7815.65	1	7815.65	1577.103	< 0.0001
D	9857.71	1	9857.71	1989.165	< 0.0001
Residual	12.39	5	0.50		
Lack of fit	9.76	0	0.49	0.93	0.5970
Pure error	2.63	5	0.53		
Core Total	21777.32	9			

^aR-squared= 0.9994, adjusted R-squared= 0.9993, adequate precision= 389.217, Prediction R-squared= 0.9992, Coefficient of Variation (C.V.)= 0.89, Prediction error sum of squares(press)=18.04.

The modified coded equation with significant terms based on ANOVA (eq.3) indicating the contribution of main factors on the particle size.

$$\text{particulatesize} = +79.52 + 12.08A + 23.15B + 36.09C - 40.53D \quad (\text{eq. 3})$$

The results show that order of contribution of factors in the particle size follow from the following trend:

Voltage > Electrode distance > Feed rate > Wire diameter

In addition, apart from the voltage all factors show straight relationship with the particle size. The results of contour graphs indicate the particle size increases with increasing both wire diameter

and feed rate (Fig. 2a). In the other word the particle size increases with increasing electrode distance and decreasing voltage (Fig. 2b).

Dependency of size nanoparticles on EEW conditions: Voltage was the most effective factor on the particle size. The correlation coefficient factor for voltage was -0.4053 that unlike other factor, coefficients is negative and denotes an inverse relation between the particle size and voltage. This result is in agreement with previously reports [25, 26] and is due to increase in the energy deposited (j) in the wire during the increasing the voltage (eq. 4).

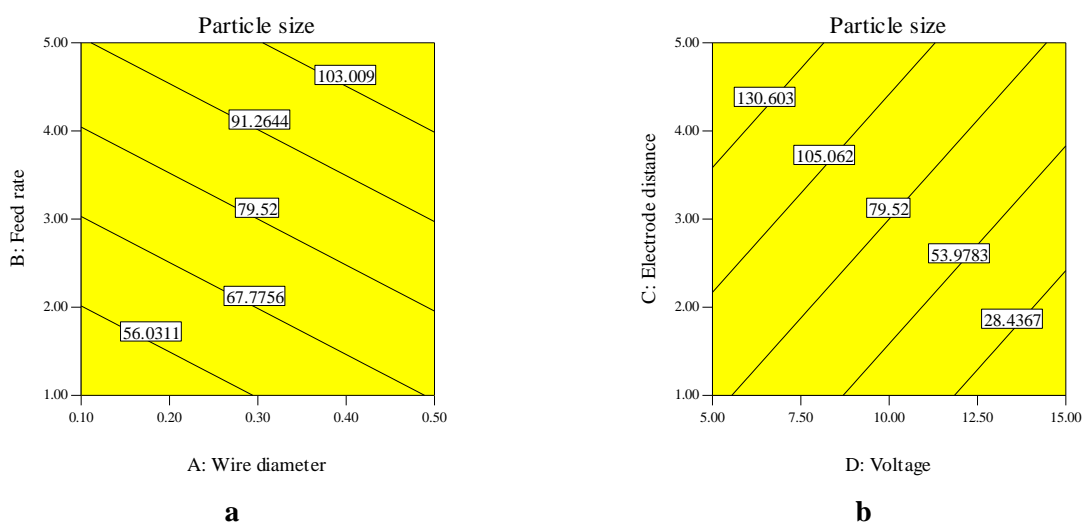


Fig. 2. Contour plots for nanoparticle size. Effect of wire diameter and feed rate on response. Actual factors (C=3.0, D=10) (a), electrode distance and voltage on the response. Actual factors (A=0.3, B=3) (b).

$$W_0 = \frac{1}{2} CV^2 \quad (4)$$

in where C, μF ; V, kV; and W_0 , J are capacity, voltage and the energy stored in the capacitor, respectively. The capacitor bank of 0.1 μF capacity was charged to a certain voltage by using an AC charger. However, the energy actually deposited to the wire, W usually is about 80–90% of the energy stored (27).

The major factor determining the particle size in the wire explosion process is superheating of the evaporated material. The particle size produced by the wire explosion process reduces substantially with increasing superheating of the metal, i.e. $K = \frac{W}{W_s}$, where W is the energy injected into the evaporating wire and W_s is the sublimation energy of the wire, which diminishes when the diameter of the wire is reduced.

This actual energy itself is related to the average size of particles (nm) formed as a result of EEW (Eq. 5):

$$D = 0.3 \times 10^3 (W/W_s)^{-3} \quad (5)$$

The energy for wire explosion can be written as (Eq. 6):

$$W_s = V_{\text{volume}} \cdot w_s = \frac{\pi}{4} d^2 \cdot \ell \cdot w_s \quad (6)$$

W_s is the energy for sublimation of the wire per volume unit (J), V_{volume} is wire volume, ℓ , length of wire (mm) and d is wire diameter (mm). w_s is specific sublimation energy of copper (47.8 J/mm³).

It was found, for example, that the energy injected to the wire, W, during the first current pulse (before the current pause) is defined by the relationship (Eq. 7):

$$W = (h_b W_0 S^2 Z)^{0.5} \quad (7)$$

that $S = \pi d^2 / 4$ is the cross sectional area of the wire, mm²; d is the wire diameter, mm; $Z = (L/C)^{0.5}$ is the circuit impedance, ohm; and h_b equals with eq. 8:

$$h_b = \left(\int_0^{t_3} i^2(t) dt \right) / S^2 \quad (8)$$

with the dimensionality $\text{A}^2\text{S}/\text{mm}^4$ and denotes the specific action before the explosion or the thermal resistance of the metal heated by a current pulse.

It can be seen from (Eq. 7) that, if $W_0 = (h_b S^2 Z)$ and the circuit loss is neglected, then: $W \approx W_0$. In other words:

$$W_0 = (h_b S^2 Z) \quad (9)$$

is one of the conditions for the consistent explosion.

Considering Eq. (9), the superheating may be expressed as shown in Eq. (10):

$$K = W / w_s S l = (h_b W_0 Z)^{0.5} / w_s l \quad (10)$$

The effect of all the mentioned factors is quite clear. As K increases, the expansion rate accelerates and the degree of ionization of explosion products rises. Ions probably represent primary condensation centers. Since the vapor super-saturation is high, condensation starts at the very beginning of expansion and progresses at a maximum rate. Therefore, the increase in the expansion rate and the number of condensation centers favors the decrease in the size of particles. For a typical experiment (Run 10), we calculated particle size by using above equations that this is equal to 33 nm.

It is evident that with increasing voltage, deposited energy, and finally superheating increases and value of the particle size will be finer. In case of low $\frac{W}{W_s}$ value the total explosion process time could be increased and thereby a growth of powder particle seemed to occur [27, 28].

With increasing electrode distance the particle size increases. Correlation coefficient factor for electrode distance is 0.3609 that denotes a linear relationship between factor and response. Its value exception voltage is larger than other factors. This means that this factor is second effective factor on particle size.

From eq.10, the effect of electrode distance is quite clear. Since overheat is inversely proportional to ℓ , it is seen the K value will decrease in proportion to the increase in electrode distance that the result is that increasing the length wires.

With increasing feeding rate, particle size increases. Correlation coefficient factor for this factor is 0.2315 that is less than voltage and electrode distance effects and represents less important feed rate on particle size. A low feed rate allows a low plasma volume. This leads to low number concentration of the substance during particle growth, resulting in small nanoparticles [11].

As it is seen in Eqs. 3, 5, and 6, with increasing wire diameter, h_b decreases, consequently K decreases and the particle size increases. Correlation coefficient factor for wire diameter is 0.1208. This factor is in the fourth place, in terms of nanoparticle size. This result is compatible with the experience [28].

Process optimization and point prediction: There are thirty desired solutions for a selected particle size range 25 ± 5 nm. The highlighted area on the overlay plot in Fig. 3 shows one of these solutions. Interestingly in this solution, the minimum required voltage was 8.84 kV while the

maximum amount of required wire diameter was 0.50 mm.

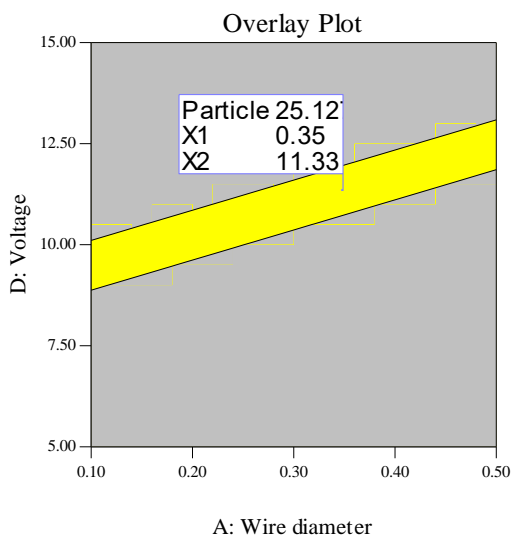


Fig. 3. Typically overlay plot for the optimal regions using response surface method (Actual factors: B= 1.89, C= 1.13).

An independent experiment (wire diameter, feed rate, electrode distance, and voltage = 0.2, 2, 4, and 10, respectively) was carried out to check and verify the model. The particle size measured with XRD was 80.65 nm which is in agreement with the value 79.95 nm predicted.

Semi large scale synthesis: In order to investigate the potent of semi large scale synthesis, the experimental run 10 was performed in the conditions (wire diameter=0.2, feed rate=2, electrode distance=2, and voltage=12.5) in 60 min. The prepared nanoparticles were collected and analyzed. The yield was 52.6 g (65%).The power

consumption was calculated about 0.5 kWh/gCu with 0.05 \$ cost (according to world electrical power average cost= 0.1 \$/1 kWh).According to this magnitude of power supply, it can be concluded that the nanoparticle prepared in this way were economically affordable compared with the other method [29].

In compare with previous studies on the EEW method for synthesis of CNPs [11, 30-32],we obtained desired particle size very selective and cost-effective.

CHARACTERIZATION

*CNPs analyses:*Typical TEM image of CNPsis shown in Fig. 4a. The CNPswere spherical in shape. A bar graph depicting the size distribution of the CNPs was determined based on total particle population taken from TEM micrograph shown in Fig. 4b.The number-average particle size obtained 23.80 nm and the particle distribution was in the range of 10–50 nm.

A typical X-ray diffraction pattern of the prepared CNPs is shown in Supplementary Fig. S3. The major peaks located at 2θ values 43.7° , 50.7° , 73.8° , 90° , 94.9° are corresponded to (111), (200), (220), (311), and (222) planes of CNPs in a face-centered cubic structure (JCPDS 5-0661, $a= b =c =3.6077 \text{ \AA}$) respectively. In almost all experiments, no characteristic peaks related of copper oxide were observed which represents the purity of the Cu nanopowder. The average crystallite size calculated from Debye-Scherer equation was 22.3 nm [4].

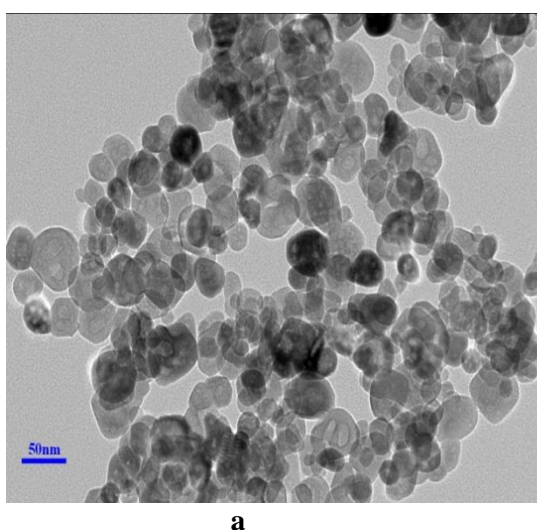


Fig. 4.TEM micrograph (a) and size distribution (b) of CNPs synthesized by EEW.

EDX spectroscopy (Supplementary Fig.S4) illustrated the chemical nature of synthesized CNPs

using EEW. The peak at the energy of 15keVwas attributed for copper. In addition, there are some

weak peaks belongs to O and Al. The latter impurity may be inserted due to the electrode materials.

The optical absorption spectrum of copper is shown in the Fig. 5. The SPR peak centered at 637 nm is characteristic for CNPs [33].

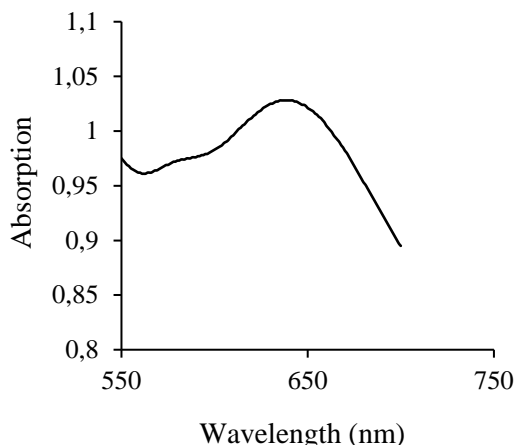


Fig. 5. UV-Visible absorption spectra of CNPs.

CONPs Analyses: A typical X-ray diffraction pattern of the prepared CONPs in the oxygen atmosphere is shown in Supplementary Fig. S5. The major peaks located at $2\theta = 35.5^\circ \pm 1^\circ$, $38.8^\circ \pm 1^\circ$, $48.7^\circ \pm 1^\circ$, and $61.4^\circ \pm 1^\circ$ are corresponded to (111), (202), (020), and (220) planes of CNPs in a face-centered cubic structure CuO (JCPDS 45-0397). There are also several trace peaks in sample which were assigned to Cu_2O peaks. The two highest peaks in the XRD patterns were chosen to calculate the size of the nanoparticles. This results show that the EEW is a very selective method for preparation of CONP. Calculations using Debye-Scherrer's equation showed that CuO nanoparticles had an average grain size of about 28.5 nm.

In the FT-IR spectrum of CuO (Supplementary Fig. S6), a broad band between 3800 and 3000 cm^{-1} , centered at 3436 cm^{-1} is assigned to OH stretching of the adsorbed water or surface OH groups. The band at 1421 cm^{-1} is due to bending of molecular water [34]. Sharp peaks between 1000 and 500 cm^{-1} could be assigned to Cu-O stretching.

CONCLUSION

In conclusion, we succeeded to synthesize nanoparticles with desired size and very selective using EEW. In addition, this method is ecologically safe, provides a sufficiently high production rate, requires a relatively small energy, and allows making powders with a small degree of contamination. This method was also used in semi large scale synthesis of nanoparticles. The process has been designed and optimized using response surface methodology by which, the weight

contribution of operational conditions has been determined. The resulting coded equation was used for point prediction and verification of other experiments.

Acknowledgments: The authors thank the Razi University Research Council for the support of this work.

REFERENCES

1. H. Suematsu, S. Nishimura, K. Murai, Y. Hayashi, T. Suzuki, T. Nakayama, W. Jiang, A. Yamazaki, K. Seki, *Rev. Scientific Instruments*, **78**, 6 (2007).
2. P. Kiran, G. DeNarayana, D. Rao, *Devices and Systems*, **150**, 559 (2003).
3. R. Soomro, A. Tufail, H. Sherazi, S. Juddin, S. Memon, N. Shah, M.R. Kalwar, N.H. Richard, K. Hallam, A. Sha, *Adv. Mat. Lett.*, **5**, 191 (2014).
4. T.M.D. Dang; T.T.T. Le, E. Fribourg-Blanc, M.C. Dang, *Adv. Nat. Sci. Nanosci. Nanotechnol.*, **2**, 2043 (2011).
5. S.P. Meshram, P.V. Adhyapak, U.P. Mulik, D.P. Amalnerkar, *Chem. Eng. J.*, **204**, 158 (2012).
6. A.H. MacDonald, *Nature*, **414**, 409 (2001).
7. C.L. Carnes, J.K. Stipp, K.J. Labunde, *Langmuir*, **18**, 1352 (2002).
8. Y. Lee, J. Choi, K. J. Lee, N. E. Stott, D. Kim, *Nanotechnol.*, **19**, 1361 (2008).
9. B. K. Park, S. Leong, D. Kim, J. Moon, S. Lim, J.S. Kim, *J. Colloid Interface Sci.*, **311**, 417 (2007).
10. Y. A. Kotov, *J. Nanopart. Res.*, **5**, 539 (2003).
11. Y. S. Lee, B. Bora, S. L. Yap, C. S. Wong, *Curr. Appl. Phys.*, **12**, 199 (2012).
12. D. Shafer, V.Tz. Gurovich, D. Yanuka, E. Zvulun, S. Gleizer, G. Toker, Ya.E. Krasik, *J. Appl. Phys.*, **117**, 015901 (2015).
13. R. Sarathi, T.K. Sindhu, S.R. Chakravarthy, *Mater. Charact.*, **58**, 148 (2007).
14. R. Sarathi, T. K. Sindhu, S.R. Chakravarthy, *Process. Mater. Lett.*, **61**, 1823 (2007).
15. R. Sarathi, R.S. Reddy, R.S. Tavarmani, A. Okamoto, H. Suematsu, P. Selvam, U.K. Mudali, M. Kamaraj, *IEEE Transactions on Plasma Sci.*, 93 (2015).
16. Y. Tokoi, T. Suzuki, T. Nakayama, H. Suematsu, F. Kaneko, K. Niihara, *Curr. Appl. Phys.*, **9**, S193 (2009).
17. L. Liu, J. Zhao, W. Yan, Q. Zhang, *IEEE T Nanotechnol.*, **13**, 842 (2014).
18. S. H. Tong, Z. X. Bing, Z. Shen, Z. X. Lei, W.X. Xin, *Acta Phys. Sin.*, **63**, 134 (2014).
19. V. S. Sedoi, Y. F. Ivanov, *Nanotechnology*, **19**, 1361 (2008).
20. M. Barmala, A. Mohe, R. Emadi, *J. Alloy. Comp.*, **485**, 778 (2009).
21. S. Vorob'ev, S. P. Malyshenko, S.I. Tkachenko, *High. Temp.*, **43**, 908 (2005).
22. Q. Zhou, Q. Zhang, W. Yun, X. Liu, J. Zhang, J. Zhao, L. Pang, *Transactions on Plasma Sci.*, **2**, 2198 (2012).

23. R. Abedini, S.M. Mousavi, *Chem. Ind. Chem. Eng. Q*, **18**, 171 (2012).
24. A. Asadi, A.A.L. Zinatizadeh, S. Sumathi, *Water Res.*, **46**, 4587 (2012).
25. Q. Li, Q.Z. Song, J.Z. Wang, Y.X. Duo, *Surf. Coat. Tech.*, **206**, 202 (2011).
26. L.N. Shiyan, N.A. Yavorovskii, A.V. Pustovalov, E.N. Gryaznova, *Mater. Sci. Engin.*, **81**, 012077 (2015).
27. Y.S. Kwon, Y.H. Jung, N.A. Yavorovsky, A.P. Illyn, J.S. Kim, *Scripta.mater.*, **44**, 2247 (2001).
28. P. Wankhede, P.K. Sharma, A.K. Jha, *J. Eng. Res. Appl.*, **3**, 1664 (2013).
29. I.V. Beketov, A.P. Safronov, A.V. Bagazeev, A. Larranaga, G.V. Kurlyandskaya, A.I. Medvedev, *J. Alloys Comp.*, **586**, S483 (2014).
30. P. Dash, K.Y. Balto, *J.Nanosci. Nanotechnol.*, **1**, 25 (2011).
31. R. Das, B.K. Das, *J Korean Phys. Soc.*, **61**, 710 (2012).
32. C. S. Wong, B. Bora, S.L Yap, Y.S. Lee, H. Bhuyan, M. Favre, *Curr. Appl. Phys.*, **12**, 1345 (2012).
33. M. P. Pileni, *J. Phys. Chem. B*, **108**, 20050 (2004).
34. T.M.H. Costa, M.R. Gallas, E.V. Benvenuti, J.A.H. da Jornada, *J. Phys. Chem. B*, **103**; 4278 (1999).

Appendix. Supplementary data

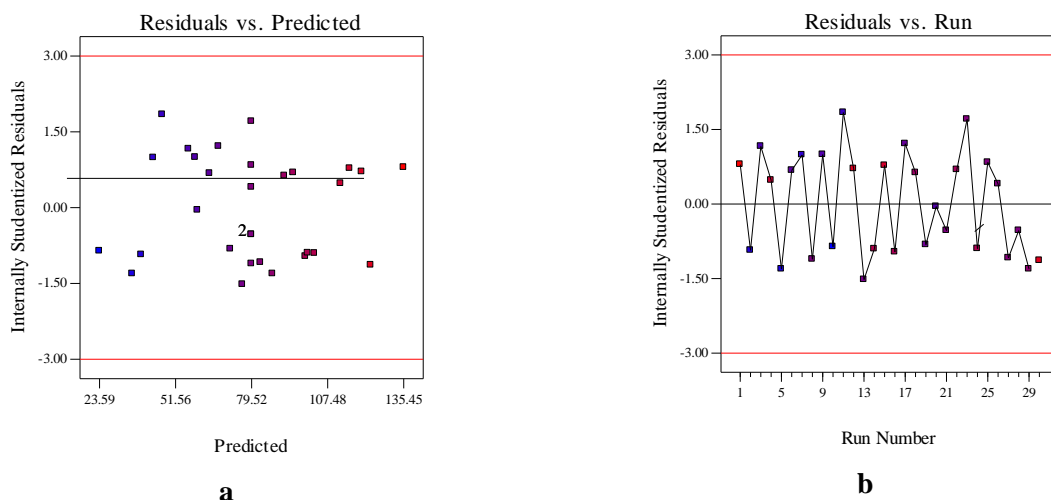


Fig. S1. Plot of residual vs. predicted response for ANPs size (a) and plot of residual vs. each run (b) based on preliminary design by Taguchi method.

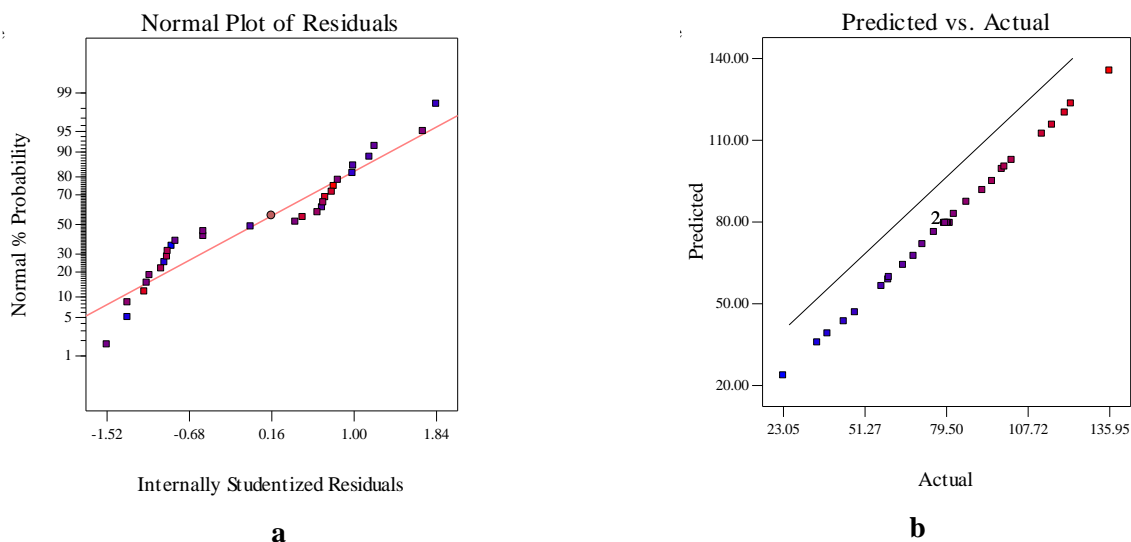


Fig. S2. Normal plot of residuals (a) and actual versus predicted (b) by response surface method for CNPs

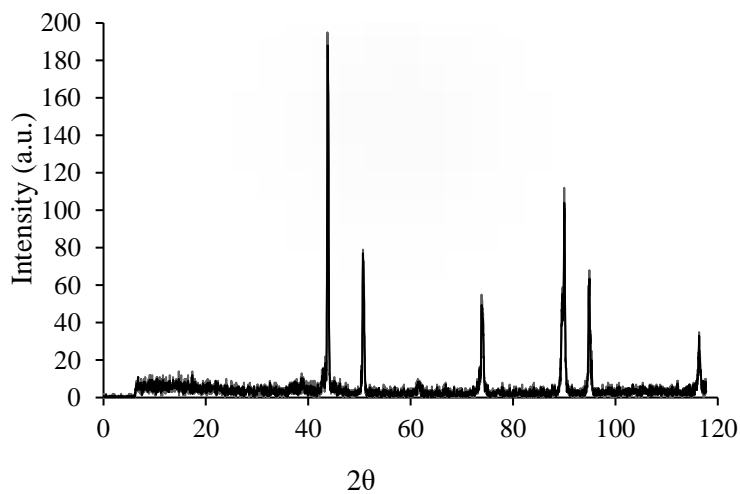


Fig. S3. XRD pattern of CNPs produced by EEW.

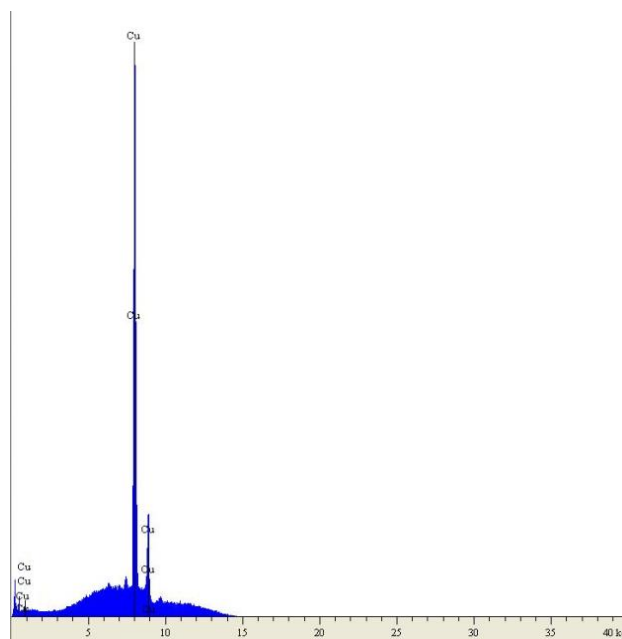


Fig. S4.EDX spectrum of CNPs synthesized by EEW.

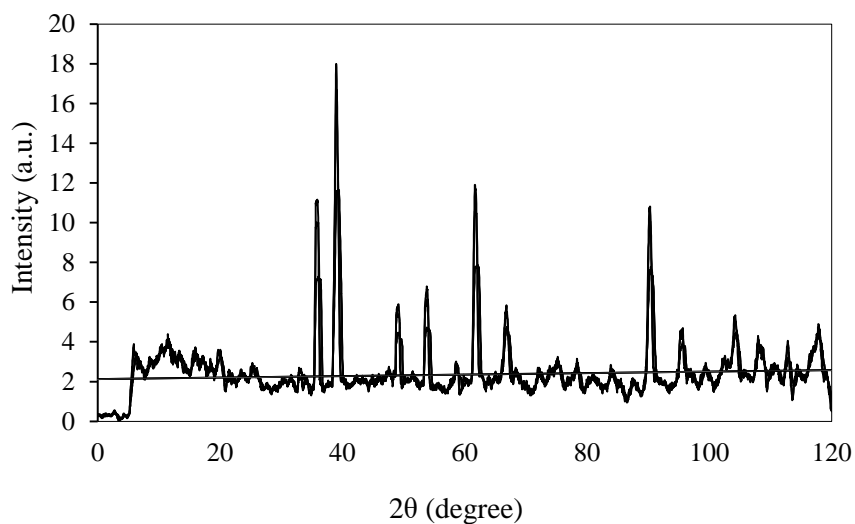


Fig. S5. XRD pattern of CONPs produced by EEW.

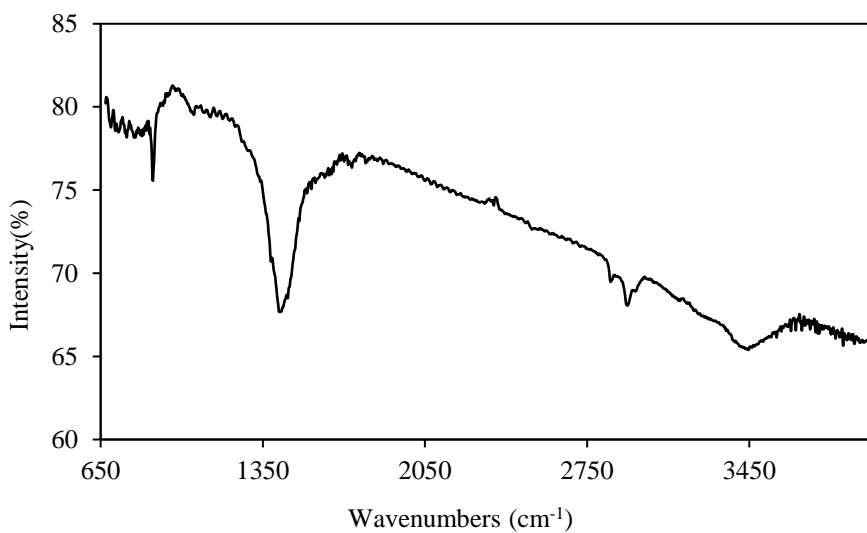


Fig. S6. FT-IR spectrum of synthesized CONPs by EEW method.

Non-thermal plasma for simultaneous NO_x and SO₂ removal from coal-combustion flue gas

Guo Bin^{1,2}, Luan Tao^{1,*}

¹ School of Energy and Power Engineering, Shandong University, Jinan 250061, Shandong Province, China

² water conservancy and civil engineering Colleges, Shandong agricultural university, Taian 271018, China

Received June 18, 2016, Revised September 10, 2016

In the laboratory, NO_x and SO₂ were removed from simulated flue gas using a plasma generator. Under normal temperature conditions, the efficiencies of desulfurization and denitrification exhibited a linear relationship with plasma input power. Dielectric barrier discharge equipment was used in the mode in which flue gas was directed through the discharge zone (direct oxidation) or that in which ozonized air was produced and injected into the flue gas stream (indirect oxidation). The SO₂ and NO_x removal efficiencies of both methods were measured and compared. Based on the experimental results, the desulfurization and denitrification efficiencies achieved using the indirect plasma were better than those achieved using the direct plasma.

Keywords: non-thermal plasma generator, denitrification, desulfurization, energy consumption

AIMS AND BACKGROUND

In recent years, coal consumption has increased by 2.2% annually, faster than that of any other type of fuel. It is anticipated that coal consumption will continue to increase until 2030. In fact, this increase in consumption will probably exceed 70% compared with the present value, with developing countries contributing 97% of this increase. By 2030, the global rate of coal use for power will increase from 40% to 45% [1]. Burning coal will release large quantities of SO₂ and NO_x, which will negatively impact air quality, produce haze, generate acid rain, severely pollute the environment, and have detrimental effects on health [2]. Controlling the discharge of SO₂ and NO_x in flue gas effectively and economically is an important strategic issue relating to sustainable development. Increasingly stringent global emission standards are inspiring researchers worldwide to exploit new technologies and develop new methods for desulfurization and denitrification. SO₂ and NO_x coexist in flue gas. However, there are no reliable chemical methods to remove these gases via a one-stage process. Therefore, it is necessary to develop new methods for simultaneous desulfurization and denitrification [3-4]. Currently, domestic and foreign research efforts have achieved breakthrough, and many advanced control technologies have been developed, including desulfurization using clean coal, desulfurization

and denitrification using ovens, desulfurization and denitrification in flue gas, desulfurization and denitrification using an electron beam in flue gas, desulfurization and denitrification in flue gas by pulsed plasma, and desulfurization and denitrification by non-thermal plasma [5-6]. Among these, non-thermal plasma technology, a new technology with great promise, is the most popular one studied currently regarding controlling SO₂ and NO_x. Non-thermal plasma is used to remove SO₂ and NO_x because NO_x can be oxidized and SO₂ can be transformed into its acid products, which can then be neutralized by mixing with NH₃. This process generates solid sulfate and ammonium nitrate, which can be subsequently recycled as agricultural fertilizers [7].

In the 1980s, scholars worldwide began to study the use of cheaper non-thermal plasma technology to replace the relatively expensive electron accelerator devices. Pulsed corona discharge plasma flue gas treatment technology is one of the most pursued research directions globally. Japanese scholars have reported that applying pulsed plasma to flue gas can achieve desulfurization and denitrification simultaneously. Based on the electron beam method, they devised a pulsed corona method to produce the plasma, which uses a high-voltage pulsed power supply to replace the electron beam accelerator, and demonstrated the effectiveness of this technique. The pulsed corona method can achieve desulfurization and denitrification simultaneously and collect dust. This technique requires only simple equipment, its operation is easy, and it is substantially cheaper

* To whom all correspondence should be sent:
E-mail: gshpsc@163.com

than electron beam irradiation. Furthermore, its by-products can be used as fertilizers, and the method does not produce secondary pollution. Therefore, it has attractive prospective applications in research addressing how to mitigate gaseous pollutants. However, this method must overcome one difficulty: how to realize easy control over a high-power, high-voltage pulsed power supply [8]. This article focuses on comparing the use of direct and indirect non-thermal plasma to achieve desulfurization and denitrification in terms of efficiency. Additionally, the efficiency of denitrification alone is compared with that of simultaneous desulfurization and denitrification when non-thermal plasma is used. Finally, the relationship between the energy consumption of the plasma generator and the efficiency of denitrification is determined to facilitate finding a way to reduce energy consumption and thus promote industrialized applications of this technology.

EXPERIMENTAL

Plasma generator

The entire body of the generator was constructed of stainless steel. The discharge area was 150 mm in length and contained a 3-mm space (single-sided). The medium tends to resist the discharge process when the space is smaller and the input and discharge voltages are lower. The thickness of the resistance medium also affects the electrodes' discharge to some extent. The components had the following dimensions: steel pipe: 25mm × 20mm; gear-shaped electrode core: 10 mm; and diameter of the raised stand: 14 mm. The structure and dimensions of the generator are shown in Figure.1.

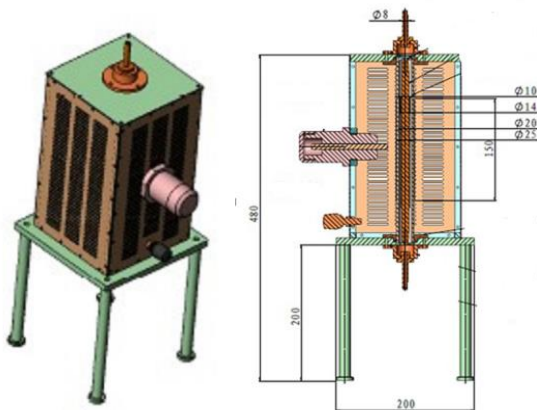


Fig. 1. Structure of the generator.

Experimental platform

(1) Gas supply system. The simulated flue gas used in the experiment consisted of N₂, O₂, NO,

NH₃, and SO₂. NO accounts for more than 95% of NO_x produced by coal-burning power stations, and the NO₂ content is only 5%; thus NO₂ exerts little influence on the behavior of the flue gas. Because NO₂ can be neglected, NO is typically used to model NO_x in experimentally simulated flue gas from power stations [9–10]. The flow of gas in the steel cylinder is controlled with a rotameter. The gas is first mixed in the commingler, and then, the uniform gas enters the tabulation and is preheated. The NH₃ enters the tabulation and subsequently reacts as the tabulation is heated. The basic information about the simulated flue gas is presented in the following table (Table 1):

The NO-removal efficiency was calculated as follows (equation (1)):

$$\text{The efficiency of removing NO(\%)} = \frac{\text{The concentration of NO at entrance} - \text{The concentration of NO at exit}}{\text{The concentration of NO at entrance}} \times 100\% \quad (1)$$

Every gas is fully mixed after entering the commingler. Then, they react with free radicals, and O₂ and steam react when passing through the exit of the plasma generator. This process is known as indirect non-thermal plasma desulfurization and denitrification. The system is shown in Figure.3.

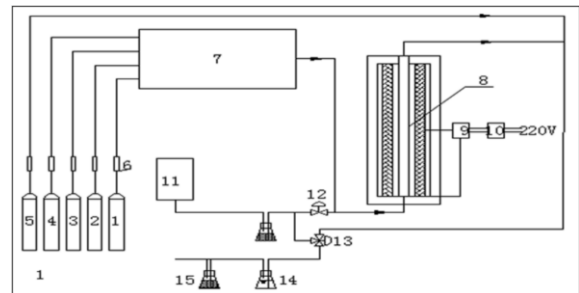


Fig. 2. The system used for direct non-thermal plasma desulfurization and denitrification.

1-O₂ cylinder, 2-SO₂ cylinder, 3-N₂ cylinder, 4-NO cylinder, 5-NH₃ cylinder, 6-flow counter, 7-gas mixer, 8-plasma generator, 9-plasma electric source, 10-voltage transformer, 11-gas analysis equipment, 12-valve, 13-three-way valve, 14-inverted bottle, and 15-dry bottle

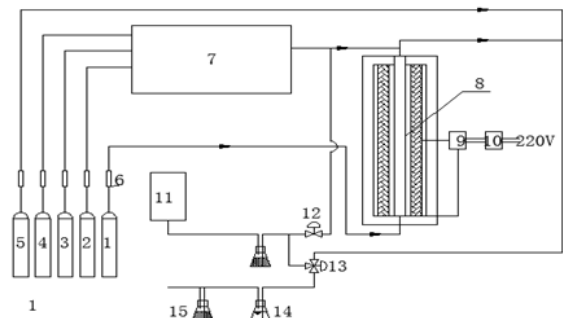


Fig. 3. The system used for indirect non-thermal plasma desulfurization and denitrification. 1-O₂ cylinder, 2-SO₂ cylinder, 3-N₂ cylinder, 4-NO cylinder, 5-NH₃ cylinder, 6-flow counter, 7-gas mixer, 8-plasma generator, 9-plasma electric

source, 10-voltage transformer, 11-gas analysis equipment, 12-valve, 13-three-way valve, 14-inverted bottle, and 15-dry bottle.

Table 1. The basic information of the experimental flue gas.

Parameter	Temperature	Initial concentration of NO	Initial concentration of SO ₂	Flow of the simulated flue gas
Numerical value	20°C	380ppm	500ppm	500ml/min

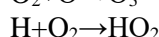
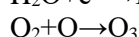
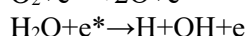
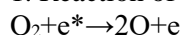
(2) Gas analysis system. Using online gas analysis equipment (MGA-5, MRU, Germany) allowed online measurement of the densities of NO, NO₂, SO₂, NH₃, CO, and O₂ with an accuracy of ±1 ppm. Once inserted, a gas-sampling pump extracted sample gas from the flue through the sampling pipe and tube. After the sampled gas was dehydrated and desooted using a gas-water filter, the inserted electrochemical sensor determined the density of each component gas. The oxygen content of the sample was measured using a two-electrode electrochemical sensor. Toxic gases, such as CO, NO, NO₂, SO₂, and H₂S, were analyzed using a three-electrode sensor. The electrochemical sensors utilized gas-diffusion technology. The advantage of this technique is that the output signal is proportional to the volume concentration (or ppm) of the analyzed gas. The three electrodes included the sensing electrode (S), counter electrode (C), and reference electrode (R). When the gas of interest reaches the sensing electrode, an oxidation or a reduction reaction occurs on the surface of the electrode, and the concentration of the gas can be obtained by measuring the resulting current (μA) and subjecting the signal to microprocessor processing.

Reaction mechanism [11-13]

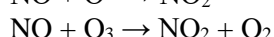
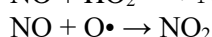
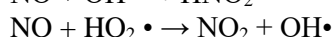
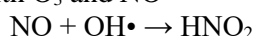
Plasma was first studied in 1808 by Davy, and in the 1930s, Langmuir proposed the concept of "plasma". Gas that is ionized at high voltage is called plasma. More specifically, plasma consists of gas that is ionized, for example, by electric discharge and heat release. When the number of particles is sufficient, plasma is formed by the particles containing electrons, ions, and atoms. The number of positive charges is equal to the number of negative charges in plasma, and it is an electrically conductive fluid. Plasma has conductive and electromagnetic characteristics, and its activity is very strong. In many ways, it is different from solids, liquids, and gases. Therefore, it is known as the fourth state of matter [14]. Dielectric barrier discharge (DBD) non-thermal plasma is a high-pressure, low-temperature, and

non-equilibrium plasma. Because it can be generated at atmospheric pressure or higher, it can obtain the active particles required to induce chemical reactions without the need for vacuum equipment. It exhibits unique light-, heat-, sound-, and electricity-related physical and chemical processes, the distance between the DBD electrodes is several millimeters, and it generates high concentrations of free radicals (O•, OH•, and HO₂•). These free radicals react with NO_x and SO₂ and result in desulfurization and denitrification. The relevant chemical reactions are as follows:

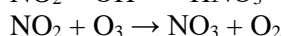
1. Reaction of wet air in a plasma reactor



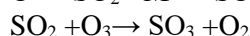
2. Reaction of free radicals (O, OH, and HO₂) with O₃ and NO



3. Further reaction of free radicals, O₃, and NO₂ generated by the reaction between the free radicals and O₃



4. Reaction of free radicals (O, OH, and HO₂), O₃, and SO₂



RESULTS AND DISCUSSION

Analysis of NO_x removal from flue gas by non-thermal plasma

When the simulated flue gas contained only N₂, O₂, and NO and the flow rate was 500 ml/min, the NO concentration in the inlet was generally controlled at 400 ppm, the plasma generator input voltage was 15 V, the generator initiates the discharge, the maximum voltage is 40 V, and the current is 1.3 A. The NO_x-removal efficiencies of

the experimental low-temperature plasma reactor at different power levels are shown in Figure.4.

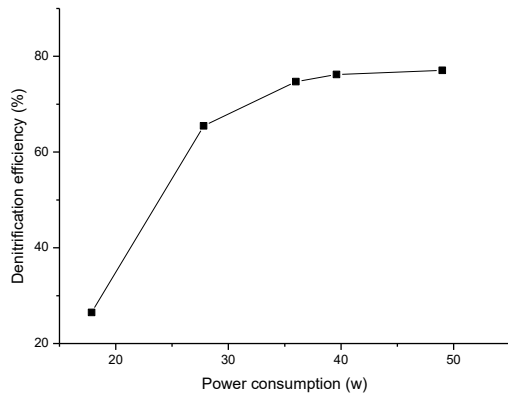


Fig. 4. Analysis of NOX removal from flue gas by non-thermal plasma.

The removal efficiency of the catalyst improved continually as the plasma input power increased. The removal efficiency exceeded 80% when the input power exceeded 35 W and reached 91.7% when the input power was 52.8 W. The removal efficiency was positively proportional to the input voltage and current; however, the increase in the removal efficiency was not large. When the voltage reached a certain level and the dielectric barrier discharge was disrupted, the removal efficiency decreased sharply.

Denitrification efficiency under simulated increased flow of flue gas

As shown in Figure.5, the denitrification efficiency increased in the context of a simulated increase in flue gas flow.

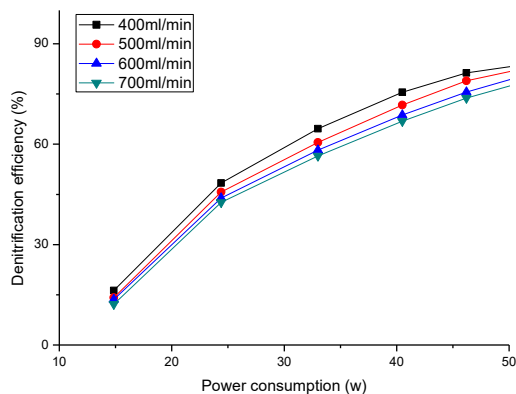


Fig. 5. Analysis of the denitrification performance as the flow is varied.

As the flue gas flow increased, the denitrification efficiency decreased. Relative to the power consumption under the same plasma reactor

conditions, the denitrification efficiency decreased by 10%, and the reaction mechanism of the plasma remained constant. Breaking more molecular bonds requires the consumption of more energy; hence, energy is conserved. Figure 5 shows the flue gas denitrification efficiencies of four different simulated flows under the same input voltage and current conditions. As the flow increased, the denitrification efficiency decreased; the top curve shows the minimum tested flow and its denitrification efficiency.

Analysis of simultaneous desulfurization and denitrification via direct oxidation

The experimentally determined removal efficiencies of simultaneous desulfurization and denitrification are shown in Figure6.

Relative to denitrification alone, the addition of SO₂ substantially influenced the removal efficiency, although the effect varied. When the input power of the reactor increased to 66 W, the denitrification efficiency was only 24.1%, as shown by the top curve of the figure above. However, increasing the input voltage to 40 V greatly affected the discharge reaction. Initially, in the discharge plasma reactor, the denitrification efficiency is very low, while before and after the test reactor, the SO₂ density is almost constant, as shown in the bottom curve in the figure above. Thus, little to no effect was observed in terms of SO₂ removal, whereas a huge effect was observed on the NO-removal performance. Several underlying reasons are possible: 1. SO₂ could inhibit the generation of O₃. 2. Previous research has shown that SO₂ consumes OH [15], which could limit the supply of OH available to react with NO [3]. The mixed gas could inhibit plasma discharge.

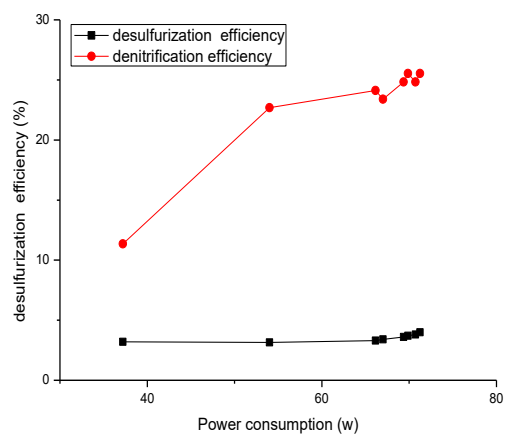


Fig. 6. Analysis of the removal efficiencies of simultaneous direct desulfurization and denitrification.

Analysis of simultaneous desulfurization and denitrification via indirect oxidation

The experimentally determined efficiencies of indirect simultaneous desulfurization and denitrification are shown in Figure 7. When the input voltage was 15 V, the reaction began in the discharge plasma reactor, and the reactor input power was 18.9 W. Then, the input voltage was increased to 23 V, the input power became 33.81 W, the flow of gas into the reactor was 500 mL/min, the initial NO concentration was 380 ppm, and the initial SO₂ concentration was 500 ppm to ensure high denitrification efficiency.

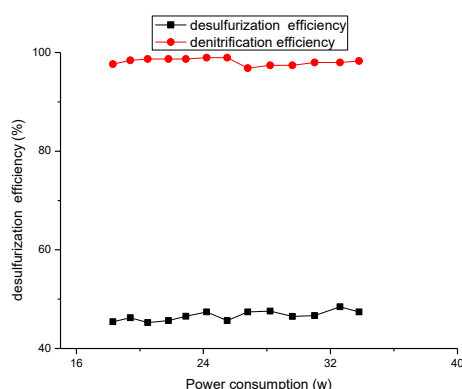


Fig. 7. Analysis of the removal efficiencies of simultaneous indirect desulfurization and denitrification.

The above figure shows that initially, the denitrification efficiency is very high (above 97%), while the desulfurization efficiency is 46%. This is different from the results observed for simultaneous direct desulfurization and denitrification, for which the desulfurization efficiency is very low. In the direct technique, the concentration of NO was controlled, and the input power was increased until the low-temperature plasma reactor achieved a high voltage, resulting in disruption of the desulfurization and denitrification efficiency. In contrast, indirect desulfurization and denitrification requires only input voltage supplied to the DBD, and even when the input power is low, this technique can achieve very efficient denitrification and desulfurization. According to its reaction mechanism, indirect desulfurization and denitrification in a plasma generator generates O₃, which reacts with and removes SO₂ and NO. However, $\text{NO} + \text{O}_3 \rightarrow \text{NO}_2 + \text{O}_2$ generates a large quantity of NO₂, which has a high activity. Therefore, this technique requires additional measures (the addition of a reducing agent or adsorbent) to remove NO₂ and thereby truly achieve denitrification.

Effect of NH₃ on denitrification performance

The addition of NH₃ somewhat improved the denitrification efficiency when the conditions were otherwise the same. The denitrification efficiency with and without NH₃ is plotted in Figure 8.

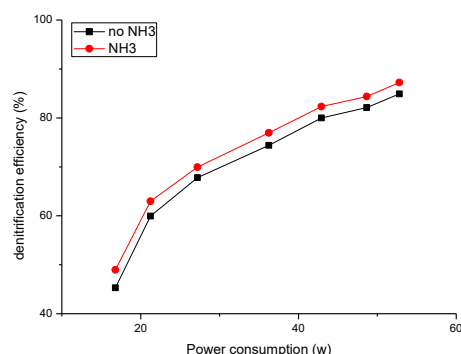


Fig. 8. Comparison of the denitrification performance with and without NH₃.

During direct non-thermal plasma desulfurization and denitrification, the efficiency can increase, although it will decline after 5 s, as shown above. The reason the plasma reactor discharge is affected at the same time remains unknown. The generator begins to discharge when the voltage is 15 V in the absence of SO₂ and at 40 V in the presence of SO₂.

During indirect simultaneous denitrification and desulfurization, the NO-removal rate is very high, but a substantial amount of NO is converted to NO₂. However, an experimental phenomenon was observed: when the O₂ input flow is reduced, NO₂ conversion is also substantially reduced. Additionally, it was found that the N₂ and free radicals produced by the plasma generator could react to produce a large quantity of NO₂. During indirect simultaneous desulfurization and denitrification, the required input voltage is the minimum voltage able to trigger the plasma reactor discharge, and increasing the input voltage and input power increases the production of free radicals and O₃. Additionally, the efficiencies of desulfurization and denitrification are not increased but the amount of NO₂ is, as demonstrated in the analysis presented above.

CONCLUSIONS

Based on our analysis of these experimental results, the following conclusions regarding the removal of NO_x from flue gas by non-thermal plasma can be reached:

The removal efficiency exceeds 80% when the input power exceeds 35 W. The removal efficiency of the catalyst improves continually as the plasma

input power increases. When the same power consumption is maintained in the plasma reactor, the efficiency decreases. This finding is in accord with the reaction mechanism of plasma: as more molecular bonds are broken, the power consumption increases, in accordance with the conservation of energy principle. During simultaneous desulfurization and denitrification, the denitrification and desulfurization efficiencies can be very high, in addition to the reaction of free radicals with NO and SO₂, O₃ can also play an important role. Furthermore, in the indirect technique, only O₃ or H₂O need to be ionized in the reactor; thus, providing a very small voltage can generate free radicals, resulting in very low power consumption and obvious energy savings. The two methods—the direct oxidation process (where gas flows through the reactor) and the indirect oxidation process (where the reactor generates free radicals and O₃ in the flue gas) - were compared in terms of their SO₂- and NO_x- removal efficiencies. It can be concluded that the direct removal of NO was more efficient, whereas indirect SO₂ removal was more efficient. During the direct oxidation of NO, in addition to NO₂ oxidation, the reverse reaction, in which NO is transformed into NO₂, occurs. In simultaneous desulfurization and denitrification, indirect oxidation is more efficient for both denitrification and desulfurization, but the reaction of free radicals, O₃, and N₂ generates substantial quantities of NO₂, which is a serious problem. It can be safely concluded that the available NO_x-removal technologies involving

non-thermal plasma remain in the experimental stage. The industrialization of this process will require additional research effort to reduce the energy consumption and enhance the removal efficiency.

REFERENCES

1. I.E. Agency, World Energy Outlook 2007, OECD/IEA, Paris, 2007.
2. Y. Gao, T. Luan, H.M. Xu, *Proc. of the CSEE.*, **32**, 143 (2013).
3. N. Ding, H.T. Huang, X. Li, *J. Safety Environ. Eng.*, **15**, 25 (2008).
4. X. Liu, S.D. Wang, *CIESC. J.*, **57**, 2411 (2006).
5. P.P. Wei, L.M. Dong, J.X. Yang, *Nat. Sci. J. of Harbin Normal University*, **17**, 68 (2001).
6. J.S. Clements, *IEEE Trans. on Ind. Appl.*, **25**, 62 (1989).
7. H.H. Kim, *Plasma Processes and Polym.*, **1**, 91 (2004).
8. X.C. Wang, X.H. Liu, K.F. Shang, *Environ. Protection Circular Economy.*, **6**, 26 (2009).
9. J. Svachula, N. Ferlazzo, P. Forzatti, *Ind. Eng. Chem. Res.*, **32**, 1053 (1993).
10. Q. Liu, Z. Liu, Z. Huang, *Catalysis Today*, **93-95**, 833 (2004).
11. Z. Hu, Fundamentals of plasma. Chemistry Chemical Industry Times, 1999.
12. F. Francis, P. Jane: Lecture Notes on Principles of Plasma Processing. Springer, Plenum/Kluwer, 2002
13. G.Q. Yan, L.L. Pan, X.H. Huang, *Environ. Technol.*, **3**, 1 (2005).
14. G.J. Zhang, K. Li, Q. Lin: *Materials Review A.*, **29**, 137 (2015).
15. Y.M. Zhu, *Advances Environ. Sci.*, **5**, 75(1997).

Experimental analysis of removal of SO₂ and NO_x for nano Mg-Al composite oxides

W. Cheng^{1*}, Y. Zhang², S. Wei³, Y. Hu¹

¹*School of Energy, Power and Mechanical Engineering, North China Electric Power University, 102206 Beijing, China*

²*Department of Administration, Sanhe Power Generation Co., Ltd. 065201 Sanhe, Hebei, China*

³*Department of Production technology, Sanhe Power Generation Co., Ltd. 065201 Sanhe, Hebei, China*

Received June 12, 2016; Revised September 10, 2016

Nano Mg - Al composite oxides were prepared through the solid state reaction synthesis method and molten salt synthesis method respectively, and efficiencies of desulfurization and denitrification were tested at the same time under the condition of flue gas, to find the optimal proportion of the material, and to investigate the adsorption mechanism of Mg-Al composite oxides. It was found that the more proportion of Mg, the efficiencies of desulfurization and denitrification are better. The removal efficiencies of the sample prepared by the molten salt synthesis method are better than that prepared by solid state reaction synthesis method. The sample, in which Mg/Al molar ratio is 4:1, has the best removal efficiency with molten salt method. The highest removal efficiency of SO₂ can reach 100%, and the highest removal efficiency of NO_x can reach 71%, whose time can maintain 150 min. It showed that the whole adsorption processes are controlled by surface adsorption reaction, and the internal diffusion and outer diffusion play a secondary role.

Keywords : Mg-Al composite oxides, desulfurization & denitrification, adsorption process, molten salt synthesis method, Solid state reaction synthesis method.

AIMS AND BACKGROUND

In China, lime slurry was adopted to reduce emissions of SO₂ from coal-fired power plants, and production of desulfurization can be used for producing gypsum board. Selective catalytic reduction method was adopted to reduce emissions of NO_x in coal-fired power plants, and N₂ and water generated by reaction of NO_x with NH₃. Separately using the above two methods are difficult to achieve the ideal effect of desulfurization and denitrification at the same time. Many scholars are researching and developing of a new technology of simultaneous control of SO₂ and NO_x emissions. Because of rich source and low cost, Mg-Al oxides as adsorbent or catalyst in removing acid gas (SO₂, NO_x and CO₂) have great potential.

As catalyst or catalyst carrier, MgO, Al₂O₃, MgAl₂O₄ used for removal of SO₂ and NO_x have been reported much [1, 2]. So far, the researches about Mg-Al oxides as sorbent used for flue gas desulfurization and denitrification is still less. Reducing the size and increasing the specific surface area are breakthroughs of desulfurization and denitrification by Mg-Al oxide [3, 4]. Nanoparticle has two important features, namely,

surface effect and volume effect, which has a very important using value and good development potential in the optical, catalyst, sensors, and many other industries. Pereira HB et al. [9] studied catalytic ability of SO_x removal by MgAl₂O₄ loaded Mn. Centi G et al. [10] studied catalytic removal ability of SO_x by CuMgAl hydrotalcite. Fornasari et al. [11] studied the influence of different Mg/Al molar ratio on the catalytic efficiency of NO_x removal. Also, application of nanometer materials in the air pollution governance also is essential to research.

In this paper, Mg-Al composite oxides were prepared with solid state reaction synthesis (SSR) method and molten salt synthesis (MSS) method. Morphology, structure and performance of Mg-Al composite oxides were tested and analytically compared, and simultaneous removal rate of SO₂ and NO_x were tested under the condition of simulate flue gas. Also the mechanism of removing was analyzed, to understand the cause of the high efficient removing.

EXPERIMENTAL

Material preparation and characterization

The reagents used in the experiment are all from Sinopharm Chemical Reagent CO.Ltd. When samples were prepared by SSR synthesis process, MgO and Al₂O₃ were used as raw materials, weighing according to the stoichiometric ratio (Mg

* To whom all correspondence should be sent:

E-mail: cwl@ncepu.edu.cn

and Al mole ratio of 1:4, 1:6, 1:8, and 4:1, 6:1, 8:1), then were put in the muffle furnace, calcining at different temperatures 1300 °C for 8 h. After muffle furnace cooled to room temperature, powders were removed out and sieved, achieve the products [5]. When samples were prepared by MSS process, MgO and Al₂O₃ were mixed together with KCl as molten salt. MgO and Al₂O₃ of different mole ratio (4:1、 6:1、 8:1) were homogeneously mixed by using ball mill, and dried. The dried power was later mixed with molten salt; the salt/oxide weight ratio was kept at 20:1. The powder mixture was grinded for 2h using an agate mortar. Later the powder mixture was placed in an alumina crucible covered with an alumina lid, heated to 1150°C and held for 4h or 8h. After

muffle furnace cooling to room temperature, the reacted mass was repeatedly washed with deionized water and filtered to remove salts. Then the resulting oxide powders were oven-dried before further characterization [6].

The obtained solid product were characterized by X-ray diffraction on a Rigaku D/Max-RB diffractometer using Cu Kα radiation (40KV, 35mA) in the range between 20°and 80°2θ. Fig.1and 2 gives the XRD patterns of samples synthesized with different mole ratio of Mg and Al. The Fig. 1 and Fig. 2 showed that when the amount of Mg is more, the main number of adsorbent is MgO and MgAl₂O₄. When the amount of Al is more, the main number of adsorbent is Al₂O₃ and MgAl₂O₄.

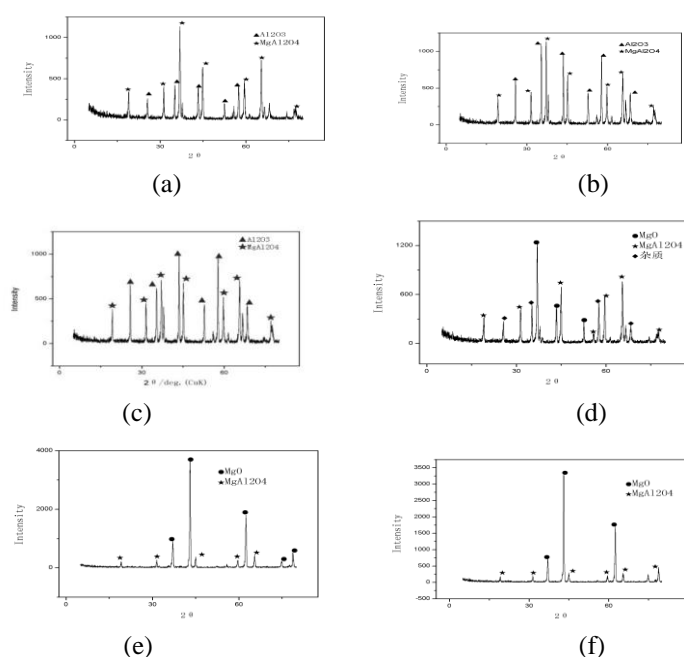


Fig.1. X-ray diffraction patterns of samples prepared by SSR with different Mg/Al mole ratio.

(a) 1:4; (b) 1:6; (c) 1:8; (d) 4:1; (e) 6:1; (f) 8:1.

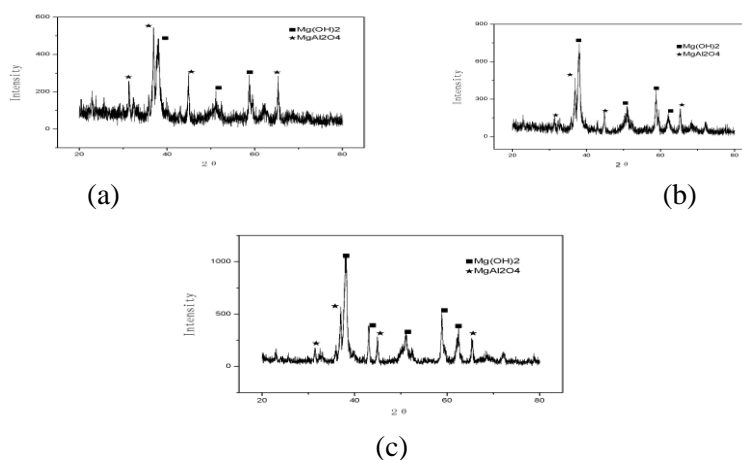


Fig. 2. X-ray diffraction patterns of samples prepared by MSS with different Mg/Al mole ratio.

(a) 4:1; (b) 6:1; (c) 8:1.

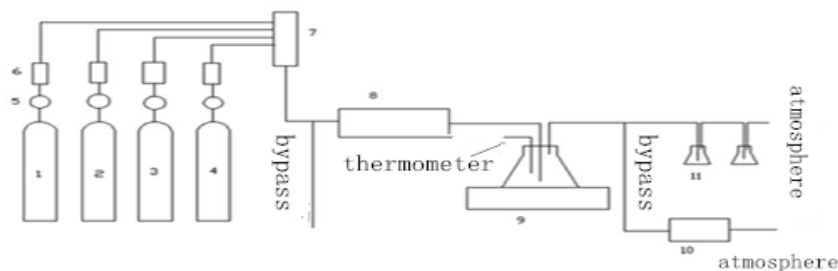


Fig. 3. The experiment system. 1. SO₂+N₂; 2.NO+N₂; 3. pure N₂ ; 4. compressed air; 5. pressure valve; 6. rotameter; 7. gas mixer;8. heater; 9. reactor ; 10. flue gas analyzer; 11. tail gas treatment.

Experiment for simultaneous desulfurization and denitrification

Fig. 3 shows the experimental system for removing SO₂ and NO_x with the Mg-Al oxide slurry [7]. The slurry was set in a quartz tube reactor and heated to 30°C. High pure N₂, O₂ and the standard gas SO₂ and NO of 9% concentration separately enter from the high pressure cylinder into gas mixer. The mixed gas was heated to 120 °C, and then flowed into the reactor. The amounts of SO₂ and NO_x removed were calculated by subtracting the amounts of SO₂ and NO_x after reaction from the total amounts of SO₂ and NO_x in the initial gas. The gas after reaction was further treated by scrubber to remove the harmful gas. Then it was discharged into atmosphere [8]. The SO₂ and NO_x gas concentration were adjusted to 1300 ppm and 900 ppm respectively. The total flow of mixed gas is 500 ml. SO₂ and NO_x in the mixed gas were quantified by the 350-pro flue gas analyzer.

RESULTS AND DISCUSSION

As is shown in Fig.4, in the samples prepared by SSR, when the number of Mg is more than Al, the removal rates of SO₂ and NO_x are not high. The removal rates of SO₂ and NO_x reach the maximum in 5 or 15 minutes. After reaching the maximum, the removal rate maintains under few time interval, and then the removal rate fell. As the proportion of Al₂O₃ in the adsorbent becomes more, the downward trend becomes bigger, and the removal effect is worse. Among the samples prepared by SSR, when Mg/Al Molar ratio is 1:4, the removal rate is best. The maximum SO₂ removal rate can reach 98.9%, maximum NO_x removal rate 50%. And after 60 minutes, SO₂ removal rate fell to 76.4%, and NO_x removal rate 41.7%. And when the number of Mg is more than Al in the samples prepared by SSR, the removal rates of SO₂ and NO_x are better. The removal rate of SO₂ reach upon 90% in 5 minutes, and the maximum removal rate all can reach about 94%. This moment the maximum removal rate can maintain a long time

and followed by a slow decline. When the Mg/Al ratio is 6:1, the removal rate is the best. The highest SO₂ removal rate can reach 99%, and the highest NO_x removal rate can reach 45%. After 60 minutes, SO₂ removal rate fell by 3.4%, and NO_x removal rate fell by 1.5%. When the same Mg/Al ratio of Mg - Al composite oxides were prepared by MSS, the removal effects of SO₂ and NO_x is better than by SSR. The maximum removal rate can maintain a more long time. However removal rates of samples of same Mg/Al ratio prepared by SSR began to decline in 60 minutes. By using MSS, the removal rates of the sample in which Mg/Al ratio is 4:1 are the highest, which can reach 100% of SO₂ maximum removal rate, 71% of NO_x, and the time interval stays for 150 minutes. It is known that the high-efficiency operation interval by MSS is 2.5 times by SSR.

Adsorption process generally includes three aspects: diffusion on particle surface, diffusion in internal pore of particle and adsorption reaction. Lagergren first order kinetic model describes diffusion on particle surface, namely the process of the adsorbate molecules diffusion is from the liquid phase to a solid surface. Lagergren secondary kinetic model describes the adsorption reaction. Weber - Morris equation describes the internal diffusion that considered a critical stage in the process of adsorption. The linear fitting result of Lagergren secondary rate equation is better. Linear correlation coefficient of Lagergren secondary rate equation is significantly greater than that of Lagergren first rate equation. It showed that the dynamic adsorption process follows the Lagergren secondary dynamic model.

The correlation coefficients of Weber - Morris equation are 0.97412 and 0.94803. Comparing with the two correlation coefficients of Lagergren secondary dynamic equation and Weber - Morris equation, the correlation coefficient of Lagergren secondary dynamic equation is larger. It reveals that in the whole process is dominated by adsorption reaction, and the diffusion between internal and surface is secondary.

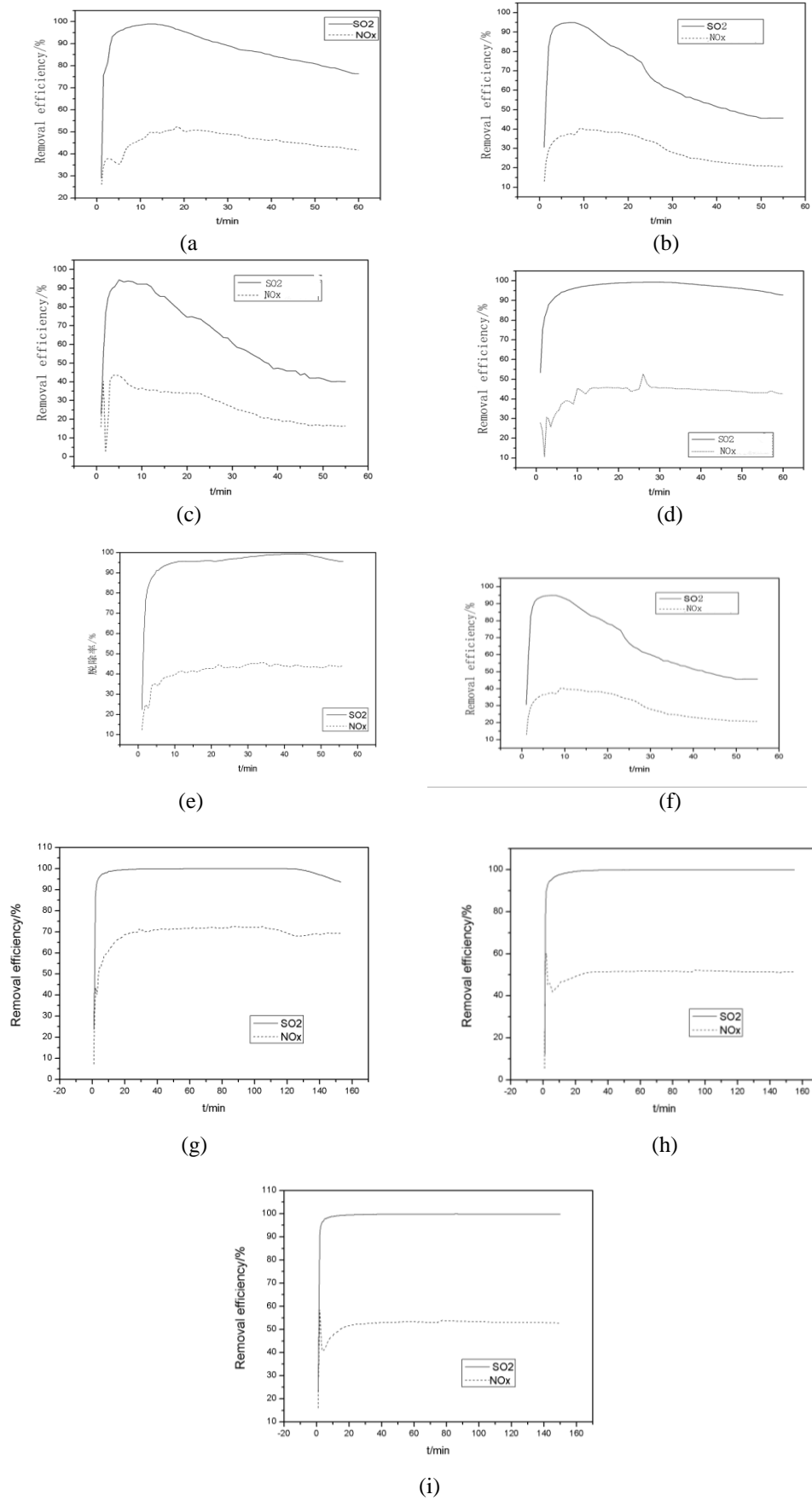


Fig. 4. The results of removal experiment of samples prepared by SSR (a, b, c, d, e, f) and MSS (g, h, i) (a)Mg/Al=1:4; (b)Mg/Al=1:6; (c) Mg/Al=1:8; (d)Mg/Al=4:1; (e) Mg/Al=6:1; (f) Mg/Al=8:1; (g) Mg/Al=4:1; (h)Mg/Al=6:1; (i)Mg/Al=8:1.

CONCLUSIONS

The Mg-Al composite oxides are prepared and characterized and simultaneous experiments of desulfurization and denitrification were done upon the condition of simulate flue gas of coal-fired powers.

For the samples prepared by SSR, when the number of Mg is more than Al, removal effects of SO₂ and NO_x are much higher. The sample in which Mg/Al mole ratio is 6:1 has the best removal effect. The highest removal efficiency of SO₂ can reach 99%, and NO_x reach 45%. After 60 minutes, SO₂ removal efficiency fell by 3.4% and NO_x removal efficiency fell by 1.5%. When samples were prepared by MSS, the sample in which Mg/Al mole ratio is 4:1 has the best removal effect. The highest removal efficiency of SO₂ can reach 100% and that of NO_x can reach 71%. And the maximum removal efficiency can maintain 150 min. The maintain time is 2.5 times than that of samples prepared by SSR. Further research shows that the adsorption process is mostly controlled by adsorption reaction, and the particle diffusion between internal and outside is under the secondary action.

Acknowledgements: This work was supported by Beijing Natural Science Foundation (No.3132017), and National Natural Science Foundation of China (No. 51476056).

REFERENCES

1. C. Kienle, C. Schinzer, J. Lentmaier, *Mater. Chem. Phys.*, **49**, 211 (1997).
2. L. Chmielarz, M. Jabl'Nska, A. Strumi'Nski, *Appl. Catal. B: Environ.*, **152**, 130 (2013).
3. T. Kameda, N. Uchiyama, T. Yoshioka, *Chemosphere*, **82**, 587 (2011).
4. D.J. Wan, H.J. Liu, R.P. Liu, *Chem. Eng. J.*, **241**, 195 (2012).
5. X.H. Su, J.G. Li, Z.J. Zhou, *J. Inorg. Mater.*, **27**, 991 (2012).
6. D.D. Jayaseelan, S.W. Zhang, S. Hashimoto, *J. Eur. Ceram. Soc.*, **27**, 4745 (2007).
7. P. Fang, C.P. Cen, X.M. Wang, *Fuel Process. Technol.*, **106**, 645 (2013).
8. J. Ding, Q. Zhang, S.L. Zhang, *Chem. Eng. J.*, **243**, 176 (2014).
9. T. Kameda, A. Kodama, Y. Fubasami, S. Kumagai, T. Yoshioka, *Chemosphere*, **88**, 250 (2012).
10. T. Kameda, A. Kodama, Y. Fubasami, *J. Environ. Sci.*, **48**, 86 (2013).
11. T. Kameda, A. Kodama, T. Yoshioka, *Chemosphere*, **93**, 2889 (2013).

Influence factor analysis of inlet spray on a natural draft wet cooling tower

W. Cheng*, C. Hou

School of Energy, Power and Mechanical Engineering, North China Electric Power University, 102206 Beijing, China

Received June 6 2016; Revised September 12, 2016

The wet cooling towers in power plants usually have the environmental pollution such as the heat and noise pollution and so on, which can bring out some energy loss at the same time. A new type of inlet water spray for cooling towers is developed which makeup water of cooling tower system is used as pre-cooling spray water. Makeup water is atomized into droplets to pre-cool the inlet air instead of putting it into water tank and it can improve the cooling performance of cooling towers. Systematic analysis for the performance of the entire cooling system with inlet pre-cooling by water spray of natural draft wet cooling towers is presented in this paper. The model consists of two parts: the pre-cooling part and the main cooling tower part. Several parameters for ambient air and makeup water are taken into consideration. The results showed that the performance with inlet water spray atomized by makeup water is better than the case putting makeup water into water tank directly; when the ambient air is hot and dry, the cooling performance of the natural draft wet cooling towers with sprayed inlet water can be improved.

Key words: Natural draft wet cooling towers, water spray, pre-cooling, makeup water, performance analysis.

INTRODUCTION

This paper presents a new type of inlet water spray for wet cooling tower with makeup water of cooling tower system. The model and the result will be given in the paper. This new idea is a new type of water spray cooling system for natural draft wet cooling towers (NDWCTs) in hot and dry places. NDWCTs are used at many power plants, so the development of the tower has become a necessity. The draft drawing air into the tower is dependent on the difference in density between the entering cold air and the internal warm air. During the high temperature the difference between the inlet and internal air density is small, the ability to draw air becomes bad, and air flow mass which cools the circulating water is decreased, eventually, the performance of cooling tower is reduced dramatically. Especially, the performance decreases sharply in hot days [1]. The way of applying water spray at the inlet of NDWCTs with makeup water can pre-cool inlet air and reduce its temperature; meanwhile it can alleviate the bad effect of the crosswind to some extent [2]; Although a number of literature has been published on droplet transport, evaporation and simulation with CFD, no study exists on analyzing an entire system of inlet pre-cooling of cooling tower NDWCTs with mathematic model.

Many efforts have been made over the past

decades to improve the performance of wet cooling systems in order to make them more efficient, such as wetted-media cooling [3, 4], and the wind-break wall [5] inlet hybrid cooling technologies. A number of studies have found that hybrid cooling technologies have the potential to alleviate this problem. Two methods of hybrid cooling were carried out, which can be classified: deluge cooling and evaporative pre-cooling. Inlet water spray cooling has become more popular due to its simplicity, low capital cost, and ease of operation and maintenance [3-6]. Inlet water spraying can reduce the temperature of inlet air, so the efficiency was increased, meanwhile, inlet water spraying can offset the bad effect of crosswind to certain extent [7], developed a typical hybrid cooling installation: spray systems on inlet of the air. In this scheme, available nozzles were placed in the path of the intake air. Water was atomized into droplets from the nozzles to cool air. The result shows inlet water spray was more effective in dry climates. Details for flow simulation can be found in [8,9]. Based on the balance equations for mass, momentum and energy, the Eulerian-Lagrangian method was used to simulate the description of the heat transfer between spray and air. The simulation regarded a single nozzle as the research object. It concluded that spray could induce flows and the air flow is mainly induced by drag effects. Abdullah Alkhedhair et al. [13] a developed 3-D numerical simulation and an experiment to study pre-cooling water spray of inlet air in the natural draft dry cooling tower, which use a single nozzle as the

* To whom all correspondence should be sent:
E-mail: cwl@ncepu.edu.cn

object of the study. It pointed out that the lower the air velocity was, the longer the residence was; the larger the evaporation mass was, the better the cooling performance was the smaller the droplet was, the faster the evaporation was. Owing to the circumstance of freezing at the inlet of cooling towers and its poor performance, Zhang Min et al. [14] and Zhang Yu et al. [15] proposed the application of the rapid freezing technology. The rapid freezing technology is a technology which uses water spray to achieve ice rapid freezing and melting at the steel wire gauze, the circulating water temperature may be adjusted automatically to optimal data according to the variation of both the environmental temperature and the unit load.

Inlet air spray cooling has been used at many applications such as gas turbine fogging and refrigerating cooling [10]. More than 1000 gas turbine stations are equipped with inlet air spray cooling [11]. When the ambient temperature was high, inlet fogging system can pre-cool the air, increase the density of the air, increase the air mass flow, and boost the power and efficiency. Water spray can also be used at heat exchangers [12] and as a curtain of a strong radiative source. A. M. Rubin et al. investigated effectiveness of using water spray to cool the inlet air in a heat exchanger experimentally. With the use of efficient atomizers, water was atomized and jetted into the air flow to pre-cool the air. Experiments showed that effective spray improved the efficiency of adiabatic cooling at a steam-electric power plant, and thereby avoided the need to reduce plant output during hot weather.

The reasonable selection and arrangement of nozzles have great influence on the cooling efficiency of water spray [13,14]. Spray nozzles are used to distribute water into the inlet air and to provide a large water-air contact surface by producing small droplets through atomization as can be seen in Figure 1.

This paper aims at a new type of inlet water spray, that is, inlet pre-cooling water spray with makeup water which can develop the efficiency loss of cooling tower during high temperature. Makeup water is atomized into droplets to pre-cool the inlet air instead of putting it into water tank and it can improve the cooling performance of cooling towers. This is the most important new highlight different from others. It avoids using the extra more water. The makeup water is pumped into the inlet of the cooling tower by nozzles and water is atomized into small droplets to pre-cool inlet air. When it comes to research methods, the present

researches on the improvement and advancement of cooling tower which carried out mainly pay attention to simulation and regarded the single droplet as the subject investigated. However, combined with practical improvement of cooling tower structure, it is necessary to settle the practical problems of cooling tower at high temperature environment and analyze the entire system of cooling tower with actual data. Few studies in this respect are carried out currently; therefore it is urgent to study it. A model of the entire cooling system, calculation and program is developed in this paper.

MODEL DESCRIPTION AND MATHEMATICAL FORMULATION

Model description

Shown in Figure 1, in the units of 300MW, at a constant load, when temperature of outlet circulating water reduces 1k, the unit efficiency increases 0.23%, coal consumption decreases 0.798g/(kw. h). The environmental and economic benefit generated from the saved coal and the increased efficiency is extraordinary considerable.

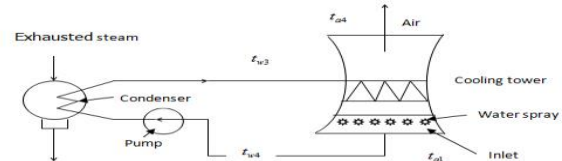


Fig. 1. Diagram of cold end system of power plant.

In order to offset the deterioration of the performance of NDWCTs which the outlet circulating water temperature is high during high temperature climate, water spray at the entrance of the cooling tower is applied[15,16]. As Fig. 1 shown, the model is shown as follow: a number of nozzles are installed and arranged around the inlet of a wet cooling tower reasonably. The direction of the nozzle points to the axe. At a given pressure, instead of putting the makeup water into water tank directly, makeup water is atomized into droplets to pre-cool the inlet air, the remaining water which is not evaporated falls into water tank. Water droplets pre-cool the inlet air and reduce the temperature of inlet air; at the same time, inlet air is induced by droplets, so more heat in circulating water will be taken away by air. Finally, the cooled air enters the cooling tower system to finish its job of cooling circulating water. The number of nozzles differs from tower dimension. Droplets can cause corrosion, scaling and fouling, so nozzles with special manufacture technology and material should be required. A calculating and analyzing model for

inlet water spray of wet cooling tower is derived, which is based on the theory of injection and gas-liquid two-phase flow. The mathematical model consists of two parts: the spray pre-cooling part and the main cooling part. Inlet air is cooled by the atomized makeup water to relative low temperature air, and pre-cooled air enters the filling area of wet cooling tower. At the region of water drenching, a combination of heat and mass transfer effect happens between the cooling water coming from the condenser and the cooled air. Therefore, when the model is built in the paper, it is necessary to take sufficient consideration to the specific situations of cooling towers, some assumptions are given as follow:

The dynamic characteristic, heat transfer property and temperature distribution between the real conic and the edge of the spray aren't uniform. The change at the real conic of the spray is much stronger than that of the edge. When the nozzle density is arranged reasonably, it is assumed that the spread of dynamic and energy is uniform, the distribution of temperature and heat transfer coefficient distribute equally;

This paper applies Y-1 nozzle, which diameter is $d=5\text{mm}$, the density is $13/\text{m}^2$;

It is assumed that the special heat capacity of water and air, are constant under the temperature range considered;

The pressure of air will decrease due to the resistance through the pre-cool spray and the area of water drenching. The pressure loss is small, so the pressure loss is ignored when study the air conditions;

The outlet circulating water temperature is the index of testing the cooling performance. When the inlet circulating water is constant, the circulating water temperature difference can be the index of testing the cooling performance instead of the outlet circulating water temperature. In general, the larger the difference between inlet and outlet circulating water temperature is, the better the cooling performance performs.

Mathematical formulation

Main purpose of the model is studied on the performance of cooling tower with cooling sprays systematically. In order to get the temperature of circulating water out of cooling towers, two steps are needed: the spray pre-cooling part and the main cooling part.

The spray pre-cooling part

Ambient air is drawn into pre-cooling parts by the suction of the cooling tower and makeup water

is atomized by the nozzles. The dry and wet bulb temperature of inlet air, air flow mass, the temperature of makeup water and makeup water mass are used to obtain the dry and wet bulb temperature of pre-cooled air. The cooling process can be described by the following three important equations:

$$A(\nu\rho)^m \mu^n = 1 - \frac{t_{s2} - t_{w2}}{t_{s1} - t_{w1}} \quad (1)$$

$$a_1 t_{s1} - a_2 t_{s2} = \mu c (t_{w2} - t_{w1}) \quad (2)$$

$$A'(\nu\rho)^{m'} \mu^{n'} = 1 - \frac{t_{a2} - t_{s2}}{t_{a1} - t_{s1}} \quad (3)$$

Where A, m, n, A', m', n' is the experimental coefficient and index, which is related to the pressure, diameter, layout density of nozzles; t_{a1}, t_{s1} , is the dry-bulb temperature and the wet-bulb temperature of inlet air, respectively; t_{a2}, t_{s2} is the dry-bulb temperature and the wet-bulb temperature of cooled air by water spraying, separately; $t_{w1}, t_{w1},$, is the temperature of inlet and outlet makeup water, respectively; $\nu\rho$ is the mass velocity of air; c stands for the specific heat capacity of circulating water; a_1, a_2 , is the ratio of enthalpy to wet bulb temperature of air; μ stands for the spray coefficient, which is given by the following expression:

$$\mu = \frac{W}{G} \quad (4)$$

Where W stands for the makeup water mass, G is the inlet air flow mass, which is calculated by the following relation:

$$Q = V_1 \rho_1 F_1 \quad (5)$$

Where V_1 is the inlet air velocity; F_1 is the area of inlet opening; ρ_1 is the density of inlet air of the cooling tower.

Equation (1) presents sensible heat transfer of gas-water which is related to the wet-bulb temperature of air and the makeup water temperature. As the difference between t_{s2} and t_{w2} becomes bigger, the heat and mass transfer becomes more imperfect; Equation (2) is based on energy balance equation which heat absorbed by water spray is equal to the heat released from the air. Equation (3) is related to the variation of air conditions. The dry and wet-bulb temperature of pre-cooled air can be achieved by simultaneous equations of (1), (2), (3) (G. Kohnen et al.[8]).

The main cooling part

At the entrance of the cooling tower, pre-cooled air by water spray enters the wet cooling tower. In the cooling tower, both heat transfer and mass transfer happens between water and air, the

enthalpy balance equation of cooling towers is applied to establish the model in the paper, and enthalpy potential method is used to circulate the outlet circulating water temperature of towers.

In the process of the heat and mass transfer inside the cooling tower, the cooling performance of the tower with a certain filling and tower type is related to the performance, structure, geometry of the filler and the cooling water flow mass. The bigger the value of the cooling loads is, the greater the heat dissipating capacity required is, and the larger the volume of the cooling fill is. In cooling tower main cooling process, the calculation process is represented by the following formula:

$$A''\lambda^{m''} = \frac{c\Delta t}{6} \left(\frac{1}{h_4'' - h_3} + \frac{1}{h_m'' - h_m} + \frac{1}{h_3'' - h_4} \right) \quad (6)$$

Where Δt_w is the temperature difference of circulating water between inlet and outlet; h_3'' , h_m'' , h_4'' is the enthalpy of saturated moist air which dry-bulb temperature is equal to inlet circulating water temperature t_{w3} , the mean water temperature t_{wm} and outlet circulating water temperature t_{w4} , respectively; h_3 , h_m , h_4 is the specific enthalpy of inlet air t_{a3} , the average mode of air t_{am} and the outlet air t_{a4} , respectively, in which the inlet air of the main cooling part is the outlet air of pre-cooling part, namely, $t_{a3} = t_{a2}$; A'' , m'' are coefficient. λ is the ratio of air to water which is given by

$$\lambda = \frac{G}{Q} \quad (7)$$

Where Q is the circulating water flow mass of cooling tower.

The draft of NDWCTs is dependent on the difference in density between the inlet and the internal air. When the resistance of air flow is equal to the pulling force generated by density difference of air, inlet air flow mass remains constant. At the normal operation of cooling towers, the resistance of air flow is balanced by the pulling force. The main model is shown as follow:

$$\Delta p' = H_e g (\rho_1 - \rho_2) \quad (8)$$

$$\Delta p = \xi \rho_m \frac{V_m^2}{2} \quad (9)$$

Where V_m stands for the average velocity at the area of water drenching; H_e is the effective air draft height of cooling tower; ρ_m is the average density of air in the tower; ξ is the total drag coefficient of cooling tower which is given by

$$\xi = \frac{2.5}{\left(\frac{4H_0}{D_0}\right)^2} + 0.32D_0 + \left(\frac{F_m}{F_2}\right)^2 + \xi_1 + \xi_2 \quad (10)$$

Where D_0 stands for the diameter of the half of inlet height; H_0 stands for the inlet height; ξ_1 and ξ_2 are the drag coefficient of bracket and drag coefficient of water eliminator, respectively; F_m is the area of water drenching; F_2 is the outlet area of cooling tower.

COMPUTATIONAL PROCEDURE

In the process of mathematical model, the emphasis here is iteration calculation which impregnate the whole computational process. An accurate prediction of cooling performance of cooling tower can be attained through iterative procedure. The sequence of calculation is shown in Figure 2:

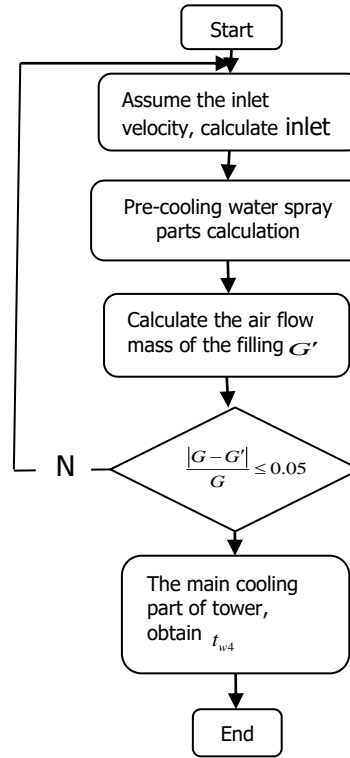


Fig. 2. The flowchart of the model.

RESULTS AND DISCUSSION

This paper is based on the following condition table 1, this paper researches the effect on the performance of the cooling tower with water spraying from two factors: ambient air and makeup water.

Table 1. Parameters of cooling tower.

the power plant capacity (MW)	135
the effective air draft height of cooling tower (m)	60
Area of water drenching (m ²)	2000
the height of inlet opening(m)	4
Mass flow rate of circulating water(kg/s)	3700

Ambient air condition

Ambient air is the mixture of dry air and water vapor, and the amount of vapor in air has great influence on the thermal performance of air. The larger the difference between dry and wet bulb temperature of air is, the smaller the relative humidity is, the stronger the ability to absorb vapor is. As to the effect of air on the NDWCT, two cases of different ambient air conditions are considered: the first case, inlet air temperature is varied while inlet air relative humidity remain constant; the second case, inlet air relative humidity is varied while inlet air dry bulb temperature remain constant. The pictures from Figure 3 to Figure6 are drawn under the following condition: $t_{w1} = 10^{\circ}C$, $t_{w3} = 40^{\circ}C$, $W = 0.06 \times Q$.

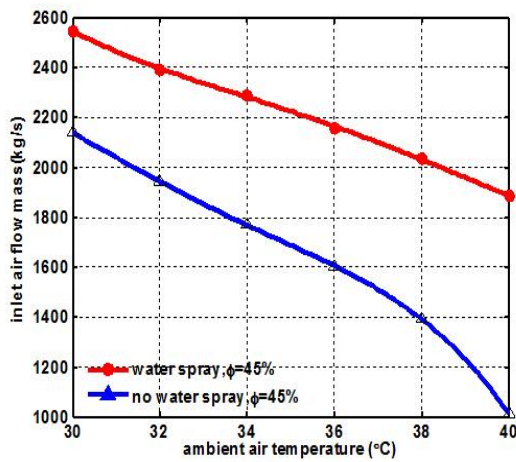


Fig. 3. The inlet air flow mass at different inlet conditions.

The inlet air flow mass at different inlet condition is illustrated in Figure 3. As the two curves shown at a given temperature and relative humidity, as ambient air ranges from 30°C to 40°C, the curve without inlet water spray changes from 2200kg/s to 1000kg/s, while the curve with inlet pre-cooling varies from 2600kg/s to 2000kg/s. It is obvious that the inlet pre-cooling can enhance the inlet air flow by a wide margin; at the same time, the development of inlet air flow become larger and bigger as the temperature rise. And it also can be seen that the inlet air flow with inlet water spray is bigger than the one without it. That is to say, the inlet air flow mass, i. e. the pulling force, decreases as the air temperature increases. The inlet pre-cooling water spray can raise the air flow mass. Therefore, inlet pre-cooling water spray can increase the draft of towers, the draft of cooling tower ascend significantly which increase the inlet air flow mass greatly, and the air flow mass has a

sharper increasing degree than that of low temperature, and the relative increase degree of air flow mass during high temperature ambient is larger.

The cooling performance at different inlet condition is illustrated in Figure 4. Three curves from top to bottom are drawn as follows: curve 1 is drawn with water spray; curve 2 is drawn without water spray; curve 3 is the comparison between the cases of the first two curves. As shown in the first two curves, the performance without water spray drops sharply at high temperature; it leads to the decline of cooling performance. As the ambient air temperature increases, the circulating water difference decreases, i. e. the thermal efficiency declines and the cooling performance decreases. Compared with the case without water spray, as shown in the curve 3, when the temperature is 30°C, the circulating water difference can increase by 1.5°C; when the temperature is 40°C, the circulating water can rise by 3°C; the difference in circulating water temperature with inlet pre-cooling spray is increased about 2°C averagely. Generally speaking, the difference between the conditions with pre-cooling and without pre-cooling rises gradually as the temperature rises, i. e. inlet water spray has a better impact on the improvement of the performance of cooling tower during the high climate. Inlet water spray can improve the cooling performance, especially in the hot day.

The cooling performance change of the wet cooling tower with the different ambient conditions is shown in Figure 5. The effect of two relative humidity values, i. e. 45%, 70% is compared on the performance with water spray. At the same air dry-bulb temperature 36, when the relative humidity values is 45%, the circulating water difference is 8.8°C; when the relative humidity values is 70%, the circulating water difference is 6.6°C; the change is about 2 °C, which is a very considerable improvement. It can be seen that a lower relative humidity results in a larger difference in circulating water temperature and higher cooling performance. Therefore, water spray have a better impact in dry days.

The effect of two relative humidity values on air flow mass is compared in Figure 6. The inlet air flow mass decreases as the temperature rises; at a given air temperature, the air flow mass, i. e. the draft of cooling tower, go up with the decease of relative humidity. The lower the relative humidity is, the smaller the internal latent heat is; the smaller air flow mass is, and the worse the heat transfer

performs. Therefore, with inlet water spray, as the lower the relative humidity is, the larger the inlet air flow mass is.

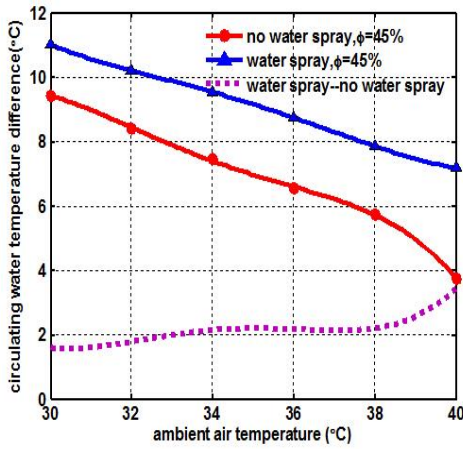


Fig. 4. The cooling performance at different inlet conditions.

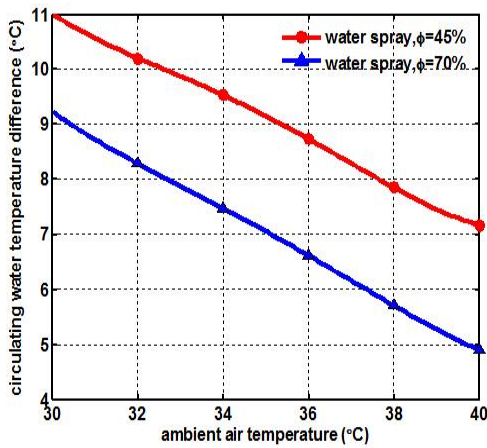


Fig. 5. Temperature and humidity curves.

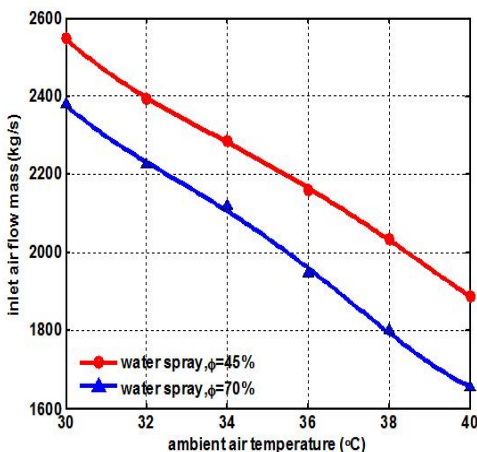


Fig. 6. The air flow mass at different temperature and humidity.

Makeup water

In the operating process of large coal-fired power plants, a large quantity of cooling water is

needed in wet cooling towers. Because of the loss caused by evaporation, wind, pollution discharge and leakage, etc. It is necessary to supply some water which is called makeup water. In present paper, instead of putting the makeup water into water tank directly, makeup water is atomized into droplets and it enters into the cooling tower along the inlet direction together with the air. Makeup water mass is also the water spray rate. The influence of makeup water of its temperature and mass is studied in the model. The curves are obtained considering the following conditions:

$$t_{a1} = 30^{\circ}C, \phi = 45\%, t_{w1} = 10^{\circ}C, t_{w3} = 40^{\circ}C.$$

The cooling performance at different makeup water masses is presented in Figure 7. With the same dimension of nozzles, the different fogging rates lead to different sizes of droplets. The ratio of makeup water flow to circulating water flow is from 4% to 6%, the difference of inlet and outlet circulating water temperature grows from 10.51°C to 10.87°C sharply, and then rise to 11°C slightly, namely, the cooling performance is enhanced. It can be seen that the driving force is also enlarged with the increasing makeup water rate, so does heat and mass transfer between air and water, eventually, the cooling effect is improved. Therefore, the larger the makeup water mass is, the better the cooling performance is.

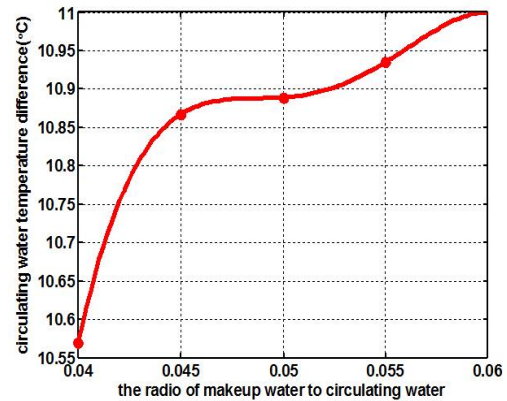


Fig. 7. The cooling performance at different makeup water mass.

The cooling performance at different makeup water temperatures is showed in Figure 8. Makeup water generally comes from deep well and deep level of rivers, lakes, and sea, for this reason, makeup water temperature ranges from 10°C to 20°C, and the temperature difference of circulating water drops linearly and gradually with the increase of the circulating water temperature. Under given ambient air condition, the temperature difference between makeup water and air becomes larger when the makeup water temperature reduces.

Therefore, a lower makeup water temperature results in a better cooling performance.

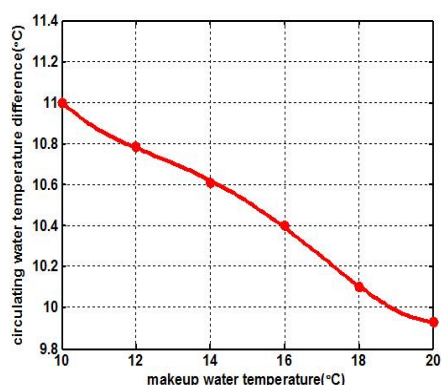


Fig. 8. The cooling performance at different makeup water temperatures.

The cooling performance at different conditions of makeup water is presented in Figure 9. There are two curves, i. e. curve 1 is the variation tendency of the cooling performance with the inlet makeup water spray; another is no spray which makeup water directly flows into tank. As shown in Figure 9, as ambient air ranges from 30 °C to 40 °C, the circulating water difference change from 10.6 °C to 5.2 °C in the curve 2, while the curve 1 varies from 7.2 °C to 3.8 °C. It can be seen from the change trend of two curves, the reduction of cooling performance with spray atomized by makeup water is smaller than the condition which put makeup water into water tank directly. The separation between the two curves increase steadily as the temperature climbs up, i. e. the higher the temperature is, the better the effect of water spray pre-cooling has relatively. Compared with the condition which let makeup water into tank, makeup water is atomized into droplets and it increases the contact area of air to water, so the heat transfer rate is enhanced. In addition, the inlet air flow mass also rises. In sum, spray cooling can enhance the total heat transfer rate of cooling tower and increase the cooling performance.

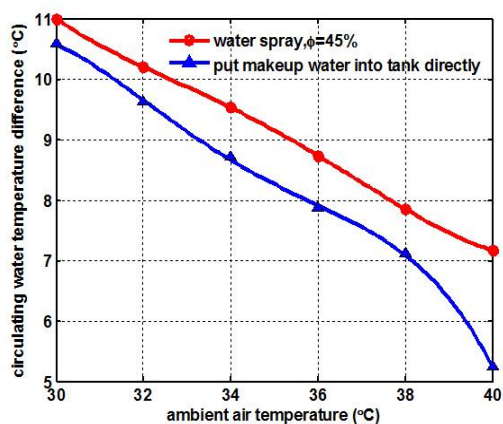


Fig. 9. The cooling performance at different conditions of makeup water.

CONCLUSIONS

In order to increase the cooling performance of NDWCTs, especially in the hot climate, water spraying for inlet air pre-cooling is applied, and it will improve the effectiveness of the cooling tower significantly. Based on the theory of injection and gas-liquid two-phase flow, a new systemic analysis model, which imitates the performance with water spraying of cooling towers, is developed. The mathematical model is used to calculate the cooling performance under different conditions of air and makeup water parameters. The main conclusions are summarized as follows:

- (1) The application of inlet water spray with makeup water can improve the cooling towers cooling effect, and it is obviously better than the effect of the case make-up water is put directly into the water tank.
- (2) Inlet pre-cooling water spray can increase the draft of towers and the inlet air flow mass.
- (3) The lower the makeup water temperature is, the larger the makeup water flow mass is, the better the cooling efficiency performs.
- (4) According to the present model, when the ambient air is very hot and dry, the water spray for pre-cooling inlet air is very suitable to obtain the high cooling efficiency in cooling towers.

Acknowledgments: The work was supported by Beijing Natural Science Foundation (No. 3132017), and National Natural Science Foundation of China (No. 51476056).

REFERENCES

1. V.D. Papaefthimiou, E.D. Rofdakakis, I.P. Koronaki, T.C. Zannis, *Appl. Therm. Eng.*, **33-34**, 199 (2012).
2. H. Ahmadikia, M. Soleimani, E. Gholami, *Therm. Sci.*, **17**, 442 (2013).
3. S.Y. He, H. Gurgenci, Z.Q. Guan, A.M. Alkhedhair, *Appl. Therm Eng.*, **53**, 67 (2013).
4. R. Al-Waked, M. Behnia, *Energy Convers. Manage.*, **48**, 2638 (2007).
5. M. Goodarz, *Wind Eng. Ind. Aerodynam.*, **98**, 858 (2010).
6. M.A. Chaker, *J. Eng. Gas Turbines Power*, **129**, 473 (2007).
7. Ashwood, D. Bharathan, Hybrid cooling systems for low-temperature geothermal power production, Nation. Lab. US, 2011.
8. G. Kohnen, M. Rüger, M. Sommerfeld, Convergence behaviour for numerical calculations by Euler/Lagrange method for strongly coupled phases,

- The Fed, Summer Meeting of the ASME, 1994, p. 191.
9. A. Collin, P. Boulet, G. Parent, D. Lacroix, *Int. J. Therm. Sci.*, **46**, 856 (2007).
 10. A.M. Al-Amiri, M.M. Zamzam, Application of inlet fogging for power augmentation of mechanical drive turbines in the oil and gas sector, ASME Turbo Expo, 2006.
 11. R.K. Bhargava, C.B. Meher-Homji, M.A. Chaker, M. Bianchi, F. Melino, A. Peretto, S. Ingistov, *Eng. Gas Turbines Power*, **129**, 443 (2007).
 12. B. D. Esterhuysen, D.G. Kroger, *Appl. Therm. Eng.*, **25**, 3129 (2005).
 13. A. Alkhedhair, Z.Q. Guan, I. Jahn, H. Gurgenci, S.Y. He, *Int. J. Therm. Sci.*, **90**, 70 (2015).
 14. M. Zhang, F.H. Zhang, Y.Q. Li, *Power Syst. Eng.*, **26**, 58 (2010).
 15. Y. Zhang, Y.H. Zhang, S.P. Chen, G.X. Song, *Turb. Technol.*, 53 (2011).
 16. M. Al-Amiri, M.M. Zamzam, M.A. Chaker, C.B. Meher-Homji, Application of inlet fogging for power augmentation of mechanical drive turbines in the oil and gas sector, ASME Conference Proceedings, 2006, p.847.

Transient modeling and performance analysis of site utilities and cogeneration systems: a case study for lubricant oil refinery utilization

H. Ahmadi^{1*}, A. Behbahani-Nia¹, F. Torabi²

¹Department of Energy Engineering, Faculty of Environment and Energy, Science and Research Branch, Islamic Azad University, Tehran, Iran

²Department of Mechanical Engineering, K.N. Toosi University of Technology, Mollasadra St., Tehran, Iran

Received June 18, 2016; Revised September 10, 2016

The heat and power demand are supplied by site utility systems. This paper aims to investigate transient modeling and performance analysis of lubricant oil refinery site utility systems. This model calculates the steam generated by boilers and CHP, steam flowrate of each header for site demand; shaft power generated by the GENSET and steam turbines with a constant isentropic efficiency, cogeneration efficiency with the objective function that maximizing total revenue. In addition, by the use of this model, the amounts of GENSET fuel consumption cogeneration efficiency and power generated by the GENSET will increase and boiler fuel consumption will decrease. Using heat recovery equipment to recover exhaust gas energy of GENSET, conformity of steam supply and steam demand and reduction the amount of steam letdown station are the reason that cause to reduce boiler fuel consumption and increase cogeneration efficacy. The reason for increased generator fuel consumption and power generation is power purchase price. Production and sale of electricity is affordable. In addition, total revenue of the site will increase. The resulting model provides a transient strategy for steam saving on total sites and modifications to the utility system as different operation conditions.

Keywords: Transient modeling, Optimization, Site utility, Total Cost, Total Revenue, Energy; Efficiency; Cogeneration

INTRODUCTION

Energy is one of the most essential commodities for sustaining people's livelihoods. Oil Refinery is one of the major energy consumers in industrial sector. Energy utilization in sites can be improved through [1]:

- Increasing energy efficiency by retrofit of site process
- Identifying the opportunities to improve utility system
- Operational optimization of existing processes or utility systems

Combined heat and power (CHP) systems, also known as cogeneration, generate electricity and useful thermal energy in a single, integrated system in different application. Varbanov *et al.* [2] studied about exergy analysis of the efficiency CHP systems in small scale utilization. Afanasyeva & Mingaleeva [3] described the detail of the Iterative Bottom-to-Top Model (IBTM) that is calculates the temperature of steam mains, steam flowrate and shaft power generated by the steam turbines. Ghannadzadeh *et al.* [4] developed the A new cogeneration targeting model that has been provided a consistent, general procedure for determining the mass flow rates and the efficiencies

of the turbines. Optimizing the site utility systems is one of the most challenging topics. To analysis a utility system, it is first necessary to develop a simulation model. Such models have been developed in [5]. Also, for estimating cogeneration potential of site utility system, using the total site profile has been suggested. The total site profile is a most useful tool to obtain a better realizing of the systems. Total site profiles can be produced by combining the grand composite curve for individual process. Furthermore, several studies have been conducted to evaluated site utility and cogeneration systems. For this reasons, various methodologies and case studies have been investigated for different approaches [6].

Most processes operate in the context of an existing site in which a number of processes are linked to the same utility system. The analysis of utility systems in industrial process to determine the value of steam savings to obtain optimizing operational energy cost and identify the energy conservation opportunities is the main target of this study. This analysis is carried out for existing utility such as steam and power in sample lubricant oil refinery [7, 8, 9].

In this paper, after energy auditing of site utility system, and collect the information of the utility systems and measuring some important parameter, the energy conservation opportunities (ECOs) are

* To whom all correspondence should be sent:

E-mail: behbahani71@gmail.com;
Eng_Hamed_Ahmadi@yahoo.com;

founded and the current situation was simulated. Next, optimizing the plant operation under the current process steam demand was studied. Considering transient condition and maximizing total revenue (or minimizing total cost) with operation research technique are new innovation in this research.

METHODOLOGY

The heat and power demand are supplied by a site utility systems. Fuels (such as NG, coal etc.) are consumed in boiler by site utility system to supplies steam for operating the process and produce power with steam turbine. Steam turbines can be divided into two basic classes: condensing and back-pressure turbines. In condensing turbines, exhaust steam pressure must be less than atmospheric pressure. Back-pressure turbines decrease steam pressure from one header to another and produce power. The algorithm of the optimization procedure is shown in Fig. 1.

The site utility scheme in maximums demand situation is presented as Fig. 2. In this case, four steam levels that are feed the four main processes are existence. This site has 3 boiler that are produce steam at 360C and 20 bar and six gas engine generator which can be produce 3.7x6 MW. The boilers and gas engine generator specification are listed as table 1 and 2. Site contains 4 is a process in which steam is used. PR1 is referred to amount of steam demand in 370 C and 35 bar that is service to first and third process of the site. PR2 is steam demand at 260 C and 25 bar that is needed for process 1, 2 and 3. PR3 and PR4 represent the amount of saturated steam required in 10 bar and 2 bar that are services to process.

This study aims to investigate transient modeling and optimization of lubricant oil refinery site utility systems. For this purpose, the annual hourly power and steam demand are extracted from CCR logging software in 3 years and the site utility systems behavior are simulated and the best solution in operation and constitutional reform is applied on site.

ENERGY MODELING

Total heat supply rate by boiler to steam circuits is calculated as below:

$$\dot{Q}_{BOILER} = \dot{m}(h_{out} - h_{in})$$

Where \dot{m} , h_{out} and h_{in} refer to flow rate of steam, enthalpy of outlet steam and boiler feed water. Total heat rate to the boiler is calculated as below:

$$\dot{Q}_{FUEL} = \dot{m}_{fuel} \times LHV$$

Where \dot{m}_{fuel} and LHV refer to boiler fuel flow rate and low heat value of the fuel. Boiler energy efficiency is calculated as below formula.

$$\eta_{BOILER} = \frac{\dot{Q}_{BOILER}}{\dot{Q}_{FUEL} + \dot{m}_{AIR} \times (h_{AIR} - h_{AMB})}$$

Where η_{BOILER} , \dot{m}_{AIR} , h_{AIR} and h_{AMB} are boiler efficiency, airflow rate, sensible specific enthalpy of supply air at the inlet to the boiler and sensible specific enthalpy of ambient air. Because of the difference of h_{AIR} and h_{AMB} is closed to zero, therefor the amount of this section is neglected.

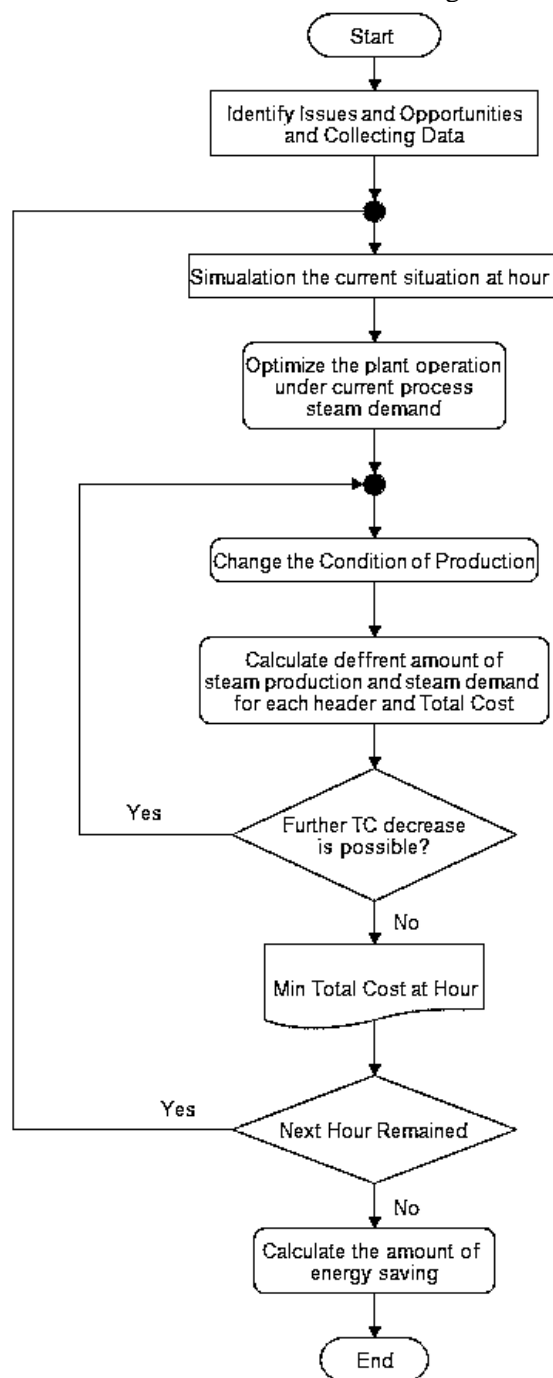


Fig. 1 The algorithm of the optimization procedure.

Therefore, the energy balance of b1, b2 and b3 are illustrated as Figure 3a,b,c. Thus the total amount of fuel that is needed to run the site utility systems is equal 8104 m³/h.

Reciprocating engine generator sets can be used in cogeneration systems, with heat recovery from their exhaust gases and cooling water jackets. In current situation the gas engine generator only produce the power but it can be equipped with heat recovery steam generator.

For the current situation (PG=1250 Kw), the reciprocating engine is simulated and shown as Figure 3d. Thus the total natural gas consumption is about 10270 m³/h.

The value of heat recovery potential, fuel consumption and electrical energy efficiency of the gas engine generator with different power generation are simulated with software and presented as Table 3.

Heat recovery potential, fuel consumption and electrical energy efficiency are regression with power production of reciprocating engine. The results of regression are listed as Table.4.

Even though the steam demand is different in each time, the utility system is produced power and steam in current situation. The total site composite curve is plotted for the maximum situation. Process stream table of process 1 to 4 are shown as Table 1.

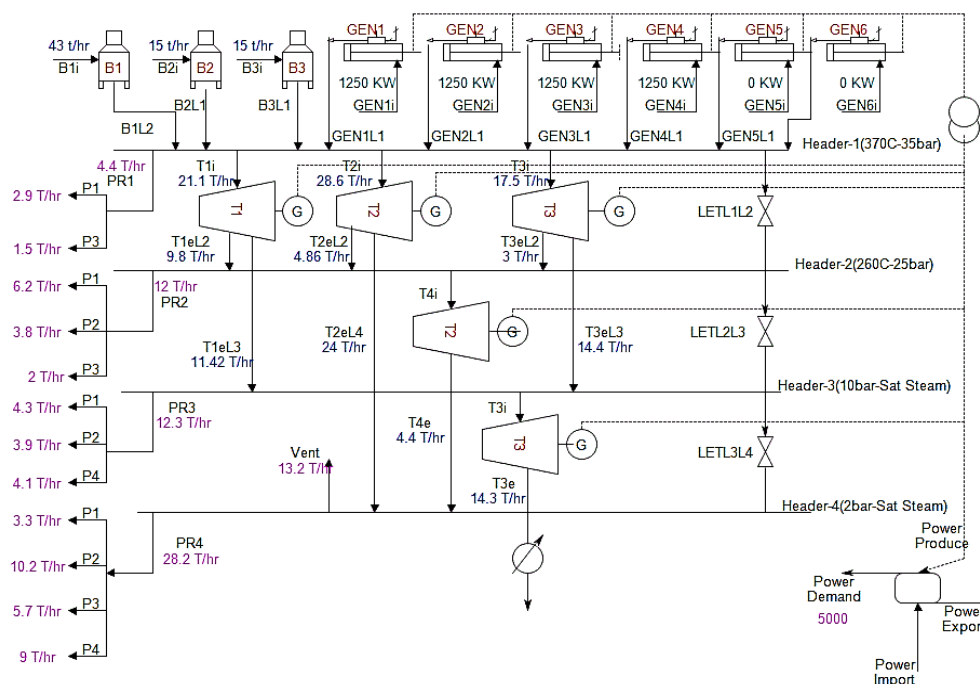


Fig. 2. The site utility scheme in maximums demand situation.

Table 1. Specifications of boilers.

Parameter	Unit	B1		B2&B3	
		Design	Current	Design	Current
Boiler Feed Water	Flow Rate	T/hr	16~80	43.68	3~15 5 98
	Temperature	°C	105	105	105
	Pressure	Bar	22.5	22.5	22.5
Steam Outlet	Flow Rate	T/hr	16~80	43	125 00 15
	Temperature	°C	360	360	360
	Pressure	Bar	20	20	20
Blowdown	Flow Rate	T/hr	-	0.68	- 0.19 8
	Temperature	°C	NA	189	NA 195
Exhaust	Oxygen	%	-	4.695	- 5.71 9

Table 2. Specifications of gas engine generators.(at 3337 kW)

Fuel Type	Mode	RPM	Freq	Power	Texh	Exh. Flow	Elec Eff
NG	C	1000	50 Hz	3337 kW	490 C	19.48 t/hr	39.5 %

Table 3. Technical information of GENSET

	PG (KW)	Heat to exhaust (KW)	Fuel consumption (t/hr)	ELEC EFF (%)	
1	3337	2832	0.657	39.49%	
2	3250	2767.1	0.644	39.29%	
3	3000	2581.7	0.604	38.66%	
4	2750	2398.3	0.564	37.94%	
5	2500	2217.3	0.524	37.11%	
6	2250	2091.4	0.484	36.14%	
7	2000	1958.5	0.444	35.01%	
8	1750	1818.7	0.405	33.65%	
9	1500	1659.6	0.365	31.99%	
0	1	1250	1490.9	0.325	29.92%
1	1	1000	1319.1	0.285	27.28%
2	1	834.2	1203.5	0.259	25.08%

Table 4. Heat recovery potential, fuel consumption and electrical energy efficiency of GENSET.

Formula	Constraint	RValue
$\eta_{ELEC} = p_1 \times PG^4 + p_2 \times PG^3 + p_3 \times PG^2 + p_4 \times PG + p_5$	$384.2 \leq PG \leq 3337$	$R = 0.99$
$M_{FUEL} = p_6 \times PG + p_7$	$384.2 \leq PG \leq 3337$	$R = 0.99$
$HEP = p_8 \times PG + p_9$	$384.2 \leq PG \leq 3337$	$R = 0.96$

Where the $p_1 = -2.703e-013$, $p_2 = 2.987e-009$, $p_3 = -1.321e-005$, $p_4 = 0.03053$, $p_5 = 7.218$, $p_6 = 0.0001593$, $p_7 = 0.1259$, $p_8 = 0.6332$ and $p_9 = 686.7$

Table 5. Current situation mass balance

1	B1L1	43	T/hr.	14	T1eL2	9.8	T/hr.
2	B2L2	15	T/hr.	15	T1eL3	11.2	T/hr.
3	B3L3	15	T/hr.	16	T2i	28.8	T/hr.
4	GEN1L1	0	T/hr.	17	T2eL2	4.8	T/hr.
5	GEN2L1	0	T/hr.	18	T2eL4	24	T/hr.
6	GEN3L1	0	T/hr.	19	T3i	17.4	T/hr.
7	GEN4L1	0	T/hr.	20	T3eL2	3	T/hr.
8	GEN5L1	0	T/hr.	21	T3eL3	14.4	T/hr.
9	GEN6L1	0	T/hr.	22	T4i	4.4	T/hr.
10	LETL1L2	1.4	T/hr.	23	T4e	44	T/hr.
11	LETL2L3	2.6	T/hr.	24	T5i	14.3	T/hr.
12	LETL3L4	1.6	T/hr.	25	T5e	14.3	T/hr.
13	T1i	21	T/hr.				

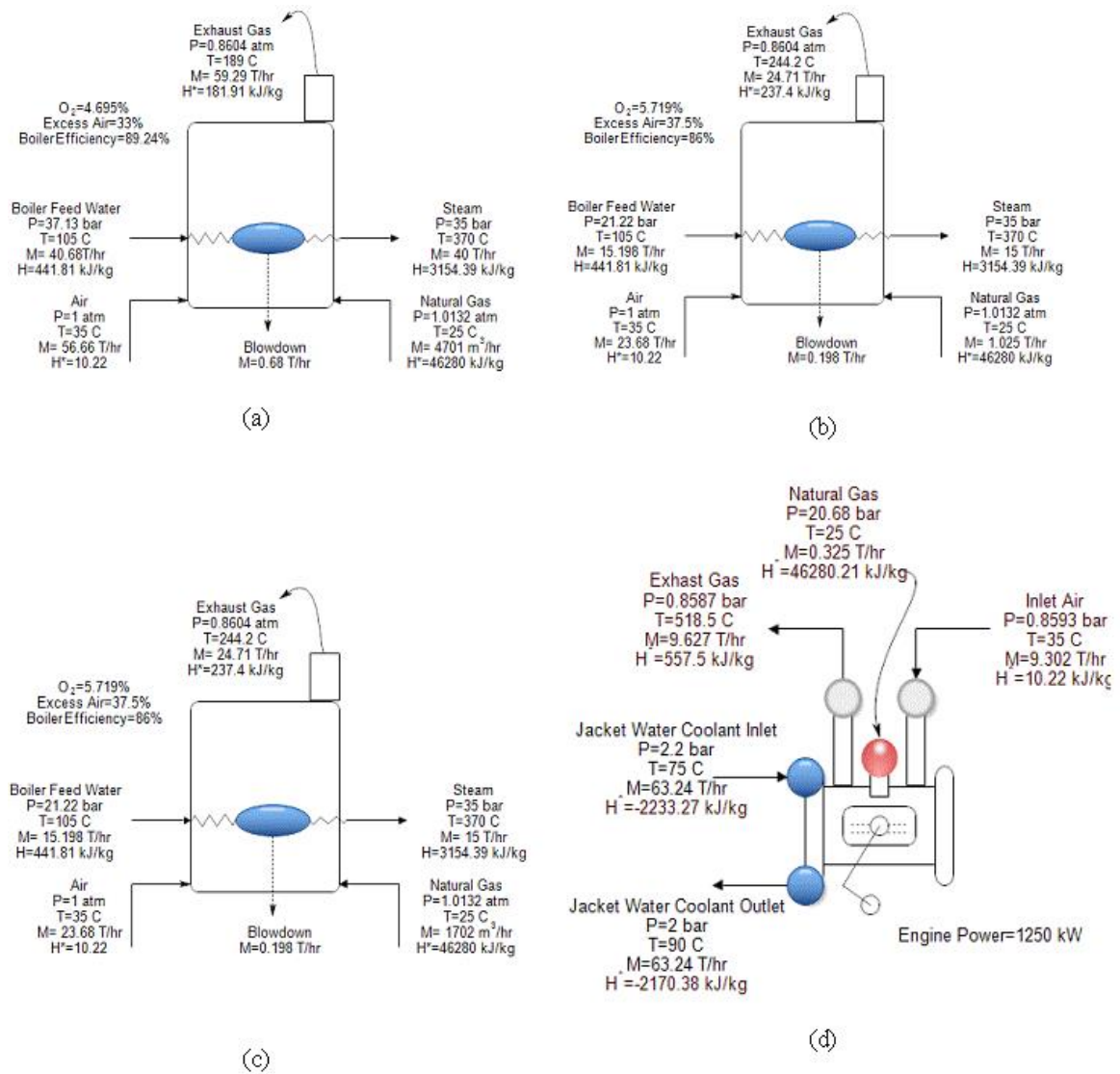


Fig. 3. Mass and energy balance of b1(a), b2(b), b3(c) and reciprocating engine(d).

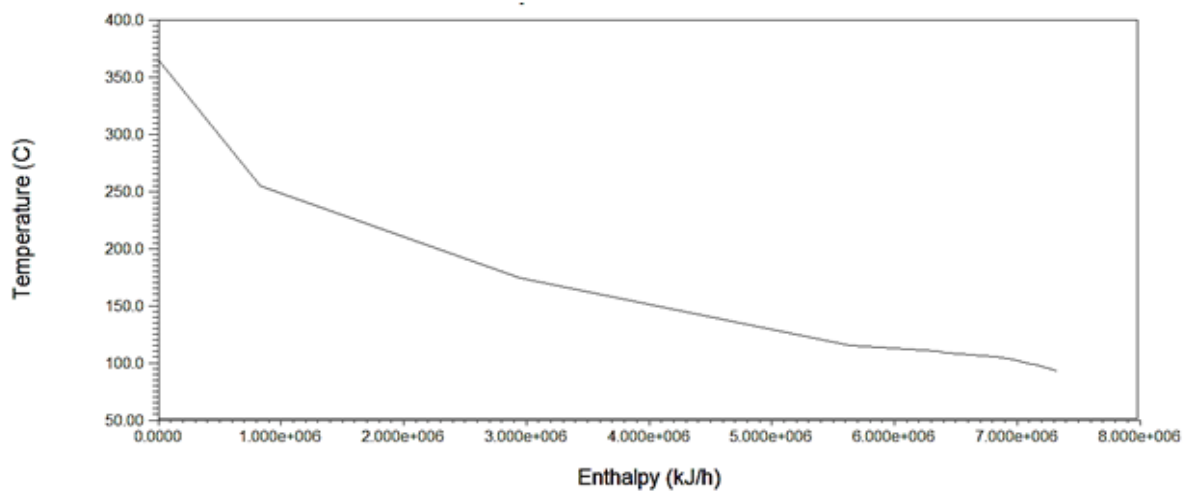


Fig. 4. Total site composite curve.

Table 6. Process stream table of total site

	Code	Flow rate	T _{in}	T _{out}	Duty
process 1	E101	2.9	370	110	1316430
	E103	6.2	260	114.3	1394864
	E104	4.3	179.9	112.4	441289.9
	E106	3.3	120.2	97.8	128145.3
process 2	E202	3.8	260	110	886131.7
	E203	3.9	179.9	113.2	394278.5
	E204	5.9	120.2	115	131282.8
	E205	4.3	120.2	108	418443.3
process 3	E301	1.5	370	105	695226
	E302	2	260	110	466385.1
	E304	5.7	120.2	98.3	215912.7
process 4	E401	4.1	179.9	103	494322.9
	E404	9	120.2	98	346058.2

As the statistical analysis, this site is operated as fixed condition during the year. The economic analysis is studied in this section. As thermal modeling of site utility, the boiler fuel consumption return to sum of fuel consumption of b1, b2 and b3. Similarly the fuel consumption of generators is equal to sum of fuel consumption of GEN1, GEN2, GEN3, GEN4, GEN5 and GEN6. Export power is calculated as different of power produce and power demand. The total cost (or total revenue) is different of fuel cost and power purchase. If the result is greater than zero total cost will be considered, else total revenue will be considered. Power and NG price are listed as below table.

The cogeneration efficiency is therefore more correctly defined as:

$$\eta_{COGEN} = \frac{W_{GEN} + Q_{SITE}}{Q_{SUPPLY}}$$

Where W_{GEN} , Q_{SITE} and Q_{SUPPLY} are total power production, total heat demand and total heat supply. Where Q_{SUPPLY} defined as:

$$Q_{SUPPLY} = Total\ fuel\ consumption \times LHV$$

The most appropriate cogeneration system for a site depends to a large extent on the site power-to-heat ratio, defined as

$$R_{SITE} = \frac{W_{SITE}}{Q_{SITE}}$$

Where R_{SITE} , W_{SITE} and Q_{SITE} are site power-to-heat ratio, power demand of the site and process heating demand for the site. R_{SITE} is equal to 0.131.

According to above discussion, economic evaluation of site utility existed condition is presented as Table 8.

For the proposed of this study, the average of hourly annual Steam and power demands in different header are extracted for 3 years from refinery's DCS and these data are plotted as fig 5,6,7,8. It should be noted that, unrealistic information (such as hot and cold maintenance, shutdown etc.) are excluded.

As shown in the figure, the amount of steam required in PR1, PR2, PR3 and conditions are equal 38509.7, 105026.7, 107652.1 and 246811.8 Ton/hr. Although the boilers are working as constant condition, that is presented as Fig 2.

Hourly total revenue of incoming power purchase after shrinking of fuel consumption cost is plotted as below figure. Annual revenue is about of 1900878 \$. This data should be used to simulate the different condition of site for optimization of operating site utility systems. For this simulation, it is assumed the efficiency of boiler is constant in different condition.

Table 7. Power and NG price

Power Export Price (¢/kWh)	NG Price of DG (¢/m^3)	NG Price (¢/m^3)
3.35	1.93	2.89

Table 8. Economic evaluation of site utility existed condition

TC (or TR) (\$)	Power Produce (kWh)	Power Export (kWh)	Power Purchase (\$/hr)	Boiler Fuel Consumption (m3/yr)	Generator Fuel Consumption (m3/yr)	Total Fuel Consumption (m3/yr)	Fuel Cost (\$/hr)	Cogeneration Efficiency
-217.4	20185	15185	509.1	8367	2587	10954	291.7	41.38%

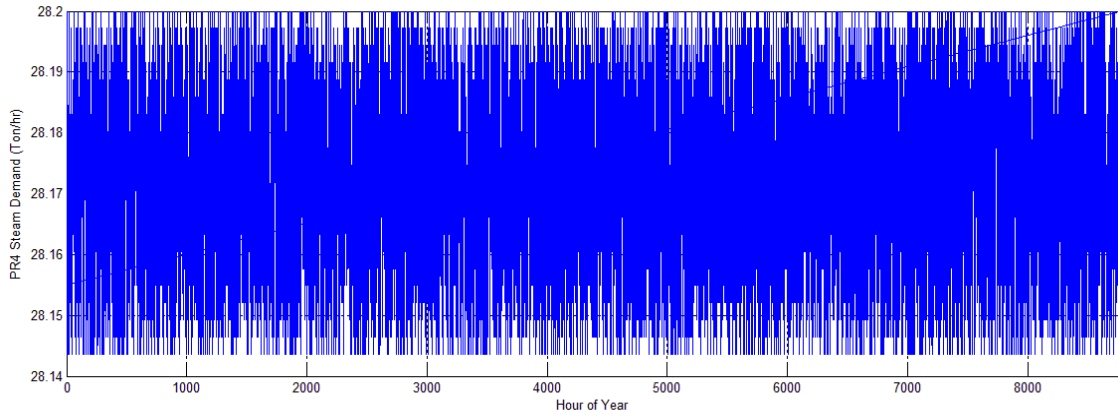


Fig. 5 Annual hourly PR4 steam demand.

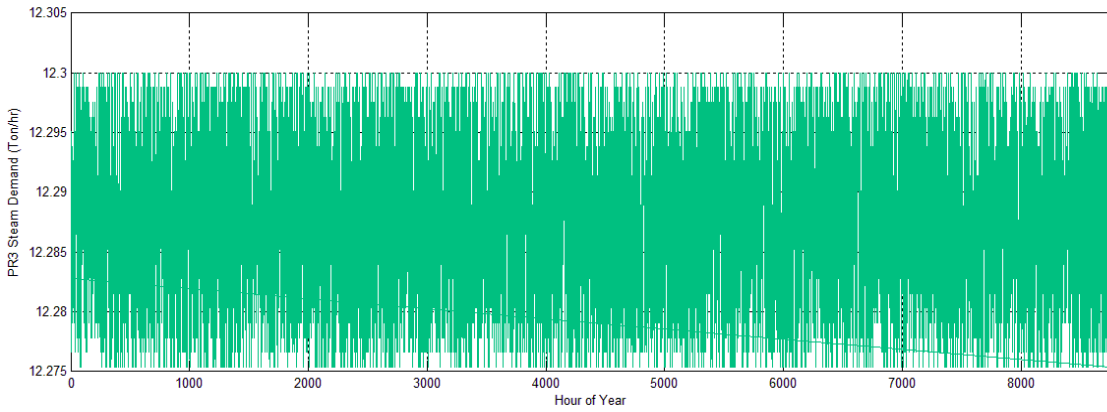


Fig. 6 Annual hourly PR3 steam demand.

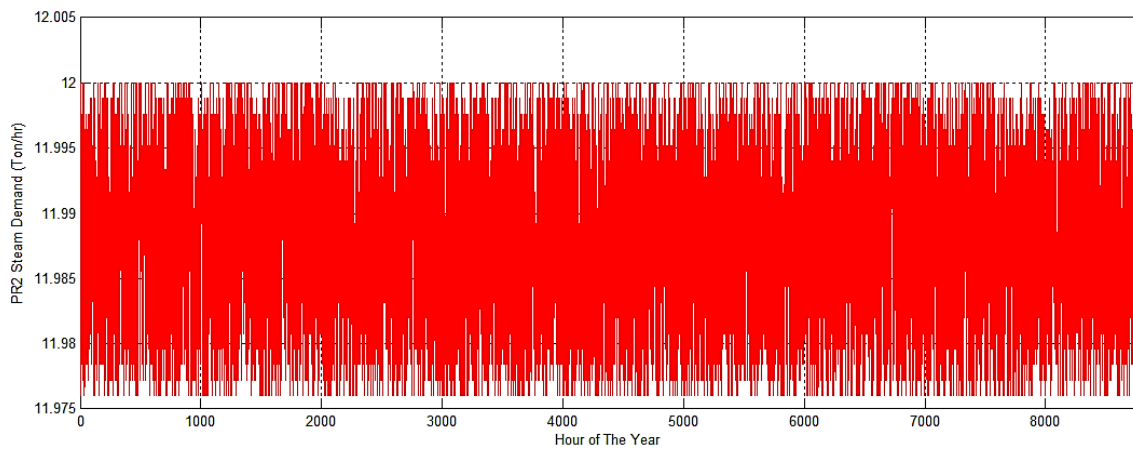


Fig. 7 Annual hourly PR2 steam demand.

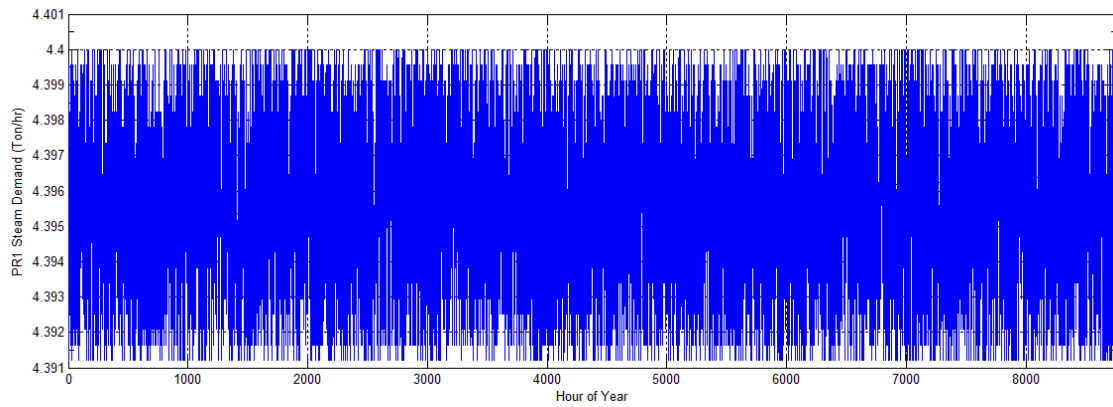


Fig. 8 Annual hourly PR1 steam demand.

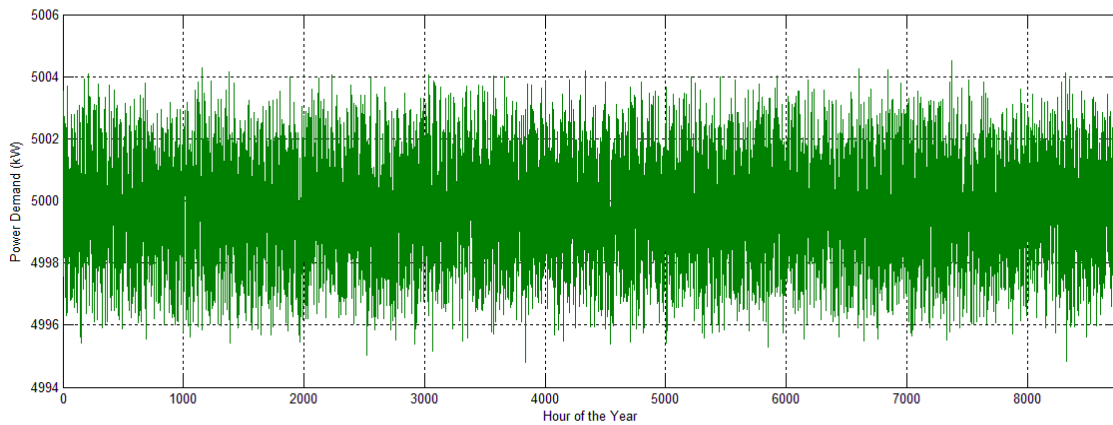


Fig. 9. Annual hourly power demand.

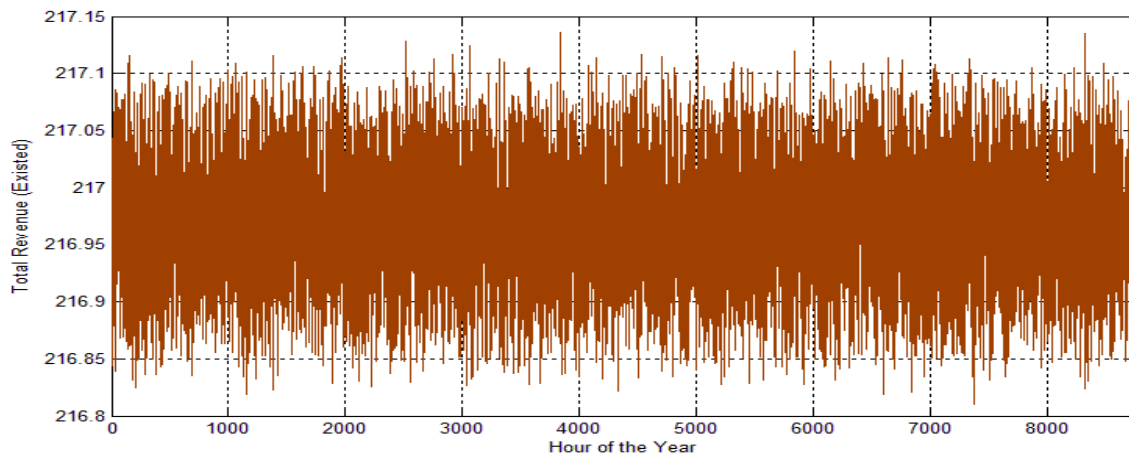


Fig. 10 Annual hourly site utility revenue

Table 9. Equal constraints of the model

$16 \leq B1L1 \leq 80;$	$3 \leq T2eL2 \leq 13.2;$
$3 \leq B2L1 \leq 15;$	$14 \leq T2eL4 \leq 37;$
$3 \leq B3L1 \leq 15;$	$8.36 \leq T3i \leq 23.3;$
$13.2 \leq Ti \leq 36.3;$	$1.4 \leq T3eL2 \leq 5.3;$
$4.2 \leq T1eL2 \leq 16.5;$	$6.96 \leq T3eL3 \leq 18;$
$9 \leq T1eL3 \leq 19.8;$	$8.8 \leq T5i \leq 16.5;$
$17 \leq T2i \leq 50.2;$	$382 \leq PG1\sim6 \leq 3337;$

The next step in this study is modeling of site utility system for transient situation of PR1, PR2, PR3 and PR4. Minimizing the total cost is the main target in this study. For this reason, the thermo-economic model is developed that finds the minimum of total cost and best solution for operation cost specified by

$$\min_x f^t x \text{ such that } \begin{cases} A \cdot x \leq b, \\ Aeq \cdot x = beq \\ lb \leq x \leq ub \end{cases} \quad (1)$$

f, x, b, beq, lb and ub are vectors and A and Aeq are matrices. The cost of energy is the sum of the costs of purchased natural gas used in the boilers and GENSET and the revenue is the sum of the power purchase. The profit is the different between the cost of energy and the revenue. Thus objective Function is presented as below formula.

$$\begin{aligned} \max Total_Revenue \text{ (or min Total_Cost)} = & \\ & FPB \times (m_FUEL_B1 + m_FUEL_B2 + \\ & m_FUEL_B3) + (M_FUEL_GEN1 + \\ & M_FUEL_GEN2 + M_FUEL_GEN3 + \\ & M_FUEL_GEN4 + M_FUEL_GEN5 + \\ & M_FUEL_GEN6) \times FPGEN - PG1 + PG2 + \\ & PG3 + PG4 + PG5 + PG6 + WPT1 + WPT2 + \\ & WPT3 + WPT4 + WPT5 - PD) \times PP; \quad (2) \end{aligned}$$

In this section the subject to the restrictions are are discussed. The mass balance around the header 1 is presented as below formula:

$$\begin{aligned} & \frac{GEN1L1}{1000} + \frac{GEN2L1}{1000} + \frac{GEN3L1}{1000} + \frac{GEN4L1}{1000} \\ & + \frac{GEN5L1}{1000} + \frac{GEN6L1}{1000} + B1L1 + B2L1 \\ & + B3L1 - T1i - T2i - T3i - LETL1L2 = \\ & PR1; \quad (3) \end{aligned}$$

Where PR1 is the amount of steam demand at 370 C and 35 bar that is presented at Fig8. Also the mass balance of header NO2 is calculated from below formula:

$$T1eL2 + T2eL2 + T3eL2 - T4i + LETL1L2 - LETL2L3 = PR2; \quad (4)$$

Where PR2 is the amount of steam demand at 260 C and 25 bar that is presented at Fig7. Then the mass balance of header NO3 is calculated from below formula:

$$T1eL3 + T3eL3 + LETL2L3 - LETL3L4 - T5i = PR3; \quad (5)$$

Where PR3 is the amount of saturated steam demand at 10 bar that is presented at Fig6. Also the mass balance of header NO4 is calculated from below formula:

$$-VENT + T4e + T2eL4 + LETL3L4 = PR4; \quad (6)$$

Where PR4 is the amount of saturated steam demand at 2 bar that is presented at Fig5. The amount of fuel consumption and steam production by three boilers is calculated from below formula.

$$Q_{B1} - B1L1 \times (HL1 - H_{FW}) \times 1000 = 0; \quad (8)$$

$$m_FUEL_B1 - \frac{Q_{B1}}{(LHV \times ETHAB1)/0.6} = 0; \quad (9)$$

$$Q_{B2} - B2L1 \times (HL1 - H_{FW}) \times 1000 = 0; \quad (10)$$

$$m_FUEL_B2 - \frac{Q_{B2}}{(LHV \times ETHAB2)/0.6} = 0; \quad (11)$$

$$Q_{B3} - B3L1 \times (HL1 - H_{FW}) \times 1000 = 0; \quad (12)$$

$$m_FUEL_B3 - \frac{Q_{B3}}{(LHV \times ETHAB3)/0.6} = 0; \quad (13)$$

The mass balance and the amount of power generated by turbine No1 is calculated as below formula

$$-T1i + T1eL2 + T1eL3 = 0; \quad (14)$$

$$-HL1 \times T1i + Ha \times T1eL2 + Hb \times T1eL3 + \frac{WPT1}{0.000277778 \times 1000} = 0; \quad (15)$$

The mass balance and the amount of power generated by turbine No2 is calculated as below formula

$$-T2i + T2eL2 + T2eL4 = 0; \quad (16)$$

$$-HL1 \times T2i + Hc \times T2eL2 + Hd \times T2eL4 + \frac{WPT2}{0.000277778 \times 1000} = 0; \quad (17)$$

The mass balance and the amount of power generated by turbine No3 is calculated as below formula

$$-T3i + T3eL2 + T3eL3 = 0; \quad (18)$$

$$-HL1 \times T3i + He \times T3eL2 + Hf \times T3eL3 + \frac{WPT3}{0.277778} = 0; \quad (18)$$

The mass balance and the amount of power generated by turbine No4 is calculated as below formula.

$$T4i - T4e = 0; \quad (20)$$

$$-HL2 \times T4i + T4e \times Hg + \frac{WPT4}{0.277778} = 0; \quad (21)$$

The mass balance and the amount of power generated by turbine No5 is presented as below formula.

$$T5i - T5e = 0; \quad (22)$$

$$-HL3 \times T5i + T5e \times Hh + \frac{WPT5}{0.277778} = 0; \quad (23)$$

The amount of heating supplied and fuel consumption by the six GENSET is calculated as the below formula.

$$M_FUEL_GEN - \frac{p_6 \times 1000 \times PG1}{0.6} = \frac{p_7 \times 1000}{0.6}; \quad (24)$$

$$(p_8 \times 3600) \times PG1 - (HL1 - H_{FW}) \times GEN1L1 = -p_9 \times 3600; \quad (25)$$

$$M_FUEL_GEN2 - \frac{p_6 \times PG2 \times 1000}{0.6} = \frac{p_7 \times 1000}{0.6}; \quad (26)$$

$$(p_8 \times PG2) \times 3600 - GEN2L1 \times (HL1 - H_{FW}) = -p_9 \times 3600; \quad (27)$$

$$M_FUEL_GEN3 - \frac{p_6 \times PG3 \times 1000}{0.6} = \frac{p_7 \times 1000}{0.6}; \quad (28)$$

$$(p_8 \times PG3) \times 3600 - GEN3L1 \times (HL1 - H_{FW}) = -p_9 \times 3600; \quad (29)$$

$$M_{FUEL_GEN4} - \frac{p_6 \times PG4 \times 1000}{\frac{p_7 \times 1000}{0.6}} =$$

$$(p_8 \times PG4) \times 3600 - GEN4L1 \times (HL1 - H_{FW}) = -p_9 \times 3600; (31)$$

$$M_{FUEL_GEN5} - \frac{p_6 \times PG5 \times 1000}{\frac{p_7 \times 1000}{0.6}} =$$

$$(p_8 \times PG5) \times 3600 - GEN5L1 \times (HL1 - H_{FW}) = -p_9 \times 3600; (33)$$

$$M_{FUEL_GEN6} - \frac{p_6 \times PG6 \times 1000}{\frac{p_7 \times 1000}{0.6}} =$$

$$(p_8 \times PG6) \times 3600 - GEN6L1 \times (HL1 - H_{FW}) = -p_9 \times 3600; (35)$$

Additional constraints are extracted from technical catalogue of boiler, turbine and GENSET are listed as table 9.

Unequal restrictions values are extracted from technical catalogue of gas engine, boiler and

turbine. Although, the constant values are listed as table 10. In accordance with state law, the price of gas to DG power plants (FPGEN) and process plant are 1.93 and 2.89 $\text{¢}/\text{m}^3$. The power export price is equal to 3.35 $\text{¢}/\text{kWh}$. Harry Taplin presented model to calculate combustion efficiency by measuring stack temperature and oxygen amount of exhaust gas and thermodynamic modeling [10-12]. ETHAB1, ETHAB2 and ETHAB3 are calculated by measuring and auditing. Enthalpies of header and turbine extraction are extracted from thermodynamic steam table.

RESULTS AND DISCUSSIONS

In the previous section, the optimal model for to achieve the best solution for operating site utility is presented. The optimum solutions of the model for boiler and turbine steam flowrate are presented as Fig. 11 to 15.

Table 10. Equal constraints of the model

PD = 5000 kW;	PR2 = Variable;	HL3 = 2584 kJ/kg;	Ha = 3121 kJ/kg;
FPGEN = 1.93 (¢/m³);	PR3 = Variable;	HL4 = 2533 kJ/kg;	Hb = 2894 kJ/kg;
FPB = 2.89 (¢/m³);	PR4 = Variable;	H _{FW} = 441.81 kJ/kg;	Hc = 3121 kJ/kg;
PP = 3.35 (¢/kWh);	LHV = 46285.6 kJ/kg;	ETHAB1 = 0.8496%;	Hd = 2598 kJ/kg;
PR1 = Variable;	HL1 = 3217 kJ/kg;	ETHAB2 = 0.8015%;	He = 3121 kJ/kg;
p₆ = 0.0001593;	HL2 = 2996 kJ/kg;	ETHAB3 = 0.8015%;	Hf = 2894 kJ/kg;
p₇ = 0.1259;	p ₈ = 0.6332 ;	p ₉ = 686.7;	Hg = 2330 kJ/kg;
Hh = 491.3 kJ/kg;	T4i = 4.4;		

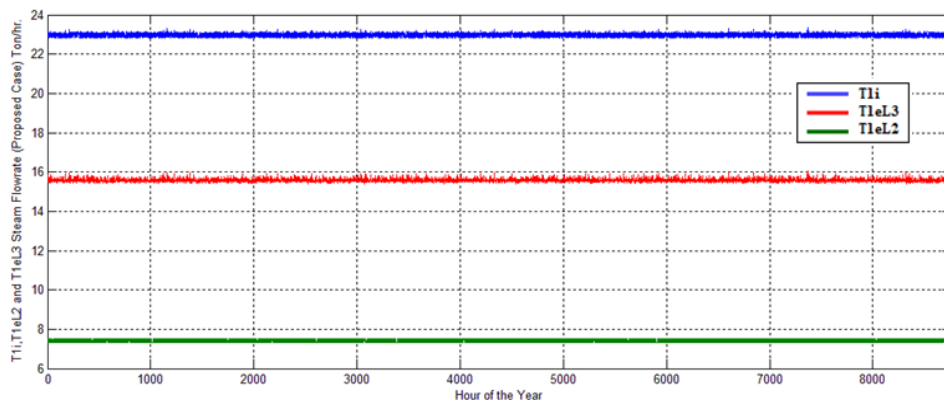


Fig. 11. Annual hourly T1i, T1eL2 and T1eL3 flowrate.

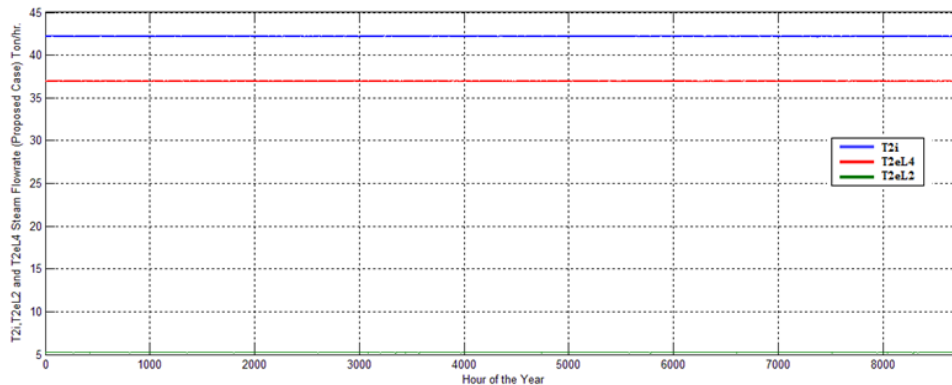


Fig. 12. Annual hourly T2i, T2eL2 and T2eL4 flowrate

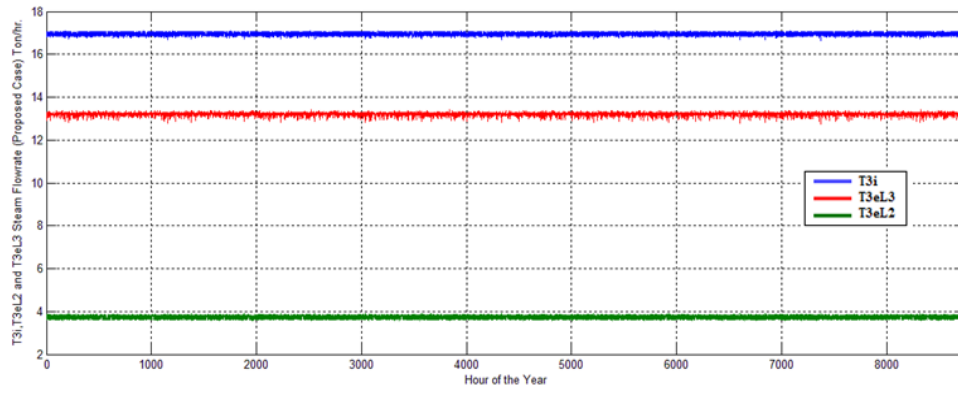


Fig. 13. Annual hourly T3i, T3eL2 and T3eL3flowrate.

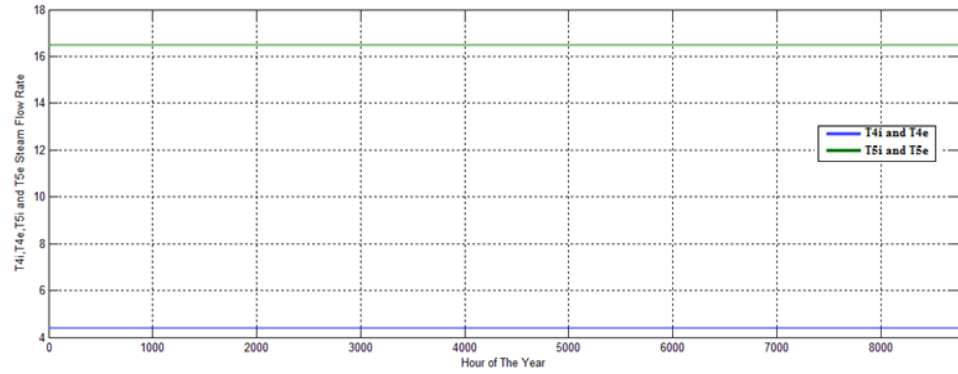


Fig. 14. Annual hourly T4i,, T4e, T5i and T5eflowrate.

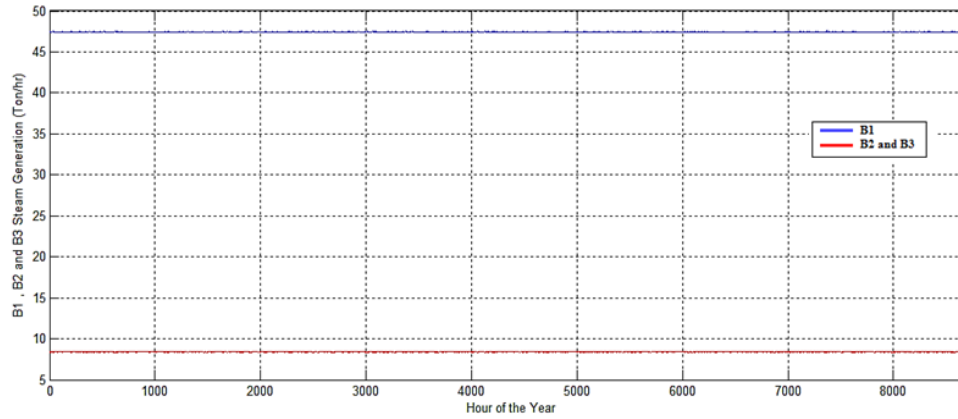


Fig. 15. Annual hourly B1, B2 and B3 steam generation.

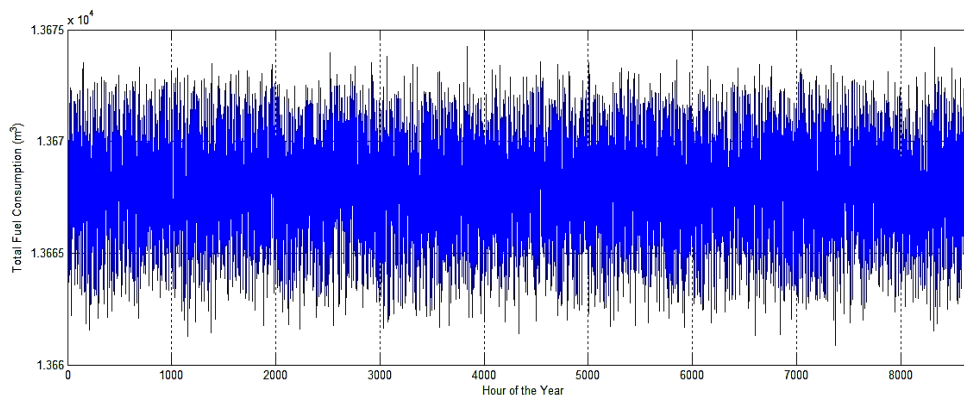


Fig. 16. Annual hourly total fuel consumption in proposed case.

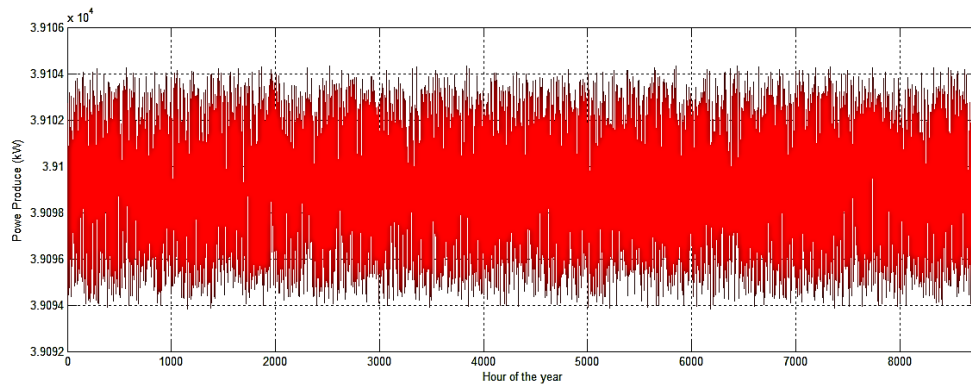


Fig. 17. Annual hourly power produces in proposed case.

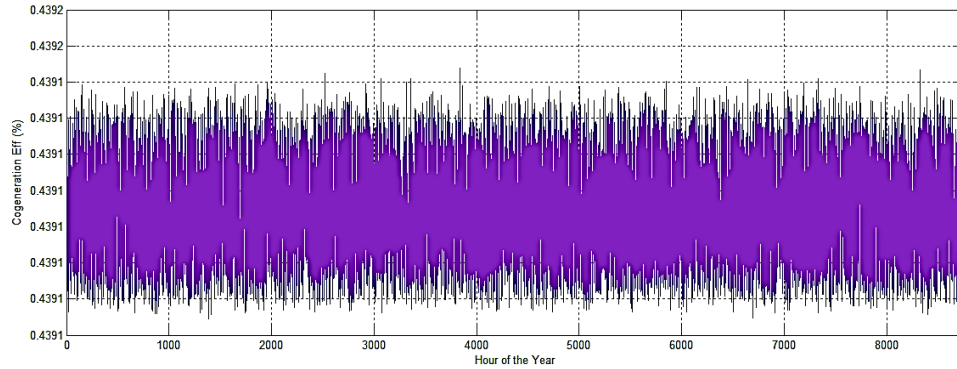


Fig. 18. Annual hourly cogeneration efficiency in proposed case.

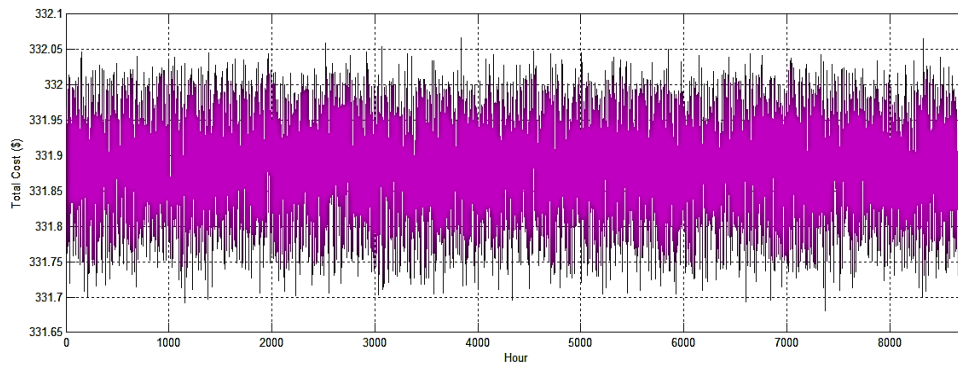


Fig. 19. Annual hourly total cost in proposed case.

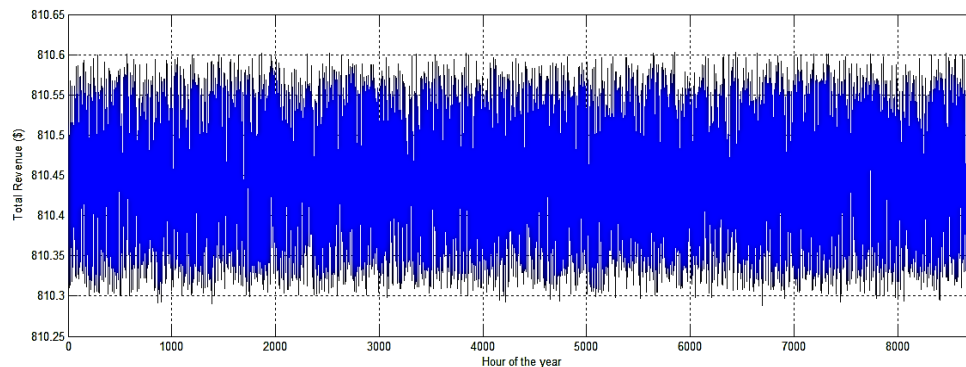


Fig. 20. Annual hourly total revenue in proposed case.

Table 11. Fuel consumption of existed and proposed case.

	Total Fuel Consumption (m ³ /yr.)	Boiler Fuel Consumption (m ³ /yr.)	GEN Fuel Consumption (m ³ /yr.)
Existed Case	95967994	73303287	22664707

Proposed Case	119744227	62142045	57602182
---------------	-----------	----------	----------

Table 12. Power Produce, Power Demand and Power Purchase in existed and proposed case.

	Power Produce (kWh/yr.)	Power Demand (kWh/yr.)	Power Purchase (kWh/yr.)
Existed Case	176840785	43802795	133037989
Proposed Case	342546981	43802795	298744185

y the use of this model, total fuel consumption in boilers and gas engine are shown as Fig16. According to the model the annual fuel consumption is equal to 119744227 m³. In existed condition the amount of fuel consumption is about 95967994 m³. By the use of proposed condition, the fuel consumption is increased about 23776233 m³, which, due to increased generators power production.

Total power produce is shown as Fig 17. The area under the power produce and time’s curve is equal annual electrical energy production. The power purchase is different between total power produce and total power demand. As result, the amount of power produces and power purchase in proposed case is equal to 342546981 and 298744185 kWh and existed case is equal to 176840785 and 133037989 kWh. The power produce and purchase are increased about 165706196 kWh.

Cogeneration efficiency is calculated by the transient model. Hourly cogeneration efficiency of the site is shown as fig18. By the averaging, the mean annual cogeneration efficiency is about 43.91%. By the use of this model and compared result with existed efficiency are shown that the cogeneration efficacy increased 2.5%.

The next important parameter that should be considered is total cost. The hourly cost of the site in optimal condition is shown as Fig. 19. By the use of this model, total cost increase about 351733\$ \$.

Finally, total revenue is another parameter that is very important to recognize economical characteristic of site utility systems. Total revenue is different between total cost and power purchase income. Hourly total revenue for optimal model is presented as Fig. 20. The amount of total revenue of site for optimal model is equal to 7100303 \$. The total revenue in existed case is about 1900878 \$.

Comparison between existed and proposed case are listed as below table. With an annual review of the above information, the following results are obtained.

- The boilers fuel consumptions are decreased and GENSET fuel consumptions are decrease in proposed case.
- Power produce and power purchase are increased in proposed case.

- Total cost and total revenue is increased in proposed case.

Table 13. Total variable cost and total revenue of site in existed and proposed case.

	Total Variable Cost (\$/yr.)	Total Revenue (\$/yr.)
Existed Case	2555893	1900878
Proposed Case	2907627	7100303

CONCLUSION

One of the most important achievements of this study is, considering the transient condition for initial assumptions of site utility to make better decisions. In the absence of consideration of this issue, the supply must be utilized in highest amount of demand. If demand decrease and supply remains constant, steam passes through the letdown stations and it cause to decrease cogeneration efficiency. If transient decisions are possible, demand and supply will compatible together and cogeneration efficiency will remain constant.

Next, the performance analysis and parameters on site utility systems has been carried. The result of different between existed and proposed case is studied. The results show that the boiler fuel consumption is reduced; generator fuel consumption, total fuel consumption, total variable cost, total revenue and cogeneration efficiency are increased. The reasons for reduced boiler fuel consumption are listed as below:

- Using heat recovery equipment to recover exhaust gas energy of DG
- Conformity of steam supply and steam demand
- Reduction the amount of steam letdown station

The reason for increased generator fuel consumption is power purchase price. Production and sale of electricity is affordable with the governmental energy price. Thus the total variable cost and total increased. There for cogeneration efficiency is increased.

It is suggested that future studies develop the exergetic analysis and consider the ambient circumstances condition in the site utility and focus more on total site grand composite curve technique.

NOMENCLATURE

B1L1	Boiler No.1 Existed Steam Flowrate
B2L2	Boiler No.2 Existed Steam Flowrate
B3L3	Boiler No.3 Existed Steam Flowrate
GEN1L1	CHP No.1 Existed Steam Flowrate
GEN2L1	CHP No.2 Existed Steam Flowrate
GEN3L1	CHP No.3 Existed Steam Flowrate
GEN4L1	CHP No.4 Existed Steam Flowrate
GEN5L1	CHP No.5 Existed Steam Flowrate
GEN6L1	CHP No.6 Existed Steam Flowrate
LETL1L2	Letdown Station from Header 1 to Header 2
LETL2L3	Letdown Station from Header 2 to Header 3
LETL3L4	Letdown Station from Header 3 to Header 4
T1i	Turbine No1. Steam Inlet
T1eL2	Turbine No1. Steam Outlet to Header 2
T1eL3	Turbine No1. Steam Outlet to Header 3
T2i	Turbine No2. Steam Inlet
T2eL2	Turbine No2. Steam Outlet to Header 2
T2eL4	Turbine No2. Steam Outlet to Header 3
T3i	Turbine No3. Steam Inlet
T3eL2	Turbine No3. Steam Outlet to Header 2
T3eL3	Turbine No3. Steam Outlet to Header 3
T4i	Turbine No4. Steam Inlet
T4e	Turbine No4. Steam Outlet
T5i	Turbine No5. Steam Inlet
T5e	Turbine No5. Steam Outlet
PG	CHP No1~6. Power Produce

m_FUEL_B	Boiler Fuel Consumption
LHV	Lower Heating Value of Fuel
ETHAB	Boiler Fuel Consumption
WPT	Power Production by Steam Turbine
M_FUEL_GEN	CHP Fuel Consumption

REFERENCES

1. R. Smith, *Chemical Process Design and Integration*. John Wiley, West Sussex, 2005.
2. P. Varbanov, S. Perry, Y. Makawana, X.X. Zhup, R. Smith, *Chemical Engineering Research and Design*, **82**, 34 (2004).
3. O.V. Afanasyeva, G. R. Mingaleeva, *Energy Efficiency*, **8**, 56 (2015).
4. A. Ghannadzadeh, S. Perry, R. Smith, *Applied Thermal Engineering*, **43**, 60 (2012).
5. M.H. Khoshgoftar Manesh, M. Amidpour, S. Khamis Abadi, M.H. Hamed, *Appl. Thermal Eng.*, **54**, 12 (2013).
6. V.R. Dhole, B. Linnhoff, *Computers & Chemical Engineering*, **17**, 101 (1993).
7. S. Perry, J. Klemes, I. Bulatov, *Energy*, **33**, 1489 (2008).
8. P.S. Varbanov, J. Klemes, *Computers and Chemical Engineering*, **10**, 44 (2010).
9. J. Klemes, V.R. Dhole, K. Raissi, S.J. Perry, L. Puigjaner, *Appl. Thermal Eng.*, **17**, 993 (1997).
10. W.F. Kenney, *Energy Conservation in the Process Industries*. Academic Press, Orlando, 1984.
11. K. Raissi Total Site Integration, PhD Thesis, UMIST, UK, 1994.
12. H. Taplin, *Combustion Efficiency Tables*, Fairmont Press, Inc., 1991.

Modeling arsenic transport in soil column and ground water

S. A. Mirbagheri*, F. G. Avili, A. H. Javid

Department of Environmental Engineering, Faculty of Environment and Energy, Tehran Science and Research Branch, Islamic Azad University, Tehran, Iran

Received June 26, 2016, Revised September 10, 2016

A mathematical and computer model for the transport and transformation of arsenic through a soil column from the surface to the groundwater is presented. The model simulates arsenic species. This model is based on the mass balance equation including convective transport, dispersive transport, surface adsorption, oxidation and reduction, volatilization, chemical and biological transformation. The governing equations are solved numerically by the method of implicit finite difference. The simulation results are in good agreement with measured values. The major finding in the present study indicates that as the time of simulation increases, the concentration of different arsenic species approaches the measured values.

Key words: arsenic transport, mathematical, computer, model, arsenic species

INTRODUCTION

Mathematical modeling is an accepted scientific practice, providing the mechanism for comprehensively integrating basic processes and describing a system beyond what can be accomplished using subjective human judgements. It is possible to construct models that better represent the natural system, and to use these models in an objective manner to guide both our future research efforts and current management practices.

Recent years have seen a variety of approaches to description of water and solute movement in soils field. A number of new models have been proposed in response to recently collected field data on solute leaching patterns. The contaminants are released from the refuse to the passing water by physical, chemical, and microbial processes and percolate through the unsaturated environment, polluting the groundwater with organic and inorganic matter.

The modeling of contaminant transport hinges on an understanding of the mechanisms of mass release from the solid to the liquid phase, and contaminant decay. These mechanisms are influenced by such factors as climatic conditions, type of waste, site geohydrologic conditions, and chemical reactions as well as microbial decomposition of organic matter.

Modeling of different kinds of contaminant was studied by several researchers, e.g. [1-9]. The objective of this paper is to address the spatial and temporal distribution of contaminant

concentrations in soil column. The work has been done in Gorgan site, Golestan province, Iran in 2014.

MATHEMATICAL MODEL

The flow and the corresponding moisture content and the concentration of a contaminant are considered here in as continuous functions of both space and time. This model considers a variety of processes that occur in the plant root zone as well as leaching to the ground water, including transient fluxes of water and contaminants, alternating periods of rainfall, irrigation and evapotranspiration, under variable soil conditions with depth.

Water flow model

Water flow is calculated using a finite difference solution to the soil-water flow equation

$$\frac{\partial h}{\partial t} c(\theta) = \frac{\partial}{\partial z} \left[K(\theta) \cdot \frac{\partial H}{\partial z} \right] \quad (1)$$

Where h is a soil water pressure head (mm), θ is volumetric water content (m^3m^{-3}), t is time (day), H is hydraulic head ($h + z$), z is soil depth, K is

hydraulic conductivity (mm day^{-1}), $c(\theta) = \frac{\partial \theta}{\partial h}$ is differential water capacity. Functions which characterized relationships between $K - \theta - h$ described in LEACHM [7] are used. There is a two-part function that described the general shape of θ (h) relationships [6],

* To whom all correspondence should be sent:
E-mail: seyedahmad_mirbagheri@yahoo.com

$$h = \frac{[1 - (\theta / \theta_s)]^{1/2} (\theta_i / \theta_s)^{-b}}{[1 - (\theta_i / \theta_s)]^{1/2}} \quad \text{for } 0 > h > h_i \quad (2a)$$

$$h = a(\theta / \theta_s)^{-b} \quad \text{for } h_i > h > -\infty \quad (2b)$$

Where $h_i = a[2b / (1+2b)]^{-b}$ and $\theta_i = 2b\theta_s / (1+2b)$ is the point h_i, q_i of intersection of the two curves, θ_s is water content at saturation, a and b are constant. The two curves are exponential and parabolic for dry and saturated soil respectively. Similarly the equation for the calculation of hydraulic conductivity is:

$$K = K_s (a/h)^2 + (2+P)/b, \quad (4)$$

Solving equation (1) using finite difference techniques provides estimated values of h at each depth node used in the differencing equation. Water contents are calculated using equation (2). Water flux densities (q) are calculated over each depth interval using Darcy's equation:

$$\left(q = K(\theta) \frac{\Delta H}{\Delta Z} \right)$$

Finally, the values of q are then used to estimate arsenic transport in the soil profile. The finite difference solution of equation (1) described in detail can be found in LEACHM (Hutson & Wagenet [7]).

Arsenic transport model

The bulk motion of the fluid, and controls contaminant transport through the soil column by molecular diffusion and mechanical dispersion. Mixing due to molecular diffusion is negligible compared to that caused by dispersion. At the same time generation of loss of mass takes place due to adsorption and desorption, and the biokinetics of the mass dissolved or suspended in the moving water. In this study arsenic was modeled. Figure 1 shows some of the arsenic transport and transformation processes and the factors affecting each of the processes.

In general for steady-state water flow condition the transport terms for arsenic are:

$$J_s = J_{DL} + J_{CL} \quad (5)$$

Where J_s is total arsenic flux ($\infty \text{ g m}^{-2} \text{ day}^{-1}$), J_{DL} is the diffusion flux in the liquid phase and J_{CL} is the convection flux in the liquid phase. In the case of diffusion in the liquid phase in a porous media, the equation represented by Fick's law as:

$$J_{DL} = D_M + (\theta) \frac{dC_L}{dz} \quad (6)$$

Where C_L is concentration in the liquid phase and $D_M(\theta)$ is the molecular diffusion coefficient.

equations for hydraulic conductivity can be derived as a function of soil water pressure head. When soil water pressure head is greater than h_i the following equation is used to calculate hydraulic conductivity:

$$K(\theta) = K_s (\theta / \theta_s)^{2b+2+P} \quad (3)$$

Where K_s is hydraulic conductivity at saturation water content (θ_s), and P is Pore water interaction parameter. When soil pressure head is less than h_i the

The value of $D_M(\theta)$ can be estimated (Kemper and Van Schaik, 1966) as:

$$D_M(\theta) = D_{OL} a \exp(b\theta) \quad (7)$$

Where D_{OL} is the diffusion coefficient in a pure liquid phase and a and b are empirical constants reported by Olsen and Kemper (1981) to be approximately $b = 10$ and $0.005 < a < 0.01$ the convective flux of arsenic can be represented as:

$$J_{cl} = -\theta D_h(q) \frac{dC_1}{dz} + qC_1 \quad (8)$$

Where q is the water flux, and $D_h(q)$ is the hydrodynamic dispersion coefficient that describes mixing between large and small pore as the result of local variations in mean water flow velocity. Combining the molecular diffusion coefficient and hydrodynamic dispersion coefficient as:

$$J_{cl} = -\theta D_h(q) \frac{dC_1}{dz} + qC_1 \quad (9)$$

Where $D(\theta, q)$ is the apparent diffusion coefficient ($\text{cm}^2 \text{ day}^{-1}$). Substituting equations 6, 8 and 9 into equation 5 the overall arsenic flux is given as:

$$J_s = -\theta D(\theta, q) \frac{\partial C_L}{\partial Z} + qC_1 \quad (10)$$

Partitioning arsenic between sorbed and solution phases, according to Alemi [2], adsorption of arsenic are assumed taken to be nonlinear equilibrium process described by:

$$C_s = C_s K^n \quad (11)$$

Where C_s is the concentration of arsenic absorbed on the soil ($\alpha \text{ mole K}^{-1}$), K_s is the adsorption coefficient for arsenic (L Kg^{-1}), C is the concentration of arsenic in the soil solution ($\alpha \text{ mole L}^{-1}$), n is the exponent in the nonlinear equation for equilibrium adsorption reaction for arsenic.

The total amount of arsenic (C_T) contained in the solution and adsorbed phases in a soil volume of one liter are:

$$C_T = \rho C_s + \theta C_L \quad (12)$$

Where ρ is the soil bulk density (g cm^{-3}). Substituting equation (11) for C_s in equation (12) one can get the convection-dispersion equation:

$$C_T = C_L + (\theta + \rho K_s) C_L \quad (13)$$

Arsenic transports in soil system occur under unsteady (transient) water flow condition. The water content (θ) and water flux (q) both vary with depth and time. Using continuity relationships of mass over space and time gives:

$$\frac{\partial C_T}{\partial t} = -\frac{\partial J_s}{\partial z} \pm \Phi \quad (14)$$

Where C_T the total arsenic concentration in sorbed and solution is phases and ϕ represents all sources or sinks of arsenic. Substituting equation (8) and (13) into (14) gives general one-dimensional transport equations for arsenic transport:

$$\frac{\partial C}{\partial t}(\theta + \rho K_s) = \frac{\partial}{\partial z} \left[\theta D(\theta, q) \frac{\partial C}{\partial z} - qC \right] \pm \Phi \quad (15)$$

Where C is concentration of all arsenic species in soil solution, and ϕ indicates all possible sources or sinks term.

Solution procedure

Prediction of the concentration of As in all phases (liquid, adsorbed, gas) as well as leaching losses at any depth for all time levels requires simultaneous solution of equations for all arsenic species.

The equations are solved numerically using an implicitly finite difference scheme and Crank-Nicholson approximation.

Using Figure 2 for the nodes and segments as well as time interval; the first term in equation (15) is evaluated at node i and time $t^{j+1/2}$ and is differenced as: $C = C_1$

$$R_1 \frac{\partial C}{\partial t} = (C_i^{j+1} - C_i^j) / \Delta t \quad (16)$$

$$R_1 = 1 + \frac{\rho}{\theta} \cdot N \cdot K S_1 \cdot C_1^{N-1}$$

The second term in equation (15) is a diffusion and dispersion term. $D(q)$ for the interval between nodes $i-1$ and i is differenced as:

$$D_{i-1/2}^{j+1/2} = \lambda q_{i-1/2}^{j+1/2} / \theta_{i-1/2}^{j+1/2} + D_{OL} a \left[\exp(-b \theta_{i-1/2}^{j+1/2}) \right] / \theta_{i-1/2}^{j+1/2} \quad (17)$$

Where

$$\theta_{i-1/2}^{j+1/2} = (\theta_{i-1}^{j+1} + \theta_{i-1}^j - \theta_i^{j+1} - \theta_i^j) / 2 \quad (18)$$

$$\frac{\partial}{\partial z} (D(\theta, q) \frac{\partial C}{\partial z}) =$$

$$\begin{aligned} & [D_{i-1/2}^{j+1/2} (C_{i-1/2}^{j+1/2} + C_{i-1}^j - C_i^{j+1} - C_i^j) / \Delta z_1 \\ & - D_{i+1/2}^{j+1/2} (C_i^{j+1} + C_i^j - C_{i+1}^{j+1} - C_{i+1}^j) / \Delta z_2] \Delta z_3 \end{aligned} \quad (19)$$

The convection term in equation (15) is differenced as:

$$\begin{aligned} v \frac{\partial C}{\partial z} &= v_i - 1/2 (C_{i-1}^j + C_{i-1}^{j+1}) / \Delta z_3 \\ &- v_i + 1/2 (C_i^j + C_i^{j+1}) / \Delta z_3 - v_i + 1/2 \\ & (C_{i+1}^j + C_{i+1}^{j+1}) / \Delta z_3 \pm \Phi \end{aligned} \quad (20)$$

Multiplying out and collecting the unknown C_i^{j+1} terms on the left-hand side and the know C^j terms on the right-hand side, the general form of equation as:

$$A_i C_{i-1}^{j+1} + B_i C_i^{j+1} + C_i C_{i+1}^{j+1} = D_i$$

Where D_i considers all the sources and sinks in equation (16). For example the sources and sinks term for equation (16) are:

$$\begin{aligned} \Phi &= \frac{\alpha_1 C_1 U(z, t)}{\theta} - [K_1 + K v_1 + K_3] C_1 \\ &+ \frac{\rho}{\theta} K_3 S_0 \end{aligned} \quad (21)$$

The finite difference forms are written similarly for all other equations for each node from 2 to $K-1$ where K is the lowest node in the profile. This set of equations, then is solved for defined boundary conditions using the Thomas tridiagonal matrix algorithm.

Upper and lower boundary conditions

The upper boundary condition for arsenic needs to be defined to represent zero flux, infiltration the value of $C_1^j = C_w$ and $D_{1+1/2}^{j+1/2} = 0$ Where C_w is concentration of arsenic in applied water and arsenic enter the profile is equal to $q_{1+1/2}^{j+1/2} (\Delta t) (C_w)$. during surface evaporation $C_1^j = 0$, $q_{1+1/2}^{j+1/2} = 0$ and $D_{1+1/2}^{j+1/2} = 0$.

The lower boundary condition for arsenic needs to be defined for zero flux, water table and unit hydraulic gradient. For zero flux $q_{K-1}^{j+1/2} = 0$, $D_{K-1/2}^{j+1} = 0$ and $CK = 0$. If water table is present, the value of $C_k = C_{gw}$ and $D_{K-1/2}^{j+1} = 0$. Finally, for unit hydraulic gradient $C_k = \text{constant}$ and $D_{K-1/2}^{j+1} = 0$ where C_{gw} is concentration of arsenic in groundwater.

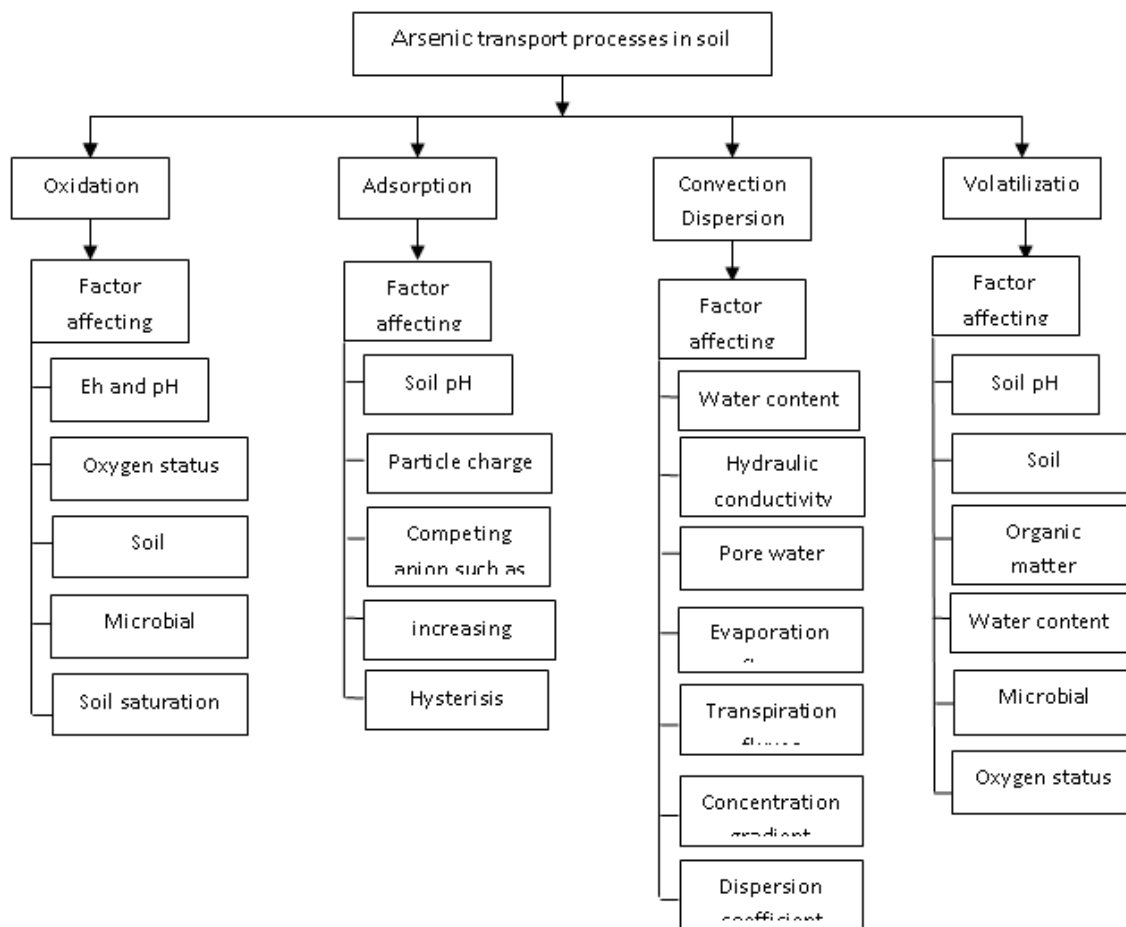


Fig.1. The transport processes and the related factors.

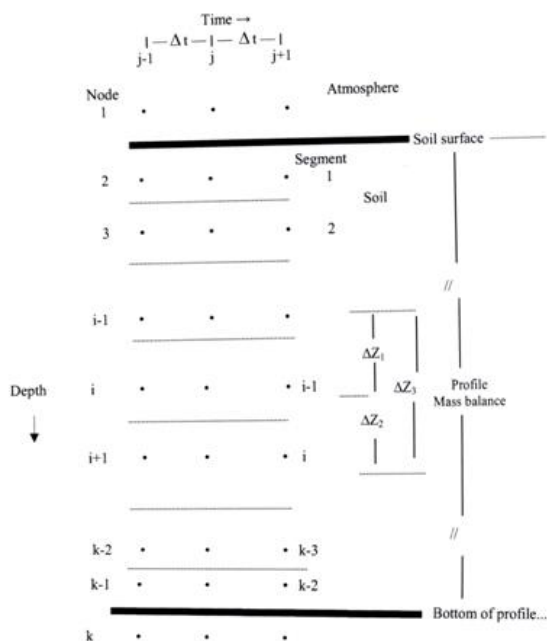


Fig. 2 Definition of nodes and segments.

RESULTS

The model was applied to simulate arsenic in soil column under steady state and transient water

flow conditions. The soil column was assumed to be unsaturated under both conditions. The model was applied to simulate the transport and transformation of As in soil column under steady – state and transient water flow conditions , The soil column was assumed to be unsaturated under both conditions for the validation of model under transient state , the data sets collected [8, 10] from Gorgan site, Golestan province, Iran 2014 , was used. In this experiment, vertical soil columns were in uniformly layered in 30 cm thick with 150 cm long.

In this Table 1 shows the soil texture details and properties. Study under transient water flow conditions, 240 liters of influent solution containing 0.2 and 0.4 mg.L⁻¹ of As in the form As₂O₃.

In this study under steady – state water flow conditions , 240 liters of influent solution containing 0.2 mg.L⁻¹ of As in the form of As₂O₃ were applied to the soil Also in the same time 240 liters of influent solution containing 0.4 mg.L⁻¹ of As were applied to the another pilot in this site . The experiment was run for 10 days.

Table 1. The soil texture details

Sand%	Silt%	Clay%	Organic Carbon %	Total saturated acidity	Electric Conductivity EC*10 ³
39	41	20	1.5	6.9	8.1

At the end of each run the concentration of As was measured in soil and ground water table .The data from the results of As transport and transformation modeling in experiment was used to run model . The time and distance interval in vertical direction for running the model were 0.25 day and 30 cm respectively .The results indicate that transport and transformation model adequately simulates the measured quantities at time =1 (day) , t= 10(day) as shown in Figures 3 to 6.

The simulation results for total time from 0.25 day to 10 days indicate that as the time increases the influent concentration approaches the inflow, which is comparable with the measured values.

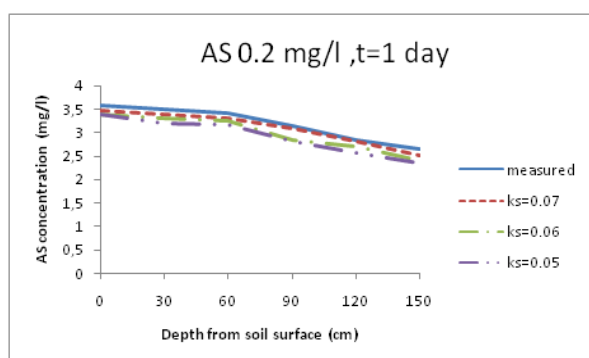


Fig. 3. Comparison of simulated and measured concentration of arsenic for different depths (t = 1 day, As = 0.2 mg.L⁻¹)

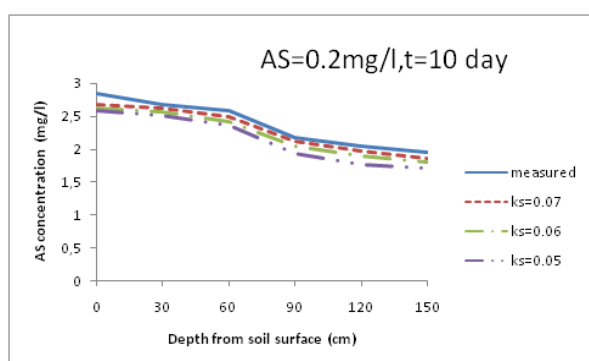


Fig. 4. Comparison of simulated and measured concentration of arsenic for different depths (t = 10days, As = 0.2 mg.L⁻¹).

The sensitivity analysis of the model to some parameter at steady state water flow condition shows that the model is very sensitive to the adsorption coefficient, K_s , such that when K_s is equal to 0.07 liter kg⁻¹ , the simulation results get closer to measured values. The computed results for

measures As concentration in $K_s = 0.07$ have mean relative error =4.43 These results imply that the model can produce a less than 5% error in predicting measured arsenic concentration in the soil zone and groundwater .LEACHM model was used for the simulation of water content and water flux .

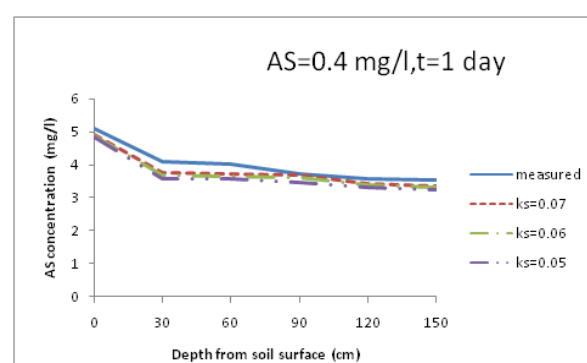


Fig. 5. Comparison of simulated and measured concentration of arsenic for different depths (t = 1 day, As = 0.4 mg.L⁻¹).

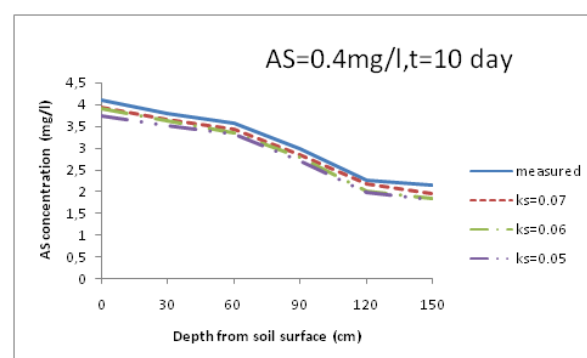


Fig. 6. Comparison of simulated and measured concentration of arsenic for different depths (t = 10days, As = 0.4mg.L⁻¹)

DISCUSSION AND CONCLUSION

One-dimensional water flow and contaminant transport model was applied to simulate arsenic in soil column. The model predicts the concentration of different contaminant in ground water. The simulation results indicate as the total time from the beginning to the end of simulation increases, the concentration of arsenic approaches the measured values, as indicated in the results section the model is sensitive to adsorption coefficient, K_s . The results also shows the variation of water flux with times steps in soil column, as the time increases from 1

days to about 10 days the water flow approaches the steady state.

LEACHM, which is the Leaching Estimation and Chemical Model, was used for the simulation of water flux and hydraulic conductivity of soil used in the study area. The model was very useful tool for the estimation of water content. The model can be used for the prediction of water pollution in groundwater systems.

NOTATION

θ = Volumetric water content
t = time
h = soil water pressure head
H = hydraulic head
K = hydraulic conductivity
 θ_s = Water content at saturation
a = constant
b = constant
 K_s = hydraulic conductivity at saturation
P = pore water interaction parameter
q = water flux
z = soil depth
J_t = total arsenic flux
J_{OL} = diffusion flux in liquid phase
J_{CL} = convection flux in liquid phase
C_l = concentration in liquid phase
C_s = concentration of adsorbed arsenic
 ρ = Soil bulk density

REFERENCES

1. M. H. Alemi, D. A. Goldhamer, D. R. Nielson, *J. Environ. Qual.*, **17**, 608 (1988).
2. M. H. Alemi, D. A. Goldhamer, D. R. Nielson, *J. Environ. Qual.*, **20**, 89 (1991).
3. J. S. Ahlrichs, L. R. Hossner, *J. Environ. Qual.*, **16**, 95 (1987).
4. D. Copoulos, E. Sehayek, *J. of Environ Eng.*, **112**, 5 (1986).
5. G.S. Hooshmand, Selenium transport and transformation modeling in soil column under transient unsaturated flow field, M.S. Thesis, 1992
6. J. L. Hutson, J. Cassvan, *Soil Sci., Soc., Amer. Proc.*, **30**, 534 (1987).
7. J. L. Hutson, R. J. Wagenet, Leaching estimation and chemistry model. A process based model of water and solute movement transformations, plant uptake and chemical reactions in the unsaturated zone, Department of Agronomy, Version 20, Cornell University, New York, 1989, p. 148.
8. S. A. Mirbagheri, K. K. Tanji, *J. Environ. Eng.* Submitted, 1995
9. F. Shifang, Selenite adsorption /desorption in the California soils, Ph. D. Dissertation, Soil Science, 1991, p. 259.
10. E. T. Thompson – Eagle, W. T. Frankenberger, *J. Environ. Qual.*, **19**, 125 (1990).

Modeling Pb transport in soil column and ground water

S. A. Mirbagheri *, N. Javadifar, A. H. Hasani

Department of Environmental Engineering, Faculty of Environment and Energy, Tehran Science and Research Branch, Islamic Azad University, Tehran, Iran

Received June 18, 2016; Revised September 10, 2016

A mathematical and computer model for the transport and transformation of Pb through a soil column from the surface to the groundwater is presented. The model simulates Pb species. This model is based on the mass balance equation including convective transport, dispersive transport, surface adsorption, oxidation and reduction, volatilization, chemical and biological transformation. The governing equations are solved numerically by the method of implicit finite difference. The simulation results are in good agreement with measured values. The major finding in the present study indicates that as the time of simulation increases, the concentration of different Pb species approaches the measured values.

Key words: Pb transport, mathematical, computer, model, Pb species

INTRODUCTION

Mathematical modeling is an accepted scientific practice, providing the mechanism for comprehensively integrating basic processes and describing a system beyond what can be accomplished using subjective human judgements. It is possible to construct models that better represent the natural system and to use these models in an objective manner to guide both our future research efforts and current management practices.

Recent years have seen a variety of approaches to description of water and solute movement in soils field. A number of new models have been proposed in response to recently collected field data on solute leaching patterns. The contaminants are released from the refuse to the passing water by physical, chemical, and microbial processes and percolate through the unsaturated environment, polluting the groundwater with organic and inorganic matter.

The modeling of contaminant transport hinges on an understanding of the mechanisms of mass release from the solid to the liquid phase, and contaminant decay. These mechanisms are influenced by such factors as climatic conditions, type of waste, site geohydrologic conditions, and chemical reactions as well as microbial decomposition of organic matter.

Modeling of different kinds of contaminant was studied by several researchers [1-2-3-4-5]

The objective of this paper is to addresses the spatial and temporal distribution of contaminant

concentrations in soil column. The work has been done in Gorgan site, Golestan province, Iran in 2014.

Mathematical Model

The flow and the corresponding moisture content and the concentration of a contaminant are considered here in as continuous functions of both space and time. This model considers a variety of processes that occur in the plant root zone as well as leaching to the ground water, including transient fluxes of water and contaminants, alternating periods of rainfall, irrigation and evapotranspiration, under variable soil conditions with depth.

Water flow model

Water flow is calculated using a finite difference solution to the soil-water flow equation

$$\frac{\partial h}{\partial t} c(\theta) = \frac{\partial}{\partial z} \left[K(\theta) \cdot \frac{\partial H}{\partial z} \right] \quad (1)$$

Where h is a soil water pressure head (mm), θ is volumetric water content (m^3m^{-3}), t is time (day), H is hydraulic head ($h + z$), z is soil depth, K is hydraulic conductivity (mm day^{-1}), $c(\theta) = \partial\theta/\partial h$ is differential water capacity. Functions which characterized relationships between $K - \theta - h$ described in LEACHM [6-7] are used. There is a two-part function that described the general shape of $\theta(h)$ relationships [7-8].

* To whom all correspondence should be sent:
E-mail: cwl@ncepu.edu. cn

$$h = \frac{[1 - (\theta / \theta_s)]^{1/2} (\theta_i / \theta_s)^{-b}}{[1 - (\theta_i / \theta_s)]^{1/2}} \quad \text{for } 0 > h > h_i \quad (2a)$$

$$h = a(\theta / \theta_s)^{-b} \quad \text{for } h_i > h > -\infty \quad (2b)$$

Where $h_i = a[2b / (1+2b)]^{-b}$ and $\theta_i = 2b\theta_s / (1+2b)$ is the point h_i, q_i of intersection of the two curves, θ_s is water content at saturation, a and b are constant. The two curves are exponential and parabolic for dry and saturated soil respectively. Similarly the equations for hydraulic conductivity can be derived as a function of soil water pressure head. When soil water pressure head is greater than h_i the following equation is used to calculate hydraulic conductivity:

$$K(\theta) = K_s (\theta / \theta_s)^{2b+2+p} \quad (3)$$

Where K_s is hydraulic conductivity at saturation water content (θ_s), and P is Pore water interaction parameter. When soil pressure head is less than h_i the equation for the calculation of hydraulic conductivity is:

$$K = K_s (a / h)^2 + (2+P) / b, \quad (4)$$

Solving equation (1) using finite difference techniques provides estimated values of h at each depth node used in the differencing equation. Water contents are calculated using equation (2). Water flux densities (q) are calculated over each depth

$$\left(q = K(\theta) \frac{\Delta H}{\Delta Z} \right)$$

interval using Darcy's equation. Finally, the values of q are then used to estimate Pb transport in the soil profile. The finite difference solution of equation (1) described in detail can be found in LEACHM [9].

Pb transport model

The bulk motion of the fluid, and controls contaminant transport through the soil column by molecular diffusion and mechanical dispersion. Mixing due to molecular diffusion is negligible compared to that caused by dispersion. At the same time generation of loss of mass takes place due to adsorption and desorption, and the biokinetics of the mass dissolved or suspended in the moving water. In this study Pb was modeled. Figure 1 shows some of the Pb transport and transformation processes and the factors affecting each of the processes.

In general for steady-state water flow condition the transport terms for Pb are:

$$J_s = J_{DL} + J_{CL} \quad (5)$$

Where J_s is total Pb flux ($\infty g m^{-2} day^{-1}$), J_{DL} is the diffusion flux in the liquid phase and J_{CL} is the convection flux in the liquid phase. In the case of diffusion in the liquid phase in a porous media, the equation represented by Fick's law as:

$$J_{DL} = D_M + (\theta) \frac{dC_L}{dz} \quad (6)$$

Where C_L is concentration in the liquid phase and $D_M(\theta)$ is the molecular diffusion coefficient. The value of $D_M(\theta)$ can be estimated (Kemper and Van Schaik, 1966) as:

$$D_M(\theta) = D_{OL} a \exp(b\theta) \quad (7)$$

Where D_{OL} is the diffusion coefficient in a pure liquid phase and a and b are empirical constants reported by Olsen and Kemper (1981) to be approximately $b = 10$ and $0.005 < a < 0.01$ the convective flux of Pb can be represented as:

$$J_{CL} = -\theta D_h(q) \frac{dC_1}{dz} + q C_1 \quad (8)$$

Where q is the water flux, and $D_h(q)$ is the hydrodynamic dispersion coefficient that describes mixing between large and small pore as the result of local variations in mean water flow velocity. Combining the molecular diffusion coefficient and hydrodynamic dispersion coefficient as:

$$D(\theta, q) = D_M(\theta) + q D_h(q), \quad (9)$$

Where $D(\theta, q)$ is the apparent diffusion coefficient ($cm^2 day^{-1}$). Substituting equations 6, 8 and 9 into equation 5 the overall Pb flux is given as:

$$J_s = -\theta D(\theta, q) \frac{\partial C_L}{\partial Z} + q C_1 \quad (10)$$

Partitioning Pb between sorbed and solution phases, according to Alemi [2], adsorption of Pb are assumed taken to be nonlinear equilibrium process described by:

$$C_s = C_s K^n \quad (11)$$

Where C_s is the concentration of Pb adsorbed on the soil (α mole K^{-1}), K_s is the adsorption coefficient for Pb ($L Kg^{-1}$), C is the concentration of Pb in the soil solution (α mole L^{-1}), n is the nonlinear equilibrium adsorption reaction exponent for Pb.

The total amount of Pb (C_T) contained in the solution and adsorbed phases in a soil volume of one liter are:

$$C_T = \rho C_s + \theta C_1 \quad (12)$$

Where ρ is the soil bulk density ($g cm^{-3}$). Substituting equation (11) for C_s in equation (12) one can get the convection-dispersion equation:

$$C_T = C_T + (\theta + \rho K_s), \quad (13)$$

Pb transports in soil system occur under non-steady (transient) water flow condition. The water content (θ) and water flux (q) both vary with depth

and time. Using continuity relationships of mass over space and time gives:

$$\frac{\partial C_T}{\partial t} = -\frac{\partial J_s}{\partial z} \pm \Phi \quad (14)$$

Where C_T the total Pb concentration in sorbed and solution is phases and ϕ represents all sources or sinks of Pb. Substituting equation (8) and (13) into (14) gives general one-dimensional transport equations for Pb transport:

$$\frac{\partial C}{\partial t}(\theta + \rho K_s) = \frac{\partial}{\partial z} \left[\theta D(\theta, q) \frac{\partial C}{\partial z} - qC \right] \pm \Phi \quad (15)$$

Where C is concentration of all Pb species in soil solution, and ϕ indicates all possible sources or sinks term.

Solution procedure

Prediction of the concentration of Pb in all phases (liquid, sorbed, gas) as well as leaching losses at any depth for all time levels requires simultaneous solution of equations for all Pb species.

The equations are solved numerically using an implicitly finite difference scheme and Crank-Nicholson approximation.

Using Figure 2 for the nodes and segments as well as time interval; the first term in equation (15)

is evaluated at node i and time $t^{j+1/2}$ and is differenced as: $C = C_1$

$$R_1 \frac{\partial C}{\partial t} = (C_i^{j+1} - C_i^j) / \Delta t \quad (16)$$

$$R_1 = 1 + \frac{\rho}{\theta} \cdot N \cdot K S_1 \cdot C_1^{N-1}$$

The second term in equation (15) is a diffusion and dispersion term. D (q) for the interval between nodes i-1 and i is differenced as:

$$D_{i-1/2}^{j+1/2} = \lambda q_{i-1/2}^{j+1/2} / \theta_{i-1/2}^{j+1/2} + D_{OL} a [\exp(-b \theta_{i-1/2}^{j+1/2})] / \theta_{i-1/2}^{j+1/2} \quad (17)$$

Where

$$\theta_{i-1/2}^{j+1/2} = (\theta_{i-1}^{j+1} + \theta_{i-1}^j - \theta_i^{j+1} - \theta_i^j) / 2 \quad (18)$$

$$\frac{\partial}{\partial z} (D(\theta, q) \frac{\partial C}{\partial z}) =$$

$$[D_{i-1/2}^{j+1/2} (C_{i-1/2}^{j+1/2} + C_{i-1}^j - C_i^{j+1} - C_i^j) / \Delta z_1 - D_{i+1/2}^{j+1/2} (C_i^{j+1} + C_i^j - C_{i+1}^{j+1} - C_{i+1}^j) / \Delta z_2] \Delta z_3 \quad (19)$$

, (19)

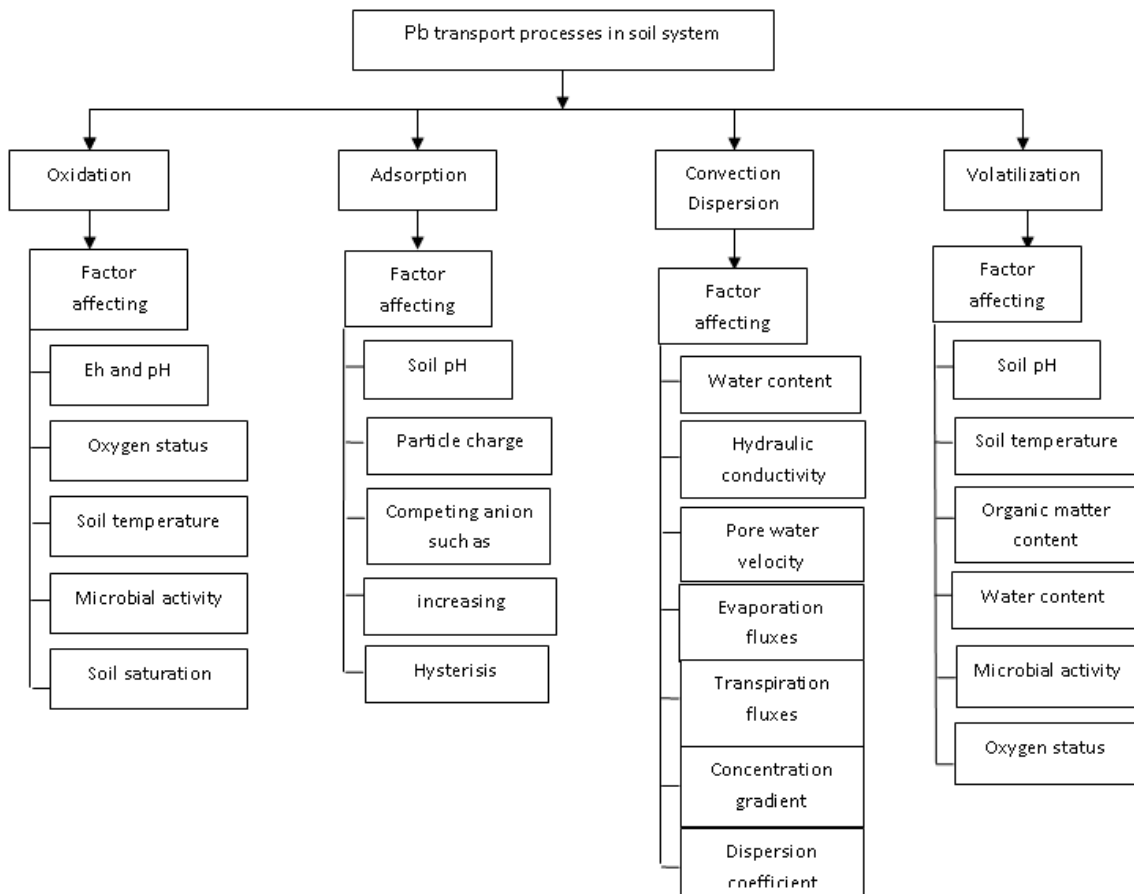


Fig.1. The transport processes and the related factors.

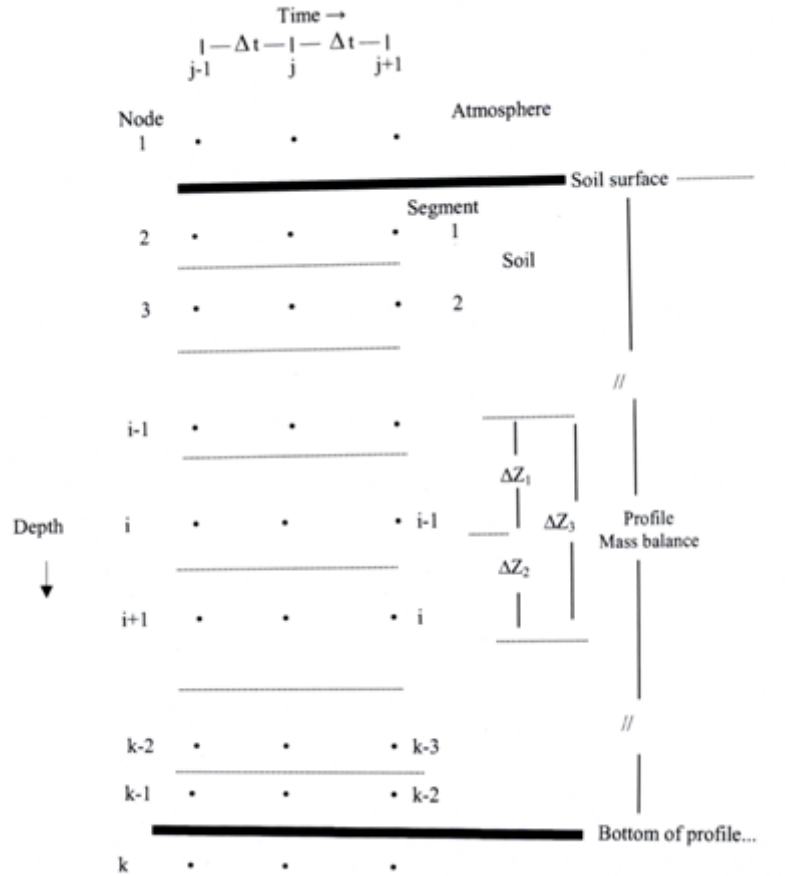


Fig. 2. Definition of nodes and segments.

The convection term in equation (15) is differenced as:

$$v \frac{\partial C}{\partial z} = v_i - 1/2 (C_{i-1}^J + C_{i-1}^{J+1}) / \Delta z_3 - v_i + 1/2 (C_i^J + C_i^{J+1}) / \Delta z_3 - v_i + 1/2 (C_{i+1}^J + C_{i+1}^{J+1}) / \Delta z_3 \pm \Phi \quad (20)$$

Multiplying out and collecting the unknown C_i^{J+1} terms on the left-hand side and the known C^J terms on the right-hand side, the general form of equation as:

$$A_i C_{i-1}^{J+1} + B_i C_i^{J+1} + C_i C_{i+1}^{J+1} = D_i$$

Where D_i considers all the sources and sinks in equation (16). For example the sources and sinks term for equation (16) are:

$$\Phi = \frac{\alpha_1 C_1 U(z,t)}{\theta} - [K_1 + K_1 v_1 + K_3] C_1 + \frac{\rho}{\theta} K_5 S_0 \quad (21)$$

The finite difference forms are written similarly for all other equations for each node from 2 to K-1 where K is the lowest node in the profile. This set of equations, then is solved for defined boundary

conditions using the Thomas tridiagonal matrix algorithm.

Upper and lower boundary conditions

The upper boundary condition for Pb needs to be defined to represent zero flux, infiltration the value of $C_1^J = C_w$ and $D_{1+1/2}^{J+1/2} = 0$ Where C_w is concentration of Pb in applied water and Pb enter the profile is equal to $q_{1+1/2}^{J+1/2} (\Delta t)(C_w)$. during surface evaporation $C_1^J = 0$, $q_{1+1/2}^{J+1/2} = 0$ and $D_{1+1/2}^{J+1/2} = 0$.

The lower boundary condition for Pb needs to be defined for zero flux, water table and unit hydraulic gradient. For zero flux $q_{K-1}^{J+1/2} = 0$, $D_{K-1/2}^{J+1} = 0$ and $CK = 0$. If water table is present, the value of $C_k = C_{gw}$ and $D_{K-1/2}^{J+1} = 0$. Finally, for unit hydraulic gradient $C_K = \text{constant}$ and $D_{K-1/2}^{J+1} = 0$ where C_{gw} is concentration of Pb in groundwater.

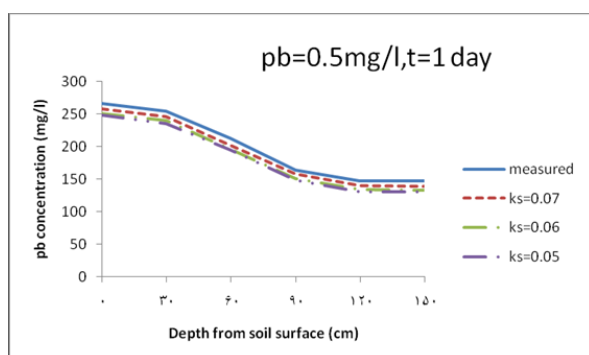


Fig. 3. Comparison of simulated and measured concentration of Pb for different depths ($t=1$ day, $Pb = 0.5 \text{ mg.L}^{-1}$)

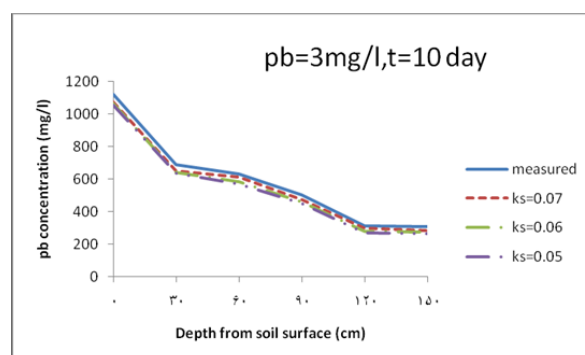


Fig. 6. Comparison of simulated and measured concentration of Pb for different depths ($t=10$ day, $Pb = 3 \text{ mg.L}^{-1}$)

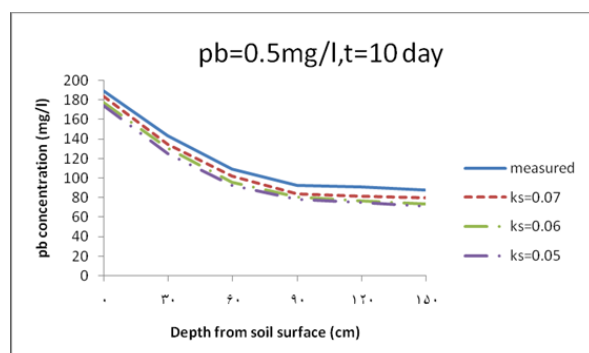


Fig. 4. Comparison of simulated and measured concentration of Pb for different depths ($t=10$ day, $Pb = 0.5 \text{ mg.L}^{-1}$)

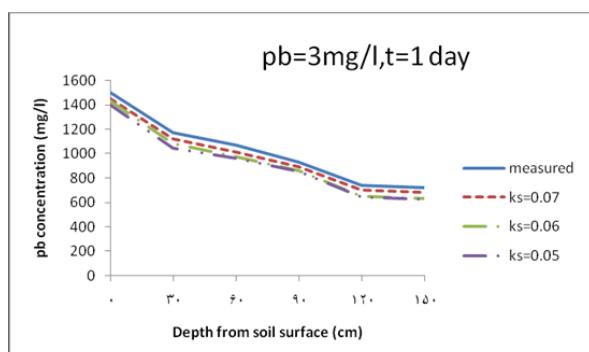


Fig. 5. Comparison of simulated and measured concentration of Pb for different depths ($t=1$ day, $Pb = 3 \text{ mg.L}^{-1}$)

RESULTS

The model was applied to simulate Pb in soil column under steady state and transient water flow conditions. The soil column was assumed to be unsaturated under both conditions. The model was applied to simulate the transport and transformation of Pb in soil column under steady – state and transient water flow conditions , The soil column was assumed to be unsaturated under both conditions for the validation of model under transient state , the data sets collected by Javadifar, et al from Gorgan site, Golestan province, Iran 2014, was used. In this experiment, Vertical soil columns were in uniformly layered in 30 cm thick with 150 cm long.

In this Table 1 shows the soil texture details and properties. Study under transient water flow conditions, 240 liters of influent solution containing 0.5 and 3 mg.L^{-1} of Pb in the form $\text{Pb}(\text{NO}_3)_2$.

In this study under steady – state water flow conditions, 240 liters of influent solution containing 0.5 mg.L^{-1} of Pb in the form of $\text{Pb}(\text{NO}_3)_2$ were applied to the soil Also in the same time 240 liters of influent solution containing 3 mg.L^{-1} of Pb were applied to the another pilot in this site . The experiment was run for 10 days. At the end of each run the concentration of Pb was measured in soil and ground water table. The data from the results of Pb transport and transformation modeling in experiment was used to run model. The time and distance interval in vertical direction for running the model were 0.25 day and 30 cm respectively.

Table 1. The soil texture details

Sand%	Silt%	Clay%	Organic Carbon %	Total saturated acidity	Electric Conductivity $\text{EC} \cdot 10^3$
39	41	20	1.5	6.9	8.1

The results indicate that transport and transformation model adequately simulates the measured quantities at time = 1 day, t= 10 days as shown in Figures 4 to 7. The simulation results for total time from 0.25 day to 10 days indicate that as the time increases the influent concentration approaches the inflow, which is comparable with measured values.

The sensitivity analysis of the model to some parameter at steady state water flow condition shows that the model is very sensitive to the adsorption coefficient, K_s , such that when K_s is equal to 0.07 liter kg^{-1} , the simulation results get closer to measured values. The computed results for measures Pb concentration in $K_s = 0.07$ have mean relative error =4.36. These results imply that the model can produce a less than 5% error in predicting measured Pb concentration in the soil zone and groundwater. Mirbagheri model was used for the simulation of water content and water flux.

DISCUSSION AND CONCLUSION

One-dimensional water flow and contaminant transport model was applied to simulate Pb in soil column. The model predicts the concentration of different contaminant in ground water. The simulation results indicate as the total time from the beginning to the end of simulation increases, the concentration of Pb approaches the measured values, as indicated in the results section the model is sensitive to adsorption coefficient, K_s . The results also shows the variation of water flux with times steps in soil column, as the time increases from 1 days to about 10 days the water flow approaches the steady state.

LEACHM, which is the Leaching Estimation and Chemical Model, was used for the simulation of water flux and hydraulic conductivity of soil used in the study area. The model was very useful tool for the estimation of water content. The model can be used for the prediction of water pollution in groundwater systems.

NOTATION

θ = Volumetric water content
t = time
h = soil water pressure head
H = hydraulic head
K = hydraulic conductivity
 θ_s = Water content at saturation
a = constant
b = constant
 K_s = hydraulic conductivity at saturation
P = pore water interaction parameter
q = water flux
z = soil depth
J_t = total lead flux
J_{OL} = diffusion flux in liquid phase
J_{CL} = convection flux in liquid phase
C_l = concentration in liquid phase
C_s = concentration of adsorbed lead
 ρ = Soil bulk density

REFERENCES

1. M.H. Alemi, D.A. Goldhamer, D.R. Nielson, *J. Environ. Qual.*, **17**, 608 (1988).
2. M.H. Alemi, D.A. Goldhamer, D.R. Nielson, *J. Environ. Qual.*, **20**, 89 (1991).
3. J. S. Ahlrichs, L.R. Hossner, *J. Environ. Qual.*, **16**, 95 (1987).
4. D. Copoulos, E. Sehayek, *J. Environ Eng.*, **112**, 5 (1986).
5. G.S. Hooshmand, Selenium transport and transformation modeling in soil column undertransient unsaturated flow field. M.S. Thesis, 1992.
6. J. L. Hutson, J. Cassvan, *Soil Sci., Soc., Amer. Proc.*, **30**, 534 (1987).
7. J. L. Hutson, R.J. Wagenet, Leaching estimation and chemistry model. A process based model of water and solute movement transformations, plant uptake and chemical reactions in the unsaturated zone, Version 20 Department of Agronomy, Cornell University, New York, , 1989, p. 148.
8. S. A. Mirbagheri, K. K. Tanji, Selenium transport and transformation in soil column. *J. Environ.*, **12**, 3 1995.
9. F. Shifang, *J. Environ. Qual.*, **19**, 125 (1990).
10. S.R. Olsen, W.D. Kemper, *Adv. Agronomy*, **20**, 91, (1968).

Investigation and optimization of reactive orange-3R dye surface absorption by nano-MMT/NZVI composite absorbent in a process of textile industry wastewater treatment

E. Gharekhani

Department of Chemistry, Faculty of Engineering, Islamic Azad University, Saveh Branch, Saveh, Iran

Received June 18, 2016, Revised September 10, 2016

Removal of the dye pollutants of factories effluents always have been a challenge. In this study zero-valent iron montmorillonite nanocomposite as an absorbent for removing azo-dye from industrial wastewater and in different test situations in a batch process was used. Synthesized Fe_3O_4 nanoparticles and nanocomposite absorbent were verified by conventional XRD and SEM methods. Then by provision of water-based solution from well-known reactive orange-3R, surface absorption ability of the absorbent was investigated. In this method, NZVI was applied as reducer for dye removing, and the factors such as absorbent quantity, contact time, solution initial pH, dye concentration and temperature influence were studied. For exploring of removed dye quantity, UV spectroscopy and Beer-Lambert law were used. According to the achieved results of MMT/NZVI absorbent efficiency, by increasing the absorbent content, the removed dye quantity was increased, but by application of 0.5 g absorbent in pH=6 for removing 50 ppm dye concentration in 10 ml solution, orange-3R was removed effectively. In investigation of temperature parameter, the test results in different temperatures showed that dye removing of solution increases in higher temperatures up to 40 °C. At last, Langmuir and Freundlich isotherm absorption models for orange-3R dye removing by application of MMT/NZVI nanocomposite were predicted and also isotherm model parameters and correlation coefficient of ion removal were achieved. According to achieved results Langmuir isotherm model in comparison of Freundlich isotherm model showed more correlation with practical values. The most dye absorption capacity of solution in pH=6 at 40 °C, for Langmuir model was determined. Dye absorption process on absorbent was exothermic and the kinetic data was in accordance to pseudo-second order model. Also dye desorption from absorbent was done using 0.1 M NaCl solution.

Keywords: Absorption isotherm and kinetics; treatment; azo dye; nanocomposite; zero valent iron; montmorillonite

INTRODUCTION

One of the most important environmental pollutants is wastewater containing textile industry chemical materials that makes pollution for humans and environment. Textile dyes through diffusion to surface and ground water lead to dye pollution of water resources [1]. Furthermore, not degradation of these dyes and absorption of them into the plants can lead to genetic mutations in next generations. Therefore, it seems really necessary to treatment of colored wastewater and removal of these pollutants before discharging them into environment. Discharged wastewater of dyeing factories contains colored wastewater including different kinds of dyes such as complex and fully aromatic structures [2]. Azo dyes are from the most applicable industrial dyes and always we had needed to use this kind of dyes regarding to the varieties of their chemical structures. Most of this kind of dyes is stable in expose of UV-visible and heat, so making them resistant to whitener, sun light and oxidation doesn't lead to elimination of them by conventional water waste treatment systems. Totally, the

treatment methodologies are divided to 3 methodologies of physical methodology [3 & 4] (surface absorption, ionic exchange), chemical methodology [5-7] (oxidation, coagulation and sedimentation) and biologic methodology [8] (aerobic and unicellular). Nowadays, among existed methodologies, utilization of absorbents for removing pollutants in surface absorption method has attracted almost of researchers attention [9 & 10]. In general, absorbents can be divided to 2 types of conventional absorbents (that the most famous of them is activated carbon) and low cost absorbents (unconventional) those rather entrap the pollutants based on reaction with absorbed particles. However the activated carbon is one of the most proper absorbent for removing several types of pigments, but its use is limited in some cases because of its high prices. Also after using, the activated carbon (for cleaning waste water) will be saturated and cannot absorb more pigments. When activated carbon is saturated, its recycling needs different methods such as thermal, chemical, oxidation, electrochemical methods that all of them are expensive. In addition, in the recycling process some activated carbon is destroyed and also its absorption capacity will be less than initial state. Therefore, the use of low cost and effective

* To whom all correspondence should be sent:
E-mail: e.gharekhani@iau-saveh.ac.ir

alternative absorbents to the activated carbon seems to be essential [11]. The absorbers that are used for absorption of pollutants should be having sufficient porosity and surface area for trapping pollutants constituents. Moreover, the low prices, availability, mechanical and thermal stability, recycling and reusing capability are also characteristic of a suitable absorbent. Among these absorbers, using inorganic nanoparticles such as titanium dioxide (TiO₂) [12], zinc (ZnO) [13] and iron (Fe₃O₄) [14] oxides as an absorbent for polluted wastewater is a developing process and has been reported as very effective process. In recent Years, the use of nano ZVI particles to remove toxic chemicals from contaminated water has attracted widespread attention. The ZVI is a strong reducing agent and also cheap. The results have shown that this method is doing well to remove contaminations such as heavy metals cations [15], chlorinated organic substances [16], aromatic nitro compounds [17], insecticides [18] and the nitrates [19]. Recently has reported an optimal performance of ZVI complex with multi-walled carbon nanotubes in a quasi-Fenton catalytic process to eliminate herbicide atrazine too [20]. In many methods and recent researches, nano ZVI particles have been used simply [21-23], with surface modification [24 & 25] or as a composite with a suitable substrate [26-28]. However, using these nano particles has been reported very effective, rapid and cheap in all cases. Here is evaluated how to produce ZVI nanoparticles on montmorillonite substrate and its application for removing orange-3R dye from water. Montmorillonite is nanoclay based on layered silicates that because of its special properties has significant importance, but so far it hasn't been used in this way. This combination can produce a suitable composite with ZVI nanoparticles for removing reactive orange-3R dye.

EXPERIMENTAL

Materials

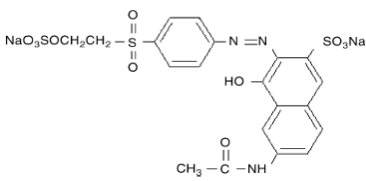
Used materials in this project included iron (III) chloride hexahydrate (FeCl₃.6H₂O), sodium borohydride (NaBH₄), sodium hydroxide (NaOH), and hydrogen chloride (HCl) and montmorillonite salts those were prepared from Merck (German) Co. In order to prepare the industrial reactive orange-3R dye, the product of Hamedan Alvan Sabet Co. was used. This dye is one of the reactive dyes and is one of the most widely used dyes in Iranian textile industry. Table (1) shows some characteristics of the investigated dye.

The Investigated parameters in this study included pH (in the range of 4-12), contact time (0.5, 1, 1.5, 2, 2.5, and 3 hours), initial dye concentration (50,100,150, and 200 ppm), the initial absorbent value (0.01, 0.1, 0.2, 0.3, 0.4 and 0.5 g), temperature range (10, 20, 30, and 40 °C) and in order to adjust the pH, NaOH (0.1 M) and HCl (0.1 M) solutions were used.

Apparatus

A double beam UV-visible Shimadzu spectrophotometer (spectrophotometer model 6320 D) equipped with a cm⁻¹ quartz cell was used for recording the visible spectra and absorbance measurements. Infrared measurements were performed on a Bruker-IFS48 FTIR spectrometer (Ettlingen, Germany). The spectra of solids were carried out using KBr pellet. Vibrational transition frequencies are reported in wave numbers (cm⁻¹). X-ray diffraction patterns (XRD) were performed at room temperature on an X-ray diffractometer (Siemens model D 5000, Germany) using Ni-filtered CuK α radiation (40 kV, 25 mA) with scanning rate of 3°/min. Field emission scanning electron microscope (FE-SEM), model Hitachi S-4160, 30 KV, on gold-coated powders. A Metrohm 692 pH meter was used for monitoring the pH values. A water ultrasonicator (Sonic VCX750, USA) was used to disperse the nanoparticles in solution and a super magnet Nd-Fe-B (1.4 T, 10×5×2 cm) was used.

Table1. Some characteristics of the investigated dye.

Characteristic	Molecular formula	Molecular Weight (g/mol)	Class	λ _{max} (nm)	Chemical structure
Reactive Orange-3R	C ₂₀ H ₁₇ N ₃ Na ₂ O ₁₁ S ₃	617.54	azo (-N=N-bond)	388, 494 (2nd)	

Preparation methods

Synthesis of iron nanoparticles

At first, a 250 ml balloon of NaBH₄ (0.8 M) was prepared. NaBH₄ due to its instability in the water reduction property loss was prepared just as much as needed amount in each stage. In other balloon, 250 ml FeCl₃ (0.2 M) was prepared and were placed on the electromagnetic shakers with magnet for 1 hour. The prepared NaBH₄ solution in the presence of nitrogen gas was added to FeCl₃ solution slowly, by burette. Experiment lasted 10 minutes in the shakers with 500 rpm. After a while the nanoparticles were gathered at its end. Brown iron (III) chloride hexahydrate (FeCl₃.6H₂O) solution was in a distillation balloon and nitrogen gas was passed over it. Sodium borohydride solution was added to the solution containing iron chloride (FeCl₃) by burette to form nanoparticles for appearing black sediment. In the next phase, the iron nanoparticles deposition was filtered by filter paper for two times and was washed with deionized water and acetone. At last, the dark obtained deposition was collected, dried in an oven and powdered, respectively.

Preparation of NZVI/MMT nanocomposite

For preparing the absorbent, 3 grams of montmorillonite was mixed in 30 ml of distilled water and 1 gram of prepared nanoparticles was added to the solution and was placed for 1 hour in oven at 300 °C to be dried and then was collected in form of solid powder. Dark brown powders were obtained.

Measuring the absorption of orange-3R by spectrometry method

The wavelength of maximum absorption was scanned using a uv spectrometer in the wavelength range of 100-700 nm and the maximum absorption was obtained at wavelength of 494 nm. The calibration curves for the solutions with different concentrations were drawn around maximum adsorption wavelength(λ max). According to the results, increasing dye concentration in solution leads to growing absorption intensity. Finally, knowing absorption quantity and regarding to linearity of the calibration curve and using Beer-Lambert equation, dye concentration was determined in each stage. To calculate the percentage of removal and absorption capacity, the equations 1 and 2 were used, respectively.

$$R (\%) = \frac{C_o - C_e}{C_o \times 100}, \quad (1)$$

$$q_e = \frac{(C_o - C_e) \times v}{w}, \quad (2)$$

That R is removal percentages, C_o and C_e are initial and equilibrium concentration after adsorption respectively, v is solution volume, and w is absorbent mass. The calibration curve of orange-3R at wavelength number of 494 nm in a straight line for 0,5, 10, 15, and 20 mg.l⁻¹ was drawn. It is illustrated in figure (1).

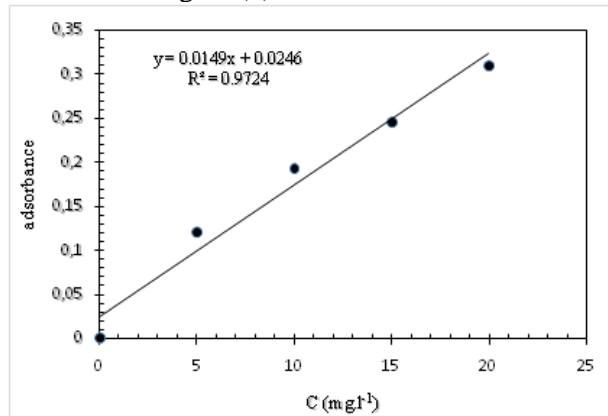


Fig.1. Calibration curve of orange-3R at wavelength number of 494 nm.

RESULTS AND DISCUSSION

Characterization

X-ray diffraction pattern (XRD)

The X-Ray diffraction method, because of being a direct method for determining phase types and material crystalline structures has significant importance. According to performed studies on the X-Ray diffraction of Fe₃O₄ nanoparticles in 2θ, 18, 21, 30, 35.5, 43.5, 54, 57.5, 64, the peaks with different intensities appear. In this experiment, the obtained results of XRD analysis was shown in Figure 2.

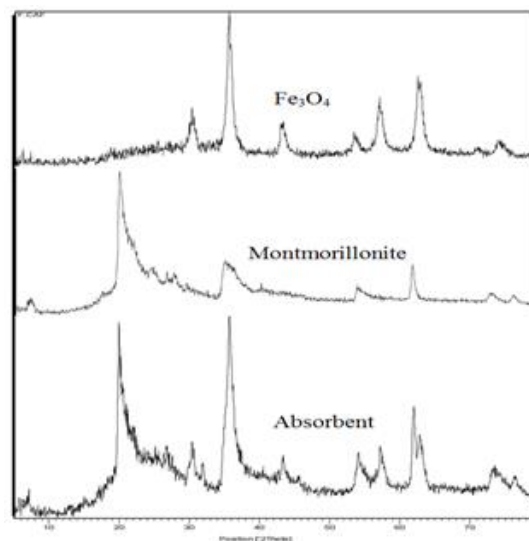


Fig. 2. XRD patterns of Fe₃O₄, nanoparticles, MMT and MMT/ZVI composite.

The maximum peak (35.5) is related to cubic crystals of iron oxide (Fe_3O_4) nanoparticles that actually this analysis confirms the presence of Fe_3O_4 particles. As shown in Figure 2, in X-Ray diffraction pattern of the prepared nanocomposite, the presence of both magnetic iron oxide and montmorillonite nanoparticles is quite evident.

Surface study of used absorbents using scanning electron microscopy (SEM)

Obtained results of SEM_EDX analysis of synthesized absorbent sample showed that in magnetic composite there are Fe, Silica, Mg, and MMT parts, produced peaks of Fe in this study confirms that MMT as a substrate includes iron nanoparticles.

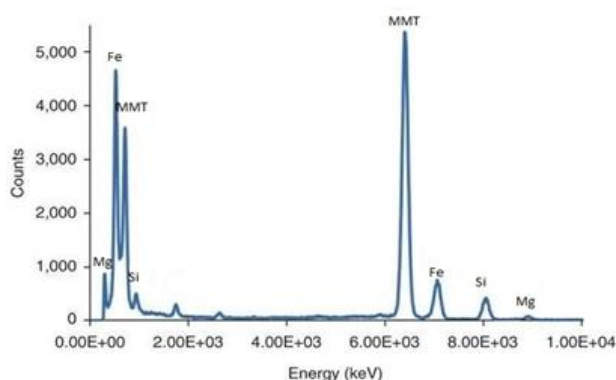


Fig.3. EDX analysis of prepared absorbent sample.

As it shown in electronic microscope images, magnetic nanoparticles were synthesized in nano scale and well dispersed in the entire montmorillonite matrix. They located into cavities of MMT in absorbent without agglomeration.

Study of effective factors to optimize absorption process of reactive orange-3R using MMT/ZVI nanocomposite. Study of pH influence on dye removal efficiency

In different bottles, 50 ml of the dye syrup in pH (4, 5, 6, 7, 8, 9, 10, 11 and 12) were prepared. To adjust pH of dye syrup, NaOH (0.1 M) and HCl (0.1 M) solutions were used and measured by pH meter. 0.1 gr absorbent was added to each one of solutions. For proper mixing of absorbable and absorbent, the samples were placed in a shaker machine with 320 rpm. The test was performed at 25 °C and was lasted 3 hours. After 180 minutes, the absorbent was separated from the solutions using a magnet during less than 1 minute. For each solution, the absorption quantity was measured using a spectrophotometer. In order to more accuracy, the test was repeated in two stages.

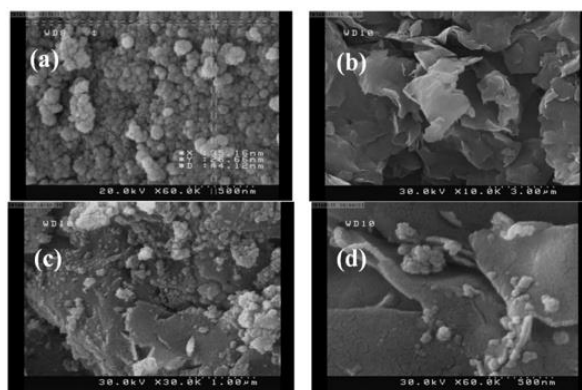


Fig.4. SEM images of Fe_3O_4 (a), montmorillonite (b), synthesized absorbent (c), and (d)

The figure (5) shows the effect of pH on absorption capacity and absorption efficiency. In this figure, it can be seen that the absorption process at pH=6 has better efficiency in comparison of other pH. So by increasing the pH from 6 to 10, both of percentage of absorption and absorption capacity are reduced. At pH=6 due to electrostatic attraction between the negatively charged molecules of dye and positively charged of absorbent surface, the absorption efficiency is high. But at higher pH, the absorbent surface is negatively charged and therefore, the electrostatic repulsive force between negatively charged ions of anionic dye and absorbent, lead to decrease the amount of dye absorption. So pH=6 was selected as the optimal value for the next tests of absorption process.

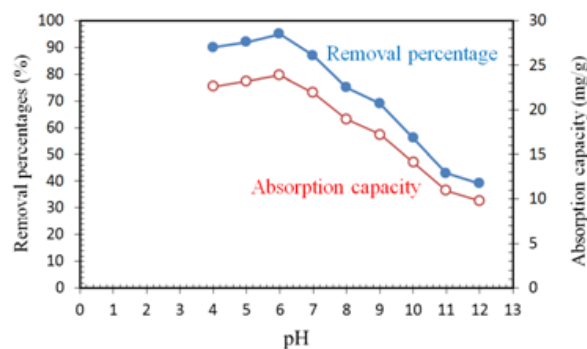


Fig.5. Diagram of pH effect on removal amount of dye (Absorbent doze: 0.1 g, temperature= 25 °C and initial dye concentration= 50 mg/l)

Study of contact time and absorption kinetics

In order to obtain the suitable for maximum removal efficiency in an Erlenmeyer flask, the dye (pH=6) was prepared and 0.02 gr of absorbent was added to the solution and it was placed on the shaker machine (T= 25 °C and 320 rpm) in time periods of 10, 20, 30, 40, 50, 60, 90, 120, 150, 180 minutes. It was observed that in the first hour the curve has sharp slope and absorption capacity

increases rapidly. This may be due to many active and unsaturated sites in outer surface of absorbent. In continue, the slope decreased during the time gradually and finally after 1 hour, the absorption amount has stabilized approximately at the room temperature and has balanced, so one hour, was evaluated as a suitable balance time at the room temperature.

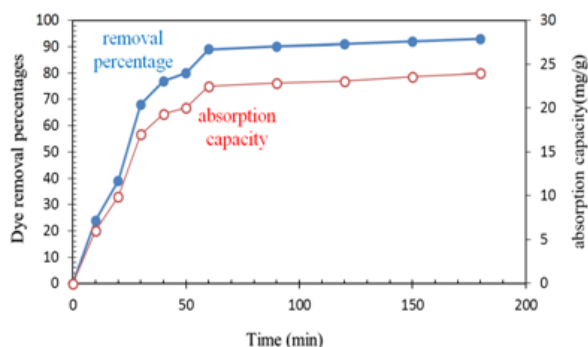


Fig. 6. Diagram of contact time effect on removal efficiency (absorbent dose: 0.1 g, pH=6, Temperature= 25 °C and dye concentration = 50 mg/l)

Kinetic equations were applied to describe the transfer of azo dye molecules per time unit or to evaluate the variables affecting the reaction rate. In this study, the pseudo-first and pseudo-second kinetic models those are mostly used to examine factors influencing the reaction rate of reactive dye absorption process on the NZVI / MMT absorbent were used. Linear kinetic equations are as follows:

$$\ln(q_e - q_t) = \ln q_e - k_1 t, \quad (3)$$

$$\frac{t}{q_t} = \frac{1}{q_e^2 \cdot k_2} + \frac{1}{q_e} t, \quad (4)$$

Which, (k_1), rate coefficient constant (min^{-1}) and (k_2), pseudo-second reaction rate constant in terms of $\text{mg} \cdot (\text{g} \cdot \text{min})^{-1}$, q_e , is balanced absorption capacity in terms of $(\text{mg} \cdot \text{g}^{-1})$, (q_t) is absorption capacity at time of (t) in terms of $(\text{mg} \cdot \text{g}^{-1})$, (q_e) and (k_1) values are determined as linear intercept and the slope of $\ln(q_e - q_t)$ versus (t) and also (q_e) values and (k_2) through the slope and intercept of linear graph $[(t) \cdot (q_t)^{-1}]$ in terms of (t^{-1}) are determined.

Study of temperature effect on removal efficiency and gaining thermodynamical coefficients

To evaluate the effect of temperature, solutions were prepared at pH = 6. The amount of 0.1 g of absorbent was added to the solutions. The solutions for 30 minutes on a shaker with 320 rpm were placed. Temperature ranges were selected as 10, 20, 30, and 40°C. It is visible that increasing the temperature increases the absorption capacity in all the initial absorbents concentration. This increasing can be due to raise of dye solubility and

consequently increasing of effective contacts of absorbable and absorbent materials and growth of pores size on absorbent surface that it leads to pollutant absorption.

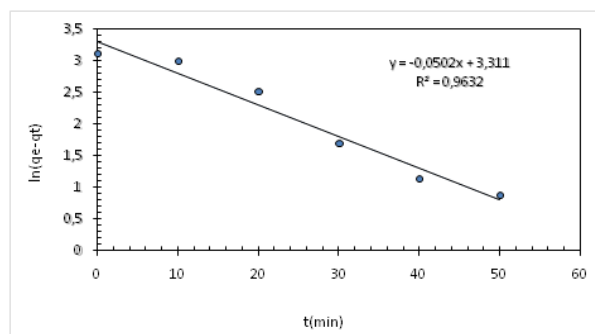


Fig. 7. The pseudo-first kinetic model.

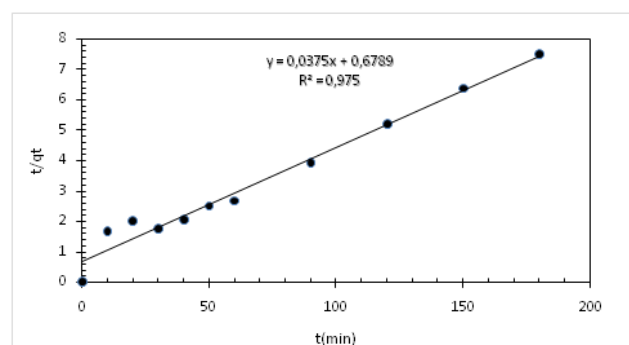


Fig.8. The pseudo-second kinetic model

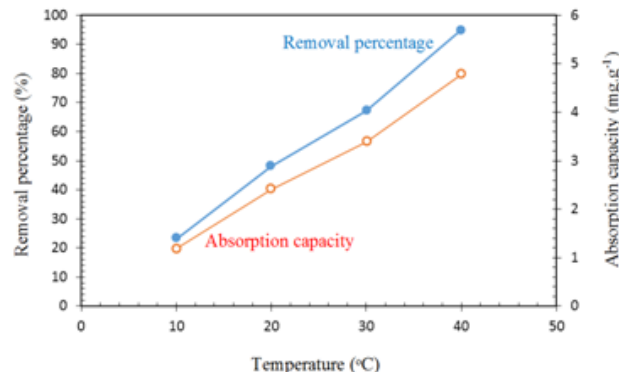


Fig. 9. Graph of temperature effect on removal efficiency [absorbent dose of 0.1 g, pH =6, time of 30 minutes and 50 ($\text{mg} \cdot \text{l}^{-1}$) of dye concentration]

In order to study the thermodynamic absorption process, determination of three factors of standard enthalpy ΔH , standard free energy ΔG and standard entropy ΔS is essential.

The obtained ΔH and ΔS values were obtained using Van'tHoff equations: [17]

$$\text{Ln}k_d = \frac{\Delta S}{R} - \frac{\Delta H}{RT}, \quad (5)$$

$$K_d = \frac{q_e}{c_e}, \quad (6)$$

That (R) is constant equals to 0.0082 and (K_d) is the ratio of absorbed dye on adsorbent to its remaining in the solution. ΔH and ΔS values are obtained from drawing linear graph of ($\ln K_d$) versus ($1/T$) those are the slope and intercept of the linear graph. ΔG values are calculated by following equation:

$$\Delta G = -RT \ln K_d \quad (7)$$

The calculated values of thermodynamic variables are shown in the table (3). According to the positive values of (ΔH), can be said that adsorption process has endothermic nature and with previous results based on increasing the amount of absorption by increasing of the solution temperature is compatible, this positive values also represents forming a strong chemical bond between azo dye molecules and the adsorbent surface. The obtained values of Gibbs free energy (ΔG) represents the absorption reaction is a spontaneous reaction and the increased values by increasing the temperature, shows high intention of adsorbent to absorb dye in higher temperatures.

Study of the adsorbent dosage effect on the removal amount

At this stage, 6 bottles of dye solution were prepared with pH = 6 and 0.08, 0.1, 0.2, 0.3, 0.4 and 0.5 gr of adsorbent were added to each solution. The temperature of 25 ° C and 1 hour of

contact time were selected. The solution was placed on a shaker with 320 rpm. It was observed that by increasing the amount of adsorbent, the dye removal percentages are increased and as well as the absorption capacity is reduced. Increasing of the removal percentage is due to increase of adsorbent surface and consequently augmentation of the absorbable molecules access to absorption sites on NZVI-MMT versus of fixed values of orange-3R molecules. Reduction of absorption capacity can be due to unsaturation of active site on adsorbent surface during the absorption process and the particle reactions, such as compaction or aggregation due to high absorption concentrations [29]. Finally, 0.5 gram of NZVI-MMT composite was selected as an optimal amount of adsorbent to remove orange-3R.

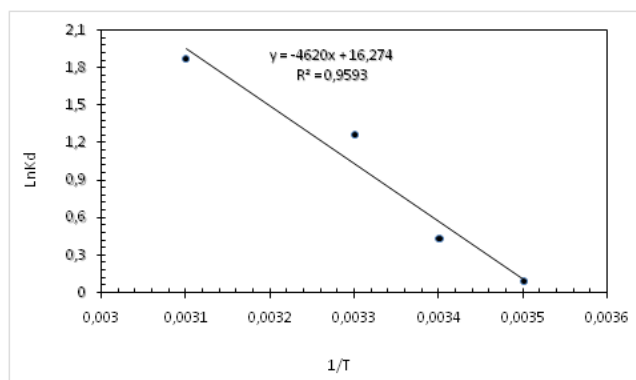


Fig.10. Van't Hoff diagram of absorption.

Table2. Calculated values to thermodynamic study

Solution Temperature (K)	C _e	q _e	K _d	lnK _d
283	15.5	17.25	1.10	0.09
293	12.14	18.93	1.55	0.43
303	6.17	21.89	3.54	1.26
313	3.54	23.23	6.54	1.87

Table3. Thermodynamic variables

Solution Temperature (K)	ln K _d	ΔG (kj.mol ⁻¹)	ΔH (kj.mol ⁻¹)	ΔS kj.(mol.K) ⁻¹
283	0.09	- 0.2	37.88	0.133
293	0.43	- 1.03		
303	1.26	- 3.13		
313	1.87	- 4.79		

Table4. Comparison of the obtained results of experimental data and Langmuir and Freundlich isotherm models.

Freundlich model			Langmuir model		
R ²	K _F (mg/g)(l/mg) ^{1/n}	1/n	R ²	K _L (l/mg)	q _m (mg/g)
0.833	4.46	0.0842	0.987	0.123	7.34

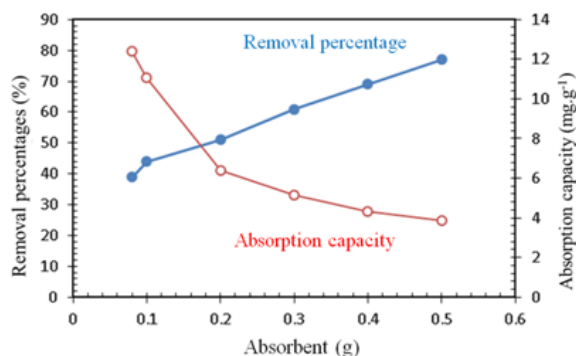


Fig. 11. The effect of adsorbent dosage on removal efficiency diagram (pH= 6, 1 hour, adsorbent dose of 0.08, 0.1, 0.2, 0.3, 0.4 and 0.5 g, temperature of 25°C and dye concentration of 50 ppm).

Study of the initial dye concentration effect and its impact on the isotherm adsorption models

At the last stage, the effect of orange-3R initial dye concentration on the removal efficiency of it by the adsorbent in different primary concentration ranges of dye was examined. Then the obtained results were used to draw the Langmuir and Freundlich isotherms. The isotherm is often used to determine the equilibrium adsorption potential and to evaluate the effectiveness of different environmental masses that in this model was used to describe the performance of montmorillonite in dye removal. In the Langmuir isotherm, surface bonds caused by physical forces are observed so the absorption is done only in form of single layer and it is assumed that the absorbing affinity of all sites is the same [30]. This model corresponded well with the vast values of experimental data and its linear form, is as the equation (3). Freundlich model in 1907 was presented as an experimental relationship by Freundlich. But then was used to multi-layer modeling on the heterogeneous surfaces or surfaces with different active sites in action and binding affinity to absorbing material. In this model it was assumed that at first, the stronger sites are filled and the bonding force is decreased by increasing the amount of the filled sites, where (Kf) and (nf) are Freundlich isotherm constants. In Freundlich isotherm, (Kf) and (nf) show the absorption amount and the absorption intensity, respectively [31]. The solutions with pH = 6 and 50, 100, 150, 200 mg.l⁻¹ of dye were prepared. 0.5 g of adsorbent was added to the solution and the solutions were placed on the shaker with 320 rpm at temperature of 40°C, for 60 minutes. It was observed that with increasing the initial dye concentration from 50 mg to 200 mg, the dye removal percentage was reduced. Probably, this decreasing trend was due to the fixed quantity of active sites on the adsorbent versus the increased quantity of dye molecules or in other words,

saturation of the absorbent surface in high dye concentrations

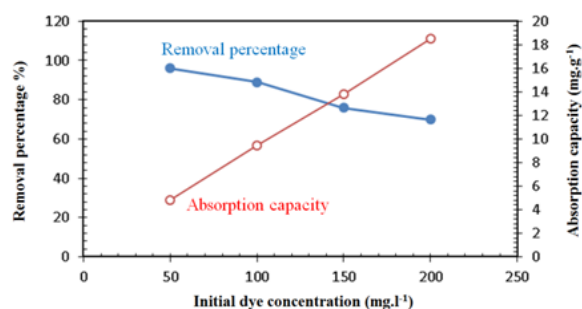


Fig.12. Effect of initial concentration (adsorbent dosage of 0.5 g, pH= 6, 1 hour, temperature of 40°C and dye concentration of 50, 100, 150 and 200 mg.l⁻¹)

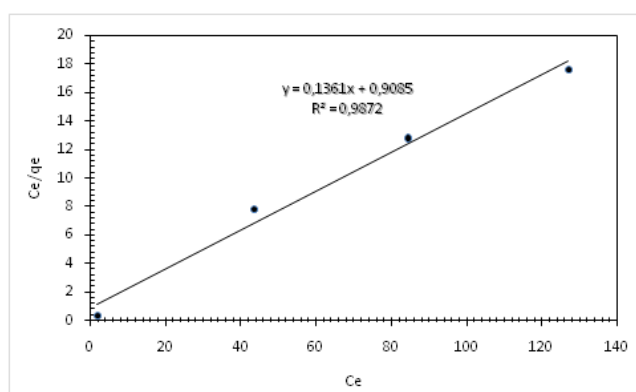


Fig. 13. The Langmuir isotherm model

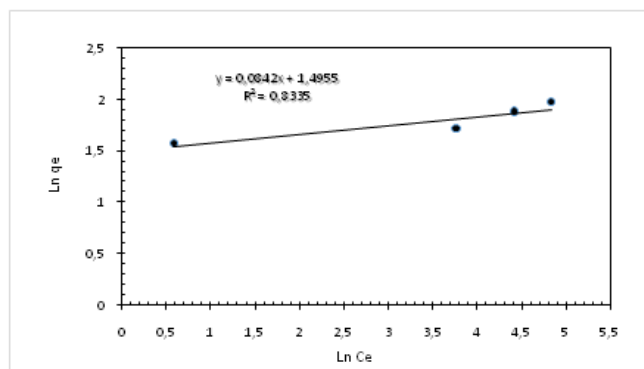


Fig. 14. The Freundlich isotherm model.

CONCLUSION

In the process of removal dye contaminants from water by adsorbent of NZVI/MMT nanocomposite, produced in optimized conditions, desired results were achieved. The results of the study showed that at pH = 6, azo dyes removal efficiency by the adsorbent was better and adsorption reaction time by increasing the temperature from 25 to 40 °C, (15 °C), was reduced from an hour to half an hour and the obtained results for the thermodynamic parameters showed that dye removal increased with increasing the

temperature and it has endothermic and spontaneous nature and has formed a strong chemical bond between the molecules of dye and absorbent surface. According to the investigations can be concluded that adsorbed Fe₃O₄ nanoparticles onto a suitable substrate of montmorillonite, has very good effectiveness and efficiency in removing dye contaminants of orange-3R. In this regard, the removal percentage, with increasing of initial concentration of dye and the amount of absorption was decreased and increased, respectively. Due to the widespread use of zero-valent iron (ZVI) nanoparticles as an appropriate adsorbent for the removal of contaminants and to remove toxic chemicals from contaminated water is expected that this method is an effective way to solve problems and remove pollutants. According to the obtained results from the performance of nanocomposite zero-valent iron montmorillonite adsorbent, however, that by increasing the amount of absorbent, dye removal amount increases but by increasing it to the amount of half a gram, at ambient temperature at, to remove 10 ml dye solution with concentration of 50 ppm can completely remove orange-3R According to the Langmuir isotherm model results in comparison of Freundlich isotherm model, there is the most correlation with experimental results. There is the most dye adsorption capacity of the solution at 40°C in pH = 6 that shows it is correlated with Langmuir adsorption process model. In this study, the positive variations of absorption heat has proved the exothermic nature of absorption process and the negative variations of free energy has proved spontaneous of absorption process and reduction of free energy associated with increasing of temperature means more effective absorption of metallic ions in higher temperatures.

REFERENCES

1. B. Ventura-Camargo, M. Aparecida, M. Morales, *Journal of Health Science*, **2**, 85 (2013).
2. K Dwivedi, G. Kumar, *Journal of Environmental and Public Health*, **13**, 25(2015).
3. M Joshi, R Bansal, Purwar, *Indian Journal of Fibre and Textile Research*, **29**, 239 (2004).
4. P.Poni, *Ion Exchange Letters*, **3**, 7 (2010).
5. H. J. Mansoorian, E. Bazrafshan; A. Yari; M. Alizadeh, *International journal of Health Scope*, **3**(2), 1(2014).
6. <http://dx.doi.org/10.1155/2013/820165>.
7. T. Moghaddam, M.R. Alavi; A. Mokhtar, *Environmental Engineering & Management Journal* **13**(3), 557 (2014).
8. R.G. Saratale, G.D. Saratale, J.S. Chang, S.P. Govindwar, *Journal of the Taiwan Institute of Chemical Engineers*, **42**, 138 (2011).
9. A. Szyguła, E. Guibal, M. Ruiz, A.M. Sastre, *Colloids and Surfaces A: Physicochemical and Engineering Aspects*, **330**(2–3), 219 (2008).
10. A. Berez, F. Ayari, N. Abidi, G. Schäfer, M. Trabelsi-Ayadi, *Clay minerals*, **49**(5), 747 (2014).
11. S.M. Kanawade, R.W. Gaikwad, *Int. J. Chem. Eng. Applications*, **2**, 317 (2011).
12. M. Lučić, N. Milosavljević, M. Radetić, Z. Šaponjić, M. Radoičić, M.K. Krušić, *Separation and Purification Technology*, **122**, 206 (2014).
13. M.H. Dehghani, P. Mahdavi, *Desalination and Water Treatment*, **54**, 3464 (2015).
14. A. Mohagheghian, R. Vahidi-Kolur, M. Pourmohseni, J.-K. Yang, M. Shirzad-Siboni, *Water Air Soil Pollut*, **226**, 321 (2015).
15. K. Kalantari, M.B. Ahmad, H.R.F. Masoumi, K. Shameli, M. Basri, R. Khandanlou, *Int. J. Mol. Sci.*, **15**, 12913 (2014).
16. R. Cheng, G. Li, C. Cheng, L. Shi, X. Zheng, Z. Ma, *An international journal to further the chemical sciences*, **5**, 66927 (2015).
17. F. Zamani, S. Kianpour, *Catalysis Communications*, **45**, 1 (2014).
18. T. Alka, B. Anita, *Int. Res. J. Environment Sci.*, **3**, 41 (2014).
19. S. Sepehri, M. Heidarpour, J. Abedi-Koupai, *Soil & Water Res.*, **9**, 224 (2014).
20. L. Yu, X. Yang, Y. Ye, D. Wang, *RSC Adv.*, 46059 (2015).
21. Y.-T. Lin, C.-H. Weng, F.-Y. Chen, *Separation and Purification Technology*, **64**, 26 (2008).
22. Z. Chen, X. Jin, Z. Chen, R. Naidu, *Journal of Colloid and Interface Science*, **363**, 601 (2011).
23. X. Yunfei, M. Megharaj, N. Ravendra, *Applied Clay Science*, **53**, 716 (2011).
24. L. Peng, P. Qin, M. Lei, Q. Zeng, H. Song, J. Yang, J. Shao, B. Liao, J. Gu, *Journal of Hazardous Materials*, **209–210**, 193 (2012).
25. A. Dalvand, R. Nabizadeh, M.R. Ganjali, M. Khoobi, S. Nazmara, A.H. Mahvi, *Journal of Magnetism and Magnetic Materials*, **404**, 179 (2016).
26. K. Kalantari, M.B. Ahmad, H.R.F. Masoumi, K. Shameli, M. Basri, R. Khandanlou, *Int. J. Mol. Sci.*, **15**, 12913 (2014).
27. M. Farrokhi, S.-C. Hosseini, J.-K. Yang, M. Shirzad-Siboni, *Water Air Soil Pollut.*, **225**, 2113 (2014).
28. S. Hanif, A. Shahzad, *Journal of Nanoparticle Research*, **16**, 2428 (2014).
29. N.M. Mahmoodi, B.M. Hayati, *Ind. Crop. Prod.*, **35** 295 (2012).
30. Z. Aksua, S. Ertugrul, Donmez, *J. Chem. Eng.*, **158**, 474 (2010).
31. M. Shafiq, A.M. Ranjha, M. Yaseen, S.M. Mehdi, A. Hannan, *Journal of Agric. Res.*, **46**, 141 (2008).

The size effect of titanium dioxide particles on desulfurization in a power plant

W. Cheng^{1*}, Y. Li¹, H.I. Schlager²

¹School of Energy, Power and Mechanical Engineering, North China Electric Power University, 102206 Beijing, China

²School of Control and Computer Engineering, North China Electric Power University, 102206 Beijing, China

Received June 8, 2016, Revised September 15, 2016

To study the effect of the different states and structures of titanium dioxide on the catalytic behavior of desulfurization during a combustion process, a titanium dioxide nano-catalyst was prepared, finding that its agglomeration is serious when calcined at 100°C. As the calcination temperature increased to 500°C, the agglomeration gradually weakens, and the uniformity of particles is enhanced, while remaining in the anatase structure. When the temperature was increased to 700°C, the titanium dioxide was converted into the rutile structure, and fusion growth phenomenon occurs. Then calcium oxide desulfurization experiments with the titanium dioxide catalyst were carried out and it was found that when the calcination temperature is 500°C, the maximum desulfurization efficiency in the sample is achieved. Another sample became fully rutile at 900°C and the desulfurization efficiency began to improve.

Keywords: titanium dioxide, size effect, desulfurization, calcium oxide, burning.

AIMS AND BACKGROUND

Coal combustion processes will bring a lot of emissions, such as dust, CO₂, SO₂, NO_x and heavy metals, which can cause pollution problems such as the greenhouse effect, acid rain, ozone depletion, smog and other environmental problems. Currently, these problems have raised extreme concerns at home and abroad, and the problems are so serious that they affect the human environment and need to be addressed.

For the removal of sulfur pollutants in coal-fired power plants, in general, the basic technological principles of desulfurization is that through chemical reactions between a desulfurization agent and the emissions, the gaseous emissions are solidified into a reaction product of solid state, so as to achieve the elimination of the polluting emissions. In this case, whether the desulfurization agent is renewable or not, has a relationship with the running costs of the system and waste of land resources and secondary pollution of the environment.

The TiO₂ catalytic action stems mainly from the transition metal characteristics of titanium. Under different reaction conditions, it directly affects the reaction substance or indirectly affects the reaction process. The bond energy of Ti and the corresponding ligands are weak, and the catalytic action tends to be of an ionic character. As a new environmentally -friendly material and being non-toxic and harmless, it has garnered much

attention in recent years due to its many excellent properties and can be used as a catalyst or carrier in many of these reactions. The preparation method, application and development of TiO₂ materials have become one of the main points of its study [1].

Ruan et al. [2] investigated an industrial honeycomb catalyst in a power plant, adding different amounts of arsenic in the catalyst to study the performance effects of arsenic on a commercial V₂O₅-WO₃ / TiO₂ catalyst. A remarkable effect on the activity of the catalyst was observed. Only a little arsenic can result in the decrease of the catalyst activity. When As / V is 0.2, the activity of the initial 92.02 percent is down to about 74%. When increasing the catalyst, its activity declined. Arsenic majorly impacted VO_x species on the catalyst surface, and made the vanadium species diverse, but did not affect the chemical character of V₂O₅/ TiO₂. It has a certain influence on the acidic sites of the catalyst surface, reducing Bronsted acid sites of the adsorbed NH₃.

The Hg oxidation activities of several commercial V₂O₅/WO₃ (MoO₃)/TiO₂ honeycomb and plate type DeNO_x catalysts were identified for the DeNO_x inactive case and compared with their DeNO_x activities [3]. In this way, it was possible to show that the velocities of Hg oxidation and DeNO_x reactions are of the same order of magnitude. The DeNO_x-active state of the catalysts had a strongly negative impact on the oxidation of elemental Hg that could not be explained solely by an inhibition effect of ammonia. Under these conditions, even reduction of oxidized Hg occurred on the catalyst. Our understanding of the control variables for Hg oxidation in SCR DeNO_x plants has to be amended in light of these slowing effects

* To whom all correspondence should be sent:
E-mail: cwl@ncepu.edu.cn

and has to take the induced reduction into account.

Xi, et al. [4] have investigated a composite SCR carrier prepared with 10% cordierite and titanium dioxide. And it did not become rutile when calcined at 600°C, meanwhile samples of V₂O₅ and WO₃ crystal diffraction peaks did not appear. The catalyst wear rate, water absorption and shrinkage rate is not heavy, avoiding cracking of the honeycomb catalyst in the heat treatment to improve the thermal stabilization. In the experiments, the reaction temperature ranges between 250 - 460°C, the denitration rate is more than 80%. Hg⁰ oxidation by chlorine over CeO₂-TiO₂ catalysts with different CeO₂/TiO₂ ratios was investigated both in the absence and the presence of SO₂ [5]. An addition of SO₂ did not inhibit the adsorption of HCl on pure CeO₂; however, it inhibited reactions between Hg⁰ and chlorine species over pure CeO₂, hence resulting in a decrease of Hg⁰ oxidation efficiency. The desulfurization ability of CaO-Al₂O₃-SiO₂-TiO₂ slag at 1 873 K was studied through a slag-metal desulfurization experiment [6]. The experimental indices considered were the sulfur distribution coefficient of the slag and the desulphurization ratio. The effect of the mass percentage of Al₂O₃ and TiO₂ is significant. Under optimal experimental conditions, the slag system with TiO₂ can meet the desulfurization requirements of steelmaking, which is a good way for resource utilization of solid waste containing titanium. The oxidative desulfurization of several sulfur compounds with a mixture of hydrogen peroxide and formic acid was studied [7]. The catalytic activity of a nanocomposite was tested on oxidative desulfurization of actual gas oil and results are compared with that of model sulfur compounds. This Keggin-type supported catalyst was shown to be able to have oxidative desulfurization of model sulfur compounds and actual gas oil with a high yield.

As a typical photocatalytic material, titanium dioxide has been applied extensively in technical applications. In recent years, some scholars have reported research developments in titanium dioxide used in desulfurization.

Zhao et al [8,9] studied experimentally supported TiO₂ photocatalysts in simultaneous desulfurization and denitrification in flue gas. Increasing removal efficiency by aerobic participation; the NO removal efficiency increased when the water vapor content was increased to a certain extent. When the exposure time is maintained for 100 min, the optimum SO₂ and NO removal efficiency is obtained. The concentration of sulfate and sulfite in the removal process

increased with the increase of the initial concentration, and the removal product SO₄²⁻ is the dominant species. When the SO₂ concentration is low, the oxidation action is dominant. But with the concentration going up, the oxidation advantages are weakened and the dissolving and absorption abilities are enhanced.

A TiO₂-aluminum silicate fiber nanocomposite, synthesized by a sol-gel method, is proposed to be used as a photocatalyst for the removal of multiple pollutants of SO₂, NO and Hg⁰ in a simulated coal combustion flue gas [10]. The TiO₂-aluminum silicate fiber calcined at 500 °C exhibited the biggest BET surface area and highest photocatalytic activity. In experiments, the removal efficiencies for SO₂, NO and Hg⁰ at 120°C and with a UV intensity of 3 mWcm⁻² can reach 33%, 31% and 80% respectively. However, the addition of water vapor to the simulated flue gas inhibited the oxidation of SO₂, NO and Hg⁰. The UV intensity was the most important factor in the photocatalytic oxidation.

Han et al. [11] prepared a nano- TiO₂ composite photocatalyst supported by activated carbon fibers, and carried out research by simultaneously removing high concentrations of sulfur dioxide and nitric oxide under ultraviolet and visible light conditions. Under visible light conditions, SO₂ and NO removal efficiency were higher. The TiO₂ photocatalytic action is dominant in the desulfurization and denitrification process.

Titanium dioxide supported by multi-walled carbon nanotubes (MWCNTs/TiO₂), and Cu doped TiO₂ supported by MWCNTs (MWCNTs/Cu-TiO₂) were synthesized via a sol-gel method [12]. The oxidation and removal efficiencies of SO₂ and NO in a simulated flue gas were investigated experimentally in a fixed-bed reactor. The optimal conditions (73 mg/m³ NO, 155 mg/m³ SO₂, 8% O₂, 5% H₂O) were determined, and 62% and 43% of total SO₂ and NO removal were achieved on 15% MWCNTs/Cu-TiO₂. The integrated desulfurization and denitration efficiencies were lower than that in the baseline experiments due to SO₂ and NO competing for adsorption sites.

Wang et al [13] have compared the impact of nano-titanium dioxide on the desulfurization during the combustion in two kinds of coals. The desulfurization performance in the coal combustion of nano- TiO₂ and CaO changes the microstructure of ash, the ash loses pores, the CaO lattice structure which makes the CaO aperture larger, increases the number of pores and the specific surface, improving the CaO sintering characteristics that promote SO₂ and CaO becoming calcium sulfate. Nano- TiO₂ has some adaptability for different

coals, especially high-sulfur coal. The optimal reaction conditions for nano- TiO_2 are a dosage of 8% TiO_2 nanoparticles, Ca / S molar ratio of 2, a combustion temperature of 850°C in the desulfurization experiments. Nanosized titanium oxide powder was prepared via the sol-gel process [14]. The calorific value of the coal and the fusion temperature of the coal ash were lowered by adding CaO, while on the other hand adding nano- TiO_2 to coal effectively increased the calorific value and the melting temperature. Meanwhile, the coal combustion efficiency and desulfurization in the combustion could be effectively improved by the co-action of TiO_2 .

Photocatalysts with different mass ratios of $\text{TiO}_2/\text{g-C}_3\text{N}_4$ were prepared by a two-step method [15]. The photocatalytic oxidation activity of the samples was evaluated by photooxidation of dibenzothiophene. Reaction conditions, such as the amount of H_2O_2 and TiO_2 loading, were investigated in detail. The results showed that the removal of dibenzothiophene could get to 98.9% under optimized conditions after 2 h at room temperature. The oxidation reactivity of the different sulfur compounds was found to be in the order of dibenzothiophene > benzothiophene > n-dodecanethiol (RSH). Further studies showed that dibenzothiophene and its derivatives were converted to the corresponding sulfone, which could be extracted by a polar solvent. The catalytic activity of titanate nanotubes in the oxidation of dibenzothiophene by using H_2O_2 was investigated [16]. Titanate nanotubes were synthesized by alkaline hydrothermal treatment of anatase TiO_2 followed by washing either with water to produce titanates with high sodium content or with aqueous HCl to obtain protonated titanates. These results were correlated with the production of reactive radicals as observed by electron paramagnetic resonance and with dibenzothiophene adsorption capacity. Favorable reaction conditions were found to be low temperatures (25°C) and $\text{H}_2\text{O}_2/\text{dibenzothiophene} = 4$. Reactions at elevated temperatures and H_2O_2 concentrations lead to significant reduction in catalyst activity, associated with partial phase transformation and premature deactivation of the catalytic sites. A.H.M. Silver supported on mixed oxides $\text{Ag}/\text{TiO}_2\text{-Al}_2\text{O}_3$ shows promise as an advanced organosulfur adsorbent with deep desulfurizing ability and scalability to be fitted into on-board fuel cell systems [17]. This paper presents the performance, characterization, and desulfurization mechanism of $\text{Ag}/\text{TiO}_2\text{-Al}_2\text{O}_3$ adsorbent for applications in pre-reformate cleaning of Proton Exchange Membrane fuel cells.

Anatase- TiO_2 dispersion on Al_2O_3 provided increased adsorbent activity, higher surface acidity and exerted in more defect sites for Ag incorporation. $\text{TiO}_2\text{-Al}_2\text{O}_3$ provided both strong and weak Bronsted sites.

By using two specific titanium dioxide materials, such as the anatase of 5,10,50 nm and rutile mine of 10×40 , 30×40 , the experiments were carried out to obtain the features of titanium dioxide nano-materials on deposition and aggregation in sodium chloride aqueous solution¹⁸. The stability between 10×40 rutile and 50 nm anatase at pH = 7 is the best, but the morphology and the chemical structure is not related to this. And impurities in raw materials such as silicon and phosphorus components have something to do with the surface charge. In the aggregation experiment, the critical concentration of 50nm anatase material is the highest, followed by 10×40 rutile and 5nm anatase.

Roncaroli et al. [19] studied two different titanium dioxide samples. It showed that their equilibrium properties are relatively similar, and the influence of the particle size and specific surface area on the adsorption rate is large in the dynamics of titanium dioxide thin films. That is why the internal diffusion capacity, in which the finer the particles are, the higher the porosity is. Dittmann et al. [20] found that very fine particles may be solidified into a dense ceramic material at low temperatures in a sintering process when grain growth and pore generation are avoided. During the sintering of titanium dioxide nanoparticles by adding elemental chlorine, the influence of phase transformation, the thickening rate and particle growth are considered. It was found that at 900 degrees, the doped chlorine leads to strong particle growth, but the thickening rate and phase transition temperatures are low, and the final density decreased by 1.5 %.

Gondek et al. [21] using the sol - gel and pull coating method, prepared a TiO_2 film attached to a sodium calcium glass lining, discovering the size effect. For a comparative analysis of TiO_2 films and TiO_2 films with an intermediate silica oxide layer, and the width of the energy gap and the Urbach energy were measured, resulting in the energy gap in the range of TiO_2 the film thickness between the glass substrate and the TiO_2 thin film, which was caused by sodium ions. The impact of silicon ions on the direct energy gap was found in the TiO_2 film adhered to a soda-lime glass substrate with pre-coated SiO_2 layer.

Due to the advantages of TiO_2 materials such as being non-toxic, cheap, efficient, non-corrosive and

so on, TiO_2 is widely used as a catalyst or catalyst carrier in the preparation of adsorbents or catalysts in desulfurization and denitrification. Obviously, different sizes of TiO_2 will have different impacts on the catalytic efficiency of desulfurization and denitration, so different sizes of TiO_2 have great significance for desulfurization and denitration.

In this paper, titanium dioxide of several sizes were prepared by hydrolysis of titanium grease, and the size effects of experimental desulfurization were studied on the basis of systematic characterization of titanium dioxide.

EXPERIMENTAL

Titanium dioxide nanopowders were prepared by the sol - gel method, using tetrabutyl titanate and deionized water as raw materials. Tetrabutyl titanate with deionized water at a volume ratio of 1:2. A beaker with 300 ml of deionized water was placed in an electric mixer. The mixer was adjusted to a certain speed, and then 150 ml of tetrabutyl titanate was added dropwise into deionized water while continuously being stirred. After continuous stirring for 6h, the solution was placed in the shade

and left standing for 24h. The mixture was then dried to get a solid yellow powder. The powder was divided into five equal parts, respectively calcinated in a muffle furnace at 100, 300, 500, 700 and 900°C for 4h. This made a series of nano-sized titanium dioxide powders. The samples were defined as Sample 1, Sample 2, Sample 3, Sample 4 and Sample 5 by the calcination temperature.

The experimental combustion desulfurization system is shown in Figure 1. Firstly, lignite coal and titanium dioxide nano-powder sample were mixed, and put into a porcelain boat which can be taken into the tube furnace. This is then connected to an absorption bottle, introducing oxygen. Secondly, the samples were preheated to 500°C for 5 min to discharge volatiles and prevent coal deflagration, then further heated to a specified combustion temperature, combusting takes place for 25min using pure oxygen, and the SO_2 of the exhaust gas is absorbed by a lime solution. Finally, the SO_2 content of the flue gas was measured by adding iodine liquid which has the effect of desulfurization. For subsequent samples 2 to 5, the same experimental desulfurization methods were applied.

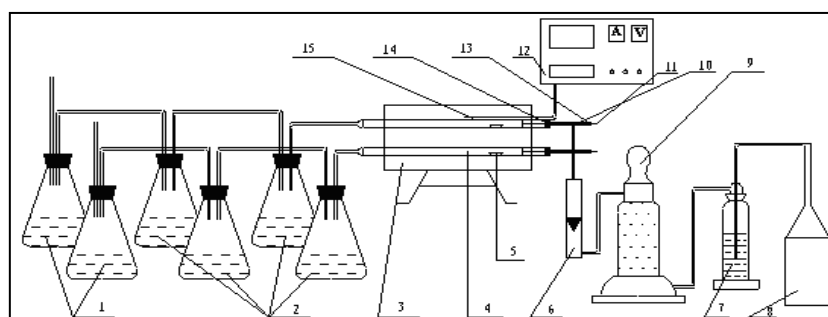


Fig. 1. Burner gas desulfurization experimental apparatus. 1 lime solution; 2 absorption bottle; 3 tube furnace; 4 burner tube; 5 porcelain boat; 6 meter; 7 scrubber; 8 storage cylinder; 9 drying tower; 10. T -tube; 11 push rod; 12 temperature controller; 13 turn plastic cap; 14 rubber stopper; 15 thermocouples.

RESULTS AND DISCUSSION

Changes in the structure of titanium dioxide

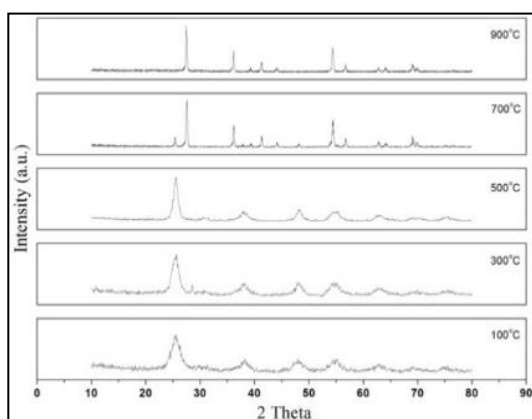


Fig. 2. XRD titania obtained at different temperature.

X -ray diffraction (XRD) pattern analysis can be used to find variation of the size and configuration, a case is shown in Figure 2. As can be seen, at a temperature of 100°C, 300°C, 500°C, a series of peaks in the diffraction pattern are consistent with anatase titanium dioxide, and showed that the obtained crystalline powder has the anatase structure. In addition, the half-width of the diffraction peaks of the sample 1, 2, and 3 are wider than sample 4 and 5, and show that the particles sizes of the three powders are small. As the temperature increases, the diffraction peaks gradually sharpened. When the temperature exceeds to 500°C, the diffraction peaks of sample 4 are obviously refined at 700°C. When the peaks increase, the powder particle size becomes large, and at that time the structural phase transition

appears. Comparing with the standard rutile Atlas, each peak corresponds with titanium dioxide rutile. Through the above analysis, it is easy to find that for the samples in the range of 500-700°C an obvious structural phase transition occurs, namely, the structure transition from anatase to rutile happens.

To further carry out the quantitative analysis of the phase change process, Figure 3 shows the description of the rutile phase transition rule with a phase transformation. In Figure 3 using the following formula is used to calculate the phase variables:

$$\text{Variable phase (\%)} = \frac{\Sigma \text{ rutile peak}}{(\Sigma \text{ rutile peak} + \Sigma \text{ anatase peak})} \quad (1)$$

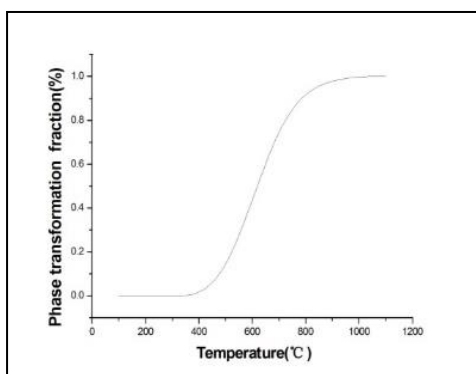


Fig. 3. The different temperatures to obtain titania phase transition diagram.

Size effect of titanium dioxide

A scanning electron microscope (SEM) was used to study the change mechanism of the particle size in calcined titanium dioxide at different temperatures, discussing the phenomenon of agglomeration and fusion grown in the process. The size effect refers to the fact that the reaction efficiency of desulfurization and denitrification can be improved after the character of the particle changes because agglomeration and fusion changes the size of the particle. The size effect is not an effect due to the original particle size but rather due to the grain size after undergoing a calcination process at different temperatures. In Figure 4, SEM pictures of titanium dioxide particles of (a), (b), (c), (d) and (e) correspond to calcination temperatures of 100, 300, 500, 700, 900 °C respectively. From the SEM scanning, it can be seen that the calcination temperature has a great influence on the particle size of titanium dioxide. Figure 4(a) clearly shows that at a calcination temperature of 100 °C, the particle size is about 1.3540 μm, while the grain size of the titanium dioxide in the sample is typically 6 nm. Thus, the agglomeration of titanium particles at this time is quite serious.

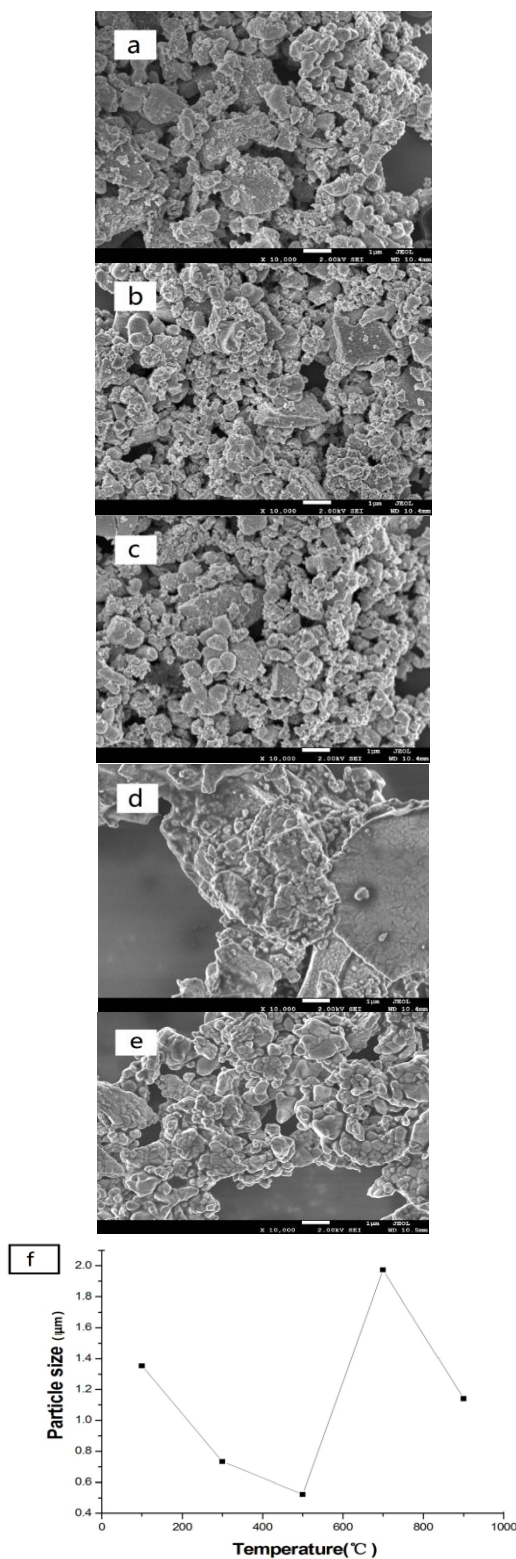


Fig. 4. Titanium images and synthetic curves at different temperatures:

- (a) calcining temperature 100 °C;
- (b) calcining temperature 300 °C;
- (c) calcining temperature of 500 °C;
- (d) calcining temperature 700 °C;
- (e) calcining temperature 900 °C;
- (f) grain size versus temperature.

When the calcination temperature is 300 °C, Figure 4b shows that the agglomeration of titanium dioxide grain at this time has been reduced compared to Figure 4a, but there still is agglomeration of large pieces of particles. When the calcination temperature is 500°C, Figure 4c, shows a change of the titanium dioxide particles which are now relatively small and uniform, while the specific surface area is still relatively large. At 700 °C as shown in Figure 4d, the fusion growth phenomenon of titanium dioxide particles appears, this being different from Figure 4a and Figure 4b where the agglomeration of titanium dioxide takes place. When the calcination temperature is 900 °C, Figure 4e, the grain growth phenomenon of titanium dioxide particles is quite obvious and cracking occurs, the grain growth size of the particles is significantly less than that at 700 °C. Figure 4f describes the curves that the particle size of titanium dioxide with calcination temperature. Observed at 500°C, the titanium dioxide particles are smallest, while the biggest are found at 700 °C.

Desulfurization effect analysis

Each of the five samples which had 8% calcium oxide was mixed with pulverized coal, then the experiments of desulfurization during combustion were carried out. The experimental data can be described as a curve which shows the relation between the different samples and the desulfurization efficiency, as shown in Figure 5. The desulfurization efficiency is related to the calcination temperature of the titanium dioxide sample. The curve rises in the beginning, then falls, and finally rises. The Desulfurization efficiency of sample 1 was low, and desulfurization efficiency of samples 2 to 3 gradually increased. Sample 3 was prepared at 500°C, and its desulfurization efficiency was the highest. The desulfurization efficiency of sample 4 is lower. With the experiment of sample 5, the desulfurization efficiency increased again.

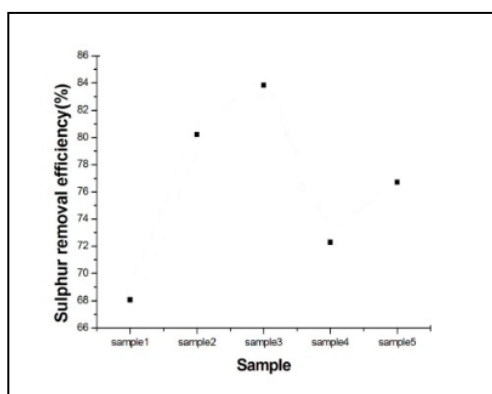


Fig. 5. Desulfurization efficiency varies with different samples of the curve.

The differences of particle size of titanium dioxide in the reaction are large, which represents different effects. Under normal ambient conditions, the crystal size of a titanium sample is about 6nm. However under other special physical and chemical conditions, the group size of some particles will multiply thousands of times, then the physical and chemical influences are not same. When the micelle size of a titanium dioxide particle is under certain range, the size effect will happen [18], at that time, the electronic energy levels near the Fermi level range from quasi-continuous to discrete, as the energy gap becomes wider. When the difference of the energy level is bigger than that of heat, light, electromagnetic energy, it results in a significant difference in the characteristics of the nanoparticle's magnetic, optical, acoustic, thermal, electrical, superconducting properties. Moreover, from the point of view of the crystal structure of titanium dioxide, the chemical composition of anatase and rutile ore are formed by titanium dioxide, and both ores are tetragonal, but their arrangement and connections are different. In Figure 6, each of the octahedral are connected with ten surrounding octahedral in the rutile crystal, wherein there are two shared edges and eight shared vertices. In the anatase crystal, each is connected with the surrounding eight octahedral, wherein there are four shared edges and four shared vertices. In contrast, the anatase crystal structure is more open than the rutile structure, so the catalytic activity of anatase is relatively stronger than rutile.

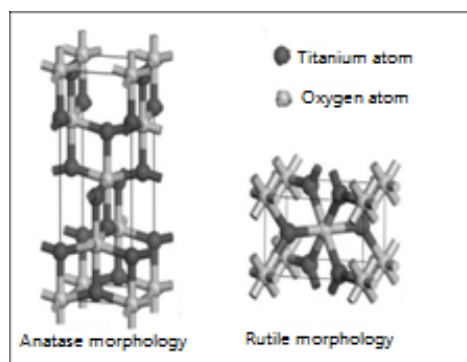


Fig. 6. Molecular structure of anatase and rutile titanium mine.

In the sample preparation process, when the calcination temperature is increased from 100°C to 500°C, the agglomeration of titanium dioxide gradually decreases, the specific surface area increases, and the adsorption capacity increases, at this stage the particle sizes are relatively small. In the coal combustion experiment when mixed with both calcium oxide and the titanium sample, in the beginning, the desulfurization efficiency gradually

improves, at this stage, it is all in the anatase state. When the experiment is in the temperature interval between 500°C and 700°C, the anatase structure gradually transforms to the rutile structure, at the same time the desulfurization efficiency begins to decline gradually. After the temperature reaches 700°C, the anatase structure completely transforms to the single-phase rutile structure, at this time the dioxide particles of the fusion growth start cracking, resulting in the particle size becoming smaller, and the adsorption capacity of sample 5 rises.

In summary, for titanium dioxide sample 3, the agglomeration phenomenon is very weak, the size is small, the specific surface is large, and the adsorption ability is stronger, but the opposite happens in the case of anatase.

CONCLUSIONS

When the nano- titanium oxide catalyst was prepared at calcination temperatures from 100°C to 500°C, the phenomenon of agglomeration appeared, the resulting particles had an anatase structure. In the calcination temperature range of 500°C-700°C, the anatase structure significantly transforms to rutile, and the fusion growth phenomenon occurs. After the calcination temperature reaches 700°C, the structure is completely in the rutile state, cracking of the fusion growth particles appears and the particle size becomes smaller.

In the coal combustion experiments with titanium dioxide and calcium oxide, the size effect of titanium dioxide on desulfurization is very obvious. No matter whether TiO₂ is in either the anatase or rutile state, the agglomeration and fusion growth phenomenon influences the desulfurization because of the particle size change. The particles of sample 1 are fairly small, thus agglomeration is serious and desulfurization efficiency is not high. For sample 2 and sample 3, the desulfurization efficiency gradually increases. For the samples 4 and 5 which completely converted to the rutile structure, the desulfurization efficiency decreases and then rises.

Acknowledgements: This work was supported by Beijing Natural Science Foundation (No.3132017), and National Natural Science Foundation of China (No. 51476056).

REFERENCES

1. J.W. Xu, L.Y. Wang, S.H. Chen, Y. Pang, *Mod. Chem. Ind.*, **31**, 21(2011).
2. D.L. Ruan, S.W. Pan, Z.L. Wei, B.C. Huang, H. Cheng, *Chem. Ind. and Eng. Prog.*, **33**, 925 (2014).
3. R. Stollea, H. Koesera, H. Gutberleb, *App. Cata. B: Environ.*, **144**, 486 (2014).
4. W.C. Xi, Q.C. Liu, *Chin. J. Environ. Eng.*, **7**, 2262 (2013).
5. H.L. Li, C.Y. Wu, L.Q. Li, *Fuel*, **113**, 726 (2013).
6. K. Dong, L. Wu, W.J. Liu, R. Zhu, *Iron Steel Inst. Japan International*, **54**, 2248 (2014).
7. A.F. Shojaei, M.A. Rezvani, M.H. *Fuel Process. Technol.*, **118**, 1 (2014).
8. Y. Zhao, J. Han, *J. Power Eng.*, **27**, 411 (2007).
9. Y. Zhao, L. Zhao, J. Han, *Proceedings of the CSEE*, **27**, 51 (2007).
10. Y. Yuan, J.Y. Zhang, H.L. Li, *Chem. Eng. J.*, **192**, 21 (2012).
11. J. Han, Y. Zhao, *Environ. Sci.*, **30**, 997 (2009).
12. H. Liu, X.Q. Yu, H.M. Yang, *Chem. Eng. J.*, **243**, 465 (2014).
13. S.Q. Wang, C.R. Su, Y. Zhao, *J. North China Elec. Pow. Univ.*, **38**, 89 (2011).
14. Y. Zhao, S.Q. Wang, Y.M. Shen, X.J. Lu, *Energy*, **56**, 25 (2013).
15. C. Wang, W.S. Zhu, Y.H. Xia, H. Xia, *Ceram. Int.*, **40**, 11627 (2014).
16. E. Lorencon, D.C.B. Alves, K. Kramvrock, E.S. Avila, *Fuel*, **132**, 53 (2014).
17. A.H.M. Shahadat Hussain, B.J. Tatarchuk, *Fuel Process. Technol.*, **126**, 233 (2014).
18. X.Y. Liu, G.X. Chen, C.M. Su, *J. Colloid. Interf. Sci.*, **363**, 84 (2011).
19. F. Roncaroli, M.A. Blesa, *J. Colloid. Interf. Sci.*, **356**, 227 (2011).
20. R. Dittmann, E. Wintermantel, T. Graule, *J. Eur. Ceram. Soc.*, **33**, 3257 (2013).
21. E. Goneded, P. Karasinski, S. Drewniak, *Phys. E: Low-dimen. Sys. Nanostr.*, **62**, 128 (2014).

Calculation of particle size field in hydrocyclones

Yuekan Zhang, Peikun Liu*, Junru Yang, Lanyue Jiang, Yulong Zhang

College of Mechanical & Electronic Engineering Shandong University of Science and Technology, Qingdao-266590, China

Received June 18, 2016, Revised September 10, 2016

A study of particle motions in the hydrocyclone based on fluid rotational motion formula and fluid vortex rotation theory is proposed. The effects of radial flow on the flow field were included, as well as the Magnus lift force on particles at high rotational speeds. Also, equations for axial motion, radial motion and trajectory of particles were established and a regular distribution of particles was demonstrated. These were achieved by analysis of the motion of and forces on solid particles in the hydrocyclone. This study serves as a reference to future studies of hydrocyclone separation.

Keywords: Hydrocyclone, Particle size field, Calculation, Magnus lift force

INTRODUCTION

A hydrocyclone refers to a device that can realize heterogeneous separation based on the differences in particle size and density [1-4]. Upon entering the hydrocyclone, solid particles would experience rotational, axial and radial motions due to the effects of fluids and the velocity and direction of particle motion are dependent on the forces applied on the particles. As the separation of solid particles and fluids can be attributed to the relative sliding motion, it is of great significance to understand the interaction between solid particles and fluids. In this study, the effects of radial flow on the flow field and the Magnus lift force on particles in the hydrocyclone, which were neglected in previous studies, were considered. Based on the proposal that particles in the hydrocyclone were affected by various forces, including centrifugal force, gravity, centripetal buoyance, fluid resistance, and Magnus lift force [5-7], a more accurate force model of particles was developed and a regular distribution of particles was demonstrated.

DISTRIBUTION OF PARTICLE SIZE FIELD IN THE HYDROCYCLONE

To precisely predict the forces experienced by solid particles in the hydrocyclone, the effects of fluid radial motions on the particles should be included to develop an effective force model for the particles.

The equations of centrifugal and centripetal buoyance are as follows:

$$F_c = \frac{\pi}{6} d^3 \rho_s \frac{u_t^2}{r} \quad (1)$$

$$F_f = \frac{\pi}{6} d^3 \rho \left(\frac{u_t^2}{r} - u_r \frac{du_r}{dr} \right) \quad (2)$$

Where F_c and F_f are the centrifugal force and centripetal buoyance on the particle, respectively; d is the particle diameter; ρ_s and ρ are the densities of particles and fluid in a continuous phase, respectively; u_r is the radial speed.

The drag force on particles by the fluid can be described by:

$$F_d = \xi A \frac{\rho u^2}{2} \quad (3)$$

Where ξ is the resistance coefficient, which is a function of the Reynolds number (Re); u is the relative speed of fluid and particle; A is the area of particle projection in the radial direction:

$$A = \frac{\pi d^2}{4}$$

However, the forces experienced by particles are more complicated in real cases. Besides the centrifugal force, the centripetal buoyance and the fluid resistance, revolution caused by internal frictions between different laminar flows was observed as the particles are in a vortex with high rotational speeds. The rotational directions of particles in forced vortex zone and semi-free vortex zone (with the radius corresponding to the maximum tangential velocity (r_m) as the demarcation line) are opposite. The difference in the flow rate and pressure at the internal and external sides of the particle, which can be attributed to the gradient of particle velocity in the radial direction, results in a radial Magnus lift force towards the wall or the axis. In the semi-free vortex zone, the Magnus lift force is towards the axis as

* To whom all correspondence should be sent:
E-mail: lpk710128@163.com

the flow rate at the internal side is higher than that at the external side; in the forced vortex zone, the Magnus lift force is towards the wall as the external side is higher than that at the internal side. The significant laminar frictions experienced by particles at high rotational speeds in the hydrocyclone lead to rapid revolution and the effects of the Magnus force should be included. Cen et al[8] proposed an equation of Magnus lift force:

$$F_M = \frac{1}{8} \pi \rho d^3 u \omega \quad (4)$$

Where ω is the rotational angular speed of particles.

In the field of radial centrifugal forces in the hydrocyclone, the directions of Magnus lift forces are different in different vortex zones. Therefore, the forces on particles in the semi-free vortex zone and the forced vortex zone shall be discussed separately.

For particles in the semi-free vortex zone, centrifugal force (Fc), centripetal force by the fluid in continuous phase (Ff), dragging force by the fluid (Fd) and Magnus lift force (FM) are observed. The radial sedimentation of particles in the centrifugal force field can be described by:

$$F_c - F_f - F_d - F_M = m \frac{du}{dt} \quad (5)$$

Namely

$$\frac{\pi}{6} d^3 \rho_s \frac{u_t^2}{r} - \frac{\pi}{6} d^3 \rho \left(\frac{u_t^2}{r} - u_r \frac{du_r}{dr} \right) - \xi A \frac{\rho u^2}{2} - \frac{1}{8} \pi \rho d^3 u \omega = m \frac{du}{dt} \quad (6)$$

Where m is the particle mass. In cases where forces on the particles are balanced, uniform radial motion ($\frac{du}{dt} = 0$) was observed and the size of particles in the centrifugal force field of the hydrocyclone particle can be described by:

$$d = \frac{3\xi \rho u^2 r}{4(\rho_s - \rho)u_t^2 + 4r\rho u_r \frac{du}{dr} - 3r\rho u \omega} \quad (7)$$

Based on the tangential speed of the fluid $u_t r^n = c_1$ (constant), the following equation can be obtained:

$$\frac{u_t^2}{r} = \frac{c_1^2}{r^{2n+1}} \quad (8)$$

Based on the empirical formula of fluid radial speed $u_r r^m = -c_2$ (constant), m is the index number and $0 < m < 1$, the following equation can be obtained:

$$u_r \frac{du_r}{dr} = -\frac{mc_2^2}{r^{2m+1}} \quad (9)$$

By substituting Equation (8) and (9) into Equation (7), we can obtain:

$$d = \frac{3\xi \rho u^2 r^{2m+1}}{4c_1^2(\rho_s - \rho)r^{2m-2n} - 4c_3\rho - 3\rho u \omega r^{2m+1}} \quad (10)$$

Where $c_3 = mc_2^2$ (constant).

For particles in the semi-free vortex zone, the Magnus lift force is towards the wall and the radial sedimentation of particles in the centrifugal force field can be described by:

$$\frac{\pi}{6} d^3 \rho_s \frac{u_t^2}{r} - \frac{\pi}{6} d^3 \rho \left(\frac{u_t^2}{r} - u_r \frac{du_r}{dr} \right) - \xi A \frac{\rho u^2}{2} + \frac{1}{8} \pi \rho d^3 u \omega = m \frac{du}{dt} \quad (11)$$

In cases where forces on the particles are balanced, the size of particles in the centrifugal force field of the hydrocyclone particle can be described by:

$$d = \frac{3\xi \rho u^2 r}{4(\rho_s - \rho)u_t^2 + 4r\rho u_r \frac{du}{dr} + 3r\rho u \omega} \quad (12)$$

By substituting Equation (8) and (9) into Equation (12), we can obtain:

$$d = \frac{3\xi \rho u^2 r^{2m+1}}{4c_1^2(\rho_s - \rho)r^{2m-2n} - 4c_3\rho + 3\rho u \omega r^{2m+1}} \quad (13)$$

ξ is a function of Re , which can be described by:

$$Re = \frac{ud\rho}{\mu} \quad (14)$$

Where μ is the fluid viscosity.

If the relative motion between particles and the medium is regarded as a laminar flow, $Re < 1$. The viscosity force is the dominant resistance by the fluid and the Stoke's resistance coefficient is utilized as ξ . With $\xi = \frac{24}{Re}$ and Equation (14)

substituted into the Stoke's Equation, the following equation can be obtained:

$$\xi = \frac{24\mu}{ud\rho} \quad (15)$$

Herein, $d < 0.1$ mm.

If the relative motion between particles and the medium is regarded as a transition flow, $1 < Re < 1000$. The Allende's resistance coefficient is utilized as ξ . With $\xi = \frac{10}{\sqrt{Re}}$ and Equation (14)

substituted into the Allende's Equation, the following equation can be obtained:

$$\xi = \frac{10}{\sqrt{\frac{ud\rho}{\mu}}} \quad (16)$$

Herein, $0.1 \text{ mm} < d < 1.5 \text{ mm}$.

If the relative motion between particles and the medium is regarded as a turbulent flow, $Re > 1000$. The inertia resistance is the dominant resistance and the Newton's resistance coefficient is utilized as ξ ($\xi = 0.44$). Herein, $d > 1.5 \text{ mm}$.

If Re of particles is within the laminar flow zone, we can obtain the particle size distribution in the semi-free vortex zone and forced vortex zone by substituting Equation (15) and (10) into Equation (13), as follows:

$$d = \left(\frac{72u\mu r^{2m+1}}{4c_1^2(\rho_s - \rho)r^{2m-2n} - 4c_3\rho - 3\rho\omega r^{2m+1}} \right)^{\frac{1}{2}} \quad (17)$$

$$d = \left(\frac{72u\mu r^{2m+1}}{4c_1^2(\rho_s - \rho)r^{2m-2n} - 4c_3\rho + 3\rho\omega r^{2m+1}} \right)^{\frac{1}{2}} \quad (18)$$

If Re of particles is within the transition flow zone, we can obtain the particle size distribution in the semi-free vortex zone and forced vortex zone by substituting Equation (16) and (10) into Equation (13), as follows:

$$d = \left[\frac{30\mu^{\frac{1}{2}}\rho^{\frac{3}{2}}u^{\frac{3}{2}}r^{2m+1}}{4c_1^2(\rho_s - \rho)r^{2m-2n} - 4c_3\rho - 3\rho\omega r^{2m+1}} \right]^{\frac{2}{3}} \quad (19)$$

$$d = \left[\frac{30\mu^{\frac{1}{2}}\rho^{\frac{3}{2}}u^{\frac{3}{2}}r^{2m+1}}{4c_1^2(\rho_s - \rho)r^{2m-2n} - 4c_3\rho + 3\rho\omega r^{2m+1}} \right]^{\frac{2}{3}} \quad (20)$$

If Re of particles is within the turbulent flow zone, we can obtain the particle size distributions in the semi-free vortex zone and forced vortex zone by substituting $\xi = 0.44$ into Equation (10) and (13), as follows:

$$d = \frac{1.32\rho u^2 r^{2m+1}}{4c_1^2(\rho_s - \rho)r^{2m-2n} - 4c_3\rho - 3\rho\omega r^{2m+1}} \quad (21)$$

$$d = \frac{1.32\xi\rho u^2 r^{2m+1}}{4c_1^2(\rho_s - \rho)r^{2m-2n} - 4c_3\rho + 3\rho\omega r^{2m+1}} \quad (22)$$

According to the equations obtained, the particle size at r is proportional to the gyration radius, although the specific relation is complicated. Briefly, the gyration radius of the particle increases with its size and a regular distribution of particles along the radial direction is observed in the hydrocyclone. As a result, coarse particles are directed towards the underflow opening and fine

particles are directed towards the overflow opening.

Besides radial motions mentioned above, axial motions (upwards or downwards) of particles caused by internal vortex are also observed in actual cases. Gravity, buoyance, fluid resistance and Magnus lift force are applied on particles in the axial direction. The axial motion of particles can be described by:

$$\begin{aligned} & \frac{\pi}{6}d^3g(\rho_s - \rho) - \xi \frac{\rho u_b^2 \pi d^2}{8} - \frac{\pi}{8}\rho d^3 u_b \omega \\ & = \frac{\pi}{6}d^3\rho_s \frac{du_b}{dt} \end{aligned} \quad (23)$$

Where u_b is the relative sliding speed of particle and fluid in the radial direction.

Assuming that the accelerating stage in sedimentation is negligible, uniform radial motion ($\frac{du}{dt} = 0$) was observed and size of particles in the axial gravity field can be described by:

$$\frac{\pi}{6}d^3g(\rho_s - \rho) - \xi \frac{\rho u_b^2 \pi d^2}{8} - \frac{\pi}{8}\rho d^3 u_b \omega = 0 \quad (24)$$

The size distribution of particles in the axial direction can be described by:

$$d = \frac{3\xi\rho u_b^2}{4g(\rho_s - \rho) - 3\rho u_b \omega} \quad (25)$$

According to Equation (25), the particle size in the axial direction is determined by the physical properties of particles and fluids and not affected by the flow rate in the hydrocyclone. The size distribution of particles is dependent on the field of radial centrifugal force.

TRAJECTORY OF PARTICLES IN THE HYDROCYCLONE

For solid particles in a hydrocyclone, gravity, buoyance, fluid resistance and Magnus lift force are observed in the axial gravity field, while centrifugal force, centripetal buoyance, fluid resistance and Magnus lift force are observed in the radial centrifugal field. The accelerating stage is negligible as the forces on particles reach an equilibrium state in a short time. Due to the low Re in the axial sedimentation process, this process can be regarded as a Stoke's sedimentation.

The particle motion was investigated in a cylindrical coordinate system by substituting Equ (15) into Equ (25). The relative axial sedimentation rate of particles can be described by:

$$u_b = \frac{4g(\rho_s - \rho)d^2 - 3\rho\omega d}{72\mu} \quad (26)$$

The sedimentation rate of the fluid in the field of

axial gravity is defined as v and the sedimentation rate of particles in the fluid can be obtained by:

$$v + u_b = v + \frac{4g(\rho_s - \rho)d^2 - 3\rho\omega d}{72\mu} \quad (27)$$

In cases where both axial and radial forces experienced by particles are in equilibrium, particles would rotate along the axis at ω . At the same time, sedimentation along the axis at the speed described in Equation (27) is observed for these particles. Therefore, the location of a particle at time = t can be described by:

$$\begin{aligned} x &= r \cos \omega_r t \\ y &= r \sin \omega_r t \\ z &= \left[v + \frac{4g(\rho_s - \rho)d^2 - 3\rho\omega d}{72\mu} \right] t \end{aligned} \quad (28)$$

Equation (28) are the combined spiral vortex parameter formula for particle sedimentation and equation of particle trajectory. At a certain pressure, particles would get into the hydrocyclone with the fluid and be distributed to their respective rotational tracks in a short time. A regular spatial distribution due to the effects of particle size on its rotational radius can be observed.

CONCLUSIONS

The separation of solid particles and fluids can be attributed to the relative sliding motion caused by forces experienced by the particles. Besides centrifugal force, gravity, centripetal buoyance and

fluid resistance, Magnus lift force is also applied on the particles in a hydrocyclone. Based on conventional rotating flow theory, a force model of particles in a hydrocyclone was established with effects of radial flows and the Magnus lift force taken into consideration. Additionally, equations for the trajectory of particles were established and a regular distribution of particles was demonstrated. This study serves as a reference to future studies of hydrocyclone separation.

Acknowledgments: This work is supported by the National Natural Science Foundation of China (No.21276145) and Natural Science Foundation of Shandong Province (ZR2013EEM016).

REFERENCES

1. D. Bradely, The hydrocyclone. London: Pergamon Press, 1965.
2. L. Svarovsky, Hydrocyclones, Holt, Rinchart and Winston, London, 1984.
3. K. Rietema, *Eng. Sci.*, **15**, 298 (1961).
4. J. Dueck, O. Matvienko, *Theoretical Foundations of Chemical Engineering*, **34**, 428 (2000).
5. M. Ghadirian, E.R. Hayes, J. Mmbaga, *The Canad. J. Chem. Eng.*, **91**, 950 (2013).
6. E.W. Chuan-Lim, Y.R. Chen, C.H. Wang, *Chem. Eng. Sci.*, **65**, 6415 (2010).
7. H.L. Wang, Y.H. Zhang, J.G. Wang, H.L. Liu, *Chin. J. Chem. Eng.*, **20**, 212 (2012).
8. K.F. Cen, J.R. Fan, *J. Zhejiang Univ.*, **21**, 111 (1987).

Change characteristics of chlorophyll content and high spectrum in soybean leaves under the stress of CO₂ leakage

Ruijuan Hao^{1,2}, Zhoufeng Wang^{1,2}, Wenke Wang^{1,2*}, Yaqian Zhao^{1,2}

¹ Chang'an University, Environmental Science and Engineering College, Shaanxi Xi'an, 710054, China

² Key Laboratories for Underground Hydrology and Ecological Efficiency of the Education Ministry of China, Shaanxi Xi'an, 710054, China

Received June 23, 2016, Revised September 14, 2016

The carbon capture and storage (CCS) may have the problem of leakage and ecosystem equilibrium may be changed due to the affected soil biological system and plants after CO₂ leaking into the soil. By measuring the hyperspectral reflectance and chlorophyll content in soybean leaves under the stress of CO₂ leakage as well as the continuum removal disposal and derivative spectrum calculation for hyperspectral data within the wavelength range of 400~800nm, 10 spectral feature parameters of absorption valley position, normalized reflectance at the absorption valley position, absorption depth, green peak position, normalized reflectance at the green peak position, red edge position, normalized reflectance at the red edge position, red shoulder position, absorption width and spectrum symmetry could be achieved. The correlation analysis of high spectrum and change characteristics of chlorophyll content in soybean leaves based on analysis of physical significance for above parameters is thus conducted. The result has shown that, under the stress of CO₂ leakage, the chlorophyll content change, absorption valley position, normalized reflectance at the green peak and red edge position are closely related and in this way, the chlorophyll content equation: $Y = -19575 + 11.9X_1 - 45.1X_2 + 17.6X_3$ is obtained. The result of study in this paper has an important practical significance and application value for ground surface eco-environment monitoring and evaluation of CCS projects and remote sensing monitoring of CO₂ leakage points.

Key Words: Hyperspectral reflectance, Chlorophyll content, Stress of CO₂ leakage.

INTRODUCTION

Intergovernmental Panel on Climate Change (IPCC) has pointed out in 2014 Report that, the global surface temperature was increased an average of 0.85 °C from 1880 to 2012. It was mainly caused by greenhouse gases, to be specific, the emission of CO₂ [1]. The carbon capture and storage (CCS) can capture, liquefy and geologically sequester the CO₂, which helps reduce the emission of CO₂. For this reason, it is a novel initiative to cope with the global climate changes [2]. CCS engineering projects operate well and no CO₂ leakage examples are reported, but leakages may also occur in the storage period. The ecosystem equilibrium may be changed due to affected soil biological system and plants after CO₂ leaking into the soil [3-5]. How to formulate a set of effective means to rapidly detect the CO₂ leakage points in the CCS period is the key link for geological storage of CO₂. The surface monitoring can only be applied for small areas, while in large areas, lots of manpower and equipment investment

response of plants. Based on this, leakage points of CO₂ may be found out by monitoring spectral characteristics of stressed plants by the remote sensing monitoring technique [6].

The chlorophyll is a basic composition of plant leaves, whose content is an important condition for exchange of substance between plants and the outside world as well as a significant index for plant nutritional stress and growing development state [7-9]. The growth of plants could be monitored and stress degree of plants could be estimated upon monitoring for chlorophyll content changes in the Soybean leaves. The conventional chlorophyll measurement methods would take a long time period and cause damages to the vegetation. The measuring accuracy may be affected by the chlorophyll content changes due to the lost part of chlorophyll during the transportation and sample preparation from field to laboratory [10]. As a non-invasive chlorophyll measurement method, high spectrometer could measure the chlorophyll content by measuring the reflectance, transmittance and absorptive of green plant leaves [11]. Therefore, it decides the unique effect for high spectrum technology in the measurement of chlorophyll content. The spectral characteristics of ground vegetation and bio-physical parameters present a significant correlation. The study result of Yunhao

To whom all correspondence should be sent:
E-mail: wenkew@chd.edu.cn

are required. The plants are often covered in geological storage areas of CO₂, so leakage may lead to the increased CO₂ concentration and stress

CHEN, et al [12] found that, the stress of CO₂ leakage may obviously reduce the beet chlorophyll content and leaf water content, wherein the leaf reflectance is reduced at 550nm and increased at 680nm. The study result of Jinbao JIANG, et al [13] found that, if the volume fraction of CO₂ in the soil is equal or greater than 15%, Area (510~590 nm) index can better recognize the stressed soybeans of higher separation ability and stability. However, if the volume fraction of CO₂ in the soil is smaller than 15%, Area (510 ~ 590 nm) index cannot exactly identify the stressed soybeans during the whole growth period.

The reports for change laws of chlorophyll content by hyperspectral characteristic parameters under the stress of CO₂ leakage are based on the artificially controlled CO₂ release concentration and there's no report on change laws of chlorophyll content by hyperspectral characteristics under the stress of natural CO₂ leakage. There are abundant data materials available by high spectrum remote sensing technique. There's no unified definition to determine which parameter could have a more significant reflection on change characteristics of vegetation stressed by the CO₂ leakage. Hence, this paper used the soybeans grown under the stress of natural CO₂ leakage as experimental materials, analyzed the differences in reflectance spectrums of soybean leaves by measuring multi hyperspectral parameters and chlorophyll contents in different leakage conditions, delved into hyperspectral characteristic parameters under the stress of natural CO₂ leakage as well as selected and calculated the built-up model of spectral characteristic parameters that could effectively reflect the stress influence of soybeans.

SELECTION OF TEST AREA AND TESTING METHOD

Selection of test area

The test area is located in First-Terrace Trailing Edge of Qijiachuan River Valley, 0.5km away from Sanhe Town, Ping'an County, Xining City, Qinghai Province, wherein an artesian hot well of CO₂ gas-water mixing high pressure is drilled out. The well is located at 36°25'29"E and 101°56'28"N, whose depth is 192.08m, aquifer thickness of CO₂ gas-water mixing is 35.09m, artesian discharge at the well mouth is 156.82m³/d and water temperature is 17 °C.

Testing method

Measurement on effect of CO₂ leakage stress in test area. This test area is an area dividing the

vegetation effects in the shape of half round, which is centered by the artesian hot well of CO₂ gas-water mixing high pressure, in where soybean plants were randomly selected in testing areas for measurement of spectrum and chlorophyll content. A CO₂ testing probe was installed in each testing area to measure the CO₂ leakage concentration and hence to determine the heavy stress area, medium stress area and mild stress area. At the same time, the local soybean plants free from CO₂ are selected to act as the control blank (CK).

Measurement on simple-leaf spectrum. This paper measured the soybean leaf spectrum by blade clip allocated by ASD Field Spec 4 from 10AM to 2PM on 10 August 2015. The measurement was conducted under the condition of stable light and cloudless sky with the wind power less than level 3. In order to measure the influence on spectrum measurements by rolled leaves, the measurement on each leaf for 4 times and each time for 90°. The correction using the standard white plate was conducted for once on each leaf. For measurement, 10 leaves of same growth conditions were selected in each test area and the mean was selected as the spectral value of leaves in this testing area.

Measurement on chlorophyll content. The measurement on chlorophyll content in soybean leaf by CCM-300 chlorophyll measurement instrument at the moment the spectroscopic data was collected. This paper selected different leaves of upper, middle and lower vertical layers of soybean plants on each collection point to avoid the venation, wherein 10 soybean leaves were selected from each layer and totally 30 soybean leaves in each test area. The mean value was thus acted as the data of chlorophyll content in soybean leaf.

Pre-processing of spectral data

Five-spot smoothing method. The smoothing process of spectral data could effectively remove the interference of high-frequency noise, wherein the denoising capacity may be enhanced due to the increased smoothing points. But if the selected smoothing points were too large, they would remove some useful signals as well and thus lead to the signal distortion. This paper made the smoothing preprocessing of spectral data by using the five-spot smoothing method and after thus processing, the spectral outline was more clear [14].

Continuum removal. The reflectance is not only affected by the biophysical and biochemical parameters of vegetation, but also is sensitive to light conditions when sampling. The absorbed electromagnetic waves by the vegetation mainly occur within the scope of visible spectrum. For this

ground, continuum removal was used for normalized processing of reflectance spectrum within the waveband of 400-800nm. In this way, weakening the influence of light conditions when collecting the spectrum could achieve the comparability between data, whose values reflect the differences in amount of information carried in the absorption characteristic waveband period by spectrum with different exchange ways. Due to these reasons, the continuum removal is a spectrum analysis method effectively enhancing the interested absorption characteristics [15].

Derivative spectrum. The spectrum position represented by maximum value of first-order differential in the reflectance spectrum within the vegetation red edge waveband is called as “red edge” [16]. The calculation way for the first-order derivative of reflectance spectrum is presented as follows:

$$D_{\lambda_i} = \frac{R(\lambda_{i+1}) - R(\lambda_{i-1})}{\lambda_{i+1} - \lambda_{i-1}}$$

In the equation, D_{λ_i} is the first-order derivative spectrum of wave length λ_i and $R(\lambda_i)$ is the spectral reflectance of wave length λ_i , wherein λ_i is the wave length of each waveband.

RESULTS AND ANALYSIS

Biology characteristic of soybean under different CO₂ leakage stressed level

If CO₂ of certain concentration was leaked into the vadose zone, replacement reaction between it and oxygen in the soil may occur and thus lead to the soil acidification. Hence, the photosynthesis and respiration of plants may be limited and biology characteristics of vegetation may be changed [17-19]. This paper observed and recorded the leaf shape, color, plant height, stem growth situations and biology characteristics of legume under different CO₂ leakage stressed level, and the results are presented in Table 1.

Table 1. Biology characteristics of soybean under the stress of CO₂ leakage

Biology Characteristics	Heavy Stress	Medium Stress	Mild Stress	Control Blank
Leaf Shape	Mostly Curved	Partly Curved	Slightly Curved	No curve
Leaf Color	Yellow Green	Yellow Green	Green	Green
Plant Height	140cm	145cm	152cm	159cm
Plant Stem	Partly Lodged	Slightly Lodged	No Lodge	No Lodge
Legume	Mostly Curved	Partly Curved	Slightly Curved	No curve
CO ₂ Concentration	30-40%	20-30%	10-20%	0.3%

From Table 1, the soybean leaf and legume under different CO₂ leakage stressed level are curved in varying degrees and when the CO₂ stressed level reaches over 20%, the leaf color may be affected. Specifically, those plants may present a color of yellow green than healthy leaves, stems may lodge at different levels and the plants may present the feature of small size. It can thus be seen that, the CO₂ concentration in normal soil is relatively low; if CO₂ concentration is increased to 10%, it may cause a significant adverse effect on the growth of plants; if CO₂ concentration is increased to 20%, it may obviously impact the biology characteristics of plants; if CO₂ of high concentration may exist on land surface for a long time, which plants are hard to live.

Spectral characteristics analysis

Absorption valley position and absorption depth. The wavelength corresponded by the lowest point on the reflection curve of soybean leaf was acted as the absorption valley position and the absorption extent of that wavelength point was calculated as the absorption depth to reflect change

features of absorption valley position on the leaf spectrum under different CO₂ leakage stressed level.

Figure 1 is the reflectance spectrum of disposed soybean leaf by five-spot smoothing method and continuum removal method. The photosynthetic pigment in palisade tissue may strongly absorb the blue and red light and relatively reflect green light, the soybean spectrum curve may thus lead to an absorption valley (red light of about 670nm) and a reflection peak (green light of about 550nm) in the visible spectrum (400-800nm).

The largest absorption valley position among all kinds of CO₂ leakage stress and control blanks is located at approximately 670nm with the biggest variability rate of 5nm, showing that the position of absorbed valley bottom is determined by characteristics of the absorbed substance (refer to Table 2). The green peak height of soybean leaf stressed by CO₂ leakage was obviously greater than that in the control blank and the depth of absorbed valley bottom was shallower than that in control blank. As the CO₂ leakage stress increases, the absorption depth presents the reduction trend (refer to Figure 1). It is mainly caused by the

reduced absorption capacity when the soybean leaves were stressed by the CO₂ leakage. It can be seen that, the absorption depth of the absorbed valley bottom is determined by the absorption capacity of visible light by the soybean leaves.

Green peak position and red edge position.

From Table 2, the difference between green peak positions in CO₂ leakage and control blank is not significant. The green peak position in the heavy and medium stress area is at approximately 554nm, while the green peak position in the mild stress area and control blank is at approximately 552nm. It has indicated that the green peak position has no determined numerical relationship between the CO₂ leakage stress extent (refer to Table 2). However, as CO₂ leakage stress enhances, the chlorophyll content in soybean leaves would

present an obvious reduction trend and the reflectance of soybean leaves in different CO₂ leakage areas may increase due to the reduced chlorophyll content in areas centered by 550 nm (refer to Figure 1). It has indicated that the CO₂ leakage stress may exert some impacts on the green peak characteristics by exerting the impact on the chlorophyll content.

As the most conspicuous symbol of plant spectrum, the red edge is caused by the strong reflection, which is formed by strong absorption of chlorophyll in red waveband and multiple scattering inside of leaf in the near-infrared waveband of plants [20]. This paper showed that, when the leaves were stressed by the CO₂ leakage, the red edge wavelength may have the following

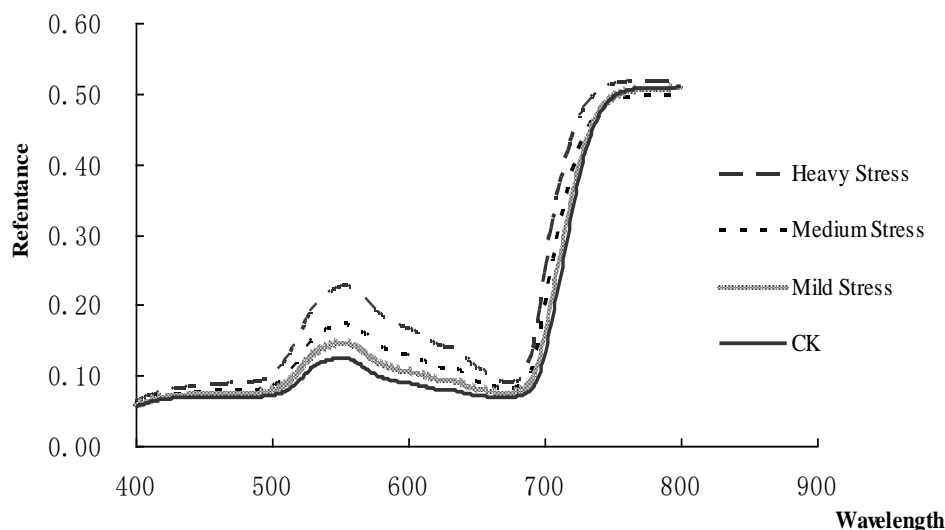


Fig. 1. The leaf reflectance curve of soybean after the pretreatment.

Table 2. Spectral characteristics of soybean under the stress of CO₂ leakage and control blank.

Spectral Characteristics	Heavy Stress Area	Medium Stress Area	Mild Stress Area	Control Blank
Maximum Absorption Wavelength (nm)	673	672	671	668
Reflectance at Maximum Absorption Wavelength	0.0898	0.0808	0.0738	0.0681
Maximum Absorption Depth for Spectral Band	0.9102	0.9192	0.9262	0.9319
Green peak Wavelength (nm)	554	554	552	552
Reflectance at Green peak Wavelength	0.2266	0.1734	0.1456	0.1249
Red Edge Wavelength (nm)	699	702	707	715
Reflectance at Red Edge Wavelength	0.0137	0.0115	0.103	0.0107
Red Shoulder Wavelength (nm)	774	785	791	799
Absorption Width (nm)	220	231	239	247
Degree of Symmetry	0.3254	0.2320	0.2262	0.1898
Chlorophyll Content	720.07	763.27	840.47	946.23

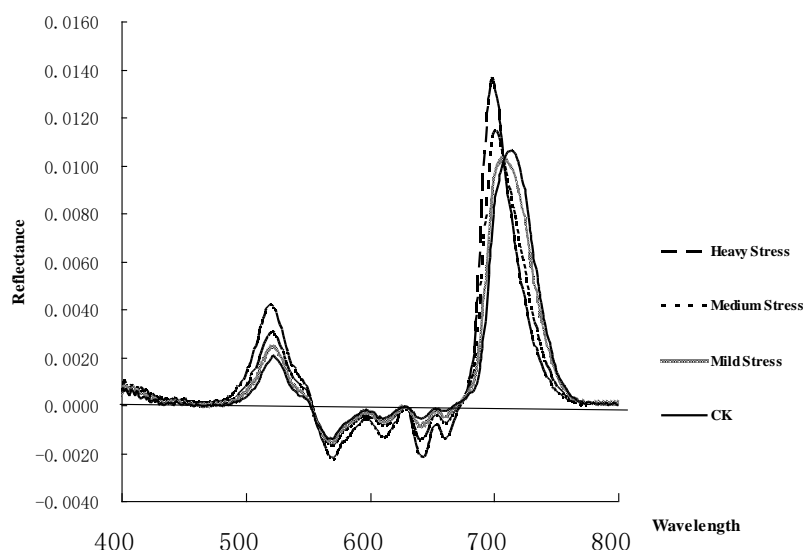


Fig. 2. Derivative spectrum of soybean leaf under the stress of CO₂ leakage.

relationship: heavy stress area (699nm) <medium stress area (702nm) <mild stress area (707nm) <CK (715nm). That is to say, the red edge of soybean leaf may move to the short wave direction as the CO₂ leakage stress extent enhances, i.e. blue-shifted phenomenon (refer to Table 2). It thus appears that the red edge position is a good index to reflect the CO₂ leakage stress.

Absorption width and red shoulder position.

Absorption width refers to the wavelength difference between red shoulder position and green peak position. This study has demonstrated that, the variation tendency for absorption width and stress level of soybean leaf spectrum curve stressed by the CO₂ leakage may be opposite. The larger the stress level is, the smaller the absorption width would be (refer to Table 2).

Red shoulder position refers to the wavelength position where the maximum reflectance in visible light waveband located. This study has demonstrated that, the red shoulder position has something to do with the effect of CO₂ leakage stress, wherein the maximum reflectance wavelength at the red shoulder position in the unstressed areas is the largest. It is unanimous to the red edge position and so does the change law of absorption width (refer to Table 2).

Degree of symmetry. The degree of symmetry refers to the ratio between left side area of absorption and the absorption area, reflecting the symmetry of spectral reflectance characteristics. This study demonstrated that, as the CO₂ leakage stress level increases, the spectral curve may present an increased trend in areas in the direction of short wave (refer to Table 2).

Measurement and analysis for chlorophyll content

Variance about the chlorophyll content.

This paper made the single factor variance analysis for chlorophyll contents of soybean with control blank and under different measured CO₂ stresses, and under the condition of variance analysis results significantly.(as shown in Table 3). Based on this, the least significant difference (LSD) method was adopted to make multiple comparisons in stress and control blanks and thus to determine the difference of chlorophyll content in all kinds of treatments. The results are presented as below:

Table 3. Variance about the change of chlorophyll content of soybean under CO₂ stress.

Source of variation	SS	S ²	F
Among treatment	3 920822.42	306940.81	44.11**
Within treatment	16 807174.57	6958.40	
Total variation	119 1727996.99		

*) F (3,116)x0.05=2.69; F (3,116)x0.01=3.96

Table 4. The results of multiple comparisons about the change of chlorophyll content of soybean under CO₂ stress (LSD).

Treatment	Chlorophyll Content	0.05	0.01
CK	946.23	a	A
Mild Stress	840.47	b	B
Medium Stress	763.27	c	C
Heavy Stress	720.07	d	C

From factor variance analysis and multiple comparison results for changes of chlorophyll content, the chlorophyll content in the control blank is significantly greater than other treatments stressed by the CO₂ stress to an extreme extent; a significant

difference, but not an extremely significant difference, exists between the heavy stress and medium stress treatment, while there's a significant difference to an extreme extent between the heavy stress and mild stress (refer to Table 4). It follows that, if the soybean was suffered from the effect of CO₂ stress, its chlorophyll content may be reduced as the stress level increases.

Stepwise multiple regression equation for chlorophyll content. By taking the above 10 spectrum parameters as the independent variable and chlorophyll content as the dependent variable, the following relationship is obtained by the stepwise multiple regression:

$$Y = -19575 + 11.9X_1 - 45.1X_2 + 17.6X_3$$

Wherein, X₁ is the absorption valley bottom position, X₂ is the normalized reflectance at the green peak position, X₃ is the red edge wavelength and coefficient of determination is R²=0.8942. It has shown that, the absorption valley position and normalized reflection at green peak of soybean leaf obtained by measuring the soybean leaf spectral curve as well as the red edge wavelength achieved by the derivative function could invert the relation between the hyperspectral curve and chlorophyll content changes stressed by the CO₂ stress. Besides, chlorophyll content respectively has a negative correlation with the normalized reflection at green peak and positive correlation with red edge wavelength. The normalized reflection at absorption valley bottom, absorption depth, green peak wavelength, normalized reflection at red edge, red shoulder wavelength, absorption width and degree of symmetry cannot better reflect the changing relationship between the soybean leaf spectral curve and chlorophyll content stressed by the CO₂ stress. For these grounds, these parameters are not suitable to be selected to invert the law of change for the stressed chlorophyll content.

DISCUSSIONS

The absorption, reflection and scattering effect on light by plants constitute characteristic spectrum. The reflection low valley in the visible band (blue light and red light at 0.45 and 0.67μm) is mainly caused by strong absorption of photosynthetic pigments inside of palisade tissue. The "reflection plateau" formed at the near-infrared band (0.7-1.3μm) is caused by multiple reflections and scatters of "water-air interface" in the internal structure of plant leaves (spongy tissue). There are 3 obvious absorption valleys in the middle-infrared band greater than 1.3μm (located at 1.45, 1.94 and 2.7 μm, respectively), which is mainly caused by the

strong absorption of liquid water in the leaves [21]. The "blue edge" (transited from blue to green) in the visible band, green peak, "yellow edge" (transited from green to red), red light low valley and near-infrared "red edge" transited from the red light are important indicating bands to describe the leaf pigment situation and physical condition. This paper found that, affected by CO₂ of high concentration, the visible band and near-infrared band of plants both present a relatively significant difference, having a better correlation with CO₂ concentration. It also demonstrated that the information materials stressed by CO₂ leakage by measuring the plant spectral data could be obtained under the field in-situ conditions.

Some studies on response problems of aboveground vegetation caused by leakage of CO₂ geologic sequestration at home and abroad have been conducted, but most were made under the condition of artificially controlled CO₂ concentration, which has some differences with the natural CO₂ leakage method and law. This paper employed the natural CO₂ leakage conditions to analyze physiological responses and hyperspectral characteristics of plants, whose results may better reflect the actual CO₂ leakage situation. Upon study on spectral change characteristics of the aboveground vegetation stressed by CO₂ leakage, Yunhao CHEN, et al designed ratio R550/R680 to recognize the beet stressed by CO₂ leakage. The study made by Jinbao JIANG, et al was designated to adopt the area vegetation index Area (510~590nm) to recognize the soybean stressed by CO₂ leakage. But among relatively many parameters reflecting spectral characteristics changes of vegetation, which parameter(s) would better reflect the spectral characteristics stressed by CO₂ leakage? There's no unified definition to answer such question. Then spectral feature parameters were selected by this paper to conduct the analysis. By selecting ten main spectral parameters and making analysis for these parameters, this paper demonstrated that, the red edge position, absorption width, red should position, degree of symmetry and other important element have a significant difference under different CO₂ concentrations, respond to the varying environment at all kinds of levels and the indicated technology indexes would also have certain difference. Hence, the single-factor indication and discrimination method may undervalue or overvalue the reaction to the external environment by plants. This paper used the stepwise regression to find out 3 characteristic parameters closely related to the chlorophyll content of soybean leaf, preliminarily established the regression equation integrating the responsive

technical indexes and thus obtained a more reliable result in theory. Featured in the low cost, large monitoring area and instantaneity, the hyperspectral remote sensing is a possible effective means to judge the leakage of CO₂ geological storage by the spectral change characteristics of vegetation.

The morphological characters and anatomic structure of plant leaf has an extremely active change response and adaptation to environmental factors. By revealing the hyperspectral curve response of soybean leaf stressed by CO₂ leakage condition, this paper found out the significant change of the spectral characteristics in visible, infrared and near-infrared bands, which may have something to do with adaptive changes in the leaf shape, epidermis characteristics and basic anatomical structure, etc. Some studies have demonstrated that, under the condition of CO₂ with high concentration, the leaf thickness often presents an increasing tendency, wherein the change trends may vary due to the different thickness of tested plant epidermis, mesophyll parenchyma and collenchymas as well as the proportion taken account in the total thickness [22]. The morphological characters and anatomic structure of plant leaf from different photosynthetic pathways have a difference on the response to CO₂ with high concentration. The multiplied CO₂ concentration would significantly increase the C₃ leaf thickness and reduce the number of top surface porosity and remain insignificant changes on C₄ leaf thickness and increase the number of surface porosity. Besides, the chlorophyll content of C₃ leaf as well as the number and volume of chlorophyllin in bundle sheath cells were reduced to a great extent than that of C₄ leaf [23]. Upon the analysis for hyperspectral data stressed by the CO₂ leakage, this study has demonstrated that the chlorophyll content of soybean leaf would present an obvious reduction trend as the stress level enhances, wherein such change trend has something to do with the CO₂ stress response. The existing studies on morphological anatomy of soybean leaf is not sufficient, so this part should be appropriately added in future work based on the spectral data to conduct the corresponding analysis with spectral characteristics changes.

CONCLUSIONS

This paper calculated and obtained spectral feature parameters related to the soybean stressed by CO₂ leakage by measuring the hyperspectral data and chlorophyll contents of soybean leaf stressed by CO₂ leakage. By the stepwise regression analysis of spectral feature parameters and chlorophyll content, this paper obtained the change law that can be used to analyse the chlorophyll content with hyperspectral

remote sensing and thus analysed the extent of CO₂ leakage stress.

The reflection spectrum feature analysis for soybean leaf stressed by CO₂ leakage has shown that, the absorption depth, normalized reflection at absorption valley, normalized reflection at green peak, red edge position, red shoulder position, absorption width and degree of symmetry of spectral characteristic parameters for soybean leaf during the mature period have a definite relation with the change of CO₂ leakage stress and have no definite numerical relationship with the absorption valley position and green peak position.

The multiple stepwise regression analysis for chlorophyll content by using the spectral feature parameters has shown that, chlorophyll content respectively has a negative and positive correlation with the normalized reflection at green peak and red edge wavelength, whose inversion equation is $Y = -19575 + 11.9X_1 - 45.119X_2 + 17.573X_3$.

It has indicated that, the inversion model for hyperspectral chlorophyll established based on the stepwise regression can be used to reflect the relation between the hyperspectral reflectance curve and chlorophyll content.

Mastering the chlorophyll content and spectrum characteristics of soybean leaf stressed by CO₂ leakage, especially the normalized reflection at green peak and red edge position, may be conducive to analyse the extent of stress on the soybean, offering theoretical foundations for CCS project site selection, monitoring and evaluation of ground surface eco-environment and remote sensing CO₂ leakage points, etc.

Acknowledgements: This work was supported by the National Science Foundation of China (NSFC, Grant No. 41202164), State Key Laboratory of Loess and Quaternary Geology, Institute of Earth Environment, CAS (SKLLQG 1012), Special Fund for Basic Scientific Research of Central Colleges, Chang'an University (Grant No 2013G1291069), and the Open Research Fund of Key Laboratory of Subsurface Hydrology and Ecological Effect in Arid Region, Ministry of Education (2013G1502041).

REFERENCES

1. IPCC Fifth Assessment Report (AR5). IPCC Fifth Assessment Report on Climate Change. Cambridge University Press, Cambridge, UK, (2014).
2. M. Shigeo, F. Yuichi, *IEEJ Trans. Electrical Electronic Eng.*, **3**, 37 (2008).
3. I. Macek, H. Pfan, V. Francetic, *Environ. Exp. Botany*, **54**, 90 (2005).
4. S.E. Beaubien, G. Ciotoli, P. Coombs, *Int. J. Greenhouse Gas Control*, **2**, 373 (2008).

5. M.A. Celia, C.A. Peters, S. Bachu, Geological storage of CO₂: leakage pathways and environmental risks, *American Geophysical Union, Spring Meeting*, (2002).
6. L. Bateson, M. Vellico, S.E. Beaubien, *Int. J. Greenhouse Gas Control*, **2**, 388 (2008).
7. I. Nijs, T. Behaeghe, I. Impens, *J. Biogeography*, **22**, 173 (1995).
8. Zhang J.H., Wang K., Wang R.C., Study on hyper spectral remote sensing in estimate in estimate vegetation leaf chlorophyll content, *J. Shanghai Jiaotong University: Agric. Science*, **21**, 74 (2003).
9. C.S.T. Daughtry, C.L. Walthall, M.S. Kim, *Remote Sens. Environ.*, **74**, 229 (2000).
10. A.C. Madeira, A. Mendonca, M.E. Ferreira, *Soil Science Plant Analysis*, **31**, 631 (2000).
11. E.W. Chappelle, M.S. Kim, J.E. McMurtry III, *Remote Sens. Environ.*, **39**, 239-247 (1992).
12. Chen Y.H., Jiang J.B., D.S. Michael, *Spectroscopy&Spectral Analysis*, **32**, 1882 (2012).
13. Jiang J.B., D.S. Michael, He R.Y., *Trans. Chinese Soc. Agric. Eng.*, **29**, 163 (2013).
14. Zhang L., Lu H.S., Yan H.W., *Spectroscopy& Spectral Analysis*, **33**, 3212 (2013).
15. Zhang L.P., Zhang L.F., *Hyperspectral Remote Sensing*, Beijing: Surveying and Mapping Press, 2011, pp. 98-99.
16. Wang X.Z., Wang R.C., Huang J.F., *Trans. Chinese Soc. Agric. Eng.*, **18**, 9 (2002).
17. D. Bergfeld, W.C. Evans, J.F. Howle, *J. Volcanology&Geothermal Research*, **152**, 140 (2006).
18. C.D. Farrar, M.L. Sorey, W.C. Evans, *Nature*, **24**, 675 (1995).
19. B.A. Martini, E.A. Silver, D.C. Potts, *IEEE Int. Geosci. Remote Sens. Symp. Honolulu, HI*, 2000, pp. 24-28.
20. G.A. Carter, *Amer. J. Botany*, **80**, 239 (1993).
21. Pu R.L., Gong P., *Hyperspectral Remote Sensing and its Applications*, Beijing: Higher Education Press, 2000.
22. G.A. Carter, R. Bahadur, R.J. Norby, *Environ. Exper. Botany*, **43**, 267 (2000).
23. Ou Z.Y., Peng C.L., *J. Trop. Subtrop. Botany*, **11**, 190 (2003).

The development and in vitro evaluation of Coenzyme Q10 long-circulating liposomes

Shuoye Yang

College of Bioengineering, Henan University of Technology, Zhengzhou, P. R. China

Received June 18, 2016; Revised September 10, 2016

To prepare Coenzyme Q10 (CoQ10) long-circulating liposomes by three most commonly used preparative methods, dry-film, reverse phase evaporation and ethanol injection. The resulting samples were contrasted through morphology observation, particle size and zeta potential analysis. Free drugs and liposomes were separated using protamine aggregation method and entrapment efficiency was determined. HPLC assay for determination of CoQ10 in vitro was developed, and its release property was studied by using dialysis method. The results showed that liposomes prepared by dry-film method were of best quality and stability. The HPLC assay developed was specific, rapid and reliable, which can be used to determine lomustine and iohexol in vitro accurately. In vitro release tests showed that the release profile of CoQ10 from liposomes at 37 °C fitted to the Weibull release kinetics, with the equation of $\ln \ln [1/(1-Q)] = 2.0352 \ln t - 4.6143$. The formulation and preparative method can be used to prepare CoQ10 long-circulating liposomes with high entrapment efficiency and good release behavior.

Key words: Coenzyme Q10, long-circulating liposomes, Preparative methods, Encapsulation efficiency, in vitro release.

INTRODUCTION

Coenzyme Q10 (CoQ10) is one of ubiquinone compounds, as an endogenous fat-soluble molecule, it plays an essential role in the production of cellular energy in mitochondria in the form of ATP [1]. CoQ10 consists of a redox active quinoid moiety and is also a vitamin-like substance present in many organisms. Through functioning as an electron carrier in the electron transport chain, CoQ10 can help to energy conservation, while the reduced form of CoQ10 is capable of scavenging free radical oxygen intermediates [2]. Furthermore, CoQ10 efficiently decreases the damage from peroxidation and free-radical-induced oxidative reaction to the membrane phospholipids, mitochondrial DNA and membrane proteins [3, 4]. Thus its ability to scavenge free radicals makes CoQ10 a promising potential anti-cataract agent.

Nowadays, potential health benefits and therapeutic value of CoQ10 supplementation have been well recognized, and it has been widely consumed as one kind of food supplement or drug. It was reported that insufficiency of CoQ10 causes a series of health disorders resulting from mitochondrial dysfunction. Numerous studies have indicated that CoQ10 deficiencies may lead to cardiovascular disease, neurodegenerative disorders, diabetes, and even cancer [5,6]. However, as a synthesized compound inside the human body,

CoQ10 would be reduced by increasing age [7]. On the other hand, despite the nutraceutical and pharmaceutical benefits, the application of CoQ10 is largely hampered as a therapeutic agent due to its low bioavailability with high variability after oral administration [8]. The incomplete bioavailability of CoQ10 should attribute to its extreme hydrophobicity, large molecular weight, instability to light and thermolability, especially the insignificant solubility in aqueous media might be the critical factor for its poor bioavailability and poor delivery properties [9]. To promote the uptake by peripheral tissues and the blood brain barrier and improve the oral absorption of this bioactive molecule, numerous approaches have been undertaken to enhance the solubility of CoQ10, involving the use of oil solutions, solid dispersion system, nano- and micro-emulsions and the self-emulsified drug delivery system [10-12]. Among the above novel formulations, colloidal drug delivery systems, such as liposomes, are regarded as the effective means to obtain improved bioavailability in comparison with liquid formulations [13]. Liposomes are preferable because they have good characteristics such as easy delivery, no interference with vision, stabilizing effect and high drug loading efficiency. Nevertheless, liposomes are generally rather unstable and tend to degrade or aggregate under ordinary conditions, leading to leakage of entrapped drug during storage or after

To whom all correspondence should be sent:
E-mail: yangshuoyecpu@163.com

administration. To prevent these disruptive influences, a number of research efforts have been made, including surface modification by using long-circulating materials, which is an effective way to improve liposomal stability both in vitro and in vivo.

The present study was undertaken to develop a new CoQ10 long-circulating liposomes, with DSPE-PEG (2000) as long-circulating material. The liposome prepared by three different methods was investigated with particle size and zeta potential as assessment index. The protamine aggregation method was developed to determine the encapsulation efficiency, and their in vitro release characteristics were investigated in details, to provide elementary experiment reference for the practical use in clinic.

MATERIALS AND METHODS

Chemicals and reagents

CoQ10 was purchased from Aladdin Industrial Corporation, soybean phospholipid (SP) was purchased from Shanghai Tywei Pharmaceutical Co., Ltd, DSPE-PEG (2000), DPPG and cholesterol were purchased from Avanti Polar Lipids (Alabaster, AL, USA). Protamine Sulfate injection was provided by Shanghai No.1 Biochemical Pharmaceutical Co., Ltd, vitamin E (VE) was purchased from Guangzhou rekon Food Chemicals Co., Ltd. Methanol and n-hexane were of chromatographic pure and purchased from Tianjin Shield Specialty Chemical Ltd. Co. and Tianjin Kemiou Chemical Reagent Co., Ltd., respectively. Trichloromethane was purchased from Luoyang haohua Chemical Reagent Co. Ltd. All other reagents were of analytical grade.

Preparation of liposomes

Dry-film method (DF). Briefly, CoQ10, SP 98, DPPG, DSPE-PEG (2000) and cholesterol were dissolved in 10ml chloroform and the solution was evaporated for about 15min at 25 °C. After the dried film was formed, N₂ gas was used to remove there siduary solvent. The dried film was hydrated with deionized water. After sufficient hydration, the film was suspended by vortexing. The liposomes were then sonicated.

Reverse phase evaporation method (RPE). A lipid mixture of CoQ10, SP 98, DPPG, DSPE-PEG (2000) and cholesterol was dissolved in chloroform, deionized water was added to the lipid solution to form an emulsification automatically, and subsequently the organic solvent was dried under vacuum through attaching to a rotary evaporator.

Ethanol injection method (EI). In brief, lipids and drugs were dissolved in 8 ml ethanol, and the

ethanol was removed in rotary evaporator leaving behind about 4 ml solutions. Next, a constant volume of deionized water was added to the ethanol solution. Liposomes formed spontaneously after further evaporation of the residual solvent.

Finally, the liposome suspension was further disrupted by using ultrasonic probe. Resulting liposomes were sterilized by extruding through a 0.22 μm sterile filter. Cationic liposomes were prepared the day before the experiment, stored overnight at 4°C.

The liposomes prepared above were all semi-transparent solutions with light yellow color. The processing operations were performed under shade environment due to CoQ10 is not to be exposed to daylight.

Morphology observation

The morphologies of liposomes were observed using transmission electron microscopy apparatus (JEM-200CX); samples were negatively stained with 1% phosphotungstic acid.

Particle size and zeta potential measurement

Long-circulating prepared by different methods were stored at 4°C for 3 months. Samples were taken on the 0 day, 1 and 3 months for particle size and zeta potential analysis to assess the stability of vesicles. For determination process, each sample was dispersed in deionized water to a final volume of 3 ml, their particle size and zeta potential were analyzed using Laser particle analyzer (Malvern Zetasizer 3000HS, Malvern, UK). Volume-weighted Gaussian size distribution was fit to the autocorrelation functions and particle size values were obtained.

Encapsulation efficiencies (EE) determination

Protamine aggregation method was developed to separate free drugs and liposomes; EE was determined by using high performance liquid chromatography (HPLC).

Effect of protamine dosage on separation for liposomes. The proper amounts of protamine sulfate injection (10 mg·ml⁻¹) was taken and diluted by different folds. 100 μl liposomes and 100 μl dilution were taken and mixed, placed for about 3 min, centrifugated with the relative centrifugal force 350×g for 10 min after diluting with 5 ml purified water precisely. The supernatant was selected to measure absorbance by using an ultraviolet spectrophotometer at 540 nm, signed as A1. Another 100 μl liposomes were mixed with purified water directly, centrifuged and collected the supernatant to determine turbidity, signed as A0, the clarity was

calculated according to the formula: $(A_0 - A_1) / A_0 \times 100\%$. By the same method, the clarities of supernatant from the series of dilutions by separate liposomes were determined.

Effect of protamine dosage on EE. 100 μ l liposomes and 100 μ l protamine sulfate were taken and mixed; the free drugs and liposomes were separated as described above. The supernatant was collected for HPLC analysis. The chromatography separation was performed with a DiamonsilTMC18 Column (200mm \times 4.6mm, 5 μ m), the flow rate was 1.5 ml \cdot min⁻¹, with column temperature of 30 °C, the mobile phase was methanol-n-hexane (4:1), the drug was detected at 275 nm for determining the content of CoQ10. By the same method, EE of CoQ10 from the series of dilutions by separating liposomes were determined.

Determination of recovery of CoQ10. Different concentrations of CoQ10 solutions (80%, 100% and 120%) were prepared with methanol. The proper amounts of blank liposomes were mixed with CoQ10 solutions, 100 μ l mixtures was taken to separate by protamine sulfate and centrifugation. The supernatant was collected for HPLC analysis to determine the recovery.

EE determination. 100 μ l liposomes were taken precisely and mixed with 100 μ l protamine sulfate, after centrifugation the supernatant was collected for HPLC analysis to determine the amounts of free drug (W1). Meanwhile, another 100 μ l liposomes were taken and dissolved by 4 ml methanol; samples were taken to determine the total amount of lomustine (W0). EE was calculated according to the formula: $EE = (1 - W1 / W0) \times 100\%$.

Development of release assay method for CoQ10

Specificity. The reference solution of CoQ10, demulsification solution of blank liposomes (no

CoQ10 contained) and demulsification solution of liposomes were taken and injected for HPLC analysis, respectively.

Linearity. The CoQ10 testing solutions of different concentrations were prepared. The calibration curve samples were assayed in triplicate, using concentration (C) as abscissa (X) and peak area as ordinates (Y).

Recovery. The proper amounts of blank liposomes were mixed precisely with different volumes of stock solution, after filtering through a 0.45 μ m sterile membrane, filtrate was collected for determination. Recoveries were calculated by comparing the mean concentration obtained from the tested solutions with that of the neat standard samples.

Study on the in vitro release of CoQ10 in long-circulating liposomes

Assay method. Dislysis method was applied to determine release rate [14,15]. 1000 ml release medium was taken to dissolution glass at predetermined temperature, 1 ml liposomes were precisely transferred into the semipermeable membrane with leak sealing ends and located in release solvent. Release medium was agitated by stirring blades and sampled at 10, 30min, 1, 2, 4, 6, 8 and 12 hours after experiment initiating. 5 ml sample was collected and filtered through a 0.45 μ m membrane, filtrate was selected to determine at 37°C.

CoQ10 content at each time point was determined by HPLC analysis, meanwhile, the proper amounts thermosensitive compound liposomes was demulsified by methanol for the total drug amounts (W), the accumulative release amounts and release percent were calculated according to the formula:

$$Q_n = C_n V_0 + \sum_{i=0}^{n-1} C_i V_i \quad \text{Accumulative release percent (\%)} = \frac{Q_n}{W} \times 100\%$$

Noting: Q_n was the accumulative release amounts at each time point, C_n was the measured concentration at each time point, V_0 was the bulk volume of release medium, V_i was the sampling volume, C_i was the measured concentration at time point i , W was the total drug amounts in liposomes.

Release medium investigation. The in vitro release feature of CoQ10 was assessed using purified water, HCL and phosphate buffer (PBS, pH7.4) as release solvent, respectively, with the stirring blades rotation speed of 50 r \cdot min⁻¹.

Mathematical model fitting. The in vitro release data of CoQ10 was processed by using zero-order kinetics, first-order kinetics, Higuchi, Ritger-

Peppas and Weibull equations, and the data obtained from all the time points set was selected to simulate.

RESULTS

Morphology of long-circulating liposomes

The morphologies of liposomes were observed by transmission electron microscopy. All the liposomes were spherical particles with integrated bilayers and fingerprint-like surface on the liposomes was distinct. There was no difference in the morphology of the samples prepared by different methods.

Characterization of liposomes prepared by three methods

As shown in Tables 1 and 2, for particle size analysis results, there was significant difference between liposomes prepared by three methods, the lipid vectors prepared by RPE experienced great size increase during storage, by contrast, the EI-liposomes remained more or less unchanged over long periods, while the size distributions were most uneven (Polydispersity index, PDI were higher than 0.4). Among the three vehicles, samples produced by

DF method showed better stability and distribution feature within 3 months, without the tendency to aggregate and become larger. For zeta potential analysis results, samples prepared by DF method possessed lower potential, as well as were more stable compared with their counterparts prepared by the other two methods. Based on an overall consideration, DF method was selected as the best alternative to prepare liposomes.

Table 1. Results of particle size (nm) analysis for liposomes prepared by three methods (n= 3). Data represent average \pm standard deviation.

Days	DF	PDI	RPE	PDI	EI	PDI
0	165.6 \pm 1.4	0.291	171.2 \pm 0.7	0.194	163.2 \pm 2.1	0.438
30	215.8 \pm 4.1	0.243	459.5 \pm 28.8	0.448	166.3 \pm 5.7	0.410
90	188.5 \pm 4.4	0.121	515.6 \pm 16.8	0.330	165.3 \pm 4.0	0.409

Table 2. Results of zeta potential (mV) analysis for liposomes prepared by three methods (n=3). Data represent average \pm standard deviation.

Days	DF	RPE	EI
0	-27.7 \pm 0.9	-29.5 \pm 3.2	-4.02 \pm 0.4
30	-33.9 \pm 0.6	-25.7 \pm 1.4	-17.5 \pm 2.0
90	-11.0 \pm 0.3	-1.26 \pm 0.6	None

Development of protamine aggregation method

Effect of protamine dosage on separation for liposomes. The clarities determination results were summarized, we can conclude that free drugs and liposomes are well separated (Clarities were higher than 95%) by using very low amounts of protamine sulfate (0.5 mg).

Effect of protamine dosage on EE. The results showed that while protamine dosage was between 0.1-1.0 mg, EE of CoQ10 determined were 82%-90 %, thus there were little effects of protamine dosage on the EE of CoQ10.

Determination of recovery. Through HPLC analysis and calculation, recovery of CoQ10 were 100.4 %, 104.5 % and 99.6 %, RSD=4.41 % (n=3).

EE determination results. The EE of CoQ10 liposomes for the three batches were 94.0 %, 94.2 % and 91.4 %.

Development of release assay method for CoQ10

The HPLC chromatograms of CoQ10 were shown in Fig 1, it was indicated that the retention time (RT) of CoQ10 was about 11.0 min, lipid and other pharmaceutical necessities were eluted within 4 min, without interfering the determination.

Further, the calibration curve of CoQ10 was calculated as: $A=9.9232\times C+1.9675$ ($r=0.9999$),

indicating the good linear relationship from 5.0 to 150.0 $\mu\text{g}\cdot\text{ml}^{-1}$. The recovery were 97.0 %, 102.3 % and 101.5 %, with RSD of 1.74 %, 1.61 % and 0.63 % (n=5).

Study on the in vitro release of CoQ10

Release condition investigation. The release curve of CoQ10 in three medium were shown in Fig 2. It can be drawn that the accumulative release percents calculated in different medium all reached over 80 % at the last time point. However, it should be noted that the release of CoQ10 was affected by the medium to some extent; CoQ10 was released relatively slower within 8 h in HCL, but became more rapidly in subsequent time, PBS has also great influences on release characteristic and properties. Purified water showed little effects on the release of CoQ10 from liposomes. Therefore, purified water was selected as release medium in order to make complete release.

Release results of CoQ10 in liposomes. The release curve of liposomes were shown in Fig.3. We can conclude that CoQ10 in different batches of samples was released with nearly the same property, and release rates increased continuously along with the time.

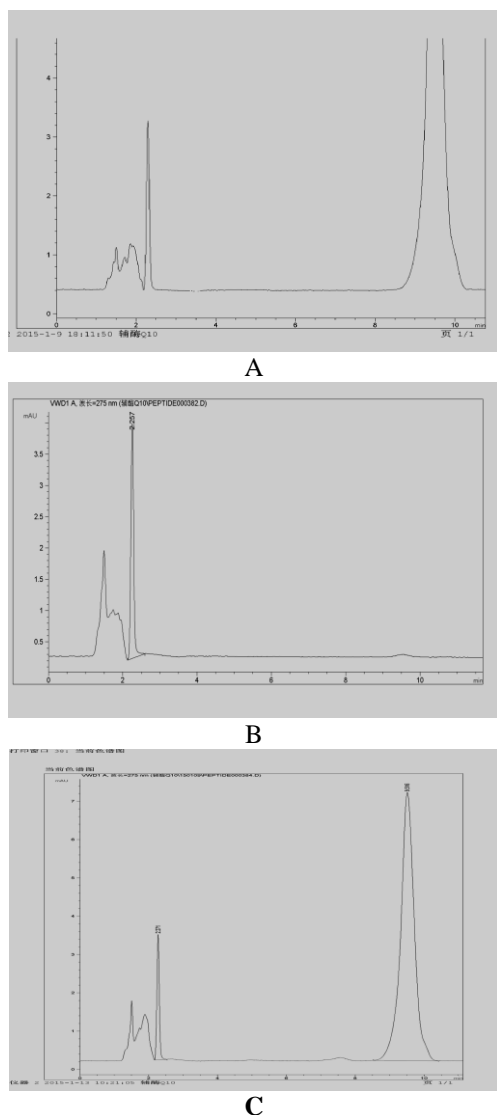


Fig. 1. Chromatograms of CoQ10 standard (A), blank liposome (B) and long-circulating liposomes (C).

Mathematical model fitting

As shown in Table 3, through regression model parameters analysis, the drug release from liposomes were with closest agreement with the Weibull

Table 3. The different release models of CoQ10 in liposomes in vitro.

Model	Equation	k	C	r
Zero-order kinetics	$Q\% = kt + C$	0.0013	0.2007	0.9051
first-order kinetics	$\ln(100-Q) = kt + C$	-0.0044	4.4926	0.9958
Higuchi equation	$Q\% = kt^{1/2} + C$	0.0398	0.0108	0.9818
Ritger-Peppas equation	$\ln Q = k \ln t + C$	0.6181	0.7615	0.9772
Weibull equation	$\ln \ln [1/(1-Q)] = k \lg t + C$	2.0352	-4.6143	0.9986

DISCUSSION

Particle size and zeta potential are generally considered as most important parameters in liposomes quality evaluation [16,17], stable particle size indicated liposomes did not show to aggregate

release kinetics, with the equation of $\ln \ln [1/(1-Q)] = 2.0352 \lg t - 4.6143$ ($r = 0.9986$).

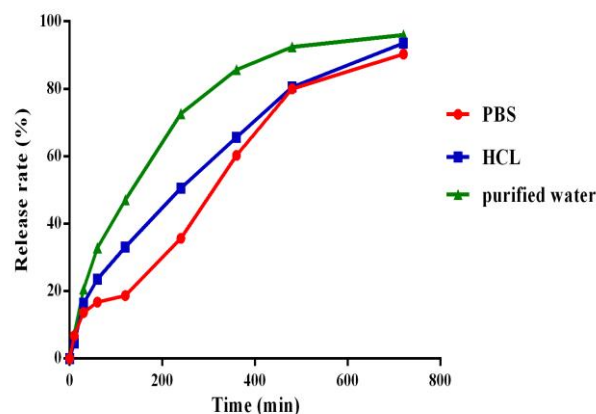


Fig. 2. Effects of mediums on in vitro release of CoQ10.

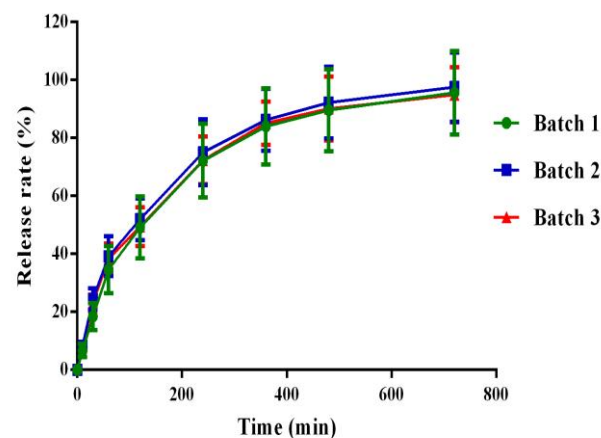


Fig.3. The release curves of the CoQ10 in liposomes, with purified water as the release medium at the rotation speed of 50 rpm.

Release results of CoQ10 in liposomes. The release curve of liposomes were shown in Fig.3. We can conclude that CoQ10 in different batches of samples was released with nearly the same property, and release rates increased continuously along with the time.

and cluster swimmingly during the use or deposit. On the other hand, conventional lipid carriers with low zeta potential were more negatively charged, which were capable of absorbing and binding to protamine sulfate molecule better, leading to

efficient separation from free drugs in EE determination. For the preparative methods selection, although as many as a dozen methods have been used to prepare long-circulating liposomes in recent research, most of them, such as extrusion method, freeze thawing method, etc., were less frequently employed in report or only used as supplement and substitution for the three methods investigated in the present study. It was suggested that long-circulating vectors prepared by DF method had more advantages over ones produced by the other two from the results of particle size and zeta potential analysis.

EE is one of the most important evaluation parameters for liposomal carriers. In general, the free drugs and liposomes are separated, and the amounts of free drug as well as the total amounts are both determined to calculate EE [18, 19, 16]. As to the EE determination for CoQ10 liposomes, organic solvent extraction was widely used in literature, in which mixed solutions composed of tween 80 and other organic solvent were used for multistage separation by solubilizing and eluting liposomes. However, as a multistep approach, this method was more labor-intensive to process, and more numerical error would be brought for determination. Protamine sulfate is one kind of polycation macro molecule and composed of basic amino acids. After mixing with liposomes protamine sulfate can adsorb their surface through electrostatic interaction, thus the density of liposomes would be increased and may be separated effectively with free drugs by lower centrifugal force. For the advantages of quickness, simple operation and high efficiency, furthermore, the separation is based on electrostatic attraction and independent of the drugs enveloped in liposomes, thus this method is applicable for EE determination of most of the drugs.

For the CoQ10 assay method, UV spectrophotometry was also used in literature, nevertheless, lipid necessities in formulation could not be effectively separated from drug by UV method, as well as lead to erroneous results. Furthermore, it was reported that methanol-anhydrous alcohol mixed solvent (with the ratio of 5: 95, 1: 9 or 1: 1) was the frequently used mobile phase, in this paper the mixed solvent was also used and the results indicated that these two organic solvents could be well miscible with each other, and CoQ10 was eluted within 3 min. However, chromatographic peak shapes became abnormal, while pharmaceutical necessities were not completely separated from drug. Methanol-n-hexane (4:1) mixed solvent was studied through experiments, by which pharmaceutical necessities

could be completely separated from drug, with longer retention time and symmetrical peak. Through large experimental validation and comparison, it was selected for in vitro release determination.

Acknowledgements: This work was financially supported by the Plan for Scientific Innovation Talent of the Henan University of Technology (No: 2014CXRC07), and the Natural Science Research Program of the Education Department of Henan Province (15A350006).

REFERENCES

1. U. Singh, S. Devaraj, I. Jialal, *Nutr Rev*, **65**, 286 (2007).
2. B. Frei, M.C. Kim, B.N. Ames, *Proc Natl Acad Sci USA*, **87**, 4879 (1990).
3. K.S. Echtay, E. Winkler, K. Frischmuth and M. Klingenberg, *Proc Natl Acad Sci USA*, **98**, 1416 (2001).
4. C.H. Huang, J.P. Sipe, S.T. Chow, R.B. Martin, *Proc Natl Acad Sci USA*, **71**, 359 (1974).
5. M. Mancuso, D. Orsucci, L. Volpi, V. Calsolaro, G. Siciliano, *Curr Drug Targets*, **11**, 111 (2010).
6. S. Suzuki, Y. Hinokio, M. Ohtomo, M. Hirai, A. Hirai, M. Chiba, S. Kasuga, Y. Satoh, H. Akai, T. Toyota, *J Diabetologia*, **41**, 584 (1998).
7. R. Wajda, J. Zirkel, T. Schaffer, *J Med Food*, **10**, 731 (2007).
8. P. Balakrishnan, B.J. Lee, D.H. Oh, J.O. Kim, Y.I. Lee, D.D. Kim, J.P. Jee, Y.B. Lee, J.S. Woo, C.S. Yong, H.G. Choi, *Int J Pharm*, **374**, 66 (2009).
9. N.K. Swarnakar, A.K. Jain, R.P. Singh, C. Godugu, M. Das, S. Jain, *J. Biomaterials*, **32**, 6860 (2011).
10. K.H. Bhandari, M. Newa, J.A. Kim, B.K. Yoo, J.S. Woo, W.S. Lyoo, H.T. Lim, H.G. Choi, C.S. Yong, *Biol Pharm Bull*, **30**, 1171 (2007).
11. T.R. Kommuru, M. Ashraf, M.A. Khan, I.K. Reddy, *Chem Pharm Bull*, **47**, 1024 (1999).
12. A. Palamakula, M.A. Khan, *Int J Pharm*, **273**, 63 (2004).
13. A.S. Monem, F.M. Ali, M.W. Ismail, *Int J Pharm*, **198**, 29 (2000).
14. C.H. Huang, J.P. Sipe, S.T. Chow, R.B. Martin, *Proc Natl Acad Sci USA*, **71**, 359 (1974).
15. S.C. Semple, A. Chonn, P.R. Cullis, *J. Biochemistry*, **35**, 2521 (1996).
16. B. Ma, S. Zhang, H. Jiang, B. Zhao, H. Lv, *J Control Release*, **123**, 184 (2007).
17. M. Ramezani, M. Khoshhamdam, A. Dehshahri, B. Malaekheh-Nikouei, *Colloids Surf B Biointerfaces*, **72**, 1 (2009).
18. L. Ciani, A. Casini, C. Gabbiani, S. Ristori, L. Messori and G. Martini, *J. Biophysical chemistry*, **127**, 213 (2007).
19. H. Farhood, N. Serbina, L. Huang, *Biochim Biophys Acta*, **1235**, 289(1995).

Study on intragenic methylation of the aromatase P450 gene from different rice field eel tissues

Zheming Cao, Weidong Ding, Jianxin Wang, Xuwen Bing*

Freshwater Fisheries Research Center, Key Laboratory of Freshwater Fisheries and Germplasm Resources Utilization, Ministry of Agriculture, Wuxi 214081, China

Received February 11 2016, Revised April 2 2016

The gonads of ricefield eels show differential expression of brain and ovarian aromatase P450 as compared other tissues. We determined whether these differential expression patterns were related to the level of genomic DNA methylation by detecting DNA methylation in different tissues with seven pairs of primers. As a result, we found that the two types of aromatases in eel testis and ovary were all methylated. By contrast, in peripheral blood, some regions of both aromatases were demethylated, and the CpG islands of ovarian aromatase in the kidney were demethylated. To determine if there were demethylation epialleles in the tissues expressing aromatase P450 gene methylation, we designed an artificial adaptor and a series of primers in a two-step amplification of the methylated tissue-specific aromatases. The results suggested that there was evidence of demethylation epialleles in most of the tissues where the aromatase P450 gene was methylated. Most of the demethylated regions in the blood were located at heterozygous methylation sites, whereas there were barely any demethylation epialleles in the methylated regions. This study demonstrated that the aromatase P450 gene was universally heterozygous in some regions of different tissues. In these tissues, the methylation state, demethylation state and extent of demethylation exerted some regulatory effects on the expression of aromatase. To determine whether the expression of brain and ovarian aromatase P450 was related to its differential methylation sites, the expression of the two types of aromatase was detected in different tissues using semi-quantitative PCR, and we found that both of aromatases was low expressed in most experiment tissues. The expression of ovarian aromatase was relatively high in blood and kidney and weakly detectable expression was found in other tissues. The brain aromatase was weakly expressed in all combinations. We suggested that gene expression of aromatase was weakly influenced by methylation of the internal sequence.

Keywords: Aromatase P450, methylation, ricefield eel, gene expression.

INTRODUCTION

Ricefield eels (*Monopterus albus*) belong to the *Monopterus* species, *Synbranchiformes* family, *Synbranchiformes* order, *Actinopterygii* subclass, and the *Osteichthyes* phylum. Widely distributed in countries and regions such as China, America and Oceania, ricefield eel is an important economic freshwater fish in China. It is an animal characterized by natural unidirectional sex reversal, which remains female since childhood to its first sexual maturation, but turns intersex and finally male after spawning. Therefore, ricefield eel species are important in fish breeding research to study sex determinative mechanisms.

Aromatase is an important member of the P450 family, which is a critical enzyme for estrogen synthesis and does so by catalyzing some androgens like testosterone and rostadienone into estrogens like estrone and estradiol. Thus, we chose the aromatase P450 gene as the target gene of eel

There are two types of the aromatase P450 gene found in research on fish, including ovarian aromatase P450 and brain aromatase P450 [1-4]. Yu et al. isolated ricefield eel ovarian aromatase P450 from fresh ovary, and identified this gene in the brain [5]. Li *et al.* [6] isolated ricefield eel brain aromatase P450, and found relatively high expression in the brain and testis, low expression in skin, and no detectable expression in the liver, heart, small intestine and muscle. We conclude from the above observations that both types of aromatase P450 expressed in ovary and testis are different genes, and are both expressed in the ricefield eel brain. Yann Guiguen *et al.* believed that ovarian aromatase P450 was the key to trigger and sustain ovary and testis differentiation, since blocking the expression of ovarian aromatase 450 could induce virilization [7]. Diotel *et al.* believed that brain aromatase P450 was only expressed in radial glial cells and distributed in neural tissues like the hypothalamus, spine and preoptic area [7]. This group also believed that brain aromatase P450 was controlled by estrogen and aromatized androgen, and involved in the reproduction of fish in addition to regulating brain sexual differentiation and sexual

To whom all correspondence should be sent:
E-mail: bingxw@ffrc.cn

related research.

activities. These observations were discordant with the conclusions of others who also thought that brain aromatase P450 was also expressed in the testis [3]. There has not been a reasonable explanation for the differences.

DNA methylation is an important modification of nucleic acids that shuts off gene activity, while demethylation induces gene reactivation and expression. Therefore, DNA methylation is a critically important area of epigenetics research, with relevance to understanding diseases like cancer, senescence and dementia. The major product of DNA methylation is 5-methyl cytosine (5-mC), which is ubiquitous in the genome of eukaryotes. The latest research findings in the field of human genomic methylation, suggests that most cells show stable methylation patterns, and 70-80% of the CpGs are methylated. It is believed that although every CpG can potentially change their methylation status, only a fraction of them are regulated and ready to change their methylation status [9]. Other groups are convinced that CpG methylation and demethylation are associated with gene expression although the degree of DNA methylation is not well correlated with gene expression [10].

To determine whether the differential expression of aromatase P450 in the gonad organs and other tissues is related to its differential internal methylation status, our current research study used methylation sensitive *HpaII* to treat genomic DNA of the ovary, testis, degenerated ovary and other tissues. Further, we amplified them by segments and investigated the methylation status of both types of aromatase by comparing the amplification products before and after digestion. Additionally, we annealed the digested genomic DNA with an artificial adaptor. Appropriate primers were designed according to the sequences of the adaptors to amplify these fragments so that we could verify whether these methylation sites were in the apparent heterozygous state, which would imply the coexistence of both methylation and demethylation.

MATERIALS AND METHODS

The search for a CpG island

There were two searching results relevant to the genomic DNA sequence of aromatase P450 found on the NCBI website. One of them was EU840259, with a full-length sequence of 4869 bp, which was of the ovarian type, and uploaded on July 29, 2008. The other was EF640940, which was of the brain type, with a full-length sequence of 3754bp, and uploaded on May 19, 2008. No CpG island sequences were found following an analysis with

the genomic DNA CpG island analyzing software provided by the European EBI website (<http://www.ebi.ac.uk/emboss/cpgplot/>). There were a total of 11 CCGGs found in the sequence in EU840259 and 10 CCGGs short sequences in EF640940. We designed several pairs of primers (Table.1) for each sequence that essentially covered all of the potential methylation regions. The orarian aromatase P450 is divided into 3 amplified regions and the brain aromatase P450 is divided into 4 amplified regions.

Genomic DNA extraction in different ricefield eel tissues

The ricefield eel samples were collected at September 2014. Ten samples (five male and five female)were obtained from Central Fish Nursery Farm of Fresh Water Fishery Research Institute of Chinese academy of Fishery Sciences.

In this procedure, 450 μ l STE buffer (150 mmol/L NaCl, 50 mmol/L Tris and 1 mmol/L EDTA), 12.5 μ l 10% SDS and 10 μ l proteinase K (20 mg/ml) were added to 0.1 g tissue (muscle, liver, kidney, blood, testis, ovary and degenerative ovary), mixed and digested at 55°C overnight. The mixture was extracted with phenol/chloroform, precipitated with equal volumes of isopropanol, and then centrifuged at 12000 rpm for 20 min. The pellet was washed twice with 70% ethanol, dissolved in 60 μ l double distilled water, and resolved on a 0.8% agarose gel to measure the mass and concentration of DNA. Since eels are bred in captivity as edible fish in China, and samples were taken after sacrificing eels by cervical dislocation, there were no ethical issues with regard the experimental animals involved in this research.

Genomic DNA digestion in different ricefield eel tissues

The total volume of the digestion system was 20 μ l, including 2 μ l sample genomic DNA, 2 μ l (10 u/ul) restriction endonuclease *HpaII*, 2 μ l 10x digestion buffer, and 14 μ l double distilled water. One blank control without restriction endonuclease and the other control with restriction endonuclease *MspI* were included in each group. The mixture was digested for 4 hrs at 37°C.

Sequence amplification and methylation statistics of aromatase P450

The total volume of the amplification system was 25 μ l, including 1.0 μ l template, 2.5 μ l 10 \times PCR buffer, 5 pmol forward primer, 5 pmol reverse primer, 1.5 μ l dNTPs (2.5 mmol), 2U Taq DNA polymerase, and deionized water to 25 μ l. The

amplification procedure was as follows: an initial denaturation at 94°C for 2 min, followed by 35 cycles of amplification (denaturation at 94°C for 30 s, annealing at 58°C for 45s, elongation at 72°C for

1min), and a final elongation at 72°C for 10 min. The PCR products were detected on 1.0% agarose gels.

Table 1. Primers for amplification of different regions in brain and gonadal aromatase P450.

Primer for ovarian aromatase P450		Primer for brain aromatase P450	
F11	tgttaccacaacgagggagg	F21	Gtgagctttgaagctactgtaatg
R11	tttaaatgtccttgggcaaac	R21	tatgagcctgtgcccttgact
F12	ggttgagtgattgggatgga	F22	cagtggcactaatcaactgg
R12	gatgaaactctggaccgtctgt	R22	cagcaactgaggacatccac
F13	gacagtgcccagtccttctt	F23	gttaacctgtgtgcagagaa
R13	tccaattcctcgtgcacgt	R23	cctgtagcaactgcagctcc
		F24	gaccgatgatcatagatggc
		R24	tcaagcccttatgaggcaact

To measure aromatase P450 methylation, the common PCR products of the blank control group without restriction endonuclease, and the group digested with restriction endonuclease were designated as methylation regions, while the regions in the PCR product of the blank control group, but not in the product of the digested group were demethylation regions.

Epiallele amplification of aromatase P450

The 20 µl the digestion product was precipitated with 50 µl of 100% ethanol, centrifuged at 12 000 rpm for 10 min to obtain the pellet, and dried at room temperature to remove ethanol. Next, 14 µl of distilled water, 2 µl of 10x T4 ligase buffer, 2 µl of T4 ligase and 2 µl of the adaptor sequence (50 mm adaptor) were added, mixed and incubated at 16°C for 4 hrs. The adaptor sequence was 5-cgagtcggctggctcctcaattgtatc-3, and 5-tcagccgaccgaggagtaacatag-3.

The total volume of the first step amplification was 25 µl, including 1.0 µl of the template, 2.5 µl of 10×PCR buffer, 10 pmol of the first step primer (caattgaggagccagccgact and the forward primer, 5 pmol each), 1.5 µl of dNTPs (2.5 mmol), 2U taq DNA polymerase, and deionized water to a final volume of 25 µl. The amplification procedure was as follows: an initial denaturation at 94°C for 2 min, followed by 30 cycles of amplification (denaturation at 94°C for 30 s, annealing at 58°C for 45s, elongation at 72°C for 1 min), and a final elongation at 72°C for 5 min.

The total volume of the second step amplification was 25 µl, including 1.0 µl of the PCR product from the first step, 2.5 µl of 10×PCR buffer, 10 pmol of the second step primer which was one of the four primers of: ttgaggagccagccgactcggt, ttgaggagccagccgactcgga, ttgaggagccagccgactcggc, ttgaggagccagccgactcggg and the forward primer at 5 pmol each, 1.5 µl of

dNTPs (2.5 mmol), 2U of Taq DNA polymerase and deionized water to a final volume of 25 µl. The amplification procedure was an initial denaturation at 94°C for 2 min, followed by 30 cycles of amplification as follows: denaturation at 94°C for 30 s, annealing at 66°C for 45s, elongation at 72°C for 1 min, and a final elongation at 72°C for 5 min. The PCR products were detected with a 1.5% agarose gel. To confirm whether the PCR product was the target digestion product, the PCR product was annealed to a T vector and subsequently sequenced.

Semi-quantitative PCR of aromatase P450

Samples of different tissues of ricefield eel was added to 500µL RNAiso Plus reagent. and was incubated for 5minutes at room temperature. The mixture was added 100µL of chloroform and shaken vigorously and then was centrifuged at 12,000g for 15 minutes at 4°C. The aqueous phase of the sample was removed into a new tube. Equivalent volume of 100% isopropanol was added and the tube was shaken vigorously. The sample was centrifuged at 12,000g for 10 minutes at 4°C. The supernatant was removed and the RNA pellet was collected and washed by 75% ethanol (500µL). The sample was centrifuged at 7500g for 5 minutes at 4°C and the wash was discarded and the residue was dried. The RNA pellet was then dissolved in DEPC water and was detected by electrophoresis analysis in 1.0% Argrose gel.

cDNA synthesis was according to M-MLV First strand cDNA Synthesis Kit(Sangon Biotech, SK2435).

Semi-quantitative PCR primers: actin, cttcgacatcacggctgatgg/caggacctgtatgcttcagg; brain aromatase P450, gttaacctgtgtgcagagaa/cctgtagcaactgcagctcc; ovarian aromatase P450, gacagtgcccagtccttctt/tccaattcctcgtgcacgt.

Adjust the concentration of the different cDNA

and the primers to make sure all amplification have the nearly equivalent result, then detect the brain and ovarian aromatase P450. 0.5µL Primers(10mmol/L), 0.5µL dNTPs(10mmol/L), 0.5µL *Taq* enzyme(5U/L), total volume 25.0µL. 94.0°C for 5minutes, (94.0 °C for 30s, 58.0 °C for 30s, 72.0 °C for 45s) 29 cycles, 72.0 °C for 5minutes. Electrophoresis analysis in 1.5% Argrose gel.

RESULTS

Methylation detection of different regions in aromatase P450 sequence

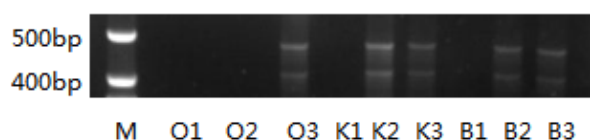


Fig. 1. Methylation amplification of aromatase from different tissues; B: blood; O: Ovary, K: Kidney; 1: digested with *MspI*, 2: digested with *Hpa I* 3: contrast.

Figure 1 represents the amplification result of region 3 in the ovarian aromatase P450. There was no band in the lanes digested with *MspI* of three samples, while there were bands seen in the control

group. But there were bands seen in the lanes digested with *Hpa II* of kidney and blood. This suggested that there was demethylation of region 3 in the blood and kidney. There were no bands in ovary suggesting methylation status .

Methylation analysis of aromatase P450 in different tissues

Table 2 described the statistics of methylation in different tissues. It could be seen that most CCGG regions in both types of aromatase P450 were methylated. All of the CCGG regions of both aromatase P450 genes found in the testis, ovary, degenerative ovary, muscle and liver were methylated. Ampiliated region 2 and 3of ovarian aromatase P450 of blood were demethylated while region 1 was methylated. Ampiliated region 1 and 2 of ovarian aromatase P450 of kidney were methylated and region 3 was demethylated. Ampiliated region 2 and 4 of brain aromatase P450 of blood were demethylated while region 1 and 3 were methylated. All amplified regions of brain aromatase P450 of kidney were methylated. The result of ten samples suggested methylation patterns of two genes in different tissues may be universal

Table 2. Methylation analysis of two types of aromatase P450.

Amplified region	Ovarian Aromatase P450			Brain Aromatase P450			
	1	2	3	1	2	3	4
Blood	+	—	—	+	—	+	—
Liver	+	+	+	+	+	+	+
Kidney	+	+	—	+	+	+	+
Muscle	+	+	+	+	+	+	+
Ovary	+	+	+	+	+	+	+
Testis	+	+	+	+	+	+	+
Degenerated ovary	+	+	+	+	+	+	+

Table 3. Methylation analysis of the two types of aromatase.

Amplified region	Ovarian Aromatase P450			Brain Aromatase P450			
	1	2	3	1	2	3	4
Female	+	—	—	+	—	+	—
Male	+	—	—	+	—	+	—

Table 3 show intragenic methylation patterns of two aromatase P450 gene of blood from five male individuals and five female individual. No differences were found between them.

Amplification of the aromatase P450 epiallele

If there is indeed coexistence of methylation and demethylation epialleles of a diploid nature, methylation fragments should be theoretically detected after digestion and amplification. It transpired, that we did not know if there were also demethylation epialleles in the above mentioned

methylation positive samples. To further study these samples and to determine if there were demethylation epialleles, we designed an artificial adaptor that could be annealed with the genomic fragments that were digested by *HpaII*. Moreover, we designed a first step amplification primer according to the adaptor sequence. In case there were four possible bases downstream of CCGG, we conducted a two-step amplification of the samples that were connected with adaptors, and sequenced the amplification product. If there was an obvious amplification band of the second step primer (with anyone as its selective base) in the amplification

result, we concluded coexistence of methylation and demethylation epialleles.

Table 4. Amplification of the epiallele of two types of aromatase.

Amplified region	Ovarian Aromatase P450			Brain Aromatase P450			
	1	2	3	1	2	3	4
Blood	—			—		—	
Liver	—	—	+	—	—	—	+
Kidney	—	+		—	+	—	+
Muscle	—	+	+	—	+	—	+
Ovary	—	+	+	—	+	—	+
Testis	—	+	+	—	+	—	+
degenerated ovary	—	—	+	—	—	+	+

In Table 4, (+) means that there was an amplification product, (—) means that there was no amplification product, and blank represents regions demonstrated to be de-methylated in the previous experiment. It could be seen that most regions that were de-methylated in the blood had demethylation epialleles in other tissues, while most methylated regions in the blood did not have demethylation epialleles. Thus, we believe that there might be two types of CCGG region in aromatase P450; one of the regions is essentially permanently methylated, while the other is dynamically methylated. Furthermore, they are relatively stable. However, there is also a very low rate of demethylation in the permanently methylated regions, and complete methylation in dynamically methylated regions of some tissues.

Semi-quantitative PCR of two aromatase P450

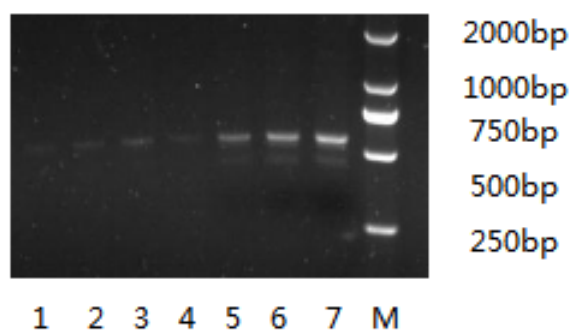


Fig. 2. Semi-quantitative PCR of ovarian aromatase P450 in seven tissues. 1: degenerated ovary, 2: muscle, 3: liver, 4: testis, 5: ovary, 6: kidney, 7: blood. Ovarian aromatase P450 expressed more in peripheral blood, less in kidney and ovary, little in other tissue.

According to our previous experience, using different pairs of primers to detect the expression level of a same gene by quantitative PCR will lead to different results. To avoid this, we use the more easy and intuitive semi-quantitative PCR to detect the expression differences of aromatase P450 in different tissues. We use *actin* of ricefield eel as inner control and adjust the amplification factors to get the consistent results in different tissues, and

then detect the expression of two types of aromatase P450. The result suggested that brain aromatase P450 expressed rarely in all experiment tissues. The highest expression level of ovarian aromatase P450 shown in Fig.2 was found in peripheral blood, followed by kidney and rarely in the rest. A slight difference in expression of ovarian aromatase in blood and kidney was found among ten samples, but higher than other tissues. Difference in other tissues can't be detected because of low expression. We also can't find difference of brain aromatase among ten samples with the same reason.

DISCUSSION

The result that most of CCGG regions of two aromatase P450 genes were methylated, was consistent with the conclusions from a previously published human genomic study (Michael, *et al.*, 2013)[9]. The result suggests that most CCGG regions in the ricefield eel genome were most likely methylated. In the methylation study of the human genome, the methylation of CpG islands is normally given greater emphasis. However, since there are no CpG islands in the both aromatase P450 sequences, we believe that part of the CCGG sequence outside of the CpG islands are involved in the regulation of methylation.

Our result of methylation research contradicts observations made by Yu *et al.*, [5] and Li *et al.*, [6]. The difference is that we can't find intragenic demethylation of ovarian aromatase P450 of which the expression can be detected in ovary. But the result of semi-quantitative PCR shown expression of ovarian aromatase P450 can be detected in ovary, which was consistent with that of Yu *et al.* [5]. So we think there was no direct correlation between the extent of methylation of the internal sequence and the expression of both of these genes in these ricefield eel tissues (testis, ovary, degenerative ovary, muscle and liver). From Figure 2, we found the expression of ovarian aromatase in kidney was slightly lower than that in blood. Because amplified region 2 was methylated in kidney while

demethylated in blood, we think intragenic methylation can effect the expression of some genes to some extent in special tissues.

Nearly all tissues can detect the weak expression of brain aromatase P450. High intragenic demethylation of brain aromatase P450 in blood don't improve the expression of the gene. Nicolas Diotel *et al.* held the opinion that brain aromatase is directly related to adult sex hormone levels, and is only expressed in the adult brain tissue [7]. However, this research was not consistent with his conclusion. We tend to think that the high expression of brain aromatase P450 in the brain tissue should require the addition of regulation mechanisms and intragenic methylation may have weak regulatory effect on the expression.

Both research reports of Yu *et al.* [5] and Li *et al.* [6] don't involve the expression of both aromatases in blood. The result shows that the tissue in which expression of ovarian aromatase P450 is the highest is blood. It is consistent with the intragenic demethylation of the gene. We guest that the activity of aromatase P450 in the blood should be relatively high, playing an important role in lowering blood androgens. To confirm whether there was a difference in the methylation status between either type of aromatase in male and female eel blood, we collected and compared the blood of male and female eels individually, but failed to find a difference. Thus, the expression of blood cell aromatase P450 had no direct effect on the sexual reversal of the eel, and the existence of other effects remains to be further elucidated. Guiguen *et al.* [8] believed that ovarian aromatase P450 played a role in testicular differentiation, since the decline in aromatase P450 was essential for testicular development. We don't think the aromatase in blood plays an important role in sex reversal of rice field eel. Maybe their main role is to maintain stable blood concentration of hormone [8].

Zhang Y *et al.* [18] considered that the methylation of the CpG island of long-distance cAMP element and the TATA box of the short-distance SF1/Adrenergic Binding Protein 4, acetylation and trimethylation of histone 3 in regulation region I and II and phosphorylation of cAMP element binding protein could affect the expression of aromatase . Our result suggested that inner methylation and demethylation of CpG island of aromatase P450 may also have slightly regulation. The biological significance of this kind of regulation needs further digging [18].

The study shows both aromatase P450 genes in some cells is apparently heterozygous, although we cannot be certain that aromatase P450 is at an

apparent heterozygous state in every cell of the tissues with the allele.

Most of the reports regarding epialleles were focused on paramutations [11-16]. Arteaga-Vazquez *et al.* [16]. reported a pair of epialleles "b1" (low expressed B' and high expressed B-I) specifically expressed in maize. Methylation of a seven-repeat sequence located 100 Kb upstream of the b1 coding region played an important role in establishing and maintaining B' gene silence. Arteaga-Vazquez *et al.* [16] and Wolfgang & Joachim [17] reported a pair of epialleles P1-rr and P1-pr in the Myb-like transcription factor, which mediates the coloring of flowers in maize. The difference between them was the methylation state in the regulatory regions [17]. These results were collectively focused on the methylation study of some special sequences, and were mostly based on previous studies with no direct reference value for the methylation state and function of most genomic CCGG regions. Our results showed that there were corresponding demethylation sequences for partially methylated genomic CCGG regions of aromatase P450. Consequently, we believe that epialleles could exist in many areas outside the regulatory region, which might serve to regulate gene expression.

There are many reports studying aromatase in fish, and most results are paradoxical, reflecting a very complicated mode of regulation that has evolved. This research showed that aromatase is a crucial enzyme that is not only regulated by its upstream and downstream regulative sequences, but also maybe by the methylation and demethylation of its internal CCGG regions. The apparent heterozygous state of partially methylated regions might be vital to the regulation of gene expression.

Acknowledgements: This study was supported by the special fund for the Fundamental Research for Central Public-Interest Scientific Institutions (Fresh Water Fishery Research Center, Chinese Academy of Fishery Sciences, Grant # 2013JBFM02), the Special Fund for Agro-Scientific Research in the Public Interest (201003076), Science and technology support program of Jiangsu province (BE2013315), Jiangsu Natural Science Foundation (SBK2014021567).

REFERENCES

1. K.R. Von Schalburg, M. Yasuike, W.S. Davidson, B.F. Koop, *Comp. Biochem. Physiol. B Biochem Mol Biol*, **155**, 118 (2010).
2. V.L. Dalla, A. Ramina, S. Vianello, *Steroid Biochem. Mol. Biol.*, **82**, 19 (2002).
3. M. Kishida, G. Callard, *Endocrinol.*, **142**, 740 (2001).

4. A. Tchoudakova, G. Callard, *Endocrinol.*, **139**, 2179 (1998).
5. Yu J.H., Wu T.T., Li J.L., Cao L.P., Xia D.Q., *Acta Hydrobiologica Sinica*, **29**, 550 (2005).
6. Li W., Liu G.Y., Luo C.Y., *Fisheries Science*, **8**, 458 (2009).
7. N. Diotel, *Frontiers Neuroendocrinol.*, **31**, 172 (2010).
8. GuiguenY., A. Fostier, F. Piferrer, C.F. Chang, *Gen. Comp. Endocrinol.*, **165**, 352 (2010).
9. J.Z. Michael J.Z., Charting a dynamic DNA methylation landscape of the human genome, *Nature*, **7463**, 477 (2013).
10. M. Kulis, *Nat. Genet.*, **44**, 1236 (2012).
11. J.B. Hollick, *Ann. Rev. Cell. Dev Biol.*, **26**, 557–579 (2010).
12. V.L. Chandler, *Science* (New York, NY), **330**, 628 (2010).
13. M. Haring, R. Bader, M. Louwers, A. Schwabe, R. R. van Driel, M. Stam, *Plant J.*, **63**, 366 (2010).
14. G. Rangani, M. Khodakovskaya, M. Alimohammadi, U. Hoecker, V. Srivastava, *Plant Mol. Biol.*, **79**, 191 (2012).
15. D. Zilberman, S. Henikoff, *Development*, **134**, 3959 (2007).
16. M. Arteaga-Vazquez, L. Sidorenko, F.A. L. Rabanal, R.L. Shrivistava, K. Nobuta, P.J. Green, B.C. Meyers, V.L. Chandler, *Proc. Natl Acad. Sci. USA*, **107**, 12986 (2010).
17. G. Wolfgang, M. Joachim, *Theor. Appl. Genet.*, **126**, 159 (2013).
18. Zhang Y., Zhang S., Liu Z., Zhang L., Zhang W., *Endocrinol.*, **154**, 2881 (2013).

Effects of bull serum albumin on corrosion of carbon steel under water with different Larson ratio

Yajun Zhang¹, Lingfeng Yao², Lihua Sun^{1*}, Tingting Du²

¹ Key Laboratory of Urban Stormwater System & Water Environment, Beijing University of Civil Engineering and Architecture, Beijing 100044, China

² School of Environment and Energy Engineering, Beijing University of Civil Engineering and Architecture, Beijing 100044, China

Received February 4 2016, Revised April 16 2016

The corrosion of metal material has brought great harm to energy, economy and water quality. Corrosion scales formed by the accumulation of corrosion products would be disturbed and release microbes, heavy metals and other contaminants into water which would seriously influence the use of people, even pose a threat to human health. Comparison of corrosion of carbon steel between with and without BSA (Bull Serum Albumin) under water with different Larson ratio would be provided in this work. The comparison was around corrosion rate, rate of iron release, morphology of corrosion scales, composition changes of corrosion scales and so on. Compared to the work condition without BSA, the one with BSA had lower corrosion rate. The mechanism of corrosion without BSA mostly matched electro-chemical corrosion and was around redox reaction of iron. The corrosion scales had few CaCO₃ in the early period due to BSA. In the last period, the composition of corrosion scales with BSA was similar to the one without BSA and mainly included γ -FeOOH, α -FeOOH and CaCO₃. The effect of proteins mainly included the adsorption film and microbial action which inhibited corrosion. Though proteins have obvious inhibition effect, it does not work when LR is high. The use of BSA as inhibitor should be after considering the water quality especially with high or low LR (Larson ratio).

Keywords: Corrosion scale, BSA, LR, Adsorption film, Microbial action, Inhibition.

INTRODUCTION

Metal material is still holding a large proportion in water distribution systems in many countries, such as 56.6% in USA, 67.2% in Italy [1] and 75.5% in China [2]. The corrosion of metal material has brought great harm including energy waste due to corrosion scales limit the flow area and reduce the flow velocity and economic losses due to the replacement and reparation of the systems resulted from the faster pipe ageing, especially the threat for the water quality [3-4]. Formed by the accumulation of corrosion products, corrosion scales act as the breeding ground for microbes and sinks for heavy metals or other contaminants [5]. Corrosion scales would be disturbed and biofilms would be damaged resulted by the changes of water quality or hydraulic condition, so that microbes, heavy metals and other contaminants would be released into the water, which would result in quality problems of water such as "Red water". Those problems would seriously influence the use of people, even pose a threat to human health [4,6]

The formation process and structure of corrosion scales in water distribution systems are always

complex. According to the most popular model called dissolved oxygen (DO) model [7], the corrosion scales always consists of four layers: a surface layer, a hard shell-like layer, a porous core layer and a corroding floor [8-9]. The structure and characteristics of corrosion scales always depend on the metallic materials of pipes, the contacted water quality, and possibly the hydraulic conditions, etc. Compared to materials and hydraulic conditions which are easily controlled, the water quality changed more frequently. The water quality parameters related to corrosion include pH, alkalinity, dissolved oxygen (DO), temperature, natural organic matter (NOM), microorganisms, Larson ratio and so on [10-14]. Among them, the anionic groups represented by Larson ratio in water obviously affect corrosion [11]. It was found that chlorine and sulfate could promote the corrosion of iron while alkalinity slowed down the corrosion [12]. It was proposed that Larson ratio (LR) could be used to distinguish the corrosiveness of water which was widely accepted [13-15]. A lot of studies concentrated on how Larson ratio influenced corrosiveness of water, but few studies paid attention to the effects on corrosion scales due to different Larson ratio.

To ease and solve corrosion problems of water distribution systems, a lot of strategies have been

To whom all correspondence should be sent:
E-mail: sunlihuashd@163.com

used and worked to some extent. Among them, corrosion inhibitor is one of the most convenient and effective method. However, lots of the traditional corrosion inhibitors have been abandoned due to the environmental impact and health risk issues. It is urgent that new corrosion inhibitors which are “green”, safe and multifunctional should be developed [13-15]. As one kind of new inhibitors, protein was attracted much attention due to its characteristics of safe, green and abundance. Lots of studies were conducted around its detection, modification and action mechanism [13-14], but studies combined with water quality in real water distribution systems were still less.

The aim of this work is to provide comparison of corrosion of carbon steel between with and without BSA (Bull Serum Albumin) under water with different Larson ratio. The comparison was around corrosion rate, rate of iron release, morphology of corrosion scales, composition changes of corrosion scales and so on. The mechanism of effect by BSA on corrosion was studied and probable explanation of different effects under different Larson ratio was given. The findings of this work would help to complete the mechanisms of proteins inhibition and provide reference for effects by proteins.

MATERIALS AND METHODS

Experiment planning

The experiment was run in six rotary coupon reactors. The reactor mainly consists of 4 parts including rotary barrel, constant temperature equipment, pump, water tank. There were 21 coupons of carbon steel in every reactor. The water was stored in the tank and got into the barrel through the pump. The barrel was cylindrical with capacity of 6L. The temperature was maintained at 25 ± 1 °C. The motor speed was 80r/min. The reactor was placed in the dark to prevent the growth of phototrophic organisms. The experiment cycle was 16 days. Horizontal hydraulic circulation was used to simulate water flow in the real systems. The water flowed into the barrel continuously and the average hydraulic retention time (HRT) was 24h.

The size of coupon is 50mm×25mm×2mm. The chemical composition (wt.%) of the coupons was as follows: C (0.07-0.13%), Si (0.17-0.37%), Mn (0.35-0.65%), P (<0.035%), S (<0.035%), with the remainder consisting of Fe.

The water was based on pure water and was prepared by adding chemical components. The main water qualities parameters are presented in Table 1. W1 to W6 represent the working conditions.

Table 1. Main water quality parameters in the experiment.

Water quality parameter	W1	W2	W3	W4	W5	W6
pH	8.1	8.1	8.1	8.1	8.1	8.1
Turbidity (NTU)	1.3	1.3	1.3	1.3	1.3	1.3
Hardness(mg/L CaCO ₃)	50	50	50	50	50	50
Cl ⁻ (mg/L)	26.6	106.5	213.0	26.6	106.5	213.0
SO ₄ ²⁻ (mg/L)	36.0	144.0	288.0	36.0	144.0	288.0
BSA (mg/L)	0	0	0	20.0	20.0	20.0
PO ₄ ³⁻ (mg/L)	0.8	0.8	0.8	0.8	0.8	0.8
HCO ₃ ⁻ (mg/L)	180.0	180.0	180.0	180.0	180.0	180.0
LR	0.5	2.0	4.0	0.5	2.0	4.0

Larson ration (LR)=[Cl⁻]+2[SO₄²⁻]/[HCO₃⁻], units of [Cl⁻], [SO₄²⁻] and [HCO₃⁻] in mol/L.

Coupon treatment

Before experiment, the coupon was treated as following steps: (1) soaked in acetone and wiped by cotton 2 times; (2) put on the clean filter paper and dried by cold wind; (3) washed by distilled water for 10s and put into anhydrous ethanol; (4) put on the clean filter paper and dried by cold wind; (5) wrapped in clean filter paper, then put into dryer and weighed after 24 hours.

During experiment, 3 coupons were taken from each reactor each time. One was put into 80mL pure water and ultrasonic oscillation was used for 5min. Then took it out and put into ultra-low temperature freezer (50°C) for 2h with other two coupons. After

that, 3 coupons were put into vacuum cooling dryer for 12h. At last, put them into dryer.

After experiment, 3coupons were washed by cleaning fluid (10%HCl and 0.5%HMTA (hexamethylenetetramine)). Then washed by pure water for 10s and put into Sodium hydroxide solution (60g/L) for 1min. Then washed by pure water for 10s and soaked in anhydrous ethanol for 1min. At last, put them into dryer and weighed after 24h.

SEM-EDX

The microphotographs of corrosion scales on the coupon were taken by Scanning Electronic

Microscope (SEM, Quanta 200 FEG, Holland) and the relevant elemental composition of targeted area was measured by using Energy Dispersive X-ray Spectrum (EDX).

XRD

The composition of corrosion scales on the coupon were tested by X-Ray Diffraction (XRD, X'PERT-PRO MPD, Holland)and the operation parameters were: Cu radiation at 40 kV and 40 mA, the 2θ ranged from 5° to 90° with a 0.04° step, and a 0.4s count time at each step.

ICP-OES

The concentration of total iron was determined by the Inductively Coupled Plasma-Optical Emission Spectrometer (ICP-OES, PerkinElmer Optima 8300, USA) after joining 1mol/LHNO₃.The concentration of dissolved iron was determined by ICP-OES after filtered through 0.45 μ m microfiltration membrane.

In the experiment, water flowed out from the top of the reactor so that the insoluble iron was intercepted and accumulated. The release rate of the insoluble iron was calculated as follows:

$$R = \frac{(c-c')-(c_0-c'_0)}{T-T_0} \quad (1)$$

Where R is the release rate(mg/(L·d)); C₀ is the concentration of total iron in last time(mg/L); C₀' is the concentration of dissolved iron in last time (mg/L); C is the concentration of total iron in this time (mg/L); C' is the concentration of dissolved iron in this time (mg/L); T₀ is the last sampling time (d); T is this sampling time (d).

HPC

The microorganism was counted for by Heterotrophy Plate Counts (HPC).

RESULTS

Corrosion rate

BSA inhibited corrosion because the corrosion rate with BSA was always below the one without BSA according to Figure 1-a, b and c. When LR was 0.5 and 2.0, the rate got the peak at the 2nd day, then decreased quickly and decreased slowly after 8 days. The inhibition ratios of BSA were 22.9% and 22.2%. When LR was 4.0, the rate got the peak at the 1st day, then decreased quickly and decreased slowly after 8 days. The inhibition ratio of BSA was only 9.1% and the effect of BSA became very little especially after 4 days. Compared to the inhibition ratios of which LR was 0.5 and 2.0, the inhibition ratio of which LR being 4.0 was smaller so that the inhibition effect reduced significantly with BSA and LR being 4.0.

Overall, the corrosion rates of W4, W5 and W6

were ranked as W4<W5<W6 which was consistent with LR according to Figure 1-d. The phenomenon showed that the inhibition effect of BSA was poor under the condition of LR being high.

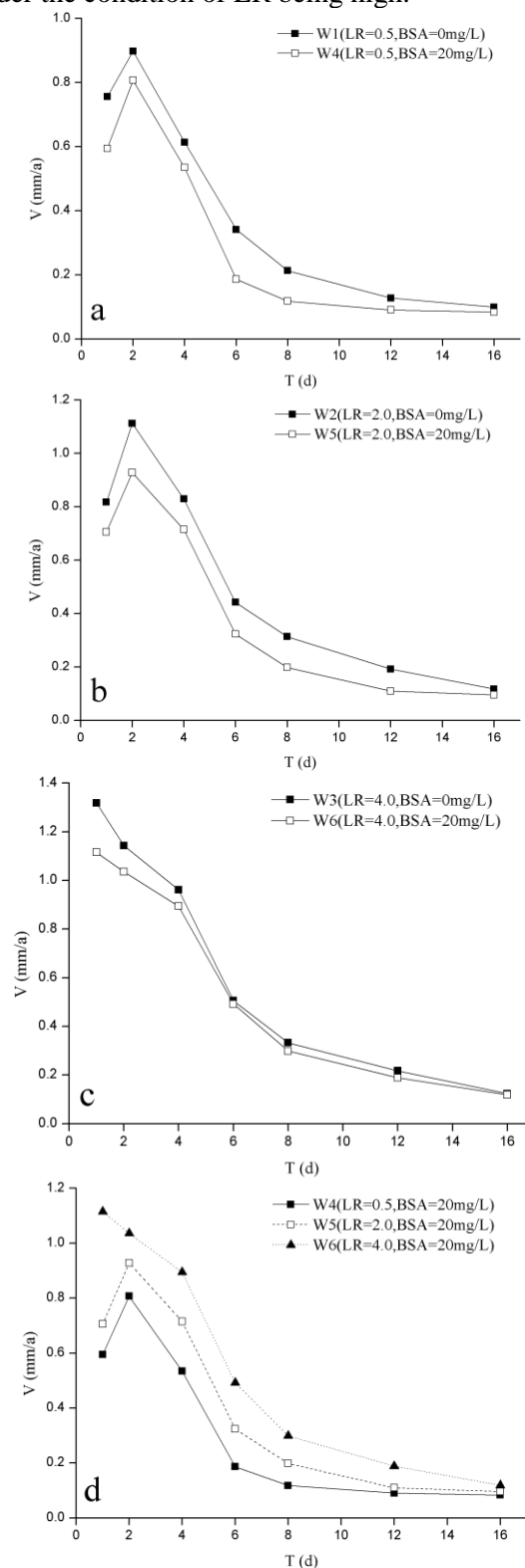


Fig. 1. Corrosion rate of coupons in 16 days. (a) LR=0.5, (b) LR=2.0, (c) LR=4.0, (d) BSA=20mg/L.

Morphology of corrosion scales

Based on SEM analysis, the calcium oxide which

had regular shape formed much with the thin iron oxide on the surface of corrosion scales in the 1st day without BSA (Figure 2-a). The size of calcium oxide became bigger and some areas became bare due to the scales fell off in the 4th day (Figure 2-b). The calcium oxide became bigger and more and the scales became thicker in the 16th day (Figure 2-c).

Compared to the scales without BSA, there were some iron oxide and less calcium oxide in the first 4 days (Figure 2-d,e). The phenomenon of scales fell off still occurred (Figure 2-e). However, much calcium oxide appeared on the scales in the 16th day (Figure 2-f).

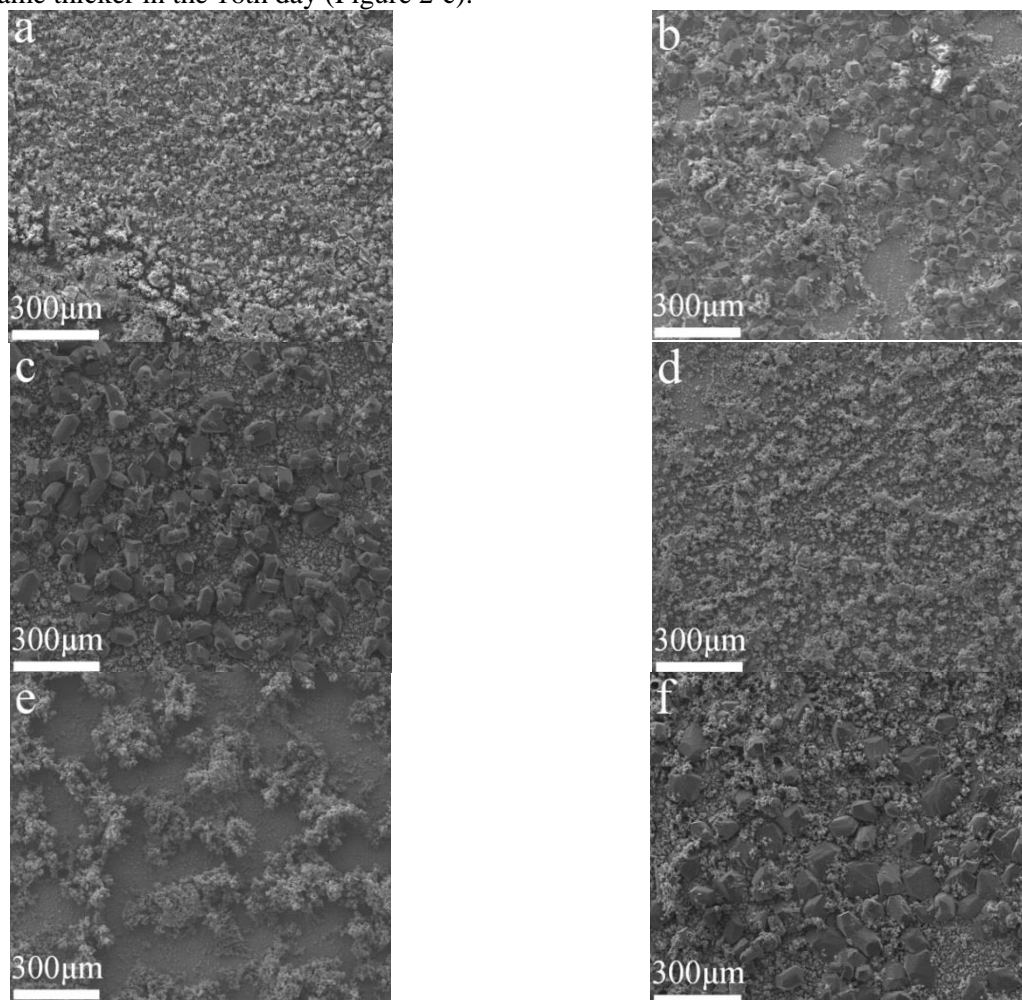


Fig. 2. SEM images of corrosion scales without (W1) and with (W4) BSA. (a) W1 in 1st day; (b) W1 in 4th day; (c) W1 in 16th day; (d) W4 in 1st day; (e) W4 in 4th day; (f) W4 in 16th day.

Composition of corrosion scales

Composition of corrosion scales changed with time in W1 (without BSA) (Figure 3-a). In the 1st day, the corrosion scales were comprised mainly of γ -FeOOH (41.8%), CaCO_3 (16.9%) and $\text{Fe}(\text{OH})_3$ (22.4%). The proportion of γ -FeOOH and $\text{Fe}(\text{OH})_3$ decreased much, but the proportion of α -FeOOH and CaCO_3 increased while the remainder changed little. In the 16th day, the corrosion scales were comprised mainly of γ -FeOOH (16.8%), α -FeOOH (23.6%) and CaCO_3 (24.2%) while each remain composition was about 9%.

Differ from W1, the composition of corrosion scales W4 (with BSA) was mainly γ -FeOOH

(46.7%), α -FeOOH (11.9%) and $\text{Fe}(\text{OH})_3$ (21.7%) with few CaCO_3 (2.3%) in the 1st day (Figure 3b). Similarly, the proportion of γ -FeOOH decreased much and α -FeOOH and CaCO_3 increased while the remainder changed little. In the 16th day, the corrosion scales were comprised mainly of γ -FeOOH (16.9%), α -FeOOH (34.5%) and CaCO_3 (19.4%) while each remain composition was about 6%.

Overall, composition of corrosion scales after 16 days was similar and mainly contained γ -FeOOH, α -FeOOH and CaCO_3 . However, the formation of CaCO_3 was inhibited in the water with BSA while α -FeOOH increased and became main part of scales.

The effect of inhibition worked in the first 4 days and weakened in the following days.

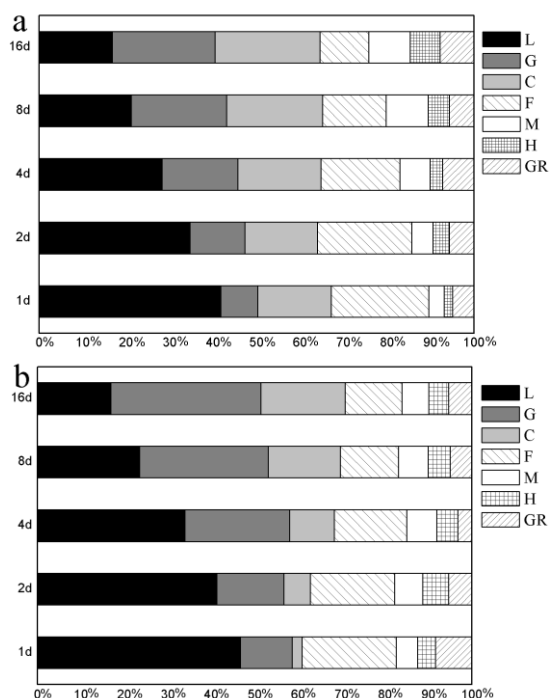


Fig. 3. Crystalline composition variation of corrosion scales. (a) W1, (b) W4.

[L: Lepidocrocite, γ -FeOOH; G:Goethite, α -FeOOH; C: Calcite, CaCO_3 ; F: $\text{Fe}(\text{OH})_3$; M: Magnetite, Fe_3O_4 ; H: Hematite, Fe_2O_3 ; GR: green rust (CO_3 , SO_4 , or PO_4)]

Rate of insoluble iron release

The rate of insoluble iron release in the water with BSA was below the one without BSA in the first 6 days was shown as Figure 4. But the condition after the 6th day was opposite and rate of insoluble iron release in the water with BSA was above.

Figure 4-d shows that the changes of rate of insoluble iron release were similar even LR was different. The rate of insoluble iron release decreased fast in first 4 days, then increased and got the peak in the 8th day. Overall, the rates of insoluble iron release were ranked as $W4 < W5 < W6$ which was consistent with LR increasing. The phenomenon was similar to the corrosion rate.

The total number of microorganism

Compared to the condition with BSA, the total number of microorganism was too small. Figure 5 shows that the changes of total numbers of microorganism of W4, W5 and W6 was similar even they had different LR. The total number of microorganism of them decreased in first 2 days then increased. W5 and W6 reached the peak value as $8.64 \times 10^8 \text{CFU/L}$ and $12.56 \times 10^8 \text{CFU/L}$ in the 6th day, and then decreased fast. But W4 reached the peak value as $13.08 \times 10^8 \text{CFU/L}$ in the 8th day and

then decreased fast. The total numbers of microorganism of three work conditions have little differences with same concentration of BSA and do not straightly related to changes of LR

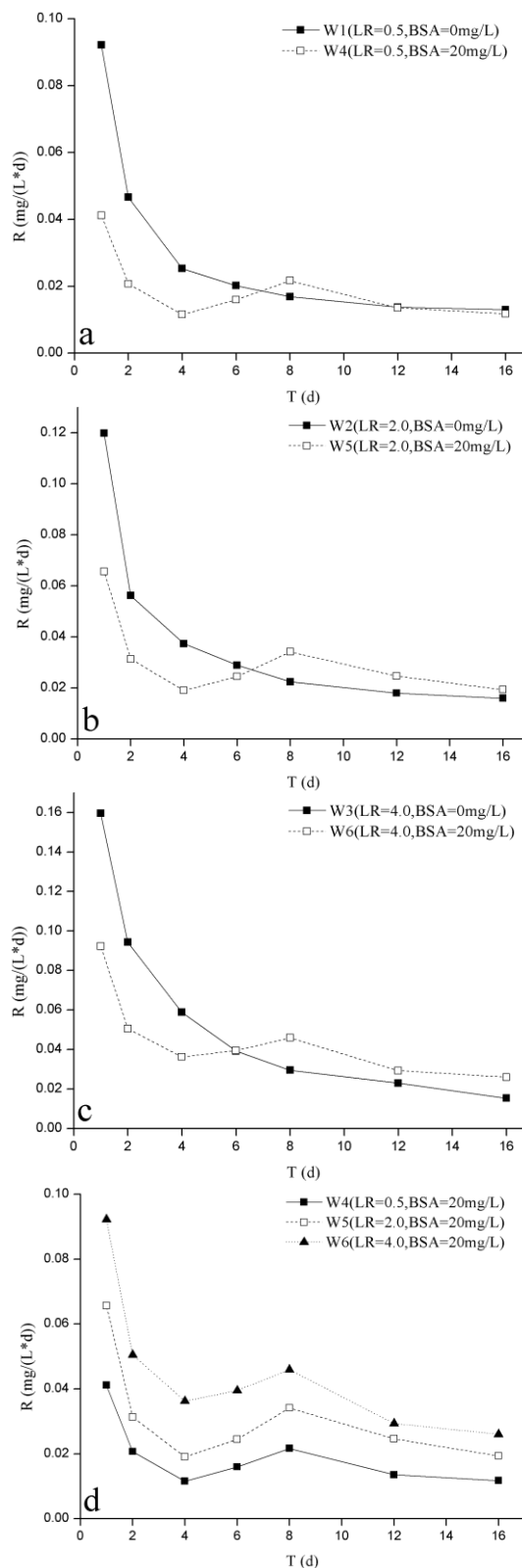


Fig. 4. The insoluble iron concentration under different conditions.(a) LR=0.5, (b) LR=2.0, (c) LR=4.0, (d) BSA=20mg/L.

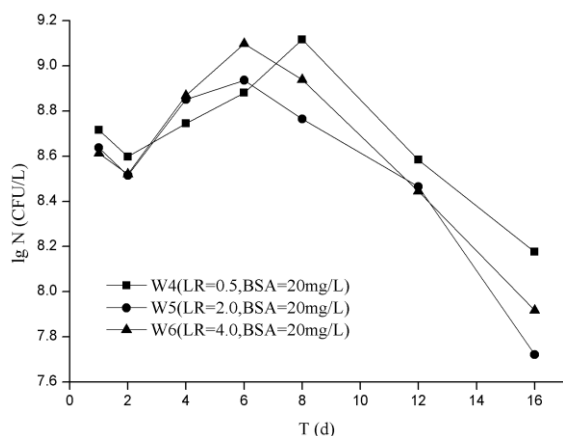


Fig. 5. The total number of microorganism under different conditions.

DISCUSSION

Corrosion mechanism under water without BSA

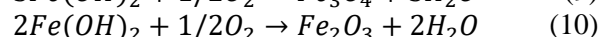
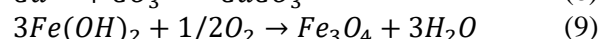
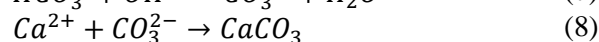
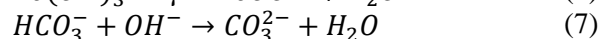
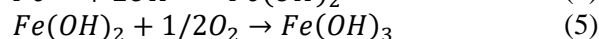
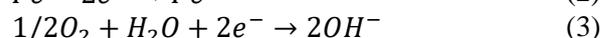
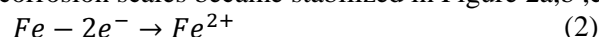
In this experiment, the main type of corrosion is electrochemical corrosion without BSA (W1, W2, W3) due to low concentration of microorganism.

The electrochemical corrosion of carbon steel was mainly about the iron-based redox reaction [15] which was in accordance with dissolved oxygen model theory. In the early, steel exposed to water, which develops galvanic effect under the condition of water and dissolved oxygen. Iron in anode was oxidized into Fe^{2+} and dissolved into the water (Eqs.2). Dissolved oxygen at the cathode was reduced to OH^- (Eqs.3) which combined with Fe^{2+} to form $Fe(OH)_2$ (Eqs.4). $Fe(OH)_2$ was easy to be further oxidized to form $Fe(OH)_3$ in the presence of high concentration of DO (Eqs.5). Some $Fe(OH)_3$ were easily occurred to dehydration and formed γ -FeOOH (Eqs.6). And the local concentration of OH^- increased which would lead to move balance to the right in Eqs.7 and form CO_3^{2-} , then further formed $CaCO_3$ (Eqs.8). These reactions happened when the iron directly contacted with water and sufficient DO, so these reactions mainly happened at the beginning of the corrosion or the top layer of corrosion scale. This also explained the formation of calcium scale and iron oxide layer in Figure 3-a and the product was mainly composed of γ -FeOOH, $Fe(OH)_3$ and $CaCO_3$ in Figure 4-a in the 1st and 4th day.

Along with the corrosion layer growing, the transmission of DO was restrained and would be insufficient. New formation of $Fe(OH)_2$ was transformed to Fe_3O_4 or Fe_2O_3 through intermediate products (green rust) (Eqs.9,10). At the same time, some γ -FeOOH became α -FeOOH while corrosion going on. It can be found in Figure 4a that γ -FeOOH was dominant in the early period, then would become α -FeOOH due to particle-particle interactions [16]. Therefore, shortage of DO would

happen when corrosion layer became thicker. The proportion of Fe_3O_4 , Fe_2O_3 , green rust and α -FeOOH would rise while the proportion of $Fe(OH)_3$ and γ -FeOOH reduced, which was consistent with the change of proportion in Figure 4-a.

The thick corrosion scale formed in the last period and the corrosion layer becomes a hinder to the transmission of DO so that anaerobic circumstance was created. The oxidation of $Fe(OH)_2$ became slow and made the balance in Eqs.6 tend to move left which made the concentration of Fe^{2+} too high near the corrosion floor. Therefore, the iron dissolution of carbon steel was inhibited which was the reason why the corrosion tended to be flat and the corrosion scales became stabilized in Figure 2a,b,c.



Effect on corrosion by BSA

In this experiment, compared with W1, W2 and W3, more protein was added to W4, W5 and W6, which had obvious influence on the corrosion of carbon steel. The effect of protein can be divided into two parts: (1) the effect of film formed of the protein on carbon steel surface by adsorption; (2) the effect of the microorganism produced by the protein on the corrosion.

The adsorption film

After the contacting of protein and carbon steel, a thin layer of protein formed by adsorption would be attached to the surface of the carbon steel within a few minutes [17]. The adsorption of the protein on surface was mainly affected by three kinds of effects, electrostatic force, hydrogen bond and dispersion force. Among them, the electrostatic force produced by the electric field between the protein and the surface of material was the strongest, and then the electrostatic force between intra molecular amino acids and surface, the weakest was dispersion force produced by instantaneous dipole [18]. The adsorption process of protein was not only the process of mixing effect of both physical adsorption and chemical adsorption, and it was a complex physiological process. It was related to the surface hydrophilic/hydrophobic property, chemical composition and microstructure, and also related to the size, charge and structure stability of the protein

molecule [19].

It can be seen from Figure 3 and Figure 4, compared to condition W1, W2 and W3 which without BSA, the corrosion fouling layer of the condition W4, W5, W6 which with protein did not form a significant layer of calcium scale layer in the early stage and it was mainly composed of ordinary iron oxide. However, Figure 2 and Figure 5 showed that the conditions with protein inhibited the corrosion and iron release in the early stage, showing that the protein in the early stage does have the effect of inhibiting corrosion. Researchers showed that [20-21] water of hydration and the opposite charged ions which were released by contact between proteins and surface would increase the entropy. With the promotion of increase of the entropy, the adsorption of proteins began by active patch on the groups in the microcell riveting with material surface. As the extension of time, some chemical bond in the molecule of adsorbed proteins opened and formed more locus combination with surface. Consequently, molecular conformation of proteins changed. This change may be the reason resulting in calcium scale layer difficult to form greatly in the early stage, and the formed part can be also loose off due to the effect of protein film.

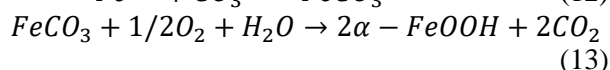
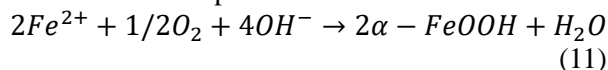
At the same time, protein film in the one hand could fill the pores formed during the formation of iron oxide layers, making the scale layer more compact, thus having good corrosion inhibition effect in the early stage; on the other hand, due to the mobility and the vulnerability of protein film, along with the corrosion process more corrosion products formed, the protein film gradually cracking and parts of iron oxide coming into the water, resulting in an increase in iron release. This can explain that the release of iron have a short period of rise after 6 days in Figure 5-d. This was a kind of original balance broken between protein film and iron scale layer, and new corrosion scale forming process, and the calcium scale could also be well adhered to on the scale layer, as can be seen in Figure 3-f.

Microbial action

Figure 6 shows that there were lots of microorganisms in the corrosion scales in W4, W5 and W6. But the total numbers of microorganism of three work conditions did not straightly related to changes of LR. The total numbers of microorganism of work conditions without BSA were too small which indicated that microbial action was the important reason for corrosion scales differences between with and without BSA.

Different microorganisms had different effects during the formation of corrosion scales. It was

found that anaerobic bacteria groups in the deposit sediment would induce the formation of Fe_3O_4 with high pH and low redox potential [22]. Genin et al. [23] found similar phenomenon in their study. It was indicated that there was microbial mechanism which could induce the formation of products such as Fe_3O_4 and affect with the electrochemical corrosion. Bonneville et al. [24] found the iron-reducing bacteria was related to the reduction reaction of Fe^{3+} and controlled release of iron. Yang et al. [25] and Wang et al. found the iron-reducing bacteria could promote to form protective layer and control the release of iron so that the corrosion would be inhibited. Jin et al. [26] found that density of iron-reducing bacteria directly influenced the formation of green rust in the core layer. Under the effects of iron-oxidation bacteria, Fe^{2+} would be directly oxidized to α - $FeOOH$ (Eqs. 11, 12 and 13) [27]. Additional explanation for the proportion of α - $FeOOH$ was higher than the one without BSA was provided.



Influence on corrosion under BSA by Larson ratio

Based on Figure 1-d and Figure 5-d, corrosion rate and rate of insoluble iron release were ranked as $W4 < W5 < W6$ which was consistent with LR. It is indicated that corrosiveness of water which is characterized by LR obviously influences the corrosion of carbon steel. In the early period, the inhibition effect of BSA due to the formation of film and the microbial action slowed down the electrochemical corrosion and inhibited the total corrosion. In the last period, the inhibition effect of BSA weakened and the corrosion condition gradually close to the one without BSA until steady due to the main electrochemical corrosion.

The inhibition ratio of corrosion rates were ranked as $W6 (9.1\%) < W5 (22.1\%) < W4 (22.9\%)$. The inhibition ratio of corrosion rate decreased fast when the LR increased. It indicates that the electrochemical corrosion always dominates the corrosion.

CONCLUSIONS

This work was aimed at trying to find effect mechanism of proteins and give probable explanation of different effects under different Larson ratio by comparing the corrosion of carb on steel between with and without BSA.

Compared to the work condition without BSA,

the one with BSA had lower corrosion rate. The corrosion scales had few CaCO₃ in the early period due to BSA. In the last period, the composition of corrosion scales with BSA was similar to the one without BSA and mainly included γ -FeOOH (16.8%), α -FeOOH (23.6%) and CaCO₃ (19.4%). The rate of insoluble iron release with BSA was lower in first 6 days and higher in last days. The total numbers of microorganism of three work conditions had little differences with same concentration of BSA and did not straightly related to changes of LR.

The mechanism of corrosion without BSA mostly matched electrochemical corrosion and was about redox reaction of iron. The effect of proteins mainly included two aspects: (1) the adsorption film which was mainly composed of proteins changed the surface properties of corrosion scales and made the scales denser to inhibition corrosion. It also could make calcium oxide easier to fall off so that calcium scale layer could not form; (2) microbial action might accelerate corrosion by promoting the redox reaction of iron or inhibit corrosion by promoting to form a protective layer and reducing release of iron. At last, the electrochemical corrosion dominates the corrosion. Though proteins have obvious inhibition effect, it does not work when LR is high. The use of BSA as inhibitor should be after considering the water quality especially LR.

Acknowledgments: This work was supported by the Funds for the National Natural Science Foundation of China (Grant No. 51278026).

REFERENCES

1. J. Świetlik, U. Raczyk-Stanisławiak, P. Piszora, J. Nawrocki, *Water Res.*, **46**, 1 (2012).
2. Wang L.P., Study of Iron Stability Problem and Pipes Corrosion in Drinking Water Distribution System [dissertation], Tianjin, China, Tianjin University, 2007.
3. S.A. Imran, J.D. Dietz, G. Mutoti, *J. Amer. Water Works Assoc.*, 93 (2005).
4. Chen L., Jia R.B., LR L., *Environ. Sci. Processes & Impacts*, **15**, 1332 (2013).
5. S. Eichler, R. Christen, C. Hölftje, *Appl. Environ. Microbiol.*, **72**, 1858 (2006).
6. Wang H., Hu C., Hu X., *Water Research*, **46**, 1070 (2012).
7. A. Kuch, *Corrosion Sci.*, **28**, 221 (1988).
8. P. Sarin, V.L. Snoeyink, J. Bebee, *Water Research*, **35**, 2961 (2001).
9. P. Sarin, V.L. Snoeyink, D.A. Lytle, *J. Environ. Eng.*, **130**, 364 (2004).
10. A. Sander, B. Berghult, A.E. Broo, *Corrosion Sci.*, **38**, 443 (1996).
11. T.E. Larson, R.V. Skold, *J. Amer. Water Works Assoc.*, 1294 (1957).
12. T.E. Larson, R.V. Skold, *Corrosion*, **14**, 43 (1958).
13. K. Merritt, S.A. Brown, *J. Biomed. Mat. Research*, **22**, 111 (1988).
14. Zhang F., Pan J., P.M. Claesson, *Electrochimica Acta*, **56**, 1636 (2011).
15. W. Stumm, B. Sulzberger, *Geochimica et Cosmochimica Acta*, **56**, 3233 (1992).
16. M. Yamashita, H. Miyuki, Y. Matsuda, *Corrosion Sci.*, **36**, 283 (1994).
17. S. Haemers, M.C. van der Leeden, G.J.M. Koper, *Langmuir*, **18**, 4903 (2002).
18. B.D. Ratner, A.S. Hoffman, F.J. Schoen, Biomaterials science: an introduction to materials in medicine, Academic press, Pittsburgh, 2004.
19. C.M.A. Brett, E. Jorge, C. Gouveia-Caridade, Passivation of Metals & Semiconductors & Properties of Thin Oxide Layers, 351 (2006).
20. W. Norde, *Adv. Colloid & Interface Sci.*, **25**, 267 (1986).
21. W. Norde, J. Lyklema, *J. Colloid & Interface Sci.*, **71**, 350 (1979).
22. F. Jorand, A. Zegeye, J. Ghanbaja, *Sci. Total Environ.*, **409**, 2586 (2011).
23. J.M.R. Génin, P. Refait, M. Abdelmoula, *Hyperfine Interactions*, **139**, 119 (2002).
24. S. Bonneville, T. Behrends, P. Van Cappellen, *Geochimica et Cosmochimica Acta*, **70**, 5842 (2006).
25. Yang F., Shi B., Gu J., *Water Research*, **46**, 5423 (2012).
26. Jin J., Wu G., Guan Y., *Water Research*, **71**, 207 (2015).
27. Sun H., Shi B., Lytle D.A., *Environ. Sci.: Processes & Impacts*, **16**, 576 (2014).

Removal of nitrate nitrogen from water via aerobic denitrification under static and dynamic experimental settings

Daping Xia^{1,2,3}, Xinyi Wang^{1,3,4*}, Zhen Wang², Shunan Zhang¹

¹ School of Resources and Environment, Henan Polytechnic University, Jiaozuo, China

² School of Energy Science and Engineering, Henan Polytechnic University, Jiaozuo, China

³ Collaborative Innovation Center of Coalbed Methane and Shale Gas for Central Plains Economic Region, Henan Province 454000, China

⁴ Institute of China Pingmei Shenma Group, Pingdingshan 467000, China

Received June 3, 2016; Revised September 20, 2016

A strain of aerobic denitrifying bacteria was isolated from mine water and further investigated for its characteristics of growth and denitrification. As both of optimal C/N ratio and rotational speed were determined through static-sample experiments, batch-fermentor experiments were subsequently conducted respectively with one-time addition and continuous equivalent additions of nitrate nitrogen (NO_3^- -N). A phase of exuberant metabolism and rapid denitrification was noted after 20 h of cultivation, the logarithmic growth phase was observed at the 25th hour, and the duration of the entire lifecycle was determined to be 120 h as a whole. The most effective denitrification was achieved during static-sample experiments under such conditions as nitrate concentration of 360 mg/L, 10% bacterial inoculum, initial pH of 7.5, C/N ratio of 10:1, and rotational speed of 100 rpm, as compared to that of batch-fermentor experiments conducted under similar conditions, but only with lower nitrogen gas production. Although the addition of 10% bacterial inoculum led to the highest NO_3^- -N removal rate, the addition of 15% bacterial inoculum accomplished an increased NO_3^- -N removal rate after pH adjustment. Continuous equivalent additions of NO_3^- -N in the denitrification experiments resulted in a more complete use of carbon sources, more stable pH changes, and more effective denitrification, comparing with one-time NO_3^- -N addition. The achieved results provide a critical experimental and industrial reference for the bio-removal of nitrate nitrogen in groundwater.

Keywords: Aerobic denitrification, Batch-fermentor experiment, Bio-removal of nitrate nitrogen, Mine water, Static-sample experiment.

INTRODUCTION

Nitrate and nitrite have been universally accepted as environmental contaminants widely present in groundwater, surface water and then being enriched altogether with the nitrogen cycle in ecosystem and consequently consumed by animals and humans [1]. Nitrate and nitrite are toxic and they can be inter-convertible through a series of chemical and biological processes, during which nitrite is reduced to various compounds or oxidized to nitrate, while nitrate is metabolized to nitrite, which is approximately 10-fold more toxic [2]. High levels of nitrate and nitrite in groundwater mainly result from human and animal wastes and excessive use of chemical fertilizers. The other most common sources are including uncontrolled land discharges of municipal and industrial waste waters, overflowing septic tanks, processed food, dairy and meat products, and decomposition of decaying organic matters buried in the ground [3].

Nitrate released into environment can lead to serious problems, such as eutrophication,

deterioration of water quality and potential hazard to human health [4, 5]. Conventional techniques including coagulation, filtration and disinfection are not effective enough to eliminate nitrate and nitrite contaminants from water. Other methods such as reverse osmosis, ion exchange, adsorption, electrodialysis and chemical treatment have also been developed in order to remove nitrate nitrogen, which are only suitable for lower concentration nitrate wastewater [6, 7, 8, 9]. Other than these physical and chemical processes mentioned above, the biological denitrification process is a comparatively promising as well as low-cost technique for removing the nitrogen-source pollutants from groundwater and has been widely used for total nitrogen (TN) removal from water in recent decades [10, 11, 12, 13, 14], which is in fact a so-called “bio-removal” process involving the transformation of nitrate into nitrogen gas (denitrification). Denitrifying bacteria are one of the significant bioresources applicable in groundwater management by oxidizing organic carbon using nitrate as the electron acceptor under anoxic and aerobic conditions [15, 16, 17]. Our Previous study has proved the presence of

To whom all correspondence should be sent:
E-mail: wangxy@hpu.edu.cn

indigenous denitrifying bacteria in mine water of post-mining operations, to great extent indicating the possibility for removing the nitrate/nitrite pollutants from groundwater through the denitrification of the isolated indigenous bacteria [18].

However, the entire process of denitrification is so complex [19, 20, 21], for it comprises a series of reductions and electron transports and is influenced by some of the factors responsible for this process such as oxygen, temperature, pH, carbon source, C/N ratio, etc, making the biological denitrification of water usually slow and lasting a quite long period. Thus, a highly efficient denitrification process is needed. Some efforts were made previously concerning the simulation of denitrification [22, 23, 24], basically by introducing a prior single experimental setting, which to some extent did not consider the potential influence of the variations of external experimental conditions on denitrification performances.

In present study, we conducted the static-sample and batch-fermentor experiments simultaneously as pilot scale tests to investigate the denitrification performances of indigenous aerobic denitrifying bacteria isolated from mine water under static and dynamic experimental settings respectively. By using glucose as sole carbon source and KNO_3 as electron acceptor, we further introduced the continuous equivalent additions and one-time additions of nitrate nitrogen (NO_3^- -N) separately for the batch-fermentor experiments with the removal rates of NO_3^- -N in groundwater as the performing indicators, aiming to investigate the differences of the variations of external experimental settings and the influences on biological denitrification for the removal of nitrate nitrogen in groundwater. We intend to provide a valuable reference for future study and industrial use regarding the biological treatment of nitrate- and nitrite-polluted groundwater.

MATERIALS AND METHODS

Materials

The aerobic denitrifying bacteria, which were isolated from mine water after being cultivated for 96 h in liquid culture medium, were used as inocula for the following experiments. The medium

adopted in this study was composed of glucose, peptone, beef extract, yeast extract, Na_2CO_3 , and L(+)-Cysteine, as tabulated in Table 1.

Table 1. Constituents of culture medium for isolated bacteria.

Constituent	Mass (g)
Glucose	5–20
Peptone	10–15
Beef extract	2–3
Yeast extract	5–10
Na_2CO_3	3–4
L(+)-Cysteine	0.2–0.6

Analytical methods

Nitrogen and other gaseous co-products produced during fermentation were examined using gas chromatography (SP-2100A, BFRL). The concentrations of reducing sugar that had not been consumed were determined by ultraviolet spectrophotometer (UV5200, Metash), with the curve of glucose as the standard. The concentrations of nitrate ions were determined using phenol disulfonic acid spectrophotometry. The OD_{600} values (optical density) of the cultivated bacteria were determined by ultraviolet spectrophotometer (UV5200, Metash), with distilled water as the control.

Experimental set-up

A glass fermentor with a working volume of 1 L was employed in this study, and its schematic diagram was shown in Figure 1. The fermentor was equipped with a heating pad for controlling the temperature at 35°C and a magnetic stirring apparatus for maintaining a rotational speed of 100 rpm. Besides, pH and ORP meters and an advanced computing system were also applied for monitoring the experimental process.

Determination of the growth cycle of aerobic denitrifying bacteria

A 250-mL conical flask containing 200 mL of the culture medium was inoculated with 10% of the prepared denitrifying bacteria after the pH was adjusted to around 7.0. The flask was sealed and placed in a shaker for cultivation at $(37\pm 1)^\circ\text{C}$ and 100 rpm, and the OD_{600} values were determined at specific intervals.

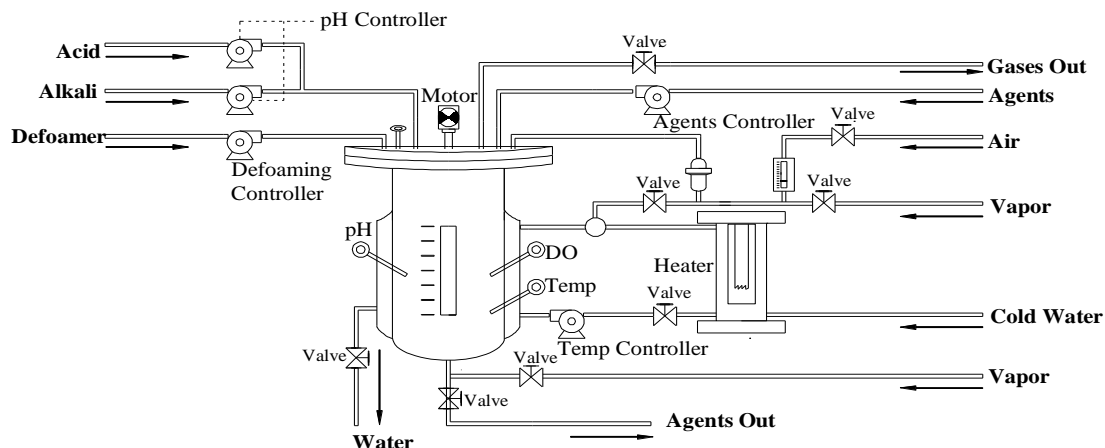


Fig. 1. Schematic diagram of fermentor used in experiments.

Static-sample experiments

The denitrification experiments were performed in a set of simply-connected experimental units (as shown in Figure 2), in which glucose was used as the carbon source and C/N ratios were pre-adjusted to 3:1, 7:1, 10:1, and 20:1. In addition, 200 mL of the culture medium and 360 mg/L NO_3^- -N were employed. The experiment was conducted at a constant temperature of 35°C for static cultivation in shakers at 60, 80, 100, and 120 rpm, respectively.

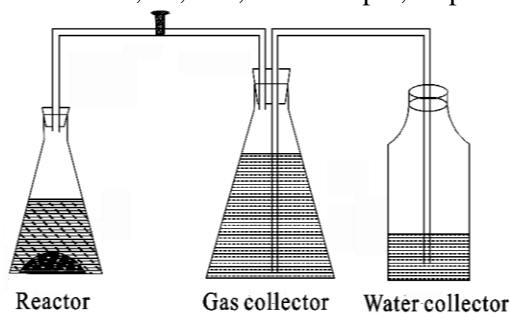


Fig. 2. Static-sample experimental units.

Batch-fermentor experiments

Based on the optimal C/N ratio and rotational speed acquired from static-sample experiments, the batch-fermentor experiments with one-time addition of NO_3^- -N were conducted under the same conditions of inoculum, temperature, and pH as those of the static ones. Furthermore, the pH of the cultures with each concentration of the bacterial inoculum was adjusted to 7.5 by adding HCl and the denitrification process was monitored. Furthermore, batch-fermentor experiment with NO_3^- -N added as the electron acceptor to the fermentor at specific intervals (continuous equivalent additions) was conducted under the same conditions.

RESULTS AND DISCUSSION

Growth cycle of aerobic denitrifying bacteria

The OD_{600} value of the aerobic denitrifying bacterial culture was 0.291, and 10% of the culture was inoculated into 200 mL of the culture medium and incubated for 72 h. The growth cycle of the inoculated aerobic denitrifying bacteria successively comprised the lag phase, logarithmic growth phase, stable growth phase, and decline phase, as shown in Figure 3. After 10 h of cultivation, the OD_{600} value of the culture, which was nearly 0.2 prior to inoculation, significantly increased during the logarithmic growth phase that occurred at 12–63 h. Then, after 70 h, stable growth phase was observed, during which the amount of bacteria did not exhibit excessive fluctuation.

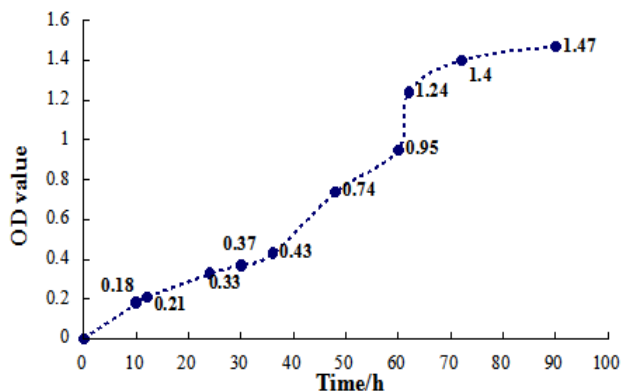


Fig. 3. Growth cycle of isolated bacteria.

Determination of the optimal C/N ratio and rotational speed

As can be observed in Table 2, the removal rate of NO_3^- -N was used as an indicator for obtaining the optimal C/N ratio and rotational speed. It reached an appreciable level of 87.30% when the C/N ratio was adjusted to 10:1, the temperature was

maintained at 35°C, and the initial pH was controlled at 7.5. The rotational speed had a major effect on the dissolved oxygen level, and higher rotation speed generally resulted in greater consumption of dissolved oxygen. In the present study, the removal rate of NO₃⁻-N reached a maximum of 88.13% when the rotational speed was 100 rpm, whereas relative lower removal rates were achieved at 60 and 120 rpm, respectively.

Table 2. Optimal C/N ratio and rotational speed determined by static-sample experiments.

C/N ratios				Rotational speeds (rpm)			
3:1	7:1	10:1	20:1	60	80	100	120
Removal rates of NO ₃ ⁻ -N							
42.96	69.50	87.30	74.50	73.25	84.11	88.13	69.34
%	%	%	%	%	%	%	%

Static-sample and batch-fermentor experiments

The batch-fermentor and static-sample experiments were compared on the basis of optimal C/N ratio and rotational speed. Considering the experimental reality and feasibility, the dosages of all the required reagents for batch-fermentor experiments were noted to be 5-fold higher than those needed for static-sample experiments. With regard to the nitrogen gas production rate and NO₃⁻-N removal rate, batch experiments yielded a slightly higher nitrogen gas production rate, but lower NO₃⁻-N removal rate, as compared to static-sample experiments (Figure 4).

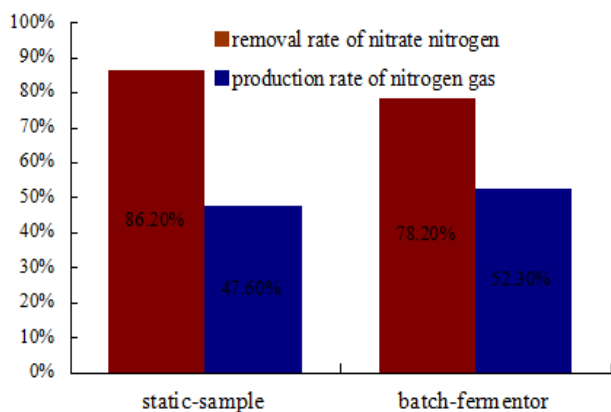


Fig. 4. Comparisons of static-sample and batch-fermentor.

Batch-fermentor experiments with various bacterial inoculum concentrations

Batch-fermentor experiments with different bacterial inoculum concentrations, such as 50, 100, 150, and 200 mL/L, respectively, 1000 g of KNO₃, and a constant OD₆₀₀ value of 0.219 were performed. As shown in Figure 5, the highest NO₃⁻-N removal rate was achieved at a bacterial inoculum concentration of 100 mL/L, because a

modest addition of bacterial inoculum neither resulted in the condition of “rich consumers but poor nutrients” nor “rich nutrients but poor consumers,” both of which did produce lower NO₃⁻-N removal rates. Furthermore, when 1 mol/L HCl was used for adjusting the pH to 7.0 in the post-reactive solution with an inoculum concentration of 150 mL/L (Table 3), both the glucose consumption rate and NO₃⁻-N removal rate increased at varying degrees possibly owing to the improvement in the growth environment and further enhancement in the metabolic activities of the bacteria in the culture.

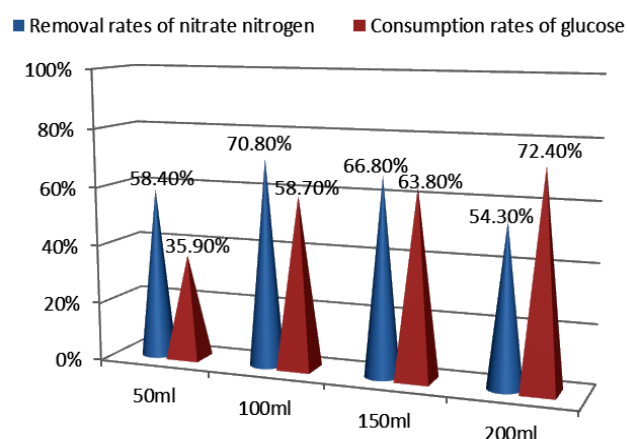


Fig. 5. Effects of various bacterial inocula concentrations.

Table 3. Effects of pH adjustment in culture containing 150 mL/L bacterial inoculum concentration.

150mL bacteria liquid	Consumption rate of glucose	Removal rate of NO ₃ ⁻ -N
Pre-adjustment of pH	63.80%	66.80%
Post-adjustment of pH	81.24%	75.07%

Continuous equivalent additions of NO₃⁻-N

The major difference between reactions performed with one-time addition of NO₃⁻-N and continuous equivalent additions of NO₃⁻-N was the time at which NO₃⁻-N was added. In other words, in reactions performed with “continuous” equivalent NO₃⁻-N additions, nitrates were added at specific intervals during the experimental process, whereas in reactions conducted with one-time NO₃⁻-N addition, nitrates were added at the beginning of the batch experiments. Fig. 6 shows that during the first 4 days (96 h) of continuous NO₃⁻-N additions, the concentration of the residue in the solution was at a relatively low but rather stable level; however, it slightly fluctuated in the last 2 days, particularly reaching a final removal rate of 88.74% at the 120th h. Therefore, the most effective denitrifying period

during reactions conducted with continuous additions of NO_3^- -N could be the first 4 days. Besides, a low pH of 6.8–8.7 was maintained throughout the entire reaction process, indicating the lack of accumulation of volatile fatty acids (VFAs) possibly due to neutralization with the OH^- ions produced during the denitrification process.

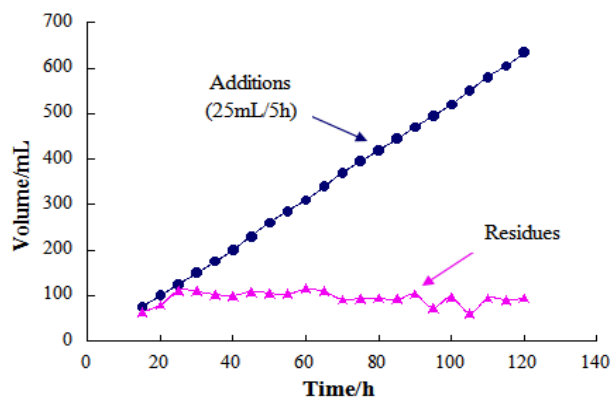


Fig. 6. Batch-fermentor performance with continuous equivalent additions of NO_3^- -N.

CONCLUDING REMARKS

The C/N ratio of 10:1 and rotational speed of 100 rpm were determined to be optimal through static-sample experiments. An optimal rotational speed can be predominant for maintaining a dissolved oxygen level suitable for the growth of bacteria.

The accumulated denitrification rate of the batch-fermentor experiments was 78.2%, which was 8% less than that of static-sample experiments. The total gas production was 600 mL, of which 68.73% was determined as nitrogen gas. After the adjustment of pH of the culture media to 7.0 with the addition of 1 mol/L HCl, 150 mL/L inoculum achieved the highest denitrification rate of 80.65% among the various bacteria inocula concentrations; however, an inoculum concentration of 100 mL/L exhibited the highest denitrification rate before the pH adjustment.

Furthermore, we concluded that the continuous equivalent additions of NO_3^- -N exhibited a 7.7% higher denitrification rate for the batch-fermentor experiments prior conducted, as compared with that performed with one-time addition of NO_3^- -N, which was evidenced by the lack of VFA accumulation during the entire process as the pH value reached nearly 7.0, indicating the function of the continuous equivalent additions of NO_3^- -N could lead to a higher biological denitrification efficiency.

Acknowledgments: This work was financed by the National Natural Science Foundation of China (No. 41272250, 41502158, 41472127), and

Technological Innovation Team of Colleges and Universities in Henan Province of China (Grant 15IRTSTHN027). The authors have declared no conflict of interest.

REFERENCES

1. P. Jakszyn, C.A. Gonzalez, *World J. Gastroenterol.*, **12**, 4296 (2006).
2. K.L. Sublette, R. Kolhatkar, K. Raterman, *Biodegradation*, **9**, 259 (1998).
3. P.C. Mishra, R.K. Patel, *J. Environ. Manag.*, **90**, 519 (2009).
4. H. Bouwer, *Water Environ. Technol.*, 292 (1989).
5. R.H. Liao, K. Shen, A.M. Li, P. Shi, Y. Li, Q.Q. Shi, Z. Wang, *Bioresour. Technol.*, **134**, 190 (2013).
6. J. Hoek, P. Ven, A. Klapwijk, *Water Research*, **22**, 679 (1988).
7. I. Mikami, Y. Sakamoto, Y. Yoshinaga, T. Okuhara, *Appl. Catalysis B Environ.*, **44**, 79 (2003).
8. H. Song, Y. Zhou, A. Li, S. Mueller, *Desalination*, **296**, 53 (2012).
9. Y. Wang, Y. Sakamoto, Y. Kamiya, *Appl. Catalysis A General*, **361**, 123 (2009).
10. B. Delanghe, F. Nakamura, H. Myoga, Y. Magara, E. Guibal, *Water Sci. Technol.*, **30**, 157 (1994).
11. X. Dong, E. Tollner, *Bioresour. Technol.*, **86**, 139 (2003).
12. H. Lemmer, A. Zaglauer, A. Neef, *Water Resources*, **31**, 1903 (1997).
13. H. Odegaard, Treatment of anaerobically pretreated effluents. In: Hall, E.R., Hobson, P.N. (Eds.), Proceedings of 5th International Symposium on Anaerobic Digestion, Pergamon Press, Bologna, Italy, 1998, pp. 225–238.
14. S. Sözen, D. Orhon, *J. Chem. Technol. Biotechnol.*, **74**, 790 (1999).
15. M. X. Xin, Y. Zhao, J. Zhou, W. C. Gao, *Microbiol. China*, **34**, 773 (2007).
16. N. Takaya, M. A. B. Catalan-Sakairi, Y. Sakaguchi, I. Kato, Z. M. Zhou, H. Shoun., *Appl. Environ. Microbiol.*, **69**, 3152 (2003).
17. L. W. Xiao, M. Rodgers, J. Mulqueen, *Bioresour. Technol.*, **98**, 739 (2007).
18. D. P. Xia, Z. Wang, X. B. Su, J. Q. Ma, *Asian J. Chem.*, **26**, 3270 (2014).
19. R. Beristain-Cardoso, A. C. Texier, E. Razo-Flores, *Rev. Environ. Sci. Biotechnol.*, **8**, 325 (2009).
20. A. De la Torre-Velasco, R. Beristain-Cardoso, P. Damian-Matsumura, J. Gómez, *Bioresour. Technol.*, **139**, 220 (2013).
21. Z. Y. Zhang, Z. F. Lei, X. Y. He, Z. Y. Zhang, Y. N. Yang, N. Sugiura, *J. Hazard. Mat.*, **163**, 1090 (2009).
22. P. An, X. C. Xu, F. L. Yang, L. F. Liu, S. T. Liu, *Chem. Eng. J.*, **222**, 32 (2013).
23. R. Li, C. P. Feng, N. Chen, B. G. Zhang, C. B. Hao, T. Peng, X. Zhu, *Ecol. Eng.*, **73**, 536 (2014).
24. B. Ovez, *Process Biochemistry*, **41**, 1289 (2006).

Fractions distribution of arsenic and cadmium in arable land soils in vicinity of mining area

Dengfeng Wang^{1,†}, Tingzhong Wang^{2,*}, Huande Feng^{1,†}, Haijie Huang¹, Di Zeng³

¹ Tropical Crops Genetic Resources Institute, CATAS, Hainan Danzhou 571737, China

² Hainan Soil and Fertilizer Station, Haikou 570203, China

³ College of Applied Science and Technology, Hainan University, Danzhou 571737, China

Received June 18, 2016; Revised September 10, 2016

Toxicity heavy metals in soil to ecological system were determined by chemical associations. It is significant to identify the distribution of heavy metals in arable land soil, due to the reflection of the bioavailability of heavy metals to crops, especially to the area of high anthropogenic heavy metals input. Sequential extraction procedures were applied to define As and Cd into six fractions, including water soluble (WS), exchangeable (EX), carbonate-bound (AC), Fe & Mn oxidized-bound (OX) and residual (RES), in arable land soil of iron deposit area. The arable land soil of mining area was contaminated by As and Cd either or both, the average concentrations of As and Cd were 59.44 and 1.403 mg kg⁻¹, respectively. The ratio of residual fraction was the topped among the six fractions of these two contaminants. The total ratio of liable fractions (AC, OX, OC) of As and Cd were 11.8% and 27.1%, and it was mainly determined by the processes of weathering of soil parent materials. The fractions of WS and EX in soil were related to the anthropogenic input of them.

Keywords: Arsenic, Cadmium, Sequential extraction procedures, Contamination.

INTRODUCTION

Mining is a mainly source of heavy metals into the environment. Mine tails and wastewaters, which cause the surrounding environment being severely contaminated by heavy metals, are created during the mining exploitation processes [1-3]. Availability, mobility, toxicity and potential ecological risk of heavy metals are determined by the chemical forms, so-called fractions [4-6]. For the purpose of estimating the bioavailability and toxicity of soil heavy metals, it is necessary to determine their chemical forms associated with different phases of soils along with the total contents. And the knowledge of how they partition among the various geochemical phases allows for a better insight into the mechanisms of retention and release involved in the process of migration and decontamination [7,8].

In order to separate the trace elements associated with the different phases, selective chemical reagents has been used, which include weak acids, chelating agents or reducing agents combined with acids [7,9,10]. One step extractions are widely used for different phases extracting due to the fact they are easy to perform, rapid and clearly show the different pollution levels of soils and sediments. Sequential extraction procedures (SEPs) provide detailed information of the differentiation of several association forms of heavy metals in soils [4,7,8,11].

And SEPs can evacuate the disadvantage of one step extractions that no potential bioavailability of heavy metals for plants can be obtained [12]. SEPs are widely applied to assess mobility and characterize the fractionation of heavy metals in sediments, soils and waste materials [4,11,13,14]. Therefore, the current study was to report on the total contents and the fractions extracted by SEPs of As and Cd in arable land soil of Shilu iron deposit area of Hainan, and identify the mainly influence factors of non-residual fractions of As and Cd in soil.

MATERIALS AND METHODS

Study area

Shilu area, which in Western Hainan Island, is very rich in mineral deposits. It is one of the most important iron ore cluster area in China. Mining in Shilu can be traced as early as three centuries ago. Along with several large scale iron mines a lot of small scale mines scattered in the area. Owing to poor mining waste management practices water and soils in the area have been contaminated by mining exploration.

Sampling and analysis

Soil samples were collected from upper 20 cm in arable land of vicinity of mine tailings. To avoid local variability, six samples within a 10 meters

diameter of each sample site

[†] The authors who contributed equally to © 2016 Bulgarian Academy of Sciences, Union of Chemists in Bulgaria

* To whom all correspondence should be sent.

E-mail: wangtingzhong2005@163.com

were mixed into one sample in the field. A total of 16 soil samples were obtained. The soil samples were air-dried at room temperature, crushed and passed through 2 mm nylon mesh sieve for soil pH and sequential extraction of As and Cd analysis. Ten grams of soil sample was ground to pass through 0.25 mm nylon sieve for organic matters (OM) and cation exchange capacity (CEC) analysis, and 0.149 nylon sieve for soil As, Cd, Ca, Si and K analysis.

The soil pH was measured using a glass electrode, at 1:5 (w/v) ratio of soil: water. After oxidized by $K_2Cr_2O_7$, the concentration of OM in soil was measured by the titration method. The CEC was determined by the Kjeldahl distillation and titration method, after extracted with NH_4OAc . The total contents of As was determined by atomic

fluorescence (AFS), Cd was measured by atomic absorption spectrometry (AAS), and Si, Ca and K were measured by ICP-AES, after digesting samples with analytically HNO_3 and $HClO_4$ [15].

The sequential extraction procedure was six-step method which proposed by Ma and Rao (Table 1) [14]. 2.5g of soil was extracted in a 100 ml polythene centrifuge tube with the corresponding extracting solution, and the samples were agitated by reciprocating shaker. The procedure was outlined in sequential order as Table 1. After each successive extraction, separation was done by centrifuging at 5000 rpm for 30 min. Supernatants were filtered with 0.45 μm microfiltration membrane and the concentrations of As and Cd were measured.

Table 1. Procedure for the sequential extraction of As and Cd in soil. † 0.25g of the residue from step 5 was digested on electric heating plate with analytically HNO_3 and $HClO_4$.

Phase/Association	Abbr.	Step	Operational definition
Water Soluble	WS	1	25ml DO- H_2O , 75rpm, 60 min
Exchangeable	EX	2	25ml 1 M $MgCl_2$ (pH 7.0), 75 rpm, 60 min
Carbonate-bound	AC	3	25ml 1M $NaOAc$ (adjusted to pH 5.0 with $HOAc$), 75 rpm, 60 min
Fe & Mn Oxided-bound	OX	4	50ml 0.25M $NH_2OH \cdot HCl$, 75rpm, 60 min
Organic-bound	OC	5	3ml 0.02M HNO_3 , 8ml 30% H_2O_2 , digestion 180 min at $85 \pm 2^\circ C$ 20ml 3.2M $HOAc/3.2M HNO_3$, digestion 600 min at $25 \pm 5^\circ C$
Residual	RES	6	Acid mixture †

Statistical analysis

All statistical analyses were performed using SAS 9.00. Analysis of variance was applied to assess significant different parameters, and the confidence interval for the Student t-test was calculated at $\alpha=0.05$. Factor analysis was applied to investigate the accumulations and distribution of fractions of As and Cd in study soil.

RESULTS AND DISCUSSION

Total contents of As and Cd in soils

Both of concentrations of these two contaminants in soils varied widely. The variations of elements contents in soils reflected the natural differences in soil genesis and the degree of anthropogenic emission. According to China's Environmental Quality Standard for Soils (GB15618-1995), the arable land soil was contaminated by one or both of As and Cd in study area (Figure 1). Due to the study area very rich in mineral deposits, the soil parent materials had relatively higher contents of heavy metals [16]. And the irrigation water for agriculture land of this area was polluted by the mining activities, which made the heavy metals accumulated on the soils in study area. Rodríguez et al. indicated that the drainage

was considered as one of the main effects causing the dispersion of pollution in mining area [17].

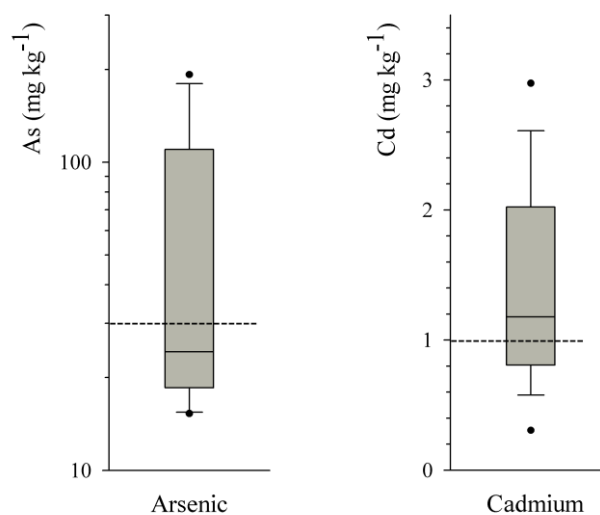


Fig. 1. Contents distribution of As and Cd in soil. -----Threshold of third grade, As 30 $mg\ kg^{-1}$, Cd 1 $mg\ kg^{-1}$ (GB15618-1995).

Fractions of As and Cd in soils

The differences between total amounts and the sum of the extracted phases were As ($2.9 \pm 1.2\%$) and Cd ($3.3 \pm 2.8\%$) of the total of the selected soil samples. This indicated that the sequential

extraction procedure and analysis techniques seemed satisfactory and practical for arable land soil of study area. Arsenic was mostly concentrated in the residual fraction (Figure 2), with the percentage of total As in the residual fraction ranging from 80.3% to 95.8%, and the average contents of residual fraction As was 50.75 mg kg^{-1} . Among the non-residual fractions, the OX fraction contained a majority content of total non-residual As in soil, partly reflecting that As tends to form OX fraction once it was in soils [18-19]. The concentration of WS fraction As was only 1.21 mg kg^{-1} , however, the ratio of this fraction only lower than RES and OX fractions. This partly attributed to that anthropogenic input of As in arable land by irrigation water, which was contaminated by heavy metals during the mining exploring processes.

The ratio of Res fraction Cd was $(54.8 \pm 16.2)\%$, which is significantly higher than other fractions (Figure 2). Among the non-residual fractions Cd in soil, the concentration of EX fraction was the highest, which was 0.742 mg kg^{-1} . The high percentage of EX fraction Cd indicated that the high potential ecological risk of Cd in study area, this may be due to the anthropogenic input Cd was mainly the EX fraction. The ratio of AC, OX and OC fractions Cd were 9.5%, 13.6% and 4.0%, respectively.

Influence factors of fractions of As and Cd in soils

The residual fractions of heavy metals in arable land soil are unlikely to be released during cropping processes. However, the WS, EX, AC, OX and OC fractions are labile and hence more available for crops and plants [20]. Due to WS and EX fractions of As and Cd are most easily to be available for crops or plants, only the AC, OX, and OC fractions of these two contaminants were taken into account

for labile fractions, which can cause potential risks to crops and human health. The contents of labile fractions of As and Cd were positive correlated with the total contents of them in soil (Figure 3). And this indicated that the concentration of labile fractions of these two elements can accumulated as the arable land soil were polluted by As and Cd.

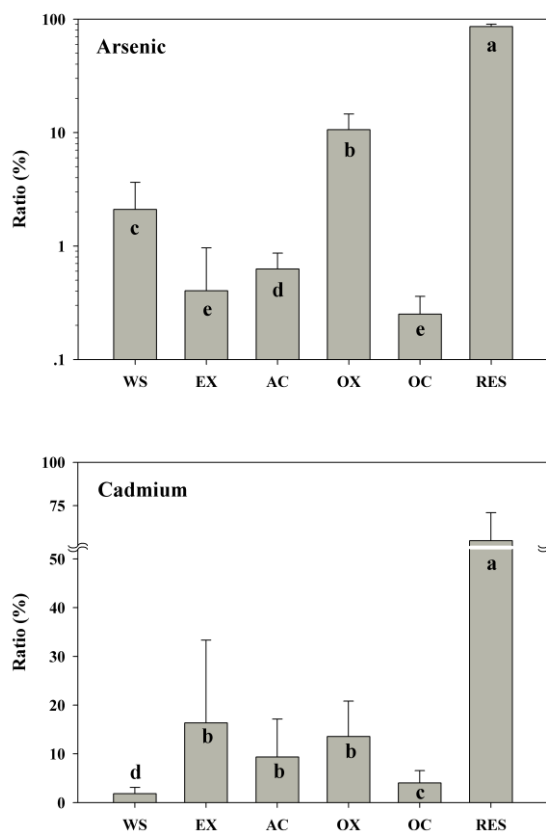


Fig. 2. The fractions distribution of As and Cd in soil. Columns with the different letters were significantly different (Sig.<0.05).

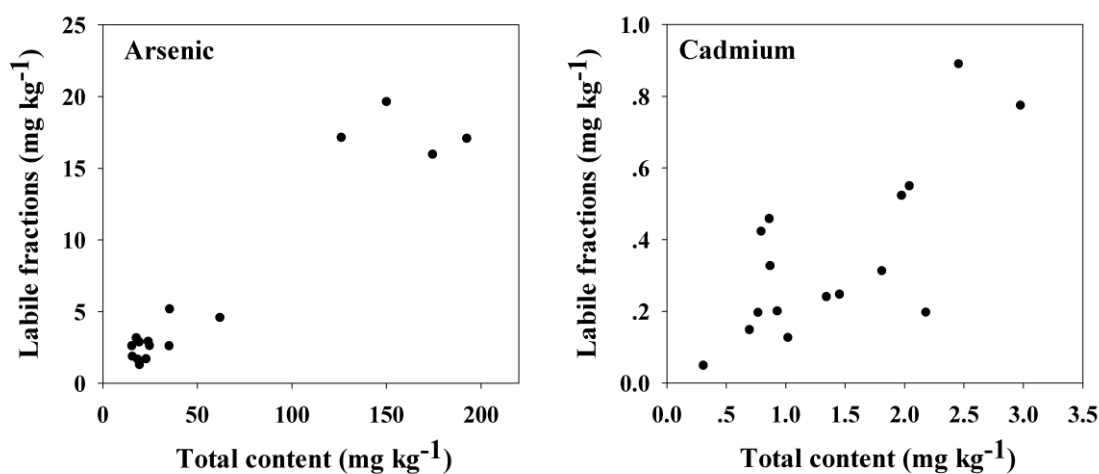


Fig. 3. Labile fractions of As and Cd with total contents in soil.

Due to both of anthropogenic input level and soil properties affected the distribution of soil As and Cd fractions, the non-residual fractions contents of these two elements cannot totally determined by their total contents in soils. Factor analysis (FA) was applied for soil properties and the proportions of total contents in the non-residual fractions of As and Cd by evaluation of principal components and

computing the eigenvectors. Three factors with eigenvalues higher than 1 (before and after Varimax normalized rotation) were extracted. The results of FA were presented in Table 2. The first three factors account for 75.1% of total variance. The high communality estimates suggested that the high portion of variance was explained by the first three factors.

Table 2. Statistical results of factor analysis.

		Factor 1	Factor 2	Factor 3	Communality estimates
pH		0.855	0.312	0.017	0.83
OM		0.004	0.839	-0.091	0.71
CEC		0.365	0.826	-0.039	0.82
SiO ₂		-0.752	-0.529	0.020	0.85
K ₂ O		0.812	0.362	-0.107	0.80
CaO		0.896	0.229	0.007	0.86
Ratio of As _(WS+EX)		0.062	-0.197	0.920	0.89
Ratio of Cd _(WS+EX)		-0.438	0.058	0.619	0.58
Ratio of labile fractions As		0.678	-0.151	-0.339	0.60
Ratio of labile fractions Cd		0.741	-0.014	-0.183	0.58
Initial	Eigenvalues	4.88	1.41	1.22	
	% of variance	48.84	14.10	12.18	
After Rotation	Eigenvalues	4.10	2.01	1.40	
	% of variance	40.99	20.13	14.01	

Factor 1 explained 40.99% of total variance with a high positive loading from soil pH, K₂O, CaO, Ratio of labile fractions of As and Cd, and high negative loading from SiO₂. Factor 1 may explain the processes of weathering of soil parent materials. During the weathering processes, the metallic cations were released from soil parent materials and labile fractions of As and Cd were accumulated. Factor 2, which had the high positive loading from Organic matters, CEC and moderate positive loading from soil pH, K₂O and CaO, and moderate negative loading from SiO₂, was considered as the second stage of the formation of soil from parent material, pedogenesis. During the pedogenesis processes, contents of organic matters, CEC and some metallic cations were increased, while soil SiO₂ content was decreased. The fractions distribution of As and Cd have not significant relationship with Factor 2 in this study. Factor 3 was considered present the anthropogenic input of As and Cd in soil, since it had high positive loading from Ratio of As_(WS+EX) and Cd_(WS+EX) and negative loading from Ratio of labile fractions of As and Cd. The As and Cd were accumulated in arable land soil mainly as WS and EX fractions, since the irrigation water of study area were contaminated by mining and smelting activities. The concentration increasing of WS and EX fractions will affect the ratio distribution of fractions.

The weathering processes were the main determined factors of labile fractions ratio of total

As and Cd contents in soil. However, the main influence factors of WS and EX fractions ratio of these two contaminants in soil were the anthropogenic input. Although the concentrations of As_(WS+EX) and Cd_(WS+EX) were quite lower, both of WS and EX fractions of them were highly available for crops and plants [9,20]. So, the potential ecological risk, which shed by anthropogenic input As and Cd, should not be ignored.

CONCLUSION

The arable land soil in vicinity of mining area was contaminated by As and Cd, and the contents of As and Cd in study soil were 59.44 and 1.403 mg kg⁻¹ respectively. Both of As and Cd were mainly distributed in residual fraction, and the ratio of their labile fractions (AC, OX, OC) was determined by the processes of weathering of soil parent materials. The mainly influence factor of WS and EX fractions, which were highly available for crops and plants, were anthropogenic input. Therefore, measures should be taken to control the anthropogenic emission of As and Cd in vicinity of mining area.

Acknowledgements: This research is jointly supported by The National Natural Science Foundation of China (41501225) and National Nonprofit Institute Research Grant of CATAS-TCGRI (1630032014035).

REFERENCES

1. J.R. Bacon, N.S. Dinev, *Environ. Pollut.*, **134**, 247 (2005).
2. X.Y. Bi, X.B. Feng, Y.G. Yang, G.L. Qiu, G.H. Li, F.L. Li, T.Z. Liu, Z.Y. Fu, Z.S. Jin, *Environ. Int.*, **32**, 883 (2011).
3. C.B. Zhang, L.H. Wu, Y.M. Luo, H.B. Zhang, P. Christie, *Environ. Pollut.*, **151**, 470 (2008).
4. L.M. Shuman, *Soil Sci.*, **140**, 11-20 (1985).
5. I. Maiz, I. Arambarri, R. Garcia, E. Millán, *Environ. Pollut.*, **110**, 3 (2000).
6. C.R.M. Rao, A. Sahuquillo, J.F.L. Sanchez, *Water Air Soil Poll.*, **189**, 291 (2008).
7. C. Gleyzes, S. Tellier, M. Astruc, *TRAC-Trend. Anal. Chem.*, **21**, 451 (2002).
8. F.M. Tack, M.G. Verloo, *Int. J. Environ. An. Ch.*, **59**, 225 (1995).
9. N.S. Bloom, E. Preus, J. Katon, M. Hiltner, *Anal. Chim. Acta*, **479**, 233 (2003).
10. M.O. Mendez, J.W. Neilson, R.M. Maier, *Appl. Environ. Microb.*, **74**, 3899 (2008).
11. A. Tessier, P.G.C. Campbell, M. Bisson, *Anal. Chem.*, **51**, 844 (1979).
12. M. Almendras, M. Carballa, L. Diels, K. Vanbroekhoven, R. Chamy, *J. Environ. Eng.*, **135**, 839 (2009).
13. F.X. Han, A.T. Hu, H.Y. Qi, *Geoderma*, **66**, 121 (1995).
14. L.Q. Ma, G.N. Rao, *J. Environ. Qua.*, **26**, 259 (1997).
15. R.K. Lu, *Analysis Methods of Soil Agricultural Chemistry*, China Agricultural Science and Technology Press, Beijing, (2000).
16. D.F. Wang, *Asian J. Chem.*, **26**, 5773 (2014).
17. L. Rodríguez, E. Ruiz, J. Alonso-Azcárate, J. Rincón, *J. Environ. Manage.*, **90**, 1106 (2009).
18. K.H. Goh, T.T. Lim, *Appl. Geochem.*, **20**, 229 (2005).
19. T.K. Van, Y. Kang, T. Fukui, K. Sakurai, K. Iwasaki, Y. Aikawa, N.M. Phuong, *Soil Sci. Plant Nutr.*, **52**, 701 (2006).
20. A. Kabata-Pendias, H. Pendias, *Trace Elements in Soils and Plants*, 2nd ed. CRC Press, Boca Raton, FL, (2001).

Gas-particulate distribution of polycyclic aromatic hydrocarbons (PAHs) in Chengdu, China

Ju Yang, Wenlai Xu*, Min Tang, Yue Jian, Jing Wang

State Key Laboratory of Geohazard Prevention and Geoenvironment Protection, Chengdu University of Technology, Chengdu 610059, China

Received June 13, 2016, Revised September 5, 2016

Research of gas-particle phase distribution characteristic and source profile distribution characteristics of atmospheric polycyclic aromatic hydrocarbons (PAHs) can help control atmospheric PAHs pollution. Typical southwestern city of Chengdu is selected as study area for long-term continuous sampling monitoring, to analyze change of atmospheric concentrations of PAHs levels, source profile distribution characteristic and gas – particle distribution pattern. The results show that Σ PAHs concentration in study area is between 95.57-930.62ng m⁻³, PAHs concentration decreases with increasing temperature, which concerns increased amount of coal, biomass fuel combustion in low temperature seasons; atmospheric gas phase PAHs concentration is higher than that in particle phase, gas – particle distribution ratio (G / P) is between 1.4 and 7.5, gas - particle distribution ratio (G / P) shows relatively good positive linear correlation with temperature ($r = 0.61$, $p < 0.01$); Nap, Acy, etc. 2-4 ring of low ring PAHs exist mainly in gas form, and BbF, BaP and other 5,6 ring PAHs are mainly adsorbed in atmospheric particulate matters.

Keywords: PAHs, Atmosphere, Source Profile, Gas-Particle Distribution, G/P.

INTRODUCTION

Polycyclic aromatic hydrocarbons (PAHs) are the most widely distributed persistent organic pollutants (POPs) in the atmosphere with greatest harm, which has “three-induced” effect of “mutagenesis, carcinogenesis and teratogenesis”. Among 129 kinds of priority control pollutants published by United States Environmental Protection Agency (USEPA), PAHs account for 16 kinds (USEPA, 2002). PAHs exist in two forms of gas / particle in the atmosphere. Small molecular weight PAHs mainly exist in gas form while high molecular weight PAHs mainly in the form of particulate. When the atmospheric conditions change, the two can be transformed into each other.

Overseas research on atmospheric PAHs began in the early 1980s, with relatively comprehensive study of PAHs concentration level and pollution characteristics in air of different cities. Domestic report on atmospheric PAHs pollution shows an upward trend in recent years, but mainly concentrated in PAHs concentration changes in atmospheric particles in the coastal city of Beijing - Tianjin area. Moreover, sampling coverage time is relatively short, lacking of long-term continuous sampling and monitoring.

In this study, typical southwestern city of Chengdu is selected as the study area for long-term continuous sampling and monitoring, concentration

change of atmospheric PAHs levels, source profile distribution characteristics and gas - particle distribution pattern are analyzed, which is of important significance for transformation and conversion processes of PAHs in the environment, population exposure, environmental pollution control.

MATERIALS AND METHODS

Sample collection and analysis

Chengdu Plain is located in the western Sichuan Plain, with an average elevation of 540 meters and surrounded by hills and mountains with relatively high elevation. This particular terrain condition will certainly affect relocation diffusion of atmospheric pollutants, showing unique pollution feature. In this paper, the study area is located in the Chengdu Plain heartland (east longitude 102 ° 54 ' - 104 ° 53' and north latitude 30 ° 05 ' - 31 ° 26'). In this study, the sampling site is located within a university campus in Chengdu east area, with sampling height at 15m. The sampling ran from August 2008 to July 2009, once a week, with a total of 98 samples collected (49 gas phase samples, 49 particle phase samples).

Collected gas and particle phase samples underwent separate sample preparation, with Soxhlet extraction to extract target substance. GC-MS (Agilent GC6890 / 5973 MSD) was used for analysis and determination of 16 kinds of USEPA priority control PAHs.

To whom all correspondence should be sent:
E-mail: xuwenlai1983@163.com

Gas-particle distribution coefficient K_p

Gas-solid distribution relationship of PAHs in gas phase and particle phase is described with distribution coefficient K_p ($m^3 \mu g^{-1}$), and K_p is calculated according to the following formula:

$$K_p = \frac{F/C_{TSP}}{A} \quad (1)$$

In the formula: F is PAHs volume concentration in particle phase ($ng m^{-3}$)

A is PAHs volume concentration in gas phase ($ng m^{-3}$)

C_{TSP} is atmospheric concentration of total suspended particles ($\mu g m^{-3}$)

RESULTS AND DISCUSSION

PAHs pollution characteristics

Atmospheric 16-PAHs concentration in gas - particle phase in the study area is shown in Table 1. In gas phase, 16-PAHs annual average concentration is $217.09 \pm 117.09 ng m^{-3}$, the highest concentration of $634.98 ng m^{-3}$ appeared on December 15, 2008, while the lowest concentration of 79.98 appeared on April 4, 2009, with mean concentration about 10 times [1] of PAHs concentration ($26.0 ng m^{-3}$) in atmospheric gas phase of central district of Athens, capital of Greece, which is lower than Chicago ($144-853 ng m^{-3}$) [2]. In comparison with studies of domestic cities, PAHs concentration in atmospheric gas phase is lower than the of the Beijing ($492 ng m^{-3}$) [3], higher than cities like Harbin ($46.47-132.41 ng.m^{-3}$) [4]. The

annual average concentration of 16-PAHs in atmospheric particle phase is $82.16 \pm 53.31 ng m^{-3}$, the highest concentration of $295.63 ng m^{-3}$ appeared on December 15, 2008, while the lowest concentration of $15.75 ng m^{-3}$ appeared on August 29, 2008. PAH monomer with highest concentration in gas phase is 3-ring phenanthrene ($187.87 ng m^{-3}$), followed by fluorene ($122.01 ng m^{-3}$). the highest content in particle phase appears in high ring 5 ring PAH benzo (b) fluoranthene ($47.87 ng m^{-3}$), followed by 4-ring chrysene ($44.06 ng m^{-3}$). in this study, average concentration of benzo (a) pyrene (BaP) is $7.68 ng m^{-3}$, which is lower than China's atmosphere standard value of $10 ng m^{-3}$ EPA 1996, with particle concentration higher than that of gas phase.

Figure 1 shows concentration and temperature variation characteristic of PAHs in atmospheric gas phase and particle phase within a year of sampling period. During the sampling period, atmospheric PAHs concentration in gas phase, particle phase of the study area shows a similar variation, with higher PAHs concentration in winter and spring with lower temperature and lower PAHs concentration in summer and autumn with higher temperature. Peak value appeared in December, January, February with low temperature, with gradual concentration decrease with temperature rise. Atmospheric PAHs concentration peak appeared on December 15, 2008. Atmospheric PAHs concentration variation characteristic in the study area is similar to that in northern China city of Harbin [5]. Studies suggest that this is associated with increased biomass burning capacity in winter and spring.

Table1. PAHs concentration ($ng m^{-3}$) statistics in atmospheric gas - particle phase in Chengdu

PAHs	Gas			Particular		
	Max	Min	Average	Max	Min	Average
Naphthalene(Nap)	32.00	0.85	7.15	0.57	0.12	0.25
Acenaphthylene(Acy)	116.69	0.12	13.79	0.44	0.03	0.10
Acenaphthene(Ace)	24.14	0.09	4.26	0.12	-	0.03
Fluorene(Flu)	122.01	2.09	28.90	0.70	0.05	0.17
Phenanthrene(Phe)	187.87	0.50	92.06	9.01	0.56	2.27
Anthracene(Ant)	35.00	1.21	7.55	1.16	0.06	0.26
Fluoranthene(Flua)	79.04	11.73	36.47	42.54	0.93	6.98
Pyrene(Pyr)	49.13	6.08	22.04	38.70	0.80	6.02
Benzo(a)anthracene(BaA)	4.78	0.16	1.29	29.16	0.63	6.11
Chrysene(Chr)	9.30	0.45	2.96	44.06	1.20	10.50
Benzo(b)Fluoranthene(BbF)	1.89	0.03	0.31	47.87	2.58	14.33
Benzo(k)Fluoranthene(BkF)	0.93	0.03	0.19	22.15	1.75	7.85
Benzo(a)Pyrene(BaP)	0.34	0.01	0.06	26.53	1.37	7.68
Indeno(123-c,d)Pyrene(IcdP)	0.23	-	0.02	23.42	2.20	7.71
Dibenzo(ah)anthracene(DahA)	0.05	-	-	7.53	0.47	1.95
Benzo(g,h,i)Perylene(BghiP)	0.29	-	0.03	26.91	2.61	8.90
Σ16PAHs	217.09±117.09 ng m⁻³			82.16±53.31 ng m⁻³		

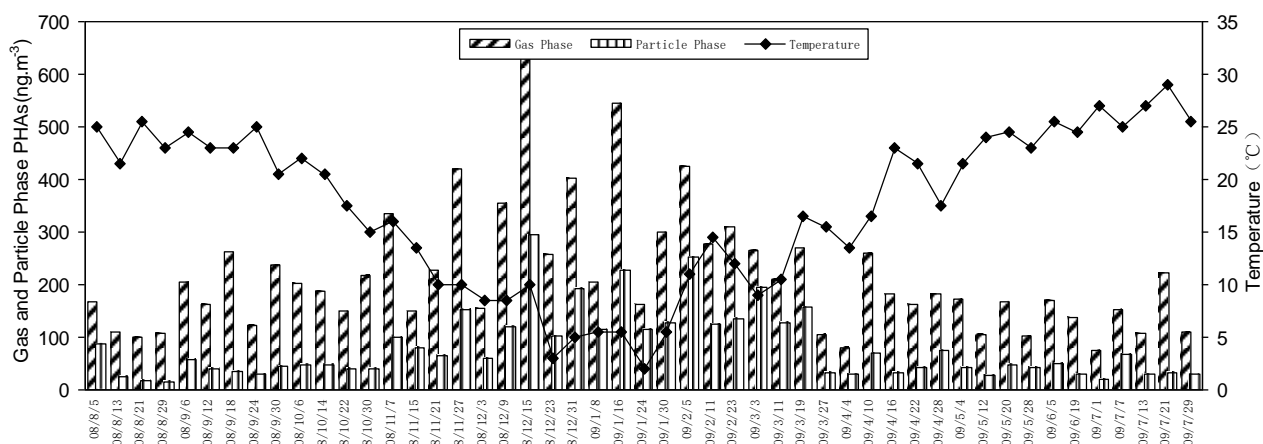


Fig. 1. Atmospheric PAHs gas - particle concentration distribution in Chengdu and temperature change map.

PAHs gas-particle distribution characteristics

PAHs gas-particle source profile distribution characteristic. In view of concentration distribution of atmospheric PAHs in the two phases (Figure 2), PAHs monomer with the highest content in gas phase is 3-ring Phe, whose contribution rate in gas phase reaches 42.5%, followed by: Flua (16.8%)>

Flu (13.3%)> Pyr (10.1%)> Acy (6.3%)> Ant (3.5%)> Nap (3.3%). What contributes most in particle phase is 5-ring benzo [b] BbF. Ranking of PAHs contribution rate in particle phase is respectively: BbF (17.9%)> Chr (12.8%)> BghiP (11.0%)> BkF (9.7%)> BaP (9.6%)> IcdP (9.5%)> Flua (8.4%)> BaA (7.6%)> Pyr (7.3%).

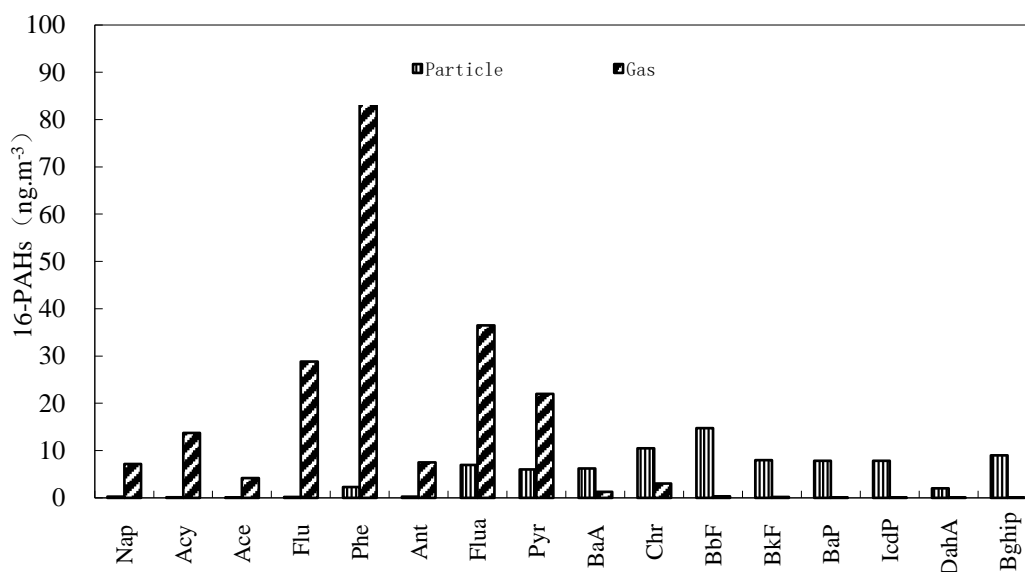


Fig. 2. PAHs source profile distribution characteristic in gas - particle.

Thus, low ring PAHs with low molecular weight mainly exists in gas state. With increase in molecular weight and number of rings, PAHs gradually tends to exist in particle state. In gas phase, contribution rate of 2,3 ring PAHs monomer to concentration is greater than that of high-ring PAHs. However, in particle phase, contribution rate of 5,6 high ring PAHs monomer to concentration is greater than that of low ring, which is opposite to the situation in gas phase. Contribution rate of 4 ring PAHs monomer in two phases is roughly equal, but Flua and Pyr concentration in gas phase is

higher than that in particle phase, which is easier to concentrate in gas phase, while concentration of BaA and Chr in particle phase is higher than that in gas phase, which is more easily absorbed in particulate matters.

PAHs gas - particle ratio (G/P). PAHs in atmospheric environment exists in two forms of gas and particle. Proportion of gas phase PAHs in total atmospheric PAHs is greater than that of particle phase. PAHs concentration distribution ratio (G / P) in gas and particle phase in the study area is between 1.4 and 7.5, with average gas - particle ratio (G / P) at

3.12, which shows relatively good positive correlation with temperature change ($r = 0.61$, $p < 0.01$) (Figure 3). Compared with the findings in different regions at home and abroad, it is higher than Seoul, South Korea in Asian countries 2.3[6],

China Harbin 1.2[5]; lower than Turkey in European region 9.36 [7], Birmingham, UK 5-6 [8], Guangzhou, China 13.2 [9], Nanjing 8.9[10], Shanghai > 10[11]; comparable to Athens, Greece 5.2 [1], western region of circum-Bohai Sea <5 [12].

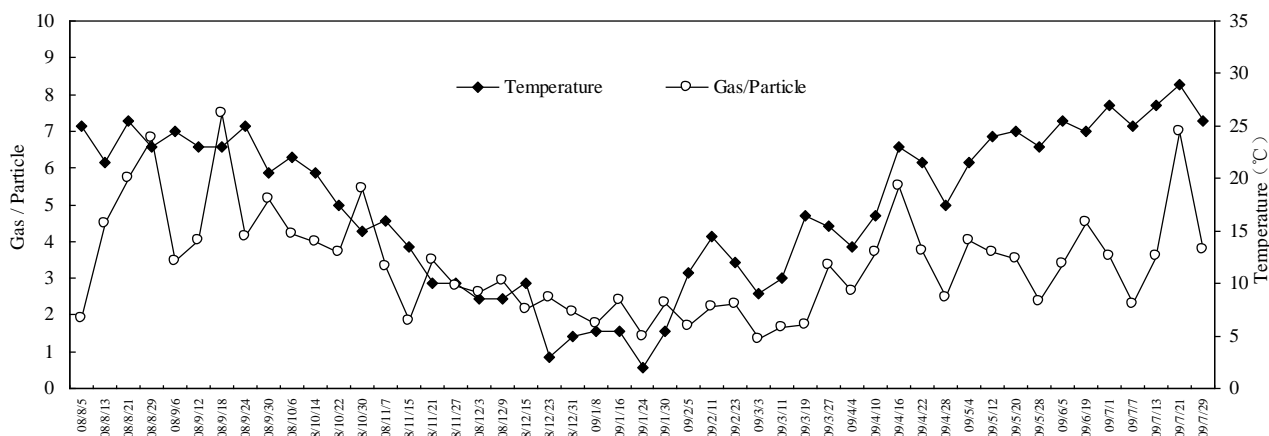


Fig. 3. PAHs gas – particle distribution ratio and temperature change trends.

Distribution and gas - solid balance of atmospheric PAHs in different particles vary. A lot of 3-4 low ring, volatile PAHs mainly exist in gas form in gas phase, while 5,6 ring hardly volatile PAHs are mainly adsorbed in atmospheric particles[9][13]. PAHs content in small particles is high, but low in larger particles. Studies have shown that PAHs contained in inhalable particle accounts for about 95% of the total amount, while PAHs contained in tiny particles with particle size <1.1 μm account for 60% to 70% of the total [14][15].

PAHs gas - particle distribution characteristic.

In this study, as IcdP, DahA, BghiP and other PAHs were not detected in part of gas phase samples, the

remaining 13 PAHs are selected for fitting analysis. Sampling period is divided into four seasons of spring, summer, autumn and winter, and concentration average of 13 PAHs is substituted to formula (1) for calculation. Distribution coefficient K_p of 13 PAHs components is between 3.34×10^{-5} -2.49. 2,3 ring Nap, Acy, Ace, Flu, Phe, etc. have low boiling point and are volatile, with occurrence ratio in gas phase higher than that in particle phase, and therefore K_p value is minimum. K_p value of Ant, Flua, Pyr, etc. is between 1.08×10^{-4} - 9.17×10^{-4} . 5,6 ring PAHs mostly exist in particle phase, with higher K_p value.

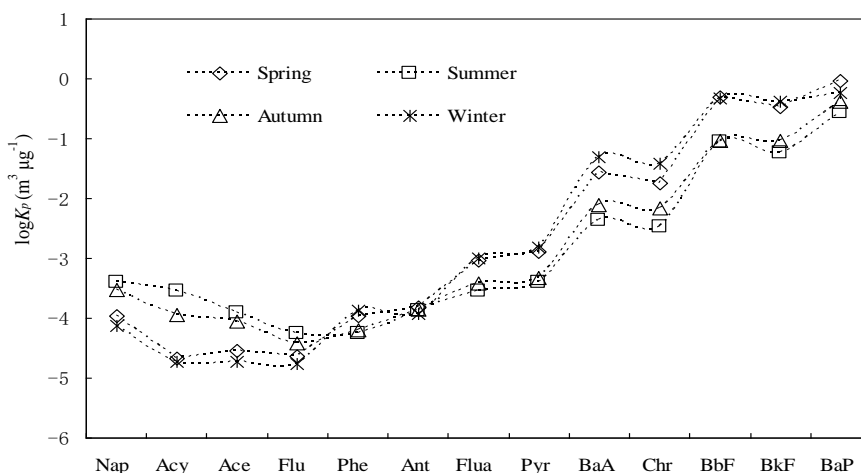


Fig. 4. Seasonal variation diagram of 13-PAHs monomer logKp.

As shown in Figure 4, $\log K_p$ value of 13 kinds of PAHs increases with increase in molecular weight,

components with small molecular weight are volatile, mainly in gas phase. Distribution

coefficient of various substances of PAHs also shows certain seasonal variations, with $\log K_p$ value of lower ring of 2, 3 ring PAHs: summer > autumn > spring > winter; $\log K_p$ value of high ring of 4, 5, 6 ring PAHs shows change law of: winter > spring > autumn > summer. Seasonal variation characteristic of $\log K_p$ value is temperature-related. In high-temperature season, PAHs components are more volatile, especially highly volatile low ring material with small molecular weight [16][17]. Distribution and transformation of PAHs in gas-particle phase has a close relationship with meteorological elements such as temperature, wind direction, etc. When environmental conditions change, gas-solid phase transformation will occur [18].

CONCLUSIONS

In the study area, atmospheric Σ PAHs average concentration in gas - particle phases is respectively $217.09 \pm 117.09 \text{ ng m}^{-3}$ and $82.16 \pm 53.31 \text{ ng m}^{-3}$; PAHs in atmosphere mainly exists in the form of gas (73%), gas - particle distribution ratio (G / P) is between 1.4 and 7.5, gas - particle distribution ratio shows relatively good positive linear correlation with temperature ($r = 0.61$, $p < 0.01$); Nap, Acy, etc. 2-4 ring of low ring volatile PAHs exist mainly in gas form in gas phase, and BbF, BaP and other 5,6 ring hardly volatile PAHs are mainly adsorbed in atmospheric particulate matters.

Acknowledgements: The research was funded by the Natural Science Foundation of China (No. 41502333), the State Key Laboratory of Geohazard Prevention and Geoenvironment Protection Foundation (No. SKLGP2015Z012, SKLGP2014Z001), the specialized research fund for the doctoral program of colleges and

universities (No.20135122120020), the scientific research plan of education department of Sichuan Province (No.14ZB0073).

REFERENCES

1. M. Mandalakis, M. Tsapakis, A. Tsoga, *Atmos Environ*, **36**, 4023 (2002).
2. Y. Tasdemir, F. Esen, , *Atmos Res*, **84**, 1 (2007).
3. Zhang Y.X., Tao S., *Environ Pollut*, **156**, 657 (2008).
4. Ma W.L., Li Y.F., Sun D.Z., *Environ Sci*, **30**, 3167 (2009).
5. Ma W.L., Li Y.F., Qi H., *Chemosphere*, **79**, 441 (2010).
6. Park, S.S., Kim Y.J., Kang C.H., *Atmos Environ*, **36**, 2917 (2002).
7. Yang, J., PhD. Dissertation, Chengdu University of Technology, Chengdu, 2010.
8. Harrison R.M., Smith D.J.T., Luhana L., *Environ. Sci Technol*, **30**, 825 (1996).
9. Li J., Zhang G., Li X.D., *Sci. Total Environ.*, **355**, 145 (2006).
10. Liu Y., Tao S., Yang Y.F., *Sci. Total Environ.*, **383**, 98 (2007).
11. Wang Y., Li P.H., Li H.L., *Atmos Res.*, **95**, 1 (2010).
12. Wan X., Chen J.W., Tian F.L., *Atmos Environ.*, **40**, 6666 (2006).
13. Hong H.S., Yin H.L., Wang X.H., *Atmos Res.*, **85**, 429 (2007).
14. Offenbergh J.H., Baker J.E., *Atmos Environ*, **34**, 1509 (2000).
15. Zhou J., Wang T., Huang Y., *Chemosphere*, **61**, 792 (2005).
16. Tan J.H., Bi X.H., Duan J.C., *Atmos Res.*, **80**, 250 (2006).
17. Zhou J., Wang T., Huang Y., *Chemosphere*, **61**, 792 (2005).
18. Pankow J.F., *Atmos Environ., Part A, General Topics*, **25**, 2229 (1991).

Vertical flow constructed wetland on the slightly polluted water denitrification and phosphorus removal test parameters optimization research

Xingguan Ma, Tao Jiang*, Pengfei Yu

Shenyang Jianzhu University, School of Municipal and Environmental Engineering, Shenyang, Liaoning province, China, 110168.

Received June 18, 2016, Revised September 10, 2016

The test is mainly aimed at ceramsite matrix vertical flow constructed wetland for slightly polluted water denitrification and phosphorus removal test parameters optimization research. According to reed, canna, water bamboo, water celery several hygrophilous plant of slightly polluted water treatment, examining the best treatment effect advantage as artificial wetland plants; Then examines the several key factors influencing the artificial wetland, such as plant density, height of filling and HRT, through the determination of $\text{NH}_3\text{-N}$ in water, $\text{NO}_3\text{-N}$, TN, TP, pH value, analysis the relationship between them to determine the optimal parameters. Screening tests of the plant: discovery of canna in denitrification and dephosphorization has obvious superiority than other several plants, so choose canna as the test plant. Parameter optimization experiment: artificial wetland system of HRT for 12h, the density of canna for 6 strains, haydite filling height of 40 cm when the optimal parameters, remove the best effect.

Keywords: Slightly polluted water, ceramsite matrix vertical flow constructed wetland, hygrophilous plant, nitrogen and phosphorus, parameters optimization.

INTRODUCTION

At present, with the rapid development of industrialization, the growing strength of the use of water resources, river pollution is increasingly serious. According to the survey, 50% of the river channel in our country and more than 80% of the pollution of lake, river and lake eutrophication problem on a nationwide scale appear constantly, causing damage to the original benign cycle [1]. As a result, the river water quality purification and restoration in the spotlight. River restoration is the purpose of river ecosystem restoration leads to a more natural state, make the river ecosystem sustainability [2], at present, the main pollution of river restoration methods are physical method, chemical method and biological method, has made some progress in both the three [3]. One of the most widely used, the most advantage is biological method, constructed wetland is one of the commonly used method.

It is the mechanism of sewage flows through long plant medium, resulting in a filtration, sedimentation, adsorption, such as physics, chemistry and pollutants and various kinds of biochemical reaction matrix [4]. Artificial wetland treatment process has: investment and maintenance cost is low; Low energy consumption; Suitable for non-point source pollution control and management. Wetlands can store surface runoff; they have the advantages of landscape function [5-6], and

therefore they are widely used. Artificial wetland by category and three classes of surface flow, undercurrent, vertical flow. The vertical flow constructed wetland of denitrification and phosphorus removal in the first two effect is more outstanding. So the experiment selected vertical flow constructed wetland. Ceramsite filler selection. Choose wet raw edge species reed, canna, water celery, water bamboo compared after the screening.

Test apparatus and materials

This test USES vertical flow constructed wetland, ceramsite matrix hygrophilous plant plants in rivers investigation advantage of reed, canna, water celery, water bamboo, the above several selected plants separately for a period of training, for all kinds of plants grow after normal, then the transplanting 40*60*60cm of the experiment in the organic glass box.

Planting density of each plant reference actual planting density, such as reed, canna, water bamboo plants / 5 barrels, water celery plants / 10 barrels, with no plants to control (CK), a total of 5 groups, each group to deal with 3 replications. Plant after transplanting, injection test the water volume of 30 l a barrel. The experimental set repeat 3 times. Immediately after experimental period for 63 days, the water samples were determined, measurement indicators include: $\text{NH}_3\text{-N}$ and $\text{NO}_3\text{-N}$, TN and TP.

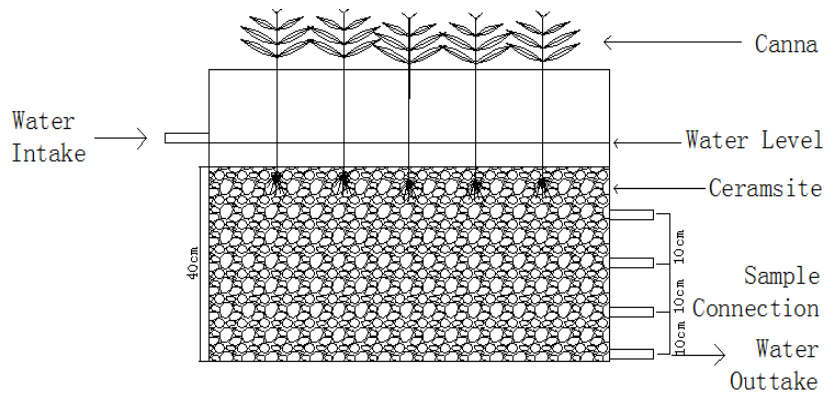


Fig. 1. Test unit.

Table 1. The water quality indicators.

Analyze project	NH ₃ -N	NO ₃ ⁻ -N	TN	TP	pH
Unit	mg/L	mg/L	mg/L	mg/L	-
The average value	2.13	1.76	5.36	0.48	6.87-7.45

NH₃-N AND TP REMOVAL EFFICIENCY ANALYSIS

In addition to water bamboo, other plants maximum removal rate of NH₃-N in 3 days, with

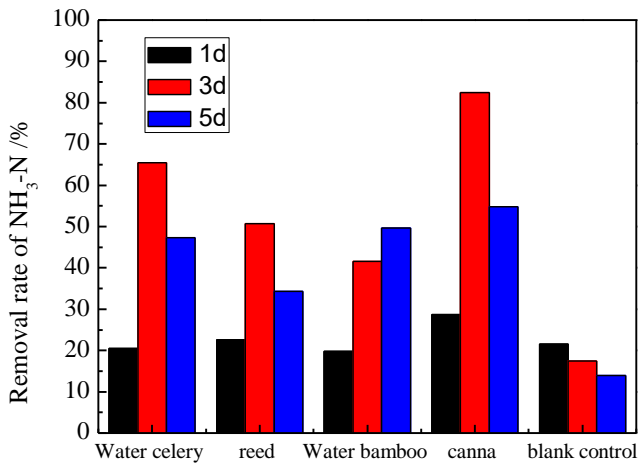


Fig. 2. Different wetland plants on the removal rate of NH₃-N contrast effect.

The Figure 2 shows that all kinds of plants are certain removal effect of TP, besides canna, other plants on the removal rate of TP with increased with the extension of time, the removal efficiency of the control group was 22%, phosphorus content is higher, shows that particle state deposits play an important role, and canna removal rate reduced to 28.5% in the third day, that may be its the second release of phosphorus in the body effect is stronger, result in higher effluent total phosphorus content, therefore, adjust good hydraulic retention time for the p removal is very important.

Found in the process of screening plant cannas has more advantage in removing nitrogen and phosphorus, NH₃-N and TP removal rate is better

canna removal effect is best, removal rate reached 84.3%, followed by water celery, reed. So it can be seen that canna advantages in terms of NH₃-N removal.

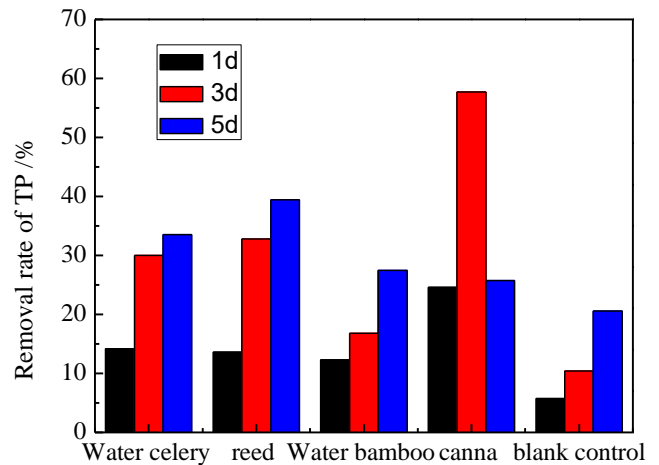


Fig.3. Different wetland plants on the removal rate of TP contrast effect.

than that of reeds, water celery, water bamboo. Canna has strong vitality and adapt better on the surrounding environment, so canna was chosen as the test plant.

Artificial wetland system of jointly by packing, plants and microbes, and in these three aspects in the operation of the system became conditions to limit its role, so to study the best conditions for system operation. Optimize the influence the effect of vertical flow constructed wetland to remove nitrogen and phosphorus several limiting factors, mainly including packing height, plant density and hydraulic retention time. The following parameter optimization was studied respectively.

PARAMETER OPTIMIZATION TEST

Height of packing

Another limiting factor of artificial wetland system, i.e., height of packing, so this experiment device based on the size of the set up three kinds of packing height, 25 cm and 35 cm, 45 cm haydite filling height, plant planting density of 6 strains canna, hydraulic retention time for 24 hours, the run of five cycles, experimental determination of NH₃-N in and out of the water, NO₃⁻-N, TN, TP of several indicators.

By Figure 4 and Figure 6, three different packing height of vertical flow constructed wetland

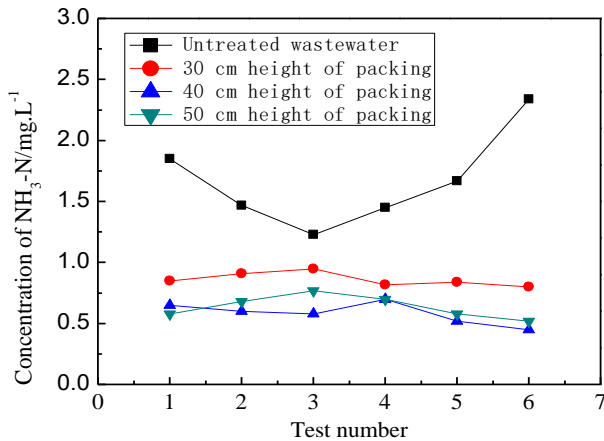


Figure 4 packing height on the influence of NH₃-N

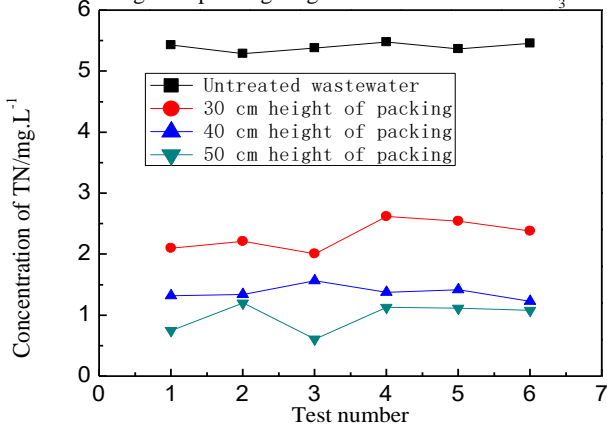


Figure 6 packing height on the influence of TN

The Figure 5 shows that when the haydite filling height of 30 cm, unstable system water NO₃⁻-N concentrations. The system packing height is low, in the digestion of microbes cannot provide stable anaerobic environment, should be appropriate to improve packing height; And when the filling height of 40 cm and 50 cm, stable effluent NO₃⁻-N concentrations of the two systems, two system NO₃⁻-N average removal rate of 35.8% and 49.2%, in terms of nitrogen removal effect, 40 cm of height of packing is good.

Canna vertical flow constructed wetland system

system of effluent NH₃-N and TN concentrations were significantly lower, and is very regular, namely the ceramsite filler elevation, water quality, the better, packing height of 40 cm system, the system of the water NH₃-N average and TN removal rate has reached 67.5% and 54.3%. When packing height is 50 cm in the system, system of the water NH₃-N and TN removal rate to an average of 71.8% and 57.7%, two kinds of packing height system NH₃-N and TN concentrations of a smaller gap height of packing, continue to increase the system of the wetland system of NH₃-N and TN removal efficiency is affected.

of total phosphorus in water to remove significant correlation, the higher the packing, the removal rate of system the better, that in addition to the plant absorption, the change of phosphorus content in the water, the adsorption of packing and interception effect is also one of the important influencing factors, when the filler height of 30 cm, 40 cm, 50 cm, the system average removal rate of total phosphorus were 32.6% and 65.5% and 78.3%. 00cm and 50cm packing height on the wetland system of TP removal efficiency is affected. Considering all factors, choose 40 cm of height of packing as best highly artificial wetland system.

Research on the best condition of system operation, plant planting density is one of the influencing factors. This experiment according to the size of the experimental apparatus, set up three different plant density, respectively 4 strains, 6 strains, 8 strains of canna, HRT is set to 24 h, test run five cycles, each sampling measurement in time, every time determination of repeat 3 times average. Planting density of three plants in the Figure 8 shows that the effluent concentration of NH₃-N are significantly decreased, and there was no significant difference, NH₃-N removal in systems that have no obvious correlation with plant, mainly is the packing of adsorption and microbiological nitrification, the main means of NH₃-N removal are nitrification is transformed into NO₃⁻-N, so the system of NO₃⁻-N concentration increase, NH₃-N others rely on ammonia volatilization removal, the removal rate of NH₃-N in the system are higher, respectively, 70.5%, 78.1% and 82.6%, among them 6 strains and 8 plant density of artificial wetland system of NH₃-N removal rate.

The Figure 9 shows that three kinds of plant density of artificial wetland system of NO₃⁻-N were not removed, instead, three kinds of NO₃⁻-N concentrations in the water system had increased,

but the three system water NO_3^- -N concentrations 4 seedlings > 6 strains, > 8 strains, which may indicate NO_3^- -N concentrations is associated with canna

plant number, the more number of plants, the more conducive to denitrification.

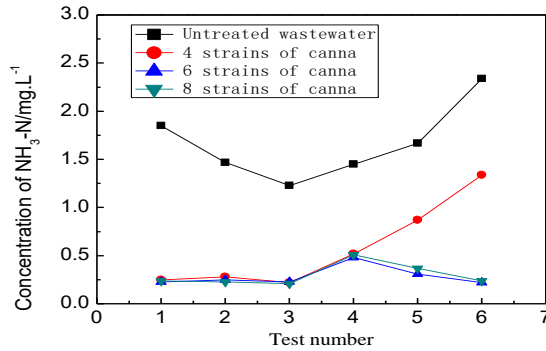


Figure 8 plant density on the influence of $\text{NH}_3\text{-N}$

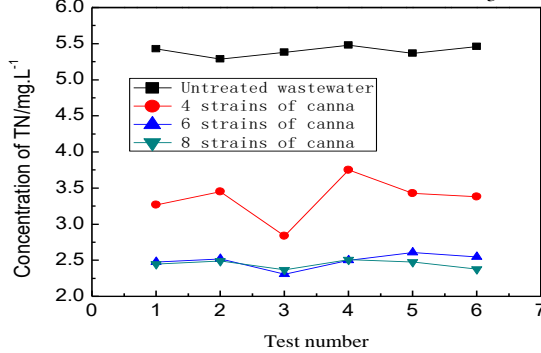


Figure 10 plant density on the influence of TN

The Figure 10 shows that present the lower effluent TN content of three kinds of system state, including plant a total of 4 canna plant effluent TN removal rate to an average of 24. 2%, and 6 cases and 8 strains of canna effluent TN removal rate to an average of 39. 5% and 41. 3%, thus can draw, 6 strains and 8 strains of canna device is superior to the 4 strains of canna device, it could be a canna in removing other forms of nitrogen removal has played a role.

By Figure 11 shows, 4 strains and 6 strains of canna two plants density of vertical flow constructed wetland system of the water from raw water TP concentrations were significantly lower, and the five test cycle, plant a total of eight canna TP water-quality wetland system of raw water was increased, the average TP is higher than that of original water 47. 6%, which can be judged, 8 strains of canna planting density is too high, can lead to canna plant competition for nutrients, thus some canna, death happened in the process, the second release of phosphorus, which can lead to system effluent is higher than that of raw water quality, plant a total of 6 canna vertical flow constructed wetland system with the minimum of TP concentration, removing effect is good, the average removal rate reaching 51. 1%.

In conclusion, can choose 6 strains for parameters of the system plant density.

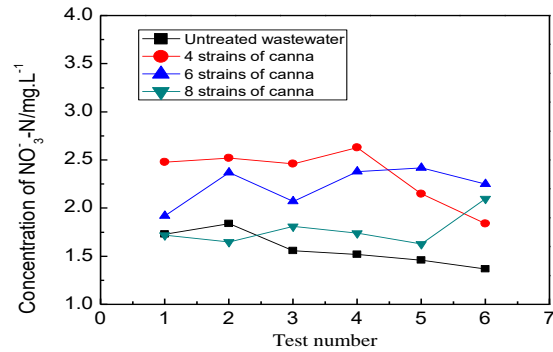


Figure 9 plant density on the influence of NO_3^- -N

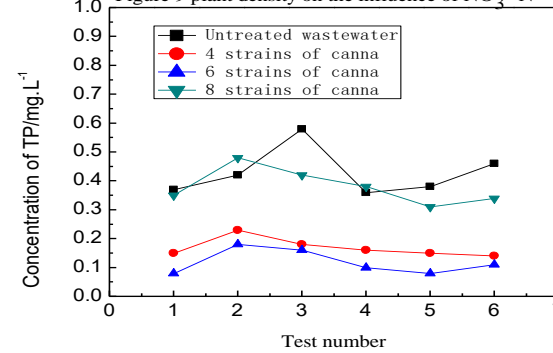


Figure 11 plant density on the influence of TP

HRT

Study found that HRT could theoretically use geometry average flow, system operation, such as water level, the initial porosity to estimate, because of the influence of geographical factors such as the application of artificial wetland technology in various areas in need of operation parameters. The appropriate extension of HRT can improve the removal rate of organic matter in wetland system. Visible, choose different HRT parameters in the artificial wetland can directly affect the efficiency of the artificial wetland.

Device select early screening advantage plant cannas, in the process of the test set different HRT, respectively is 12 hours, 24 hours, 36 hours, 48 hours, a total of four different residence time to determine water quality.

The Figure 12 shows that water of artificial wetland system in HRT for 12 h, the removal rate of $\text{NH}_3\text{-N}$ concentration has reached 72. 4%, during the water removal rate of $\text{NH}_3\text{-N}$ is stable, and with the HRT increases, the removal rate of $\text{NH}_3\text{-N}$ revealed a general trend, first the lowered after the removal rate of $\text{NH}_3\text{-N}$ best in HRT for 48 h, during the water removal rate of $\text{NH}_3\text{-N}$ the highest reached 93. 5%, than high removal rate of HRT for 12 h best 21. 1%, and the cycle time is 4 times as much, so the analysis by $\text{NH}_3\text{-N}$ removal efficiency, HRT for this system, the optimal time of 12 h.

The Figure 13 shows that the system effluent NO_3^- -N concentrations in HRT for 12 - within 48 h, were higher than water NO_3^- -N concentrations, system within 48 h, is superior to the nitrification and denitrification effect, because denitrification

need anaerobic conditions, but with the extension of time, the concentration of NH_3 -N can reduce water, nitrification will gradually weaken, denitrifying bacteria play a major role at this time, start lower NO_3^- -N concentrations.

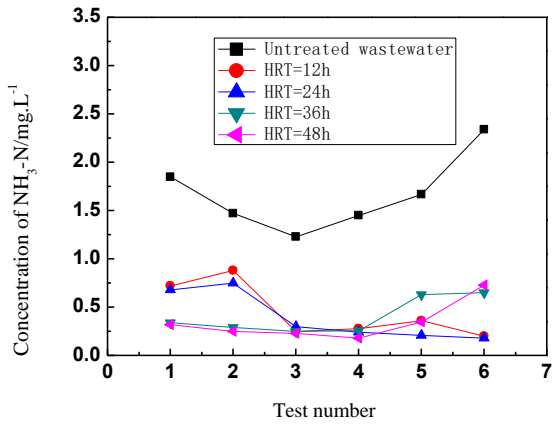


Figure 12 The influence HRT of NH_3 -N

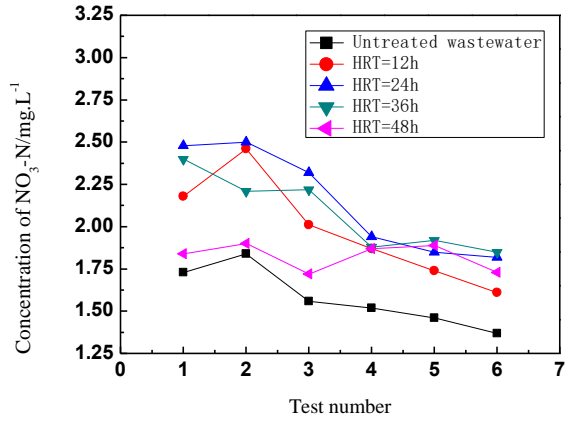


Figure 13 The influence of HRT of NO_3^- -N

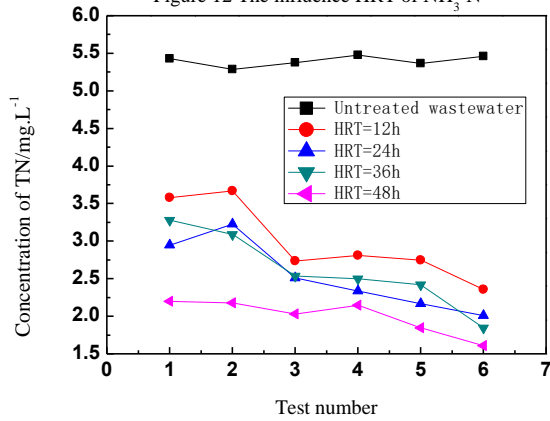


Figure 14 HRT effect on TN

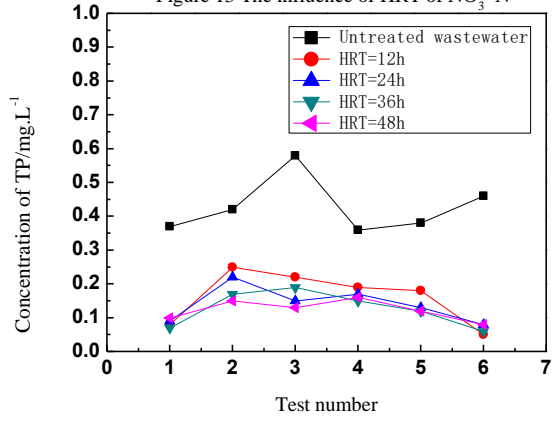


Figure 15 The influence of HRT of TP

By Figure 14, the TN concentration in the system under the condition of different hydraulic retention time, out of the water have significant changes in concentrations of TN, TN removal rate with the increase of time, gradually increases, when the HRT for 48 h, TN removal effect is best, removal rate reached 62.4%.

By Figure 12 shows, in different HRT system effluent TP is lower than the water concentration, and with a continuation of the time, the concentration of the two measures are, in turn, reduce the water, namely in the experiment of six different HRT, 48 h effluent TP concentration, the lowest average removal rate of up to 63.5%. And when HRT is 12 h, the system average removal rate of TP water has reached 48.7%, while a quarter of their time only for 48 h, so you can determine the optimal hydraulic retention time of artificial wetland system for 12 hours.

Taken together, determine the optimal hydraulic retention time of artificial wetland system for 12 h.

CONCLUSION

(1) the test in the process of screening plant found that canna has advantage in removing nitrogen and phosphorus, total nitrogen, total phosphorus removal rate is respectively 84.5% and 57.3%, respectively, better than the reeds, water celery, water bamboo, canna strong vitality and adapt better, on the surrounding environment in the whole process of plant selection, canna nitrogen and phosphorus removal is more significant in the lake, so choose canna as the test plant.

(2) the canna vertical flow constructed wetland plants in total nitrogen removal is mainly due to the system in the process of growth need nutrients supply, ceramsite filler on nitrogen removal efficiency of phosphorus removal effect is better than, slightly polluted water during the trial run period, a little change of nitrogen and phosphorus concentration in the artificial wetland in the purification effect is stable. Canna artificial wetland system on phosphorus removal effect is remarkable, the main reason in the period of system stable

operation, including canna root absorption ability is good, plant growth condition is good, the plants need to grow and phosphorus absorbed by plant roots in great quantities, which is transformation in plants and thus out of the water concentration is low.

(3) according to the economic benefit and nitrogen and phosphorus removal effect analysis of artificial wetland system of HRT = 12 h, plant density of 6 strains of canna and 40 cm ceramsite filler height as the optimal parameters.

Acknowledgements: *The authors wish to thank the China Fund program: National Science and Technology Major Project for the Control and Treatment of Water Pollution (2014ZX07202-011).*

REFERENCE

1. Y.Y. Zhang, *J. Environ. Sci. Manag.*, **5**, 126 (2009).
2. A.M. Pires, I.G. Cowx, M.M. Coelho, *J. Fish Biol.*, **2**, 235 (1999).
3. R.B. Fu, Strengthen the artificial wetland restoration of eutrophication of water bodies and mechanism study, Tongji University, (2007).
4. C.K.C. Hatano-Trettin, C.H. House, Microbial populations and decomposition activity in the subsurface flow constructed wetlands, In: *Constructed wetlands for water quality improvement*, A.M. Gerald, Florida, Lewis Publishers, 1993, pp.540-547.
5. X.L. Wang, *J. River Ecol. Restoration Technol. Hydraulic Electric Eng.*, **361**, 6 (2010).
6. M.A. Palmer, E. Bernhardt, E. Chomesky, *Science*, **304**, 1251(2004).

Geology, mineralogy and geochemistry of the Mazayjan massive sulfide deposit (Southern Sanandaj - Sirjan, Iran)

Kamal Noori Khankahdani*, Mehrdad Karimi

Islamic Azad University, Shiraz Branch, Department of Geology, Shiraz, Iran

*-Corresponding author, Noorikamal@yahoo.com

Received June 26, 2016, Revised September 10, 2016

Copper mineralization of Mazayjan area occurred in Carboniferous metabasites of Suriyan metamorphic Complex (northeast Fars province) and within the southern part of Sanandaj–Sirjan structural province in Iran.

Metallic minerals composition observed in the region is simple and includes pyrite, chalcopyrite, malachite, covellite and iron oxides. The geological settings forming the deposit environment including mineralization at metabasitic section of Suriyan complex with the basaltic to andesitic primary composition, The nature of sub-alkaline tholeiitic related to oceanic basins for this metabasites and occurrence of subsequent metamorphic processes, presence of pyrite mineral as main sulphide phase, massive, layered and shearing structures, all indicate that Mazayjan copper deposit is a volcanogenic massive sulfide (VMS deposits) and probably of the besshi type. Point analysis studies (EPMA) showed that in terms of chemical composition, pyrite and chalcopyrite are uniform and homogeneous due to metamorphic processes in the area of interest. This indicates that metamorphic events in the region occurred after sulfide mineralization. In the other words, metamorphic processes cannot be introduced as the origin of copper mineralization in Mazayjan. Microscopic and probe analyses have shown that inclusions of chalcopyrite within pyrite, while valuable elements were not found within these minerals.

Keywords: Iran, Sanandaj-Sirjan, Mazayjan, Massive sulfide, Probe analysis.

INTRODUCTION

Massive sulfide deposits were introduced in the 1950s for the first time as a distinct group of deposits. Due to their relation with volcanic activities, they are commonly known as VMS, an acronym with different words, but very close concepts. For example, Sawkins [20] called these deposits volcanic-associated massive sulfide deposits. Large *et al.* [9] named them as volcanic-hosted massive sulfide deposits. Also volcanogenic massive sulfide deposits has been used by Franklin *et al.* [6].

VMS deposits are major source for copper and zinc elements, and secondary source for elements such as Pb, Ag, Au, Cd, Sc, Sn and Bi. Also the supply of a VMS mass is variable and ranges between 2.7 to 7.1 million tonnes have been reported [8-11].

It should be noted that massive sulfides mineralization at the Sanandaj- Sirjan structural state of Iran is well known and have been introduced by many researchers [1,2,5,12,14,15,18,19,21-24].

In the current study, after an introduction to the study area and research methods, we discuss issues related to copper mineralization at the Mazayjan area in the southern Sanandaj-Sirjan in three sections: geology, mineralogy and geochemistry.

The results of these sections are presented separately.

GEOLOGICAL BACKGROUND

Study area

Mazayjan is located in the most eastern part of Bavanat city in Fars province and is bordered with Kerman (in east) and Yazd (in northern) (Fig. 1).

Mazayjan area is located in 240 Km northeast of Shiraz and at the southern part of Sanandaj- Sirjan state; therefore, follows the general geological conditions of the state.

Geology

Fig.2 shows the simplified geological map of Mazayjan area based on Noori's studies [13, 14] and Noori *et al.* [16]. This map is part of the Tootak White Mountain anticline which has a Northwest – Southeast trend same as most of the anticlines in Sanandaj-Sirjan [18-19]. The core of White Mountain anticline includes older Tootak series and its limb is made of Suriyan complex schists. In a geological section from the northeast to southwest of Mazayjan region three main geological units are exposed. These units in terms of age from older to younger include: Tootak metamorphic complex marbles, age of Devonian-Carboniferous, Suryan metamorphic complex schists, age of Carboniferous and non-metamorphic carbonate rocks, age of

To whom all correspondence should be sent:

E-mail: Noorikamal@yahoo.com

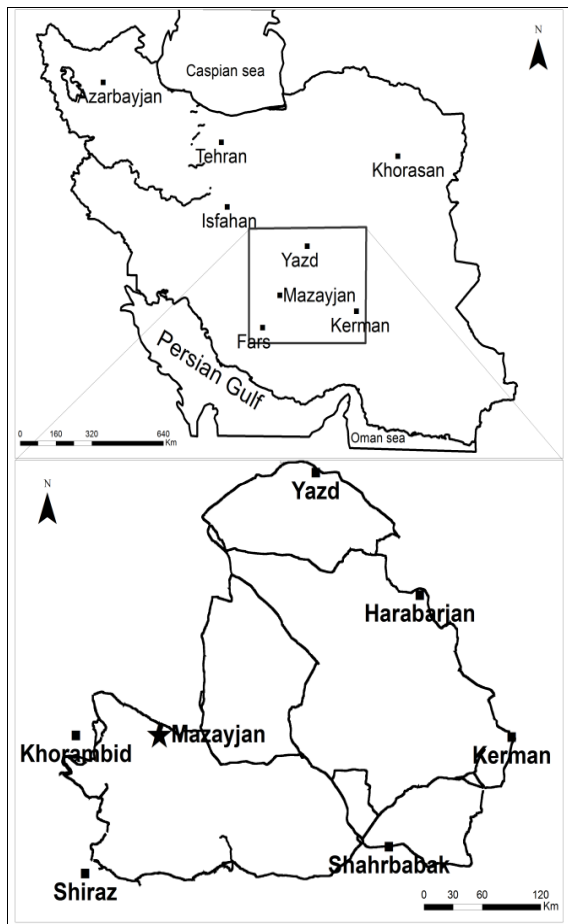


Fig. 1. Geographical location and access routes of Mazayjan.

Jurassic-Cretaceous. Since Suriyan metamorphic complex schists acted as the host rock of copper mineralization in Mazayjan region, therefore, will be discussed in more details (Fig. 3).

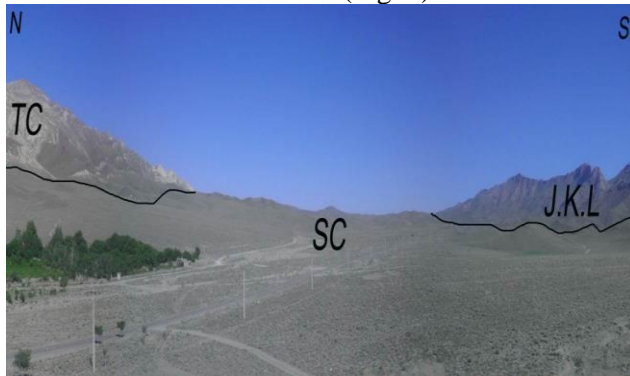


Fig. 3. Outcrop of rock units, view towards east. J.K.L: Jurassic-Cretaceous Limestone SC: Suriyan complex(greenschist & micaschist) TC: Tootak Complex

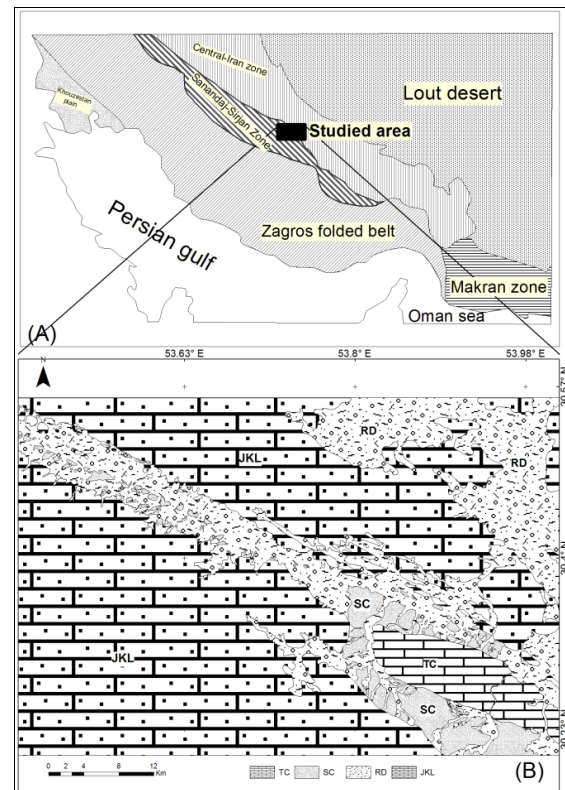


Fig. 2. (A) Study area in structural provinces map of Iran and (B) Simplified geological map of Mazayjan [22].

- J.K.L: Jurassic-Cretaceous Limestone
- RD: Recent deposit
- SC:Suriyan complex(greenschist & micaschist)
- TC:Tootak complex
- TC: Tootak Complex

Stratigraphic column of the Mazayjan study area is shown in (Fig.4). Suriyans complex schists are between Tootak complex rock units and jurassic–cretaceous non-metamorphic carbonate rocks.

Based on studies of [7], protolith of Suriyan metamorphic complex schists is divided into two groups. The first group are metapelites commonly composed of micaschist and some phyllite and represent metamorphosed clastic sedimentary facies, and the second group are metabasites that mostly made of greenschist and are rarely associated with amphibolites and indicate metamorphosed submarine basaltic volcanism. Most of the Suriyan metamorphic complex in Mazayjan area, are metabasites or greenschists, which is accompanied by a smaller micaschist and phyllite (Figs 5, 6).

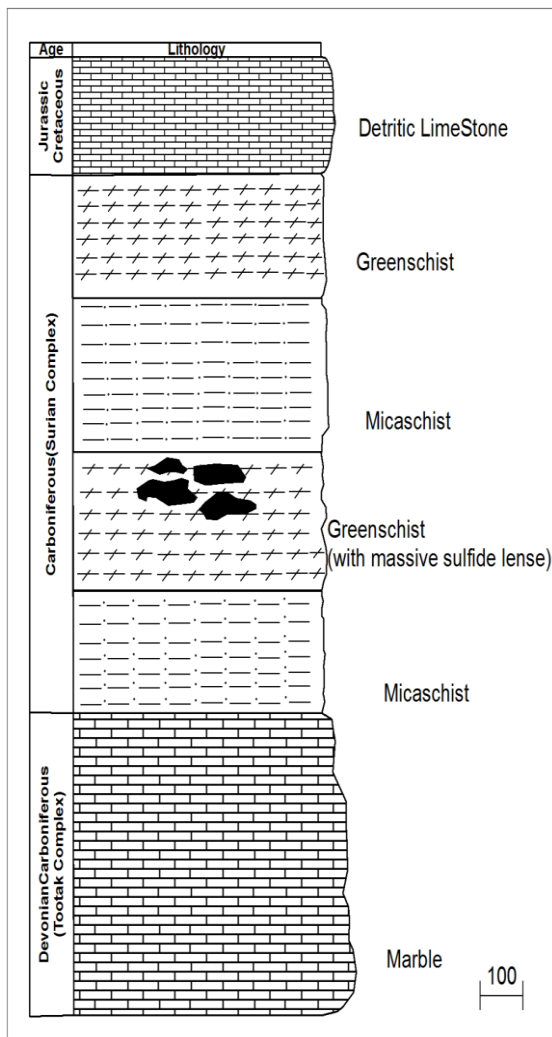


Fig. 4. Stratigraphic column of Mazayjan area.

Based on current studies, metabasites section of Suriyan metamorphic complex has played as Cu mineralization host rock (Figs. 7 and 8). This idea is in accordance with the findings of other researchers such as Musivand [12], Noori&Amiri [15], Fahandezh [5].

Field studies conducted in the area reveal that this section of the sedimentary basin of southern Sanandaj-Sirjan has been extremely active during the Devonian to Carboniferous and left behind clastic sediments. Later on, these sediments were accompanied by submarine basaltic eruptions. Then after metamorphism during either Hercynian [25] or former Cimmerian [24], Suriyan metamorphic complex was formed with a thickness of 3750m. This metamorphic complex is associated with the copper mineralization in parts of its outcrop area such as [20-25]. Field evidences suggest that



Fig. 5. The contact region of marbles of Tootak complex (TMC) with schists of the Suriyan complex (SSC) in the east of Mazayjan, view towards east.



Fig. 6. Greenschist of Suriyan complex Outcrop in north of Mazayjan.



Fig. 7. Copper mineralization as chalcopyrite in metabasites of the Suriyan complex in Mazayjan area.



Fig. 8. Malachite mineralization in oxidation zone of Mazayjan Cu deposit, greenschist of Suriyan metamorphic complex was host rock of this mineralization.

Mazayjan copper deposit was formed in a volcanic–sedimentary environment. Comparing with the origin of copper deposits, it reminds massive sulfides where high volume of submarine eruptions is associated with clastic sedimentary rocks. Another important observation in the Mazayjan is that specific alteration of massive sulfide deposits such as sericitization and chloritization is scarce or can be seen on a small extent, indicating these massive sulfide deposits are close to besshi type [13-15]. Occurrence of regional metamorphism after the alteration in besshi deposits is the reason for less exposure of altered rocks. Formation of iron hat or gossan in the upper part of studied basic schists is one of the special effects of alteration in Mazayjan area (Fig.9). Based on the studies in this iron hat, which represents supergene oxidant zone, a variety of secondary minerals such as malachite, chrysocolla, hematite, goethite and limonite have been formed. During the field studies, Iron hat is very important in identification of metal impregnation areas.

STUDY METHODS

First, Stratigraphic column of the study area was mapped to determine the rock units and their relationship in the field. Thin sections were prepared from hand samples and studied using Nikon polarizing microscope. During microscopic experiments, mineralogical and texture studies, were implemented while suitable samples were separated for detection and analysis device tests. Chemical analysis XRF and ICP was done by Kansaran Binalud Company.

After reviewing the regional studies, field surveys and samplings were carried out and then office studies were begun.



Fig. 9. Metabasites with chlorite alteration in greenschist of Suriyan complex.

Microscopic studies

This study has several major goals: detection of metallic and non-metallic minerals and exploring their relationship, identification of available textures, naming rocks, examination of rock alteration phenomenon in order to determine the origin of copper mineralization in the area, and selection of suitable samples for analysis device. All these items are presented separately.

Non-metallic minerals

Suriyan metamorphic complex metabasites are introduced as the host rock of copper mineralization; therefore, it is expected that most non-metallic minerals observed in thin sections include: Plagioclase (sometimes with sericitic alteration), tremolite–actinolite (occasionally chloritized), calcite, biotite and quartz (Fig.10). The integration of this mineralogy complex indicates minerals of greenschist facies that have experienced some alteration phases. Based on study of polished sections, opaque minerals presented in this set are pyrite and chalcopyrite.



Fig. 10. Limonite with goethite and other iron oxides in a samples of rocks in oxidant supergene zone (gossan or iron cap) in Mazayjan area.

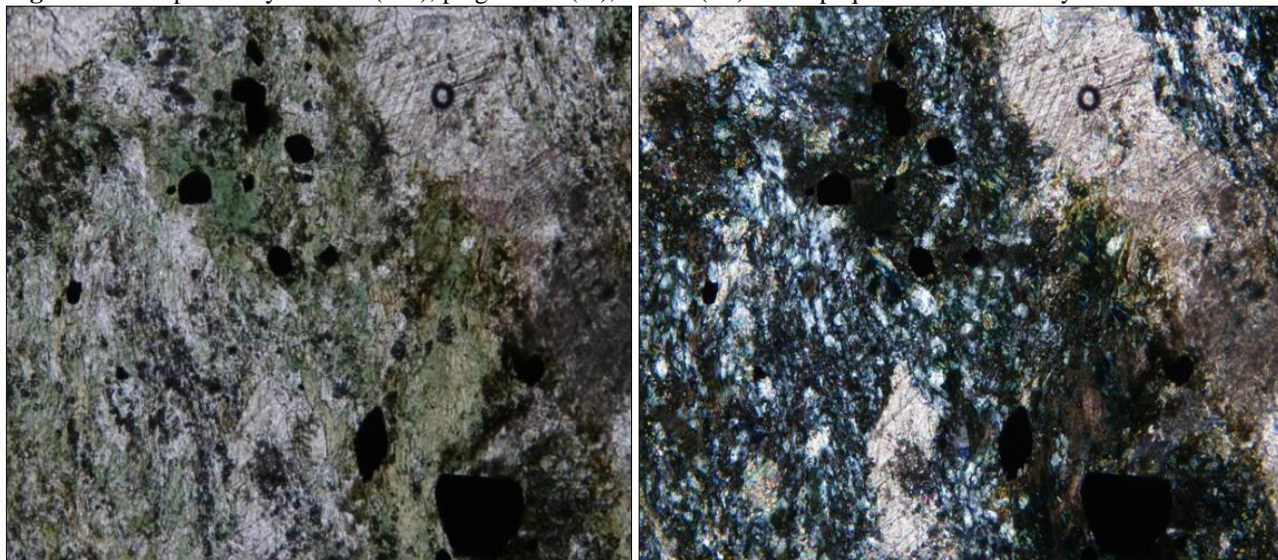
Metallic minerals:

Chalcopyrite, pyrite, marcasite, covellites and iron oxides are the most important metallic minerals found in rocks of this region.

Chalcopyrite. Chalcopyrite is the most important mineral containing Cu at Mazayjan area. Its dimension is usually about 20 to 50 microns, and its abundance is between 5 to 10 percent. In some sections, chalcopyrite has been observed as inclusions within pyrite and these two minerals, together, show the layered texture (Fig.11).

Moreover, growth of sulfides, in some cases indicates massive texture for them (Fig. 12). Both of these textures are important in determining the origin of these deposits.

Fig. 11: Accompanied by chlorite (Chl), plagioclase (Pl), calcite (Cc) whit opaque minerals in Suriyan basic schists.



Pyrite

Pyrite is the most common sulfide mineral of Suriyan basicschists in Mazayjan area. The abundance of this mineral is about 5 to 20 percent. Dimensions of pyrite is about 10 to 200 microns, rarely appears up to 2 mm in size (Figs. 11, 12, 13). The difference in grain size of pyrite in basicschists of Mazayjan area represents the graded bedding phenomenon which is commonly observed in the other massive sulfide deposits [20]. This phenomenon in pyrite is assumed to be related to periodic changes in super saturated degree of fluids at the time of discharge at the sea floor [20]. Pyrites observed in the Mazayjan area are mainly in the form of a banded texture (Fig.11) and in some cases sparse texture (Fig.13). In both cases, they usually show forms of brecciations.

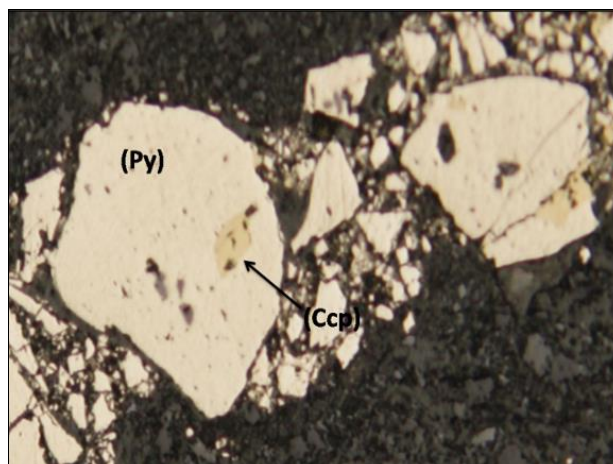


Fig. 12. Shearing bedded texture in Pyrites (Py) of Suriyan basicschist, Mazayjan. Pyrite crystals in this section contain inclusions of chalcopyrite (Ccp).



Fig. 13. Delayed crystallization of chalcopyrite compared whit Suriyan basicschists, Mazayjan area.



Fig. 15. Marcasite crystals with inclusions of chalcopyrite in Mazayjan metabasites.

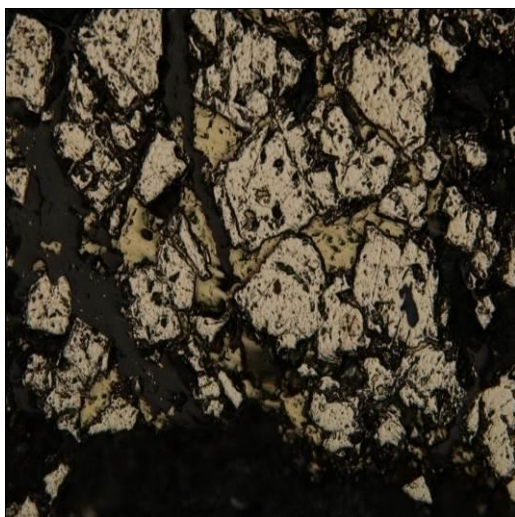


Figure 14: Pyrite automorph crystal with traces of embayment in Mazayjan basicschists

Marcasite

In polished sections can be seen as rectangular-shaped crystals, retaining crushing traces and cataclastic textures created by tectonic forces (Fig.15). Marcasite abundance is about 2 to 4 percent. Presence of chalcopyrite inclusions is another characteristic of this mineral. Formation of marcasite instead of pyrites in Mazayjan schist, is related to decrease in temperature during crystallization of iron sulfides. Based on Deer et al. [4] marcasite has a lower crystallization temperature comparing to pyrite.

Covellite

Covellite is formed as a secondary mineral because of the conversion of chalcopyrite, so often appears in the form of chalcopyrite as a pseudo-morph (Fig.16). Also, Covellites as a secondary

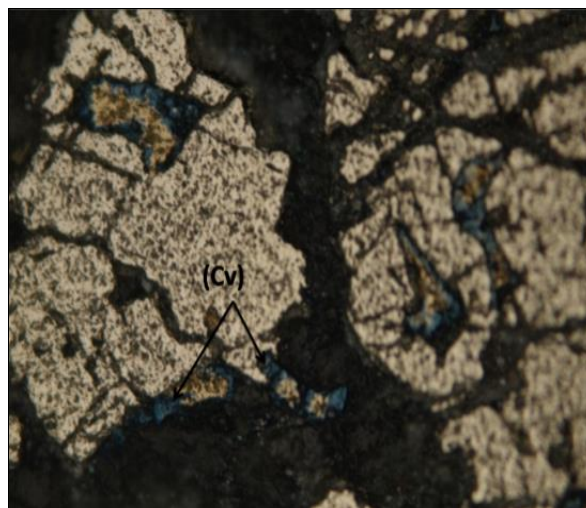


Figure 16: Chalcopyrite mineral is converted to Covellite (Cv) in Mazayjan Basic schists.

mineral can grow into empty spaces. Its abundance is up to 3 percent in some sections.

Minerals of supergene zone

Malachite is the most important secondary mineral containing Cu in Mazayjan area. Its characteristic color is a great clue to identify areas of copper dissemination in the field. In thin sections, it fills fractures and pore spaces irregularly (Fig.17). This mineral is often associated with hematite and chrysocolla and is indicator of minerals of supergene zone.

In Fig.17 Chrysocolla shows banded colloidal texture, while hematite has a concentric colloidal texture in some sections of supergene zone rocks (Fig.18). But in both cases, it is assumed that colloidal texture is an indicative of rapid deposition of material from super saturated fluids during their mixing with the sub saturated fluids.

Table 1: Paragenetic sequence of minerals in Mazayjan copper index, according to microscopic studies

	Initial stage	Delay stage	Supergene stage
Chalcopyrite	●		
pyrite		●	
Markasit		●	
Hematite		●	
Colitis			●
Goethite			●
Limonite			●
Malachite			●
Krizokoola			●
Quartz	●		
Calcite	●		
Chlorite	●		
Sericite	●		

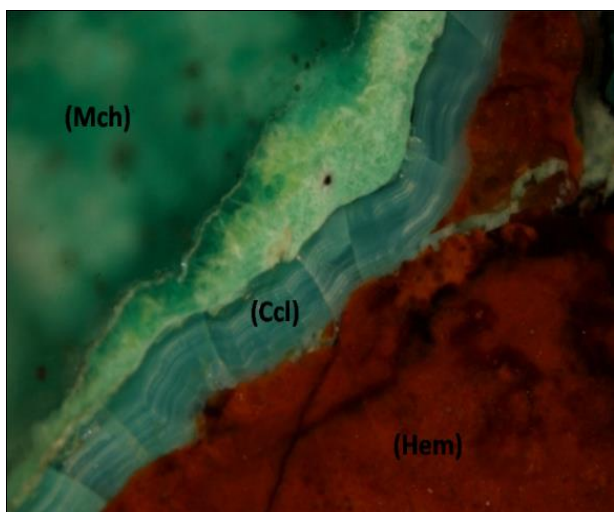


Fig. 17. Accompanied malachite (Mch) whit chrysocolla (Ccl) and hematite (Hem) in the rocks of iron hat zone in Mazayjan area.

Paragenetic sequence of minerals

Table 1 shows paragenetic sequence of minerals extracted from microscopic studies of Mazayjan area. Since chalcopyrite has been seen commonly as inclusions within other minerals such as pyrite and marcasite, it is related to the first stage of crystallization. In the next step, pyrite and marcasite are formed and then, secondary supergene minerals such as covellitis, malachite and chrysocolla are developed. Secondary silicate minerals such as quartz, calcite, chlorite and a bit later sericite are formed in the early and late stages

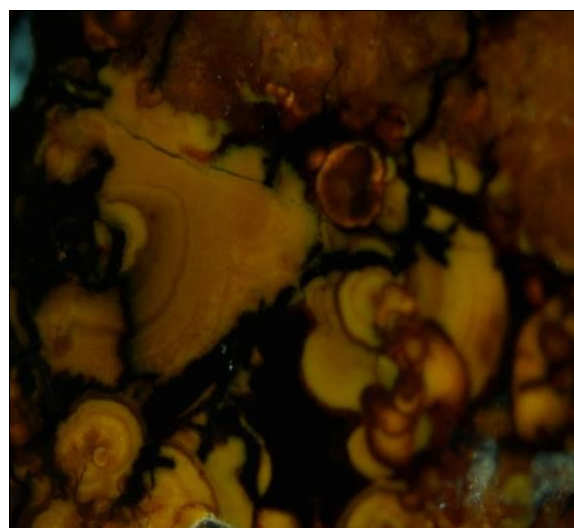


Fig. 18. Concentric colloidal texture in hematite, supergene zone of Mazayjan copper index.

and show simultaneous crystallization with sulfide. minerals in the area. They can be considered as a guide for exploration operations

Geochemical studies

Geochemical studies include analysis of 6 samples to determine the abundance of major and minor elements using XRF (Table 2), 4 samples to determine the abundance of major, minor and trace elements using ICP (Table 2) and 7 samples to perform Point analysis identification (EPMA). The results of this data processing are presented as follows.

Table 2. Chemical analysis results (XRF& ICP)

Sample		B2S16	B2S8	B5S13	B5S1	S10	S9	Sample	S1	S2	S4	S6	S7	B1S32	B1S6	B1S38
XRF								ICP								
SiO2		45.11	46.57	48.68	49.12	61.15	48.75	Ag	0.11	0.16	3.7	0.19	1.6	0.17	0.15	0.17
TiO2		2.540	1.303	1.460	1.312	0.554	0.667	Al	73213	68957	11487	17081	22785	76871	54331	73376
Al2O3		12.35	14.88	13.25	14.35	16.87	15.65	As	5.9	1.7	1.8	6.5	2.1	1.8	2.3	1.8
Fe2O3		17.45	12.40	14.52	9.85	7.84	7.66	Ba	53	56	14	17	14	41	49	170
MnO		0.256	0.285	0.233	0.265	0.033	0.051	Be	0.3	0.2	<0.2	<0.2	<0.2	0.3	0.3	0.2
MgO		7.85	7.59	6.22	6.98	1.85	1.96	Bi	0.43	0.38	0.88	0.45	0.69	0.41	0.41	0.44
CaO		7.71	9.35	10.58	10.96	2.52	9.85	Ca	53823	69103	1391	2319	3535	75657	101071	42088
Na2O		0.82	1.84	1.67	2.64	3.05	0.93	Cd	0.25	0.23	1.9	0.23	3.6	0.24	0.24	0.24
K2O		0.45	0.16	0.15	0.03	1.70	2.53	Ce	14	11	2	5	4	16	11	9
P2O5		0.307	0.099	0.104	0.083	0.149	0.158	Co	188	149	218	540	324	32	41	33
SO3		0.429	0.001	0.328	0.001	0.002	1.248	Cr	127	111	19	38	31	193	98	174
LOI		4.40	5.02	2.33	3.86	4.05	10.28	Cu	14566	16542	117287	6974	54052	104	35	133
Cr (ppm)		37	173	105	197	8	24	Fe	66057	63934	15702	153765	119335	49945	44996	56592
Ni (ppm)		55	138	74	114	35	50	K	1449	1709	122	403	106	1630	1864	3724
Co (ppm)		1	3	2	5	6	4	La	5	5	1	6	2	8	4	4
V (ppm)		446	224	286	218	145	166	Li	10	9	4	9	9	11	16	16
Zn (ppm)		159	73	82	74	69	59	Mg	19235	17101	7985	10305	13104	18045	15853	20753
Rb (ppm)		17	17	16	16	50	73	Mn	2070	1968	157	331	581	922	1575	807
Cl (ppm)		54	56	62	58	58	56	Mo	0.83	0.89	1.1	1.05	1	1.01	1.13	1.01
Ba (ppm)		126	56	51	91	116	69	Na	11785	7841	188	216	268	13500	8776	12267
Sr (ppm)		128	237	179	253	247	376	Ni	409	76	89	35	64	97	37	33
Cu (ppm)		76	76	62	100	73	85	P	691	553	747	261	489	663	526	375
Pb (ppm)		10	9	13	4	11	12	Pb	5	5	14	15	7	6	6	6
Ce (ppm)		3	23	17	31	4	38	S	138	151	125547	195341	86837	970	5603	7289
La (ppm)		1	10	7	15	1	17	Sb	1.11	1.02	1.08	1.08	1.02	1.03	1.03	1.19
W (ppm)		7	6	5	3	1	9	Sc	37.4	31.4	7.3	10	13.4	28.7	29.6	37.2
Zr (ppm)		132	107	84	89	103	125	Sn	3.5	3.1	4.1	4.1	3.4	3	2.9	3.2
Y (ppm)		39	22	22	15	23	33	Sr	121	173	11	4	11	352	207	133
As (ppm)		137	65	9	75	21	90	Th	5.3	6.2	2.9	3.4	3.2	6.1	6.3	5.6
U (ppm)		3	4	2	6	5	3	Ti	8659	7271	1282	1833	2524	7624	5368	4422
Th (ppm)		1	2	3	5	3	2	U	2.7	1.8	3.3	3	2.4	2.5	19	2.8
Mo (ppm)		2	4	3	6	2	3	V	301	274	44	81	100	199	145	245
Ga (ppm)		16	13	15	14	17	17	W	5.39	6.77	5.98	1.03	16.56	6.67	7.48	4.12
Nb (ppm)		32	25	23	21	32	25	Y	34	36	8	7	14	24	24	18
								Yb	4.3	4.3	1.6	1.6	1.9	3	2.9	2.6
								Zn	189	185	946	102	955	60	47	77
								Zr	60	54	27	33	31	77	29	36

RESULTS

Chemical analysis results of XRF and ICP:

The mean frequencies of major elements of Mazayjan area are listed in table3. It can be seen that the mean frequency of copper in the analyzed samples is 2.62%. This value is considered purely economical for other massive sulfide deposits which are similar to Mazayjan area, and hence reminds the necessity to complete the exploratory studies in the area.

Table 3. Mean frequency of the major metal elements.

Mean frequency in ICP	Element name
2.62%	Cu
7.13 %	Fe
0.03%	Zn

The results were processed using Minpet software. At first, basic schists were named. These rocks generally sit in the range of basalt and sometimes andesite (Fig.19). It is confirmed by assuming that studied basic schists are sourced from submarine basaltic eruptions.

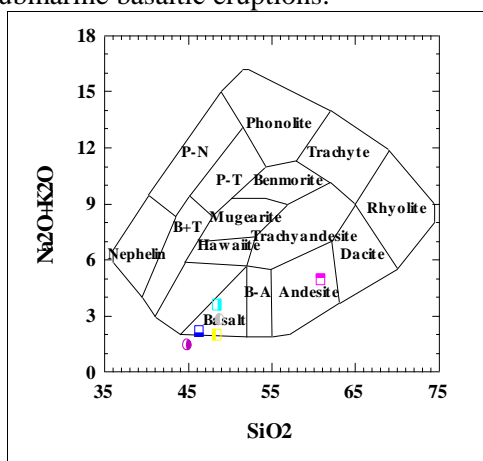


Fig. 19. Position of studied rock in (Base graph of Cox *et al.* [3])

[24-25] are used to determine the magma series. Based on these charts, studied rocks are located within the sub-alkaline and tholeiitic zones (Figs. 20, 21). Since oceanic crust is the origin of these rocks, the identified magma series would be correct.

Another important note in the geochemical study of these rocks is determination of their tectonic environment. After applying necessary corrections to the percentage of iron oxides using the Irvine and Baragar method, tectonic environment of Mazayjan basic schists were determined using the chart of Pierce *et al.* [17], (Fig.22). On this basis, environment of studied rocks is within the range of mid-oceanic and oceanic islands. This environment is consistent with Mazayjan field observations, because shows

accompaniment of hosted copper basic schists with metamorphosed clastic rocks. On the other

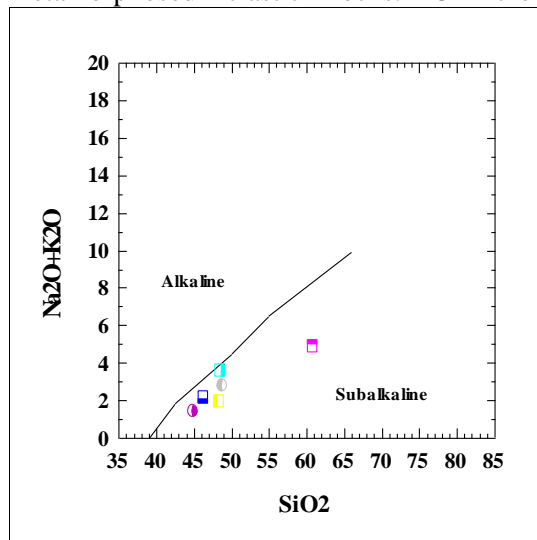


Fig. 20. Position of studied rock in Irvin and Baragar chart (1971).

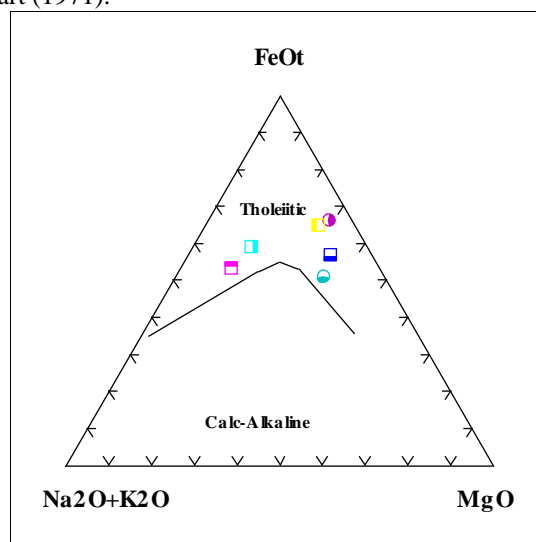


Fig. 21. Position of Mazayjan basicschists in Irvin and Baragar chart (1971) to determine the magmatic series.

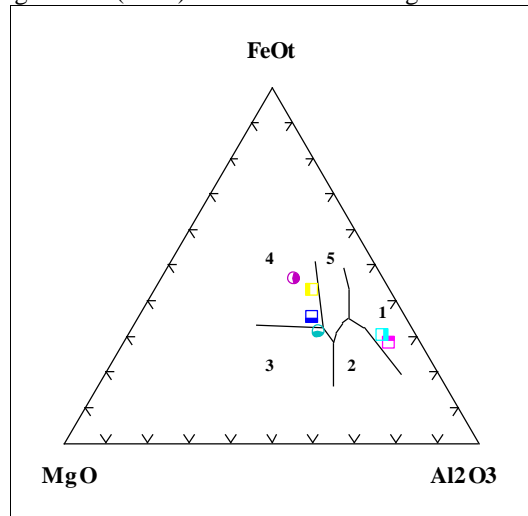


Fig. 22. Position of Mazayjan basic schists in oceanic environments (MORB and oceanic islands) in Pierce and *et al* chart (1997).

hand this could represent relationship between Mazayjan copper deposits with oceanic sedimentary basins similar to massive sulfide deposits. In order to study distribution of trace element, abundance of these elements in studied rock samples were normalized relative to the oceanic crust and the spider diagram was drawn (Fig. 23). The diagram shows that in comparison with the abundance of elements in the oceanic crust, abundance ratio of most normalized minor elements in the Mazayjan basic schists are in the range of 1. This fact points to their common origin. Based on these spider diagrams, one can conclude that the basic schists which hosted copper mineralization in Mazayjan area are similar to oceanic crust basic rocks in terms of distribution of trace elements.

Abundance of element such as Rb, Th and U relative to normalized oceanic crust (Figure 23), is higher. Considering the lithophile geochemical behavior of these elements and their low concentration in the oceanic crust, this situation can be explained as a result of the impregnation of these samples.

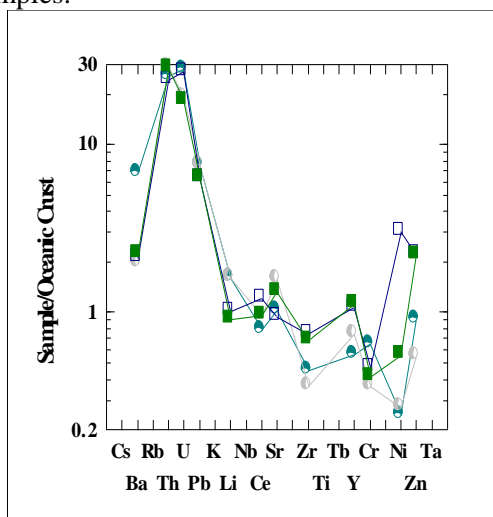


Fig. 23. Spider diagram of trace elements frequency of normalization studied rocks relative to the oceanic crust.

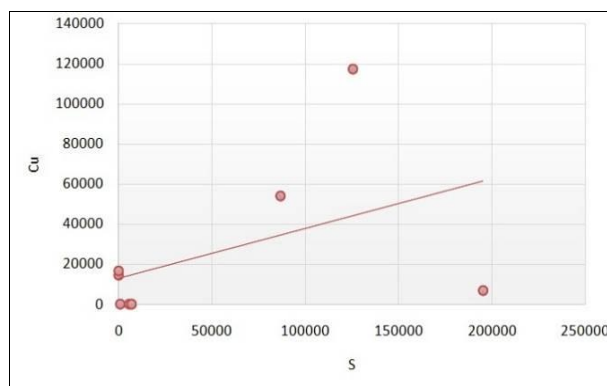


Fig. 24. Correlation chart of copper- sulfur for Basic schists, host of Cu mineralization in Mazayjan area.

Correlation charts between copper and iron with sulfur were drawn using the results of chemical analysis of samples (Figs. 24-25). As one can see correlation between metals with sulfur is a strong and positive value. Both copper and iron elements are concentrated in sulfide phases such as pyrite and chalcopyrite. The idea is completely consistent with the results of microscopic studies and point analysis.

Results of EPMA point analysis

Microscopic studies and device analyses showed that Pyrite and chalcopyrite are the main phases of metallic minerals in the study area. At the next stage point analysis started on these minerals. The current study follows several major goals: First, accurate determination of chemical and mineralogical composition of the main metallic mineral phases; Second, identification of probable inclusion minerals in major phases; third, identification of probable precious elements present in the primary phase.

Sample No. 891-MZ4 is one of the pyrite samples studied using probe analysis. In order to accurately identify the chemical composition of

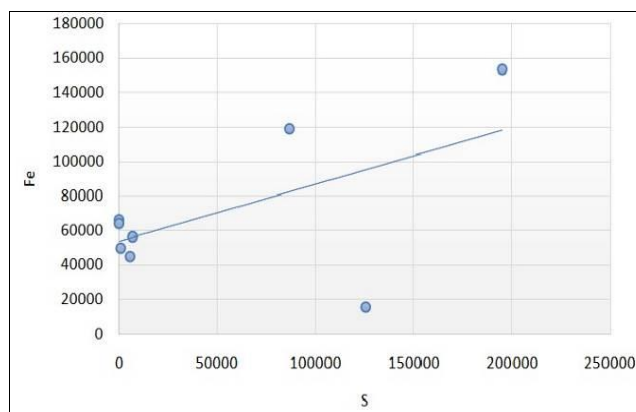


Fig. 25. Iron-sulfur correlation diagram for Mazayjan studied samples

mineral and potential zonings, three points were analyzed. Point 1 is located in the center and points 2 and 3 are at the margins of mineral (Fig.26).

Concentrations of iron and sulfur elements are lower in the margin and higher in center. It may be related to the alteration processes because these processes generally begin from margin of mineral.

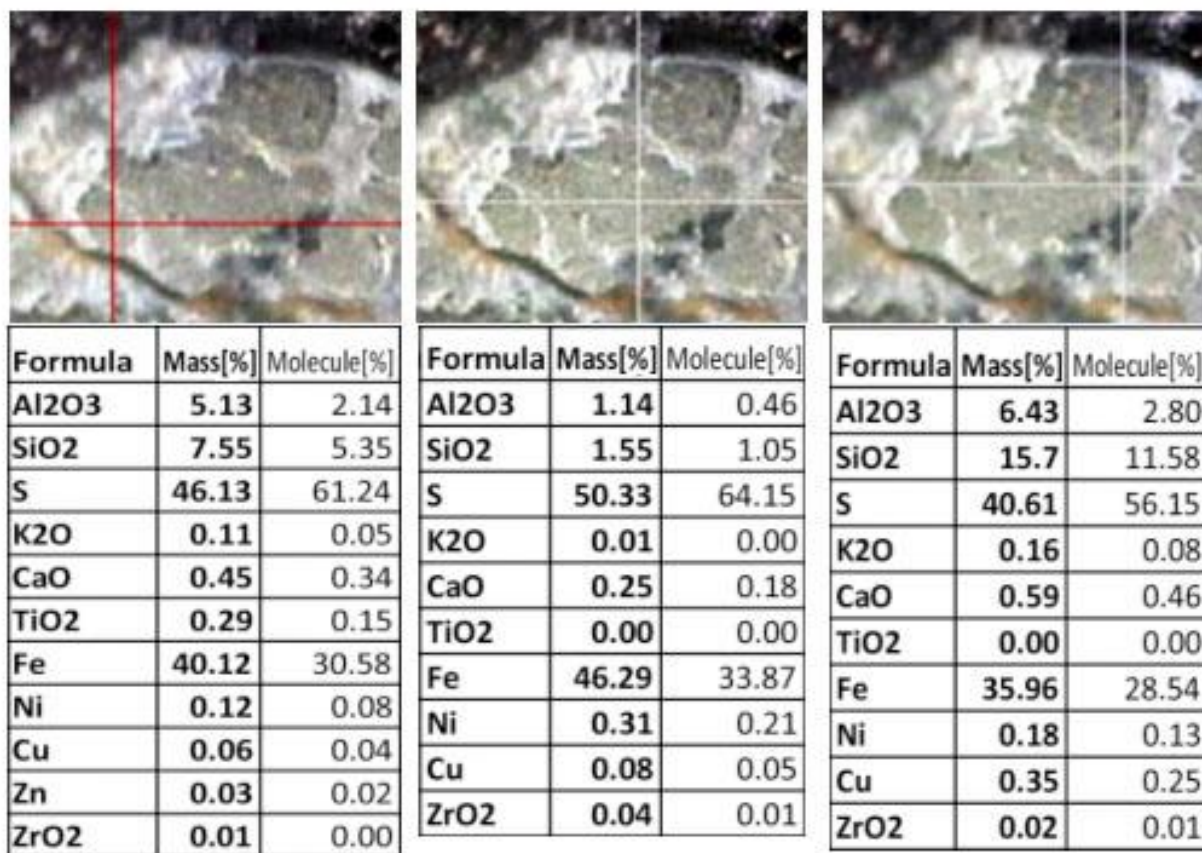


Fig. 26. Electron probe micro-analysis (EPMA) in a sample of pyrite from Mazayjan area in a central point and two marginal points.

Concentration of valuable elements such as copper, nickel and cobalt is low. Another important observation is that there is not any specific zoning among the present elements. This indicates the influence of metamorphic processes on pyrites of Mazayjan area. It has been proved that recrystallization processes due to metamorphism eliminate the combination zoning and homogenization of sulphides which generally have primary combination zoning inherited from environmental conditions and several physico-chemical changes (Mizuta, 1988).

The lack of combination zoning in the pyrites of Mazayjan area suggests that this mineral in terms of age has formed before taking place of metamorphic processes in the area. In the other words, metamorphism of plates and basic rocks has occurred after formation of pyrite. As a supplementary confirmation it worth mentioning

that chalcopyrite samples of studied area also don't have combination zoning (Fig.27).

In case of S-16 sample, as the backscatter images show, the context of studied mineral consists of sulfur, iron and copper without any regional structure. The chemical composition of mineral is quite uniform and homogeneous. It should be noted that marginal regions of the S-16 sample in (Fig.27), show a weak zoning, which can be due to the occurrence of subsequent alteration and contamination. With this reasoning, one can conclude that metamorphism processes are not responsible for copper mineralization in the Mazayjan area, but have led to some other subsequent changes such as homogenization. According to the probe studies, valuable elements have not been observed as impurity in pyrite and chalcopyrite samples.

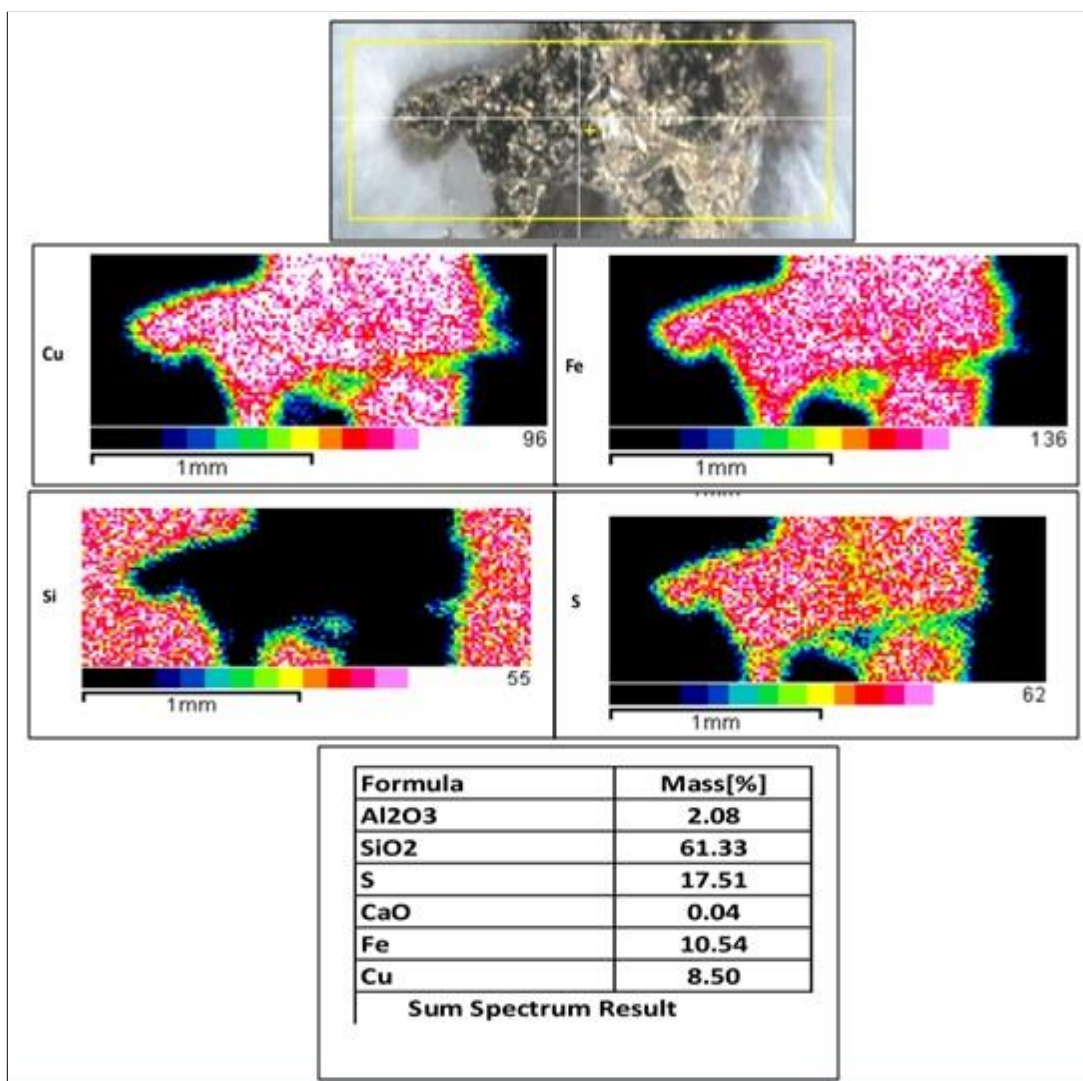


Fig. 27. Back scattering images and probe point analysis in a chalcopyrite (samples of Mazayjan area).

Comparing characteristics of Mazayjan copper deposits with various massive sulfide deposits suggest that this deposit is very similar to besshi type massive sulfide deposits (Table 4). Some of these characteristics include the geological environment, geochemistry of magmatic series in Mazayjan deposit, lithological conditions, mineralogy and mineralization of the region. Therefore the origin of Mazayjan deposit can be included in massive sulfide deposits Sanandaj-Sirjan structural province of Iran.

DISCUSSION AND CONCLUSIONS

The most important results of the current study can be summarized as follows:

- Metamorphosed basic rocks such as green schist and amphibolite are host of Cu mineralization in Mazayjan area. These rocks and metapelitic rocks such as micaschist and phyllite all together, form Suriyan metamorphic complex. So, the geological environment of host rock for Cu mineralization in Mazayjan area can be assumed to

be the ocean floor basic eruptions similar to massive sulfide deposits.

- The most important metallic minerals identified in the study area are pyrite, chalcopyrite and covellite. These minerals in addition to other minerals such as chlorite, calcite and epidote make up the Suriyan complex metabasites. Secondary minerals such as malachite, chrysocolla, limonite and goethite were also observed in gossan zone.

- Geochemical studies showed basic rocks which are generally in the range of basalt and some in the range of andesite, are considered as sub-alkaline rocks and imply oceanic environments (MORB and oceanic islands). Spider diagrams prove the latter issue.

- According to probe studies, pyrite and chalcopyrite samples have a uniform chemical composition. This suggests the influence of metamorphic processes on the studied samples, and is interpreted as the time of copper mineralization in Mazayjan, has been earlier than the time of metamorphism in the area.

Table 4: Comparative study of Mazayjan copper deposit whit besshi type massive sulfides.

Geology Establishment Environmental	Geochemistry of magmatic series	Metallic minerals	Structural properties	Characteristics of the host rock	Type of deposit
Mid-ocean ridges and oceanic islands	Sub-alkaline and tholeiitic basic rocks	Often Pyrite whit lesser amounts of Chalcopyrite, inclusions of Chalcopyrite in Pyrite	Stratiform and in direction to Surian basic Schists	Upper Paleozoic metapelites and metabasites of the Surian complex	Mazayjan Deposit
oceanic basins, such as Mid-ocean ridges	Sub-alkaline and tholeiitic basic rocks	Mainly pyrite with inclusions of Chalcopyrite	Generally stratiform to Lenticular form and often in shistosity direction	Paleozoic- Mesozoic Volcanogenic stratiform deposits and usually metamorphosed	Bashi deposits ★

* Gibson *et al.* [8]

- For various reasons, environmental conditions of Mazayjan copper deposit, is similar to massive sulfides conditions. First, eruptive basic rocks in the sedimentary basins have been host of copper mineralization, and due to metamorphism transformed to metabasites afterwards. Second, metallic minerals are limited to sulfide minerals such as pyrite, chalcopyrite and covellite and Mazayjan deposit has a simple mineralogy composition. And third, elements such as copper and iron have been positively correlated with sulfur. This behavior comes from geochemical characteristics of massive sulfides.

- In terms of comparison, characteristics of Mazayjan copper deposits are close to besshi type massive sulfide deposits. This comparative study has been shown in Table 4.

Acknowledgements. *This paper represents a part of results obtained from the research project of "Study of Copper mineralization in Bavanat region" which has been approved and performed in the Research deputy department of Islamic Azad University of Shiraz. We are grateful from partners in this department. We also acknowledge Dr. Mosayeb Sabzeie for his comments on the improvement of interpretations.*

REFERENCES

1. Z. Badrzadeh, M. Sabzei, A. Rastad, M. Emami, D. Khimno, *J. Earth Sci.*,76, (2010).
2. Z. Badrzadeh, Petrology and geochemistry of basaltic pillow lava in Northwest Jiroft, with Special Reference on Copper mineralization VMS accompanying them, Ph.D. Thesis, Tarbiat Modares University, 2009..
3. K.G. Cox, J.D. Bell, R.J. Pankhorst, The interpretation of igneous rocks, Allen&Unwi, 1979, p.450.
4. W.A. Deer, R.A. Howie, J. Zussman, An Introduction to the Rock Forming Minerals. Longman, 1991, p .528.
5. M. Fahandezh, Mineralogy and geochemistry study of Tootak mining index in east of Bavanat Fars province, Economic Geology MS thesis, Islamic Azad University of Shiraz, 2012.
6. J.M. Franklin, H.L. Gibson, I.R. Jonasson, A.G. Galley, In: Volcanogenic Massive Sulphide Deposits; J.W. Hedenquist, J.F.H. Thompson, R.J. Goldfarb, J.P. Richards (eds). The Economic Geology Publishing Company, 2005, pp. 523-560.
7. J.M. Franklin, J.W. Lydon, D.F. Sangster, *Eco. Geo.*, pp. 485-627 (1981).
8. H.L., Gibson, R.L. Allen, G. Riverin, T.E. Lane, The VMS Model: Advances and Application to Exploration Targeting, Fifth Decennial International Conference on Mineral Exploration, 2007, pp. 713-730.
9. R.R. Large, R.L. Allen, R.L., M.D. Blake, W. Herrmann, *Econ. Geol.*, **96**, 1055 (2001).
10. T. Mariko,T, Y.Kato, *Resource Geol.*,**44**, 353 (1994).
11. T. Mizuta, *Mining Geology*, **38**, 263 (1988).
12. F. Mousivand, Mineralogy, geochemistry and genesis of copper mineralization in Suriyan volcanic

- sedimentary complex in Fars Bavanat region, Economic Geology MA thesis. Tehran Tarbiat Modarres University, 2003.
13. K. Noori Khankahdani, Investigation of genetic and constructional relationship of Bon-do-no gneiss whit Tootak metamorphic complex .Petrology PhD thesis, Islamic Azad University, Science and Research Branch of Tehran, 2005.
 14. K. Noori Khankahdani, Application of satellite data in separation of rock units of Totak and Suriyan metamorphic complexes. Report of research project, Islamic Azad University, Shiraz, 2009.
 15. K. Noori Khankahdani, A. Amiri, Exploration of mining potential in Bavanat region, Final report of the research project, Islamic Azad University, Shiraz branch, Research Assistant Domain, 2007.
 16. K. Noori Khankahdani, A. Zarei, M. Karimi, A. Mousavi Makoui, Application of principal components analysis method (PCA) linear data in separation of Surian metamorphic complex rocks units – Fars Bavanat, National Conference Advances of Geosciences, Islamic Azad University of Behbahan, p. 1388, 2009.
 17. T.H. Pearce, B.E. Gorman, T.C. Birkrtt, *Earth Planet Sci* ,**36**, 121(1977).
 18. M. Sabzei, A.Gh. Yusefi, Introduction to geology and mining exploration of Sargez massive sulfide Jiroft mountain, southeast of Iran, Sabzevaran armanpazhouh company, 2000, 59 pages.
 19. M. Sabzei, A.Gh. Yusefi, Final report of exploration Jiroft Mountain Sargaz Copper mine, Arman pazhouhe sabzevaran, 2000, 52 pages.
 20. F.J. Sawkins,. (1984) Metal Deposits in Relation to Plate Tectonics, Berlin, 1984, p. 325.
 21. F. Soroushnezhad, Mineralogy and geochemistry of Mazayjan copper index northeast Fars province, Economic Geology MS Thesis, Islamic Azad University of Shiraz, 2012.
 22. J Stocklin, Structural History and Tectonic of Iran - Geo. B. V.52 -No.7 (1968).
 23. H. Tajeddin, A. Rastad, A. Yaaghoubpour, M. Mahjal, *J. Econ. Geol.*, **1**, 97 (2010).
 24. A. Yarmohammadi, A. Rastad, M. Mahjal, M.J. Shamsa, *Science Journal of Tehran University*, 1985.
 25. Yui, S., *Econ. Geol.*, **5**, 231 (1983).

Geochemistry and genesis of Qareh Qotoo copper index, Sanandaj-Sirjan, Iran

F. Amiri¹, K. Noori Khankahdani^{*2}, M. Lotfi¹, M. Karimi²

1-Department of Geology, North Tehran Branch, Islamic Azad University, Tehran, Iran

2-Department of Geology, Shiraz Branch, Islamic Azad University, Shiraz Iran

**Corresponding Author: Noorikamal@yahoo.com*

Received June 26, 2016, Revised September 10, 2016

The Qareh Qotoo copper deposit has been located in the south of Kerman province and Sanandaj-Sirjan metamorphic belt. Petrologically, the study area has been formed from crystalline limestone, phyllite, amphibolite, serpentinite, green schists, calcareous sediments, tuff and diabase units. The host rocks of copper mineralization in this area are generally the greenschists which their protoliths are basic to intermediate igneous rocks (basalt to dacite), based on geochemical studies. The nature of these igneous rocks are tholeiitic sub-alkaline and are related to igneous arcs basalts in terms of geological dispositional environment. The main copper minerals of the ore deposit are chalcopyrite, malachite and covellite. The average grade of copper in the analyzed specimens was calculated equal to 0.92%.

Keywords: Sanandaj-Sirjan, Qareh Qotoo copper deposit, geochemistry, genesis

INTRODUCTION

The Qareh Qotoo region has been located in the southern part of Sanandaj-Sirjan metamorphic belt. This belt is one of the structural states of Iran which has been named by Stocklin [20] for the first time. The Sanandaj-Sirjan state in south is separated from Zagros folded state by the main thrust of Zagros. The metamorphic activities in the state have continued from Paleozoic to Cenozoic and cause this state have the uttermost metamorphic rocks out cropping among Iran's structural states. Some of these activities have resulted copper mineralization at various points of Sanandaj-Sirjan that has been reported by different researchers [1, 3, 10-17, 19, 21]. One of these copper mineralization areas is Qareh Qotoo region that its geochemistry and genesis has been investigated in the current studies.

GEOLOGICAL SETTING

Sanandaj – Sirjan is a narrow strip of the southwestern of central Iran which is in the immediate North-East of the main thrust of the Zagros zone. The lithological and structural features of the state represents a trough or a bloc crevasse in the Precambrian Shield of Iran and Saudi Arabia [5-6]. Therefore, its geological features have obvious differences with the adjacent zones. The significant differences of this zone has attracted the geologists'

attention since distant past. The most original lithic collection of Sanandaj-Sirjan zone are gabbro and metamorphic ultramafic rocks which mainly have Precambrian age. Lithologically, Qareh Qotoo region has been formed from crystalline limestone, phyllite, amphibolite, serpentinite, green schists, calcareous sediments, tuff and diabase units (Figure 1). Among the mentioned rocks, green schists are the host of copper mineralization event in the area and Figures 3 to 5 have displayed an outcrop of that important geological unit. Figures 6 and 7 have been prepared from microscopic sections of the schists, hosting copper mineralization.

STUDY METHOD

In order to identify the rocks and minerals, the handy specimens as well as thin and polished sections were studied after field investigations. Then, 10 specimens were selected from stones suitable for chemical analyses and were analyzed using XRF method. Considering the data obtained from the chemical analyses, the changes in the magmatic phases in the region were perused, the primary chemical composition of the magma was recognized, and type of magmatic series governing the region was identified and regional tectonic environment that the results of this part of studies will be presented accordingly.

To whom all correspondence should be sent:
E-mail: *Noorikamal@yahoo.com*

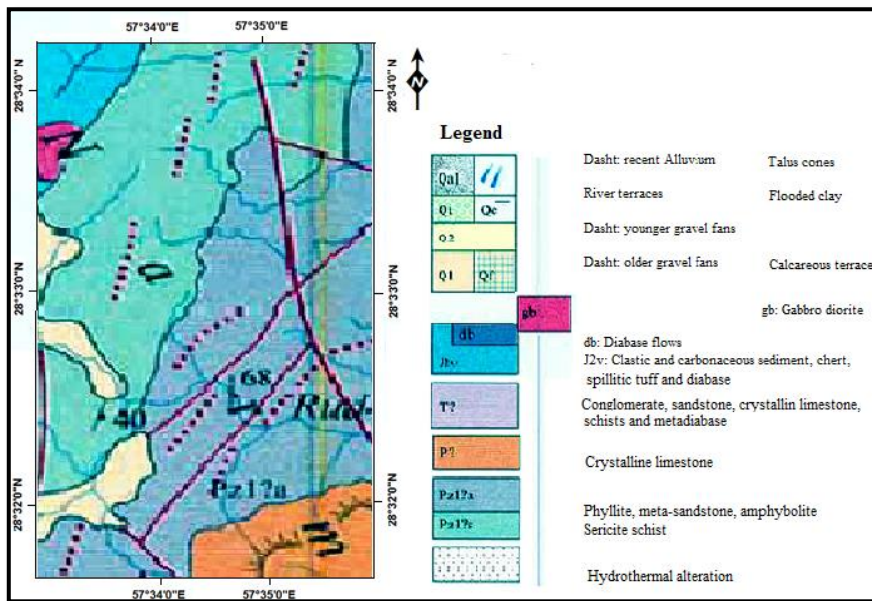


Fig. 1. The geological map of the range of Qareh Qotoo's copper (derived from the Sabzevaran's 1: 100,000 scale map).



Fig. 2. A close-up from green schists out cropping in Qareh Qotoo's mineral range (the host rock of copper mineralization).



Fig. 3. The general state of outcropping of alteration basic rocks (green schists) within the range of Qareh Qotoo's copper. The field and microscopic studies has determined the combination of these rocks from green schists to amphibolite.

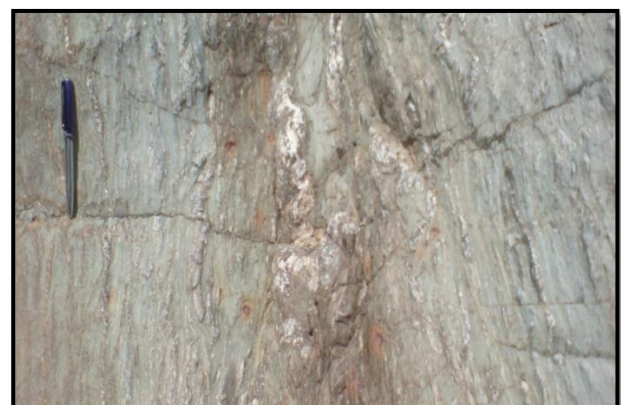


Fig. 4. The sulfidic mineralization (pyrite and chalcopyrite) in the green schists of mineral range of Qareh Qotoo. In this picture, nota bene to the effects of analysis and sulfide minerals alteration which has led to the release of iron oxides and hydroxides.

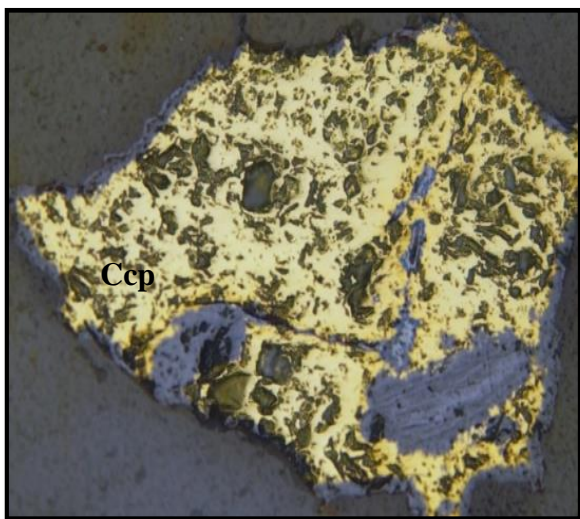


Fig. 5. The Chalcopyrite mineral with a vein tissue in green schists of the region.

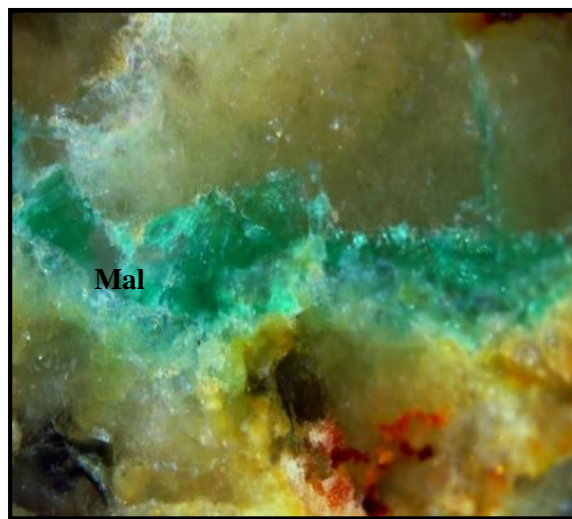


Fig. 6. The Malachite mineral in green schists of the region.

STUDY RESULTS

The results obtained from the chemical analyses on rocks in the environment of GCDKit and Minpet software have been processed that its results will be presented separately.

The results of geochemical studies

The XRF method was used to study the basic elements. In this method, the values of major oxides including SiO₂, Al₂O₃, Fe₂O₃, CaO, Na₂O, K₂O, MgO, TiO₂, MnO, P₂O₅, S, LOI was determined. Here, considering the diversity of taken specimens, 8 specimens of copper ore were selected for the geochemical study. The studies show that the oxides of silicon, iron and aluminum are the most important oxides available in the rocks (Table 1). Also can see that the average frequency of Cu in the sample is 0.92% and its maximum rate was determined equal to 2.69% that it is considered economic for copper massive sulfide deposits resembling Qareh Qotoo region in Jiroft and it confirms the need for further exploratory studies. In this research, Le Bas et al. diagram [9] were used

to determine the type of rocks (Figure 8). The obtained results show that the Protolith of green schists of the region, or in fact, the primary rock, hosting the copper mineralization in Qareh Qotoo region have been basalt to dacite rock series. Additionally, according to this diagram, the rocks under study have been located within the range of sub-alkaline. The AFM diagram was used to determine the magmatic series type (Figure 9). The resulting graph shows that most of the specimens have been positioned within the tholeiitic range. Therefore, the Protolith of rocks hosting the copper mineralization in the studied specimens are part of tholeiitic sub-alkaline series.

The genetic studies results

Verma et al. (2006) diagram has been used to determine the origin of protoliths, hosting copper mineralization in Qareh Qotoo region (Figure 10). According to the diagram, the majority of the investigated specimens have been located within the igneous arc basalts (IAB) range that this issue is confirmed considering the tholeiitic nature of these rocks.

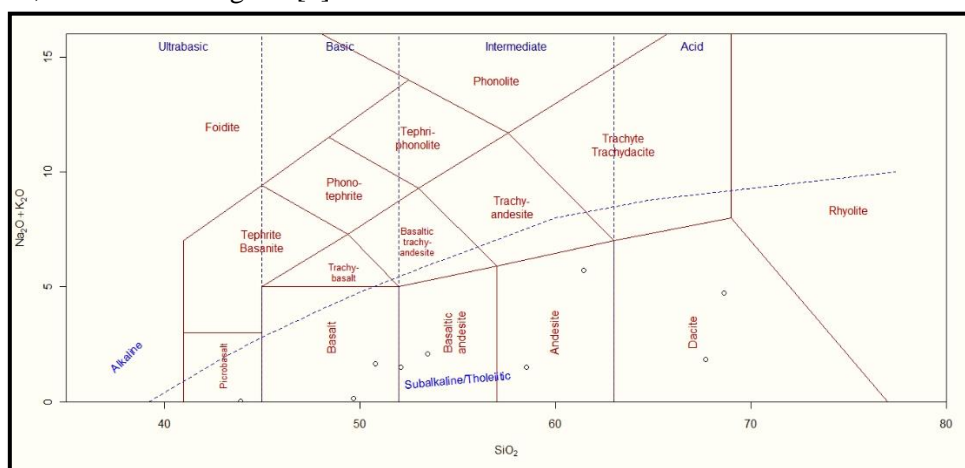


Fig. 7. The position of protoliths of green schists in Qareh Qotoo region in the Le Bas et al. diagram [9].

Table 1. The results of XRF analysis.

Sample	Si ₂ O	Al ₂ O ₃	Fe ₂ O ₃		CaO	Na ₂ O	K ₂ O	MgO	TiO ₂	MnO	P ₂ O ₅	S	L.O.I
	%	%	%		%	%	%	%	%	%	%	%	%
T4S3	40.03	14.85	14.62		14.58	0.02	0.01	6.75	0.166	0.148	0.043	0.147	4.87
T4S5	48.75	10.74	12.61		11.79	1.39	0.02	7.85	1.654	0.275	0.142	0.001	3.64
T4S13	60.68	15.21	12.01		0.23	0.01	0.23	9.41	0.398	0.370	0.103	0.002	0.020
T4S15	44.25	13.75	12.02		6.54	1.35	0.37	8.25	1.114	0.475	0.064	0.002	9.35
T4S15	11.68	0.58	80.12		0.35	0.02	0.02	0.04	0.121	0.007	0.002	0.204	6.55
T5S4	95.85	1.22	0.96		0.31	0.14	0.08	0.02	0.001	0.002	0.002	0.183	0.48
T5S10	52.78	9.35	10.59		11.41	0.62	0.72	2.78	0.216	1.862	0.071	0.002	9.12
T6S1	72.85	1.77	2.14		11.76	0.15	0.01	1.81	0.070	0.029	0.009	0.002	9.05
T6S2	58.35	17.85	3.49		3.96	9.73	0.15	2.57	0.230	0.061	0.010	0.113	3.13
T6S4	45.68	15.68	18.30		0.60	1.45	0.03	7.85	0.674	0.302	0.032	0.002	5.77
AVR	53.09	10.10	16.69		6.15	1.49	0.16	4.73	0.464	0.353	0.048	0.066	5.18
MAX	95.85	17.85	80.12		14.58	9.73	0.72	9.41	1.654	1.862	0.142	0.204	9.35
MIN	11.68	0.58	0.96		0.23	0.01	0.01	0.02	0.001	0.002	0.002	0.001	0.02

Sample	Cl	Ba	Sr	Cu	Zn	Pb	Ni	Cr	V	Ce	La	W
	ppm	ppm	ppm	ppm	ppm	ppm	ppm	ppm	ppm	ppm	ppm	ppm
T4S3	73	89	265	27451	38	1	134	94	164	8	3	1
T4S5	59	5	197	8654	170	4	158	494	259	6	4	1
T4S13	97	43	32	6879	1934	139	35	82	124	30	13	1
T4S15	62	61	65	15424	924	16	120	366	258	21	8	1
T4S15	456	2	43	1013	241	4	31	372	168	17	11	2
T5S4	94	34	18	4785	14	41	46	26	22	21	15	3
T5S10	61	112	208	246	109	4	140	149	146	46	18	1
T6S1	88	16	18	338	66	13	42	5	26	14	9	1
T6S2	90	34	135	674	43	8	61	28	56	16	11	5
T6S4	66	74	14	26857	412	3	157	203	286	22	14	1
AVR	114.6	47	99.5	9232	395.1	23.3	92.4	181.9	150.9	20.1	10.6	1.7
MAX	456	112	265	27451	1934	139	158	494	286	46	18	5
MIN	59	2	14	246	14	1	31	5	22	6	3	1

Sample	Zr	Y	Rb	Co	As	U	Th	Mo	Ga	Nb
	ppm	ppm	ppm	ppm	ppm	ppm	ppm	ppm	Ppm	ppm
T4S3	45	5	15	1	116	2	2	1	6	1
T4S5	96	22	13	2	71	1	1	1	8	1
T4S13	57	13	21	2	860	2	8	1	8	2
T4S15	67	34	29	112	25	1	1	1	4	1
T4S15	11	2	18	4	88	1	3	1	19	1
T5S4	37	5	13	7	39	1	1	1	11	1
T5S10	92	32	32	2	117	1	1	1	12	1
T6S1	27	4	12	2	4	1	1	1	9	1
T6S2	62	12	15	1	36	1	1	1	14	1
T6S4	40	21	17	562	164	2	3	1	4	1
AVR	53.4	15	18.5	69.5	152	1.3	2.2	1	9.5	1.1
MAX	96	24	32	562	860	2	8	1	19	2
MIN	11	2	12	1	4	1	1	1	4	1

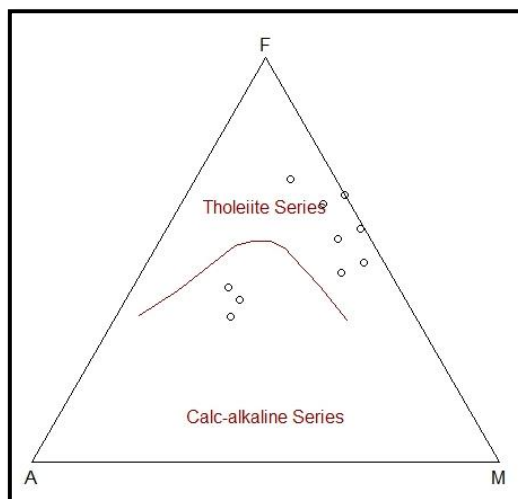


Fig. 8. The position of protoliths hosting the copper of Qareh Qotoo region in the AFM diagram (basis diagram of Irvine&Baragar [8]). The majority of specimens have been located within the range of tholeiitic series.

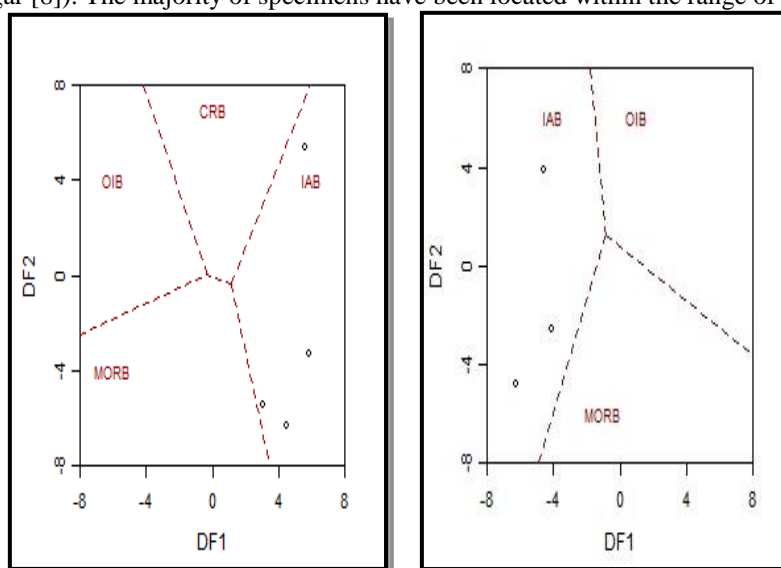


Fig. 9. The position of protoliths of basic schists containing copper in position of igneous arc basalts, basis diagram of Verma *et al.* [22].

DISCUSSION AND CONCLUSION

The most important results obtained from this study can be summarized as follows:

- The Qareh Qotoo region in the south of Jiroft is a part of Sanandaj–Sirjan. Thus, it follows the lithological and tectonic features of this state.
- The copper minerals of the region generally consist of chalcopyrite, malachite and covellite which can be seen in keeping with the minerals such as hematite and goethite which are as a host rock in the green schists.
- The protolith of green schists, hosting copper mineralization in Qareh Qotoo region, were basic igneous rocks up to intermediate within the range of basalt to dacite.
- The Protolith of green schist, were geochemically in tholeiitic sub-alkaline series

and were originally very similar to geological environments of igneous arcs basalts rocks.

- Based on geological geochemical evidence as well as identification depositional environment for Protolith of green schists, hosting copper mineralization in Qareh Qotoo region, it can be concluded that studied copper deposit is very similar to the copper deposit of massive sulfides type. Accompaniment with basic igneous rocks up to intermediate with the submarine origin, the existence of sub- tholeiitic alkaline series, impact of alteration processes on rocks hosting copper mineralization, confirms that the copper deposit of Qareh Qotoo in the south of Jiroft, is very similar to the Besshi-type massive sulfide copper deposits. Table 2 has shown a comparative study of the results in more details and using studies carried out by Cox [2], Seal *et al.*[18], Fox [4] and Hy [7].

Table 2. A comparative study of copper deposit of Qareh Qotoo with Besshi-type massive sulfide.

Geological conditions \ Deposit type	Besshi-type massive sulfide*	Qareh Qotoo deposit
Host rock	Altered basic rocks	Greenschist, amphibolite
Associated rocks	Carbonate and siliciclastic sedimentary rocks	Crystalline limestone, phyllite and schist
Protoliths	Basic igneous rocks up to intermediate	Basalt to dacite rock series
Magmatic series	Sub-alkaline and tholeiitic	Sub-alkaline and tholeiitic
Geological environment	Sedimentary basins, such as back-arc basins	Igneous arcs basalts
Metamorphic processes	Up to greenschist to amphibolite	Generally in the range of green schist, sometimes amphibolite
Geological age	Upper Paleozoic	Permian (upper Paleozoic)

*According to Cox [2], Seal et al. [18], Fox [4] and Hy [7].

REFERENCES

1. Badrzadeh, Z., (2009) -Petrology and geochemistry of basaltic pillow lava in Northwest Jiroft, with Special Reference on Copper mineralization VMS accompanying them, Petrology Ph.D. thesis, Tarbiat Modares University.
2. D.P. Cox, Descriptive model of Besshi Massive Sulfide, in: Cox, D.P., and Singer, D.A.(eds.) Mineral deposit Models. U.S. Geological Survey Bulletin, 1986, pp.136-138.
3. M. Fahandezh, Mineralogy and geochemistry study of Tootak mining index in east of Bavanat Fars province, Economic Geology MS thesis, Islamic Azad University of Shiraz, 2012.
4. J.S. Fox, *Canad. Inst. Mining Met. Bull.*, **77**, No.864, 5 (1984).
5. M. Ghorbani, "Economic geology of natural and mineral resources of Iran", Pars (Arian Zamin Geology Research), 2007, p. 492.
6. V. Grabeljsek, S. Cvetic, S., R. Mitrovic, D. Stoilovic, Sabzevaran Geological Map (1:100000), GSI.
7. T. Hy, Besshi Massive Sulphide, In: Selected British Columbia Mineral Deposit Profiles, Vol. 1 (Metallics and Coal), Lefebure, D.V. and Ray, G.E. (eds), British Columbia Ministry of Energy of Employment and Investment, Open file 1995-20, p.40-50.
8. T.N. Irvin, W.R.A. Baragar, *Canad. J. Earth Sci.*, **8**, 523 (1971).
9. M.J. Le Bas, R.W. Le Maitre, A. Streckeisen, B. Zanettin, *J. Petrology*, **27**, 745 (1986).
10. F. Mousivand, Mineralogy, geochemistry and genesis of copper mineralization in Suriyan volcanic – sedimentary complex in Fars Bavanat region, Economic Geology MA Thesis. Tehran Tarbiat Modarres University, 2003.
11. K. Noori Khankahdani, Petrological and Geochemical Investigation in Bavanat Area ", Final report of the research project, Islamic Azad University, Shiraz Branch, Research Assistant Domain, 2002.
12. K. Noori Khankahdani, A. Amiri, Exploration of mining potential in Bavanat region, Final report of the research project, Islamic Azad University, Shiraz branch, Research Assistant Domain, 2007.
13. K. Noori Khankahdani, A. Zarei, M. Karimi, A. Mousavi Makoui, Application of principal components analysis method (PCA) linear data in separation of Surian metamorphic complex rocks units – Fars Bavanat, National Conference Advances of Geosciences, Islamic Azad University of Behbahan, p. 1388, 2009.
14. K. Noori Khankahdani, M. Karimi, (2013) Mineralogical and geochemical studies of copper mineralization in the Surian metamorphic complex (Bavanat, Fars); Final report of the research project, Islamic Azad University, Shiraz Branch, Research Assistant Domain, 2013.
15. K. Noori Khankahdani, *Adv. Biores.*, **6**, 146 (2015).
16. M. Sabzehei, A.Gh. Yusefi, Introduction to geology and mining exploration of Sargez massive sulfide Jiroft mountain, southeast of Iran, Sabzevaran Armanpazhouh Company, 2000.
17. M. Sabzehei, A.Gh. Yusefi, Final report of exploration Jiroft mountain Sargaz copper mine, Arman Pazhouh Sabzevaran, 2002.
18. R.R. Seal, J.M. Hammarstrom, N.K. Foley, C.N. Alpers, Geoenvironmental models for seafloor massive sulfide deposits, U.S., Geol. Survey Open File Report, 2001, pp.196-212.
19. F. Soroushnejad, "Mineralogical and geochemical index of Mazayjan copper – north-east of Fars province" M.S. Thesis of Economic Geology, Islamic Azad University, Shiraz branch, 2012.
20. J Stocklin, Structural History and Tectonic of Iran - Geo. B. V.52 -No.7 (1968).
21. H. Tajeddin, A. Rastad, A. Yaaghoubpour, M. Mahjal, *J. Econ. Geol.*, **1**, 97 (2010).
22. S.P. Verma, M. Guevara, S. Agrawal, *J. Earth System Sci.*, **115**, 485 (2006).

Geochemistry and genesis of Darb-e-Behesht porphyric copper index, South Kerman, Iran

K. Noori Khankahdani^{1*}, H. Motavassel¹

¹ Department of Geology, Shiraz Branch, Islamic Azad University, Shiraz, Iran

*Corresponding Author: Noorikamal@yahoo.com

Received June 26, 2016; Revised September 10, 2016

The Copper Deposit area of Darb-e Behesht is located in south of Kerman province, at a 45 km distance from South Rayen. In terms of structural states the study area is considered as a part of the magmatic Urmia-Dokhtar belt. Main rocks of the region include Andesite, Andesite Tuff and Granodiorite. In some areas, Copper mineralization is observed as Malachite, Azurite, Chalcopyrite and Colic in Granodiorites and rocks in their contact zones. Field and geochemical studies indicated that Darb-e-Behesht Copper index is most similar to Porphyry type deposits because copper mineralization in granitoid intrusive rocks has happened along with propylitic, argillic and sericitic alterations. In addition to this, the geochemical combinations of studied rocks fall under the sub-alkaline, calc-alkaline type rocks category. This matter along with their geological environment, are recognized as the plates 'convergent boundaries are among the most important geochemistry reasons to introduce this deposit as a propylitic one.

Key words: Urmia-Dokhtar, Darb-e-Behesht, Porphyric Copper, Geochemistry, Genesis

INTRODUCTION

Porphyric copper deposits have always been under earth science researchers due to their high importance. Guilbert&Park [6] introduce porphyric copper deposits as deposits with high tonnage, low-grade non-twin which are generally associated with acidic to intermediate plutonic igneous rocks. Sawkins [10] has analyzed time and place of the geological formation of porphyry deposits. He believes that although porphyry deposits have always had a chance to be formed in geological times, their most important has been from the Late Cretaceous until now. Also, on the geological environment of these deposits' formation, Sawkins [10] believed that the malicious borders of the layers have been most likely to form these deposits and in fact, areas with subduction are the geological environment position for porphyric deposits; thus, identification and exploration of porphyry deposits are most likely in the magmatic or island arcs. Copper mineralization in the magmatic belt of Urmia-Dokhtar in central Iran has long been of interest to geologists because many of them believe the magmatic belt of Urmia-Dokhtar is in fact a magmatic arc which's most activity has occurred during the Eocene [3]. As an example, Waterman& Hamilton [12] have evaluated the Sarcheshmeh copper deposit in the magmatic belt of Urmia-Dokhtar and concluded that this deposit is Porphyric type. Shahabpour [11] has studied the alteration and mineralization of copper – molybdenum in Sarcheshmeh's copper mine and concluded that it is a porphyric copper deposit.

Aftabi and Ataapour [1] have studied the magmatic activities' geochemistry and petrologic characteristics in Sarcheshmeh and DehSiahan regions in the magmatic belt of Urmia-Dokhtar and concluded that the deposits have similar conditions to Porphyricdepostis. Hezarkhani [7] has investigated the evolution of hydrothermal systems in Midook copper mine of Urmia-Dokhtar magmatic belt and concluded that copper mineralization in Midook has the conditions of Porphyric deposits. Copper deposit of Darb-e-Beheshtis located in south Rayen and the magmatic belt of Urmia-Dokhtar. Geochemistry and genesis of this deposit has been studied for the first time which's results will be presented separately but before that the geology of the region is described.

GEOLOGICAL SETTING

Darb-e-Behesht area is located in central Iran and magmatic belt of Urmia-Dokhtar in terms of Iran's structural state divisions [5] (cf. Figure 1) and is also considered as a part of Dehaj-Sarduiehbelt based on Kerman area divisions. The Dehaj-Sarduiehbelt with a length and width of 450 km and 90km respectively begins from northwest and west of Kerman, Anar and Dehajareas, and continues to southeast of the province (Jabālbārez Jiroft). Wide parts of this layer are covered by Eocene volcanic complex including Andesitic, Andesitic- Basaltic, Basaltic- Trachyte, Rhyolite, Trachyte- Andesitic, Trachyte- Basaltic along with related pyroclastic. This volcanic complex is penetrated by granite and granodiorite

To whom all correspondence should be sent:

E-mail: Noorikamal@yahoo.com

intrusive and hydrothermal solutions have caused extensive alterations and copper mineralization in the area. Volcanic-plutonic belt of Dehaj-Sarduieh is a part of the Sahnd-Bazman zone in Kerman province which is formed from extrusive (basalt, track basalt, andesite, dacite and rhyolite) and intrusive igneous rocks (diorite, granodiorite, quartz and granite) of Eocene and Neogene which are cut by granitoid masses with combination of

diorite, granodiorite-quartz, quartz and granite oligomiocene.

Granitoids generally have the condition for potassic, sericitic and propylitic alteration. Being tourmaline is also seen in a large number of samples. The abundance of alkali feldspar in field and microscopic observations indicate that these rocks are rich in potassium.

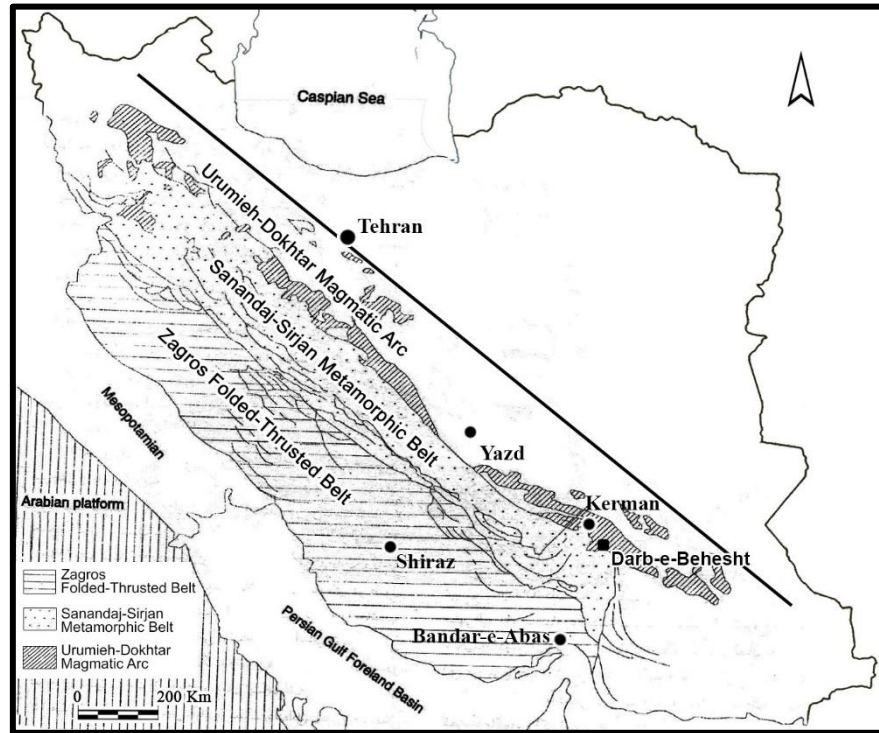


Fig. 1. Condition of Darb-e Behesht area in the Magmatic Arc or Urmia-Dokhtar in the Structural States Map of Iran, (Base Map from Ghorbani [5]).

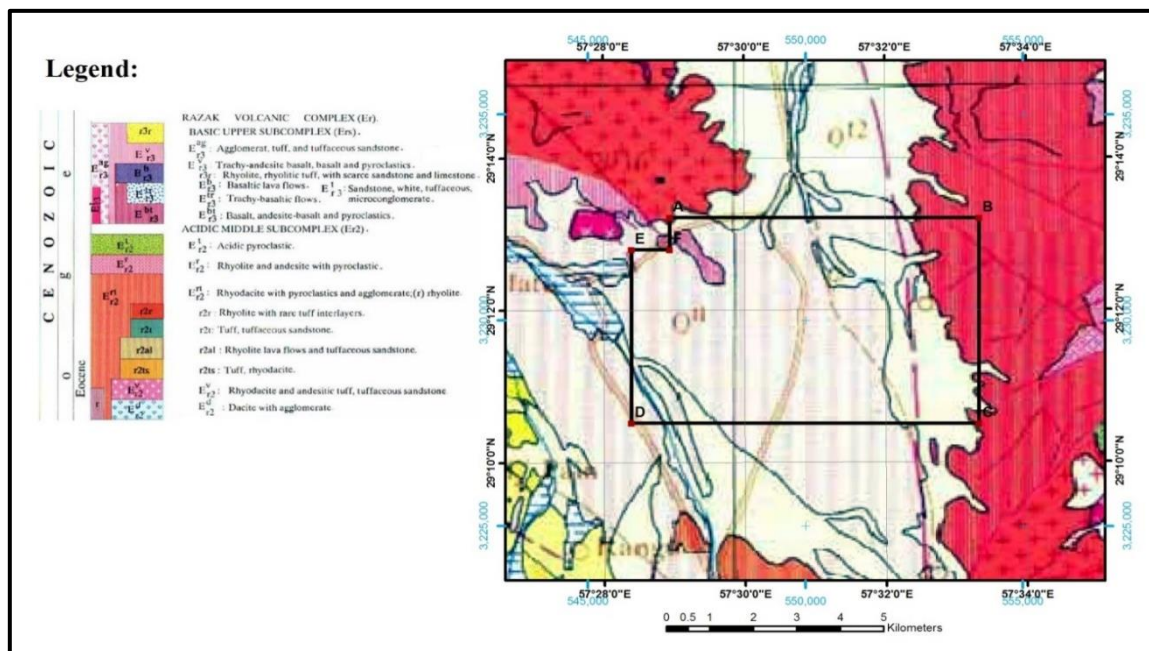


Fig. 2. - Geological map of copper deposit of Darb-e Behesht area (derived from 1: 250,000 map of Bam [4]).

Figure 2 shows a slice of the geological map of the area. Large parts of this layer is covered by volcano-sedimentary complex of Eocene including andesitic, andesitic- basaltic, basaltic- trachyte, rhyolite, trachyte- andesitic, trachyte- basaltic along with related pyroclastic. This volcanic complex is penetrated by granite and granodiorite intrusive and hydrothermal solutions have caused extensive alterations and copper mineralization in the area.

According to field studies conducted in the region it was concluded that the main stones in the area include andesite (Fig.3), granodiorite (Fig. 4) and andesitic tuffs (Fig.5).Surface copper mineralization is often seen as malachite (Fig. 6) but sometimes azurite and a less amount of chalcopyrite are also observed on the surface. Studying the microscopic sections has also confirmed the existence of copper minerals such as malachite (Fig. 7).



Fig. 3. Outcrop of andesitic rocks in Darb-e Behesht area.



Fig. 4. Close-up of granodioritic intrusive rocks in Darb-e-Behesht deposit.



Fig. 5. Andesitic tuff outcrop in Darb-e-Behesht area with propylitic alteration.



Fig. 6. Mineralization as malachite in epidotic alteration zones.

CHEMICAL STUDY OF ROCK SAMPLES

In order to complete geological studies, analysis of rock samples of Darb-e-Behesht area was on the agenda. Chemical analysis took place by XRF method in Kansaran Binalud laboratory in Tehran. Table 1 shows the results of the chemical analysis. The results of chemical analysis of rocks were processed by Minpet software which will be presented separately later.

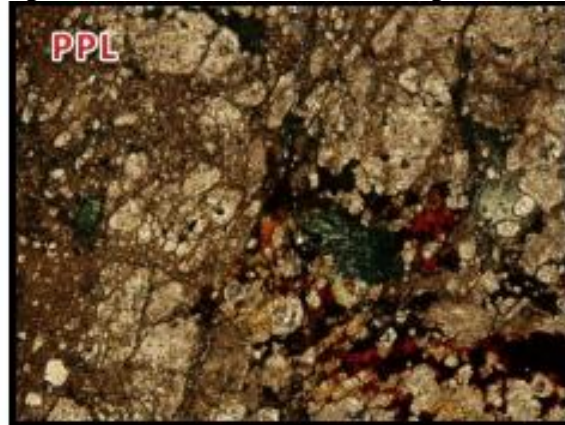


Fig. 7. Malachite (green) in altered volcanic rocks, Darb-e-Behesht area (Magnification x40).

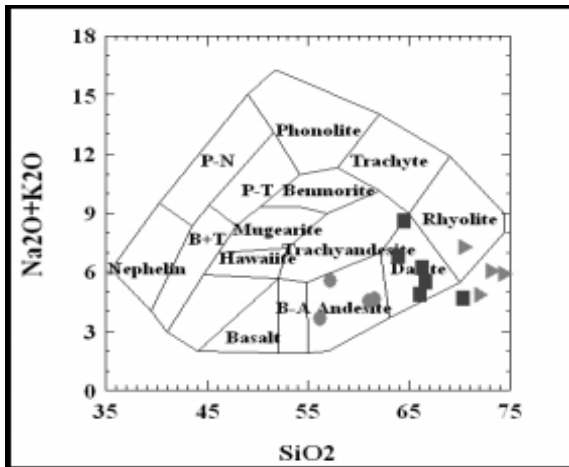


Fig. 8. Position of Darb-e-Behesht volcanic rocks in Cox et al. charts [2].

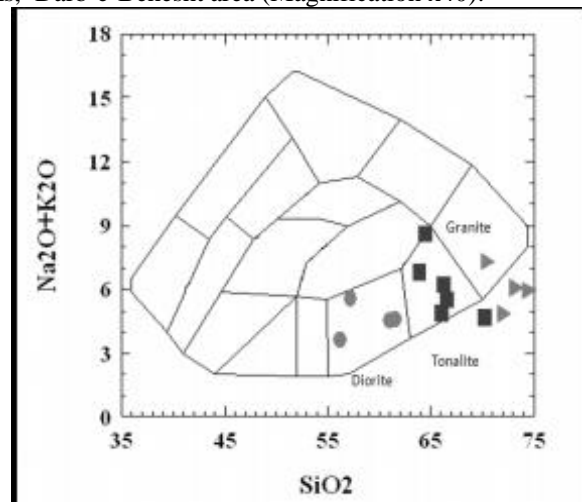


Fig. 9. Position of Darb-e-Behesht Plotunic rocks in Cox et al. charts [2].

Geochemistry Study

After chemical classification of rocks, a geochemical study was on the agenda to determine their magmatic series. According to the plotted graphs it was found that decomposed rocks are in the magmatic sub-alkaline series (Fig. 10); also, geochemical studies demonstrated that the majority of the analyzed samples are within the calc-alkaline series (Fig. 11).

DETERMINING THE GENESIS

In order to determine the geology environment of Darb-e-Behesht magmatic rocks' genesis, the results of chemical analysis of rock samples were used. For this purpose, the results of these analyses were processed in Minpet environment and using Pierce rock samples of Darb-e-Behesht copper

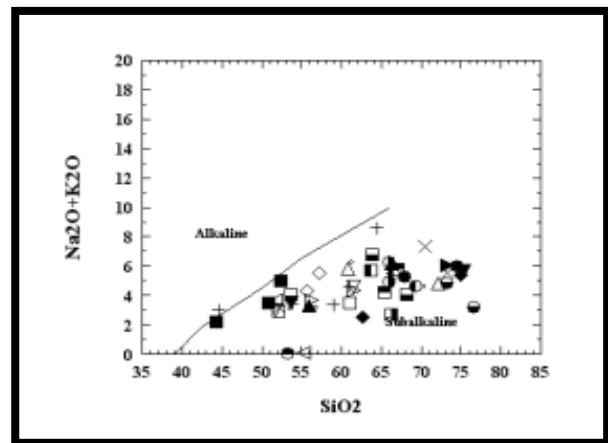


Fig. 10. Situation of Darb-e-Behesht rocks in Irvine and Baragar, chart [8].

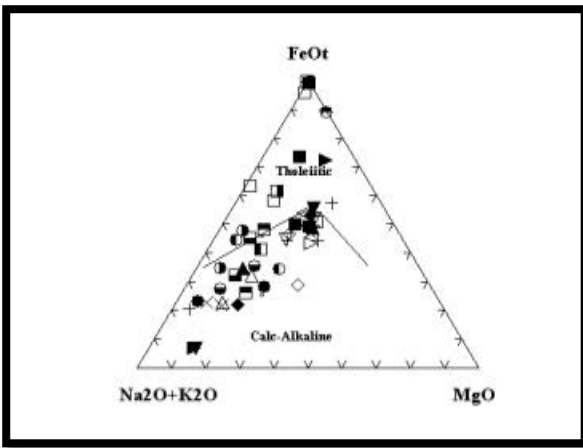


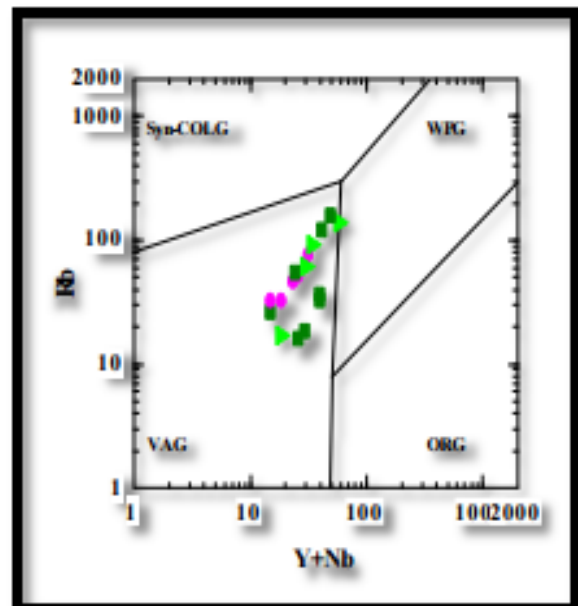
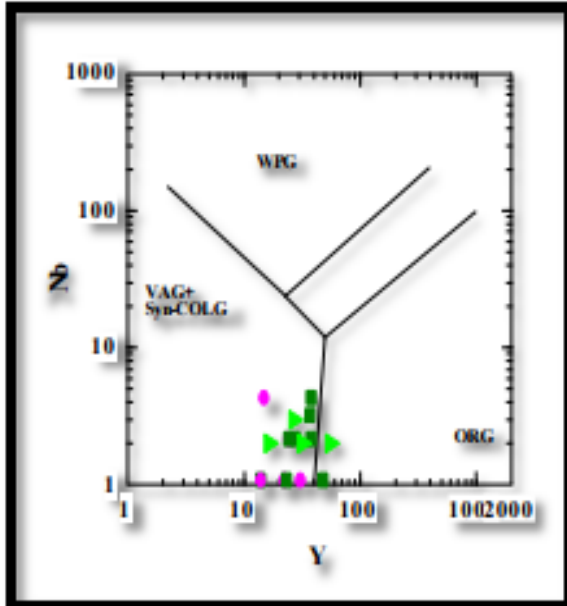
Fig. 11. Situation of Darb-e-Behesht rocks in AFM chart.

index are within Volcanic arc granitoids (Fig. 12 & 13). With such assumption, mineralization origin of copper can be considered the same as deposits related to magmatic arcs, that is Porphyry copper deposits.

DISCUSSION AND CONCLUSION

The results of this study can be summarized in the following cases:

- Copper deposit of Darb-e-Behesht is located in Dehaj-Sarduieh zone of Urmia-Dokhtar magmatic belt and thus it follows this region's lithology, mineralization and structural characteristics.
- In lithology terms, andesite, granodiorite and andesitic tuff are the most important occurrences of the region.
- Copper mineralization of this region is observed as chalcopyrite, malachite, azurite and sometimes covellite.
- The magmatic rocks of Darb-e-Behesht area are within calc-alkaline to sub-alkaline magmatic series.
- Granodiorites of Darb-e-Behesht area are within granodiorite groups related to magmatic arcs, that is layers' convergent boundaries. Thus, considering their magmatic series it can be assumed that copper mineralization in this area is related to copper porphyry deposits. Field evidences including alterations observed in this area, including the Sericitic and epidotic alterations confirm this matter. Epidotic alteration is considered a kind of propylitic alteration which occurs in copper porphyry deposits.



Figures 11 and 13 - Position of Darb-e-Behesht rocks in Pierce et al. [9] charts (VGA: Volcanic Arc granitoids).

Table 1- The results of chemical analysis of Darb-e-Behesht rock samples.

Sample	Cl	Ba	Sr	Cu	Zn	Pb	Ni	Cr	V	Ce	La	W	Zr	Y	Rb	Co	As	U	Th	Mo	Ga	Nb	
	ppm	ppm	ppm	ppm	ppm	ppm	ppm	ppm	ppm	ppm	ppm	ppm	ppm	ppm	ppm	ppm	ppm	ppm	ppm	ppm	ppm	ppm	
T1S1	120	87	198	29	149	31	37	3	153	12	5	3	119	35	76	2	25	1	1	1	1	17	1
T1S2	272	146	361	53	89	13	33	1	213	7	4	2	103	23	35	2	64	1	1	1	1	15	1
T1S3	196	37	163	33	49	9	31	2	122	48	32	2	88	15	16	1	133	1	1	2	13	1	
T1S4	362	173	865	110	123	16	39	1	132	20	7	1	160	27	51	4	79	1	1	1	1	13	1
T1S5	129	128	209	48	42	21	37	2	52	21	8	1	180	58	139	4	55	2	5	2	16	2	
T1S7	219	77	294	6400	69	12	41	10	85	12	5	1	194	41	112	8	46	1	2	3	15	4	
T1S10	113	129	283	8	58	19	34	4	63	32	11	4	297	64	111	3	67	1	1	1	1	15	1
T1S11	233	182	271	20	65	17	51	22	83	7	3	1	148	32	94	2	138	1	2	2	12	3	
T1S12	216	97	419	116	47	24	37	33	127	29	12	1	139	19	26	1	126	1	1	1	1	14	1
T1S13	120	125	444	15	42	22	38	15	123	44	18	4	179	27	25	5	2	1	2	3	14	2	
T1S14	136	103	391	28	43	15	38	2	126	25	11	2	159	27	24	2	30	1	1	2	16	1	
T1S15	283	140	419	28	39	24	46	29	141	12	5	1	156	27	62	2	134	1	1	2	16	1	
T2S2	183	41	381	30	50	35	37	4	83	19	12	5	136	18	18	1	31	1	1	1	1	13	3
T2S5	159	118	288	52	43	19	43	20	102	28	5	2	135	20	28	1	194	1	1	1	1	13	1
T3S4	125	153	184	32	34	14	34	2	42	32	21	3	115	39	105	1	67	1	2	1	18	1	
T3S6	67	146	362	161	76	13	40	1	172	12	3	1	128	33	70	2	37	1	1	1	1	16	1
T3S8	113	113	444	12	48	10	35	1	120	29	15	1	146	24	41	4	87	1	1	1	1	13	1
T3S9	135	143	367	74	77	9	39	2	140	8	6	2	137	26	48	1	1	2	1	1	1	16	2
T3S10	97	55	570	23	41	27	37	1	31	5	3	1	293	30	17	3	2	1	1	2	17	2	
T3S12	135	66	4	164900	86	34	18	1	57	11	5	1	9	2	15	2	58	1	7	48	2	1	
T3S13	106	132	361	102	62	12	38	2	137	21	10	4	139	24	43	5	118	1	1	2	16	1	

Sample	Cl	Ba	Sr	Cu	Zn	Pb	Ni	Cr	V	Ce	La	W	Zr	Y	Rb	Co	As	U	Th	Mo	Ga	Nb
	ppm	ppm	ppm	ppm	ppm	ppm	ppm	ppm	ppm	ppm	ppm	ppm	ppm	ppm	ppm	ppm	ppm	ppm	ppm	ppm	ppm	ppm
T4S10	166	183	355	14	29	17	40	31	124	20	11	2	152	25	50	4	27	1	1	3	15	1
T4S13	141	10	29	21500	77	64	33	7	35	4	2	3	11	1	15	3	531	1	2	2	7	1
T4S14	128	3	2	5	32	35	34	9	104	5	3	1	4	2	16	4	200	1	2	1	6	1
T4S15	264	99	405	79	40	24	31	11	70	35	12	3	126	41	30	3	152	1	1	2	16	2
T4S23	828	205	404	25	32	10	48	34	149	9	4	1	150	52	147	3	2	2	1	2	16	1
T4S24	157	52	277	24	32	30	34	5	40	15	5	2	127	15	24	4	1	1	2	1	13	1
T4S26	381	186	646	281	74	18	42	3	79	18	11	1	233	41	75	1	173	1	1	2	18	3
T4S27	347	151	508	167	55	22	37	9	56	36	14	4	191	38	90	1	12	1	1	3	15	1
T5S1	74	136	317	60	99	14	83	54	135	26	10	5	162	35	72	2	2	2	2	2	15	1
T5S2	75	124	329	72	99	24	63	47	217	23	8	1	117	27	47	2	21	1	1	4	16	1
T5S3	98	105	542	97	78	7	36	7	170	3	2	2	102	15	22	3	69	1	1	2	16	1
T5S4	87	146	328	70	99	22	84	78	136	44	15	1	159	37	69	3	2	1	1	4	16	2
T5S7	115	58	514	27	71	2	52	28	111	7	4	1	126	16	30	4	126	1	1	2	16	4
T5S8	68	22	247	107	80	12	28	4	146	40	15	2	100	15	30	4	42	1	1	1	10	1
T5S9	85	155	398	64	107	25	77	65	129	57	21	2	156	33	63	4	19	1	1	1	14	1
T5S10	94	172	311	56	107	21	85	106	148	48	11	1	180	36	66	2	4	1	1	2	15	1
T5S11	98	141	450	62	85	19	57	48	120	9	5	1	157	29	58	1	1	1	1	2	15	2
T5S13	72	155	305	89	99	21	81	98	134	70	18	2	184	38	71	1	77	1	1	3	13	3
T6S1	113	163	387	46	80	16	77	55	106	7	3	1	163	30	61	1	1	1	1	1	15	1
T6S2	108	174	313	48	100	29	102	90	134	46	11	2	184	38	62	1	1	2	2	3	15	2
T6S3	103	179	306	52	80	25	103	98	125	10	5	1	189	38	75	2	17	1	1	5	14	2
T6S4	84	173	288	48	91	24	106	106	124	62	7	3	171	37	80	3	24	1	1	2	15	3

REFERENCES

1. A. Aftabi, H. Atapour, *Res. Bull. Isfahan University*, **9**, 127 (1997) (in Persian).
2. K.G. Cox, J.D. Bell, R.J. Pankhorst, The interpretation of igneous rocks, Allen& Unwin, 1979, p. 450.
3. M. Darvishzadeh, *Geology of Iran*, Danesh e Emrooz publications, 1992, pp. 25-38.
4. Geological Map of Bam (1:250,000), Geological Society of Iran, 1998, pp. 35-41.
5. M Ghorbani,. "Economic geology of natural and mineral resurces of Iran", Pars (Arian Zamin Geology Research), 2007, p.492.
6. J.M. Guilbert, C.F. Park, *The Geology of Ore Deposits*, Freeman and Company, 2007, pp. 12-22.
7. A. Hezarkhani, *Int. Geol. Review*, **50**, 1 (1999).
8. T.N. Irvin, W.R.A. Baragar, *Canad. J. Earth Sci.*, **8**, 523 (1971).
9. J.A. Pearce, N.B.W. Harris, A.G. Tindle, *J. Petrology*, **25**, 956 (1984).
10. F.J. Sawkins, *Metal Deposits in Related to Plate Tectonic*, 2nd edition, Springer, 1990.
11. J. Shahabpour, *Aspects of alteration and mineralization at the Sarcheshmeh copper-molybdenum deposit*, Kerman, Iran. Ph.D. Thesis, University of Leeds, England, 1982.
12. G.C. Waterman, R.L. Hamilton, *Econ. Geol.*, **70**, 568 (1975).

Investigation of drilling fluid loss and its affecting parameters in one of the Iranian gas fields

M. Nasiri, I. Jafari*

Faculty of Chemical, Petroleum and Gas Engineering, Semnān University, Semnan, Iran

Received June 15, 2015; Revised October 13, 2015

Received June 26, 2016; Revised September 10, 2016

Drilling fluid loss is one of the most important subjects in drilling industry causes the time waste and costs increase. As a result of formation and drilling fluid pressure difference, fracture, formation properties and other factors this loss is occurred. Different ways, such as mud weight loss, reducing the flow rate into formation, using the controller loss materials and cement plug are used to avoid this problem. In order to access gas resources of Dahram group. During drilling in the Asmari and Jahrum formation in section 24" in field "A" we encounter the connected numerous sections and fractures. Drilling mud loss is developed due to low fluid pressure of fluids within the pores in comparison with drilling fluid. The mud loss occurs due to several reasons, some of them are geological and the others are drilling factors. For this reason, the study tries to investigate the loss reasons, determination of the areas and given solutions using the daily drilling reports, mud, geology and mud logging report to solve the problem. Drilling optimal parameters and drilling fluid application program for cleaning section 24 are suggested through our aim of loss control.

Keywords: Formation, Drilling fluid, Drilling optimal parameters, Fracture, Fluid Loss.

INTRODUCTION

Drilling fluid loss problem has been evident since the first time of being to drill oil and gas wells. This issue becomes serious when drilling deeper or drained wells were placed on the agenda. Oil companies spent millions of dollars to solve the problems such as stuck pipe, lost rig time, Blowout, the loss of large volumes of drilling fluid and the formation damage caused by loss. Stuck drill string during loss, because of the pressure difference between mud and formation the pipes stuck the in the well. Fishing operation should be done costly to solve this problem. Damage to the layers in many cases, after the well tests indicates that as a result of partial or total loss mud, especially in fractured reservoir, intensity damage to high-permeability production formations. Mud loss can transfer the fine particles into the pores and reduce the permeability of the formation near the well. In addition, the filtration may cause a chemical reaction between the mud and the reservoir fluid compositions through sediment reduce the permeability of the reservoir around the well. To eliminate this problem formation acidizing and stimulation operations have to be performed costly [1,2].

Waste drilling fluid or cement grout in void spaces during drilling operations is called loss. in the industry loss is classified as leakage (less than bbl / hr 10), mild (bbl / hr 10-100), intense (bbl / hr 100-500) and complete (more than bbl / hr 500) [3]. It

should be noted that the mud volume reduction from the total volume because of the extraction diminish and filling the new well, is quite different from the loss [4]. Loss is different in type, severity and location of the well. Knowing the type and location loss help to choice the control materials of loss. Loss location is determined by using information from previous drilling, formation changes and different techniques of mud logging report [5]. A systematic approach is known to control loss economically and effectively. This includes both the prevention and treatment [6].

Many parameters may affect the intensity of drilling fluid loss. The fracture pressure gradient of formation, drilling fluid properties, petrology and the type of drilling formation, the existence of fractures and caves in formation, drilling parameters such as pressure and flow rate of the pump and the known and unknown parameters made the anticipation of the amount of fluid loss during drilling of wells in a particular formation, problematic [1,7].

In all of the drilling wells in field "A", loss occurred and caused the waste time so that after the waste time for waiting and remaining the most wasted time dues to loss. And the waste time for the improvement and further drilling some time is more than the section time. During Asmari and Jahrom drilling in section 24" of the field "A" in order to achieve gas resources of Dehram group, we see multiple fractures and joined cavities.

In comparison with the drilling fluid, as a result of low fluid pressure of vein inside the sections, drilling mud loss occurred in this formation. As a section the mud loss occurs due to several reasons,

To whom all correspondence should be sent:
E-mail: jafari3760@gmail.com

some of them are geological and the others are drilling causes. so this study investigates the drilling causes and determination drilling areas and the ways to solve this problem in section 24 at field "A".

DESCRIPTION OF ISSUE

Field "A" placed in the northern part of the Persian Gulf. This field is the largest known gas field with estimated reserves of 14 trillion cubic meters (8% of the world's proven reserves of natural gas) and 17 billion barrels of natural gas liquids and 5 billion barrels of condensate, which is followed by the line in Qatar, called North Field. Development of field "A" is divided into several areas of development or planed phases. A total of 24 phases, between 1990 and 1992 a total of 4 exploratory and descriptive wells were drilled in the main phase. This field is geology placed on the bulging bow which is always higher than the surrounding areas. Therefore sediments residual speed on it is less than the surrounding areas, so the sediment thickness of various layers of the geological periods on the scale with the surrounding is less.

The hydrocarbon field was formed in the Permian and Triassic period and includes Dalan and Kangan formation. The highest point of the reservoir is approximately at a depth of 3,800 meters above sea level. Reservoir thickness is approximately 400 meters.

The Fars group formation such as Asemari and Jahrom exist in this section. Jahrom sediment cycle, after upper Cretaceous series movements in the early Tertiary, the Zagros was covered with a progressive Sea. Sachun formation in coastal areas, carbonate formation in shallow areas and Pabdeh shale formation in deep areas were deposited. Asmari cycle in late Eocene-oligocene, northeast of Lorestan and internal platform of Fars remained out of the water but Fars and Khuzestan, deep sedimentary Pabdeh formation continued. At the end of the Oligocene as a result of slow and limited progress of the sea, the small Asmari cycle, Chattian age, was formed.

In oligocene-miocene boundary, in the areas of Ahwaz, sandstone was deposited as Ahwaz sandstone from Asmari formation. The lower limit of Jahrom formation in sample section is harmonically placed on silt and dolomite of Sachun formation. Jahrom formation is placed above the Ilam formation in the field "A". Existence of Glauconite at the end of Jahrom formation shows this boundary. According to the study [8] the formation's age in two sections around Shiraz related to Paleocene to Middle Eocene. Upper boundary of Jahrom formation with Asmari formation is erosive discontinuity so that in the cutting sample of the boundary there are limestone and conglomerate with irregular layered

iron compounds. But in the field, Asmari and Jahrom are considered together but empirically the border is placed at the change location of limestone to dolomite and dolomitic [9].

METHODOLOGY

Development of field "A" is divided into several areas of development areas or planned phase that drilling wells in phases 13, 22 and 24 were studied. In phase 13 there were 4 places and in total 48 wells were drilled, in phase 22 there was and 11 drilling wells and in phase 24 there were 2 places and 20 wells were drilled. In this study, the daily reports of daily drilling, geological and mud logging of wells in the section 24", following the analysis of the loss reasons, determination of the loss areas and provide solution to prevent it. We aim to control loss, give the optimal drilling parameters and the best drilling program for section 24" to increase the speed for drilling, give the best applied program of drilling fluid and reduce costs.

Drilling in the section 24"

After placing the casing 32" at the depth of 172 meters, the section 24" was drilled by insert bit size 24. Drilling the section was done by sea water and pumping cells with high viscosity to clean the section. Drilling in the Fars group is slow due to the pre predominant lithology of the marl and marl sticky. But drilling in Asmari formation has higher speed because of the lithology of calcic - dolomite and at Jahrom formation drilling is slow and done with a special program, due to falling Dolomites and the possibility of mud loss, the stuck pipe and the closed well wall. These programs are used to control the weight on bit, maximize the mud pump with Hi-Vis pumping and lubricants with pumping loss controller materials. After arrival in Ilam Formation drilling was continued for about 30 meters and casing shoe of 5/8 18" was placed in this formation and cementing operations were done based on plan.

Loss in the section 24"

At first using the daily drilling reports, mud drilling and geological drilling wells, all drilling parameters and mud properties were extracted and through the mud logging reports, affecting parameters on the loss size were noted and they have been set as table. The diagram related to the amount of loss and the influencing loss factors to the depth was plotted and the results were adapted with the lithological data. Accordingly the Asmari-Jahrom formation is created by two mainly parameters: lithology and drilling parameters.

Effect of the drilling parameters on the fluid loss

In this section, through study the daily drilling reports and logging of well drilling parameters such

as WOB, ROP, RPM, Flow in and mud weight was extracted and shown in Figure 1 and 2. These parameters versus depth were plotted by Excel in cross plots and the results were compared and discussed. Many drilling factors can increase or decrease the loss of drilling such as WOB, ROP, RPM, Flow in. if the effect of these factors on loss is known, it is easy to control and prevent the occurrence of severe loss. Based on diagram some of these parameters have direct relation with the mud loss and some of them are inverse. For example, if these parameters in A and B wells are compared with the diagram, in both well there will be four loss zones, each of these zones show different factors, including lithological and diagenetic factors and drilling parameters. This means that in some of these zones, lithological factors are determining factors and the others intensify the loss degree or vice versa. these four zones are

Zone A'A

This zone started from a depth of about 780 meters and continued to 620 meters, in this zone the amount of loss is insignificant due to not very porous lithology, and the drilling parameters determine the loss degree. In this area lithology related to the dolomitic limestone with anhydrite cement that layers of anhydrite and limestone, argillite can be found among them. As shown in the diagram, the loss degree is below of 50 barrels and drilling parameters such as WOB have an important effect on this section. So the parameter of bit weight must be controlled in this zone because if it is higher than conventional degree, the formation will be broken and cause the complete loss.

Zone B'B

This zone started at the depth of 780 meters and continued to a depth of about 900 meters, the diagrams show that the maximum loss occurred in this depth, and the zones are known as loss zone. Based on the obtained samples in this section and analysis of their lithology we realized that this zone includes some algae and coral reefs that are highly porous. If drilling parameters especially the speed and weight on the bit is not controlled and set out the plan in this depth, enormous costs may be included in addition to many hours of rig time is wasted. Using Draw plots in this zone, it is indicated that the drilling parameters are controlled For example, the drilling rate, weight on bit, and rotation of the drill pipe one minute decreased and flow in increased due to the more mud pumps for cleaning wells. This factor could slightly increase the loss degree.

Zone C'C

This zone started from a depth of about 900 meters and continued to a depth of 1060 meters. In this zone the loss degree is less than 250 barrels. In this zone the loss degree is variable and is a function of lithology and drilling parameters. In areas where the loss degree is high the section porosity figures, fissure porosity and inter granular porosity due to the conversion of calcite to dolomite can be seen. However, in this zone increase the weight on the bit and drill speed make the high loss degree.

Zone D'D

This zone started at a depth of about 1060 meters and continued to a depth of 1150 meters. In this zone sometimes the loss degree reached 400 barrels per hour. As a result of increased amount of anhydrite cement, like the previous zone is not porous, but sugar grained porous dolomite figures help to increase porosity. In this zone More drilling parameters have a significant role to intensify the loss.

Proposed drilling fluid plan and well cleaning in the section 24"

According to the definition 4 the loss area in Asmari and Jahrom and the daily drilling reports of the major oil companies in the other field "A" phases to drill this section, drilling fluid and cleaning plan as well as follows.

Sea water and well cleaning through cells with high viscosity

The seawater is used as the main and cleaning fluid through the cells with high viscosity concerning the areas and the lithology according to the following plan. Since the diameter of the section was large, rubble evacuation and dug wells with high speed combined mechanism and scanning with high viscosity were occurred. Viscous scanning composed of xanthan gum and a pre-hydrated gel .analyze offset well indicates that the main problem of loss is on the bottom of the section so the hydrostatic pressure drop occurred within the well. This hydrostatic pressure drop leads to break the mouth of the well, poor well cleaning, stuck pipe and the close well wall. in order to minimize these problems ,the well should be cleaned at the depth of 780 to 172 meters in which the formation of the Fars and A'A Asmari and Jahrom zone existed. In drilling of 9 meters scan of cell 30 barrel with high viscosity should be pumped to clean wells. At every 14 meters of drilling scanning of pre-hydrated gel should be pumped to clean the walls of the well. At the end

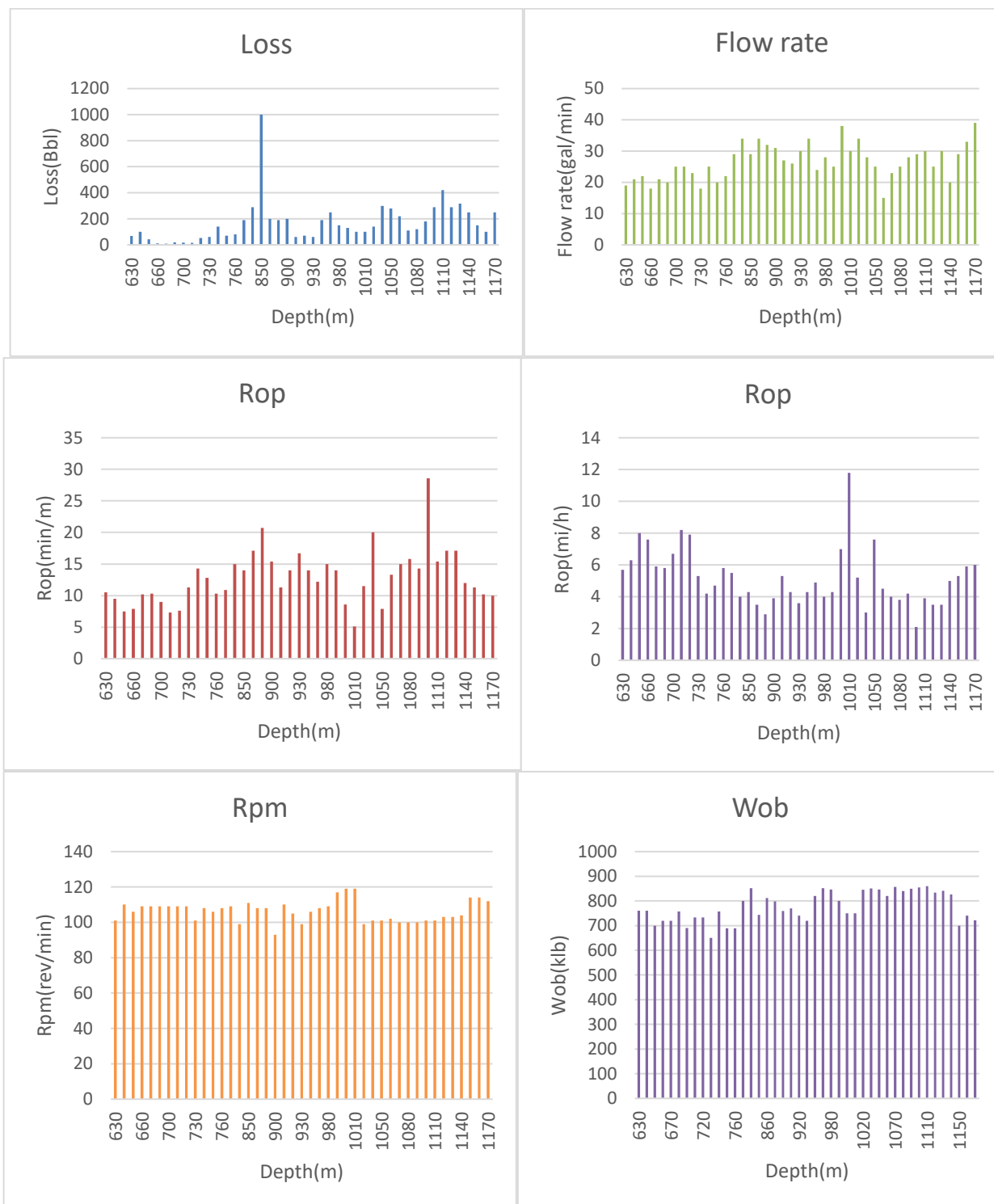


Fig. 1. The effect of different parameters of the depth on drilling in wells A.

stand of the drill pipe with high viscosity was pumped in 30 barrels and the mud was circulated for 5 minutes. Then 40 barrels of pre-hydrated gel were pumped and mud was recirculated for 15 minutes. The drilled distance back reamed and reamed down at the flow rate of 700 gallons per minute with the drill pipe rotation rate of 30 rpm and at the bottom of the well, 30 barrels of pre-hydrated gel were pumped and when it exited from bit the flow rate stopped

and the new stands were prepared and drilling continued. At a depth of 780 meters the well cleaning way should be changed. Based on the depth of about 780 meters to a depth of about 900 meters of B'B zone and according to the results, this zone is made of some algae and coral reefs that are highly porous that is the main reason of the loss. But based on the current situation there are two methods to control or minimize the loss. The controlled drilling

Parameters are used according to the cleaning following plan. Otherwise if the full loss is occurred the cement plug will be placed and then the cement and the formation is drilling. it leads to control the

loss. C'C zone started from a depth of about 900 meters and continued to a depth of 1060 meters. In this zone the loss degree is variable and as a function of geology and drilling parameters. The loss was

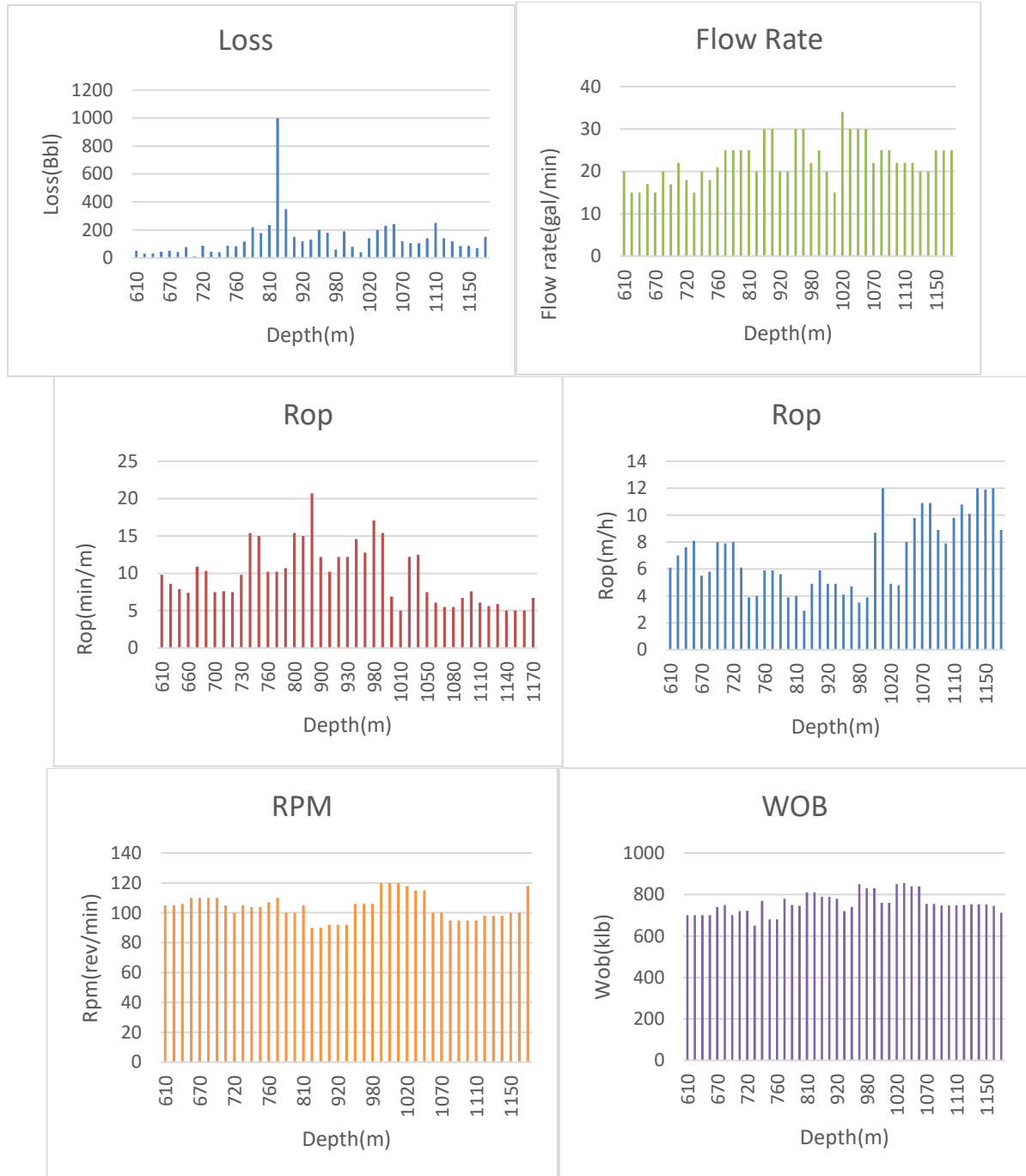


Fig. 2. The effect of different parameters of the depth on drilling in wells B.

prevented by controlling the drilling speed. D'D zone started from a depth of about 1060 meters and continued to a depth of 1150 meters. This zone like the previous zone was not porous due to the increased amount of anhydrite cement, but sugar grained dolomite figures increased porosity. In this zone, the drilling parameters intensify the loss degree. it can be reduced by controlling the drilling speed. From a depth of 780 to 1150 meters the

cleaning program was at every 5 meters of drilling wells in which scanning of cell of 30 barrels with high viscosity was pumped to clean wells. In each 9 meters of drilling of the hydrated gel scanning was pumped to clean the walls of the well. At the end the stand drilling pipe of 40 barrels with high viscosity was pumped. Then the mud circulated for 10 minutes and then 50 barrel of pre-hydrated gel were pumped. The mud re-circulated for 20 minutes

to of the flowers have become. The drilled distance back reamed and reamed down at the flow rate of 800 gallons per minute with the drill pipe rotation rate of 30 rpm and at the bottom of the well, 30 barrels of pre-hydrated gel were pumped and when it exited from bit the flow rate stopped and the new stands were prepared and drilling continued. The maximum level of 2000 ppm hydrogen sulfide has been recorded in offset wells. To protect the drill

pipes, CONQOR 202B should be used as a protective element, which used as a Slough spray while raising the pipes. The Table 1 shows the optimal properties of section mud.

Yield point, of a pre-hydrated gel should be kept between 25-18 to prevent the close of the wells that can be caused by the additional accumulation of particles around the BH.

Table 1: Properties of section mud.

pH	Funnel viscosity (sec/qt)	Mud Wt. (ppg)	Depth TVD (m)	Mud System
7	26	6.8	1150	Sea water
5.10-10	<120	6.8	1150	PHG Sweeps
6-8	<100	6.8	1150	Polymer Sweeps(Hi-Vis)

The use of bentonite based mud

This mud is an appropriate chance to prevent the rise of hydrogen sulfide is a good option But due to the fact that excessive weight gain goal, regardless of lithology feature will be off Due to the large volume of drilling sections in the mud weight increased the loss. Because of the costly drilling fluid and the complete loss at second zone is generally this way is not used.

RESULTS

According to the above statement, section 24 started at the depth of 172 meters after cement drilling of section 32 starts and continued to 1150 meters which is the Fars formation. This formation was made of limestone, marl and clay limestone. The loss did not occur in this formation and its drilling rate was proper and the drilling can be occurred with no problem at the rate of 25 -15 m. But it should be noted that because of clay limestone and the use of the seawater as a drilling fluid, the formation was swollen, that makes the closed walls. So no time should be given to wells and drilling was done as soon as possible to prevent the walls tight hole. Usually at a depth of 620 meters we entered into Asmari and Jahrom formations which most problems of drilling occurred in this part of field "A" gas. Most oil companies drill the Fars and Jahrom formation without using engine to avoid waste and saving the possible cost. Accordingly, four zones of loss were defined. Each of them was affected by one of the loss factors such as Lithological and digenetic and drilling parameters. Many factors increased or decreased the loss which can be defined as dependent or independent parameters. The weight on the bit, flow in and the pipe rotation in minute are the dependent parameters and the rate of drilling and the output pressure pump were defined as independent parameters. It should be noted that the

dependent parameters were the function of the weight on the drill and the flow. So zone A'A started at a depth of 620 meters and continued about 780 meters .In this zone, the loss degree was insignificant due to the lithology and more drilling parameters determined the loss degree. So the drilling rate was at 8-6 meters per hour and weight on bit should be corresponding to the drilling rate, flow in was 800 gallons per minute and drilling pipe rotation in a minute was determined based on BHA. If the engine was used in well the rotation would be rpm 40 and otherwise 110-90 rpm. B'B zone started at a depth of 780 meters and continued to 900 meters, the maximum loss degree was occurred in this depth so this zone is known as the loss zone. This zone includes some algae and coral reefs that are highly porous the drilling speed was 6.4 meters per hour. The corresponding weight on bit with the speed drilling should be controlled. If this action was done out of the determined depth, there would be the enormous costs. It should be noted that the rate of flow in about 800 gallons per minute was suitable. If the flow rate became low, the well cleaning was not done properly that could stick pipe. C'C zone started from a depth of about 900 meters and continued to a depth of 1060 meters. The loss degree was variable and as a function of geology and drilling parameters in this zone. In areas where the loss degree is high, the section porosity figures, fissure porosity and inter granular porosity due to the conversion of calcite to dolomite can be seen. However, in this zone the increase weight on the bit and the high drilling speed increased the loss degree. The drilling must be controlled at the drilling rate of 7-5 meters per hour and the weight on the bit was corresponding with the drilling speed and flow in of 850 gallons per minute that would be the ideal. Zone D'D started at a depth of about 1060 meters and continued to 1150 meters. Sugar grained Dolomite figures increase the porosity. The drilling parameters in the

zone intensified the loss degree. The most loss was occurred due to lithology type.

Two proposed programs are given for the main drilling fluid and cleaning wells. The justifiable use of sea water as the main fluid and cleaning programs are offered which is the best choice to reduce the cost and increase the drilling speed.

CONCLUSION

According to the division of the loss areas and its selection and optimization of drilling parameters in each section and the application of the proposed mud plan and cleaning wells can be expressed as the following results:

1. Comparison the affected drilling parameters at wells A and B with the related diagram of the loss degree in section "24, show that there are four zones, each zone indicates the factors such as lithological and diagenetic factors and drilling parameters. This means that in some of these zones, lithological factor and other factors are determining factors and the others intensified the loss degree or vice versa.

2. Many factors can increase or decrease the loss that the most important include the weight on bit, drilling speed, drill pipe rotation in one minute, flow in and the mud weight. Through study the effect of these factors on the loss can be easily to control the loss due to the influence of various parameters or even prevent the occurrence of acute loss.

3. Drilling parameters can reduce or increase the loss which is defined as the dependent and independent parameter. The drill pipe rotation in one minute as independent parameters and the rate of drilling and output pump pressure are defined as the independent parameters. Note that the dependent parameters are the function of the weight of the drill and the flow in.

4. The optimal method to fluid loss control is the application of controlled drilling parameters of weight on bit, flow in and drilling speed.

5. The loss control indicates the logical consequence with the pump pressure. So based on

the specific areas the increased and decreased flow in should be controlled. The cleaning wells should be considered to prevent the possible problems.

6. According to two proposed drilling fluid plan, using sea water as the main fluid and cleaning wells in different geological zones the best choice to manage the loss and drilling speed is proper.

7. Since increasing the mud weight is one of the reasons to occur the loss, the use of the Betonite based mud due to the higher weight than the sea water and increased weigh during drilling due to high volume of cuttings and its high cost, this type of fluid is not recommended.

8. The pre-hydrated gel with high viscosity is used to clean the well it is the best choice to clean wells.

9. There is an inverse relation between the loss degree and fracture pressure. If the pressure of the fracture is low the loss degree will be high.

REFERENCES

1. E. Davidson, "Control of Circulation in Fractured Limestone Reservoir," IAD/SPE, 2000, p. 9.
2. E. Fidan, Halliburton, T. Babadaghli. Use of Cement as Lost Circulation Material-Field Case Studies, paper SPE/IADS 88005 Presented at the IADC/SPE Asia Pacific Drilling Technology Conference and Exhibition held in Kuala Lumpur, Malaysia, 13-15 September 2004.
3. H. Bahmani, Principles of engineering and eruption and control operations and of oil and gas field of Tehran. Tehran University Science and Technology Park, 2013.
4. A. Bahadori, F. Khybari, *Exploration&Production Magazine*, **3**, Number 47, July 2010.
5. R.S. A. F. K. Cole, "A new environmentally safe cross linked polymer for fluid-loss control," *SPE* 29525, 1985.
6. A.N. Moazeni, M. Naba'i, *J. Eng.*, Islamic Azad University of Mashhad, No.3, September 2010.
7. G. Daccord, Cement-Formation Intraction, Houston: Schlumberger, 2006
8. M.J. Sadegholvad, A. Faghieh, *Geophysical Research Abstracts*, **9**, 120 (2007).
9. Y. Lasemi, *Sedimentary Geology*, **99**, 151 (1995)

Characteristics and correlation analysis between soil magnetic susceptibility and heavy metal content in soil along the North shore of Xinjiang Bosten Lake

Yonghui Wang*

College of geography and tourism, Xinjiang Normal University, Urumqi, PR China

Received February 18, 2016; Revised September 10, 2016

Coupling relationship between soil magnetism characteristic and soil heavy metal is one of the hottest topics of current environmental study. Bosten Lake is a major freshwater lake in arid region of Xinjiang, which plays a vital role in regulating this regional ecosystem. In order to explore the soil magnetic susceptibility, soil heavy metal characteristics as well as the correlation between them, in this paper, we selected 10 soil profiles along north shore of Bosten Lake for the determination of soil magnetic susceptibility, and heavy metal content. Through statistic analysis, we can see that: (1) Low frequency magnetic susceptibility of soil along north shore of Bosten Lake gradually increases with the depth of soil layer from 0 to 60cm, and gradually increases to the top value within the soil depth range of 40-60cm, while gradually decreases with the soil depth from 60 to 100cm; According to the variation of magnetic susceptibility content in different soil layers, we can see that within the soil layer with depth range from 0-20cm, 20-40cm, 60-80cm, 80-100cm, it exhibits the intermediate variation, while in the soil layer from 40-60cm, it shows the strong variation. Based on the average value of frequency-dependent magnetic susceptibility, we can see that there are less super paramagnetic particles within soil layer with depth of 20-40cm, while in other soil layer, the super paramagnetic particles contents are all over 10%. The analysis result of variation coefficient shows within 20-40cm soil layer, it exhibits medium variation, and in other soil layers, it exhibits strong variation. (2) The content order of heavy metal in soil along the north shore of Bosten Lake is $Mn > Cr > Zn > Cu > Ni > As > Pb > Hg$, and the vertical distribution rule is that the element Cr and Mn contents gradually increase with the deepening soil layer range from 0-80cm, while gradually decrease with the deepening soil layer range from 80-100cm; There is no obvious change occurring to the Cu content in all soil layer; contents of other elements in 20-40cm soil layer are all lower than that in 0-20cm soil layer. The variation rule of heavy metal content is that Cu, Ni, Pb, Zn, As, Cr show the medium variation, while the Mg and Hg show strong variation. (3) The relation characteristics between heavy metal content and magnetic susceptibility of soil along the north shore of Bosten Lake: the contents of Cu, Mn, Pb, Hg are positively correlated with the low frequency magnetic susceptibility, wherein the Cu element content is related with low frequency magnetic susceptibility in largest degree; Contents of Cr, Pb, Cu, Ni, Zn, Mn are positive correlated with frequency-dependent magnetic susceptibility, wherein the correlation between contents of Mn and Cu elements are mostly and frequency-dependent magnetic susceptibility is the biggest. By above analysis, we can provide scientific reference to regional environmental governance and protection.

Keywords: North shore of Bosten Lake, soil, Magnetic susceptibility, Heavy metal, Correlation.

INTRODUCTION

The soil magnetic susceptibility can reflect informations including soil weathering degree, climate, vegetation, and ecological environment. The diagnose of soil heavy metal pollution by soil magnetism characteristic has become one of most important approaches in soil environmental research [1]. As an important magnetic parameter of environmental magnetism research, the magnetic susceptibility can be put into consideration together with some geochemical elements for exploring the effect of environmental change on magnetic property as well as for analyzing the correlation between magnetic susceptibility and geochemical elements, which is one of the new development

tendencies in environmental magnetism study of recent years [2]. As a result, we can indirectly monitor the effect of human activities on environment through analyzing the magnetic characteristics soil particles [3]. Weiguo ZHANG et al who studied the magnetic property of sediments in tidal flat of the Changjiang estuary, believed that the magnetic parameter values of sediments are related with soil heavy metal contents [4]. Due to the magnetic mineral in pollutant source as well as the close relation between magnetic minerals and heavy metals, the magnetic measurement method can be quickly applied in the research of environmental pollution monitoring and environmental evaluation [5]. The magnetic measurement method can achieve an excellent application in monitoring heavy metal pollution in

To whom all correspondence should be sent:
E-mail: wyhsd_3011@163.com

soil and sediments[6]. As a major component of soil, the magnetic mineral particles exist in soil by large amounts [7]. The magnetic minerals can be divided as naturally formed minerals and man-made minerals [8]. Since secondary pollution will be formed after toxic metal elements entering into water, the monitoring and evaluation of heavy metal pollution in river sediment are of important practical significance [9]. The heavy metal pollution in lake water is mainly caused by industrial pollution, traffic pollution, agricultural pollution and living garbage pollution [10]. The iron particles in industrial waste water greatly affect the source of magnetic materials and material behavior, leading an increased magnetism of the soil, which is far beyond the local soil background value [11]. Large amounts of research results show that for the sediments, soil and street dust that are polluted by various heavy metals, their mass fraction is greatly positively related with their magnetic parameters [12]. Currently, researchers from home and abroad have conducted large amounts of studies on soil heavy metals, which reveals roles of regional climate, environmental conditions and magnetic parameters in effectively indicating the content of certain pollutant in soil, revealing the potential value of magnetic parameters in indicating pollutants[13-15]. Some researches mainly focus on the source and space distribution of pollutants [16], with China's urbanization process is accelerated unceasingly, human activities exert a more and more bigger influence on soil environmental quality [17]. Therefore, it is imperative for us to research and design an more advanced and effective monitoring technique of soil heavy metal pollution [18]. The magnetic susceptibility is closely related with the content of some heavy metals in soil [19], and the heavy metal pollution has been prescribed in China's "twelfth five-year" as a major environmental issue [20]. Large amounts of researches have shown that the magnetic susceptibility χ is positively correlated with contents of Pb, Zn, Cu, Mn [21], and the soil magnetic susceptibility values are obvious positively related with the heavy metal Cu, Zn, Pb [22]. Some researches indicate that in the heavy metal polluted soil, there is a strong correlation between heavy metal content and soil magnetic parameters [23], also other researches show that regarding the soil being polluted by modern industrial waste, its magnetic susceptibility will increase [24], all these researches play an vital role in evaluating the heavy metal pollution in various regions [25]. Based on above research results, in

this paper, we conducted determination on the soil magnetic susceptibility and heavy metal content in soil along north shore of Bosten Lake, and analyzed the relation between them for the purpose of knowing the magnetization characteristics of Bosten Lake environment and exploring the correlation between soil magnetic susceptibility and soil heavy metal content. The research result can play a scientific reference in regional environmental governance and protection.

MATERIALS AND METHODS

Overview of the researched area

As the biggest inland freshwater lake, Bosten Lake locates near southern Tianshan piedmont of Bohu County, Bayingolin Mongol Autonomous Prefecture in Xinjiang. Located in east longitude $86^{\circ}15'-87^{\circ}00'$, north latitude $41^{\circ}45'-42^{\circ}15'$, it is a mesozoic depression lake, and serves as the main water source for urban and rural people's living as well as the industry and agriculture in Bayingolin. Bosten Lake has vast water area, with length from east to west of 55 km, and width from south to north of 20km. In 2005, the total area of Bosten Lake was registered as 1360.5 square kilometers, which consists of big lakes, small lakes and reed marshes, wherein, the big lakes account for 1036km^2 with average water depth of 7.38m and total volume of $7.15 \times 10^9\text{m}^3$; The small lake group, composed by 16 small lakes, accounts for 44.5km^2 , with water depth of 2-4m, and volume of $1.2 \times 10^8\text{m}^3$; The total area for reed marshes is 280km^2 , which distributed along the southwest shore to the northwest shore. Bosten Lake area is blessed with sufficient sunshine and abundant heat, and the climate here is of dry air and less rain, the average precipitation for the past few years is 68.2mm, and annual evaporation capacity is 1800-2000mm. In recent years, with the industrial and agricultural development as well as the increasing human activities such as reclamation of lakes, land clearance, heavy grazing, more and more pollutants pouring into the lake, robbed development, irrational utilization of natural resource, the original function of Bosten lake wetland as severely damaged, resulting in destroyed lake ecosystem, extinction of rare species and threatened biodiversity. In addition, due to the higher content of heavy metal, the soil along the lake shores is polluted, negatively affecting the environment.

Collection of soil samples

The soil samples were collected along north shore of Bosten Lake, in February, 2014. By

randomly setting 10 sites as the sample collection site, each site can be divided into 5 soil layers with depths of 0—20cm, 20---40 cm, 40---60 cm, 60--80

cm, 80--100 cm, respectively, so there should be collecting 50 samples (see Figure 1.)



Fig. 1. Distribution of the soil sampling site.

Soil sample analysis method

The collected soil samples were firstly subjected to room dry, and then removed the impurities such as fallen leaves, plant roots, rocks and animal residues, followed by pulverized them into powders which will be selected by 100-mesh nylon mesh for the final samples for the test. The heavy metal Cr, Cu, Mn, Pb, Ni, Zn in the soil samples were put into the hydrochloric acid-nitric acid-hydrofluoric acid microwave digestion system, after being fully digested, removed the acids, and conducted ICP determination; With regard to the element As and Hg, also firstly being digested in hydrochloric acid-nitric acid-hydrofluoric acid microwave digestion system, then removed acids under reflux, and conducted AFS determination instead. The determination method of soil magnetic susceptibility: firstly natural drying the soil sample and then grinding it into powders. Then pick some quantity of powders into the 100cm³ magnetics special sample box, being compacted and sealed, we used Bartington MS2 magnetic susceptibility instrument to determine the low frequency magnetic susceptibility (X_{lf},470HZ) and the high frequency magnetic susceptibility(X_{hf},4700HZ) . According to the X_{lf} and X_{hf}, we calculated the X_{fd} of the sample.

RESULTS AND ANALYSIS

Analysis of magnetic susceptibility characteristics of soil along the north shore of Bosten Lake

The Table 1. reflects the statistical characteristic of low frequency magnetic susceptibility of soil along the north shore of Bosten Lake. The low

frequency magnetic susceptibility varies from soil layer to soil layer: magnetic susceptibility 1.45-2.43 in 0-20cm soil layer, 1.60-3.45 in 20-40cm soil layer, 2.57-12.56 in 40-60cm soil layer, 1.81-2.62 in 60-80cm soil layer, 1.76-3.05 in 80-100cm soil layer; According to the mean value analysis, we can see the low frequency magnetic susceptibility gradually increase within 0-60cm soil layer, and reaching the peak value within 40-60cm soil layer, while gradually decrease within 60-100cm soil layer; When the coefficient of variation (CV)<10%, it exhibits the weak variation, when Cv=10-100%, it exhibits the medium variation, while Cv>100%, it shows strong variation [1]. Based on this, the variation results of soil low frequency magnetic susceptibility in different soil layers along north Bosten Lake indicate: in soil layers with depth range of 0-20cm, 20-40cm, 60-80cm, 80-100cm, it exhibits medium variation, only in 40-60cm soil layer, it will show strong variation. The possible causes for above result may be diverse, on one hand, due to the water pollution in river basin, the soil properties are inevitably affected, resulting in such variation of low frequency magnetic susceptibility. On the other hand, the underground water level may also exert influence for such results, and the lower-middle part of soil profile is of higher water content, and the soil displays cinerous color. The anaerobic environment caused the reductive dissolution of magnetic minerals, which may be the major cause for the decrease of magnetism in soil profile under 60 cm, which is also similar to the research conclusion by Guo ZHANG et al. [8].

Table 1. Characteristics of low-frequency magnetic susceptibility.

$X_{fd}/10^{-8}m^3kg^{-1}$	Average	Max	Min	Median	SD	CV
0-20cm	1.45	2.43	0.76	0.95	0.56	0.39
20-40cm	1.60	3.45	0.64	1.47	0.94	0.59
40-60cm	2.57	12.56	0.55	1.76	3.56	1.38
60-80cm	1.81	2.62	0.51	1.90	0.71	0.39
80-100cm	1.76	3.05	0.46	1.41	0.78	0.44

Table 2 reflects the variation of frequency-dependent magnetic susceptibility in different soil layer. The frequency-dependent magnetic susceptibility is used to determine the content of super paramagnetic particles in soil, and normally when the X_{fd} value is about 5%, it means the content of super paramagnetic particles is high; when the $X_{fd}>10\%$, the content super paramagnetic particles is considerably high [8]. According to the average value of frequency-dependent magnetic susceptibility in soil along the north shore of Bosten Lake, we conclude that there is less super paramagnetic particles in soil layer with depth range from 20-40cm, and in

other soil layer, the content of super paramagnetic particles is over 10%, which is a considerable content. The analysis result of variable coefficient shows that in 20-40cm soil layer, it exhibits medium variation, while in other soil layers, it shows strong variation. The major cause for above results is that the soil in Xinjiang is generally weakly magnetic, the soil-forming process is weak, and the frequency-dependent magnetic susceptibility is normally low. In addition, less human disturbance occurs in north shore of Bosten Lake, which also leads to the low frequency-dependent magnetic susceptibility in soil.

Table 2. Characteristics of frequency magnetic susceptibility.

$X_{fd}/10^{-8}m^3kg^{-1}$	Max	Min	Average	Median	SD	CV
0-20cm	0.91	0.07	0.29	0.21	0.32	1.10
20-40cm	0.05	0.01	0.02	0.02	0.01	0.50
40-60cm	0.99	0.03	0.26	0.05	0.37	1.42
60-80cm	0.99	0.01	0.23	0.02	0.38	1.65
80-100cm	0.97	0.01	0.25	0.07	0.37	1.48

Statistical characteristics of soil environment background value of Bosten Lake Wetland

Table 3. shows the statistical content of soil environment background value of Bosten Lake wetland area, and the statistical results show: the order of heavy metal content is : Mn>Cr>Zn>Cu>Ni>As>Pb>Hg, Mn top the rank, and the content of Hg element is the lowest. the vertical distribution rule of these 8 elements is: In the depth of 0-80cm, the content of Cr and Mn increase with the deepening of soil layer, while in depth 80-100cm, their content become less; There is no obvious change to Cu content, which stays within the range of 21.83-24.69mg/kg; With regard to other elements, their contents in soil depth of 20-40cm are lower than that in soil depth of 0-20cm. According to the classification of variable coefficients, when $Cv<10\%$, it means lower variation, $Cv=10-100\%$ represents the medium variation, while when $Cv>100\%$, it means strong variation. As for the heavy metal soil pollution in

the Northern shore of Bosten Lake, the variation rule is: Cu, Ni, Pb, Zn, As, Cr is in the range of medium variation, while Mg and Hg show the strong variation. The above characteristics and mechanism of soil heavy metal pollution in north shore of Bosten Lake are caused by complex factors including internal factors and external factors. The internal factor is the mainly the landform of Yanqi basin, while the external factors are the three major pollution source including farmland drainage, industrial wastewater and domestic wastewater, Among which, the farmland drainage is the major cause for salt pollution of Bosten Lake, and the other two are the main cause for the eutrophication of Bosten Lake. The objective reason is the insufficient coming water from the upstream Kaidu River, and the subjective reason is due to the extensive production mode and unreasonable production structure, resulting in a unoptimistic environmental governance situation.

Table 3. Environmental background concentrations in the soils.

Indicators	Depth	No.	Average	Max	Min	Medin	SD	Cv
Cr	0-20	10	49.81	87.88	30.58	51.33	1.52	3.05
	20-40	10	50.18	66.56	21.43	48.33	1.85	3.68
	40-60	10	56.45	75.76	41.38	60.24	3.79	6.71
	60-80	10	60.61	95.89	27.8	58.83	2.08	3.43
	80-100	10	56.11	65.74	44.66	60.49	4.38	7.8
Cu	0-20	10	21.94	55.76	16.06	29.5	7.56	34.45
	20-40	10	22.83	43.53	13.15	20.06	2.77	12.1
	40-60	10	21.83	29.28	13.5	21.02	0.81	3.7
	60-80	10	23.2	31.13	14.48	26.75	3.55	15.3
	80-100	10	24.69	36.28	14.87	23.24	1.45	5.9
Mn	0-20	10	410.25	719.38	262.25	424.75	14.5	735.3
	20-40	10	472.01	662.63	281.25	432.88	39.13	82.9
	40-60	10	484.25	642.63	407.25	497.15	12.93	26.7
	60-80	10	1121.2	673.93	253	535.94	585.26	56.19
	80-100	10	468.9	550.88	255.25	5406.69	37.79	77.61
Ni	0-20	10	19.52	23.26	10.93	19.58	0.06	3.07
	20-40	10	18.08	26.68	10.06	20.45	2.37	13.1
	40-60	10	21.79	29.81	12.75	25.14	3.35	10.78
	60-80	10	23.2	36.39	18.6	24.52	1.32	5.69
	80-100	10	22.02	27.93	17.53	23.98	3.78	17.17
Pb	0-20	10	9.18	17.96	-2.96	8.7	6.633	72.19
	20-40	10	4.64	19.125	-2.96	0.78	6.56	141.14
	40-60	10	8.76	25.325	0.05	7.85	7.16	81.74
	60-80	10	11.96	30.93	1.025	9.4	8.08	67.5
	80-100	10	9.825	19.68	3.1875	5.71	4.46	45.74
Zn	0-20	10	52.6	85.62	26.96	45.78	16	30.37
	20-40	10	45.78	67.95	25.66	44.85	13.94	30.46
	40-60	10	58.7	92.83	34.16	81.01	20.33	34.63
	60-80	10	56.67	89.96	31.12	42.25	17.52	30.91
	80-100	10	62.62	148.87	33.2	48.31	31.76	50.72
Hg	0-20	10	0.97	5.91	0	0.75	1.8	141.57
	20-40	10	0.86	4.24	0.074	2.7	1.22	141.58
	40-60	10	0.37	1.25	0	1.04	0.45	196.14
	60-80	10	0.56	3.81	0	0.11	1.167	206.43
	80-100	10	0.37	0.84	0	0.421	0.3	82.31
As	0-20	10	9.75	16.26	6.79	10.89	2.84	29.2
	20-40	10	9.39	12.5	6.2	9.08	1.86	19.82
	40-60	10	10.87	18.39	7.45	11.18	2.99	27.57
	60-80	10	9.85	15.86	0	10.52	4.35	44.21
	80-100	10	10.93	32.06	0.67	7.29	8.28	75.73

Analysis of correlation between soil magnetic susceptibility and heavy metal content in soil along Northern shore of Bosten Lake

Table 4. reflects the correlation between soil low frequency magnetic susceptibility and heavy metal content in soil along north shore of Bosten Lake. When $|r|=1$, it means the two variables are in completely linear correlation. When $r=0$, there is no linear correlation between the two variables. Normally it can be divided into 3 levels: $|r|<0.4$ represents low degree linear correlation; $0.4\leq|r|<0.7$ represents significant linear correlation; $0.7\leq|r|<1$ represents high degree linear correlation [26]. On

this basis, the analysis result of correlation between soil low frequency magnetic susceptibility and heavy metal content in soil along north shore of Bosten Lake: the correlation coefficient between Element Cr and soil low frequency magnetic susceptibility shows a gradually increasing trend, reaching its highest value in 80-100cm soil layer, representing high degree linear correlation. The same situation happens to the variation of correlation coefficient between Ni and soil low frequency magnetic susceptibility; Cu content is significantly related to the soil low frequency magnetic susceptibility, while Hg content is low degree related to the soil low frequency magnetic

susceptibility; Mn content is significantly related to the soil low frequency magnetic susceptibility only in 80-100cm soil layer, while in other soil layers, low degree correlation exists. Regarding the contents of Zn, Hg, As, they share the equal

correlation with soil low frequency magnetic susceptibility, reaching peak value of linear correlation coefficient in 40-60cm soil layer, which is the significant linear correlation.

Table 4. Correlation analysis between low frequency magnetic susceptibility and heavy metal contents.

depth	Cr	Cu	Mn	Ni	Pb	Zn	Hg	As
X _{lf} 0-20cm	0	0.57	0.14	0	0.24	0	0.1	0
X _{lf} 20-40cm	0.14	0.37	0.36	0.28	0.14	0.24	0.22	0.22
X _{lf} 40-60cm	0.1	0.53	0.36	0.24	0.68	0.48	0.32	0.45
X _{lf} 60-80cm	0.2	0.48;	0.32	0.35	0.22	0.33	0.14	0.22
X _{lf} 80-100cm	0.7	0.65	0.42	0.62	0.1	0.2	0.25	0

Table 5 reflects the characteristics of correlation between soil low frequency magnetic susceptibility and heavy metal content in soil along north shore of Bosten Lake. Contents of Cr, Pb, Hg are in low degree correlation with soil low frequency magnetic susceptibility; Mn and As share the equal variation trend of correlation with soil low frequency magnetic susceptibility, reaching peak value of correlation coefficient in 20-40cm soil layer which represents the significant linear correlation, while in other soil layers, low degree linear correlation exists. The correlation coefficient between Zn content and soil frequency-dependent

magnetic susceptibility shows a gradually decreasing trend, reaching the peak value of correlation coefficient in 80-100cm soil layer, which represents the significant correlation. In 0-20cm, 40-60cm, 80-100cm soil layers, the Cu content is significantly correlated with the frequency-dependent magnetic susceptibility, while in other soil layers, the low degree linear correlation exists; In 40-60cm and 80-100cm soil layers, Ni content is significantly linear related to the soil frequency-dependent magnetic susceptibility.

Table 5. Correlation analysis between frequency magnetic susceptibility and heavy metal content.

depth	Cr	Cu	Mn	Ni	Pb	Zn	Hg	As
X _{fd} 0-20cm	0.22	0.52	0.33	0.27	0.1	0.26	0.22	0
X _{fd} 20-40cm	0.14	0.24	0.56	0.2	0.1	0.37	0	0.55
X _{fd} 40-60cm	0.26	0.66	0.45	0.46	0.1	0.28	0.3	0
X _{fd} 60-80cm	0.24	0.6	0.33	0.4	0.29	0.56	0.2	0.32
X _{fd} 80-100cm	0.37	0.39	0.51	0.51	0.1	0.68	0.14	0.32

RESULTS AND CONCLUSION

(1) The characteristics of magnetic susceptibility of soil in north shore of Bosten Lake are: differentiation characteristics of low frequency magnetic susceptibility vary from soil layer to soil layer, in 0-60cm soil layer, it gradually increases, reaching its peak value in 40-60cm soil layer, and then gradually decreases in 60-100cm soil layer; The variation result of magnetic susceptibility and heavy metals contents show: In 0-20cm, 20-40cm, 60-80cm, 80-100cm soil layers, it exhibits medium variation, only in 40-60cm soil layer, it exhibits strong variation. Through determining the average value of frequency-dependent magnetic susceptibility, we find that the 20-40cm soil layer contains less superparamagnetic particles, while in other soil layers, the contents of superparamagnetic particles are all over 10%, which is a considerable value. The analysis results of variation coefficient show that in 20-40cm soil layer, it exhibits medium variation, while in other soil layers, it exhibits

strong variation. (2) The characteristics of heavy metals contents in soil along north shore of Bosten Lake show that the order of heavy metals contents is Mn>Cr>Zn>Cu>Ni>As>Pb>Hg, wherein the Mn element tops the rank, while the Hg content is the lowest. The vertical distribution rule of heavy metals shows that the Contents of Cr and Mn increase with the deepening of the soil layer depth of 0-80cm, while gradually decrease with the deepening of the soil layer depth of 80-100cm; There is no significant variation occurs to the content of Cu in all soil layers; The contents of other elements in 20-40cm soil layer are generally lower than that in 0-20cm soil layer. The variation trend of heavy metals contents is: contents of Cu, Ni, Pb, Zn, As, Cr show medium variation, while the contents of Mg and Hg show strong variation. (3) The correlation between soil magnetic susceptibility and heavy metal content in soil along north shore of Bosten Lake shows that the contents of Cu, Mn, Pb, Hg are positively related to the low

frequency magnetic susceptibility, wherein the Cu content is related in largest degree; There is no correlation between other four heavy metal elements and magnetic susceptibility of surface soil; The correlation results between soil frequency-dependent magnetic susceptibility and heavy metal contents in soil show contents of Cr, Pb, Cu, Ni, Zn, Mn are positively related with soil frequency-dependent magnetic susceptibility, wherein the correlation coefficient between Mn and Cu contents and soil frequency-dependent magnetic susceptibility is the highest in each soil layer.

Acknowledgement: This work was supported by the China National Natural Science Foundation (project No. U1138302).

REFERENCES

1. X.D. Chen, X.W. Lu, G. Yang, *Environ. Sci.*, **34**, 1086 (2013).
2. Jiang, H.F. Yin, R.H. Wang, *J. Jilin University, Earth Sciences*, **35**, 653 (2005).
3. X.G. Chen, J. Wei, H.L. Sun, *Arid Land Geography*, **37**, 265 (2014).
4. Y.H. Wang, G.Z. Zheng, *Mountains Normal University, Natural Sci.*, **25**, 98 (2011).
5. Q. Yan, S. Dai, J. M. Liu, *China Environ. Sci.*, **31**, 1731 (2011).
6. J.H. Chen, X.W. Lu, *Shanxi Normal University, Natural Sci.*, **39**, 76-82 (2011).
7. F. Fang, X.Y. Li, *Environ. Monitor. Manag. Technol.*, **23**, 78 (2011).
8. G. Zhang, X.F. Hu, X.H. Wu, *Soil Sinica*, **48**, 429 (2011).
9. B. Wang, S. Zhao, D.S. Xia, *Environ. Sci.*, **32**, 1430 (2011).
10. X.J. Yu, X.L. Huo, G.C. Zhao, *J. Environ. Eng.*, **7**, 439 (2013).
11. B. Wang, D.S. Xia, J. Jia, *Jilin University, Earth Sci.*, **43**, 962 (2013).
12. D.S. Xia, B. Wang, Y. Zang, *Lanzhou University, Natural Sci.*, **49**, 173 (2013).
13. T. Muyassar, A. Jilil, F.Q. Jiang, *China Eco-Agriculture*, **21**, 883 (2013).
14. S.F. Deng, T.B. Yang, B. Zeng, *Soil Sci.*, **43**, 1054 (2012).
15. B. Wang, D.H. Xia, J. Jia, *Chinese Science Bulletin*, **57**, 3078-3089 (2012).
16. Q. Yan, S. Dai, H.J. Liu, *China Environmental Science*, **31** 1732-1737 (2011).
17. S. Li, X.F. Hu, Y. Du, *Soil Sinica*, **49**, 9-17 (2012).
18. H.M. Going, R.J. Ma, Y. Ye, *Chinese Agric. Sci. Bull.*, **29**, 140 (2013).
19. W. Liu, X.W. Lu, C.C. Chen, *Soil Sci.*, **44**, 993 (2013).
20. J.Y. Song, K.D. Fu, B. Su, *Environ. Chem.*, **32**, 1730-1736 (2013).
21. L.T. Zeng, Y.K. Chen, X.S. Wang, *Environ. Sci.*, **34**, 987 (2014).
22. T.N. Chen, Y.Q. Zhang, X.Y. Zhang, *Arid Land Res. Environ.*, **28**, 85 (2014).
23. D.X. Liu, J.H. Ma, K.L. Sun, *J. Soil*, **51**, 1242 (2014).
24. Y. Li, *Soil Sci.*, **45**, 1089 (2014).
25. X.S. Tian, H. Zhang, J.Z. Hang, *Environ. Sci. Technol.*, **35**, 6 (2012).
26. Y. Zhao, X.H. Xie, Y.F. Fu, *Southwest Univ.*, **37**, 39 (2015).

Numerical simulation and experimental study on thermal properties of trailer house composite envelope with vacuum insulation panels

Haijun Lou, Ankang Kan*, Zhipeng Guo

Merchant Marine College, Shanghai Maritime University, Shanghai, 201306, P.R.China

Received June 5, 2016, Revised September 16, 2016

Due to distinguished thermal performance of vacuum insulation panels (VIPs), i.e. the thermal conductivity is approximately 5-10 times lower than that of traditional thermal insulation material, it has been widely applied for energy conservation purpose, especially as building envelope. To research the thermal characteristic of VIPs composite envelope for trailer house, the VIPs are employed, based on the climate characteristics of the cold zone, and three typical models, namely, the interior adiabatic, sandwich and exterior adiabatic models are constructed. The physical and mathematic models are developed and the numerical comparative analysis of the thermal performance is made under the larger temperature difference condition. Compared among those constructions with the same continuous temperature waves, the damping factor, the delay time, the temperature vibration of interior wall surface, heat transfer flux and the thermal bridge are theoretically analyzed. The results of the simulation imply that, interior adiabatic model of the VIPs composite envelope is the best for the energy conservation, especially in thermal bridge region, reduction the range of the interior temperature fluctuation, radiation thermal cool sensation and improvement thermal comfort index. The work provides the theoretical foundation for the VIPs development and application in building contracture.

Key words: Vacuum insulation panels, Trailer house, Composite envelope construction, Thermal performance, Energy conservation.

INTRODUCTION

The development of cold regions is important for regional economic, military significance and research value. The trailer house can be the temporary working and living place for researchers or staff. As the special outdoor climate in winter, that is, the temperature difference between interior and exterior can be up to 60 °C, thermal performance of the building envelope is vital for energy conservation and personal thermal comfort.

Excellent adiabatic performance of envelope construction, not only can reduce energy consumption, improve indoor thermal comfort, but also can avoid moisture condensation problems of inner wall surface [1]. Due to the distinguished low thermal conductivity, i.e. approximately 5-10 times lower than traditional thermal insulation materials [2-3-4], Vacuum insulation panels (VIPs), has significant advantages as the adiabatic component for trailer house envelope. The VIPs are already introduced to the market in large-scale production, such as reefer containers, civil building envelopes, refrigeration storage room, ice boxes and so on[5]. Some theoretical calculations have been proposed and amount of study has been carried out on the possibilities of VIPs insulated systems. But the

reports for the VIPs installation and thermal operation in system are rare.

The objective of this paper was to analyse theoretically the thermal insulation models, the internal interface temperature, delay time, thermal inertia index, etc., model the trailer houses wall structure with VIPs and compare the models combined with the exterior temperature variation in cold regions [5].

THERMAL PERFORMANCE OF TRAILER HOUSE ENVELOPE

The envelopes of trailer house, including one door panel, three side panels, one roof panel, and one floor panel, mainly used to reduce the heat leakage and maintain the room temperature. According to the thermal comfort index, interior wall surface temperature closed to the indoor environment temperature means the comfortable feeling [6]. However, the interior surface wall temperature mainly depends on the indoor air temperature and the thermal resistance of the wall. According to some relevant provisions, heat transfer coefficient of trailer house envelope in cold region must be: $k \leq 0.14 \text{ W}/(\text{m}^2\cdot\text{K})$, and temperature difference between interior surface and design ambient temperature must be: $\Delta t \leq 4.0\text{K}$ [7-9]. Too thick wall means high initial investment

To whom all correspondence should be sent:
E-mail: ankang0537@126.com

and transportation costs, while too thin wall means energy consumption and even moisture condensation. Optimal construction of the trailer house envelope can not only provide comfortable living environment, but can also reduce energy consumption. In addition, trailer house belongs to reusable building, which is beneficial to environmental protection, economic.

Minimum thickness of trailer house envelope construction

The minimum heat transfer resistance of building envelope in cold region should meet the requirements of the GB50176-1993, Can be calculated by Eq.(1):

$$R_{0,\min} = \frac{(t_{in} - t_{ex})}{[\Delta t]} n R_{in} \quad (1)$$

where: $R_{0,\min}$ is minimum heat transfer resistance of the envelope, $m^2 \text{ K/W}$; t_{in} is indoor design temperature of the trailer house in winter, K; t_{ex} is outdoor design temperature of the trailer house in winter, K ; n is temperature difference correction factor, $n = 1.0$; R_{in} is internal surface heat transfer resistance; $R_{in} = 0.11 \text{ m}^2 \text{ K/W}$; Δt means allow error between indoor air and interior wall surface, $\Delta t = 2.5 \text{ K}$.

So, $R_{0,\min} = 2.99 \text{ m}^2 \text{ K/W}$. According to the design Code [8], its heat transfer resistance should be:

$$R = \frac{1}{k} = \frac{1}{0.14} \geq 7.143 \text{ m}^2 \cdot \text{K/W} \quad (2)$$

VIPs and polyurethane (PU) as trailer house envelope construction of filling materials, and the thickness of PU layer can be calculated by Eq. (3):

$$R = \sum_1^4 R_i = R_{in} + \frac{\delta_f}{\lambda_f} + \frac{\delta_{vip}}{\lambda_{vip}} + R_{ex} \quad (3)$$

Where: R_{ex} is the design exterior surface heat transfer resistance, $R_{ex} = 0.04 \text{ m}^2 \text{ K/W}$; λ_f is thermal conductivity of PU, $\lambda_f = 0.032 \text{ W/(m K)}$; λ_{vip} is thermal conductivity of VIPs, $\lambda_{vip} = 0.007 \text{ W/(m K)}$; δ_{vip} is thickness of VIPs, $\delta_{vip} = 0.02 \text{ m}$.

The exterior protective layers of the trailer house envelope are made of steel plate and galvanized sheet and the interior protective layer is made of stainless steel plate. All the protective layers are very thin and the excellent thermal conductors. R_{ex} and R_{in} are ignored in the calculation. Combined with the Eqs. (2) and (3), the PU layer thickness is 133 mm. In fact, PU layer thickness is 150 mm in this research.

The thermal characteristic parameters of trailer house envelope construction

VIPs cannot be used alone as the envelope of the trailer house, but in form of composite panels with other thermal insulating materials. The following parameters should be confined before the study.

(1) *The damping factor.* The damping factor refers to the interior air temperature stability of the trailer house envelope, the exterior envelope effect by outdoor integrated temperature or outdoor air temperature harmonic. The damping factor is the ratio of outdoor integrated temperature or outdoor air temperature harmonic amplitude to interior surface temperature harmonic amplitude. For the multilayer envelope, the damping factor can be calculated by the Eq. (4) [8]:

$$v_0 = 0.9e^{-\frac{\sum D_i}{\sqrt{2}}} \frac{S_1 + \alpha_{in}}{S_1 + Y_1} \cdot \frac{S_2 + Y_1}{S_2 + Y_2} \dots \frac{S_n + Y_{n-1}}{S_n + Y_n} \cdot \frac{Y_n + \alpha_{ex}}{\alpha_{ex}} \quad (4)$$

where: v_0 is the damping factor of the multilayer envelope; D_i is thermal inertia index of the layer i ; h_{in} is interior surface thermal convective coefficient of the trailer house, $\text{W/(m}^2 \cdot \text{K)}$; h_{ex} is exterior surface thermal convective coefficient, $\text{W/(m}^2 \cdot \text{K)}$; S_1, S_2, \dots, S_n are heat storage coefficients of each layer materials from inside to outside, $\text{W/(m}^2 \cdot \text{K)}$; Y_1, Y_2, \dots, Y_n is surface heat storage coefficient of each layer materials from inside to outside, $\text{W/(m}^2 \cdot \text{K)}$.

(2) *The delay time.* The delay time is the time difference between the moment that highest (or lowest) interior surface temperature harmonic appears and the moment that the highest (or lowest) outdoor integrated temperature or the highest (or lowest) outdoor air temperature harmonic appears. It can be calculated by Eq. (5) (GB50176-1993):

$$\xi_0 = \frac{1}{15} (40.5 \sum_1^n D_i - \arctan \frac{\alpha_{in}}{\alpha_{in} + Y_{in} \sqrt{2}} + \arctan \frac{Y_{ex}}{Y_{ex} + \alpha_{ex} \sqrt{2}}) \quad (5)$$

where: ξ_0 is the delay time, h; Y_{in} is the heat storage coefficient of interior surface envelope, $\text{W/(m}^2 \cdot \text{K)}$; Y_{ex} is heat storage coefficient of outer surface envelope, $\text{W/(m}^2 \cdot \text{K)}$.

(3) *Thermal inertia index.* Thermal inertia index D is a dimensionless index to characterize its resistance ability of temperature fluctuations and thermal flux fluctuations. The greater the D value is, the better thermal stability of envelope is. The D of a single material layer envelope can be calculated by Eq. (6)[8] :

$$D = RS = \delta \sqrt{\frac{2\pi C_p \rho}{\lambda T}} \quad (6)$$

Where: R is thermal resistance, $m^2 \cdot K / W$; S is thermal storage coefficient, $W / (m^2 \cdot K)$; δ is thickness, m ; C_p is specific heat at constant pressure, $J / (kg \cdot K)$; ρ is density, kg / m^3 ; λ is heat conductivity coefficient, $W / (m \cdot K)$; T is period of fluctuations, s .

For multilayer composite layers envelope, the D value can be calculated by Eq. (7) [8]:

$$\sum_i^n D_i = \sum_i^n R_i S_i \quad (7)$$

(4)The thermal storage coefficient. The thermal storage coefficient is the ratio of the heat flux amplitude through the layer surface to the surface temperature amplitude. It can characterize the merits of the material thermal stability. The greater

the thermal storage coefficient is, the better thermal stability is. It's can be calculated by the Eq. (8)[8].

$$S = \frac{A_q}{A_t} = \sqrt{\frac{2\pi\lambda C_p \rho}{T}} \quad (8)$$

where: A_q is heat flux wave-amplitude of layer surface; A_t is temperature wave-amplitude of layer surface.

The types of composite envelope

As the thermal conductivity of VIPs is much less than that of traditional thermal insulated materials, the composite envelope of trailer house, according to VIPs layer location position, can be divided into three types, that is , interior adiabatic (Figure 1a), sandwich (Figure 1b) and exterior adiabatic (Figure 1c).

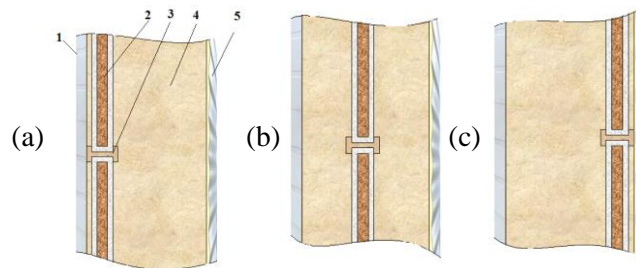


Fig. 1. The adiabatic types of the composite envelope: (a) interior adiabatic, (b) sandwich and(c) exterior adiabatic. (1)- internal stainless steel plate; (2) - VIPs layer; (3) - H-shaped fixed piece; (4) - PU layer; (5) - external steel plate.

VIPs COMPOSITE ENVELOPE CONSTRUCTION MODEL

Heat transfer through trailer house envelope under large temperature difference in cold region is a complicated unsteady process, which is not only affected by the outdoor air temperature, solar radiation, wind speed and so on, but also relates to thermal conductivity, thermal storage coefficient, specific heat at constant pressure, density and thermal performance of envelope material. As the direct calculation for the heat transfer process in trailer house envelope is very complicated, the following necessary assumptions should be made in advance. (1)No clearance exist between each layer; (2) Physical parameters of each layer material does not change with temperature;(3)Ignore the influence of "H-shape connecting piece" and heat transfers in one dimension way;(4) No internal heat source and mass transfer.

Physical model

Internal stainless steel plate and external steel plate are ignored to simplify the models and the physical models are illuminated in Figure 2. The types of composite envelope mainly depend on the

location of the VIPs layer. In this physical model, the thickness δ_{vip} of VIPs layer is a constant value, and total thickness $\delta_1 + \delta_2$ for polyurethane layer is also a constant value. When $\delta_1 = 0$, the type is interior adiabatic. While $\delta_2 = 0$, the type is exterior adiabatic. While $\delta_1 = \delta_2 \neq 0$, the type is sandwich.

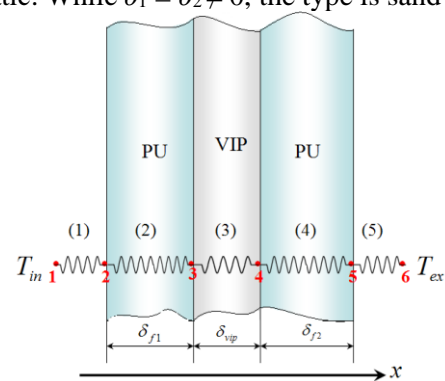


Fig. 2. The sketch of trailer house VIPs composite envelope.

Outdoor temperature

The outdoor temperature is a key variable to calculate the heat flux that transfers from interior to exterior. However, the outdoor temperature changes with time. In a period of time (for example within a

month), the diurnal variation of the temperature can be thought as a cyclical fluctuation in 24 hours. Sine (or cosine) function series are always taken to simplify temperature fluctuation for calculation in practice. The real outdoor temperature fluctuation in a certain Chinese cold region in one day of the coldest month in 2013 is collected by the national meteorological station, and the fitting curve is shown in Figure 3.

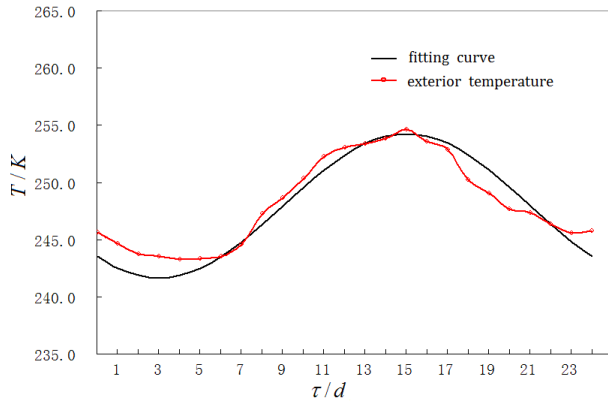


Fig. 3. Actual temperature and fitting curve in the cold region.

Outdoor comprehensive temperature fitting function is:

$$T_{ex,\tau} = 247 + 6.3 \cos\left(\frac{2\pi}{24}(\tau - 15)\right) \quad (9)$$

where: $T_{ex,\tau}$ is the corresponding outdoor temperatures at the moment τ , K.

Mathematical model

As the dimension of height and width is much larger than that of thickness of trailer house envelope, no heat source exists and materials of every layer is uniform individually, the thermal conduction of the envelope can be considered as one dimensional way. Based on Fourier's law, a corresponding unsteady differential equation (10) can be established.

$$\frac{\partial T}{\partial \tau} = \frac{\lambda}{\rho C_p} \frac{\partial^2 T}{\partial x^2} \quad (10)$$

Where, τ is time; x is finite-thickness.

According to the cold region climate characteristics, $h_{in} = 8.7 \text{ W}/(\text{m}^2 \text{ K})$, $h_{ex} = 19.0 \text{ W}/(\text{m}^2 \text{ K})$. The design indoor temperature in winter is 23°C , relative humidity 30%. That boundary condition is:

$$\begin{cases} \lambda \frac{\partial T}{\partial x} \Big|_{x=0} = 0 & T_1 = T_{in} \\ \lambda \frac{\partial T}{\partial x} \Big|_{x=L} = h_{ex}(T - T_{ex}) & T_{ex} = 247 + 6.3 \cos\left(\frac{2\pi}{24}(\tau - 15)\right) \end{cases} \quad (11)$$

Linear finite element equation of unsteady thermal conduction function can be derived by variable separation method. Supposed that indoor air temperature is constant, the heat flux, transferring through the interior surface is mainly used for heat storage at the beginning. A period later, the heat transfers from the interior surface to the exterior surface. While the thermal equilibrium is established, the exterior surface temperature reaches its maximum value. For the unsteady-state heat transfer of the envelope, its interior surface thermal transfer strength is:

$$q_{in} = h_{in}(T_{in} - T_2(\tau)) \quad (12)$$

Where: q_{in} is thermal flux density through envelope internal surface, W/m^2 ; $T_2(\tau)$ is temperature of envelope interior surface, K.

the thermal flux density is made up of two parts, that is, thermal conduction strength of envelope material q_1 and thermal storage strength of envelope material q_2 .

$$q_1 = \frac{T_2(\tau) - T_5(\tau)}{\sum_i \delta_i / \lambda_i} = q_{ex} = h_{ex}(T_5(\tau) - T_{ex}(\tau)) \quad (13)$$

$$q_2 = \sum_i \rho_i \cdot C_{pi} \cdot \delta_i \frac{dT(\tau)}{2d\tau} \quad (14)$$

Where: $\frac{dT(\tau)}{2d\tau}$ is average temperature change amount per unit time of the material, K/s

According to $q_{in} = q_1 + q_2$, Eq.(15) can be obtained.

$$T_2(\tau) = \frac{1+h_{ex}\sum R}{h_{in}+h_{ex}+h_{in}\sum R} \left(\frac{h_{in}T_{in}+h_{ex}T_{ex}+h_{in}h_{ex}T_{in}\sum R}{1+h_{ex}\sum R} - e^{-\frac{h_{in}h_{ex}+h_{in}h_{ex}\sum R}{(h_{in}\sum R)D}} \right) \quad (15)$$

Where: $D = \sum_1^n D_i$; $\sum R = \sum \delta_i / \lambda_i$.

Types and thermal parameters of VIPs composite envelope

The three envelopes are constructed according to the Figure 2. As the thermal resistances of stainless steel plate and steel plate are much smaller than that of thermal insulated materials, the stainless steel plate and steel plate are ignored in the simplified models and the following simulation. The core material of VIPs is super-fine glass fibre. And thermal properties parameters of thermal insulated materials are shown in Table 2.

Table 1. VIPs composite envelope structure.

NO.	Models	Composition (from inside to outside)
1	Interior adiabatic	Stainless steel plate and internal decoration +SCUFF panel + VIPs20mm+ PU150mm+steel plate, galvanized plate and outer decoration
2	Sandwich	Stainless steel plate and internal decoration + PU 75mm+ VIPs20mm+ PU 75mm+ steel plate, galvanized plate and outer decoration
3	Exterior adiabatic	Stainless steel plate and internal decoration + PU150mm+ VIPs 20mm +SCUFF panel+ steel plate, galvanized plate and outer decoration

Table 2. Thermal properties parameters of insulated materials.

Materials	Heat conductivity coefficient/ W/(m·K)	Density/ kg/m ³	Specific heat capacity / J/(kg·K)	Heat storage coefficient 24h / W/(m ² ·K)	Thermal inertia index/ D
PU	0.032	38	2475.2	28.06	/
VIPs	0.007	264	674.2	44.24	0.87

RESULT AND DISCUSSION

Comparison of the damping factor and the delay time

As mentioned above, the damping factor and the delay time of a building envelope are all important parameters to characterize the interior surface temperature stability. The damping factor and the delay time of the three kind trailer house envelopes are collected in Table 3.

Table 3. The damping factor and the delay time of three trailer house envelopes.

NO.	Models	Thermal inertia index $\sum D$	The damping factor ν_0	The delay time ξ_0 / h
1	Interior adiabatic	7.69	289.35	11.47
2	Sandwich	6.81	270.16	10.64
3	Exterior adiabatic	6.35	265.52	9.41

The conclusion can be easily made from Table 3 that, the damping factor of model 1 is the largest one, followed by that of model 2, and that of model 3 is the smallest one. The change trends of delay time are the same with that of the damping factor. Under the same outdoor environment wave fluctuation condition, the bigger the damping factor is, the longer the delay time is, and the smaller the internal surface temperature fluctuation is, that means the excellent anti interference ability of outdoor environment temperature and good thermal stability. So the interior adiabatic model, namely

the VIPs layer is closed to the interior in the envelope structure, is good for the internal surface temperature stability.

Interior surface temperature fluctuation

The interior surface temperature of trailer house envelope is one of the important factors of indoor thermal comfort study. It is also a vital factor of the moisture condensation on the surface of building internal wall surface, especially in cold region. The internal wall surface temperature fluctuations of three models under the same condition were numerically analyzed, and the simulation curves are exposed in Figure 4.

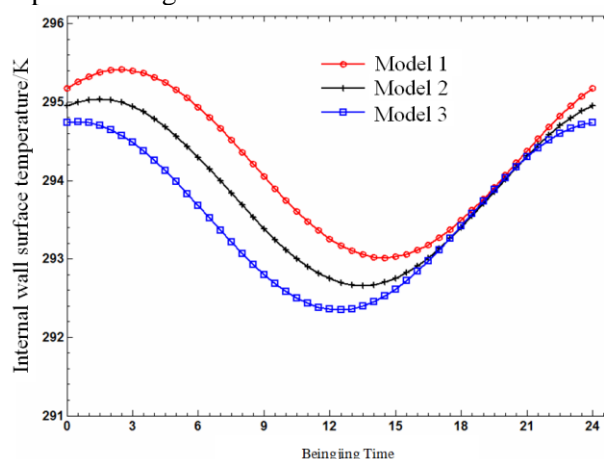


Fig. 4. Simulation curves of three internal wall surface temperatures.

All the internal wall surface temperatures kept pace with the external environment change and

appeared in manner of sine waves, while the interior temperature was constant. As the thermal inertia index is the biggest of the three, the model 1 has the longest delay time and the smallest wave amplitude. The wave trough of the model 1, that is, 293.35K, appeared at about 14:00 in Beijing time. The wave troughs of models 2 and 3 are all a little lower than that of model 1, respectively 292.89K and 292.53K, even the difference with interior air temperature is not over 4K. Obviously, the internal wall surface of model 3 will easily moisture condense while the relative humidity is up to the dew point.

Taking the indoor thermal comfort for consideration, the mean internal wall surface temperature of model 1, a little high than that of models 2 and 3, is much closer to the interior constant temperature and can reduce the cold feeling of wall radiation.

Heat transfer capacity

For the unsteady thermal process of the trailer house envelopes, the initial input heat capacity Q_L is always not equal to the output heat capacity Q_R . As the heat storage capacity of the envelopes, resulting in the delay transfer of heat, and the fluctuation effect of external temperature, Q_L and Q_R cannot be equal to each other all the time, even $Q_R > Q_L$ at some moment. But for a cycle interval, the total input heat capacity should be approximate equal to the output one, that is, $\int_0^{24} Q_L d\tau \approx \int_0^{24} Q_R d\tau$. The relate function can be expressed as:

$$\int_0^{24} Q_L d\tau = \int_0^{24} -h_{in} \frac{\partial T}{\partial n} \Big|_{x=0} \partial\tau = \int_0^{24} h_{in} (T_{in} - T_2(\tau)) d\tau \quad (16)$$

Total heat transfer capacities in 24 hours of three envelopes are summarized in Table 4.

Table 4. Heat transfer capacity of three envelopes.

NO.	Models	Heat transfer quantity /24h / kJ/m ²
1	Interior adiabatic	1 277.86
2	Sandwich	1 390.61
3	Exterior adiabatic	1 443.02

The conclusion can be made from Table 4 that, energy transmission, that is, output heat capacity of model 1 is the smallest, followed by that of model 2, and the last is that of model 3. So, interior adiabatic structure is the best one for energy conservation.

Local thermal bridge effect

In order to enhance the trailer house envelopes strength, the steel components, such as beams, reinforcing ribs, crutches, etc. are always involved.

But they can change the temperature distribution at their location, causing so called local thermal bridge. Under the cold region condition, the local internal surface temperature is much lower than that of main internal surface temperature, resulting in moisture condensation, even frost at the local space, reducing thermal comfort and causing potential danger. Although the area of the thermal bridge space is small, the heat loss is huge. As thermal bridge spots and types are various, the typical thermal bridge at the beam is selected in this research to simulation and discussion.

Three different configurations diagrams are shown in Fig. 5a, in which solid line means model 1, dotted line, model 2, dash line dot, model 3, and upper left corner area means indoor room boundary.

Combined with the third boundary condition, simulations for three models were exposed the temperature distribution and thermal bridge effect. And the results were shown in Figure 5b,c,d.

With the position of VIPs in envelopes shifting from the inside to the outside, the thermal bridge of the beam is becoming more and more significant. Isothermal trends of model 1 in Figure 5 (b) is gentle, and the local internal surface temperature, the minimum value 292.15K, even a little lower than the main internal surface temperature, is not beyond 4K difference with the interior temperature, that the code requires. Isothermal trends of model 2(shown in Figure 5(c)) and model 3(shown in Figure 5 (d)) are distorted, implying the thermal bridge effects are obviously. The lowest temperatures of model 2 and model 3, respectively, are 291.62K and 290.86K, all beyond 4K difference. So, under the large temperature difference condition, the interior adiabatic type of VIPs trailer house envelope is ideal for the reduction of energy loss and improvement of the interior thermal comfort.

Taking the temperature distribution charts for consideration, the mean temperatures of the VIPs layers are also different. For a cycle period, the mean temperature of model 1 is 287K, is higher than that of model 2, 275K, also higher than that of model 3, 255K. However, VIPs' service life is influenced by ambient temperature. It is helpful to extend the service life if the surrounding temperature is close to the room temperature. So, the model 1 is ideal for the trailer house envelope.

CONCLUSIONS

Three typical composite envelopes models for trailer house, by using VIPs, that is, interior adiabatic, sandwich, exterior adiabatic, are structured. And the thermal characteristics of the envelopes are theoretically compared under the cold region temperature condition.

(1) Combining with the three types and thermal performance in cold region, the damping factor, the delay time, the internal wall surface temperature vibration, and heat transfer flux are theoretically analyzed. Interior adiabatic model is superior to the others in energy conservation and indoor thermal comfort.

(2) The thermal bridge effects of three VIPs composite envelopes are simulated and theoretically analyzed under the unsteady condition. The conclusion can be gained that, the interior adiabatic type is excellent for energy conservation on thermal bridge regions and temperature difference decreasing between the internal wall surface temperature and indoor air temperature. Meanwhile, the interior adiabatic envelope can reduce radiation cold feeling, avoid local moisture condensation and improve thermal comfort index.

Acknowledgement: This research is financially supported by the Natural Sciences Foundation of Shanghai, China (15ZR1419900). The authors would also like to render thankfulness to Mr. Yang Baotong from Yangzhou Tonglee Reefer Container Co., Ltd. for the kind help.

REFERENCES

1. H.H. Wang, Y.Y. Zhuan, *Tongji University(Natural Sciences)*, **38**, 1641 (2010).
2. R. Baetens, B.P. Jelle, J.V. Thue, *Energy and Buildings*, **42**, 147 (2010).
3. M. Alam, H. Singh, *Applied Energy*, **88**, 3592 (2011)
4. J. Fricke, U. Heinemann, H.P. Ebert, *Vacuum*, **82**, 680 (2008).
5. J. Zhang, Z.L. Huang, *Harbin Engineering University*, **30**, 1356 (2009).
6. H.M. Li, W.L. Jin, *J. Building Struct.*, **25**, 93 (2004).
7. GB50189-2005, Design standard for energy efficiency of public buildings, China Building Industry Press, Beijing, 2005.
8. GB50176-1993, Code for thermal design of civil buildings, China Building Industry Press, Beijing, 1993.
9. CAN/CSA-Z240.2.1-1992, Canadian Standards Association Standards, *Structure Requirements for Mobile Homes*, Canada (in press), 1992.

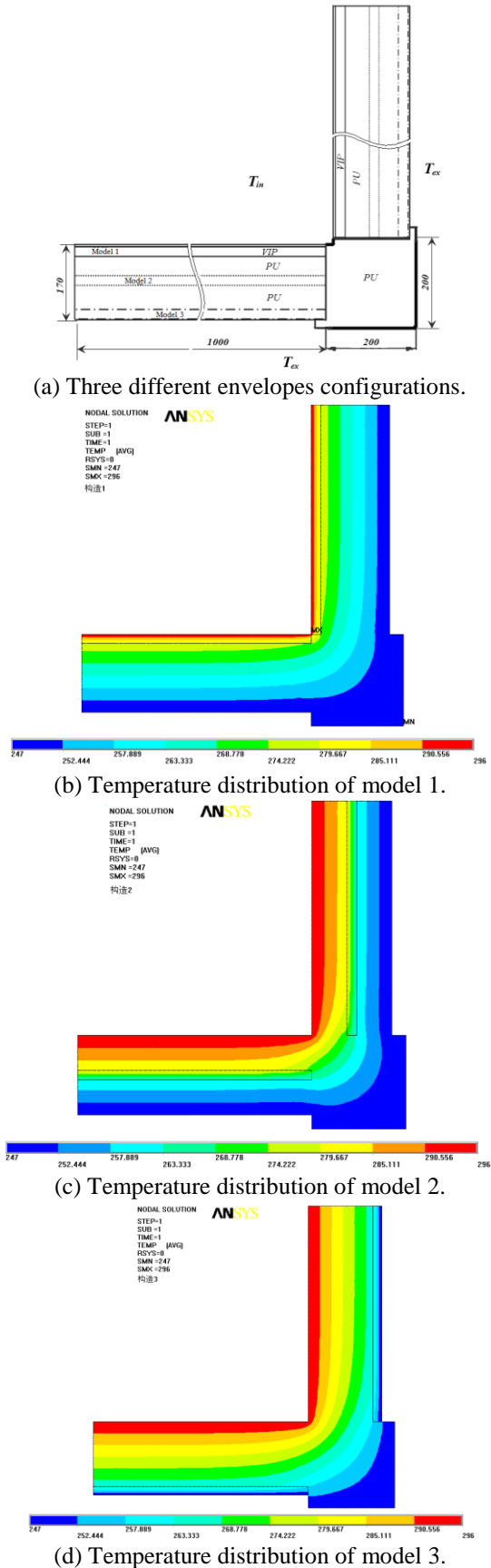


Fig. 5. Three different envelopes configuration and temperature distribution diagram.

Theoretical study on structure and properties of $B_2H_m(NO_2)_n$ ($m=2-5; n=1-4$)

Haiyan Hu^{1,2}, Yonghong Wang^{2,3}, Hongbin Wang^{2*}

¹ School of Chemical and Environment Engineering, North University of China, Taiyuan, 030051, China

² Department of Computer Science, Xinzhou Teachers University, Shanxi, 034000, China

³ School of Computer Science and Control Engineering, North University of China, Taiyuan, 030051, China

Received February 18 2016, Revised April 10 2016

This paper conducts theoretical research of $B_2H_m(NO_2)_n$ ($m = 2-5; n = 1-4$) with density functional theory, determines the most stable structure through structural optimization and frequency analysis, and calculates enthalpy of formation by applying atomization reaction method and isodesmic reaction method for the most stable structure, calculates molar volume, theoretical density and explosion heat of $B_2H_m(NO_2)_n$ ($m = 2-5; n = 1-4$) at B3LYP / 6-31G * level, and studies detonation velocity, detonation pressure and other thermodynamic properties with K-J empirical formulas. Studies show that explosion heat of $B_2H_3(NO_2)_3$, $B_2H_2(NO_2)_4$ are 1.34KJ / mol and 0.85KJ / mol respectively, less than 1.37KJ / mol of conventional explosive TNT; explosion heat of $B_2H_5NO_2$ and $B_2H_4(NO_2)_2$ are 1.83KJ / mol and 1.57KJ / mol, greater than that of TNT explosion heat; detonation velocity and pressure of adding compound $B_2H_m(NO_2)_n$ ($m=2-5; n=1-4$) more and more approach TNT as substituting cardinal number increases; ΔE_{gap} of titled compound are 5.94eV, 5.76eV, 5.10eV and 4.76eV respectively, showing that as nitro substituent increases, ΔE_{gap} value decreases. In Wiberg bond order analysis, B-NO₂ bond is relatively weak in $B_2H_m(NO_2)_n$ ($m=2-5; n=1-4$) molecule, probably pyrolysis or detonation trigger bond of titled compound.

Keywords: Enthalpy of formation, High energy compounds, Density functional theory, Explosion heat, Detonation pressure, Detonation velocity.

INTRODUCTION

Since high-energy compounds has been very widely applied in civil and military use, research on new high-energy compounds has always been a subject interested by scientists who try to find new high-energy, low-sensitivity energetic materials to meet the development needs of military and aerospace technology[1]. There are two sources of high-energy compounds, one is conventional explosives whose energy is mainly from rapid oxidation [2] of carbon chain or cage-type tension structure [3]; another is high-nitrogen compound whose energy is mainly from very high enthalpy of formation [4].

Enthalpy of formation is a fundamental thermodynamic property of compounds, moreover an important parameter to measure explosiveness and security for enthalpy of formation of explosives, as enthalpy of formation can directly affect explosion heat, indirectly impact detonation velocity, detonation pressure and capacity for work. For stable compound, their enthalpy of formation can be obtained directly by information search; while enthalpy of formation of high-energy compounds is difficult to be directly measured experimentally as there is a certain danger in actual

measurement. Therefore, to estimate enthalpy of formation of high-energy compounds with a variety of theoretical approaches has become scientists' research focus, and quantum chemistry method has opened up a new way for calculation of enthalpy of formation [5-7]. In theoretical calculation, estimation of enthalpy of formation with group adding subjects to many restrictions[8] due to consideration to bond and some group's contribution value for enthalpy of formation and correction value interactional with group, which renders theoretical calculation value not trusted. Atomization reaction method has been affirmed by scientists and widely used for calculation of enthalpy of formation. Based on density functional theory DFT-B3LYP[9-10] method, it takes into account electron correlation effect, can obtain more reliable energy in optimization of molecular structure, while reducing computing cost; however atomization reaction method is not applicable to all molecules. For those large molecular systems with cage-like or delocalized bond, calculation of enthalpy of formation with atomization reaction method will damage its system with relatively big error, also relatively complicated [11-13]. Hence, it is necessary to design a reasonable isodesmic reaction to calculate enthalpy of formation. Isodesmic reaction method based on the advantage that reactants and products have similar electronic environment offsets error caused by electron

To whom all correspondence should be sent:
E-mail: whb-163@163.com

correlation energy, and accurately calculates enthalpy of formation of titled compound [5.10.14.15].

Enthalpy of formation of B_2H_6 calculated by atomization reaction method based on B3LYP / 6-31G * level is 34.83 KJ / mol which approaches experimental value (35.60 KJ / mol), indicating reliability of atomization reaction method. Effort has been made to replace hydrogen in the molecule with nitro and generate a class of new compounds. If such compounds have good thermodynamic properties, then they are probably a class of new high-energy compounds. Thus, its research significance lies in that it is more environmentally friendly compared to traditional explosives. After reaction, B element generates B_2O_3 and boron, and there will be no CO, SO_2 and other harmful gases causing environmental pollution.

CALCULATION METHOD

This paper applies density functional theory and ab initio method in Gaussian 09 program package, combines 6-31G * basis set, conducts geometry optimization of B_2H_6 , $B_2H_m(NO_2)_n(m=2-5;n=1-4)$ and other molecules, and obtains ground state total energy. Zero-point energy and enthalpy correction energy is acquired based on vibration analysis. Default program value is adopted for calculation of convergence precision, and the resultant structures are minimum points on potential energy surface, that is, no imaginary frequency. Calculation results of the most stable structure of B_2H_6 $B_2H_m(NO_2)_n(m=2-5;n=1-4)$ is shown in Figure 2.1.

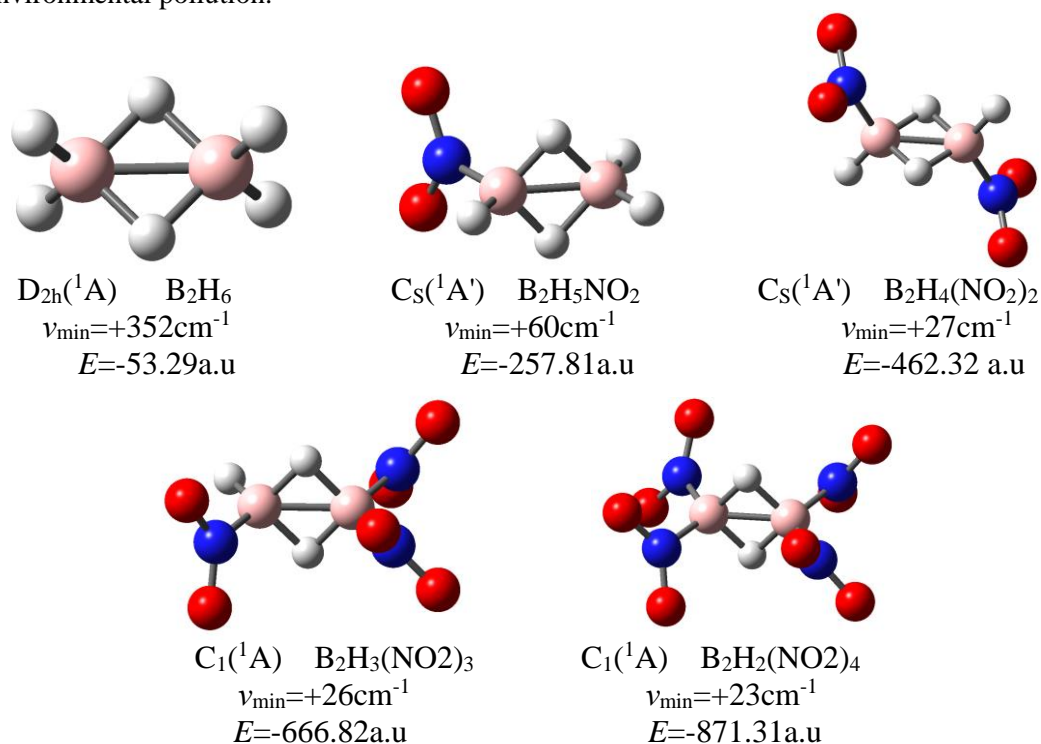


Fig. 2.1. The most stable structure of B_2H_6 $B_2H_m(NO_2)_n(m=2-5;n=1-4)$

The paper next takes compound $A_xB_yH_z$ as an example to introduce the method to calculate standard enthalpy of formation of compound at 298 K with atomization reaction method. First, decompose molecules into atoms.



Standard reaction enthalpy of the reaction at 298K is ΔH_{298}^0 (equal to atomization energy ΣD_0 of molecule)

$$\Sigma D_0(A_xB_yH_z) = [x\varepsilon_0(A)+y\varepsilon_0(B)+z\varepsilon_0(H)] - \varepsilon_0(A_xB_yH_z) - \varepsilon_{ZEP}(A_xB_yH_z)$$

In the formula, $\Sigma D_0(A_xB_yH_z)$ is atomization energy of $A_xB_yH_z$, $\varepsilon_0(A)$, $\varepsilon_0(B)$, $\varepsilon_0(H)$ and $\varepsilon_0(A_xB_yH_z)$

are ground state total energy of A, B, H and compound $A_xB_yH_z$ at Gaussian 09 program computing, while $\varepsilon_{ZEP}(A_xB_yH_z)$ is zero point energy of compound $\varepsilon_{ZEP}(A_xB_yH_z)$;

$$\Delta H_{298}^0 = \Sigma D_0(M) = \Sigma x\varepsilon_0(X) - \varepsilon_0(M) - \varepsilon_{ZEP}(M)$$

$$\Delta_f H^0(A_xB_yH_z, 0K) = \Sigma x\Delta_f H^0(X, 0K) - \Sigma D_0(A_xB_yH_z)$$

$$= [x\Delta_f H^0(A, 0 K)+y\Delta_f H^0(B, 0 K)+z\Delta_f H^0(H, 0 K)] - \Sigma D_0(A_xB_yH_z)$$

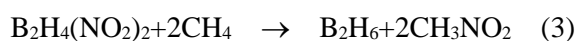
$$\Delta_f H^0(A_xB_yH_z, 298 K) = \Delta_f H^0(A_xB_yH_z, 0 K) +$$

ΔH_T

$$\Delta H_T = [H^0_{A_xB_yH_z}(298K) - H^0_{A_xB_yH_z}(0K)] - x[H^0_A(298K) - H^0_A(0K)] - y[H^0_B(298K) - H^0_B(0K)] - z[H^0_H(298K) - H^0_H(0K)]$$

In the formula, $\Delta_f H^0(A_xB_yH_z, 0K)$ and $\Delta_f H^0(A_xB_yH_z, 298K)$ are enthalpy of formation of compound at 0 K and 298 K respectively, $\Delta_f H^0(A, 0K)$, $\Delta_f H^0(B, 0K)$, $\Delta_f H^0(H, 0K)$ are enthalpy of formation of atoms A, B and H respectively at 0 K which can be obtained by checking the manual, $[H^0_A(298K) - H^0_A(0K)]$, $[H^0_B(298K) - H^0_B(0K)]$, $[H^0_H(298K) - H^0_H(0K)] \rightarrow$ are heat correction values of atoms A, B and H respectively which can also be obtained by checking the manual. Similarly, $[H^0_{A_xB_yH_z}(298K) - H^0_{A_xB_yH_z}(0K)]$ is heat correction value of compound $A_xB_yH_z$.

For $B_2H_m(NO_2)_n(m=2-5;n=1-4)$, if isodesmic reaction is adopted to calculate its enthalpy of formation, then the designed isodesmic reaction is as follows:



In the formula: B_2H_6 is the parent, CH_4 , CH_3NO_2 are reference material methane and nitromethane respectively. Reaction heat ΔH_{298} of

$$Q \cong \frac{-[\Delta_f H(\text{detonation products}) - \Delta_f H(\text{explosive})]}{\text{formula weight of explosive}}$$

Detonation velocity and detonation pressure can be estimated by K-J empirical formula, with its expression as follows:

$$D = 1.01[NM^{0.5}Q^{0.5}]^{0.5}(1 + 1.30\rho)$$

$$P = 1.558\rho^2NM^{0.5}Q^{0.5}$$

The formula is simple empirical formula to calculate detonation velocity and pressure based on experimental data analysis and summarization by Kamlet and Jacobs et al. [8]. In the formula, D is detonation velocity (km / s), P is detonation pressure (GPa), ρ is density of explosives (g/cm³), N is mole number of gaseous products generated by per gram of explosive detonation (mol / g), M is average molecular weight of gaseous products (g / mol). In the calculation process, suppose explosive reaction follows principle of maximum heat release, i.e. after explosion, hydrogen first generates H_2O

Table 3.1. The standard enthalpy of formation, Values of Thermal Correction, and Ground State Total Energy (ϵ_0) of B, H, N, O atoms.

reaction formulas (2) - (5) at 298 K can be expressed as:

$$\Delta H_{298} = \Sigma \Delta H_{f,P} - \Sigma \Delta H_{f,R}$$

In the formula: $\Sigma \Delta H_{f,P}$ and $\Sigma \Delta H_{f,R}$ are total heat formation of products and reactants respectively at 298 K. Gas phase formation heat of CH_4 and CH_3NO_2 can be obtained by checking the table. Hence, only by calculating ΔH_{298} can enthalpy of formation of titled compound be obtained.

$$\Delta H_{298} = \Delta \epsilon_0 + \Delta \epsilon_{ZEP} + \Delta H_T + \Delta nRT$$

In the formula: $\Delta \epsilon_0$ and $\Delta \epsilon_{ZEP}$ are difference between the total energy and zero-point energy of reactant and product respectively, ΔH_T is enthalpy correction term of 0-298 K; under ideal gas conditions, $\Delta(PV)$ equals ΔnRT , Δn is the difference between mole number of product and reactant. For the above formula, $\Delta n = 0$.

After enthalpy of formation of titled compound is obtained according to the above calculation method, seek explosion heat value according to explosion heat formula. Explosion heat is the maximum released energy (detonation chemical energy) per gram of explosive after explosion, i.e. negative of enthalpy change in detonation reaction, energy [15] that can be used to do mechanical work. Also, explosion heat can also be used to assess dynamite damage [14] to the environment. The formula [12-14] is as follows:

with oxygen, boron and oxygen generate diboron trioxide solid, but due to lack of oxygen, the remaining boron exists as simple substance, and all nitrogen generates nitrogen oxides.

RESULTS AND DISCUSSION

In this paper, enthalpy of formation of compounds such as B_2H_6 , $B_2H_m(NO_2)_n(m=2-5;n=1-4)$ is calculated with atomization reaction method based on level method DFT-B3LYP-6-31G*. Experimental standard gaseous enthalpy of formation, value of thermal correction and ground state energy obtained after calculation of B, H, N, O atoms are shown in Table 3.1. Total energy ϵ_0 , zero-point energy ϵ_{ZEP} , enthalpy correction value H_T and enthalpy of formation ΔH_f calculated by atomization reaction method of compounds B_2H_6 , $B_2H_m(NO_2)_n(m=2-5;n=1-4)$ at level of B3LYP / 6-31G* are shown in Table 3.2.

	ΔH_{atom}^0 [12] Cal/mol	H_T [$H^0(298)-H^0(0K)$][12] Cal/mol	ϵ_0 /(a.u) at B3LYP/6-31G* level
B	136.2	0.29	-24.654354
H	51.63	1.01	-0.5002728
N	112.53	1.04	-54.5844894
O	58.99	1.04	-75.0606214

Table 3.2. Total Energy (ϵ_0), Zero-Point Energy (ϵ_{ZEP}), Values of Thermal Correction (H_T), and Heats of Formation (ΔH_f) of the $B_4H_2, B_4HNO_2, B_4(NO_2)_2, B_2H_5NO_2, B_2H_4(NO_2)_2, B_2H_3(NO_2)_3, B_2H_2(NO_2)_4, CH_4$ and CH_3NO_2 Compounds at the B3LYP/6-31G* level

	ϵ_0 a.u	ϵ_{ZEP} a.u	H_T a.u	ΔH_f KJ/mol Atomic reaction	ΔH_f KJ/mol Isodesmic reaction method
$B_2H_5NO_2$	-257.81	0.068	17.69	-45.32	-35.09
$B_2H_4(NO_2)_2$	-462.32	0.072	24.78	-253.15	-85.16
$B_2H_3(NO_2)_3$	-666.82	0.075	31.918	-271.63	-109.22
$B_2H_2(NO_2)_4$	-871.31	0.078	39.77	-319.75	-129.08
CH_3NO_2	-244.33	0.051340	0.0053	-74.40[14]	
CH_4	-40.33	0.046354	0.0038	-74.80 [13]	

Table 3.2 shows that all enthalpy of formation of resulting compound $B_2H_m(NO_2)_n$ ($m=2-5; n=1-4$) after compound B_2H_6 's nitro-substitution of hydrogen atoms are negative, indicating that generation of this class of compound will release heat. Enthalpy of formation of CH_4, CH_3NO_2 is

experimental value in the Table.

Calculation results of theoretical density, molar volume, explosion heat, detonation velocity, detonation pressure of compound $B_2H_m(NO_2)_n$ ($m=2-5; n=1-4$) and TNT at B3LYP / 6-31G * level are shown in Table 3.3.

Table 3.3. The density, size, detonation, detonation velocity and detonation pressure of $B_2H_m(NO_2)_n$ ($m=2-5; n=1-4$) and TNT compounds at the B3LYP/6-31G* level.

	ρ g/cm ³	V cm ³ /mol	N mol/g	M g/mol	Q KJ/g	P GPa	D km/s
$B_2H_5NO_2$	1.05	69.75	0.041	17	1.83(1.86)	12.38 (12.53)	6.42 (6.45)
$B_2H_4(NO_2)_2$	1.55	75.96	0.025	21.3	1.57(1.91)	17.89 (18.89)	6.58 (6.84)
$B_2H_3(NO_2)_3$	1.61	101.60	0.028	20.4	1.34(1.73)	18.29 (21.27)	6.65 (7.10)
$B_2H_2(NO_2)_4$	1.85	112.68	0.024	27.6	0.85(1.22)	19.55 (23.48)	6.59 (7.21)
TNT[11]	1.72	132.42	-	-	1.37	23.46	7.22

Note: Figures in parentheses are calculated values of isodesmic reaction method.

Table 3.3 shows that as density of adding compounds that substitute cardinal number increases, tetra-substituted compound density is greater than TNT density; molar volume is less than TNT, while explosion heat tri-substituted compound and tetra-substituted compound are significantly less than TNT; as number of substituent group grows, detonation velocity and pressure become closer to TNT. The reason is that when nitro number increases, oxygen elements in molecule increase, B_2O_3 mole number generated in reaction increases, gas phase enthalpy of formation of B_2O_3 after calculation is -819.92KJ / mol, so there is more

energy released during B_2O_3 generation, much larger than equimolar CO_2 and H_2O , and explosion heat will be huge. From calculation formula of detonation velocity and pressure, it can be known that explosion heat and density are the main factors affecting its size, as explosion heat and density become closer to TNT, detonation velocity and pressure are closer to TNT.

Frontier orbital energy E_{HOMO} and E_{LUMO} of five titled compound stable structure at B3LYP/6-31G* level and its energy gap ΔE_{gap} value is shown in Table 3.4.

Table 3.4. Energies (a.u.) of frontier molecular orbitals and their gaps at the B3LYP/6-31G* level.

	$E_{HOMO}(a.u.)$	$E_{LUMO}(a.u.)$	$\Delta E_{gap}(eV)$
B_2H_6	-0.33	-0.030	8.14
$B_2H_5NO_2$	-0.30	-0.077	5.93
$B_2H_4(NO_2)_2$	-0.31	-0.10	5.76
$B_2H_3(NO_2)_3$	-0.33	-0.14	5.10
$B_2H_2(NO_2)_4$	-0.34	-0.17	4.76

Molecular orbital theory regards that, the highest occupied molecular orbital HOMO and the lowest unoccupied molecular orbital LUMO exert greatest impact on chemical properties of compound. HOMO orbital has priority in provision of electrons, while LUMO orbital can receive electrons [11]. Size of HOMO-LUMO energy gap value ΔE_{gap} reflects electrons' ability to transit to unoccupied molecular orbital from occupied molecular orbital, which represents molecule strength in participation into chemical reaction to a certain extent. A bigger ΔE_{gap} value means that it is more difficult to have electron transition, and that molecule is more stable. Seen

from the table, ΔE_{gap} of $B_2H_2(NO_2)_2$ is higher than that of $B_2H_2(NO_2)_3$, $B_2H_2(NO_2)_4$, indicating that as nitro substituent increases in number, ΔE_{gap} value decreases, and that as nitro substituent increases in number, compound stability decreases. B-H-B bridged bond is electron deficient bond, while nitro is electron withdrawing group, so the more nitro, the more instability of compounds, which is consistent with calculation results of this paper.

Calculation results of wiberg electronic population of compound at B3LYP/6-31G* level are shown in Table 3.5.

Table 3.5. Wiberg bond (WBIA-B) indexes of compounds at B3LYP/6-31G* level.

	$WB_{I_{B-H}}$	$WB_{I_{B-H}(2)}$	$WB_{I_{B-B}}$	$WB_{I_{B-NO_2}}$
B_2H_6	0.99	0.48	0.68	
$B_2H_5NO_2$	0.96	0.49	0.68	0.76
	0.98	0.45		
	0.98			
$B_2H_4(NO_2)_2$	0.96	0.46	0.67	0.77
		0.44		
		0.47		
$B_2H_3(NO_2)_3$		0.43	0.65	0.77
		0.48		
		0.48		
$B_2H_2(NO_2)_4$		0.45	0.64	0.77

Interatomic bond level reflects relative strength of bond. The greater interaction between the bond, the greater bond order, the smaller interaction, the smaller bond order which represents the degree of electron cloud overlap. From wiberg bond order calculation results of compound at B3LYP / 6-31G* level in Table 2.5, it can be seen that hydrogen bridge bond $WB_{I_{B-H}}$ (2) and $WB_{I_{B-B}}$ are less than $WB_{I_{B-NO_2}}$, but closed three-center two-electron stable structure forms between two B atoms and H atoms. Thus, B-H-B bond is relatively strong. In comparison, B-NO₂ bond is relatively weak, probably pyrolysis or detonation trigger bond of titled compound, which is consistent with TNT as nitro nitrogen bond is pyrolysis or detonation trigger bond of titled compound.

CONCLUSIONS

Based on density functional theory B3LYP/6-31G* method, this paper adopts atomization

reaction method for theoretical calculations of stability, enthalpy of formation, explosion heat, detonation velocity and detonation pressure and other parameters of compound $B_2H_m(NO_2)_n$ ($m=2-5; n=1-4$); and conducts simple theoretical calculation of thermal decomposition mechanism of compound, obtaining the following conclusions:

(1) Enthalpy of formation of compounds $B_2H_4(NO_2)_2$, $B_2H_3(NO_2)_3$ and $B_2H_2(NO_2)_4$ are -253.15, -271.63 and -319.75 KJ/mol respectively, indicating that a lot of energy will be released during chemical reaction of these compounds;

(2) With isodesmic reaction calculation method, detonation pressure of $B_2H_4(NO_2)_2$, $B_2H_3(NO_2)_3$ and $B_2H_2(NO_2)_4$ is obtained: 18.89, 21.27 and 23.48 GPa, very close to 23.46 GPa of TNT explosive. Calculated value of $B_2H_2(NO_2)_4$ detonation pressure even exceeds detonation pressure value of TNT; detonation velocity of $B_2H_4(NO_2)_2$, $B_2H_3(NO_2)_3$ and $B_2H_2(NO_2)_4$ are 6.84, 7.10 and 7.21 km/s

respectively, very close to TNT detonation velocity of 7.22 km/s.

(3) Through wiberg bond order analysis, it can be known that B-NO₂ bond in compound $B_2H_m(NO_2)_n$ ($m = 2-5; n = 1-4$) is relatively weak, indicating that chemical reaction of compound most likely begins from B-NO₂ bond rupture.

REFERENCES

1. A.K. Sikder, N. Sikder, *J. Hazard. Mater.*, **112**, 1 (2004).
2. D.E. Chavez, M.A. Hiskey, R.D. Gilardi, 3, 3'-Azobis (6-arnion-1,2,4,5-tetrazine), *Angew. Chemie*, **10**, 1861 (2000).
3. M.X. Zhang, P.E. Eaton, R. Gilardi, *Angew. Chemie*, **2**, 422 (2000).
4. A. Hammerl, T.M. Klapotke, P. Schwerdtfeger, *Chem. A Eur. J.*, **22**, 5511 (2003).
5. Y.L. Lu, *Nanjing Univ. Sci. Technol.*, **5**, 67 (2009).
6. X.L. Zeng, W.H. Chen, J.C. Liu, *Acta Physico-Chimica Sinica*, **2**, 192 (2007).
7. P.C. Chen, Y.C. Chieh, S.C. Tzeng, *J. Mol. Structure, Theochem*, **3**, 215 (2003).
8. S.W. Benson, F.R. Cruickshank, D.M. Golden, Additivity rules for the estimation of thermochemical properties, *Chem. Rev.*, **3**, 279 (1996).
9. L.A. Curtiss, K. Raghavachari, P.C. Redfern, *J. Chem. Phys.* **3**, 1063 (1997).
10. Z.X. Chen, J.M. Xiao, H.M. Xiao, *J. Phys. Chem. A*, **40**, 8062 (1999).
11. H.M. Xiao, Z.X. Chen, *The Modern Theort for Tetrazole Chemistry Firsted*, Science Press, Beijing (2000).
12. F. Wang, X.J. Xu, H.M. Xiao, *Acta Chimica Sinica*, **12**, 1939 (2003).
13. X.H. Ju, Y.M. Li, H.M. Xiao, *J. Phys. Chem. A*, **5**, 934 (2005).
14. H.M. Xiao, Z.X. Chen, *Modern Theories of Tetrazole Chemistry*, Beijing, Science Press, (2000).
15. J. Zhang, H.M. Xiao, X.D. Gong, *J. Phys. Org. Chem.*, **8**, 583 (2001).

TECHNOLOGY SELECTION FOR IRAN'S GAS FLARE RECOVERY SYSTEM

H. Bakhteyar¹, A. Maleki^{2,3*}, A.M. Mashat¹, S. Sattari²

¹Energy Systems Engineering, Department of Energy Engineering, Sharif University of Technology, Tehran, Iran

²Energy Policy, Department of Energy Engineering, Sharif University of Technology, Tehran, Iran

³Belfer Center's International Security Program, John F. Kennedy School of Government, Harvard University

Received June 26, 2016, Revised September 10, 2016

About 70% of gas flaring in the whole world produces in less than 20 countries whereas more than 70 bcm of it is generated in just four of the mentioned countries. Iran flared 400 bcf of gas in 2011. In this paper, five options of Iran's gas flare recovery have been compared via MCDM method. For developing the model, the weighing factor of each indicator an AHP method is used via the Expert-choice software. Two groups of cases were considered in this analysis. One group was designed with priority given to individual indicators, while the other indicators had the same value, and the second group consisted of cases where the priorities were defined always keeping one criterion in first position, while the priorities of the other criteria were defined by ordinal information defining the mutual relations of the criteria and the respective indicators.

Keywords— Flare, Gas, Iran

INTRODUCTION

It is obviously clear that by rising the living standards in Iran and also the global population growth, the greenhouse gas emissions will definitely increase during the future years.

Enormous consumption of fossil fuels to supply the demanded energy in the recent decade, causes a huge amount production of greenhouse gases which leads to global warming disaster.

Annually, over 140 billion cubic meters of natural gas are being flared and vented which is equivalent to 25% of the United States' gas demand, 30% of the European Union's gas demand, or 75% of Russia's gas exports [1].

Gas flaring in Africa is equivalent to half of that continent's power consumption. Flaring gas has a global effect on climate change by adding annually about 360 million tons of CO₂.

About 70% of gas flaring in the whole world produces in less than 20 countries whereas more than 70 bcm of it is generated in just four of the mentioned countries. Iran flared 400 bcf of gas in 2011. That would meet about a quarter of demand in South Korea. The gas is worth about \$7.3 billion on Southeast Asian spot LNG markets [2]. The associated gas in Iran is usually flared for the lack of infrastructure to be processed and transported to demand markets.

The flared natural gas was about 5% of the world's natural gas production by the end of 2012 [3]. As explained, the top 20 countries accounted for the flaring of 127 billion cubic meters, which is over 86% of the total flaring in the world by the end of 2011. The ratio of CO₂ emissions to natural gas

flaring have also been described. Russia stands on the first place of gas flaring in the world. The flaring of Nigeria alone amounts 12% of the total flaring and Iran holds the third place of gas flaring.

ENVIRONMENTAL EFFECTS OF CO₂

Iran has shown remarkable growth in total fossil-fuel CO₂ emissions since 1954, averaging 6.3% per year. In 2008 total emissions reached an all-time high of 147 million metric tons of carbon. With Iran being the world's fourth largest oil-producing country it is not surprising crude oil and petroleum products account for the largest fraction of the Iranian emissions, 46.4% in 2008. The CO₂ emissions time series for Iran, like other countries in the Middle East, shows sizeable emissions from gas flaring in the late 1960s and 1970s and a decline in these emissions during the 1980s and 1990s. This downturn reflects changes in oil field practices, improvements in oil field facilities, and increasing use of gas fuels. Emissions from gas fuels have grown 390-fold since the first reported natural gas use in 1955 and now account for 42.3% of Iran's total fossil-fuel CO₂ emissions. From a per capita standpoint, Islamic Republic of Iran is above the global average at 2.00 metric tons of carbon.

It is generally accepted that carbon dioxide is a greenhouse gas and contributes to global warming. About 75% of the anthropogenic emissions of carbon dioxide come from the combustion of fossil fuels. Flaring produces a great amount of carbon dioxide. Carbon dioxide emissions from flaring have high global warming potential and contribute to climate change. The mounting environmental pressure on the oil and gas production areas to cut

To whom all correspondence should be sent:

E-mail: maleki@sharif.edu

CO₂ emissions is directly affecting the practice of flaring [5].

CO₂ emissions from flaring have high global warming potential and contribute to climate change. Flaring also has harmful effects on human health and the ecosystems near flaring sites. The low quality gas that is flared releases many impurities and toxic particles into the atmosphere during the flaring process. Acidic rain, caused by sulfur oxides in the atmosphere, is one of the main environmental hazards which results from this process [6].

According to research performed by the World Bank's Global Gas Flaring Reduction Partnership (GGFR), the equivalent of almost one third of Europe's natural gas consumption is burned in flares each year which is about 400 million tons of carbon dioxide emission to the atmosphere (roughly 1.5% of the global CO₂ emission) [7].

Environmental and economic considerations have increased the use of flare gas recovery systems. Flare gas recovery reduces noise and thermal radiation, operating and maintenance costs, air pollution and gas emission and reduces fuel gas and steam consumption.

IRAN'S GAS STATUS

The proved natural gas reserves of Iran are about 29.6 Tcm or about 15.8% of world's total reserves. Iran has the world's first largest reserves which is estimated up to 18% of the world's share. Iran's gas production by the end of 2012 has been about 160.5 billion cubic meters, which is 4.8 percent of the world's share. Natural gas consumption in Iran by the end of 2012, was about 156.1 Gcm.

Iran's gas production

Iran is the largest gas producer in the Middle – East and holds the 3rd place in the world following U.S. and Russia respectively. Global conventional natural gas resources are concentrated geographically, with 70% in three countries: Qatar, Iran and Russia [9]. Iran's gas production by the end of 2012 has been about 160.5 billion cubic meters, which is 4.8 percent of the world's share and shows 5.4% changes over 2011.

Iran's natural gas production has increased by over 550 percent over the past two decades, and the consumption has kept pace. As demand growth rates persist, the potential for shortfalls in natural gas supply grows.

1) South Pars field

The most significant energy development project in Iran is the offshore South Pars field, which produces about 35 percent of total gas produced in Iran. Discovered in 1990, and located about 100 km

offshore in the Persian Gulf, South Pars has a 24-phase development scheme spanning 20 years. Participating foreign companies in these phases are, among others, Petronas, Total, Gazprom, ENI, Statoil and PdVSA.

The entire project is managed by Pars Oil & Gas Company (POGC), a subsidiary of the National Iranian Oil Company. Each phase has a combination of natural gas with condensate and/or natural gas liquids production. Phases 1-10 are online. The majority of South Pars natural gas development will be allocated to the domestic market for consumption and gas re-injection. The remainder will either be exported as liquefied natural gas (LNG) and/or used for gas to liquids (GTL) projects.

2) Kish field

Kish, with estimated reserves of 1,416 bcm, is expected to produce about 85 mcm per day (mcm/d) of natural gas. Phase I of the project, which experienced repeated delays is expected to come online in 2016. Phase I is expected to produce approximately 28 mcm/d and Phase II of the project will produce an additional 57 mcm/d.

In addition to Kish, there are other promising gas fields that could further boost Iran's production. However, these projects also are characterized by delays and other difficulties. These additional fields include the Golshan, Ferdowsi, and North Pars gas fields although their start-ups are unlikely to occur until the next decade.

Iran's gas production share of the Middle East by the end of 2011 is about 30% [10].

Iran's gas consumption

Iran holds the world's 3rd - largest consumer of natural gas after U.S. and Russia respectively. Natural gas consumption in Iran by the end of 2012, was about 156.1 bcm which is 4.7% of the world's share.

IRAN'S GAS IMPORT / EXPORT

Iran imports natural gas from its northern neighbor Turkmenistan. The import of natural gas from Azerbaijan and Turkmenistan was respectively equal to 0.4 and 9 billion cubic meters in 2012.

Iran exports only a small part of its total natural gas production. Natural gas exports go to Turkey and Armenia via pipeline. Turkey, an importer since 2001, received 8,190 mcm in 2011, while exports to Armenia totaled 250 mcm in 2011. Iran's natural gas exports likely will be limited due to rising domestic demand, even with future expansion and production from the massive South Pars project, and other development projects.

The Strait of Hormuz, on the southeastern coast of Iran, is an important route for oil and gas exports from Iran and other Persian Gulf countries. At its narrowest point the Strait of Hormuz is about 34 km wide, yet an estimated 70 million ton of LNG flowed through the Strait between January and October 2011.

FLARING GAS STATISTICS IN IRAN

In this section, Iran's statistics of gas flaring are presented. Iran's flaring gas amount is about 50 million cubic meter natural gas which is equivalent to the 126 million barrel oil equivalent every year. It can be indicated that flared gas from oil and gas production field is about 37 and 13 million cubic meters, respectively in Iran.

Furthermore, statistics indicate that flared gas values about eighteen million dollars a day [11] which is comparable to capital cost of 5MW photovoltaic panels.

Error! Reference source not found. study represents the historical amount of flared gas in oil fields in Iran. Despite, there are many plans for reducing the flare gas; it is increasing in recent years [11]. The study also presents the ratio of flare gas to produced oil in Iran. It can be seen that not only crude oil production decreased, but also the amount of flared gas is increased, in the recent years. The statistics shows that around 10 cubic meters of natural gas has been flared for every barrel oil production.

The average growth of which during these years is estimated about 17.97%. The Study also shows the ratio of flare gas to gas production in Iran [11]. Unfortunately, It can be indicated that the ratio of flaring gas to gas production in Iran enjoys a positive growth and more than 2.5% of Natural gas production in Iran has been flared in 2011.

This chart indicated that flaring gas from Gas production field is about 37 million cubic meters which is 40% of import natural gas. It can be concluded that by reducing flare gas, Iran can be independent of gas import. On the other hand, the Iran's gas export may be increased which leads to economic growth.

Reducing flare gas from Oil production fields causes an increase in chemical refinery production. This matter may also to higher economic growth.

The value of daily flaring gas in Iran is equal to 500 GWh per day which is equal to the 27% of annual electrical energy supply in 2012. Assuming the average efficacy of power plant in Iran around 36%, this amount of gas flaring contains a potential of Electricity production for 7.5 GW power plant rating. This is equal to the 11% of total capacity of

power plant in Iran in 2012. Every year, Iran import electricity from neighboring countries. In 2011, Iran's electricity import was about 3650 GWh/yr which was equal to 6% of electricity production from flare gas. Therefore, by converting flare gas to Electricity, not only Iran can be independent of electricity import, but also exporter of it to neighborhood countries.

The daily gas flaring in Iran is equal to the 60% of daily gas injection to the oil fields in 2011. By reducing gas flaring, the gas injection to oil fields can be increased which lead to more oil production and longer life of oil fields.

Because of social consequences, the first priority of allocation of natural gas is for residential/commercial sector in Iran. As it is clear the consumption of residential sector during the cold months especially in winter extremely increases. The Residential sector carries a high share of Natural gas consumption which is equal to 10% of light gas flaring in Iran. Indeed, reducing the residential consumption share needs medium and long term programs, while reducing the light flare gas and injecting it to Gas pipeline may be so easier at this time.

It is noticeable that gas flaring ratio to oil and gas production is increasing in recent years in Iran. Therefore, it seems the recovery of flare gas is logical in this country [3].

FLARE GAS RECOVERY METHODS

The recovery of flare gas is of importance for many advanced countries around the world due to the saving resources and reducing air pollution. There are various ways to recover flare gas. The study represents some possible strategies to recover flare gas in Iran. Statistics shows that the ratio of flare gas to oil and gas production is highly increasing in this country [11].

Moreover, it can be seen that Iran stands in the third place of top flaring countries. Consequently, providing the performance of Kyoto Protocol in Iran, the recovery of flare gas becomes very significant. As a result, in this paper, the feasibility study of the methanol production in small scales from the flare gas is studied. In the first section, for observing the significance of flare gas recovery, the detailed Iran's gas flaring data are presented. Then the simulation of mini methanol plant is described in the second part. In order to present the economic results for the simulated plant, we generate two scenarios, one scenario is with consideration of the environmental taxes of gas flaring and the second one is without considering them. Afterwards, to recognize the feasibility of the simulated plant in Iran, the

sensitivity analysis is done on the technical data such as the flow rate of input gas and economical data like flare gas cost and methanol price.

GTL technology

Gas-to-liquid (GTL) technology is a good alternative for reducing gas flaring. Recently, the high oil price has created considerable interest in the development of GTL technology for the manufacture of transportation fuels. The GTL process can be a good candidate for alleviating the current oil crisis, in which synthetic liquid fuels (e.g., gasoline, diesel, and wax) are produced from stranded natural gas. This means that "stranded natural gas" in remote areas can be converted to shippable liquid fuels through the GTL process [12]. Among the various alternatives for combustion of flare gas, there has been an increased interest in GTL technology.

Such technologies play an important role in bringing gas to markets as both fuel and/or petrochemicals [13]. The GTL products have important environmental advantages compared to traditional products, giving GTL a significant edge as governments pass new and more stringent environmental legislation. In addition, refineries are faced with the challenge that crude oil is generally getting heavier, making it harder and more expensive to meet the new stringent standards. It is highly unlikely that these improvements in fuel quality can be achieved without using a technique such as blending zero sulfur GTL diesels into the current crude based product mixture. Another environmental issue is the regulatory pressure to reduce the volume of flare gas, which has serious environmental consequences. The main issue in Nigeria is to gather gas from more than 1000 wells by building gas collection facilities at the oilfields and constructing an extensive pipeline network to carry gas to an industrial facility where it turns into liquid for transportation.

Electricity generation

Electricity generation from flared natural gases via gas turbines Flare gas conversion into electricity is another way for reducing flare gas. Although natural gas has become a key primary source of energy for electricity generation, higher fuel costs of natural gas quickly outweigh the advantages in most applications.

Compressed method

Compression and transmission of gas to practical point of view is another alternative to reduce and reuse flare gas. Initially natural gas was used only in the areas in which it was produced, with excess

production being vented to the air or flared. But the large demands for natural gas has developed fairly recently. The increased demand has also greatly increased the price obtained for the gas [14]. This made refineries to use flare gas recovery systems for lowering emissions by recovering flare gases before they are combusted by the flare.

A flare gas recovery system compresses the flare gas for reuse in the refinery gas system. A compressor is used to increase the pressure of a compressible fluid. The inlet pressure can be any value from a deep vacuum to a high positive pressure. The discharge pressure can range from sub atmospheric to high value in the tens of thousands of pounds per square inch. Compressors have numerous forms, their exact configurations being based on the application [15].

Piston compressors operate based on the displacement principle. Piston compressors are available both with one and several cylinders and also one and multiple-stage versions.

Multi-cylinder compressors are used for higher outputs while multistage compressors are used for higher pressures. The gas compressed in the cylinder in the first stage (low pressure stage) is cooled in the intermediate cooler and then compressed to the final pressure in the second stage (high pressure cylinder). In single action compressors, one compression action with one rotation of the crankshaft take place while in double action compressors there are two compression actions with one rotation of the crankshaft.

CHP

Natural gas is the most common fuel for CHP plants and this is a reflection of its price, availability, wide range of applications and the lower environmental impact of its exhaust gases.

The supply of natural gas to a user is by pipeline from the national distribution network, much of which is owned and operated by National Grid Gas.

The installation of a gas-fired CHP plant almost always increases the site's consumption of gas, as the new plant generates both heat and power and usually operates for a large proportion of the year. As well as the increase in total annual gas consumption, the maximum rate of consumption usually increases, and this often requires the uprating of an existing site gas connection. In addition, the gas supply pressure required for operating a gas turbine or a gas engine is often higher than the existing site supply pressure, necessitating the use of pressure-boosting equipment.

Petrochemical products

Low natural gas prices are a magnet for petrochemical producers, who are planning big

investments in the province and helping it realize its long-standing priority of adding value to its oil and gas resources.

The large majority of chemical products are produced from petroleum (oil) or natural gas. Several of these base chemicals may be made more readily from natural gas rather than petroleum. Synthesis gas is an obvious candidate, due to the high hydrogen content of natural gas. Moreover, the light alkenes may be made from wet natural gas (NGL) in a process known as steam cracking.

Injection

Iran is one of the largest gas rich countries in the world that production capacity exceeds domestic consumption and gas injection requirements. Gas can be utilized as feed stock in petrochemical plants and refineries or exported through pipeline or LNG. Through re-injection of gas to oil reservoirs, while increasing the oil recovery ratios, the produced gases from fields shared with other countries could be stored into domestic gas fields.

Gas consumption in domestic markets and its substitution with oil products, in addition to providing environmental benefits, will also result in optimum consumption of these products and relieving the government from the heavy burden of existing subsidies and heavy expenditures of importing these products into country.

METHODOLOGY

Multiple criteria decision making (MCDM) refers to making decisions in the presence of multiple, usually conflicting, criteria. MCDM problems are common in everyday life. In personal context, a house or a car one buys may be characterized in terms of price, size, style, safety, comfort, etc. In business context, MCDM problems are more complicated and usually of large scale. For example, many companies in Europe are conducting organizational self-assessment using hundreds of criteria and sub-criteria set in the EFQM (European Foundation for Quality Management) business excellence model. Purchasing departments of large companies often need to evaluate their suppliers using a range of criteria in different area, such as after sale service, quality management, financial stability, etc... Although MCDM problems are widespread all the time, MCDM as a discipline only has a relatively short history of about 30 years.

The development of the MCDM discipline is closely related to the advancement of computer technology. In one hand, the rapid development of computer technology in recent years has made it possible to conduct systematic analysis of complex

MCDM problems. On the other hand, the widespread use of computers and information technology has generated a huge amount of information, which makes MCDM increasingly important and useful in supporting business decision making. There are many methods available for solving MCDM problems as reviewed by [8], though some of the methods were criticized as ad hoc and to certain degree unjustified on theoretical and/or empirical grounds. There were calls in early 1990s to develop new methods that could produce consistent and rational results, capable of dealing with uncertainties and providing transparency to the analysis processes.

The ER approach and the software are now widely used in many areas. In the following section, the main characteristics of MCDM problems are summarized first, followed by a list of typical techniques used in MCDM analysis.

For multi-criteria analysis, there are a large number of combinations describing potential situations of weighting factors. In order to overcome this arbitrariness in the evaluation of these options, the multi-criteria evaluation method is introduced. This method is based on the numerical values of the indicators used in the multi-criteria analysis. The multi-criteria assessment method is based on the decision making procedure reflecting the combined effect of all criteria under consideration and is expressed in the form of a General Index of Sustainability. A selected number of indicators is taken as the measure of the criteria comprising specific information of the options under consideration. The procedure aims to express the property of the options by a respective set of indicators.

In this paper, an AHP method is used to identify the priorities of flared gas recovery in different options which are explained as follows. In order to find the priorities, Expert Choice is used as the appropriate software and the result are shown as follows.

Options

An individual criterion for evaluation of the potential flare gas recovery options is leading to a limited guidance for the respective decision making process.

In this respect, individual indicators are leading to the priorities of specific options, which will strongly depend on the selected indicator.

The different options of flare gas recovery usage are as follows:

- Liquid Fuels Production
- Electricity Production
- CHP

- Petrochemical Products
- Injection
- Pipeline Usage

Indicators

For assessing the priorities of each option different criteria are used. The criteria are as follows:

- Environment
- Economics
- Availability

The assumptions of Iran's future gas availability depend on different factors. In order to obtain the most probable ones, the three-round Delphi panel method is used in this paper.

In the first round, the Delphi process begins with an open-ended questionnaire for a 100 experts' society. This questionnaire contained a list of assumptions which have been created by the authors and is used as the survey instrument for the second round of data collection. In the second round, 50 Delphi participants received a second questionnaire and were asked to review the most probable assumptions summarized by the investigators based on the information provided in the first round. In the third and final round, the lists of all probable results are distributed to the top ten expert panelists. This round provides a final opportunity for participants to revise their answers in a meeting and discuss about their opinions.

RESULTS

For developing the model, the weighing factor of each indicator is required. In order to define the weight coefficient of each indicator an AHP method is used via the Expert-choice software. Expert Choice is decision-making software that is based on multi-criteria decision making.

Expert Choice implements the Analytic Hierarchy Process (AHP) and has been used in different fields.

SELECTION OF CASES

For evaluation of any complex system by the MCDM method, appropriate parameters, needed for its application have to be selected. In this paper, two groups of possible cases are defined, namely: a group with priority given to the single indicator, while the other indicators have equal values; and a second group with all indicators defined by the internal preference amongst the criteria.

Group 1

In evaluation of the priority list amongst the alternative options, some cases have to be selected to represent potential constraints between the indicators. This means that the cases that are to be

representative for the decision making procedure have to be defined. The evaluation procedure implies that constraints have to be defined among the options in order to obtain the respective values of their weighting coefficients. In this evaluation, attention will be focused on a number of cases to be analyzed that correspond to the individual priority of every indicator with the other indicators having the same value. In this analysis, the following cases are taken.

Case 1: Env. > Eco. = Av. Case 1 is designed with priority given to the Environmental Indicator while the other indicators have the same value of weighting coefficient.

For this case, it is noticed that priority is obtained for the Pipeline usage and the injection followed by the liquid fuel and then the petrochemical and CHP and Electricity production options respectively.

Case 2: Av. > Eco. = Env. Case 2 is designed with priority given to the Availability Indicator while the other indicators have the same value of weighting coefficient. For this case, it is noticed that priority is obtained for the CHP usage and the liquid fuel followed by the Electricity production and then the injection and Pipeline usage and Petrochemical products options as the last one.

Case 3: Eco. > Av. = Env. Case 3 is designed with priority given to the economic indicator while the other indicators have the same value of weighting coefficient. For this case, it is noticed that priority is obtained for the Injection and the Pipeline usage followed by the liquid fuel and then CHP and the petrochemical and Electricity production options respectively.

Group 2

Group 2 cases are aimed to emphasize the role of the cases when internal priorities amongst them are defined by ordinal information that defines the mutual relations of the criteria and the respective indicators. It is obvious that the number of such cases can be very much larger than that of Group 1. The cases are formed by ordering the criteria, always keeping another criterion at the first position. In this group, the results are presented as follows.

Case 4: Env. > Eco. > Av. Case 4 is designed with the aim to give the first priority to the environmental indicator and the second priority to economic indicator. The result of running the program shows that the most probable option in this case is the pipeline usage and injection, liquid fuel production, CHP, Petrochemical products and electricity production stand at the next priorities respectively.

Case 5: Eco. > Av. > Env. Case 5 is designed with the aim to give the first priority to the economic indicator and the second priority to the availability

Effect, comparison and analysis of pesticide electrostatic spraying and traditional spraying

Yujing He, Binbin Zhao, Yongchang Yu*

College of Mechanical and Electrical Engineering, Henan Agricultural University, Zhengzhou, 450002, China

Received February 14 2016, Revised April 6 2016

The plant protection effect takes up 20% of high yield factor in the practice of agricultural production, wherein the use of pesticide is an extremely important means in the agricultural production. The pesticide spraying technique and level have a direct bearing on the effective utilization of pesticide. This paper drew a conclusion from the contrast experiment of electrostatic and traditional spraying that: electrostatic spraying decreases the droplet diameter and droplet spectrum and at the same time, it increases the droplet evenness. The electrostatic spraying could also increase the blade droplet coverage rate, especially on the obverse side of target crop blade, where the coverage rate is relatively obvious. The coverage rate on the reverse side is also increased, its level is limited.

Key Words: Plant protection, Electrostatic spraying, Traditional spraying, Droplet diameter, Droplet spectrum.

INTRODUCTION

China's pesticide application technique has suspended on the traditional high-capacity and large-droplet spraying technique level [1]. Few pesticides are stuck to the surface of plants and the vast majority of them may flow or scatter on the ground [2-6]. It causes the effective utilization of pesticide to be 20%~30% and less than 1% pesticide would be actually sprayed inside of the pest body [7-10].

The effect of sprayed pesticide depends on three factors: the redistribution of droplet or powder on the plant surface and inside of the plant canopy, activity habits of pests (whether they are exposed to pesticides) as well as the physical properties of pests. As a result, improving the effect of spraying pesticides has an important realistic meaning to reduce the costs (manpower, pesticide, energy, time), improve the prevention effect, cut down the loss of pesticides (to the ground) and lessen the environmental pollution [11-12]. The spraying effect is determined by the atomization quality and sedimentary characteristics.

Utilizing the electrostatic spraying for prevention of crop diseases and pests is a novel technique in the modern plant protection spraying, which well solves the problems in the process of traditional spraying. This paper made some comparisons of electrostatic spraying and traditional spraying through the atomization quality and the sedimentary characteristics.

CONTRAST EXPERIMENT OF ATOMIZATION QUALITY

The two parameters mainly investigated by the atomization quality: droplet diameter and droplet evenness.

Experimental device

The experimental devices and equipment materials are: Wuxing 3JWB-16A knapsack electrostatic sprayer, Chunshou 3WBS-16A ordinary knapsack hand sprayer, sampling paper, dye, microscope and digital camera.

The purposes of main equipment materials are shown in Table 1.

Experimental process

The reagent this experiment used is a mixed solution of tap water and red ink without impurity.

The sample was collected by the sampling paper underneath of 0.5m away from the sprayer. Wuxing 3JWB-16A knapsack electrostatic sprayer was used for spray sampling first, then came Chunshou 3WBS-16A ordinary knapsack hand sprayer and each test was made for twice. This paper conducted the experimental records and photographing immediately it finished.

Matters needing attention during the experimental process:

1) the sampling speed must be strictly controlled. If the speed is too slow, there would be severe superposition and agglutination phenomenon and poor accuracy of reflected atomization property. If the speed is too fast, the droplets collected may not be enough and lead to an incomplete representation;

To whom all correspondence should be sent:
E-mail: 496507286@qq.com

Table 1. The purposes of main equipment materials

Equipment Materials	Purpose
Wuxing 3JWB-16A knapsack electrostatic sprayer	Atomization and charged droplets
Chunshou 3WBS-16A ordinary knapsack hand sprayer	Atomized droplets
sampling paper	Sampling for droplets
dye	Dying of droplets for better observation
microscope	Measurement for droplet diameter and droplet coverage rate
digital camera	photographing of experimental results

2) The electrostatic sprayer needs to be charged before the experiment and ensured to be in the turn-off state when completed.

Measurement and calculation of droplet diameter

The droplet diameter is a critical parameter reflecting the sprayer atomization quality, which is because it has something to do with the droplet adsorption and sedimentation capacity. If the droplet diameter is much larger, it could prevent the drift, is beneficial to capture the target crops as well as obtains a better sedimentation capacity, but it has poor coverage evenness and most droplets may fall down into the soil, causing a bad spraying effect and low pesticide efficacy. If the droplet diameter is much smaller, it may be evenly covered on plant surfaces and thus to take full advantage of pesticides. However, the long floating time for some smaller droplets may lead them to be easily drifted with the wind and causes the environmental pollution. For these grounds, the appropriate droplet diameters need to be selected as per the different objects within an optimum particle size range. In this way, the quantity of droplets captured by targets could reach up to a maximum number and thus achieve the optimal control effect. For this reason, it is of great significance to measure and delve into the droplet diameters. Considering that there has no mature theoretical model to calculate droplet diameters at present, so experiment is still a common means to determine the droplet diameters.

This experiment adopted the electrostatic copy paper for sampling. The sampling time was strictly, but the droplets would be diffused to some extent. As a result, in order to close to the actual value of droplet diameter, this paper multiplied the measured data after the diffusion by a coefficient in the process of data analysis. Again, there would be some certain errors when measuring by a microscope, so this paper should use the mean value of several measurements. The trace of droplet on the sampling paper is a roughly circular, so it shall be corrected as the diameter of a sphere. The calculation should be made according to the formula (1) as below:

$$d = kD \tag{1}$$

In the formula,

- d is droplet diameter after the correction, μm ;
- D is reading number under the microscope, μm ;
- k is correction coefficient.

The correction coefficient was determined by comparing the standard particle value of common spraying droplet and its measurement value.

Calculation of droplet evenness

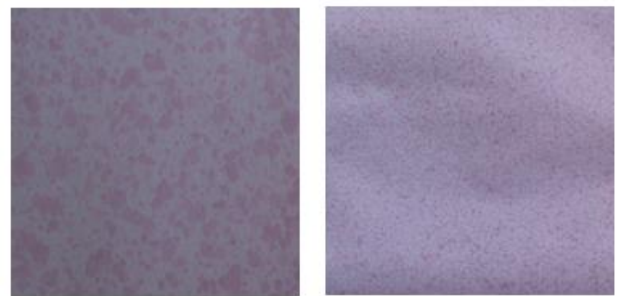
As known as the diffusion ratio, the index of droplet evenness DR is used to represent the degree of dispersion for droplet population size, which is also an important index to measure the atomization quality. DR is the ratio between NMD and VMD, which is given in formula (2):

$$DR = \frac{NMD}{VMD} \tag{2}$$

The closer the droplet evenness value is to 1, the more even the droplet partical size is. If DR is lower than 0.6, it would mean that the droplet partical size generated by the spraying machine is not even and has poorer coverage density and penetrability on the crops. If DR is higher than 0.6, it would be deemed as a relatively optimal evenness.

EXPERIMENTAL RESULTS AND ANALYSIS

Figure 1 presents the samples collected by these two sprayers under the experimental conditions:



a. common spraying b. electrostatic spraying

Fig. 1. Samples collected by these two sprayers experimental conditions.

The conclusion can be intuitively arrived at from Figure 1 that the droplet diameter for electrostatic spraying is smaller than that for common spraying on the average and it also has better droplet evenness. The common spraying may have the

phenomenon that the droplets would be converged to greater droplets.

Following the experimental steps, this paper conducted 3 groups of sampling on each sampling paper by the common spraying with 100 points for each time and totally 300 points.

The actual diameters of 300 sampling droplets of common and electrostatic spraying were calculated by employing the measurement method. This paper used Excel to draw the droplet spectrum of common spraying and electrostatic spraying, as shown in Figure 2:

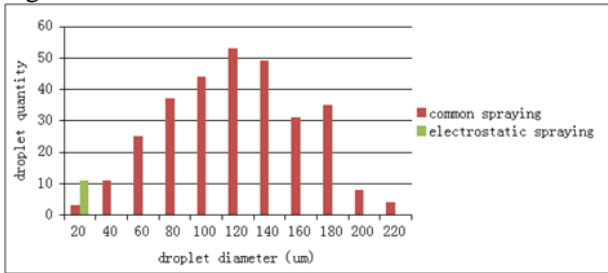


Fig. 2. Droplet spectrum of common and electrostatic spraying.

This paper used Excel to draw a percentage map for the droplet quantity within each diameter level accounting for the total droplet quantity under the common spraying and electrostatic spraying, as shown in Figure 3:

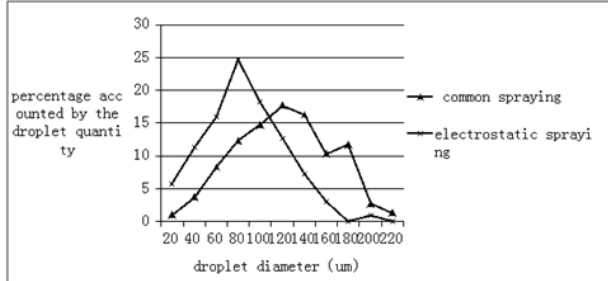


Fig. 3. Droplet percentage of common and electrostatic spraying.

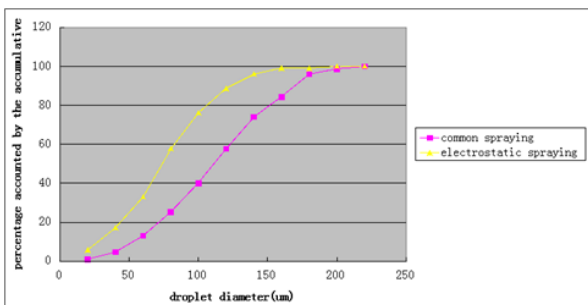


Fig. 4. Solving graph of mean diameter for droplet quantity.

The arithmetic mean droplet diameter d is the mean diameter value of 300 sampling points. Multiplying the summation for diameter values of 300 sampling points by the sampling number is the

final arithmetic mean value. The solving graph of mean diameter for droplet quantity is shown in Figure 4.

The accumulative droplet volume was solved by the graphing method as the droplet diameter of 50% of the total volume, which was also the mean diameter of the droplet volume in the experimental device. The solving graph of mean diameter for droplet volume is shown in Figure 5.

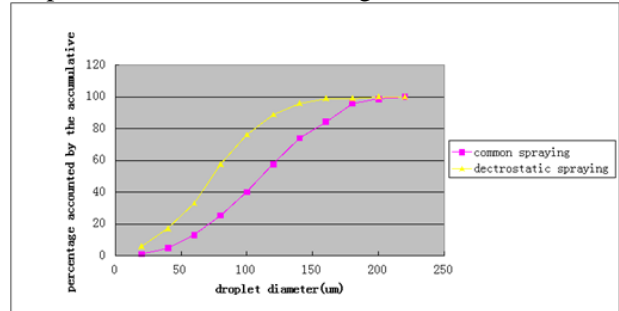


Fig. 5. Solving graph of mean diameter for droplet volume.

The evenness of droplet diameter was calculated according the formula (2), which was also recorded in Table 1.

The concrete data such as the arithmetic mean diameter, quantity mean diameter, volume mean diameter and evenness of all the sampling droplets can be seen in Table 2.

Table 2. Experimental results.

Spraying mode	Arithmetic mean diameter (μm)	Quantity mean diameter (μm)	Volume mean diameter (μm)	Evenness
Common spraying	121	112	165	0.68
electrostatic spraying	85.6	75	104	0.72

CONCLUSIONS

1) By contrast experiment, this paper found that the size of common spraying droplets varies significantly and there are lots of large droplets; while the size of electrostatic spraying droplets varies insignificantly, spraying droplets are distributed more evenly and there are increased droplets with smaller diameters.

2) Through the comparison of droplet spectrums, the electrostatic spraying tends to be narrowed down. For the common spraying, it has droplet distributed at the diameter of 20μm~220μm, while the electrostatic spraying droplets are mainly distributed at the diameter of 60μm~120μm. The droplet quantity would be quite few when the droplet diameter exceeds 160μm. The narrowing droplet

spectrum indicated that the diameter of electrostatic spraying is shrinking and more even.

3) It can be analyzed from the percentage of droplets that, by comparing the peaks for these two curves, the quantity of electrostatic spraying droplets reached to the highest level at 80µm, while common spraying droplets reached to the highest level at 120µm. It indicated that diameters of electrostatic spraying droplets were narrowed down and both of them mainly kept in a normal distribution, i.e. there were many droplets with mean diameter values and few droplets with diameter values of too large or too small. The common spraying curve is smoother than the electrostatic spraying curve, which indicated that the diameters of common spraying droplets are distributed in each level of diameters with fewer differences in the droplet quantity. However, the electrostatic spraying curve was rather pointed at the highest point 80µm, representing that 80µm aggregates its main diameters, wherein such evenly distributed diameters of droplets are required in the spraying process.

4) It can be concluded from the final experimental results in Table 3-2: the arithmetic mean diameters of common spraying droplets and electrostatic spraying droplets are 121µm and 85.6µm, respectively; the quantity diameters of common and electrostatic spraying droplets are 165µm and 104µm, respectively; it indicated that the diameters of electrostatic spraying droplets are reduced. The diameter evennesses for common and electrostatic spraying droplets are 0.68 and 0.72. The diameter evennesses for the electrostatic spraying droplets are increased, and the closer the diameter evenness is to 1, the narrower difference the whole droplet is and the better the atomization quality performance is. In a word, the electrostatic spraying has a better atomization quality than the common spraying.

CONTRAST EXPERIMENT OF SPRAYING SEDIMENTATION CHARACTERISTICS

Contrast experiment for the coverage rates of common and electrostatic spraying

This experiment is designed to delve into the coverage rates of common spraying and electrostatic spraying by designing a contrast experiment for spraying sedimentation characteristics.

The coverage rate refers to the coverage ratio between the droplet and target, which is represented by number of droplets per unit area. The formula to calculate the coverage rate is shown in the following (3).

$$CR = \frac{N}{S} \quad (3)$$

In the formula,

CR is coverage rate of droplets, number/cm²;

N is number of covered droplets;

S is area of sampling paper, cm².

Experimental design

This experiment used the model shown in Figure 6. The number of droplets sprayed on the leaves in the model cannot be easily calculated, so this paper replaces leaves by rectangles cut by the electrostatic copying paper.

The sampling method in this experiment: rectangular copying papers were fixed to the model to represent the both sides of a plant leaf and moved fast at 50cm on the model by a sprayer for sampling during the spraying process.



Fig. 6. Experimental model.

Experimental result of coverage rate

This paper took photos for droplets on the copying papers by a digital camera as soon as the experiment was finished. Figure 7 is the sampling situations of the both sides under the common spraying. Figure 8 is the sampling situations of the both sides under the electrostatic spraying. Figure 9 is the effect of the both sides under the electrostatic spraying.



a. The obseverd side

b. The reverse side

Fig. 7. Effects of both sides under the common spraying.

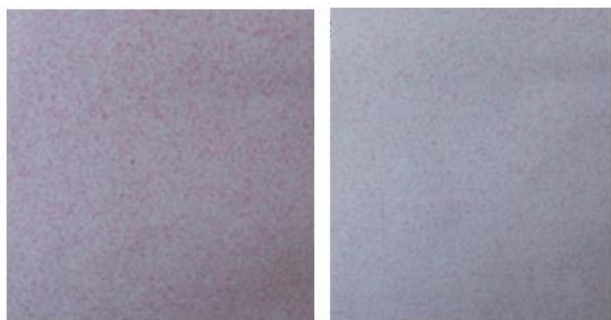


Fig. 8. Effects of both sides under the electrostatic spraying.



Fig. 9. Effects of both sides of a leaf under the electrostatic spraying.

This paper observed the number of droplets on each sampling paper (area of 15 cm²) with a microscope at the moment the photos were taken and recorded the experimental results of the droplet number by sampling groups in Table 3.

Table 3. Droplet coverage rate under common and electrostatic spraying.

Spraying mode	Unit	The obverse side	The reverse side
Common spraying			
electrostatic spraying	Number of droplets	795	0
common spraying	coverage rate (droplets/cm ²)	1080	165
electrostatic spraying		53	0
		72	11

Analysis for experimental results of coverage rate

It can be seen from Table 3 that, under the common spraying, there were 795 droplets on the obverse side and no droplet on the reverse side of the copying paper; under the electrostatic spraying, there were 1080 droplets on the obverse side and 165 droplets on the reverse side of the copying paper. By

comparing with the common spraying, the droplet number on both sides of electrostatic spraying was increased. At the same time, concerning the increase of coverage rate on both sides, the electrostatic spraying was significantly increased on the obverse side, from 53 droplets / cm² to 72 droplets / cm², an increase rate of 26.4%, while the coverage rate on the reverse side was added from 0 to 11 droplets / cm². However, compared with 72 droplets / cm² coverage rate on the obverse side by electrostatic spraying, it still has a larger difference of 84.7%. Again, the droplets of electrostatic spraying were sedimentated on the reverse side.

REFERENCES

1. Wang T., He J.G., Liao Y.L., *Auhui Agricultural Science Bulletin*, **14**, 163 (2008).
2. Asano K., *Disease Prevention for Plant (Japan)*, **40**, 12 (1986).
3. Hou J.R., Wang Z.Y., *New Agricultural Technology*, **6**, 10 (2005).
4. Yang Y., Ge X.K., *J. Agric. Mechanization Res.*, **5**, (2005).
5. Dai F.F., Development Trend of Pesticide Application Technology in China// 40th Anniversary Celebration for China Association of Agricultural Machinery Manufacturers & Proceedings of Annual Conference in 2003, Beijing: China Association of Agricultural Machinery Manufacturers, (2003).
6. Zheng L.H., Wu C.D., *J. Agric. Mechanization Res.*, **6**, 204 (2004).
7. Zheng J.Q., Xu Y.L., *Electrostatics*, **9**, 8 (1994).
8. Yu Y.C., Wang B.H., *Agricul. Technol.*, **24**, 190 (2004).
9. Yu Y., Research on Charging Effect of ULV Electrostatic Spraying Machine, Yunan Agricultural University, 9 X 3rd Period 202~206 (1995).
10. Qin H.Q., 8th Proceedings of Annual Electrostatic Conference for Chinese Physics Society, 61~64 (1999).
11. Wang Z., *Jiangsu University of Science and Technology* (1994).
12. Mechanical Engineering Research Institute. Equipment for Crop Protection-General Test Methods. P.R.C. Machine Industry Standard, (2000.4).

Characterization of indoor/outdoor PM₁₀, PM_{2.5}, PM₁ and radon concentrations in Imam Khomeini hospital

K.V. Kazemi¹, N. Mansouri^{2*}, F. Moattar², S.M. Khezri²

¹PhD Candidate, Department of Environmental Engineering, faculty of Environment and Energy, Science and Research Branch, Islamic Azad University, Tehran, Iran.

²Department of Environmental Engineering, faculty of Environment and Energy, Science and Research Branch, Islamic Azad University, Tehran, Iran.

Received October 10, 2015; Revised October 18, 2016

In this study the concentrations of PM₁₀, PM_{2.5}, PM₁ and [222] Rn and meteorological variables (atmospheric pressure, air temperature, and relative humidity) were measured simultaneously to find association of particulate matters and Radon gas emissions using multivariate statistical methods. The data (from 1512 samples for PM and 196 samples for Radon measurement) have been collected in six medical treatment floors of Imam Khomeini Hospital in Tehran (Iran) from June 2014 to June 2015, seven days per each season. In this study, we conducted a time-series analysis to evaluate the effects of indoor or outdoor PM₁₀, PM_{2.5}, PM₁ and Radon on hospital sections. During our study period, the PM₁₀ and PM_{2.5}, PM₁ average concentration were 27.75, 20.05, 15.50 and varied between 7-49 µg/m³, 6-37 µg/m³ and 5-33 µg/m³, respectively. The records showed that the average of Radon emissions in six floors of building were 2.8 Bq m⁻³, 1.8 Bq m⁻³, 2.8 Bq m⁻³, 3.2 Bq m⁻³, 1.2 Bq m⁻³, 0.83 Bq m⁻³ and 0.53 Bq m⁻³ respectively. Multivariate Manova analysis for four variables (season, day, floor no., location) and through Pillai's Trace, Wilks' Lambda, Hotelling's Trace, and Roy's Largest Root methods are used for providing table of Tests of Between-Subjects Effects for PM₁, PM_{2.5}, PM₁₀ arrays. The results summarized meaningful difference between PM₁, PM_{2.5} and PM₁₀ for some effects. For evaluating of effects of air condition (Temperature, Pressure, and Relative Humidity) on PM concentrations we applied Stepwise Linear Regression (LR) and found that increasing of pressure and decreasing of temperature cause all PM increase but the temperature is sensitive more to PM₁ and PM_{2.5} and pressure is sensitive just for PM₁₀.

We found that in the first and second half of year the Radon emissions at Nursery location had same effect but in Outdoor location and in cold seasons it has been increased. Finally, based on stepwise regression model, we can report that the concentration of [222]Rn and PM_{2.5} and ambient pressure showed reverse and direct correlation respectively. Linear model has more than 50 percent reliability in correlations but study should be continued by others to find more correlations between Radon and parameters.

To our knowledge, this is the first study in Iran, or even in Asian developing countries, to report the effect of PM₁₀, PM_{2.5}, PM₁, and [222]Rn emission simultaneously on morbidity. Our findings also suggest that Radon could serve as a valuable air quality indicator that reflects the health risks of airborne particles.

Keywords: Particulate Matter, Hospital, Radon, Characterization, IAQ.

INTRODUCTION

Nowadays, people have paid more attention to indoor air quality (IAQ) in workplace and residential environments. People spend >90% of their time indoors (Jenkins et al., 1992); therefore, the quality of indoor air is crucial to us. Many factors can cause the deterioration of indoor air quality, such as building materials [1], architectural coatings applied to building materials [2-3], heating, ventilation, and air conditioning systems [4], consumer products [5], and various indoor activities [6]. Moreover, air pollutants generated from outdoor sources can affect indoor air quality, as well as our health. Several research studies have reported significant health risks associated with exposure to particulate matter (PM) [7]. Most

studies on PM exposure consider particle mass, particularly particles smaller than 10, 2.5 and 1 µm (PM₁₀, PM_{2.5} and PM₁ respectively). Hospitals have complex indoor environment influenced by many factors such as number and age of occupants, their activities, building design, and sources of pollution inside the building, outdoor pollutant concentrations, and ventilation conditions [8-9-10]. Respirable particulates (RP) with aerodynamic diameter smaller than 10 µm (PM₁₀) has received considerable attention in recent years as it is easily inhaled and deposited within the respiratory system [11-12-13]. RP is divided into a coarse fraction (>2.5 µm in diameter) and a fine fraction (<2.5 µm in diameter) [14]. The coarse fraction is found to consist mainly of organic material, silicates and larger soot aggregates [15]. The fine fraction typically contains a mixture of particles resulting

To whom all correspondence should be sent:
E-mail: nmansourin@gmail.com

from different kinds of combustion processes (e.g., exhaust particles) and secondary particulates generated by chemical reactions in the atmosphere (acid condensates, sulfates and Studies show that RP plays a role in the incidence and severity of respiratory disease [16] and have significant associations with decline in lung function, respiratory and cardio-vascular diseases deaths.

Especially, public attention has been focused on fine particulates among the RP in aerosol highlighted for adverse health effect [17-18-19]. PM_{2.5}, the fine fraction in RP is significantly correlated with deaths from cardiopulmonary disease and lung cancer [20]. These finer particles are also the potential allergen carriers, which are probably liable to affect respiratory health, as they are able to penetrate deep into the respiratory tree [21]. Therefore, these fine particles seem to be more harmful to humans than the coarse ones. USEPA revised the primary (health-based) particulate matter standards by adding new annual and 24-h PM_{2.5} standards at 15 and 65 µg/m³ for outdoor air, respectively, to more effectively control the aerosol problem [22]. Thus, assessment of PM₁₀ and PM_{2.5} levels assumes significance from an environmental health perspective.

In the last few decades, a general social concern about the health risk associated with radon has grown worldwide. Historically, the detrimental effect on health attributed to radon came to light in connection with frequent lung disease (lung cancer) incidence among underground miners. Nowadays attention is paid to radon both at workplaces and homes. Although one usually spends less time at work than at home (the ratio is about 1:2.5), the radiation exposure from radon in the workplace can be significant in cases when the radon concentration is relatively high in work environments. The International Commission on Radiological Protection (ICRP) provides guidance to regulatory authorities on the radon action levels in its publication of ICRP-65. ICRP-65 suggests that workers who are not regarded as being occupationally exposed to radiation should be treated in the same way as the general public.

In this study, hospitals are selected for investigation. Their indoor PM₁₀/PM_{2.5}/PM₁ and associated Radon emissions were focused on. This is based on three considerations. Firstly, hospital is regarded as a special and important type of public place in Iran. The number of people is much higher in hospital every day than in other medical centers. Therefore, effect of hospital IAQ to people is more significant than other public places. Secondly, epidemiological studies showed hospital-acquired

respiratory system infection (HARSI, refer to diseases infected from hospital) is well affinity with hospital indoor aerosol that is the carrier for virus and Radon emission diffusion by adhering to aerosol particles. Thus, assessment of PM₁₀, PM_{2.5}, PM₁ and Radon levels assumes significance from epidemiology. Finally, there are few studies that focused on the indoor air quality of hospitals in world based on both particulate matters and Radon simultaneously. Our study aims to (1) characterize the indoor/outdoor RP concentrations and associated Radon emissions in Imam Khomeini hospital, (2) investigate the potential indoor and outdoor sources and their correlations based on statistical analysis. This is the first comprehensive report on quantifying RP and associated Radon emissions at the same time in an old hospital environment in Tehran, Iran.

METHODOLOGY

This study was performed in an old urban hospital that located in Tehran, Iran during the four season period from June 2014 to June 2015. The building age covers about 50 years. All six floors of the building are occupied by patients, visitors and staff all day. This hospital is located in the densely populated commercial area in urban districts and adjacent to heavy traffic road nearby (see Fig.1). Owing to the hot summer periods of sampling, this surveyed hospital is cooled by air-water coolers or air conditioners and in cold season is heated by heating radiators. Particulate matters analyzer (Dust Trak 8520), Radon meter (RADSTAR RS800), ambient air condition analyzer (Lutron MHB 38SD) were used in the medical center for sampling, monitoring and recording data (see Fig.2).

The sampling campaign took place between June 2014 to June 2015 at the 3 locations (Nursery, Treating Rooms, and Outdoor) of 6 floors of monitoring hospital to cover summer, fall, winter, and spring seasons. Totally 504 PM samples and 196 Radon samples are analyzed in this study.

From Saturday to Friday, during the hospital 24h and 3 shifts working hours in the all seasons sampling was performed in 3 locations of hospital. Sampling was performed inside and outside of the 3 selected locations of each floors. Following the WHO guideline the sampling equipment's were placed in the best position to avoid direct contamination of the conditioning systems and

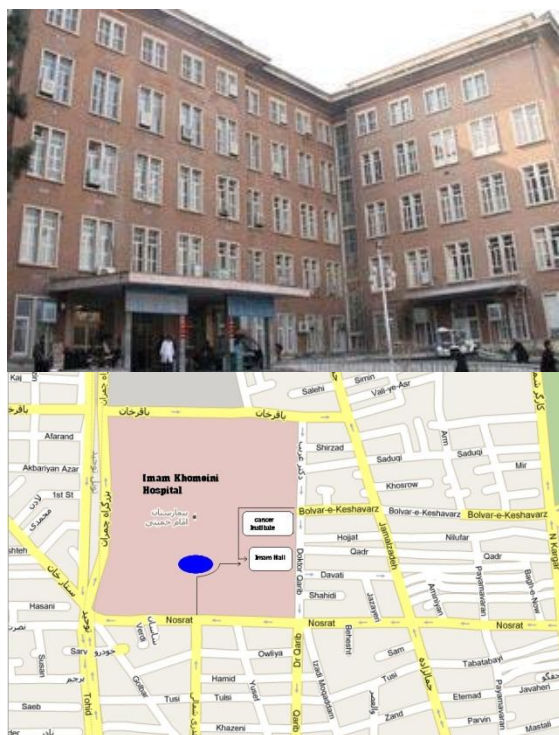


Fig. 1. Imam Khomeini hospital and its location.



Fig. 2. PM and radon analyzers.

people traffic. The sampling instruments were positioned at a distance of around 1 m from the bottom wall and at a height of about 1.5 m above

floor [23-24]. For outdoor sampling, the samplers were placed at the front side of the building. Due to the lack of multiple samplers, indoor and outdoor measurements were taken alternately after each 15 min [25]. [26] reported that a variation between 4% and 12% was observed in the mass concentration of PM between alternately and continuously sampled in indoor and outdoor measurement for one successive week. Therefore, the individual 1512 (1008 indoor and 504 outdoor) measurements at hospital were obtained through all seasons in order to cover meteorological conditions and pollutant concentrations. The ambient temperature, air pressure and relative humidity in each location were simultaneously measured at the same time with particulate matter and Radon measurement. The particle counter and Radon meter were factory calibrated, prior to the sampling campaign and the calibration was repeated every season. A Lutron MHB 38SD was used for temperature, relative humidity, and pressure measurements.

All data were normalized before application of MLR procedure. The analysis of the data was carried out using the statistical software, SPSS (Statistical Package for Social Science, version 20). Bivariate correlation analysis is used to assess the measure of pair wise association among the various variables. Pearson's coefficient (r) is used for measuring linear association, the strength and direction of the relationship between two variables. Stepwise multiple regressions were carried for PM₁₀, PM_{2.5} and PM₁ and the results were checked for multicollinearity by examining the variance inflation factors (VIF) of the predictor variables.

RESULTS AND DISCUSSION

The Radon emission measured data reported in Table 1. The PM₁₀ and PM_{2.5}, PM₁ average concentration were 27.75, 20.05, 15.50 and varied between 7-49 $\mu\text{g}/\text{m}^3$, 6-37 $\mu\text{g}/\text{m}^3$ and 5-33 $\mu\text{g}/\text{m}^3$, respectively. The records showed that the average of Radon emissions in floors of building were 2.8 Bq m^{-3} , 1.8 Bq m^{-3} , 2.8 Bq m^{-3} , 3.2 Bq m^{-3} , 1.2 Bq m^{-3} , 0.83 Bq m^{-3} and 0.53 Bq m^{-3} respectively.

The statistical Pearson analysis approved strong positive correlation between PM₁₀ and PM_{2.5}, PM₁ (Table 2).

Table 1. Statistics for Radon concentrations at nursery location in hospital (Bq m⁻³).

	Spring	Summer	Fall	Winter
min	0.1	0.1	0.9	0.9
mean	0.89	0.87	2.2	2.15
max	3.1	2.8	4.5	4.42

Multivariate Manova analysis for four variables (season, day, floor no., location) and through Pillai's Trace, 'Wilks' Lambda, 'Hotelling's Trace', and 'Roy's Largest Root' methods are used for providing table of Tests of Between-Subjects Effects for PM₁, PM_{2.5}, PM₁₀ arrays with following results:

- There is no meaningful difference between season-day for any PM's
- There is no meaningful difference between season-location for PM_{2.5}
- There is no meaningful difference between location-day for any PM_{2.5} and PM₁₀
- There are meaningful difference between PM₁, PM_{2.5} and PM₁₀ for other effects.

Table 2. Correlation analysis for PM.

	Spring	PM1	PM2.5	PM10
Pearson Correlation	1	.834**	.702**	
Sig. (2-tailed)		.000	.000	
N	504	504	504	504
Pearson Correlation	.834**	1	.810**	
Sig. (2-tailed)	.000		.000	
N	504	504	504	504
Pearson Correlation	.702**	.810**	1	
Sig. (2-tailed)	.000	.000		
N	504	504	504	504

** Correlation is significant at the 0.01 level (2-tailed)

For evaluating of effects of air condition (Temperature, Pressure, and Relative Humidity) on PM concentrations we applied Stepwise Linear Regression (LR) and found that increasing of pressure and decreasing of temperature cause all PM increase but the temperature is sensitive more to PM₁ and PM_{2.5} and pressure is sensitive just for PM₁₀.

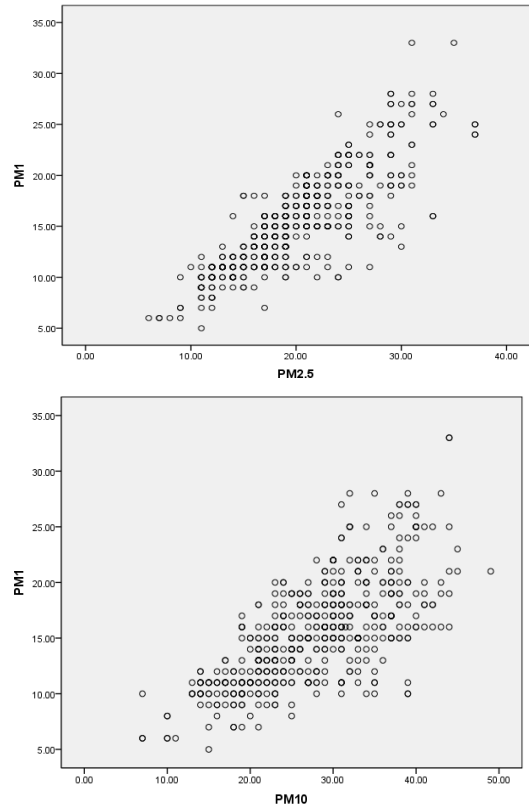


Fig. 3. Linear relation diagram of PM₁, PM_{2.5} and PM₁₀.

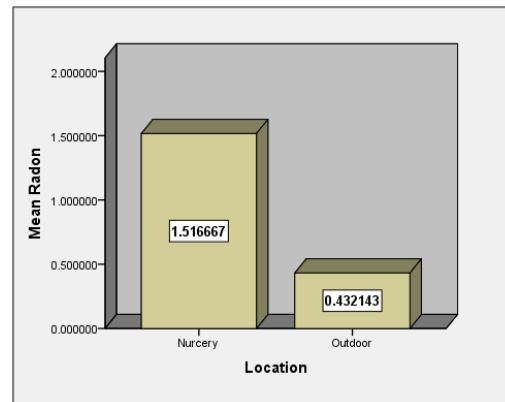
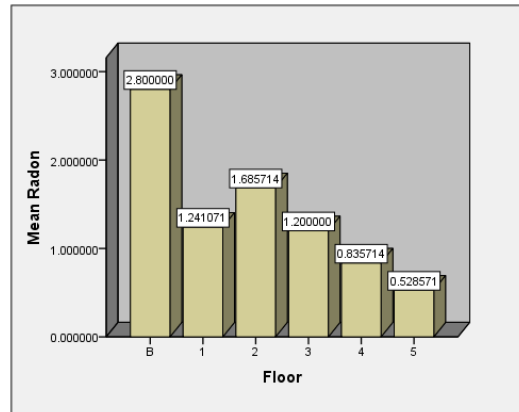


Fig 4. The radon measurements graphs.

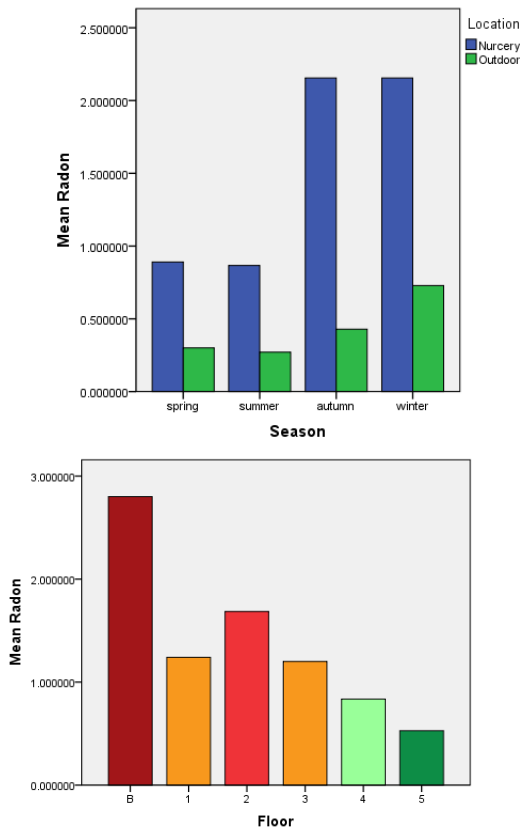


Fig. 5. The variance analysis results for season-location sources.

The Radon emission data analysis showed that the Nursery with 1.51Bq m^{-3} has the maximum emission and the hospital outdoor with 0.43Bq m^{-3} has the lowest emissions (Fig. 2).

The Variance analysis for Radon data, showed a large amount of F (44.871) for the season-location and it means that there is a strong meaningful correlation between two sources.

We found that in first and second half of year the radon emissions at Nursery location were the same but in outdoor location and in cold seasons it has been increased.

Finally, based on stepwise regression model, we can report that the concentration of $[222]\text{Rn}$ and PM_{2.5} and ambient pressure showed reverse and direct correlation respectively. Linear model has more than 50 percent reliability in correlations but study should be continued by others to find more correlations between Radon and parameters. We understood that in regression model:

- The temperature had no any meaningful correlation
- The cold seasons had meaningful correlation specially in outdoor location

The parameters of temperature, pressure and humidity had very strong correlation with each other and the pressure as their representative was

very good response variable to Radon mathematically.

CONCLUSION

To our knowledge, this is the first study in Iran, or even in Asian developing countries, to report the effect of PM₁₀, PM_{2.5}, PM₁, and $[222]\text{Rn}$ emission simultaneously on morbidity. Our findings also suggest that Radon could serve as a valuable air quality indicator that reflects the health risks of airborne particles. The study could be continued to explain more about particulate matters and Radon correlations.

Acknowledgments: The study was supported by the Department of Environment and Energy, Science and Research Branch, Islamic Azad University, Tehran, Iran and Imam Khomeini hospital management and we would like to appreciate it.

REFERENCES

1. H. Anderson, R.W. Atkinson, J. Peacock, L. Marston, K. Konstantinou, Meta-analysis of time-series studies and panel studies of particulate matter (PM) and ozone (O₃). Report of a WHO task group. Copenhagen: World Health Organization; 2004.
2. T.F. Bateson, J. Schwartz, *Epidemiology*, **15**, 143 (2004).
3. M.L. Bell, J.M. Samet, F. Dominici, *Annu Rev Public Health*, **25**, 247 (2004).
4. M.L. Bell, J.K. Levy, Z. Lin, *Occup Environ Med*, **65**, 104 (2008).
5. M.L. Bell, R.D. Peng, F. Dominici, J.M. Samet, *Circulation*, **120**, 949 (2009).
6. C. Billionnet, D. Sherrill, I. Annesi-Maesano, *Ann Epidemiol*, **22**, 126 (2012).
7. B. Brunekreef, B. Forsberg, *EurRespir J*, **26**, 309 (2005).
8. B. Brunekreef, S.T. Holgate, *Lancet*, **360**, 1233 (2002).
9. J. Cao, H. Xu, Q. Xu, B. Chen, H. Kan, *Environ Health Perspect*, **120**, 373 (2012).
10. G. Chen, G. Song, L. Jiang, Y. Zhang, N. Zhao, B. Chen, *J OccupHealth*, **50**, 41 (2008).
11. R. Chen, H. Kan, B. Chen, W. Huang, Z. Bai, G. Song, *Am J Epidemiol*, **175**, 1173 (2012).
12. F. Geng, J. Hua, Z. Mu, L. Peng, X. Xu, R. Chen, *Environ Res.*, **120**, 27 (2013).
13. G.T. Goldman, J.A. Mulholland, A.G. Russell, A. Srivastava, M.J. Strickland, M. Klein, *Environ SciTechnol*, **44**, 7692 (2010).
14. N.A. Janssen, G. Hoek, M. Simic-Lawson, P. Fischer, L. van Bree, H. T. Brink, *Environ Health Perspect*, **119**, 1691 (2011).
15. N.A.H. Janssen, M.E. Gerlofs-Nijland, T. Lanki, R.O. Salonen, F. Cassee, G. Hoek, Health effects of black carbon, WHO; 2012.

16. H. Kan, S.J. London, G. Chen, Y. Zhang, G. Song, N. Zhao, *Environ Health Perspect*, **116**,1183 (2008).
17. H. Kan, R. Chen, S. Tong, *Environ Int.*, **42**, 10 (2012).
18. T. Lanki, J.J. de Hartog, J. Heinrich, G. Hoek, N.A. Janssen, A. Peters, *Environ Health Perspect*, **114**, 655 (2006).
19. W. Lin, W. Huang, T. Zhu, M. Hu, B Brunekreef, Y. Zhang, et al., *Environ Health Perspect*, **119**, 1507 (2011).
20. Y. Ma, R. Chen, G. Pan, X. Xu, W. Song, B. Chen, *Sci Total Environ*, **409**, 2473 (2011).
21. S. Manney, C.M. Meddings, R.M. Harrison, A.H. Mansur, A. Karakatsani, A. Analitis, *Occup Environ Med*, **69**, 663 (2012).
22. R.D. Peng, H.H. Chang, M.L. Bell, A. McDermott, S.L. Zeger, J.M. Samet, *JAMA*, **299**, 2172 (2008).
23. R.D. Peng, M.L. Bell, A.S. Geyh, A. McDermott, S.L. Zeger, SametJM, *Environ Health Perspect*, **117**, 957 (2009).
24. C.A. Pope III, D.W. Dockery, *J Air Waste ManagAssoc*, **56**, 709 (2006).
25. P. Quincey, *Atmos Environ*, **41**,7964 (2007).
26. C. Reche, X. Querol, A. Alastuey, M. Viana, J. Pey, T. Moreno, *AtmosChem Phys.*, **11**, 6207 (2011).

BULGARIAN CHEMICAL COMMUNICATIONS

Instructions about Preparation of Manuscripts

General remarks: Manuscripts are submitted in English by e-mail or by mail (in duplicate). The text must be typed double-spaced, on A4 format paper using Times New Roman font size 12, normal character spacing. The manuscript should not exceed 15 pages (about 3500 words), including photographs, tables, drawings, formulae, etc. Authors are requested to use margins of 3 cm on all sides. For mail submission hard copies, made by a clearly legible duplication process, are requested. Manuscripts should be subdivided into labelled sections, e.g. **Introduction, Experimental, Results and Discussion**, etc.

The title page comprises headline, author's names and affiliations, abstract and key words.

Attention is drawn to the following:

a) **The title** of the manuscript should reflect concisely the purpose and findings of the work. Abbreviations, symbols, chemical formulas, references and footnotes should be avoided. If indispensable, abbreviations and formulas should be given in parentheses immediately after the respective full form.

b) **The author's** first and middle name initials, and family name in full should be given, followed by the address (or addresses) of the contributing laboratory (laboratories). **The affiliation** of the author(s) should be listed in detail (no abbreviations!). The author to whom correspondence and/or inquiries should be sent should be indicated by asterisk (*).

The abstract should be self-explanatory and intelligible without any references to the text and containing not more than 250 words. It should be followed by key words (not more than six).

References should be numbered sequentially in the order, in which they are cited in the text. The numbers in the text should be enclosed in brackets [2], [5, 6], [9–12], etc., set on the text line. References, typed with double spacing, are to be listed in numerical order on a separate sheet. All references are to be given in Latin letters. The names of the authors are given without inversion. Titles of journals must be abbreviated according to Chemical Abstracts and given in italics, the volume is typed in bold, the initial page is given and the year in parentheses. Attention is drawn to the following conventions:

a) The names of all authors of a certain publications should be given. The use of “*et al.*” in

the list of references is not acceptable.

b) Only the initials of the first and middle names should be given.

In the manuscripts, the reference to author(s) of cited works should be made without giving initials, e.g. “Bush and Smith [7] pioneered...”. If the reference carries the names of three or more authors it should be quoted as “Bush *et al.* [7]”, if Bush is the first author, or as “Bush and co-workers [7]”, if Bush is the senior author.

Footnotes should be reduced to a minimum. Each footnote should be typed double-spaced at the bottom of the page, on which its subject is first mentioned.

Tables are numbered with Arabic numerals on the left-hand top. Each table should be referred to in the text. Column headings should be as short as possible but they must define units unambiguously. The units are to be separated from the preceding symbols by a comma or brackets.

Note: The following format should be used when figures, equations, etc. are referred to the text (followed by the respective numbers): Fig., Eqns., Table, Scheme.

Schemes and figures. Each manuscript (hard copy) should contain or be accompanied by the respective illustrative material as well as by the respective figure captions in a separate file (sheet). As far as presentation of units is concerned, SI units are to be used. However, some non-SI units are also acceptable, such as °C, ml, l, etc.

The author(s) name(s), the title of the manuscript, the number of drawings, photographs, diagrams, etc., should be written in black pencil on the back of the illustrative material (hard copies) in accordance with the list enclosed. Avoid using more than 6 (12 for reviews, respectively) figures in the manuscript. Since most of the illustrative materials are to be presented as 8-cm wide pictures, attention should be paid that all axis titles, numerals, legend(s) and texts are legible.

The authors are asked to submit **the final text** (after the manuscript has been accepted for publication) in electronic form either by e-mail or mail on a 3.5” diskette (CD) using a PC Word-processor. The main text, list of references, tables and figure captions should be saved in separate files (as *.rtf or *.doc) with clearly identifiable file names. It is essential that the name and version of

the word-processing program and the format of the text files is clearly indicated. It is recommended that the pictures are presented in *.tif, *.jpg, *.cdr or *.bmp format, the equations are written using "Equation Editor" and chemical reaction schemes are written using ISIS Draw or ChemDraw programme.

The authors are required to submit the final text with a list of three individuals and their e-mail addresses that can be considered by the Editors as potential reviewers. Please, note that the reviewers should be outside the authors' own institution or organization. The Editorial Board of the journal is not obliged to accept these proposals.

EXAMPLES FOR PRESENTATION OF REFERENCES

REFERENCES

1. D. S. Newsome, *Catal. Rev.–Sci. Eng.*, **21**, 275 (1980).
2. C.-H. Lin, C.-Y. Hsu, *J. Chem. Soc. Chem. Commun.*, 1479 (1992).
3. R. G. Parr, W. Yang, *Density Functional Theory of Atoms and Molecules*, Oxford Univ. Press, New York, 1989.
4. V. Ponec, G. C. Bond, *Catalysis by Metals and Alloys* (Stud. Surf. Sci. Catal., vol. 95), Elsevier, Amsterdam, 1995.
5. G. Kadinov, S. Todorova, A. Palazov, in: *New Frontiers in Catalysis* (Proc. 10th Int. Congr. Catal., Budapest, 1992), L. Guzzi, F. Solymosi, P. Tetenyi (eds.), Akademiai Kiado, Budapest, 1993, Part C, p. 2817.
6. G. L. C. Maire, F. Garin, in: *Catalysis. Science and Technology*, J. R. Anderson, M. Boudart (eds), vol. 6, Springer-Verlag, Berlin, 1984, p. 161.
7. D. Pocknell, *GB Patent 2 207 355* (1949).
8. G. Angelov, PhD Thesis, UCTM, Sofia, 2001.
9. JCPDS International Center for Diffraction Data, Power Diffraction File, Swarthmore, PA, 1991.
10. *CA* **127**, 184 762q (1998).
11. P. Hou, H. Wise, *J. Catal.*, in press.
12. M. Sinev, private communication.
13. <http://www.chemweb.com/alchem/articles/1051611477211.html>.

CONTENTS

Organic Chemistry

- A. Bolouri, A. Mohammad-khah, Preparation and characterization of antibacterial nanofibrous trimethoprim/polyvinylpyrrolidone mats as an oral fast-dissolving drug delivery system..... 5
- M. Sasani, S. Khoramnejadian, R. Safari, Effect of benzophenone and zinc stearate on photodegradation of potato starch based low density polyethylene..... 15
- B. Akbari, M.E.Olya, M. Bahmaei, F. Najafi, A new study on the derivatization of malondialdehyde by anisidine reagent with use of UV-Vis, FT-IR, ¹HNMR, ¹³CNMR techniques..... 18
- M. Amini, M. Khosravi Rineh, M. Yazdani, Study of the chemical compositions of Iranian rose flower essence oil (*Rosa persica*)..... 27

Analytical chemistry

- Fashe Li, Zonghong Feng, Chengzhi Wang, Zhisong Liang, Jin Gao, Qingqing Wang, Jianhang Hu, Simultaneous quantitative analysis of inorganic anions in commercial waste-oil biodiesel using suppressed ion exchange chromatography..... 30
- A. Gholami, H. Noorizade, Preconcentration, speciation and determination of As and Sb by optimized experimental design DLLME combined with GF-AAS..... 36
- R. Parviz, M. Honari, Solidified floating organic drop microextraction (SFODME) for simultaneous separation/preconcentration and determination of cadmium by atomic absorption spectroscopy..... 43
- F. Karami, M. Khanmohammadi, A. Bagheri Garmarudi, ATR-FTIR spectroscopy and chemometrics application for analytical and kinetics characterization of adsorption of 1-butyl mercaptan (1-butanethiol) on nickel coated carbon nanofibers (CNFS)..... 51

Physical chemistry

- S.M. Tabatabaee Ghomshe, Cleaning strategy of fouled reverse osmosis membrane: Direct osmosis at high salinities (DO-HS) as on-line technique without interruption of RO operation..... 57
- Daiyin Yin, Kai Liu, Yazhou Zhou, Analysis of the effects of alcohol on displacement performance of the microemulsion system through ϵ - β -fishlike phase diagram..... 65
- Jiping Wang, Huangbo Huang, Thermodynamics of NO₃⁻ adsorption on different kinds of anion exchange resins..... 73
- Li Xu, Tao Jiang, Pengfei Yu, Qiuju Zhao, Experimental study on the effect of combined modified aluminum and magnesium and phosphorus removal of zeolite..... 80
- M. Manteghian, M. Shahbazi, Liquid-liquid equilibrium for the ternary systems of water + acetic acid + ethyl acetate at T=298.2 K..... 84
- A. Lorparizangen, M. Jafarian, F. Gobal, S. Miandari, M. Ghasem Mahjani, The effect of nitrate ions on the electrodeposition of PbS semiconducting film: electrochemical and surface analysis..... 89
- Yongliang Zhang, Wei Yu, Min Li, Application research on coating to adjust the cohesive force between dust and polar plate..... 97

Material Science

- A. Mohsenibandpey, A. Eslami, H.K. Maleh, M M. Rabori, Investigating the efficiency of nanocomposite membranes synthesized by polyacrylonitrile polymers containing single-walled carbon nanotubes in decreasing chemical and biological pollution indicators of greywater..... 102
- S. Zarinabadi, A novel modified integral PES/PVB nanofiltration membrane and its application in wastewater treatment..... 112
- Z. Izakmehri, M. Ardjmand, M. Darvish Ganji, Organic pollutant adsorption on pristine, defected and Al-doped carbon nanotube: a dispersion corrected DFT study..... 119
- Md.. Poostforush, H. Azizi, I. Ghasemi, Thermal conductivity of silane cross-linked polyethylene composites..... 125
- E. Amaki, R. Sahraei, Preparation, characterization and optical properties of nanostructured undoped and Cu doped ZnO thin films..... 131

<i>Tao Shen, Baihe Wang, Minli Yao, Weijun Yang</i> , Research on extinction performance of expanded graphite at band of 3 millimeter wave.....	138
<i>A. Sadeghian Maryan, M. Gorji</i> , Microstructure interpretation of macromechanical behaviour of polyurethane electrospun nanofiber webs.....	142
<i>A. Sadeghian Maryan, M. Gorji</i> , Synthesize of nano silver using cellulose or glucose as a reduction agent: the study of their antibacterial activity on polyurethan fibers.....	151
<i>M. Darvishpour, M. Feyzi, M. Joshaghani</i> , Optimal semi large scale synthesis of copper and copper oxide nanoparticles by electrical explosion of wire.....	156
Chemical Engineering	
<i>Guo Bin, Luan Tao</i> , On-thermal plasma for simultaneous NO _x and SO ₂ removal from coal-combustion flue gas.....	166
<i>Weiliang Cheng, Yi Zhang, Shuzhou Wei, Yuhang Hu</i> , Experimental analysis of removal of SO ₂ and NO _x for nano Mg-Al composite oxides.....	172
<i>Weiliang Cheng, Cuicui Hou</i> , Influence factor analysis of inlet spray on a natural draft wet cooling tower.....	177
<i>H. Ahmadi, A. Behbahani-Nia, F. Torabi</i> , Transient modeling and performance analysis of site utilities and cogeneration systems: a case study for lubricant oil refinery utilization.....	185
<i>S.A. Mirbagheri, F. Ghomi Avili, A.H. Javid</i> , Modeling arsenic transport in soil column and ground water.....	199
<i>S.A. Mirbagheri, N. Javadifar, A. Hesam Hasani</i> , Modeling Pb transport in soil column and ground water.....	205
<i>E. Gharehkhani</i> , Investigation and optimization of reactive orange-3R dye surface absorption by nano MMT/NZVI composite absorbent in a process of textile industry wastewater treatment.....	211
<i>Weiliang Cheng, Yanqiu Li, H. Schlaberg</i> , The size effect of titanium dioxide particles on desulfurization in a power plant.....	219
<i>Yuekan Zhang, Peikun Liu, Junru Yang, Lanyue Jiang, Yulong Zhang</i> , Calculation of particle size field in hydrocyclones.....	226
Biochemistry	
<i>Ruijuan Hao, Zhoufeng Wang, Wenke Wang, Yaqian Zhao</i> , Change characteristics of chlorophyll content and high spectrum in soybean leaves under the stress of CO ₂ leakage.....	230
<i>Shuoye Yang</i> , The development and in vitro evaluation of Coenzyme Q10 long-circulating liposomes...	238
<i>Zheming Cao, Weidong Ding, Jianxin Wang, Xuwen Bing</i> , Study on intragenic methylation of the aromatase P450 gene from different ricefield eel tissues.....	244
<i>Yajun Zhang, Lingfeng Yao, Lihua Sun, Tingting Du</i> , Effects of bull serum albumin on corrosion of carbon steel under water with different Larson ratio.....	251
Environment protection	
<i>Daping Xia, Xinyi Wang, Zhen Wang, Shunan Zhang</i> , Removal of nitrate nitrogen from water via aerobic denitrification under static and dynamic experimental settings.....	259
<i>Dengfeng Wang, Tingzhong Wang, Huande Feng, Haijie Huang, Di Zeng</i> , Fractions distribution of arsenic and cadmium in arable land soils in vicinity of mining area.....	264
<i>Ju Yang, Wenlai Xu, Yue Jian, Min Tang, Jing Wang</i> , Gas-particulate distribution of polycyclic aromatic hydrocarbons (PAHs) in Chengdu, China.....	269
<i>Xingguan Ma, Tao Jian, Pengfei Yu</i> , Vertical flow constructed wetland on the slightly polluted water denitrification and phosphorus removal test parameters optimization research.....	274
<i>K.N. Khankahdani, M. Karimi</i> , Geology, mineralogy and geochemistry of the Mazayjan massive sulfide deposit (Southern Sanandaj - Sirjan, Iran).....	280
<i>F. Amiri, K.N. Khankahdani, M. Lotfi, M. Karimi</i> , Geochemistry and genesis of Qareh Qotoo copper index, Sanandaj-Sirjan, Iran.....	294
<i>K.N. Khankahdani, H. Motavassel</i> , Geochemistry and genesis of Darb-e-Behesht porphyric copper index, South Kerman, Iran.....	300
<i>M. Nasiri, I. Jafari</i> , Investigation of drilling fluid loss and its affecting parameters in one of the Iranian gas fields.....	306

<i>Yonghui Wang</i> , Characteristics and correlation analysis between soil magnetic susceptibility and heavy metal content in soil along the north shore of Xinjiang Bosten Lake.....	313
Miscellaneous	
<i>Haijun Lou, Ankang Kan, Zhipeng Guo</i> , Numerical simulation and experimental study on thermal properties of trailer house composite envelope with vacuum insulation panels.....	320
<i>Haiyan Hu, Yonghong Wang, Hongbin Wang</i> , Theoretical study on structure and properties of $B_2H_m(NO_2)_n$ ($m=2-5; n=1-4$).....	327
<i>H. Bakhteeyar, A. Maleki, A.M. Mashat, S. Sattari</i> , Technology selection for Iran's gas flare recovery system.....	333
<i>Yujing He, Binbin Zhao, Yongchang Yu</i> , Effect, comparison and analysis of pesticide electrostatic spraying and traditional spraying.....	340
<i>K.V. Kazemi, N. Mansouri, F. Moattar, S.M. Khezri</i> , Characterization of indoor/outdoor PM_{10} , $PM_{2.5}$, PM_1 and radon concentrations in Imam Khomeini hospital.....	345
Instruction to the authors.....	351